When drug-trial subjects don't take their pills *p. 288*

European regulations and consumer genomics *p. 296*

An autoimmune target in rheumatoid arthritis *p. 363*

Science

$10
17 OCTOBER 2014
sciencemag.org

AAAS

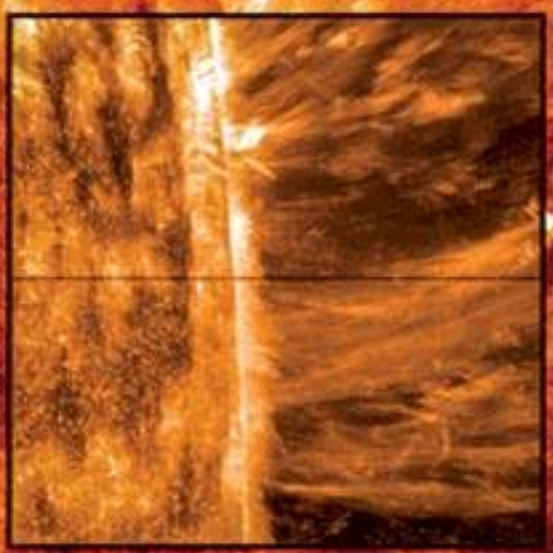

Eyeing the Sun

IRIS takes a close-up look at the solar transition region

pp. 305 & 315

CONTENTS

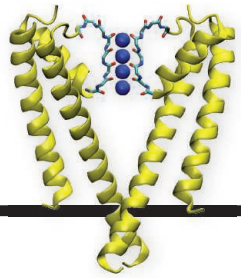

303 & 352
What pushes potassium through the channel?

17 OCTOBER 2014 • VOLUME 346 • ISSUE 6207

NEWS

IN BRIEF

284 Roundup of the week's news

IN DEPTH

287 **FOR VENEZUELAN ACADEMICS, SPEAKING OUT IS RISKY BUSINESS**
Government attacks some, snares many in red tape *By L. Wade*

288 **'NONADHERENCE': A BITTER PILL FOR DRUG TRIALS**
Drug developers seek new ways to ensure that subjects take their medicine *By K. Servick*

289 **EBOLA VACCINE TRIALS RAISE ETHICAL ISSUES**
Randomized studies may offer fastest answer *By J. Cohen and K. Kupferschmidt*

290 **LIGHT LOOPHOLE WINS LAURELS**
Chemistry Nobel winners pushed microscopes past supposed limit *By D. Clery*

291 **REGULATING INDUSTRY'S BIG BOYS**
French economist Jean Tirole wins Nobel for his analyses of oligopolies *By T. Rabesandratana*

FEATURE

292 **BABOON WATCH**
An epic baboon study shows how social interactions shape health and reproduction in all primates—including humans *By E. Pennisi*

INSIGHTS

PERSPECTIVES

296 **CHANGES ON THE HORIZON FOR CONSUMER GENOMICS IN THE EU**
Test results may no longer be available directly to consumers *By L. Kalokairinou* et al.

298 **TO LEARN IS TO MYELINATE**
The adult mammalian brain requires the production of new glial cells and myelin for learning *By P. Long and G. Corfas*
▸ RESEARCH ARTICLE P. 318

300 **NUTRIENT COMPUTATION FOR ROOT ARCHITECTURE**
Plants sense and respond to nutrients using a peptide signaling system *By T. Bisseling and B. Scheres*
▸ REPORT P. 343

301 **SENSING BIODIVERSITY**
Sophisticated networks are required to make the best use of biodiversity data from satellites and in situ sensors *By W. Turner*

303 **POTASSIUM IONS LINE UP**
Do K^+ ions move in single file through potassium channels? *By G. Hummer*
▸ REPORT P. 352

304 **IN OPTICAL PUMPING, LESS CAN BE MORE**
Creating loss in one optical resonator can initiate lasing in its coupled partner *By H. G. L. Schwefel*
▸ REPORT P. 328

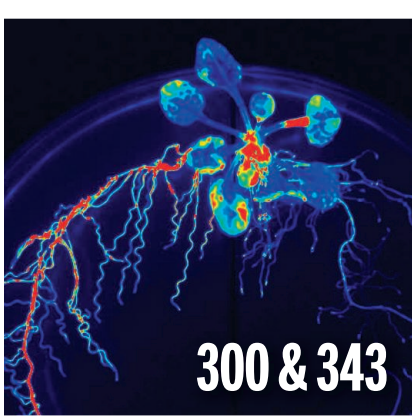

305 **LOOKING CLOSER AT THE SUN**
The space-based IRIS telescope provides a new window to view the solar atmosphere *By L. K. Harra*
▸ EYEING THE SUN SECTION P. 315

BOOKS *ET AL.*

307 **WHAT IS YOUR RACE?**
By K. Prewitt, reviewed by P. Schor

LETTERS

308 **BEFORE THE KARDASHIAN INDEX**
By G. R. Goldsmith

308 **NUANCED NEGATIVE RESULT REPORTING**
By S. K. Lhachimi et al.

308 **SUPPORT UNDERWAY FOR COASTAL ECOSYSTEMS**
By D. S. Schinn

309 **SCIENCE AND RELIGION: THINK LOCAL**
By J. M. Hanes

DEPARTMENTS

283 **EDITORIAL**
"Epicenters" of resilience *By Mary Lou Zoback*

390 **WORKING LIFE**
Life inspires applications *By Sharon Ann Holgate*

Science Staff 282
New Products 369
Science Careers 370

PHOTO: (MIDDLE) KUMIKO SUMIDA/YOSHIKATSU MATSUBAYASHI

Published by AAAS

298 & 318

Myelin and motor skills

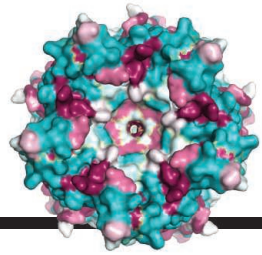

355

A bacterial homolog to probe eye disease

RESEARCH

IN BRIEF

310 From *Science* and other journals

REVIEWS

313 **APPLIED EVOLUTION**
Applying evolutionary biology to address global challenges *S. P. Carroll* et al.
REVIEW SUMMARY; FOR FULL TEXT:
dx.doi.org/10.1126/science.1245993

SPECIAL SECTION

Eyeing the Sun

INTRODUCTION

315 Probing the solar interface region *B. De Pontieu* et al.

REPORT ABSTRACTS

316 On the prevalence of small-scale twist in the solar chromosphere and transition region *B. De Pontieu* et al.

Prevalence of small-scale jets from the networks of the solar transition region and chromosphere *H. Tian* et al.

Evidence of nonthermal particles in coronal loops heated impulsively by nanoflares *P. Testa* et al.

Hot explosions in the cool atmosphere of the Sun *H. Peter* et al.

The unresolved fine structure resolved: IRIS observations of the solar transition region *V. Hansteen* et al.

SEE ALSO

▸ PERSPECTIVE P. 305
▸ VIDEO
▸ sciencemag.org/special/iris

314 **SOCIAL EVOLUTION**
Evolution of responses to (un)fairness *S. F. Brosnan and F. B. M. de Waal*
REVIEW SUMMARY; FOR FULL TEXT:
dx.doi.org/10.1126/science.1251776

RESEARCH ARTICLE

318 **SKILL DEVELOPMENT**
Motor skill learning requires active central myelination *I. A. McKenzie* et al.
▸ PERSPECTIVE P. 298

REPORTS

322 **PLANETARY GEOLOGY**
Constraints on Mimas' interior from Cassini ISS libration measurements *R. Tajeddine* et al.

325 **LAB ASTROPHYSICS**
Laboratory formation of a scaled protostellar jet by coaligned poloidal magnetic field *B. Albertazzi* et al.

328 **OPTICS**
Loss-induced suppression and revival of lasing *B. Peng* et al.
▸ PERSPECTIVE P. 304

332 **QUANTUM ELECTRONICS**
Cavity quantum electrodynamics with many-body states of a two-dimensional electron gas *S. Smolka* et al.

336 **ATTOSECOND DYNAMICS**
Ultrafast electron dynamics in phenylalanine initiated by attosecond pulses *F. Calegari* et al.

340 **STRATEGIC REASONING**
Neural correlates of strategic reasoning during competitive games *H. Seo* et al.

343 **NITROGEN UPTAKE**
Perception of root-derived peptides by shoot LRR-RKs mediates systemic N-demand signaling *R. Tabata* et al.
▸ PERSPECTIVE P. 300

346 **TROPHIC CASCADES**
Large carnivores make savanna tree communities less thorny *A. T. Ford* et al.
▸ PODCAST

349 **CLIMATE CHANGE**
Increased variability of tornado occurrence in the United States *H. E. Brooks* et al.

352 **ION CHANNELS**
Ion permeation in K^+ channels occurs by direct Coulomb knock-on *D. A. Köpfer* et al.
▸ PERSPECTIVE P. 303

355 **ION CHANNELS**
Structure and selectivity in bestrophin ion channels *T. Yang* et al.

360 **AGING**
HSF-1–mediated cytoskeletal integrity determines thermotolerance and life span *N. A. Baird* et al.

363 **AUTOIMMUNITY**
Detection of T cell responses to a ubiquitous cellular protein in autoimmune disease *Y. Ito* et al.

ON THE COVER

Ultraviolet view of a coronal mass ejection on the Sun on 9 May 2014. Images from the Interface Region Imaging Spectrograph (IRIS) (inset) and from the Solar Dynamics Observatory's Atmospheric Imaging Assembly (background) show the violent eruption of hot plasma into space. NASA launched IRIS in June 2013 to study the complex interface between the Sun's surface and outer atmosphere. See pages 305 and 315 and sciencemag.org/special/iris.
Images: IRIS and SDO/AIA, Lockheed Martin Solar & Astrophysics Laboratory, NASA/Goddard Space Flight Center

SCIENCE (ISSN 0036-8075) is published weekly on Friday, except the last week in December, by the American Association for the Advancement of Science, 1200 New York Avenue, NW, Washington, DC 20005. Periodicals mail postage (publication No. 484460) paid at Washington, DC, and additional mailing offices. Copyright © 2014 by the American Association for the Advancement of Science. The title SCIENCE is a registered trademark of the AAAS. Domestic individual membership and subscription (51 issues): $153 ($74 allocated to subscription). Domestic institutional subscription (51 issues): $1282; Foreign postage extra: Mexico, Caribbean (surface mail) $55; other countries (air assist delivery) $85. First class, airmail, student, and emeritus rates on request. Canadian rates with GST available upon request, GST #1254 88122. Publications Mail Agreement Number 1069624. **Printed in the U.S.A.**
Change of address: Allow 4 weeks, giving old and new addresses and 8-digit account number. **Postmaster:** Send change of address to AAAS, P.O. Box 96178, Washington, DC 20090–6178. **Single-copy sales:** $10.00 current issue, $15.00 back issue prepaid includes surface postage; bulk rates on request. **Authorization to photocopy** material for internal or personal use under circumstances not falling within the fair use provisions of the Copyright Act is granted by AAAS to libraries and other users registered with the Copyright Clearance Center (CCC) Transactional Reporting Service, provided that $30.00 per article is paid directly to CCC, 222 Rosewood Drive, Danvers, MA 01923. The identification code for *Science* is 0036-8075. *Science* is indexed in the *Reader's Guide to Periodical Literature* and in several specialized indexes.

Published by AAAS

Science
AAAS
1200 New York Avenue, NW, Washington, DC 20005
Bateman House, 82-88 Hills Road, Cambridge, UK CB2 1LQ

Editor-in-Chief Marcia McNutt
Executive Editor Monica M. Bradford **News Editor** Tim Appenzeller
Managing Editor, Research Journals Katrina L. Kelner
Deputy Editors Barbara R. Jasny, Andrew M. Sugden(UK), Valda J. Vinson, Jake S. Yeston

Research and Insights

SR. EDITORS Caroline Ash(UK), Gilbert J. Chin, Lisa D. Chong, Maria Cruz(UK), Julia Fahrenkamp-Uppenbrink(UK), Pamela J. Hines, Stella M. Hurtley(UK), Paula A. Kiberstis, Marc S. Lavine(Canada), Kristen L. Mueller, Ian S. Osborne(UK), Beverly A. Purnell, L. Bryan Ray, Guy Riddihough, H. Jesse Smith, Jelena Stajic, Peter Stern(UK), Phillip D. Szuromi, Brad Wible, Nicholas S. Wigginton, Laura M. Zahn **ASSOCIATE EDITORS** Brent Grocholski, Melissa R. McCartney, Margaret M. Moerchen, Sacha Vignieri **ASSOCIATE BOOK REVIEW EDITOR** Valerie B. Thompson **ASSOCIATE LETTERS EDITOR** Jennifer Sills **CHIEF CONTENT PRODUCTION EDITOR** Cara Tate **SR. CONTENT PRODUCTION EDITORS** Harry Jach, Trista Wagoner **CONTENT PRODUCTION EDITORS** Jeffrey E. Cook, Chris Filiatreau, Cynthia Howe, Lauren Kmec, Barbara P. Ordway **SR. EDITORIAL COORDINATORS** Carolyn Kyle, Beverly Shields **EDITORIAL COORDINATORS** Ramatoulaye Diop, Joi S. Granger, Lisa Johnson, Anita Wynn **PUBLICATIONS ASSISTANTS** Aneera Dobbins, Jeffrey Hearn, Dona Mathieu, Le-Toya Mayne Flood, Shannon McMahon, Scott Miller, Jerry Richardson, Rachel Roberts(UK), Alice Whaley(UK), Brian White **EXECUTIVE ASSISTANT** Anna Bashkirova **ADMINISTRATIVE SUPPORT** Janet Clements(UK), Lizanne Newton(UK), Maryrose Madrid, John Wood(UK)

News

NEWS MANAGING EDITOR John Travis **INTERNATIONAL EDITOR** Richard Stone **DEPUTY NEWS EDITORS** Daniel Clery(UK), Robert Coontz, Elizabeth Culotta, David Grimm, David Malakoff, Leslie Roberts **CONTRIBUING EDITORS** Martin Enserink(Europe), Mara Hvistendahl (Asia) **SR. CORRESPONDENTS** Jeffrey Mervis, Elizabeth Pennisi **NEWS WRITERS** Adrian Cho, Jon Cohen, Jennifer Couzin-Frankel, Carolyn Gramling, Eric Hand, Jocelyn Kaiser, Kelly Servick, Robert F. Service, Erik Stokstad, Emily Underwood **INTERNS** David Shultz, Jia You **CONTRIBUTING CORRESPONDENTS** Pallava Bagla(South Asia), Michael Balter(Paris), John Bohannon, Ann Gibbons, Sam Kean, Richard A. Kerr, Eli Kintisch, Kai Kupferschmidt(Berlin), Andrew Lawler, Christina Larson(Beijing), Mitch Leslie, Charles C. Mann, Eliot Marshall, Virginia Morell, Dennis Normile(Tokyo), Heather Pringle, Tania Rabesandratana(Brussels), Gretchen Vogel(Berlin), Lizzie Wade(Mexico City) **CAREERS** Jim Austin(Editor), Donisha Adams **COPY EDITORS** Kara Estelle, Nora Kelly, Jennifer Levin **ADMINISTRATIVE SUPPORT** Scherraine Mack

Executive Publisher Alan I. Leshner
Publisher Beth Rosner **Chief Digital Media Officer** Rob Covey

BUSINESS OPERATIONS AND ADMINISTRATION DIRECTOR Deborah Rivera-Wienhold **BUSINESS SYSTEMS AND FINANCIAL ANALYSIS DIRECTOR** Randy Yi **MANAGER OF FULFILLMENT SYSTEMS** Neal Hawkins **SYSTEMS ANALYST** Nicole Mehmedovich **ASSISTANT DIRECTOR, BUSINESS OPERATIONS** Eric Knott **MANAGER, BUSINESS OPERATIONS** Jessica Tierney **BUSINESS ANALYSTS** Cory Lipman, Cooper Tilton, Celeste Troxler **FINANCIAL ANALYST** Jeremy Clay **RIGHTS AND PERMISSIONS ASSISTANT DIRECTOR** Emilie David **PERMISSIONS ASSOCIATE** Elizabeth Sandler **RIGHTS, CONTRACTS, AND LICENSING ASSOCIATE** Lili Kiser

MARKETING DIRECTOR Ian King **MARKETING MANAGER** Julianne Wielga **MARKETING ASSOCIATE** Elizabeth Sattler **SR. MARKETING EXECUTIVE** Jennifer Reeves **SR. ART ASSOCIATE, PROJECT MANAGER** Tzeitel Sorrosa **ART ASSOCIATE** Seil Lee **ASSISTANT COMMERCIAL EDITOR** Selby Frame **MARKETING PROJECT MANAGER** Angelissa McArthur **SR. WRITER** Bill Zimmer **PROGRAM DIRECTOR, AAAS MEMBER CENTRAL** Peggy Mihelich **FULFILLMENT SYSTEMS AND OPERATIONS** membership@aaas.org **MANAGER, MEMBER SERVICES** Pat Butler **SPECIALISTS** LaToya Casteel, Javia Flemmings, Latasha Russell **MANAGER, DATA ENTRY** Mickie Napoleoni **DATA ENTRY SPECIALISTS** JJ Regan, Jaimee Wise, Fiona Giblin

DIRECTOR, SITE LICENSING Tom Ryan **DIRECTOR, CORPORATE RELATIONS** Eileen Bernadette Moran **SR. PUBLISHER RELATIONS SPECIALIST** Kiki Forsythe **PUBLISHER RELATIONS MANAGER** Catherine Holland **PUBLISHER RELATIONS, EASTERN REGION** Keith Layson **PUBLISHER RELATIONS, WESTERN REGION** Ryan Rexroth **MANAGER, SITE LICENSE OPERATIONS** Iquo Edim **FULFILLMENT ANALYST** Lana Guz **ASSOCIATE DIRECTOR, MARKETING** Christina Schlecht **MARKETING ASSOCIATES** Thomas Landreth, Minah Kim

DIRECTOR OF WEB TECHNOLOGIES Ahmed Khadr **SR. DEVELOPER** Chris Coleman **DEVELOPER** Dan Berger **SR. PROJECT MANAGER** Trista Smith **SYSTEMS ENGINEER** Luke Johnson **PRODUCT MANAGER** Walter Jones

CREATIVE DIRECTOR, MULTIMEDIA Martyn Green **DIRECTOR OF ANALYTICS** Enrique Gonzales **SR. WEB PRODUCER** Sarah Crespi **WEB PRODUCER** Alison Crawford **VIDEO PRODUCER** Nguyen Nguyen **SOCIAL MEDIA PRODUCER** Meghna Sachdev

DIRECTOR OF OPERATIONS PRINT AND ONLINE Lizabeth Harman **PRINT PRODUCTION DIRECTOR** Wendy K. Shank **PREFLIGHT MANAGER** Marcus Spiegler **ASSISTANT MANAGER ONLINE** Lisa Stanford **ASSISTANT MANAGER PRINT** Rebecca Doshi **SR SPECIALISTS** Steve Forrester, Jason Hillman, Antoinette Hodal, Tara Kelly, Anthony Rosen **SPECIALISTS** Jacob Hedrick, Nichele Johnston, Lori Murphy, Kimberley Oster

DESIGN DIRECTOR Beth Rakouskas **ASSOCIATE ART DIRECTOR** Laura Creveling **SR. ILLUSTRATORS** Chris Bickel, Katharine Sutliff **ILLUSTRATOR** Valerie Altounian **SR. ART ASSOCIATES** Holly Bishop, Preston Huey **ART ASSOCIATES** Kay Engman, Garvin Grullón, Chrystal Smith **SR. PHOTO EDITOR** William Douthitt **PHOTO EDITOR** Leslie Blizard

DIRECTOR, GLOBAL COLLABORATION, CUSTOM PUBLICATIONS, ADVERTISING Bill Moran **EDITOR, CUSTOM PUBLISHING** Sean Sanders: 202-326-6430 **ASSISTANT EDITOR, CUSTOM PUBLISHING** Tianna Hicklin: 202-326-6463 **ADVERTISING MARKETING MANAGER** Justin Sawyers: 202-326-7061 science_advertising@aaas.org **ADVERTISING MARKETING ASSOCIATE** Javia Flemmings **ADVERTISING SUPPORT MANAGER** Karen Foote: 202-326-6740 **ADVERTISING PRODUCTION OPERATIONS MANAGER** Deborah Tompkins **SR. PRODUCTION SPECIALIST/GRAPHIC DESIGNER** Amy Hardcastle **PRODUCTION SPECIALIST** Yuse Lajiminmuhip **SR. TRAFFIC ASSOCIATE** Christine Hall **SALES COORDINATOR** Shirley Young **ASSOCIATE DIRECTOR, COLLABORATION, CUSTOM PUBLICATIONS/CHINA/TAIWAN/KOREA/SINGAPORE** Ruolei Wu: +86-186 0822 9345, rwu@aaas.org **COLLABORATION/CUSTOM PUBLICATIONS/JAPAN** Adarsh Sandhu + 81532-81-5142 asandhu@aaas.org **EAST COAST/E. CANADA** Laurie Faraday: 508-747-9395, FAX 617-507-8189 **WEST COAST/W. CANADA** Lynne Stickrod: 415-931-9782, FAX 415-520-6940 **MIDWEST** Jeffrey Dembksi: 847-498-4520 x3005, Steven Loerch: 847-498-4520 x3006 **UK EUROPE/ASIA** Roger Goncalves: TEL/FAX +41 43 243 1358 **JAPAN** Katsuyoshi Fukamizu(Tokyo): +81-3-3219-5777 kfukamizu@aaas.org **CHINA/TAIWAN** Ruolei Wu: +186-0082-9345

WORLDWIDE ASSOCIATE DIRECTOR OF SCIENCE CAREERS Tracy Holmes: +44 (0) 1223 326525, FAX +44 (0) 1223 326532 tholmes@science-int. co.uk **CLASSIFIED** advertise@sciencecareers.org **U.S. SALES** Tina Burks: 202-326-6577, Nancy Toema: 202-326-6578 **SALES ADMINISTRATOR** Marci Gallun **EUROPE/ROW SALES** Axel Gesatzki, Sarah Lelarge **SALES ASSISTANT** Kelly Grace **JAPAN** Hiroyuki Mashiki(Kyoto): +81-75-823-1109 hmashiki@aaas.org **CHINA/TAIWAN** Ruolei Wu: +86-186 0082 9345 rwu@aaas.org **MARKETING MANAGER** Allison Pritchard **MARKETING ASSOCIATE** Aimee Aponte

AAAS BOARD OF DIRECTORS RETIRING PRESIDENT, CHAIR Phillip A. Sharp **PRESIDENT** Gerald R. Fink **PRESIDENT-ELECT** Geraldine (Geri) Richmond **TREASURER** David Evans Shaw **CHIEF EXECUTIVE OFFICER** Alan I. Leshner **BOARD** Bonnie L. Bassler, May R. Berenbaum, Carlos J. Bustamante, Claire M. Fraser, Laura H. Greene, Elizabeth Loftus, Raymond Orbach, Inder M. Verma

SUBSCRIPTION SERVICES For change of address, missing issues, new orders and renewals, and payment questions: 866-434-AAAS (2227) or 202-326-6417, FAX 202-842-1065. Mailing addresses: AAAS, P.O. Box 96178, Washington, DC 20090-6178 or AAAS Member Services, 1200 New York Avenue, NW, Washington, DC 20005

INSTITUTIONAL SITE LICENSES 202-326-6755 **REPRINTS:** Author Inquiries 800-635-7181 **COMMERCIAL INQUIRIES** 803-359-4578 **PERMISSIONS** 202-326-6765, permissions@aaas.org **AAAS Member Services** 202-326-6417 or http://membercentral.aaas.org/discounts

Science serves as a forum for discussion of important issues related to the advancement of science by publishing material on which a consensus has been reached as well as including the presentation of minority of conflicting points of view. Accordingly, all articles published in *Science*—including editorials, news and comment, and books reviews—are signed and reflect the individual views of the authors and not official points of view adopted by AAAS or the institutions with which the authors are affiliated.

INFORMATION FOR AUTHORS See pages 680 and 681 of the 7 February 2014 issue or access www.sciencemag.org/about/authors

SENIOR EDITORIAL BOARD
A. Paul Alivisatos, *Lawrence Berkeley Nat'l. Laboratory,* **Ernst Fehr,** *U. of Zürich*
Susan M. Rosenberg, *Baylor College of Medicine,* **Michael S. Turner,** *U. of Chicago*

BOARD OF REVIEWING EDITORS (Statistics board members indicated with **(S)**)
Adriano Aguzzi, *U. Hospital Zürich*
Takuzo Aida, *U. of Tokyo*
Leslie Aiello, *Wenner-Gren Foundation*
Judith Allen, *U. of Edinburgh*
Sonia Altizer, *U. of Georgia*
Virginia Armbrust, *U. of Washington*
Sebastian Amigorena, *Institut Curie*
Kathryn Anderson, *Memorial Sloan-Kettering Cancer Center*
Peter Andolfatto, *Princeton U.*
Meinrat O. Andreae, *Max-Planck Inst. Mainz*
Paola Arlotta, *Harvard U.*
Johan Auwerx, *EPFL*
David Awschalom, *U. of Chicago*
Jordi Bascompte, *Estación Biológica de Doñana CSIC*
Facundo Batista, *London Research Inst.*
Ray H. Baughman, *U. of Texas, Dallas*
David Baum, *U. of Wisconsin*
Mark Bear, *Massachusetts Inst. of Technology*
Kamran Behnia, *ESPCI-ParisTech*
Yasmine Belkaid, *NIAID, NIH*
Philip Benfey, *Duke U.*
Stephen J. Benkovic, *Penn State U.*
Gabriele Bergers, *U. of California, San Francisco*
Christophe Bernard, *Aix-Marseille U.*
Bradley Bernstein, *Massachusettes General Hospital.*
Peer Bork, *EMBL*
Bernard Bourdon, *Ecole Normale Supérieure de Lyon*
Chris Bowler, *École Normale Supérieure*
Ian Boyd, *U. of St. Andrews*
Emily Brodsky, *U. of California, Santa Cruz*
Ron Brookmeyer, *U. of California Los Angeles* **(S)**
Christian Büchel, *U. Hamburg-Eppendorf*
Joseph A. Burns, *Cornell U.*
William P. Butz, *Population Reference Bureau*
Gyorgy Buzsaki, *New York U. School of Medicine*
Blanche Capel, *Duke U.*
Mats Carlsson, *U. of Oslo*
David Clapham, *Children's Hospital Boston*
David Clary, *U. of Oxford*
Joel Cohen, *Rockefeller U., Columbia U.*
Jonathan D. Cohen, *Princeton U.*
James Collins, *Boston U.*
Robert Cook-Deegan, *Duke U.*
Alan Cowman, *Walter & Eliza Hall Inst.*
Robert H. Crabtree, *Yale U.*
Roberta Croce, *Vrije Universiteit*
Janet Currie, *Princeton U.*
Jeff L. Dangl, *U. of North Carolina*
Tom Daniel, *U. of Washington*
Frans de Waal, *Emory U.*
Stanislas Dehaene, *Collège de France*
Robert Desimone, *MIT*
Claude Desplan, *New York U.*
Ap Dijksterhuis, *Radboud U. of Nijmegen*
Dennis Discher, *U. of Pennsylvania*
Gerald W. Dorn II, *Washington U. School of Medicine*
Jennifer A. Doudna, *U. of California, Berkeley*
Bruce Dunn, *U. of California, Los Angeles*
Christopher Dye, *WHO*
Todd Ehlers, *U. of Tuebingen*
David Ehrhardt, *Carnegie Inst. of Washington*
Tim Elston, *U. of North Carolina at Chapel Hill*
Gerhard Ertl, *Fritz-Haber-Institut, Berlin*
Barry Everitt, *U. of Cambridge*
Ernst Fehr, *U. of Zurich*
Anne C. Ferguson-Smith, *U. of Cambridge*
Michael Feuer, *The George Washington U.*
Peter Fratzl, *Max-Planck Inst.*
Elaine Fuchs, *Rockefeller U.*
Daniel Geschwind, *UCLA*
Andrew Gewirth, *U. of Illinois*
Karl-Heinz Glassmeier, *TU Braunschweig*
Julia R. Greer, *Caltech*
Elizabeth Grove, *U. of Chicago*
Kip Guy, *St. Jude's Children's Research Hospital*
Taekjip Ha, *U. of Illinois at Urbana-Champaign*
Christian Haass, *Ludwig Maximilians U.*
Steven Hahn, *Fred Hutchinson Cancer Research Center*
Michael Hasselmo, *Boston U.*
Martin Heimann, *Max-Planck Inst. Jena*
Yka Helariutta, *U. of Finland*
James A. Hendler, *Rensselaer Polytechnic Inst.*
Janet G. Hering, *Swiss Fed. Inst. of Aquatic Science & Technology*
Michael E. Himmel, *National Renewable Energy Lab.*
Kai-Uwe Hinrichs, *U. of Bremen*
Kei Hirose, *Tokyo Inst. of Technology*
David Hodell, *U. of Cambridge*
David Holden, *Imperial College*
Lora Hooper, *UT Southwestern Medical Ctr. at Dallas*
Thomas Hudson, *Ontario Inst. for Cancer Research*
Raymond Huey, *U. of Washington*
Steven Jacobsen, *U. of California, Los Angeles*
Kai Johnsson, *EPFL Lausanne*
Peter Jonas, *Inst. of Science & Technology (IST) Austria*
Matt Kaeberlein, *U. of Washington*
William Kaelin Jr., *Dana-Farber Cancer Inst.*
Daniel Kahne, *Harvard U.*
Daniel Kammen, *U. of California, Berkeley*
Masashi Kawasaki, *U. of Tokyo*
Joel Kingsolver, *U. of North Carolina at Chapel Hill*
Robert Kingston, *Harvard Medical School*
Alexander Kolodkin, *Johns Hopkins U.*
Roberto Kolter, *Harvard Medical School*
Alberto R. Kornblihtt, *U. of Buenos Aires*
Leonid Kruglyak, *UCLA*
Thomas Langer, *U. of Cologne*
Mitchell A. Lazar, *U. of Pennsylvania*
David Lazer, *Harvard U.*
Thomas Lecuit, *IBDM*
Virginia Lee, *U. of Pennsylvania*
Stanley Lemon, *U. of North Carolina at Chapel Hill*
Ottoline Leyser, *Cambridge U.*
Marcia C. Linn, *U. of California, Berkeley*
Jianguo Liu, *Michigan State U.*
Luis Liz-Marzan, *CIC biomaGUNE*
Jonathan Losos, *Harvard U.*
Ke Lu, *Chinese Acad. of Sciences*
Christian Lüscher, *U. of Geneva*
Laura Machesky, *CRUK Beatson Inst. for Cancer Research*
Anne Magurran, *U. of St. Andrews*
Oscar Marin, *CSIC & U. Miguel Hernández*
Charles Marshall, *U. of California, Berkeley*
C. Robertson McClung, *Dartmouth College*
Graham Medley, *U. of Warwick*
Yasushi Miyashita, *U. of Tokyo*
Richard Morris, *U. of Edinburgh*
Alison Motsinger-Reif, *NC State U.* **(S)**
Sean Munro, *MRC Lab. of Molecular Biology*
Thomas Murray, *The Hastings Center*
James Nelson, *Stanford U. School of Med.*
Karen Nelson, *J. Craig Venter Institute*
Daniel Neumark, *U. of California, Berkeley*
Timothy W. Nilsen, *Case Western Reserve U.*
Pär Nordlund, *Karolinska Inst.*
Helga Nowotny, *European Research Advisory Board*
Ben Olken, *MIT*
Luke O'Neill, *Trinity College, Dublin*
Joe Orenstein, *U. of California Berkeley & Lawrence Berkeley National Lab*
Harry Orr, *U. of Minnesota*
Andrew Oswald, *U. of Warwick*
Steve Palumbi, *Stanford U.*
Jane Parker, *Max-Planck Inst. of Plant Breeding Research*
Giovanni Parmigiani, *Dana-Farber Cancer Inst.* **(S)**
Donald R. Paul, *U. of Texas, Austin*
John H. J. Petrini, *Memorial Sloan-Kettering Cancer Center*
Joshua Plotkin, *U. of Pennsylvania*
Philippe Poulin, *CNRS*
David Randall, *Colorado State U.*
Colin Renfrew, *U. of Cambridge*
Felix Rey, *Institut Pasteur*
Trevor Robbins, *U. of Cambridge*
Jim Roberts, *Fred Hutchinson Cancer Research Ctr.*
Barbara A. Romanowicz, *U. of California,Berkeley*
Jens Rostrup-Nielsen, *Haldor Topsoe*
Mike Ryan, *U. of Texas, Austin*
Mitinori Saitou, *Kyoto U.*
Shimon Sakaguchi, *Kyoto U.*
Miquel Salmeron, *Lawrence Berkeley National Lab*
Jürgen Sandkühler, *Medical U. of Vienna*
Alexander Schier, *Harvard U.*
Randy Seeley, *U. of Cincinnati*
Vladimir Shalaev, *Purdue U.*
Robert Siliciano, *Johns Hopkins School of Medicine*
Joseph Silk, *Institut d'Astrophysique de Paris*
Denis Simon, *Arizona State U.*
Alison Smith, *John Innes Centre*
Richard Smith, *U. of North Carolina* **(S)**
John Speakman, *U. of Aberdeen*
Allan C. Spradling, *Carnegie Institution of Washington*
Jonathan Sprent, *Garvan Inst. of Medical Research*
Eric Steig, *U. of Washington*
Paula Stephan, *Georgia State U. and National Bureau of Economic Research*
Molly Stevens, *Imperial College London*
V. S. Subrahmanian, *U. of Maryland*
Ira Tabas, *Columbia U.*
Sarah Teichmann, *Cambridge U.*
John Thomas, *North Carolina State U.*
Christopher Tyler-Smith, *The Wellcome Trust Sanger Inst.*
Herbert Virgin, *Washington U.*
Bert Vogelstein, *Johns Hopkins U.*
Cynthia Volkert, *U. of Göttingen*
Douglas Wallace, *Dalhousie U.*
David Wallach, *Weizmann Inst. of Science*
Ian Walmsley, *U. of Oxford*
David A. Wardle, *Swedish U. of Agric. Sciences*
David Waxman, *Fudan U.*
Jonathan Weissman, *U. of California, San Francisco*
Chris Wikle, *U. of Missouri* **(S)**
Ian A. Wilson, *The Scripps Res. Inst.* **(S)**
Timothy D. Wilson, *U. of Virginia*
Rosemary Wyse, *Johns Hopkins U.*
Jan Zaanen, *Leiden U.*
Kenneth Zaret, *U. of Pennsylvania School of Medicine*
Jonathan Zehr, *U. of California, Santa Cruz*
Len Zon, *Children's Hospital Boston*
Maria Zuber, *MIT*

BOOK REVIEW BOARD
David Bloom, *Harvard U.,* **Samuel Bowring,** *MIT,* **Angela Creager,** *Princeton U.,* **Richard Shweder,** *U. of Chicago,* **Ed Wasserman,** *DuPont*

Published by AAAS

EDITORIAL

"Epicenters" of resilience

The 25th anniversary of the magnitude (*M*) 6.9 Loma Prieta earthquake that struck the San Francisco Bay Area on 17 October 1989 is a fitting time to examine what progress has been made in increasing community resilience to minimize seismic risk. The regions affected by the 2010 *M* 7.0 earthquake that struck Port-au-Prince, Haiti, and the *M* 8.8 event near Concepción, Chile, a few weeks later illustrate the extremes in earthquake resilience. In the zone of most intense shaking, 1 of every 10 Haitians was killed, compared to 1 of every 2500 Chileans, reflecting huge differences in construction quality and community resilience. The Loma Prieta event left 63 people dead, largely the result of the collapse of a bridge, an overpass, and homes built on unconsolidated fill. But beyond the loss of life, the Bay Area was affected by more than $10 billion in disruption of economic activity and damaged infrastructure. One challenge in implementing community resilience is to use science and engineering to find solutions that not only save lives but also get communities back to business as quickly as possible after a seismic event.

Loma Prieta, 1989

"One challenge...is to use science and engineering to...get communities back to business... after a seismic event."

The Loma Prieta event catalyzed partnerships of scientists, engineers, elected and building inspection officials, and emergency managers, as well as building and infrastructure owners, members of the business community, and tenant groups, to make the region safer and speed recovery. Over the past 25 years, the Bay Area has become an "epicenter" of resilience, in which the community has made substantial investments that are driven and supported by science-informed public policy.

Translation of science, accurate and clear risk communication, and actionable risk reduction measures with specific performance goals formed the cornerstones of campaigns to generate the political will to achieve public acceptance and enable substantial investments to improve resilience. One key to the success of these campaigns was a San Francisco–based planning and urban research nonprofit organization that included citizens and members of the business community as well as public policy, science, and engineering experts. This group led a dialogue to clearly define the attributes and performance measures of a resilient city subject to earthquakes. Enlightened leadership, both public and corporate, was also key to the success. After Loma Prieta, the area's major utility and transportation providers designed programs to lower vulnerability and speed recovery after a quake, and invested more than $25 billion in upgrades to their critical infrastructure, funded almost exclusively by local ratepayers and taxpayers. At the same time, over $30 billion has been invested by business and taxpayers in extensive retrofitting of commercial and public buildings and residential structures. Mandatory seismic safety inspections and retrofit ordinances also have been passed in several communities. Over 100 local governments now work together to strengthen community resilience, using measures such as financial incentives to upgrade buildings and public service systems, postdisaster governance plans, and interjurisdictional alliances.

The citizens of Haiti, situated directly adjacent to a major fault, were unaware of their risk and built homes that would collapse in an earthquake. Chile recognized its seismic risk, developed strong building codes, and enforced them. The Bay Area's robust high-tech economy gives it the capacity and public will, more than most, to invest more than $50 billion in resilience. However, there are valuable general lessons from the response to the Loma Prieta quake that can inform resilience building elsewhere. No-cost or low-cost measures such as broad engagement by the scientific and nonscience communities working together to communicate risk and set recovery priorities and performance objectives; providing the public with actionable risk reduction measures; and forming regional governmental and community alliances to implement science-informed policy are relevant to communities at risk everywhere. These are measures with a payoff that one cannot put a price on.

– Mary Lou Zoback

Mary Lou Zoback is a consulting professor in the Department of Geophysics, Stanford University, Stanford, CA. E-mail: marylouz@stanford.edu

10.1126/science.1261788

PHOTOS: (INSET) FREDERIC LARSON/SAN FRANCISCO CHRONICLE/CORBIS; (RIGHT) COURTESY OF MARY LOU ZOBACK

Downloaded from www.sciencemag.org on October 17, 2014

Published by AAAS

NEWS

> "It lifts the last remaining cloud from the subject."
>
> **Steven Aftergood** of the Federation of American Scientists to *The New York Times*, on the release of newly declassified documents that further exonerate physicist J. Robert Oppenheimer, once suspected of being a Soviet spy.

IN BRIEF

An inside view of the complex skeleton of the scalyhead sculpin fish.

See-through swimmer

Just in time for Halloween comes this ghoulish portrait of a scalyhead sculpin fish, *Artedius harringtoni*, stained to highlight its skeleton (red) and cartilage (blue). The photo comes from the lab of Adam Summers, a biomechanics researcher at the University of Washington, Seattle, who studies how the skeletons of fish and other animals allow them to move, which can offer lessons for engineers and even animators. (Summers consulted on the film *Finding Nemo*.) The fish is among 12 images and videos chosen as winners in the third annual BioArt competition, sponsored by the Federation of American Societies for Experimental Biology in Bethesda, Maryland, "to share the beauty and excitement of biological research with the public," according to the BioArt website. Other awardees include striking microscopy images of cells—immune cells engulfing a fungal invader, the neat cells resembling bundles of hair that allow a chick to hear—and a *Fantastic Voyage*–like tour through the branching airways in a mouse's lung. The winners will go on display at the National Institutes of Health in Bethesda.

PHOTO: ADAM SUMMERS

AROUND THE WORLD

Taiwanese research ship sinks

TAIPEI | Two researchers died in the sinking of a $50 million, 2700-ton Taiwanese research ship in the Taiwan Strait on 10 October. The remaining people onboard, including 25 researchers and 18 crew members, were rescued. The *Ocean Researcher V*, the flagship research vessel of the Taiwan Ocean Research Institute, was 1 day into an 8-day expedition to study atmospheric pollution when it decided to return to port due to deteriorating weather conditions. Taiwan's Ministry of Science and Technology is investigating; high waves and strong currents related to Typhoon Vongfang may have taken the vessel off course, where it struck a coral reef before capsizing.

Protesters disrupt TMT ceremony

MAUNA KEA, HAWAII | Dozens of native Hawaiians and non-Hawaiians gathered at the entrance to Mauna Kea summit on 7 October to protest the construction of the Thirty Meter Telescope (TMT), temporarily interrupting the planned groundbreaking ceremony (*Science*, 10 October, p. 146). The protests came on top of years of delay due to concern over the construction of the $1.4 billion telescope on a mountain that is sacred to Hawaiians and is home to more than a dozen telescopes. When it obtains first light, scheduled for 2022, TMT will be one of the most powerful ground-based telescopes in the world, allowing scientists to unravel the history of the first stars and galaxies and study dark matter and dark energy.

Z machine moves toward fusion

ALBUQUERQUE, NEW MEXICO | Researchers at Sandia National Laboratories in Albuquerque, New Mexico, using the lab's colossal electric pulse generator, or Z machine, to heat and squeeze hydrogen, say they have detected significant numbers of neutrons—byproducts of fusion

Downloaded from www.sciencemag.org on October 17, 2014

Published by AAAS

reactions—coming from the experiment. Reporting in *Physical Review Letters* last week, they detected about 2 trillion neutrons coming from each shot. The result shows that a substantial number of reactions is taking place—100 times as many as the team achieved a year ago—but they will need 10,000 times as many to produce as much energy as needed to heat and contain the plasma.
http://scim.ag/_Zmachine

Scientists protest Europe cuts

BRUSSELS | In an open letter published 8 October, nine prominent science policy advocates from Spain, Italy, Greece, Portugal, France, Germany, and the United Kingdom have aired their grievances with what they called "the systematic destruction of national R&D infrastructures," "drastic" budget and hiring cuts at research institutions and universities, and an increasing emphasis on applied research. Signed by nearly 5000 scientists, the open letter is part of a broader movement that includes a 3-week cycling tour around France and a series of meetings at major Italian universities. The protest is expected to culminate later this month with a march in Paris, a protest in Madrid, and a press conference in Rome. http://scim.ag/scientistmarch

Antivenom patent case settled

MEXICO CITY | Rattlesnake bite victims in the United States may soon have their choice of antivenoms. The London-based pharmaceutical company BTG announced 10 October that it had reached a settlement with Instituto Bioclon that will allow the Mexican company to sell its pit viper antivenom Anavip in the United States, pending Food and Drug Administration (FDA) approval. In October 2013, BTG had filed a complaint with the International Trade Commission claiming that Anavip infringed on BTG's patent for Crofab, which remains the only FDA-approved treatment for pit viper bites (*Science,* 3 January, p. 16). Many antivenom experts disagreed, citing differences in the companies' formulas. Under the settlement, Anavip could be available in the United States beginning in 2018. BTG retains its patent and will receive royalties on sales of Anavip until exclusivity expires in 2028.

Record-high Antarctic sea ice

BOULDER, COLORADO | The National Snow and Ice Data Center (NSIDC) announced last week that the sea ice surrounding

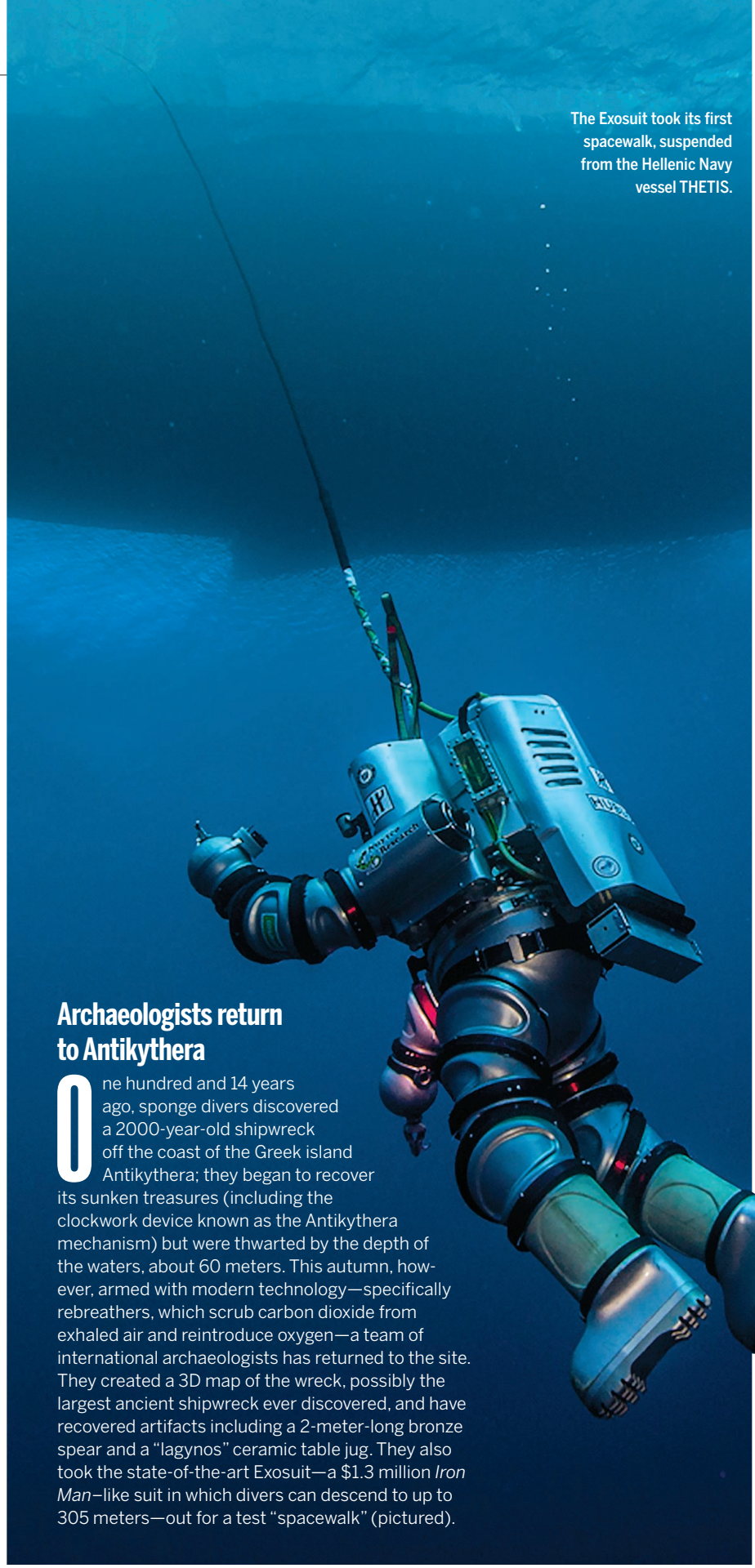

The Exosuit took its first spacewalk, suspended from the Hellenic Navy vessel THETIS.

Archaeologists return to Antikythera

One hundred and 14 years ago, sponge divers discovered a 2000-year-old shipwreck off the coast of the Greek island Antikythera; they began to recover its sunken treasures (including the clockwork device known as the Antikythera mechanism) but were thwarted by the depth of the waters, about 60 meters. This autumn, however, armed with modern technology—specifically rebreathers, which scrub carbon dioxide from exhaled air and reintroduce oxygen—a team of international archaeologists has returned to the site. They created a 3D map of the wreck, possibly the largest ancient shipwreck ever discovered, and have recovered artifacts including a 2-meter-long bronze spear and a "lagynos" ceramic table jug. They also took the state-of-the-art Exosuit—a $1.3 million *Iron Man*–like suit in which divers can descend to up to 305 meters—out for a test "spacewalk" (pictured).

PHOTO: © RETURN TO ANTIKYTHERA 2014

Published by AAAS

League of SI Superheroes, assemble!

These are no ordinary trading cards—they represent an elite group of international measurement units. The brainchild of the National Institute of Standards and Technology (NIST), the league includes The Mole, Professor Second, Monsieur Kilogram, Ms. Ampere, Dr. Kelvin, Meter Man, and Candela. A video of their adventures first appeared at the USA Science & Engineering Festival this summer, but NIST has spruced it up a bit for National Metric Week (centered around the 10th day of the 10th month), lengthening it and adding voice-overs (supplied mostly by NIST employees). NIST is now working on tie-ins aimed at middle school science teachers and students, including these trading cards and other educational materials. In their pilot episode ("Desperate Measures!"), the team helps a stranded girl by building her a new cellphone (http://www.nist.gov/pml/metric-100614.cfm). Another crisis averted—thanks to the power of measurement!

Mole, the SI unit for the amount of a substance, prepares to do battle.

Antarctica reached its maximum extent in 2014 on 22 September, at more than 20 million square kilometers. That was also a record since satellite measurements began in the late 1970s. Scientists have suggested that changes in prevailing winds and in ocean wave magnitudes might be responsible for the growth of Antarctic sea ice in some parts of the Southern Ocean, even as Arctic sea ice rapidly shrinks. NSIDC notes that this year's record might be related to changing wind patterns as well as melting of the continental ice sheet. The cold, fresh meltwater forms an extra-chilly layer on the ocean surface around the continent, favoring sea ice growth.

Big awards to mine big data

BETHESDA, MARYLAND | To tame the torrent of data churning out of biology labs, the National Institutes of Health (NIH) announced on 9 October $32 million in awards in 2014 to develop ways to analyze and use large biological data sets. The awards will fund 11 centers focused on developing tools for everything from modeling cell signaling in cancer to integrating data from mobile sensors worn by volunteers in health studies. Others will support brain data-collection efforts, including the ENIGMA project, which aims to unearth the genetic roots of psychiatric disorders. The awards will help maximize "the utility of the mammoth data sets that are emerging at an accelerated pace," said NIH Director Francis Collins in a call with reporters.

NEWSMAKERS

Three Q's

Australia's leading research agency, the Commonwealth Scientific and Industrial Research Organisation (CSIRO), has taken some heavy hits since the election of a conservative government in September 2013. The agency lost 5.4% of its budget (AU$111.4 million), up to 420 jobs will go by June 2015, and eight research facilities will be shuttered.

Newly appointed CEO **Larry Marshall**, an Australian physicist and Silicon Valley entrepreneur, faces a big challenge when he takes over next January from outgoing CEO Megan Clark—including reassuring skeptical staff that CSIRO won't become an industry-driven think thank.

Q: What's at the top of your to-do list?
A: Meeting everybody. I want them to get to know me, and I want to spend serious time at each major site.

Q: The government is keen to build stronger links between CSIRO and industry. Where will you begin?
A: Customer engagement. Opening the doors of CSIRO, obviously carefully because it's a national treasure house of intellectual property, but we're going to have to do that in some areas like information technology.

Q: Where does fundamental research sit in the innovation process?
A: They're inextricably linked. It's impossible to tell where fundamental research will lead. You have to trust the scientists.

BY THE NUMBERS

46%

Growth from 1995 to 2013 in the number of most-cited papers published in lower tier journals, according to a study at arXiv.org based on Google Scholar metrics.

$150 thousand

Asking price for the domain name Ebola.com, currently owned by Nevada-based Blue String Ventures, which specializes in buying and reselling domain names.

135%

Jump in methane emissions from venting and flaring of oil and gas wells on federal lands between 2008 and 2013, according to the Center for American Progress.

CREDITS: (TOP TO BOTTOM) NIST (4); CSIRO

Published by AAAS

Venezuelan President Nicolás Maduro took to the airwaves last month to accuse a physician of "psychological terrorism."

PHOTO: AP PHOTO/JOHN MINCHILLO

SCIENTIFIC COMMUNITY

For Venezuelan academics, speaking out is risky business

Government attacks some, snares many in red tape

By **Lizzie Wade**

When Ángel Sarmiento discovered that eight patients had died of an unidentified fever in less than 2 weeks in Maracay, the capital of Aragua state in Venezuela, he did what he was supposed to do: sound the alarm. In a press conference on 11 September, the president of Aragua's College of Physicians revealed the spate of deaths and declared, "We don't know what we're facing." But instead of applauding Sarmiento, Venezuelan President Nicolás Maduro accused the physician in a televised speech on 17 September of fomenting "psychological terrorism" and instructed his attorney general to open a case against him. Sarmiento fled the country a few days later.

The episode continues to reverberate in Venezuela, where intellectuals consider it a signal of the central government's disdain for science and the medical establishment. "What they want is to silence all of us," says Feder Álvarez, a pediatrician and secretary of Aragua's College of Physicians. "They're not just persecuting Ángel. They're persecuting the medical community."

Scientists, too, feel beleaguered. Objectivity and critical thinking—key values of science—"are very much at odds with the prevailing winds" in Venezuela, says Ricardo Hausmann, a Venezuelan economist who teaches at Harvard University. Last month, Hausmann found himself accused by Maduro, again on national television, of conspiring against the government after publishing a syndicated op-ed about the country's dire economic straits titled "Should Venezuela Default?" Hausmann worries that if he were to return to Venezuela, he could face months or years in prison, even before standing trial.

Within the country, scientists must cope with byzantine rules. The central government wants "control over every step" of an experiment, says a university-based molecular biologist who requested anonymity. For ecological fieldwork, collecting areas must be strictly specified in advance. For experiments of any sort, researchers must fill out forms every 6 months articulating the progress they've made toward predetermined goals, with little flexibility to follow new threads, the biologist laments.

Whenever scientists want to sequence nonhuman DNA, they must apply for permission from the country's environment ministry in the form of a contract for access to genetic resources. The government says that the requirement protects Venezuela's biodiversity and indigenous knowledge from capitalist exploitation. "Out of 11 contracts I've applied for, they've granted two," the biologist says. Because phylogenetics and other evolutionary studies require sequencing many related organisms, such studies are little more than pipe dreams for scientists at Venezuelan universities.

"I have to decide," the biologist says, "am I willing to spend my entire life filling out forms, asking permission, waiting for years, and in the end still be subject to the latent threat of fines or imprisonment if I access genetic resources I didn't originally ask permission for?" Sequencing human DNA is simpler, however, requiring no official permission. That opens the way to certain kinds of medical diagnostics and other tests—and may also make it easier for the central government to maintain a forensic database, the biologist says.

Some observers trace the persecution of scientists to the populist government's distrust of intellectuals. "The authority that comes from knowledge tends to be stubborn and irreverent, so [in Maduro's eyes] it's better that it's crushed," Hausmann says.

Since Sarmiento left the country, the Aragua outbreak has come into sharper focus. Last month, three doctors affiliated with the Central University of Venezuela announced that the unidentified fever is chikungunya, a mosquito-borne disease that is spreading in the Americas. "There is no mystery here," says Gustavo Villasmil, health minister of the state of Miranda. Weeks ago, he says, an independent lab confirmed that six of the first eight patients who succumbed to the fever tested positive for chikungunya. Because the disease has a mortality rate of about one in 1000, those fatalities are likely the "tip of the iceberg" of a widespread outbreak in Venezuela, says Julio Castro, health minister of the municipality of Sucre.

"We're hoping there will come a moment when the central government understands that there's no sense in denying the situation," Villasmil says. Hausmann is pessimistic: "They don't perceive [the epidemic] as a problem of public health. They perceive it as a problem of public opinion." As of 14 October, chikungunya infections and deaths were not being reported in the federal health ministry's weekly epidemiological bulletin.

Villasmil, a member of the political opposition who has stated boldly and publicly that Venezuela is in the throes of a chikungunya epidemic, says he can't help looking over his shoulder. "Here, you can never really calm down," he says. "That's the problem with police states." ■

Downloaded from www.sciencemag.org on October 17, 2014

Published by AAAS

When these pills are ingested, the chip on them sends a wireless signal.

BIOMEDICINE

'Nonadherence': A bitter pill for drug trials

Drug developers seek new ways to ensure that subjects take their medicine

By **Kelly Servick**

Phil Skolnick calls it "the crazy uncle in the attic that nobody likes to talk about." Last week in Boston, at a meeting on clinical trials for central nervous system treatments, he and a small number of drug researchers discussed how to deal with that crazy uncle—the fact that many people in drug trials stop taking their experimental medicines or don't take them as prescribed.

That's a major problem for drug developers, and for Skolnick, who directs the Division of Pharmacotherapies and Medical Consequences of Drug Abuse at the National Institute on Drug Abuse in Bethesda, Maryland. People who don't adhere to the expected drug regimen—because of unpleasant side effects, for example—can diminish the observable effects of the experimental treatment, or even mask side effects. "If you're going to spend millions of dollars of taxpayer money" on funding a trial examining a drug's safety or benefits, he says, "you should at least try to test the hypothesis."

The conventional wisdom in drug development holds that enrolling enough trial subjects can counteract low adherence rates, Skolnick says. But after watching studies flounder due to nonadherence, some drug developers are seeking other solutions, from pill-tracking technologies to trial designs that encourage adherence.

Even measuring the scope of the problem is a challenge. Most drug trials rely on participants' self-reports or a periodic count of how many pills have been used up from each patient's supply, Skolnick says, and those measures have often turned out to be misleading. While investigating a new antidepressant when he was a researcher at DOV Pharmaceutical Inc. 6 years ago, for example, Skolnick found an adherence rate of 92% using pill counts. But when blood samples were tested for levels of the drug, only 70% of the trial subjects met the minimum requirements for compliance, which could have diminished the drug's apparent performance in the trial. At last week's workshop, put on by the International Society for CNS Clinical Trials and Methodology (ISCTM), many researchers had similar experiences to share.

"It's very uncomfortable to grapple with this, because I think it challenges the way we go about our business," says psychiatrist Robert Alexander, who works on drug development at AstraZeneca in Cambridge, Massachusetts. He and colleagues there are preparing a paper that reports an average nonadherence rate of roughly 20% across eight recent AstraZeneca psychiatry studies, based on testing drug levels in blood.

But even blood or urine tests can only offer a snapshot of medication use, not a record of dosing patterns over time, Skolnick notes. To keep closer tabs on patient behavior, some studies rely on a so-called medication event monitoring system (MEMS). First developed in the 1980s, the system uses a microchip in the cap of the pill bottle to record when the bottle is opened and closed. A 2012 review of 95 clinical trials from the iAdherence database, which compiles MEMS dosing histories, found that 20% of patients had completely stopped taking their medication by day 100 of their trial, and 12% of those still participating omitted their dose on that particular day.

The study also confirmed what many in drug development have observed: Trials for psychiatric drugs have particularly low adherence. That's in part because these drugs tend to have many side effects, and because people with mental illness are often less than enthusiastic about being put on a drug to begin with, says Terrence Blaschke, a clinical pharmacologist at Stanford University in Palo Alto, California, and lead author on the study.

Some trial subjects are deliberately deceptive, says psychiatrist Thomas Shiovitz, a

(Not) following doctors' orders

Electronic monitoring data from 95 clinical studies of drugs show declines in both trial participation and adherence to prescribed doses.

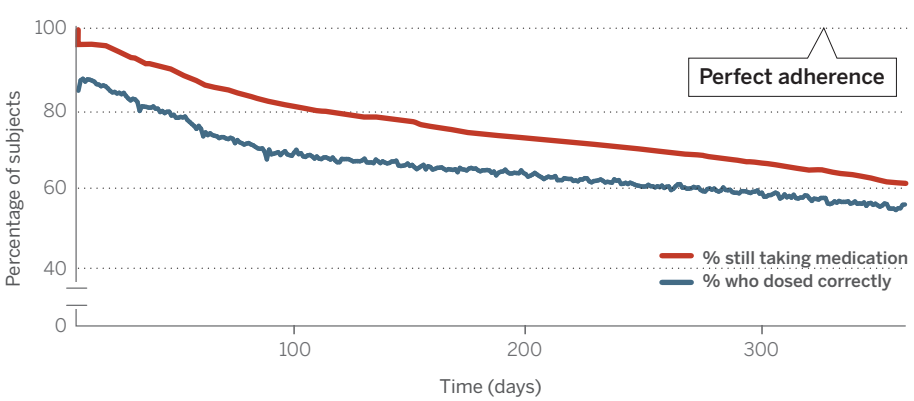

Downloaded from www.sciencemag.org on October 17, 2014

CREDITS: (PHOTO) PROTEUS DIGITAL HEALTH; (DATA) BLASCHKE TF *ET AL. ANNU. REV. PHARMACOL. TOXICOL.* 52:275-301 (2012)

Published by AAAS

principal investigator at the clinical trial site California Neuroscience Research Medical Group in Sherman Oaks, California, who co-chaired the ISCTM workshop. Alarmed by the number of subjects popping up in multiple studies he ran, Shiovitz began in 2011 to compile a database of people who enroll or go through screening with his drug sponsor clients and at other nearby trial sites.

Earlier this year, one man who came to enroll in a new schizophrenia study was flagged as a duplicate; he had visited at least seven trial sites in the last 12 months. He admitted that his strategy was to enroll in several schizophrenia trials, but take only the pills that made his head feel clearer. Either way, he got a stipend for participation, and reported to each trial that he was taking only the prescribed drug, in regular doses.

Shiovitz encourages his sponsors to prescreen for these duplicate subjects, which he estimates to make up 5% to 10% in trials for central nervous system drugs. "Scientists often don't take into account when they design their elegant studies that the subjects are real people who act in their own interest, for money or to feel better," Shiovitz says. Producing good, clean data for the investigators is "not their goal."

Some investigators are trying to track the very act of taking a drug, embedding in each pill a microchip that sends a wireless signal to a wearable device when ingested. One system, developed by Proteus Digital Health, has approval from the U.S. Food and Drug Administration and will be made commercially available this month.

But once enrolled, these nonadherent subjects can't simply be excluded from the post-trial analysis, says Craig Mallinckrodt, a statistician at Eli Lilly in Indianapolis and a member of the ISCTM working group on nonadherence, which plans to put out a white paper on the problem by 2016. Ignoring those people could create a bias of its own, because they may also be the ones who have negative effects from the drug. "At the end of the day," Mallinckrodt says, "you can only speculate about what would have happened had the patients adhered."

A 2010 report from the National Academies' Committee on National Statistics encouraged investigators to think about strategies that may help well-intentioned trial participants stick to a drug regimen. Shorter trials with less complicated dosing instructions could help, for example.

Stanford's Blaschke suggests much could be gained by better communicating the purpose of the trial, and the importance of following through with medication. Although databases and surveillance can spot the offenders, he says, "many of us feel that the problem is much bigger than that." ■

INFECTIOUS DISEASES

Ebola vaccine trials raise ethical issues

Randomized studies may offer fastest answer

By **Jon Cohen** *and* **Kai Kupferschmidt**

Come January, as many as 20,000 doses of an Ebola vaccine candidate may be ready for testing in the unprecedented epidemic racing through West Africa. The vaccine—and another one whose development is 6 weeks behind—could bring hope to a desperate, panicked population. Indeed, some scientists believe that the epidemic has grown so large that vaccines will be essential to stopping it. But difficult questions are now emerging about how to design clinical trials, who should be the first to get the shots, and when to begin mass production.

> ***"I suddenly saw a real double-blinded trial with another vaccine as the control was the way to go."***
>
> **Ira Longini,** University of Florida

Until recently, many scientists said that with Ebola, it wouldn't be ethical to use the standard procedure for testing a vaccine's efficacy: so-called randomized controlled trials (RCTs), in which some trial subjects are assigned to a control group that doesn't receive the actual vaccine. At a consultation held by the World Health Organization (WHO) on 29 to 30 September, however, there was unexpectedly broad support for the RCT design after all—but not from Doctors Without Borders (MSF), which is playing a huge role in the current outbreak.

On 2 September, one of the vaccines, made by pharmaceutical giant GlaxoSmithKline (GSK) of Rixensart, Belgium, in collaboration with the National Institute of Allergy and Infectious Diseases (NIAID), entered phase I trials, which test safety and immune responses in a small number of healthy volunteers. Preliminary results could be available as early as November. Similar studies for the other vaccine, developed by the Public Health Agency of Canada and produced by NewLink Genetics in Ames, Iowa, were launched 13 October, with early results expected in December.

If the vaccines do not cause harm and trigger the immune response scientists hope to see, WHO has recommended jumping straight into what amount to phase III efficacy tests in Liberia, Guinea, and Sierra Leone, the three hard-hit countries. It's an extraordinary, unprecedented gamble to move so quickly—but one that WHO consultants say is warranted by Ebola's extreme threat.

In RCTs, half of the participants are randomly assigned to receive the experimental shot and the other half a dummy, or placebo; ethicists say that's OK if it's unclear whether the vaccine will help, do nothing, or cause harm. If significantly more people in the placebo arm develop disease, the vaccine works. But animal experiments suggest the Ebola vaccines could well offer protection; keeping them from workers facing a disease as deadly as Ebola is unethical, some say.

The leading alternative is a trial design known as stepped-wedge, which takes advantage of the inescapable reality that a large-scale study can't give everyone the vaccine on the exact same date. Stepped-wedge trials compare the rates of infection in people already vaccinated with those who have yet to receive the shots. "People are more comfortable" with this setup because everyone in such a study gets the Ebola vaccine, says Barney Graham, a virologist at NIAID in Bethesda, Maryland, who attended the WHO meeting.

But at the meeting, Ripley Ballou, who heads the Ebola vaccine project for GSK, argued for an RCT—although the placebo would be replaced with an "active control," a proven vaccine (for instance, against hepatitis B) that would at least protect participants against another virus. An RCT, Ballou argued, offers the fastest, most acceptable route to determining whether a vaccine is safe and effective, and thus would potentially save the most lives.

Ballou described a randomized study in which 2500 people, probably health care workers, would receive the vaccine and 2500 an active control. He stressed that his team at GSK had many unknowns to wrestle with, including health care workers' infection risk, which they estimated at 10% per year spent in contact with Ebola patients. Assuming this is correct, and that the vaccine works at least 80% of the time, researchers could be "absolutely confident" about efficacy after 30 infections, which would likely

Published by AAAS

occur within 3 months, Ballou says. A vaccine that had 60% efficacy could still yield an answer with fewer than 60 infections.

That's much faster than a stepped-wedge design, he contends. Such a study would enroll participants at the same point in time, but would stagger distribution of vaccine, say, to different Ebola treatment units. But researchers would still have to observe the different communities from the same start date, introducing delays and making it harder to tell whether the vaccine works. Infection rates might change over time, too, complicating the analysis.

Ballou didn't win over MSF. "Studies on efficacy in affected countries and more so in at-risk populations should not have a placebo or active control arm as this cannot be defended ethically," says Annick Antierens, a meeting attendee who oversees experimental Ebola products for MSF. Antierens says MSF would support other Ebola vaccine efficacy trial designs, but would not specify which ones. One idea is to just distribute vaccine to health care workers and then do an "observational" study that does not have a control group but compares vaccination status in those who became ill to those who did not.

But most meeting participants sided with Ballou, says Ira Longini, a biostatistician from the University of Florida in Gainesville. Longini changed his planned talk on the stepped-wedge design after Ballou spoke. "I suddenly saw a real double-blinded trial with another vaccine as the control was the way to go," he says. Marie-Paule Kieny, a WHO assistant director-general, says "the meeting was quite tense at moments," but that there ultimately was "broad agreement" on this design. "Rip's study made sense," Kieny says.

Jeremy Farrar, an infectious disease researcher who heads the Wellcome Trust in London, cautions that people on the front lines of Ebola may disagree. An RCT may yield results faster, but if it's simply unacceptable for trial participants, a stepped-wedge design is preferable. "If you were there tomorrow and you were a health care worker, would you be willing to be in a control arm, when the next 3 months you will be looking after patients with Ebola?" Farrar asks. "I don't want us to have months of discussions about the best way of handling this."

The 20,000 doses of the GSK vaccine that may be ready by January—double earlier projections—could be enough for several trials, which might allow different groups of participants to enroll in different designs. "I would do all these trials simultaneously," Longini says.

Before the trials are launched, health officials also need to decide who should participate. An August WHO consultation recommended that efficacy trials first recruit health care workers, as they are at high risk and provide a critical service. But the latest meeting "stopped talking about health care worker and started talking about front-line caregiver," Ballou says, which means everyone from doctors and nurses to janitors, people who collect the bodies, and gravediggers.

The next issue is when to scale up production. Many researchers, including Longini, argue that massive production of Ebola vaccines should begin as soon as positive phase I data exist, to increase the likelihood that shots will be widely available when the evidence from the phase III study comes in. "I'd pull out all the stops," Longini says. "I'd try to make 30 to 40 million doses to cover at-risk West African populations." Farrar agrees. "We may come to regret that we have to throw those vaccines away if they prove not to be effective," Farrar says, "but I think that is a risk we have to take." ■

Liberian nurses pick up a dead body from the waiting area of a hospital in Monrovia.

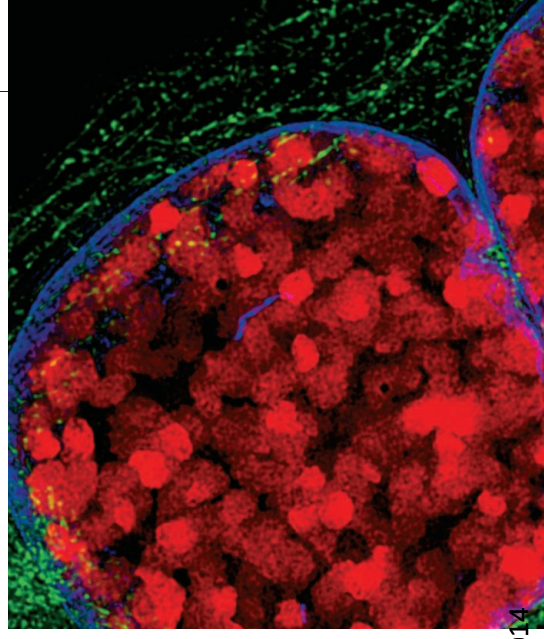

NOBEL PRIZES

Light loophole wins laurels

Chemistry prize winners pushed microscopes past supposed limit

By **Daniel Clery**

For more than 100 years, microscopists were stymied by a law of nature—or so they thought. The so-called diffraction limit meant that optical images could never reach a resolution finer than half a wavelength of light, and the fine details of living things would be forever blurry. Then, beginning in the late 1990s, three scientists found a way to blast through that limit. Their techniques, all based on getting the specimen itself to absorb and emit light, have won them this year's Nobel Prize in chemistry.

Microscopists told *Science* they are delighted about the award, announced on 8 October, which went to Eric Betzig of the Howard Hughes Medical Institute in Ashburn, Virginia; Stefan Hell of the Max Planck Institute for Biophysical Chemistry in Göttingen, Germany; and William Moerner of Stanford University in Palo Alto, California. "It's very well deserved," says Michelle Peckham, a cell biologist at the University of Leeds in the United Kingdom and a council member of the Royal Microscopical Society. "It's opened up the horizons of microscopy to new techniques, especially in the biological sciences."

The so-called Abbe diffraction limit had condemned things smaller than about 0.2 micrometers—including bacteria, cel-

PHOTOS: (LEFT TO RIGHT) EPA/AHMED JALLANZO; SCHERMELLEH ET AL./*SCIENCE*

Downloaded from www.sciencemag.org on October 17, 2014

Published by AAAS

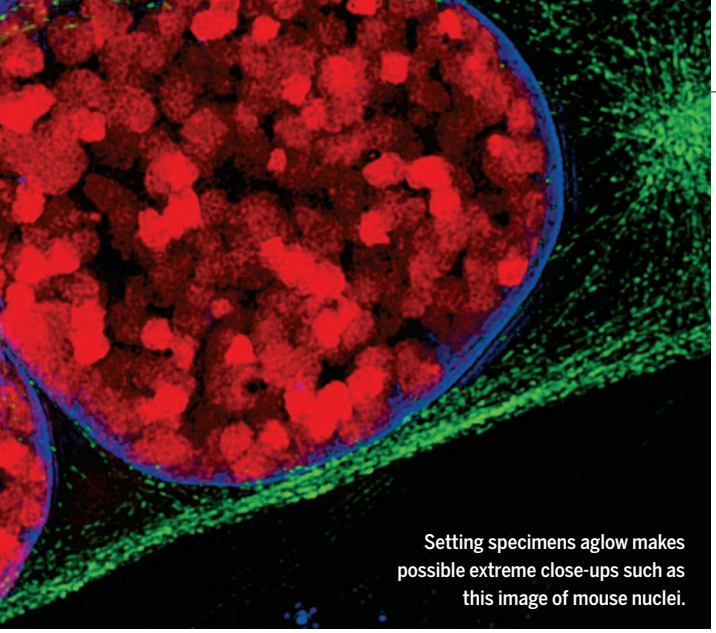

Setting specimens aglow makes possible extreme close-ups such as this image of mouse nuclei.

lular organelles, and viruses—to looking at best blurry and indistinct in visible light micrographs. The three new Nobelists overcame that limit through fluorescence, coaxing objects to reveal details by emitting their own light.

In the late 1980s, Moerner, then at IBM's Almaden Research Center in San Jose, California, was trying to develop a novel optical data storage technique. Along the way, he and his colleagues improved their lasers and detection equipment enough to track the light absorption spectra and fluorescence of single molecules. Those studies revealed that the wavelength of light given off by individual molecules can shift as molecules dance around, an insight that made possible later imaging developments.

Hell developed his technique, called stimulated emission depletion microscopy, in 2000. It uses a laser beam to excite molecules to glow and a second beam to cancel out all fluorescence except within a volume just nanometers across—hundreds of times smaller than a wavelength of light.

Shortly thereafter, Betzig developed a different method known as single-molecule localization microscopy. Instead of turning off unwanted fluorescence, his technique excites it selectively, using a precisely tuned laser to tickle just a single kind of biological molecule at a time. By separately imaging molecules that have different distributions in a sample, then superimposing the separate images, the technique can build up a complete picture of the structure. Betzig demonstrated the method for the first time in 2006 and described it in a paper in *Science* (11 August 2006, p. 748).

Hell told the Nobel press conference on 8 October by phone from Germany that he began working on the problem when he became bored by the conventional problems of microscopy and wondered if this seemingly unbreakable limit could be breached. "I was attracted to the problem. I eventually realized there was a way," he said. At first, Hell added, other scientists couldn't believe his new approach had cracked a problem that had vexed researchers since Abbe's work in 1873. "I realized you don't overcome the limit by changing the waves of light; you overcome it by playing with the molecules."

The implications were revolutionary. Using electron microscopes, researchers had been able to observe only specially prepared dead specimens. The ability to produce visible light images at a resolution of tens of nanometers meant they could now study biological molecules in living organisms. "I am thrilled by this," says Catherine Lewis, director of the cell biology and biophysics division at the National Institute of General Medical Sciences in Bethesda, Maryland. "Because these techniques allow researchers to monitor molecular movements over time, they are becoming very important for understanding things such as metastasis in cancer, and the way viruses enter cells and where they go."

Some researchers noted that, coming so soon after the techniques' discovery, the award contrasted with the Nobels' usual stately pace. "It's still quite new. It's only just starting to be adopted in the lab," says Leeds' Peckham. Susan Cox, a biologist at King's College London, agrees. "These three people are very worthy recipients," she says. "But we're still at the start. It's a little messy, and the technological development is happening as the scientific results are coming in."

CHEMISTRY NOBEL

"for the development of super-resolved fluorescence microscopy"

Eric Betzig

Stefan W. Hell

William E. Moerner

Microscopists were quick to develop variants of the Nobel-winning techniques, with a bewildering array of acronyms—SPDM, SPDMphymod, STORM, PALM, dSTORM, fPALM, SOFI, and SIM—but they remained too expensive and technically difficult for many biology labs, Cox says. In recent years, however, major optics manufacturers have begun producing off-the-shelf systems. "That's the critical thing," Cox says: "being able to push the button, and it just works." ■

With reporting by Robert F. Service.

NOBEL PRIZES

Regulating industry's big boys

French economist Jean Tirole is honored for his analyses of oligopolies

By **Tania Rabesandratana**

Big companies make their own rules—but they can still be regulated. That insight earned Jean Tirole, scientific director at the Industrial Economic Institute at the Toulouse School of Economics in France, the 2014 Nobel Prize in economics. Tirole's influential analyses of oligopolies, industries dominated by a few large firms, helps answer the question: "What sort of regulations and competition policy do you want in place so that large and mighty firms will act in society's best interest?" said Tore Ellingsen, chair of the prize committee.

ECONOMICS NOBEL

"for his analysis of market power and regulation"

Jean Tirole

Until the 1980s, regulation researchers sought simple rules that could apply to every industry. They often dealt with two extreme situations: single monopolies or perfect competition. Tirole instead used mathematical modeling from game theory and contract theory to describe how giant firms react and interact under various conditions. He also provided tools to deal with so-called asymmetric information, when public authorities have less information than the firms they are trying to regulate.

Tirole has never shied away from giving practical policy recommendations, says Reinhilde Veugelers, an economics professor at the University of Leuven in Belgium and senior fellow at the Bruegel think tank in Brussels, adding that his work is highly relevant to current debates on the regulation of telecoms, banking, and energy markets.

Indeed, Joaquín Almunia, the European commissioner for competition, praised Tirole's influence on the regulation of company mergers, among other topics, in a statement on Monday. "We owe Jean Tirole so much," Almunia said.

For a longer version of this story, see http://scim.ag/econNobel. ■

Published by AAAS

Baboon watch

By **Elizabeth Pennisi**,
in Amboseli National Park, Kenya

Several yellow baboons are sitting on their haunches pulling up grass, tearing off the stems, and shoving the corms into their mouths. The scene looks sleepy—but a frisson of sexual tension is in the air. Glenn, the troop's dominant male, clearly has eyes for Hokey, whose swollen rear end means she's ready to mate. He's hanging out nearby, hoping to get lucky.

Suddenly a commotion erupts; squealing baboons are mixing it up in a cloud of dust. Within a few heartbeats it's over. Hokey ambles away, grunting. Was she hurt? I ask. No, says Kinyua Warutere, a tall, unassuming Kenyan who has spent much of the past 20 years observing baboons here on the savanna northwest of Mount Kilimanjaro. He recounts in detail what to me had been a blur. Wily old Lobo had coaxed three other males to charge Glenn, then grabbed Hokey and mated with her. Hokey's grunt was her copulation call. To my astonishment, Glenn had lost his fertile female to a middle-aged has-been.

Similar play-by-play details, captured painstakingly over 43 years and combined with a wealth of genetic and physiological data, have brought renown to the Amboseli Baboon Research Project. Begun by Stuart and Jeanne Altmann, a husband-and-wife team, the project is the world's longest running baboon study, and it set a standard for behavioral fieldwork 40 years ago when Jeanne devised a method of making systematic observations now implemented worldwide. "They have transformed the field," says Larissa Swedell, a primatologist at Queens College of the City University of New York who has studied baboons elsewhere in Africa.

Many other primate researchers have gravitated to baboons, which spend most of their time on the ground and thus are easy to observe. Robert Sapolsky, a neuroscientist at Stanford University in Palo Alto, California, for example, has explored social interactions and stress in the animals, a theme of his captivating 2002 book, *A Primate's Memoir: A Neuroscientist's Unconventional Life Among the Baboons*. Other teams have also studied baboons over the years. But none can match the decades of cradle-to-grave observations at Amboseli, which have yielded what Sapolsky calls "stunningly

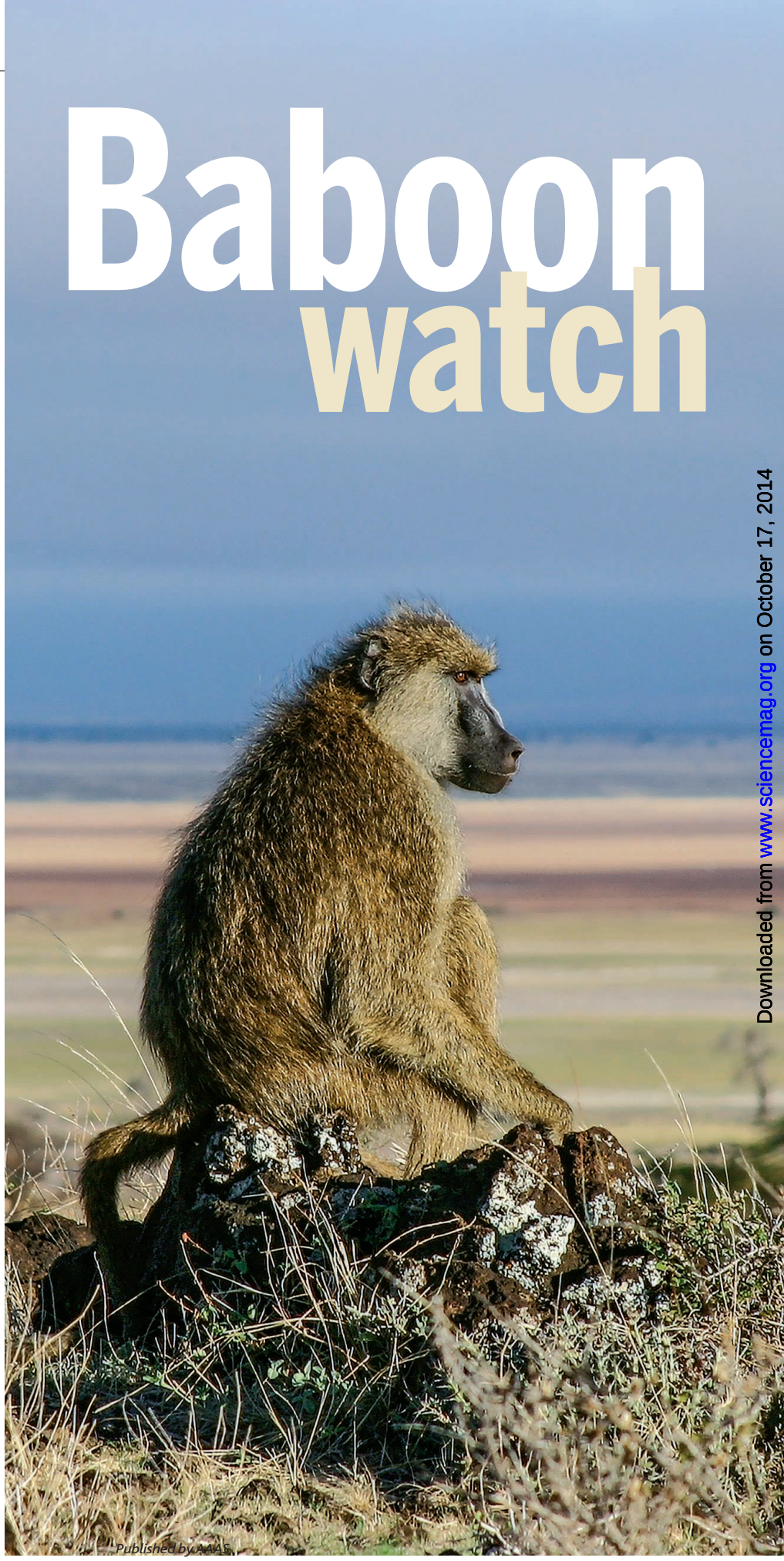

Downloaded from www.sciencemag.org on October 17, 2014

Published by AAAS

An epic baboon study shows how social interactions shape health and reproduction in all primates—including humans

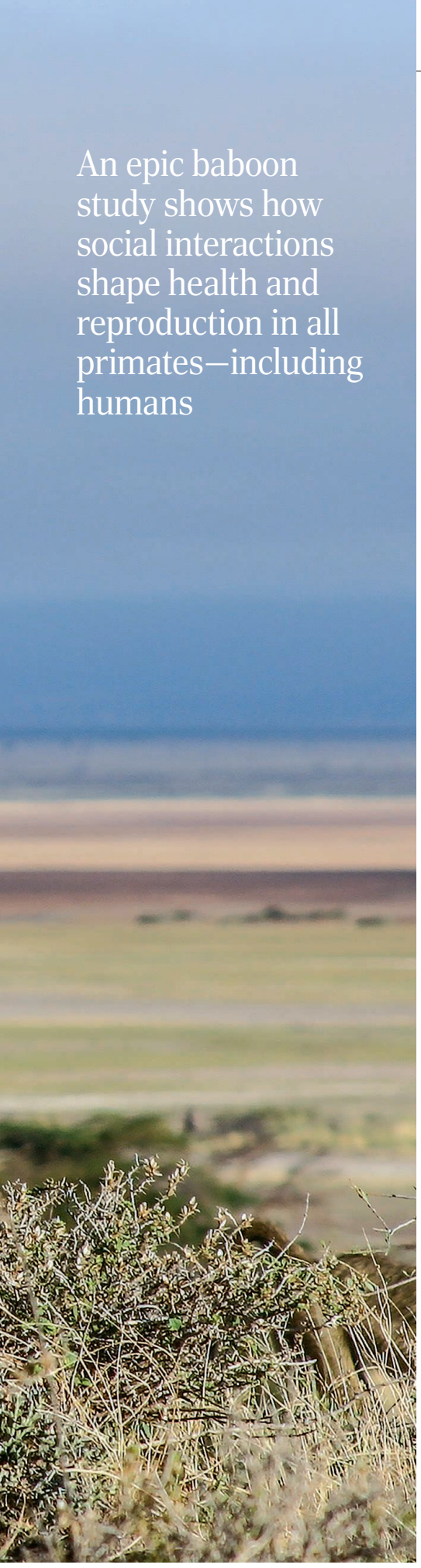

PHOTOS: (LEFT TO RIGHT) CATHERINE MARKHAM; DUTCH RESISTANCE MUSEUM AMSTERDAM

large and detailed data sets stretching over decades," from which a varying cast of researchers "mine incredibly subtle, interesting behavioral findings."

Some of those findings lay bare the workings of baboon troops, showing how conflict, habitat loss, predation, and drought shape the lives of these Old World primates. The work is also ever more relevant to our own species. Amboseli researchers are probing how baboons age to understand why women outlive men but are apparently sicker over the course of their lives. They're dissecting how social relationships among baboons influence longevity, and they are using new molecular tools to document the interplay between behavior and two hot research areas: epigenetics and the microbiome. And in an extraordinary new twist, Amboseli is helping peel away the mystery of a decades-old human catastrophe.

IN THE FINAL MONTHS of World War II, the German-occupied Netherlands cut food rations to less than one-quarter of normal caloric levels. Some 4.5 million people starved, and 18,000 died. To assess the famine's long-term toll, researchers in 2001 tracked down 2400 babies born in an Amsterdam hospital between 1943 and 1947. They discovered that the famine babies—those born in the winter of 1944 to 1945—suffered higher rates of diabetes, heart disease, obesity, and other ills in later life than babies born earlier or later.

Scientists have floated two possible explanations. One holds that the harsh conditions crippled embryonic development, cheating children out of a healthy life. The other idea holds that malnutrition during development tweaked the metabolism, brain function, and circulatory system of famine babies as a coping mechanism for starvation. Later, when food was abundant, those adaptations went awry and led to illnesses. That idea, says Laura Clamon Schulz, a reproductive physiologist at the University of Missouri, Columbia, "is one of the most provocative and difficult to test in the field."

A catastrophe offered the Amboseli team a chance to evaluate what happens when food runs short for pregnant baboons and their infants. After a dry year in 2008, severe drought hammered East Africa in 2009, taking a heavy toll on wildlife. Most baboons survived, but females stopped ovulating and some infants starved to death. The next year brought record rains.

Now, those infants are fully grown. If starvation prepared them for lean times in adulthood, then those born in 2009 should do better in later drought years than those born in 2010. But if conditions when they were in the womb left them physiologically damaged, they would do worse in later hard times—and that's what was observed. Susan Alberts, Jenny Tung, and graduate student Amanda Lea, of Duke University in Durham, North Carolina, first compared the reproductive success of female baboons born during the 2009 drought with those born in years in which food and water were not scarce. During later dry years, they found, baboons born in 2009 were less likely to conceive and much slower to resume menstruation. (Female baboons become sexually mature at age 4.5.)

Now, the Amboseli team is factoring in other stresses, such as social status or loss of a parent. Infants experiencing three or more stressors in their first year of life tend to die a year or two earlier than those who led a charmed infancy, Tung says. Alberts, Tung, and Lea also found that drought-year infants born to high-ranking mothers do better during subsequent droughts than those born to low-ranking females, perhaps because they get more food and are less harassed.

The findings suggest that infants who were malnourished in the 2009 drought suffered irreversible physiological changes. They also support a converse idea, the silver spoon hypothesis, which holds that "kids born in really good years to high-ranking moms do much better," Tung says. The same effects could explain the patterns seen after the Dutch famine. "I can certainly see the parallel between the baboon study and ours," says Tessa Roseboom, an epidemiologist at the Academic Medical Center in Amsterdam who studied the fate of the famine babies. "This is a fascinating story."

Babies born during the Dutch "Hunger Winter" of 1944 to 1945 had health problems as adults. Findings from Amboseli may help explain why.

Like Roseboom's group, the Amboseli researchers are now trying to unravel the molecular causes of these long-lasting effects. Suspecting the subtle hand of epigenetics—which modifies gene activity without altering

Published by AAAS

a DNA sequence—they are sizing up differences in patterns of methylation, in which the attachment of methyl groups to DNA can silence nearby genes. They compared baboons subsisting on wild foods with those that live near a tourist lodge and feast on calorie-rich garbage. Lodge baboons are known to forage less and have 20% body fat compared with the usual 2%, high cholesterol, and bad teeth.

The pilot study of 66 males in the two troops revealed significant differences in methylation, Lea reported in May at the Biology of Genomes meeting in Cold Spring Harbor, New York. Most intriguing are differences affecting a gene called *PFKP* that responds to insulin and is involved in breaking down sugar, and a gene called *KCNIP4* that seems to play a role in human obesity. The researchers suspect that dietary shifts trigger epigenetic changes that affect the activity of these genes, although they don't know how these changes play out in baboon health.

SUCH CUTTING-EDGE STUDIES wouldn't be possible without detailed data on the life histories and behavior of the more than 1500 baboons monitored over the decades at Amboseli. And those data are the fruits of a methodology pioneered by Jeanne Altmann. When she arrived with Stuart in Kenya in 1963, she could not have imagined immersing herself in the world of baboons. The behavior she planned to watch was that of her toddler, Michael. Stuart, however, had planned to spend a year studying baboon communication, so the Altmanns struck out in search of a field site. Baboons at Nairobi National Park had adapted to tourists, so the couple settled on Amboseli, where open savanna and passable terrain allow for easier fieldwork, and the baboons were not perturbed by their presence.

Jenny Tung, part of the third generation of women running the Amboseli project, collects a fecal sample.

After the Altmanns returned to the United States in 1964, Jeanne resumed her undergraduate studies (in math) and worked part time as a computer programmer. But her Kenya experience had kindled an interest in baboons, and eventually, egged on by Stuart, she began pondering how to reduce biases in observational studies.

Researchers of the time tended to jot down whatever caught their eye. With that approach, "the biggest, flashiest individuals doing the most dramatic things are going to be disproportionately recorded," says Jeanne, now a professor emeritus of behavioral ecology at Princeton University. In 1974, she published a method of observing individuals in a predetermined random order for preset lengths of time, greatly reducing bias.

The paper may be the most cited in animal behavior, says Karen Strier, a behavioral ecologist at the University of Wisconsin, Madison, who has studied New World monkeys for decades. "It was a bible for me."

Jeanne Altmann also drove a shift of focus away from male baboons. In 1975, she began observing females and discovered the intricate links between social relationships and raising offspring. That work earned her a Ph.D. in behavioral sciences just in time for her son Michael's high school graduation. More recently, Amboseli researchers have found that higher ranked females have more offspring, on average, than lesser peers and that their young mature faster, creating larger lineages. But rank isn't everything: No matter what a female baboon's status, having friends correlates to a longer lifespan—and it's even better if some friends are males, Amboseli researchers reported last month in the *Proceedings of the Royal Society B*.

LIKE MOST AMBOSELI NEOPHYTES, I find it impossible to tell the baboons apart. But Raphael Mututua, who keeps the Amboseli project running smoothly, is on a first-name basis with all 300-odd baboons. He and his colleagues have honed "baboon eyes": an ability to recognize individuals and notice subtle changes in behavior. With time, Mututua says, "you see them like you see human beings." He coaches me in coat color, tail shape, facial characteristics, posture, and other features. My 2 days in the field are far too few to get the hang of it.

Susan Alberts also has baboon eyes—and a penchant for molecular studies. As Jeanne Altmann's graduate student, she and Altmann in 1989 decided that the project's voluminous behavioral observations would

The baboon chronicles

Amboseli researchers have monitored their subjects for 40 years.

1963–4
Jeanne and Stuart Altmann study baboon ecology in Kenya, mostly at what is now Amboseli National Park

1971
The Altmanns return to Amboseli and launch what became a long-term study of a baboon troop called Alto's Group

1974
Jeanne Altmann publishes a methodological study that sets the standard for behavioral observations

1980
The project expands observations to a second troop, Hook's Group

1981
Raphael Mututua becomes the first of three Kenyan field assistants

1984
The project's first Kenyan student, Philip Muruthi, joins; he goes on to complete a Ph.D.

Susan Alberts joins project as an assistant; she, too, completes a Ph.D.

1989
Blood sample collection begins, leading to papers on the influence of social factors on behavior and physiology

1994
Fecal sampling starts, enabling larger sample sizes for hormone and DNA studies

2003
Amboseli team discovers that male baboons can identify their own offspring and that friends matter for females

2009
Severe drought forces baboons to spend much of their time foraging

2010
Jenny Tung and Beth Archie sign on as project associate directors under directors Alberts and Jeanne Altmann

2013
Mercy Akinyi determines that grooming leads to fewer ticks and healthier blood

PHOTO: ELIZABETH PENNISI/*SCIENCE*

Published by AAAS

Through grooming, baboons not only reduce parasites—they also cement friendships.

PHOTO: SUSAN C. ALBERTS

be more meaningful with genetic data. To explore how a male's success at fathering offspring varies with his rank and whether he has migrated from a different troop, Alberts and Altmann began collecting blood for paternity testing. Even though fertile females have multiple mates, the work showed that dominant males father most of their offspring—somehow sperm from the top-ranking males comes out ahead. Yet dominant males have limited lineages because most don't stay dominant for very long. Alberts and colleagues also discovered that contrary to expectations, fathers know their own offspring and can boost their progeny's survival odds, if they stay in the same troop.

Getting blood samples by darting and tranquilizing animals is difficult and expensive, so Alberts and Altmann honed techniques to cull DNA and hormones from fecal samples, which are now crammed by the thousands in freezers in the United States. They only collect fecal samples they see deposited, so they know the source. Hormone concentrations in the feces have taught them much about how baboons deal with stress, and DNA extracted from the samples has allowed them to build pedigrees for the more than 1500 individuals they've observed over the years.

Biologist Beth Archie of the University of Notre Dame in Indiana has come up with a new use for these samples. Over the past 5 years, studies have linked the microbiome—microbes that live in and on our bodies—to our health status. Some work has suggested that social connections lead to more similar microbiomes, but it's been hard to tease apart whether social connections or similar diets are responsible. Archie has pulled bacterial DNA out of the feces to characterize baboon microbiomes. Combining that data with behavioral observations allows her to evaluate how baboon social mores affect the microbiome. At the recent Biology of Genomes meeting, she and Tung reported that gut microbiomes are most similar within a social group, and specific bacteria and enzymes strongly correlate with how friendly baboons are to each other. "We show a striking role for social relationships," Archie says, "which has ramifications for the evolutionary costs and benefits of sociality."

For other projects, the Amboseli researchers have had to resume blood collection. This year's effort will start the day after I leave Amboseli: Mututua and colleagues will fan out among a troop, each concealing a meter-long blowgun loaded with a tranquilizing dart, until a target baboon is alone and they can take it down. "Once we cover [the darted animal] with the tarp, [others in the troop] forget all about it," Tung says.

Back at the truck, a team will weigh the drugged animal, make a cast of the teeth, take a skin punch, and check for parasites. They will also draw blood for their studies, which aim to test immune system function and correlate it with age, social rank, and other factors. Tung and Archie are pushing the limits of what can be done in the field. When their colleagues flew in from North Carolina, they brought reagents for testing immune function that must be kept frozen before they are mixed with blood and incubated at baboon body temperature. Using this test on captive primates in the United States, Tung and postdoc Noah Snyder-Mackler found that low social status often dampens immune function. Now, they have a chance to see what happens in wild baboons, which are under far greater stress and are besieged by parasites. By doing so, the baboon watchers hope to uncover a new plot twist in the epic Amboseli story—and perhaps another clue to what shapes our own health. ■

Published by AAAS

The dynamic Sun in closeup *p. 305*

Does race belong on the U.S. Census? *p. 307*

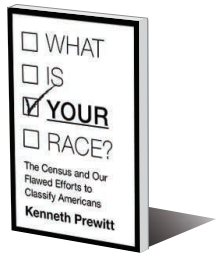

PERSPECTIVES

SCIENCE AND REGULATION

Changes on the horizon for consumer genomics in the EU

Test results may no longer be available directly to consumers

By **Louiza Kalokairinou,[1] Heidi Carmen Howard,[2] Pascal Borry[1]**

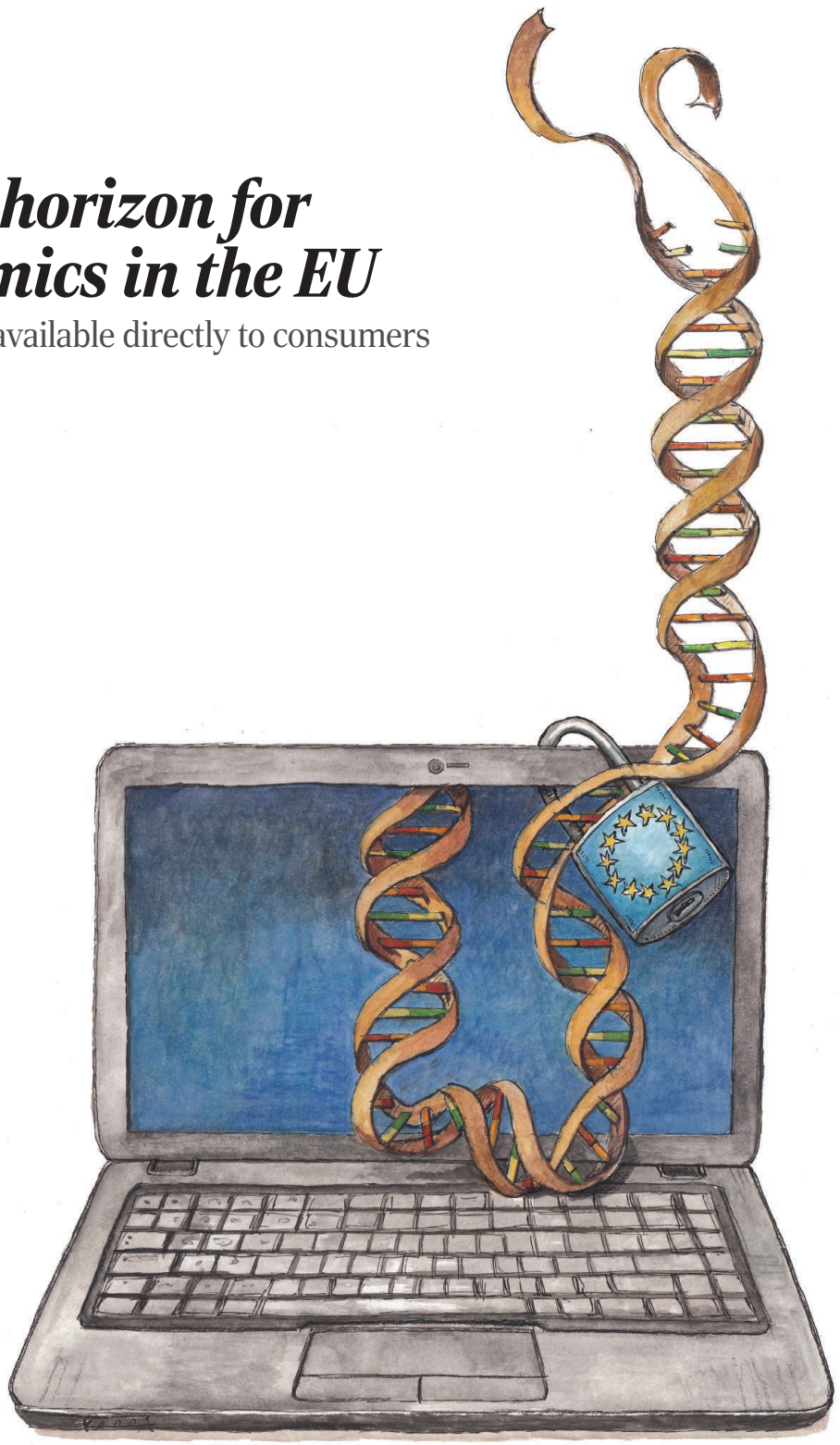

ILLUSTRATION: JORIS SNAET

Although the direct-to-consumer (DTC) genetic testing market has been developing for over a decade, effective oversight has been challenging, with regulations remaining complex and often unclear. Recent developments indicate that important changes in the regulatory landscape may be imminent. In November 2013, the U.S. Food and Drug Administration (FDA) halted the DTC genetic testing company 23andMe from marketing its "Personal Genome Service" without marketing clearance or approval, which highlighted concerns over potential adverse health consequences of the genome-wide testing offered (*1*). The company has no timeline for when it will offer health-related genetic testing again in the United States (*2*). Meanwhile, in the European Union (EU), a proposed regulation could limit availability of such test results directly to consumers. We describe this ongoing revision of the EU in vitro diagnostic (IVD) medical device directive and how this may drastically affect market authorization of genetic tests.

POLICY

The safety and performance of DTC genetic tests entering the EU market falls within the scope of Directive 98/79 on IVD medical devices. In contrast to national legislations in some EU member states, this directive has had little or no practical impact on the offer of DTC genetic tests. Above and beyond concerns over IVD medical devices for DTC genetics, the need for revision of the regulatory framework has been highlighted by the rapid evolution of the health care industry, emerging weaknesses of the current

Downloaded from www.sciencemag.org on October 17, 2014

Published by AAAS

legislation, and divergence in implementation of the rules by member states (*3*).

In this light, it is proposed that Directive 98/79 be replaced by a new regulation. Whereas a directive designates objectives and leaves member states to decide how these will be achieved, a regulation is directly binding for all member states, to be implemented uniformly across the EU by the end of the transitional period, without the need to be transposed into national law (*4*).

In September 2012, the European Commission (EC) submitted a proposal for regulation to the European Parliament and the Council of the EU. An amended version was voted on by the European Parliament in October 2013 and formalized by another parliamentary vote in April 2014. The proposed regulation is now under discussion at the council. The regulation can only be definitively adopted if both the Parliament and council approve a common version. Until this happens, amendments can be made (*5*).

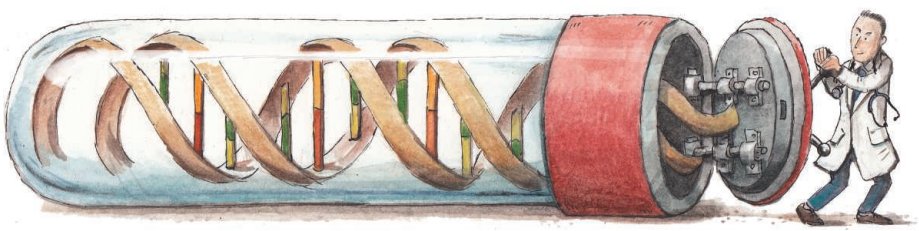

ILLUSTRATION: JORIS SNAET

CLASSIFYING RISK, VERIFYING CLAIMS. Contrary to the directive, in which the scope of genetic tests covered was unclear, genetic tests with a direct or indirect medical purpose are undoubtedly covered by the proposed regulation (*6*). The proposed regulation includes, among others, self-tests performed in a home environment; DTC tests, results of which are delivered via the Internet; and software used for direct or indirect medical purposes of, among others, diagnosis, prediction, and prognosis of disease. The proposed regulation can only regulate devices, the framework used to put these devices into service, and the use of such devices but not services per se.

The proposed regulation will implement a new risk-based classification system for medical devices—increasing in risk from A, B, C, to D—based on the Global Harmonization Task Force model (*7*). All health-related human genetic tests will be classified as class C. All such tests offered outside a health care institution will be subject to premarket review by Notified Bodies [private commercial entities designated and monitored by competent authorities of member states (often ministries of health) in order to perform conformity assessment of medical devices]. This new risk classification is a major change from the current system, which uses a list-based classification system, criticized for not being updated regularly and for lacking coherence (e.g., tests for chlamydia were on the list, but none for other sexually transmitted diseases). Furthermore, because most health-related genetic tests were, by default, considered "low" risk, they only required a self-certification before market introduction.

Although similar to the existing directive in this regard, the proposed regulation further highlights the safety and performance of devices before they can be brought to market. This includes clarifying that devices should be suitable for their intended purposes, not compromise the safety or health of users, and achieve analytical and clinical performances intended by the manufacturer (e.g., How well does the test detect some genetic variant, and how well does the variant relate to specific disease?). Safety and performance claims made by manufacturers of medical devices are evaluated by Notified Bodies before the devices are placed on the market (*8*). The proposed regulation also places an added emphasis on the need to supply clinical evidence, which could be seen as an improvement; however, the fact that the evidence provided need only be limited to uses stated by the manufacturer is potentially problematic. For example, if the manufacturer claims to test the APOE gene for the purpose of identifying risk for hyperlipoproteinemia or cardiovascular disease, yet the alleles also potentially provide information for increased risk of late-onset Alzheimer's disease, is evidence only needed for the former?

Regarding enforcement, there is no centralized European body corresponding to the FDA, as implementation and enforcement of EU law lies with the authority of the member states. Once IVD medical devices are on the market, national competent authorities conduct market surveillance and enforcement and may take any actions necessary in order to prohibit or restrict market availability of a device deemed likely to cause risks to the health and safety of the public. If, after the European Commission evaluates these interim national measures, they are deemed to be justified, it may rule to have their uniform implementation across the EU (Article 72) (*3*).

REQUIRING A MEDICAL LINK. The proposed regulation foresees that health-related genetic testing may only be provided with a medical prescription. Furthermore, Amendment 271 states that genetic tests can only be ordered by "persons admitted to the medical profession under the applicable national legislation after a personal consultation" (*6*). Although some organizations have criticized this as being disproportionate (*9*), it is in line with article 7(1) of the Council of Europe Additional Protocol to the Convention on Human Rights and Biomedicine, concerning Genetic Testing for Health Purposes. It states that "a genetic test for health purposes may only be performed under individualized medical supervision" (*10*). Whereas EU member states can voluntarily adhere to the additional protocol, if this new regulation is accepted, this provision will become obligatory in all member states.

Beyond stating who should be allowed to order tests, the proposed regulation defines, in more detail, the way in which genetic tests should be provided. The same amendment describes the obligation to provide the test applicant "with appropriate information on the nature, the significance and the implications of the genetic test" (*6*). It underlines the necessity of "appropriate genetic counseling" before the provision of a genetic test, and that "the form and extent of this genetic counseling shall be defined according to the implications of the results of the test and their significance for the person or the members of his or her family" (*6*). Not all stakeholders are in agreement with this amendment. The European Society of Human Genetics has stated that it would be "unworkable in the daily practice of genetic medicine" and questions the EU's power to enact this article by highlighting that regulating how genetic tests are to be provided is "well beyond the scope of a Regulation on the safety of IVDs" (*11*).

Through this amendment, it is clear that the offer of health-related genetic testing services is perceived as necessitating the context of a medical relationship. This clearly opposes an approach where genetic test results are made directly available to consumers. Furthermore, by declaring illegal DTC advertising of prescription-only devices, including genetic tests, the proposed regula-

[1]Department of Public Health and Primary Care, University of Leuven, B-3000 Leuven, Belgium. [2]Center for Research Ethics and Bioethics, Uppsala University, SE-751 22 Uppsala, Sweden
*E-mail: pascal.borry@med.kuleuven.be.

Published by AAAS

tion could, in essence, ban DTC genetic testing as we have known it in Europe. Whether a website providing information regarding a genetic test is advertisement per se, or simply informational, may be debatable.

These articles in the proposed regulation are likely to strengthen the trend of DTC companies incorporating physicians into their model of test provision, as well as redirecting their advertising efforts (including continuing medical education) to health care professionals. This may present problems related to impartiality similar to those observed with prescription drugs, especially when clinicians are recruited, trained by, and often remunerated by the companies selling the services (*12*).

Inclusion of a health care professional, even a clinical geneticist, does not necessarily safeguard against all the concerns surrounding scientific validity or clinical validity raised by the proposed regulation and the FDA. Given the speeds at which new tests are being developed and at which new technologies allow for genotyping and sequencing, it is unreasonable to expect that simply adding a medical professional will solve all problems raised by DTC genetic testing. Not only are such professionals not currently prepared to interpret all genetic tests offered by DTC companies, but their involvement does not necessarily assure that tests offered will have appropriate quality and/or benefit to the users.

"If the proposed regulation is approved, it is not obvious that crossing the Atlantic will make it easier for companies."

Although a decision of the Council of the EU was originally planned before the May 2014 European elections, only a June 2014 meeting providing guidance for future work has taken place (*13*), with further debates and negotiations to follow. If the proposed IVD regulation is accepted by the Council, it will clearly affect the way genetic testing is being offered beyond the clinic. It will also potentially affect the clinicians who will be sought by consumers for genetic testing prescriptions. The future of European DTC genetic testing companies—and of non-European companies in the EU market—may also be heavily affected by coming policy decisions. For example, companies may want to broaden their sales outside the United States into foreign markets, in order to circumvent FDA demands. This was showcased recently when 23andMe announced it would resume selling its Personal Genome Service in Canada (*14*). If the proposed regulation is approved, it is not obvious that crossing the Atlantic will make it easier for companies (*15*). ■

REFERENCES AND NOTES

1. FDA, FDA to 23andMe, Inc., 22 November 2013 (FDA, Silver Spring, MD, 2014); www.fda.gov/iceci/enforcementactions/warningletters/2013/ucm376296.htm.
2. In June 2014, it was announced that the FDA would review a premarket 510(k) application for Bloom syndrome submitted by the company. Such an application for a single disorder could be considered much simpler than an application (or many applications) for genome-wide testing, from which results are returned for a multitude of phenotypes.
3. European Commission, Proposal for a regulation of the European Parliament and the Council on *in vitro* diagnostic medical devices (2012); http://ec.europa.eu/health/medical-devices/files/revision_docs/proposal_2012_541_en.pdf.
4. European Union, Regulations, Directives and other Acts; http://europa.eu/eu-law/decision-making/legal-acts/index_en.htm.
5. Council of the European Union, The decision-making process in the European Union (2014); www.consilium.europa.eu/council/decision-making-process?lang=en.
6. European Parliament, Amendments adopted by the European Parliament on 22 October 2013 on the proposal for a regulation of the European Parliament and of the Council on in vitro diagnostic medical devices [COM(2012)0541 – C7-0317/2012 – 2012/0267(COD)] (2013); www.europarl.europa.eu/sides/getDoc.do?type=TA&reference=P7-TA-2013-0427&language=EN&ring=A7-2013-0327.
7. Global Harmonization Task Force, *Principles of In Vitro Diagnostic (IVD) Medical Devices Classification* (SG1 Final Document GHTF/SG1/N045:2008, GHTF, 2008).
8. The main task of Notified Bodies is to analyze claims made by manufacturers. Notified Bodies do not assess whether a test has sufficient clinical utility to be offered to patients or individuals. The proposed regulation includes rules that aim to promote transparency and similar standards to be met by Notified Bodies during assessment.
9. P. Brice, EU legal amendments threaten genomic medicine and research (PHG Foundation, Cambridge, 2013); www.phgfoundation.org/news/14842/.
10. Council of Europe, *Additional Protocol to the Convention on Human Rights and Biomedicine, concerning Genetic Testing for Health Purposes* (2008); http://conventions.coe.int/Treaty/en/Treaties/Html/203.htm.
11. European Society of Human Genetics, New legal opinion finds EU does not have the power to enact radical genetic counselling laws (2014); https://www.eshg.org/fileadmin/eshg/documents/IVD/IVDLegalOpinionExecutiveSummaryApril2014.pdf.
12. H. C. Howard, P. Borry, *J. Community Genet.* **3**, 105 (2012).
13. Council of the European Union, 3323 Council Meeting, Employment, Social Policy, Health, and Consumers Affairs [press release] (2014); www.consilium.europa.eu/uedocs/cms_data/docs/pressdata/en/lsa/143271.pdf.
14. Canada News Wire, 23andMe announces new service for Canada [press release] (2014); www.bizjournals.com/sacramento/prnewswire/press_releases/California/2014/10/01/C2766.
15. S. Locke, The FDA won't let 23andMe test your genes—so it may go to Europe (2014); www.vox.com/2014/5/12/5709766/the-fda-wont-let-23andme-test-your-genes-so-it-may-go-to-europe.

ACKNOWLEDGMENTS

Part of this work was supported by a doctoral fellowship from the Research Foundation Flanders (FWO), the Swedish Foundation for Humanities and Social Sciences, the Biobanking and Molecular Resource Infrastructure of Sweden (BBMRI.se), and the CHIP ME COST Action IS1303.

10.1126/science.1256396

NEUROSCIENCE

To learn is to myelinate

The adult mammalian brain requires the production of new glial cells and myelin for learning

By **Patrick Long** *and* **Gabriel Corfas**

Learning triggers neuronal changes in the brain that contribute to information acquisition and memory formation, including the activity and strength of existing synapses, the formation of new synapses, and possibly the birth of new neurons (*1*). Therefore, it is not surprising that neurons have been seen as the sole components of the nervous system, capable of responding to experience and responsible for learning and long-term behavioral plasticity. However, this notion is being challenged by recent findings on glial biology. On page 318 of this issue, McKenzie *et al.* (*2*) add to this argument by revealing that the generation of new oligodendrocytes—one of the brain's non-neuronal cell types—is required for learning a complex motor skill. The finding advances our understanding of brain plasticity and points to roles for glia and myelin in cognitive function.

Oligodendrocytes generate myelin, the insulating membrane that covers many neuronal axons and facilitates the propagation of electrical signals along neuronal circuits. Although oligodendrocytes and the myelin they create were assumed to be static, recent studies indicate that myelin is much more malleable than once thought. Imaging studies have shown that various forms of learning correlate with structural changes in the human brain's white matter, and animal studies have demonstrated oligodendrocyte and myelin changes in response to social and environmental conditions (*3*). These observations raise the possibility that myelin is highly dynamic and that changes in myelination are important components of brain plasticity.

Oligodendrocytes send out multiple cellular processes that attach and ensheath axons with concentric layers of compacted cellular membrane to form myelin (see the figure). Myelination increases the speed by which electrical impulses travel along neuronal processes, and differences in the de-

Published by AAAS

gree to which axons are myelinated affect the timing of the flow of information between neurons. The composition of myelinated axons in the brain is heterogeneous; axons may be highly myelinated, not myelinated, or incompletely myelinated, and the pattern of myelination may vary along a single axon (*4*).

Most myelination in the mammalian brain occurs during early life. At that stage, oligodendrocyte progenitor cells (OPCs) give rise to oligodendrocytes, which go on to myelinate axons as they mature. Remarkably, a high density of OPCs remains in the adult brain long after the developmental period of myelination is complete. Adult OPCs retain the capacity to differentiate into myelinating oligodendrocytes in response to injury or demyelinating diseases, such as multiple sclerosis (*5*). These precursor cells may also give rise to newly generated oligodendrocytes to remodel myelin along previously myelinated axons in the adult brain (*6*).

Yet, the potential functional importance of this apparent reservoir of undifferentiated cells for plasticity in the normal brain has been a mystery. McKenzie *et al.* sought to determine whether adult-born oligodendrocytes are necessary for learning to occur. They observed that young adult mice that learn to run on a "complex running wheel" with irregularly spaced rungs have a transient elevation in OPC proliferation and production of adult-born oligodendrocytes in the corpus callosum, an axon-dense area of the brain connecting the two cerebral hemispheres. To analyze the contribution of new oligodendrocyte formation to motor learning, the authors used genetically modified mice in which they had eliminated the ability of OPCs to make new oligodendrocytes without affecting preexisting oligodendrocytes or myelin. They achieved this by inactivating the myelin regulatory factor (*Myrf*) gene in adult OPCs. *Myrf* encodes a protein required for OPCs to differentiate into mature myelinating oligodendrocytes. McKenzie *et al.* discovered that mice lacking the capacity to form new oligodendrocytes also failed to develop an effective running strategy in the complex running wheel. By contrast, when mice were allowed to train on the complex running wheel before *Myrf* inactivation, they performed comparably to normal control mice. This indicates that although the production of new oligodendrocytes is not required for information retrieval, it is critical for learning new motor behavior.

How is learning linked to changes in myelination? OPCs express numerous receptors that make them responsive to neurotransmitters. OPCs can also respond to neuron-derived mitogens and trophic factors such as neuregulin-1 (NRG1) and brain-derived neurotrophic factor (BDNF), whose release is modulated by neuronal activity. Interestingly, cell-culture experiments have shown that NRG1 and BDNF influence whether neuronal activity stimulates myelination (*7*). In vivo optogenetics studies have also shown that elevated neuronal activity increases OPC proliferation and oligodendrocyte number in an area of the brain involved in motor learning in vivo (*8*). Accordingly, neuronal circuits that are preferentially recruited during learning may signal to adjacent OPCs to differentiate into myelinating oligodendrocytes. This could lead to increased strength of connectivity and efficiency of information flow along circuits as a new motor behavioral pattern emerges. Thus, it is possible that activity-dependent myelination might be toggled on and off under different physiological contexts.

How might differences in myelin generation affect cognitive function more generally? And is myelin plasticity a universal aspect of learning or is it confined to systems involved exclusively in adaptive motor behaviors? The answers to these questions have broad implications for the understanding of how cognitive function is influenced by conditions that affect myelin. Several psychiatric illnesses, such as schizophrenia and bipolar disorder, are associated with defects in myelin (*9*). Moreover, myelin appears to be particularly vulnerable to adverse life experiences, such as social isolation (*10*, *11*). The discovery that new myelin generation is essential for learning may help explain some of the cognitive disturbances associated with psychiatric disorders or the absence of strong social support. Furthermore, the efficiency with which OPCs differentiate into myelinating oligodendrocytes appears to decrease with age (*12*), raising questions about how changes in myelin plasticity might contribute to age-associated cognitive decline.

The evidence that glia can be influenced by experience, and that this process is essential for behavioral changes and cognition, has brought us to an exciting paradigm shift that opens up a new vast frontier that might help to explain the mechanisms of learning. This may bring us closer to developing new treatments for neurological and neuropsychiatric disorders. ■

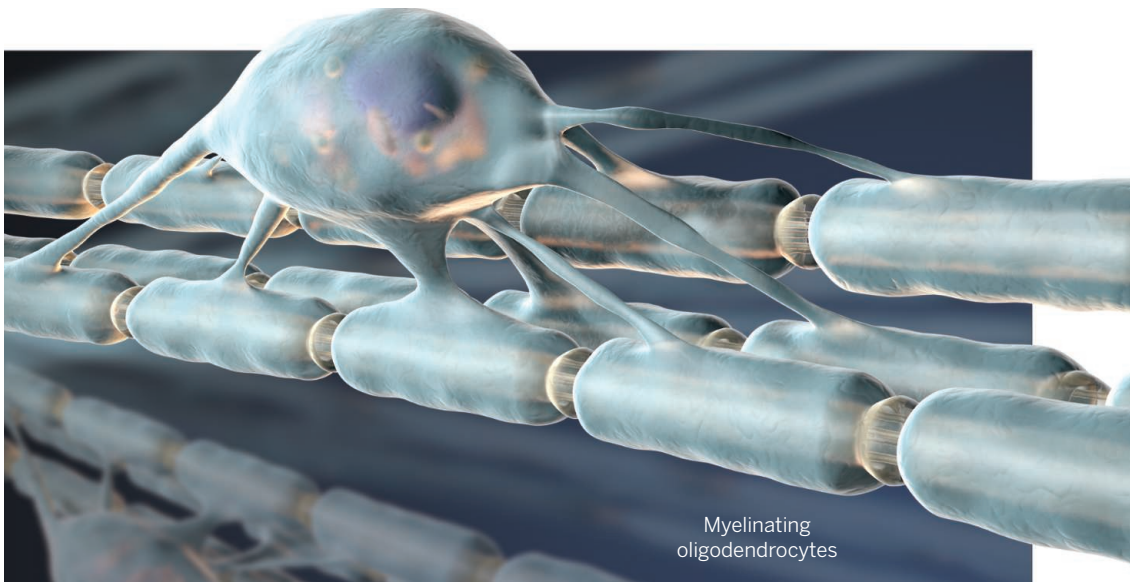

ILLUSTRATION: C. BICKEL/*SCIENCE*

Kresge Hearing Research Institute, The University of Michigan, 1150 West Medical Center Drive, Ann Arbor, MI 48109-5616, USA. E-mail: corfas@med.umich.edu

REFERENCES

1. A. Stuchlik, *Front. Behav. Neurosci.* **8**, 106 (2014).
2. I. A. McKenzie *et al.*, *Science* **346**, 318 (2014).
3. P. Long, G. Corfas, *JAMA Psychiatry* 10.1001/jamapsychiatry.2014.1049 (2014).
4. G. S. Tomassy *et al.*, *Science* **344**, 319 (2014).
5. H. Zuo, A. Nishiyama, *Neurosci. Bull.* **29**, 165 (2013).
6. K. M. Young *et al.*, *Neuron* **77**, 873 (2013).
7. I. Lundgaard *et al.*, Charles Ffrench-Constant, *PLOS Biol.* **11**, e1001743 (2013).
8. E. M. Gibson *et al.*, *Science* **344**, 1252304 (2014).
9. B. P. Sokolov, *Int. J. Neuropsychopharmacol.* **10**, 547 (2007).
10. M. Makinodan, K. M. Rosen, S. Ito, G. Corfas, *Science* **337**, 1357 (2012).
11. J. Liu *et al.*, *Nat. Neurosci.* **15**, 1621 (2012).
12. S. Shen *et al.*, *Nat. Neurosci.* **11**, 1024 (2008).

10.1126/science.1261127

Published by AAAS

PLANT SCIENCE

Nutrient computation for root architecture

Plants sense and respond to nutrients using a peptide signaling system

By Ton Bisseling[1,2] and Ben Scheres[3]

Nitrogen is a major limiting nutrient for plants. Root systems acquire nitrogen through uptake of nutrients such as nitrate from the soil. Some plants can also obtain nitrogen by establishing a root nodule symbiosis with N-fixing bacteria. Whatever the means to acquire nutrients, an investment of the plant is required in which root architecture is suitably adapted. Therefore, plants integrate local and global nutrient cues to spend resources efficiently. On page 343 in this issue, Tabata *et al.* (*1*) identify a peptide signaling mechanism by which the root locally senses N limitation in the soil, and communicates with the shoot, which then signals back to the root to stimulate lateral root growth in regions with a high nitrate content to facilitate nitrate uptake.

Nitrate, or other sources of nitrogen, can be distributed heterogeneously in the environment. Therefore, for optimal growth, it is essential that a plant can respond in a systemic manner to its global N status. Split root assays (see the figure, panel A) have been pivotal in unraveling the mechanisms that regulate this systemic control of lateral root organ formation (lateral roots and nodules). In these studies, the plant's root system is split into two and placed in separate compartments, where different nutrient levels can be applied. If conditions in compartment 1 induce a response in the root system in compartment 2, systemic communication through the shoot must have occurred.

When low nitrate (–N) is sensed, this locally reduces lateral root growth, but in the compartment with high nitrate (+N), lateral root elongation and nitrate uptake through nitrate transporters (NTRs) are stimulated (*1*–*3*). The stimulation of lateral root growth in the nutrient-rich compartment resembles the foraging behavior of roots toward soil patches with high nitrate. Tabata *et al.* demonstrate that precursors of C-terminally encoded peptide 1 (CEP1) are formed in *Arabidopsis thaliana* roots exposed to low N (see the figure, panel A). The authors used these peptides to screen a library of cultured plant cells expressing all known plant leucine-rich repeat receptor kinase (LRR-RK)–encoding genes and identified two homologous LRR-RKs that efficiently bind CEP1. When CEP1 was applied to the root system in one of the experimental compartments, it triggered increased NTR expression in the other, which required the two LRR-RKs that recognize CEP1. Exposure of roots to low N increased CEP1 levels in the xylem sap of the shoot, indicating that long-distance transport had occurred. Indeed, reciprocal grafting demonstrated that the systemic response required functional receptors in the shoot, but not in the root. The nature of the signal from the shoot that triggers lateral root foraging behavior in the +N compartment remains to be resolved.

Tabata *et al.* implicate CEP peptide signaling in the decision whether and when the plant should redirect growth under heterogeneous nutrient supply. Previous work indicates that local nutrient sensing is coupled to local inhibition of growth through nitrate transporter NTR1.1, which can also transport the growth hormone auxin (*3*). The auxin response in lateral root tips is diminished under nitrate-limiting conditions. It has been hypothesized that this contributes to reduced lateral root growth and is caused by auxin efflux activity of NTR1.1 (*3*, *4*). Furthermore, CEP peptides might—in addition to their long-distance signaling function—reduce lateral root growth at the site where they are produced, as overexpression of *CEP* genes is known to have this effect (*5*). From an engineering perspective, it makes perfect sense to decide centrally (in the shoot) whether the overall nutrient status is adequate, and then send systemic signals to stimulate growth everywhere except where the local inhibition system is active (see the figure, panels A and C).

It is interesting to consider that a peptide–LRR-RK relay also controls rhizobium-induced nodulation in legumes (see the figure, panel B). When one split-root

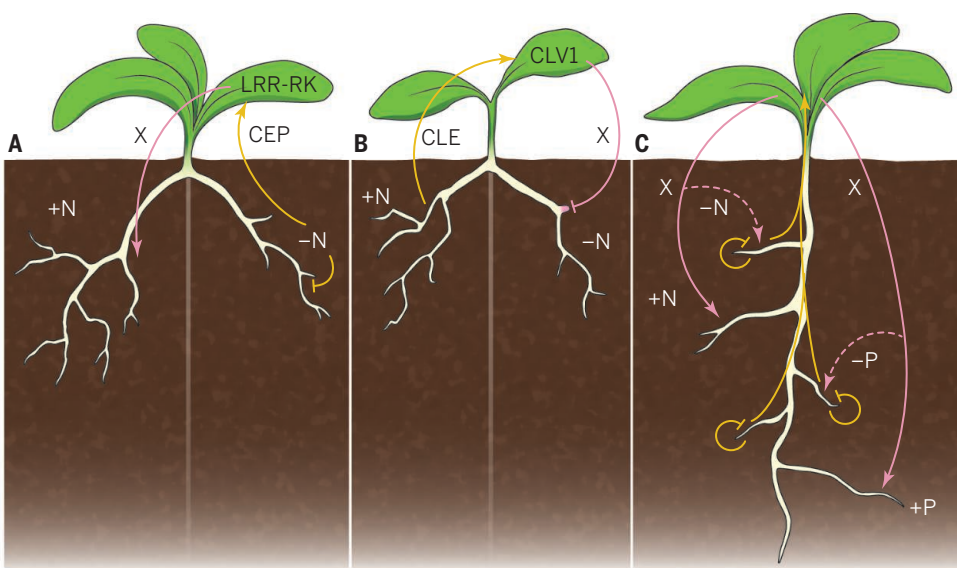

Sensing and responding to patchy nutrients. (**A**) Local N starvation inhibits lateral root growth and triggers production of CEP peptides; these are perceived in the shoot by LRR-RK receptors, leading to an unknown systemic signal X that can stimulate growth in high-N areas. (**B**) In legumes, local N supply triggers production of CLE peptides, which are perceived in the shoot by the CLV1 receptor, leading to an unknown systemic signal X that suppresses the formation of N-fixing root nodules. (**C**) A model of foraging behavior. Low nutrient concentration locally induces the production of a signal (peptide) that represses lateral root growth. In the shoot, the peptide induces production of a second signal (X) that stimulates lateral root growth in patches with high nutrient level, but cannot counteract the growth repression in lateral roots at low nutrient level. (N and P are example nutrients.)

ILLUSTRATION: P. HUEY/*SCIENCE*

[1]Department of Plant Sciences, Laboratory of Molecular Biology, Wageningen University, Droevendaalsesteeg 1, 6708 PB Wageningen, Netherlands. [2]College of Science, King Saud University, Post Office Box 2455, Riyadh 11451, Saudi Arabia. [3]Plant Developmental Biology, Wageningen University, Droevendaalsesteeg 1, 6708 PB Wageningen, Netherlands. E-mail: ton.bisseling@wur.nl

Published by AAAS

compartment contains a high (+N) and the other a low nitrate (–N) concentration, high nitrate is sensed and triggers repression of root nodule formation in both compartments (*6*). Roots exposed to +N produce a CLE (CLAVATA3/endosperm surrounding region–related) peptide that is translocated by the xylem in an arabinosylated form to the shoot (*7*), where it binds to the legume LRR-RK NARK [nodulation autoregulation receptor kinase, an ortholog of CLAVATA1 (CLV1)]. NARK is essential for CLE peptide–induced systemic suppression of nodulation in the roots. The nature of the shoot-derived compound suppressing lateral organ formation is not known.

It is possible that the CLE/CLV1 relay controlling nodulation has evolved from one controlling lateral root elongation. In *Arabidopsis*, overexpression of certain *CLE* genes inhibits lateral root growth in a CLV1-dependent manner. However, it remains to be demonstrated whether this inhibition is controlled by root- or shoot-located CLV1 (*8*).

There is ample evidence that the availability of multiple nutrients is assessed in plants and that their uptake systems interact with one another. Nitrate and phosphate levels can both trigger local growth responses and are subject to systemic control (*9*). Other important nutrients, such as potassium and sulfur, are also sensed, and this information is integrated in the overall response of the plant to nutrient status. The work of Tabata *et al.* shows that small-peptide signaling pathways play an important role in the process by which plants deal with trade-offs between nutrient demands. In addition, it suggests that plants use a general mechanism to compute multiple nutrient levels in the shoot and relay this information back to individual root tips. There, inhibition due to local nutrient deprivation might be balanced with activation signals that relay multiple global nutrient levels. Such a modular design might help to achieve optimal root foraging architecture under competing nutrient demands (see the figure, panel C). ■

REFERENCES AND NOTES

1. R. Tabata *et al.*, *Science* **346**, 343 (2014).
2. S. Ruffel *et al.*, *Proc. Natl. Acad. Sci. U.S.A.* **108**, 18524 (2011).
3. G. Krouk *et al.*, *Dev. Cell* **18**, 927 (2010).
4. T. Beeckman, J. Friml, *Dev. Cell* **18**, 877 (2010).
5. K. Ohyama *et al.*, *Plant J.* **55**, 152 (2008).
6. D. Reid *et al.*, *Ann. Bot. (Lond.)* **108**, 789 (2011).
7. S. Okamoto, H. Shinohara, T. Mori, Y. Matsubayashi, M. Kawaguchi, *Nat. Commun.* **4**, 2191 (2013).
8. T. Araya *et al.*, *Proc. Natl. Acad. Sci. U.S.A.* **111**, 2029 (2014).
9. D. P. Schachtman, R. Shin, *Annu. Rev. Plant Biol.* **58**, 47 (2007).

ACKNOWLEDGMENTS

T.B. is supported by ERC-2011-AdG29470. B.S. is supported by the NIRM consortium for stem cell research.

10.1126/science.1260942

ILLUSTRATION: C. SMITH/*SCIENCE*

CONSERVATION

Sensing biodiversity

Sophisticated networks are required to make the best use of biodiversity data from satellites and in situ sensors

By **Woody Turner**

Biodiversity loss is a global change with consequences that may exceed those of climate change (*1*). Yet, limited data on key aspects of biodiversity continue to constrain conservation efforts. Effective biodiversity conservation will require rapidly increasing understanding of the elements of biodiversity (such as the condition of ecosystems or the number and identities of species) and how they are changing through time. Satellite and airborne remote sensing are key to this effort but will only achieve their conservation potential when networked with in situ sensors (see the figure).

CONSERVATION SERIES

Remote sensing involves a wide array of tools and techniques on orbiting satellites and flying aircraft. It enables directly observing large-scale ecosystems and large organisms, depicting the broader environmental context for biodiversity, tracking climatic and other drivers of biodiversity change (often for use in ecological models), and making consistent observations across time and space for biodiversity monitoring (*2*). Remote sensing is increasingly complemented by in situ sensing with cameras on stationary objects or small drones, sound recorders, cell phones, electronic tags, and fragments of genetic material sampled directly from the environment.

INDIRECT REMOTE SENSING. Some biodiversity research and conservation efforts make good use of global satellite data that are recorded (typically for climate research) at spatial scales of 1 km or more (*3*). Most of these efforts involve indirect remote sensing of biodiversity. In this approach, climatic parameters like temperature, integrated vegetation measures such as vegetation indices, or observations of the three-dimensional structure of vegetation serve as inputs to models. Used either with species data in ecological niche models or with information about organismal physiology and/or demography in mechanistic models, remotely sensed data allow estimation of species distributions and abundance.

For example, Pearson *et al.* have used modeled climate variables and remotely sensed land cover and land surface data in a coupled ecological niche–demographic model to estimate climate change extinction risk with a mix of spatial and demographic variables (*4*).

Appropriate use of remote sensing data for species distribution modeling is challenging because it unites tools developed separately by geographers and ecologists. Doing so requires attention to sample sizes and characteristics of both remote sensing and ecological data, matching the scales of the observations and the phenomena under investigation, determining whether species absence information is needed, and defining clearly one's purpose for modeling (*5*).

DIRECT REMOTE SENSING. The scales of satellite data from climate research satellites are generally too coarse for direct observation of important elements of biodiversity. However, airborne instruments and a rapidly growing array of private-sector satellites, designed for online mapping, can directly sense and identify organisms, including large tree canopies and even big mammals and birds. These instruments have pixel sizes ranging from 50 cm to a few meters.

Fretwell *et al.* (*6*) used images from three such satellites to estimate the global population of emperor penguins. They found four new colonies and confirmed locations of three previously suspected sites while determining the total number of breeding colonies in an area of the world difficult to survey. A global population estimate for species of concern is a key conservation measure. Separating penguins, snow, shadow, and guano is unique to this and similar efforts, but the study is indicative of a growing body of work using remote sensing to distinguish organisms from their surroundings.

Very high spatial resolution sensors typically trade higher spatial resolution for much narrower coverage of Earth's surface, making it challenging to assemble global or even wide-area data sets. Also, the cost

Earth Science Division, NASA Headquarters, Washington, DC 20546-0001, USA. E-mail: woody.turner@nasa.gov

Published by AAAS

of these commercial data sets may stretch limited conservation budgets.

Imaging spectrometers or hyperspectral sensors provide very high spectral (as opposed to spatial) resolution. They generate essentially continuous spectra from visible to shortwave infrared wavelengths and have mostly flown aboard government or commercial aircraft. The spectra reflect the unique chemistries of canopy vegetation and marine phytoplankton at resolutions of meters to tens of meters. In the resulting compiled imagery, scientists can discriminate between ecological guilds and even genera and species on the ground and in the water (*7*, *8*), allowing these groups to be mapped and the composition and functioning of associated ecosystems to be delineated.

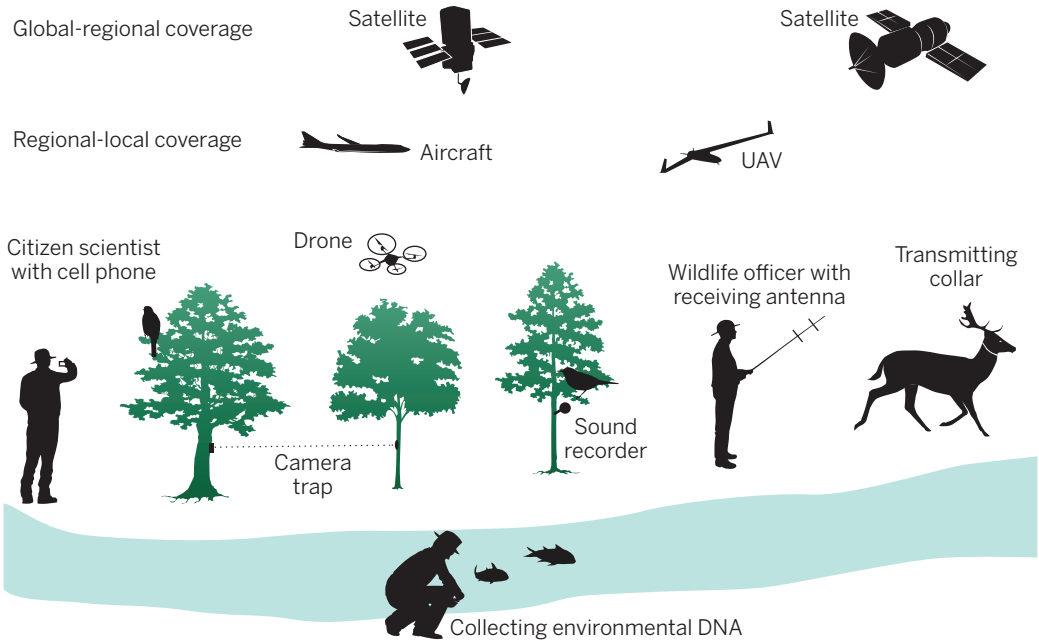

Sensor power. Networking satellite and airborne remote sensing with in situ sensing will allow changes in many elements of biodiversity to be tracked over time.

Recent combinations of imaging spectrometers and lidars or radars aboard aircraft have enabled simultaneous detection of vegetation biochemistry and its three-dimensional structure. Such combinations are powerful tools for discriminating species and ecosystem types and condition (*9*). Radar microwaves can travel through clouds, which often prohibit other forms of remote sensing in the biodiversity-rich humid tropics. At coasts, spectrometers and bathymetric lidars, incorporating water-penetrating green lasers, enable direct characterization of sea grasses, coral reefs, and other shallow benthic habitats (*10*). These airborne spectrometer-lidar/radar combinations may serve as precursors for orbiting biodiversity satellites that could offer detailed views of the composition, structure, and functioning of ecosystems.

IN SITU SENSING OF BIODIVERSITY. In parallel to advances in airborne and space-based sensing, developments in situ have also been dramatic. Transmission tags on terrestrial and aquatic animals, camera traps, sound recording devices, remotely piloted drones, and collections of environmental DNA in fresh and salt waters and soils are directly observing organisms, even the microbial components of biodiversity (*11*, *12*). These approaches also provide information on animal behavior, abundance, and community organization (*13*). The small size of these sensors, reflecting rapidly expanding computer and battery power, offers the potential for near-ubiquitous sensing of Earth's land- and seascapes. Citizen science further contributes to the growth in fine-scale biodiversity observations.

These in situ data provide insight at the levels of genes, species, and some ecosystems that remain hidden to remote sensing. In situ sensing thus brings critical fine-scale biodiversity information for use with the wider context and measures of environmental drivers obtained from remote sensing. It can also generate urgently needed time series of biodiversity observations, complementing remote-sensing time series of measures such as land cover and sea surface temperature that now span several decades.

NETWORKING NEEDS. The data from satellites, aircraft, and in situ sensors cover a vast range of spatial scales. Use of these sensing data in concert requires sophisticated networking and geostatistical analysis to fill gaps between fine-scale organismal or genetic observations and ecosystem-scale observations. Similar networks are necessary to tie biodiversity observations to data on broader environmental drivers of change.

Scale is not the only issue. The multitude of sensor types used to measure elements of biodiversity even at the same spatial scale further complicates networking, as does the integration of information from models. All observations and models come with their individual uncertainties, which must be addressed by any networking framework.

The first programmatic networks of this kind are now being created. In the United States, the National Ecological Observatory Network (NEON) proposes linking in situ sampling at sites around the country with airborne and satellite remote sensing, although the satellite component still needs to be designed. The international Group on Earth Observations (GEO) partnership, particularly its global Biodiversity Observation Network (GEO BON), is a first attempt by national governments to jointly coordinate satellite, airborne, and in situ observations across biodiversity elements through genes, species, and ecosystems (*14*). This effort is crucial for meeting governments' obligations to assess national biodiversity under the Convention on Biological Diversity and the Intergovernmental Platform on Biodiversity and Ecosystem Services. ■

REFERENCES

1. J. Rockstrom *et al.*, *Nature* **461**, 472 (2009).
2. N. Horning, J. A. Robinson, E. J. Sterling, W. Turner, S. Spector, *Remote Sensing for Ecology and Conservation* (Oxford Univ. Press, New York, NY, 2010).
3. N. Pettorelli *et al.*, *J. Appl. Ecol.* **51**, 839 (2014).
4. R. G. Pearson *et al.*, *Nat. Clim. Change* **4**, 217 (2014).
5. A. F. Cord, R. K. Meentemeyer, P. J. Leitao, T. Vaclavik, *J. Biogeogr.* **40**, 2226 (2013).
6. P. T. Fretwell *et al.*, *PLOS ONE* **7**, e33751 (2012).
7. G. P. Asner *et al.*, *Proc. Natl. Acad. Sci. U.S.A.* **111**, 5604 (2014).
8. E. Organelli *et al.*, *Appl. Opt.* **52**, 2257 (2013).
9. A. Swatantran *et al.*, *PLOS ONE* **7**, e28922 (2012).
10. L. M. Wedding, A. M. Friedlander, M. McGranaghan, R. S. Yost, M. E. Monaco, *Remote Sens. Environ.* **112**, 4159 (2008).
11. J. P. Dandois, E. C. Ellis, *Remote Sens. Environ.* **136**, 259 (2013).
12. P. F. Thomsen *et al.*, *PLOS ONE* **7**, e41732 (2012).
13. A. S. Stoeger, M. Zeppelzauer, A. Baotic, *Bioacoustics* **23**, 231 (2014).
14. R. J. Scholes *et al.*, *Curr. Opini. Environ. Sustain.* **4**, 139 (2012).

10.1126/science.1256014

ILLUSTRATION: P. HUEY/*SCIENCE*

Published by AAAS

BIOCHEMISTRY

Potassium ions line up

Do K^+ ions move in single file through potassium channels?

By **Gerhard Hummer**

Potassium channels are involved in many biological functions, most notably the generation and shaping of electrical signals in neurons. These transmembrane proteins function by conducting potassium ions selectively across biological membranes. On page 352 of this issue, Köpfer *et al.* (*1*) report molecular dynamics simulations of ion conduction through potassium channels. The results challenge the established picture derived from x-ray crystallography (*2*, *3*), electrophysiology (*4*), and earlier simulations (*5*, *6*).

In their classic 1955 study, Hodgkin and Keynes (*7*) proposed that potassium ions move through the channels "in single file along chains of potassium-selective sites." In this "knock-on" mechanism, conduction occurs as the chain of ions moves back and forth, picking up and releasing ions on opposite sides. This mechanism ensures both high selectivity for K^+ ions and high conductance despite high affinity.

This simple picture of ion conduction was spectacularly confirmed more than four decades later by the potassium channel crystal structures of MacKinnon and collaborators (*2*, *3*). These structures showed a distinct chain of four ion-binding sites inside the cylinder-shaped selectivity filter (see the figure, panel A). However, the crystal structures also put a twist on the original knock-on mechanism: Instead of forming a continuous chain, ions alternate with intervening water molecules that weaken the large Coulomb repulsion in direct cation contacts (*3*).

Molecular dynamics simulations have corroborated this picture and further elucidated the energetics and dynamics of ion transport (*5*, *6*). In these simulations, chains of alternating K^+ ions and water molecules cross the selectivity filter in a highly concerted fashion: An ion arriving on one side pushes the entire chain forward to the other side, resulting in release of water and ions (see the figure, panel B).

Köpfer *et al.* (*1*) challenge this picture. In extensive molecular dynamics simulations of K^+ conduction through various potassium channels, they find that K^+ ions contact each other directly along the single file (see the figure, panel C); intervening water molecules appear only rarely. The authors argue that the direct Coulomb repulsion between contacting cations enhances ion conductance. In effect, they suggest a return to the original model (*7*), with the "hard" knock-on of approaching ions not softened by intervening water. Earlier molecular dynamics simulations also point toward direct K^+-K^+ contacts. Free energy calculations have shown that cation pairs moving through the selectivity filter without intervening water molecules are energetically feasible (*8*), the Coulomb repulsion being counteracted by the negatively charged carbonyl oxygen atoms (see the figure). Jensen *et al.* recently performed long simulations of dynamic ion transport driven by an external electric field (*9*). They found that only half the number of water molecules expected from perfect alternation of ions and water was transported with the potassium ions.

However, the results of Köpfer *et al.* do appear to conflict with experimental results. The selectivity filter in their simulations tends to be filled with three ions over a wide range of potassium concentrations. In contrast, the crystal structures obtained in this concentration regime have pointed to alternating cations and water molecules. To resolve this conflict, Köpfer *et al.* re-refined the crystal structures, concluding that the x-ray data are indeed consistent with single-file chains of cations in direct contact.

Direct ion contacts also seem to be inconsistent with electrophysiological data. Potassium channels conduct water (*10*); measurements of streaming potentials, created by ions carried along in osmotically driven water flows through the channel, point to cotransport of at least one water molecule per ion (*4*). Given the distinct predictions for water cotransport with and without interstitial water in the ion chains, firming up the measured numbers should go a long way toward resolving the issue.

Not long ago, such molecular dynamics results might well have been brushed aside. Now simulations are taken seriously thanks to rapid improvements in the quality of the models, the extent of the sampling, and the realism of simulated experimental setups. Despite remaining challenges, not least concerning the force fields used to describe the molecular interactions, experimentalists would do well to heed Köpfer *et al.*'s results. ■

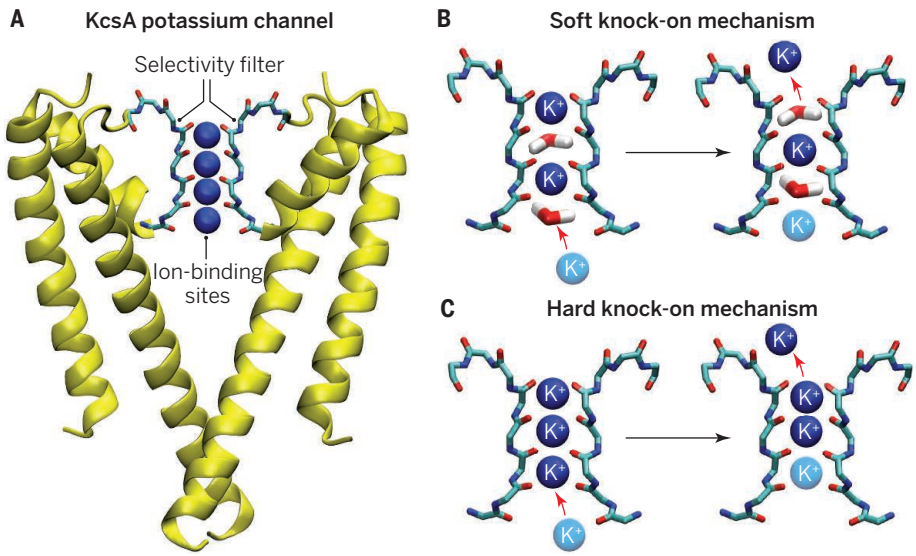

Knock-on mechanism. (**A**) A cut through the KcsA potassium channel (*3*) shows the ion-binding sites (blue) in the selectivity filter. (**B**) In the soft, water-mediated knock-on mechanism, approaching ions (light blue) alternatingly knock-out water and K^+ ions. (**C**) Köpfer *et al.* find that the filter is instead densely packed with a chain of K^+ ions in direct contact.

Department of Theoretical Biophysics, Max Planck Institute of Biophysics, 60438 Frankfurt am Main, Germany. E-mail: gehummer@biophys.mpg.de

REFERENCES AND NOTES

1. D. A. Köpfer *et al.*, *Science* **346**, 352 (2014).
2. D. A. Doyle *et al.*, *Science* **280**, 69 (1998).
3. J. H. Morais-Cabral *et al.*, *Nature* **414**, 37 (2001).
4. M. Iwamoto, S. Oiki, *J. Neurosci.* **31**, 12180 (2011).
5. S. Bernèche, B. Roux, *Nature* **414**, 73 (2001).
6. J. Åqvist, V. Luzhkov, *Nature* **404**, 881 (2000).
7. A. L. Hodgkin, R. D. Keynes, *J. Physiol.* **128**, 61 (1955).
8. S. Furini, C. Domene, *Proc. Natl. Acad. Sci. U.S.A.* **106**, 16074 (2009).
9. M. Ø. Jensen *et al.*, *J. Gen. Physiol.* **141**, 619 (2013).
10. T. Hoomann, N. Jahnke, A. Horner, S. Keller, P. Pohl, *Proc. Natl. Acad. Sci. U.S.A.* **110**, 10842–10847 (2013).

ACKNOWLEDGMENTS

Supported by the Max Planck Society.

10.1126/science.1260555

Published by AAAS

OPTICS

In optical pumping, less can be more

Creating loss in one optical resonator can initiate lasing in its coupled partner

By **Harald G. L. Schwefel**

Lasing is based on the process of optical gain. Once this gain provided through external pumping surpasses the loss in a resonator, lasing sets in and a coherent beam of laser light is emitted. Thus, loss is a natural adversary of lasing, at least in common lasers. A striking amendment to this rule is reported on page 328 of this issue by Peng *et al.* (*1*), who report an onset of lasing in a pair of coupled resonators when the total loss of the system is increased.

This special feature is possible because of the non-Hermitian nature of the system designed by Peng *et al.*, a property related to the Hamiltonian description that physicists use to calculate the time evolution of a system. When such a Hamiltonian is Hermitian, it means that the total energy is conserved, leading to real eigenvalues for the energy (as, for example, the energy of electrons in an atom). However, many realistic systems do not conserve energy. The corresponding gain and loss processes can be modeled through Hamiltonians that are non-Hermitian and which will generally have complex eigenvalues. A particular example is a laser, which features an amplifying medium (through optical gain) and radiates out a coherent laser beam (causing loss).

The physics that follows from such non-Hermitian properties shows several counterintuitive features, especially near so-called "exceptional points" (EPs) in parameter space, where two complex eigenvalues coalesce in both their real and imaginary parts. Recently, a specific subset of non-Hermitian systems with a so-called parity-time (PT) symmetry have surfaced for which the gain and the loss are carefully balanced so that the eigenvalues end up on the real axis (*2*). For such cases, surprising experimental results, such as loss-induced transparency (*3*), unidirectional invisibility (*4*), and optical isolation (*5*) have been demonstrated.

These PT-symmetric systems are, however, only a subset of the general class of non-Hermitian systems for which the eigenvalues reside in the complex plane. In particular, for systems operating near the lasing threshold, theoretical proposals indicate phenomena occurring near an EP, such as coherent perfect absorption of light (*6*) and the loss-induced onset of lasing (*7*) studied here. To venture experimentally through the vicinity of the EP, typically two independent parameters are necessary. Such parameters are accessible by coupling whispering gallery mode resonators, which efficiently trap light via total internal reflection at the rim of a convex shape made from a dielectric material (such as silica). When two spectrally identical optical resonators couple, they form a "photonic molecule," in that individual modes undergo a mode splitting similar to the transition for electronic levels when atoms form molecules (*8*, *9*). In the optical domain, individual tuning of the resonators is necessary to achieve degenerate modes and coupling between both resonators (*5*). The two independent parameters are the coupling strength, as determined by the distance between the two resonators, and the loss added by an absorptive nanotip probe in the vicinity of one of the resonator's evanescent field. Tuning of these two parameters allows the system to approach the EP.

Peng *et al.* used coupled whispering gallery mode resonators as a convenient platform to study several of the fascinating phenomena arising in the vicinity of an EP (*7*). When they brought two resonators near each other, the individual resonance modes split and supermodes formed with slightly detuned resonance frequencies (see the figure). When additional loss was induced by the optically absorbing nanotip, the resonance frequencies, given by the real part of the eigenvalues, lost their detuning when passing the EP. At this point, the imaginary parts of the eigenvalues, which describe the loss or gain of the mode, acquired a detuning at the EP that resulted in one of the two resonant modes experiencing less loss than the other. This imbalance is a direct consequence of the field distributions of the modes no longer being equally distributed between both resonators. Rather, with increasing nanotip loss, each mode is increasingly concentrated in one of the resonators alone.

To show the most striking effect resulting from this mode rearrangement at an EP, Peng *et al.* took advantage of silica microtoroids' ability to provide Raman gain when pumped by an appropriately offset pump laser (*10*). With this additional feature, the

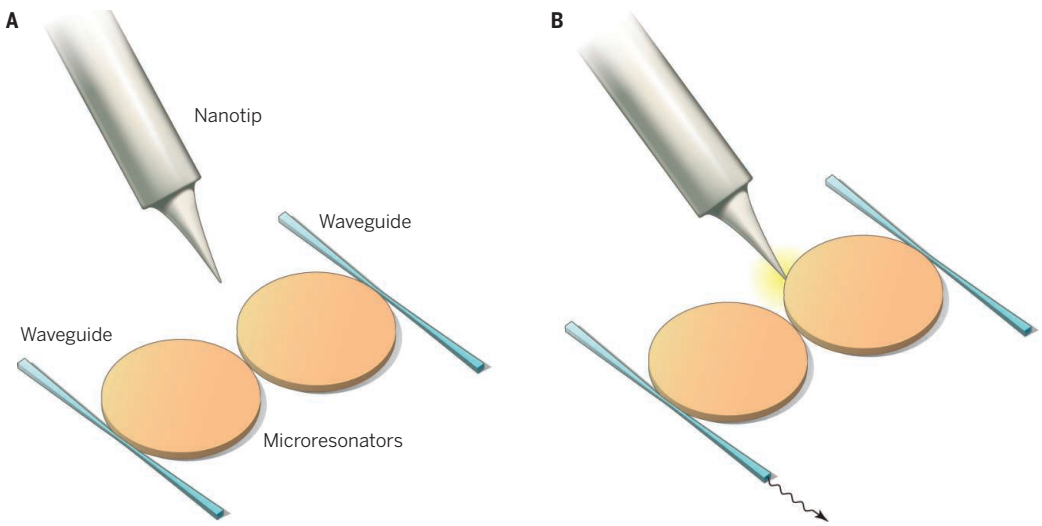

An odd laser at a loss. (**A**) Two coupled microresonators initially exhibit no lasing. (**B**) By increasing the loss in one microresonator through coupling to a nanotip (in silver), the other microresonator can suddenly start to lase (the light is coupled to the optical waveguides shown in blue). Peng *et al.* show how these effects are caused by the non-Hermitian nature of the system.

ILLUSTRATION: P. HUEY/*SCIENCE*

Max Planck Institute for the Science of Light & Institute for Optics, Information and Photonics, Friedrich-Alexander University of Erlangen-Nuremberg, 91058 Erlangen, Germany. E-mail: harald.schwefel@mpl.mpg.de

Published by AAAS

two coupled resonators were operated near the lasing regime. When adding loss by the nanotip, the detuning in the imaginary part of the eigenvalues reduced the loss of the mode in the resonator without the nanotip up to the point where the lasing threshold was reached, and the coupled system experienced a loss-induced onset of lasing.

The observation and control of an EP for a laser opens the way toward many further studies such as on self-pulsation effects in the temporal dynamics of the laser (*11*). A way to explore the fascinating topological aspects of EPs is to encircle them in the two-dimensional parameter space, parameterized by the nanotip-induced loss and the coupling strength. In passive resonators, a curious mode exchange and the accumulation of a geometric phase have been observed for this situation (*12*). How these phenomena translate to the lasing regime, where nonlinear mode interactions also play a role, is still an open question that may occupy both theorists and experimentalists in the years ahead.

"The observation and control of an exceptional point for a laser opens the way toward many further studies..."

Even beyond lasing, non-Hermitian systems can be found in many other contexts. In optical sensing, EPs can enhance single-particle detection (*13*), and in optomechanical systems, they can enable applications such as a phonon laser (*14*). Similar non-Hermitian concepts have even been applied to finance, where non-Hermitian Hamiltonians are used to describe stochastic financial instruments with striking effects that just wait to be explored. ■

REFERENCES

1. B. Peng *et al.*, *Science* **346**, 328 (2014).
2. C. M. Bender, S. Boettcher, *Phys. Rev. Lett.* **80**, 5243 (1998).
3. A. Guo *et al.*, *Phys. Rev. Lett.* **103**, 093902 (2009).
4. A. Regensburger *et al.*, *Nature* **488**, 167 (2012).
5. B. Peng *et al.*, *Nat. Phys.* **10**, 394 (2014).
6. Y. D. Chong, L. Ge, A. D. Stone, *Phys. Rev. Lett.* **106**, 093902 (2011).
7. M. Liertzer *et al.*, *Phys. Rev. Lett.* **108**, 173901 (2012).
8. S. Preu *et al.*, *Opt Exp.* **16**, 7336 (2008).
9. S. V. Boriskina, *Opt. Lett.* **31**, 338 (2006).
10. L. Yang, T. Carmon, B. Min, S. M. Spillane, K. J. Vahala, *Appl. Phys. Lett.* **86**, 091114 (2005).
11. H. Wenzel, U. Bandelow, H.-J. Wünsche, J. Rehberg, *IEEE J. Quantum Electron.* **32**, 69 (1996).
12. C. Dembowski *et al.*, *Phys. Rev. Lett.* **86**, 787 (2001).
13. J. Wiersig, *Phys. Rev. Lett.* **112**, 203901 (2014).
14. H. Jing *et al.*, *Phys. Rev. Lett.* **113**, 053604 (2014).

10.1126/science.1260707

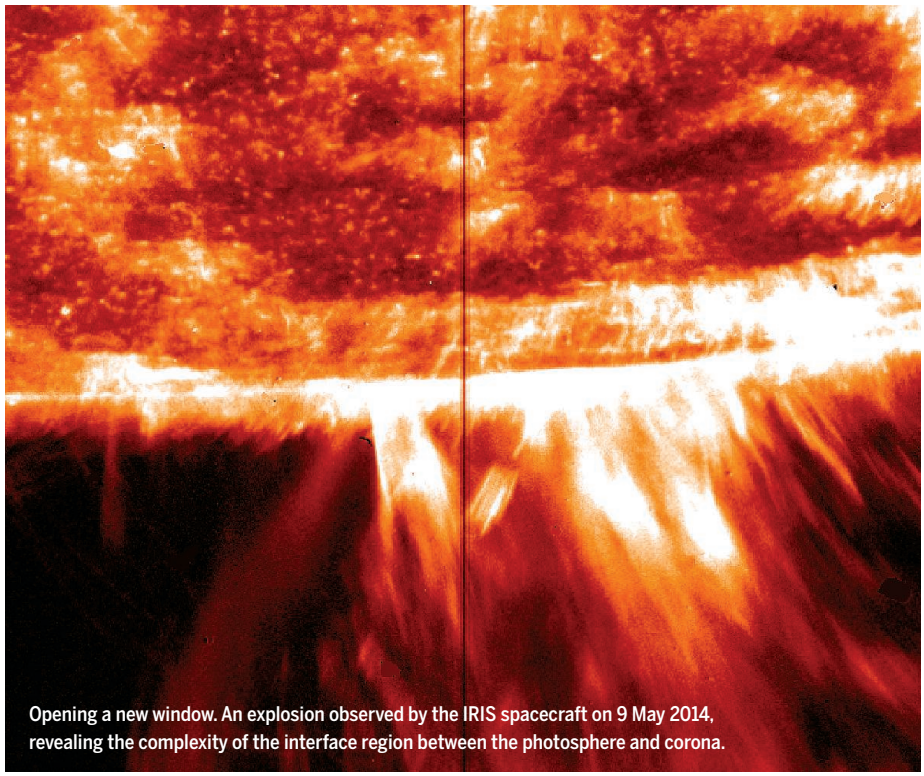

Opening a new window. An explosion observed by the IRIS spacecraft on 9 May 2014, revealing the complexity of the interface region between the photosphere and corona.

PHOTO: NASA/IRIS

ASTRONOMY

Looking closer at the Sun

The space-based IRIS telescope provides a new window to view the solar atmosphere

By **Louise K. Harra**

The Sun's atmosphere is a dramatic and dynamically changing one. The physical domains encountered as the atmosphere is explored from the Sun's surface to the outer corona differ widely. The region where the differences are more notable is the interface region, where the plasma characteristics change from optically thick to optically thin and the regime goes from gas-dominated to magnetic-dominated. NASA's Interface Region Imaging Spectrograph (IRIS) (*1–5*) is now observing this elusive region. The first results from the mission are showing a world of twisted magnetic fields throughout the region, "bombs" exploding at regular intervals, evidence of particle acceleration causing heating in coronal loops, and small jets and loops appearing at cool temperatures. These results are providing important input into how the solar atmosphere is created and maintained and how the solar wind is formed.

The Sun is the largest object in the solar system, providing the heat and light that allows us to survive. It is a middle-aged star that produces energy through nuclear fusion of hydrogen to helium at its core. The enormous energies propagate through the interior of the Sun by radiation and convection. In the convection zone, the churning hot plasma creates magnetic fields. Our first view of the energy escaping the Sun is at the surface (the photosphere). Here, evidence of the convection that occurs in the interior is seen—the magnetic fields that appear help to form the heliosphere within which the planets are shrouded. The heliosphere drives the solar wind that flows past our planet, and is the source of large explosions that can affect our delicate Earth environment.

The magnetic fields are the source of the "coronal heating problem": As you move away from the Sun's surface (and farther from the heat source in the core), the tem-

Mullard Space Science Laboratory, University College London, Holmbury St. Mary, Dorking, Surrey RH5 6NT, UK. E-mail: l.harra@ucl.ac.uk

Published by AAAS

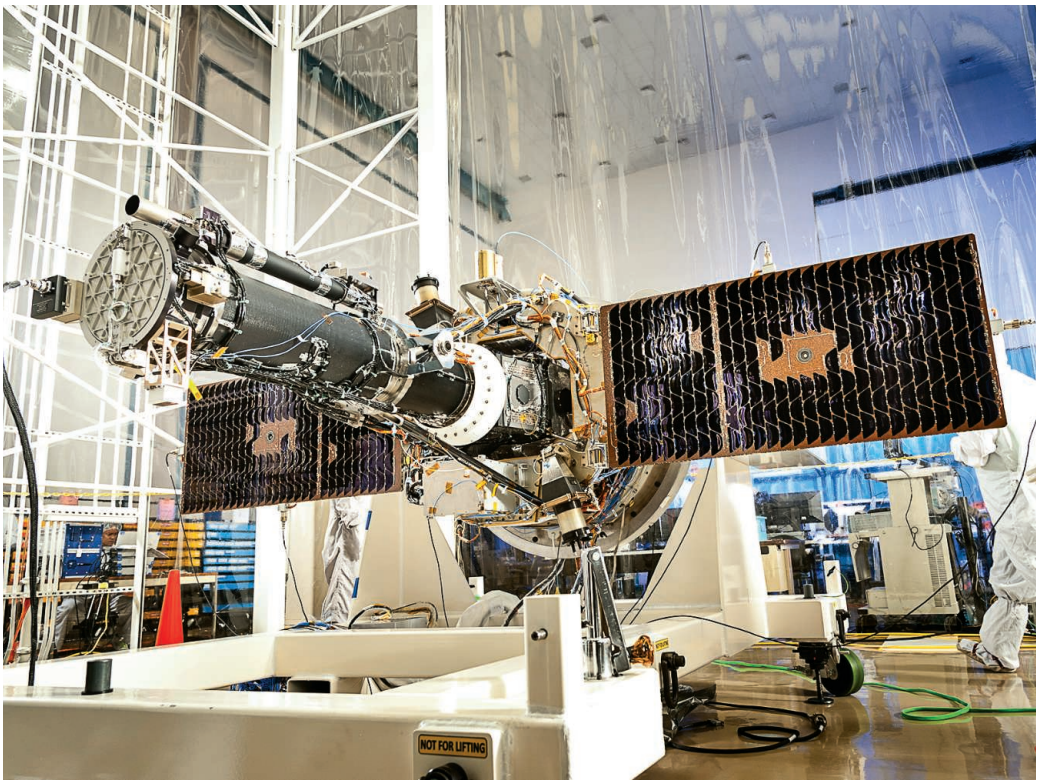

Preparing for launch. Interface Region Imaging Spectograph (IRIS) with solar wings deployed in the clean room.

perature increases. The goal for solar physicists is to determine how the Sun produces winds with speeds that can be 50 times those of the most powerful hurricanes on Earth, and can create energetic flares that release tens of millions of times the energy of a hydrogen bomb. Although the magnetic field is known to be key to this understanding, the actual details of the energy transfer through the solar atmosphere have so far remained unclear.

IRIS, launched in June 2013, is the latest in a line of solar observatories that are exploring the Sun's interface region. It is a 20-cm telescope that observes near- and far-ultraviolet light from the Sun, which is normally blocked by Earth's atmosphere. It was designed to explore spectroscopically the elusive interface region of the Sun's atmosphere between the surface of the Sun (photosphere) and the outer hot atmosphere (the corona). This region has been difficult to observe because it goes from being optically thick to optically thin, from partially to fully ionized, and from gas to magnetic domination. In recent years, advances in computation have permitted the development of 3D radiative magnetohydrodynamic models that can provide insight into the observations made by IRIS.

IRIS has exceptional spatial resolution. With its spectroscopic capability focused on the interface region, it can probe the hot plasma to determine parameters such as temperature, speed, turbulence, and density. The example image of a large explosion at the solar limb reveals the incredible complexity of the Sun's atmosphere (see the first figure). The first results from IRIS address some of the key unsolved questions in solar physics.

The high-resolution IRIS observations have revealed red- and blue-shifted plasmas that exist parallel and adjacent to each other (*2*). The evidence for twist or torsional motions is seen in every magnetic domain on the Sun, from the quietest region to the larger active region, and even in coronal holes where the magnetic field is dominantly open. Evidence of the magnetic fields being so twisted provides insight into how energy is created and how rapid heating is associated with these regions of strong twist. Another phenomenon that has been revealed for the first time is that of very short, low-lying magnetic loops in the quiet Sun (*1*), settling a debate about their existence that had been raging for many years. The measurements show that this emission cannot be accounted for just by thermal conduction back from the hot corona. These loops are short and dense and can lose their energy effectively through radiation. They are also found to occur naturally in advanced 3D magnetic models that have recently become available. IRIS observations in coronal holes have also uncovered frequent high-speed small jets (*5*) that are located in the network structures that highlight the convective cells. These fast jets may contribute plasma to the solar wind.

IRIS has also explored the larger regions of strong magnetic field, called active regions. In a newly created active region, Peter *et al.* (*3*) found small regions of plasma within the active region that reach temperatures of 100,000 K and are embedded in a region of much lower temperature. They are found in small regions where magnetic flux of opposite polarity converges, and evidence of a bidirectional jet is seen, where the magnetic field lines that are being pushed together squeeze the plasma in both directions. These "bombs" that are firing off have much greater energies than previously expected.

In active regions, the dominant features in the atmosphere are the long magnetic loops stretching from one polarity region to another. Testa *et al.* (*4*) found rapid variability at the footpoints of these loops, and investigated what could create these. They found them to be heated by accelerated beams of nonthermal particles, which are generated in very small-scale flares called nanoflares. Through comparison with advanced numerical models, they have developed diagnostics that can probe the nonthermal characteristics of the smallest-scale particle acceleration ever observed. This provides much-needed constraints on models of how these particles are accelerated to such high energies—a process that is expected to occur throughout the universe in other, more distant, astrophysical phenomena.

The early results reported by the IRIS mission show the power of spectroscopy in terms of understanding energy sources on the Sun. All the phenomena described so far are low-energy or small-scale phenomena. With the Sun close to reaching a maximum in activity, IRIS observations will continue to be important to our understanding of the solar wind that emanates from the active latitudes, solar flares, and coronal mass ejections. ■

REFERENCES

1. V. Hansteen *et al.*, *Science* **346**, 1255757 (2014).
2. B. De Pontieu *et al.*, *Science* **346**, 1255732 (2014).
3. H. Peter *et al.*, *Science* **346**, 1255726 (2014).
4. P. Testa *et al.*, *Science* **346**, 1255724 (2014).
5. H. Tian *et al.*, *Science* **346**, 1255711 (2014).

10.1126/science.1260828

PHOTO: JIM DOWDALL/LOCKHEED MARTIN

Published by AAAS

LETTERS

Edited by **Jennifer Sills**

Before the Kardashian Index

IN HER IN DEPTH News feature "Who are the science stars of Twitter?" (19 September, p. 1440), J. You explores the so-called Kardashian Index, defined as the number of followers a scientist has on the social media platform Twitter relative to their academic citation count. While this may provide insight into the profile of scientists engaging in this type of science communication, such an approach misses a larger and much more pressing problem. Although a growing number of scientists are engaging social media as a means of science communication, little information is available on whether it's actually worth our time.

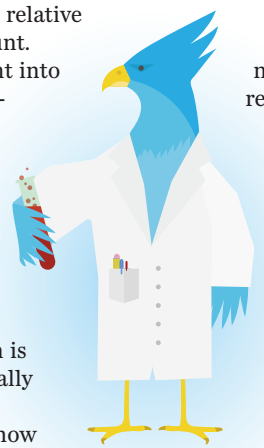

We are largely ignorant of how many people we actually reach, whom we are reaching, and whether or not 140 characters is sufficient to actually change their knowledge about, or attitudes toward, science. However, early evidence suggests that rather than communicating with a broader public, scientists using social media are largely communicating with one another (*1*). Moreover, social media may not even be the most effective means by which to promote meaningful engagement in science, as compared with other web-based approaches (*2*). Until we have a more complete body of research, perhaps we should withhold judgment on whether there is value to actually being a "Science Kardashian."

Gregory R. Goldsmith

Paul Scherrer Institute, 5232 Villigen PSI, Switzerland. E-mail: gregory.goldsmith@psi.ch

REFERENCES

1. E. S. Darling *et al.*, *Ideas Ecol. Evol.* **6**, 32 (2013).
2. G. R. Goldsmith *et al.*, *Ecosphere* (2014); http://dx.doi.org/10.1890/ES14-00206.1.

Nuanced negative result reporting

A. FRANCO, N. MALHOTRA, and G. Simonovits ("Publication bias in the social sciences: Unlocking the file drawer," Reports, 19 September, p. 1502) present convincing evidence of publication bias in the social sciences. Encouraging publication of negative results will indeed benefit the research community, but the proposed solution of creating repositories or new dissemination channels may do little to dent the "file-drawer" problem of selective reporting of research results.

Preregistration and protocols may prove unrealistic as data sets become larger and richer and data-mining techniques—for better or worse—increasingly supplement the classical single-hypothesis/experiment framework (*1*). Moreover, we have learned from experience that building a new reporting channel will not, in itself, mainstream reporting of negative results (*2*). Technical advances have removed some of the obstacles to the publication of negative results. Digital dissemination is not constrained by the availability of trees. Computational preprocessing—that is, machine sorting of large volumes of text to highlight interesting patterns that can then be checked by a skilled human researcher—may enable us to read and sort through quantities of findings we previously could not handle. For example, researchers from Baylor College of Medicine recently used an automated system to scan 23 million Medline papers and identify more proteins to target for cancer research than human medical researchers typically do in a year (*3*).

However, technology adoption and institutional reform get us only so far. Innovation, incentives, and penalties must go hand in hand with a normative basis for publishing negative results (*4*), and with clear criteria and standards for evaluating them. King notes that it may be difficult to distinguish more from less useful negative results (*5*), but it is not impossible. We must develop a more nuanced view of when, why, and how to report informative null results (*6*).

A single result may contain little truth but much information—even information about what does not work—which moves science forward. A so-called weak result, seen in context, may prove a more valuable, informative contribution than a so-called strong result in isolation.

Stefan K. Lhachimi,[1]* David Lehrer,[2] Janine Leschke,[3] Moira Nelson,[4] Brigitte Weiffen[5]

[1]Research Group for Evidence-Based Public Health, University Bremen and Leibniz-Institute for Prevention Research and Epidemiology BIPS, 28359, Bremen, Germany. [2]Department of Political and Economic Studies, University of Helsinki, 00014, Helsinki, Finland. [3]Department of Business and Politics, Copenhagen Business School, 2000, Frederiksberg, Denmark. [4]Department of Political Science, Lund University, 22100, Lund, Sweden. [5]Institute of International Relations, University of São Paulo, 05508-020, São Paulo, Brazil.

*Corresponding author. E-mail: Stefan.Lhachimi@uni-bremen.de

REFERENCES

1. D. Lazer *et al.*, *Science* **323**, 721 (2009); published online 6 February 2009.
2. D. Lehrer, J. Leschke, S. Lhachimi, A. Vasiliu, B. Weiffen, *Bull. Méthodol. Sociol.* **94**, 95 (2007); published online 1 April 2007.
3. B. Saporito, "IBM Watson's Startling Cancer Coup," Time (28 August 2014); http://time.com/3208716/ibm-watson-cancer/.
4. J. Couzin-Frankel, *Science* **342**, 68 (2013); published online 4 October 2013.
5. J. Mervis, *Science* **345**, 992 (2014); published online 29 August 2014.
6. D. Lehrer, J. Leschke, S. Lhachimi, A. Vasiliu, B. Weiffen, *Eur. Polit. Sci.* **6**, 51 (2007).

Support underway for coastal ecosystems

IN HIS PERSPECTIVE "A global strategy for protecting vulnerable coastal populations" (12 September, p. 1250), E. B. Barbier proposes the establishment of a global emergency task force, combined with international financial support to reduce vulnerability in the long-run, as a means to protect coastal populations from the threats posed by climate change. A disaster task force would be a valuable addition to existing international approaches to climate change adaptation; in fact, the proposed financing of a long-term strategy is already underway.

Barbier lists three objectives for a long-term coastal adaptation strategy: managing risks of costal storms, investing in coastal ecosystems and key infrastructure, and enhancing institutional and community response capacities. These activities conform with the strategic objectives of the Global Environment Facility's (GEF) Adaptation Program (*1*), which serves as a financial mechanism to the United Nations Framework Convention on Climate Change (UNFCCC).

The estimated need of $575 million to support coastal adaptation in the developing world overlooks existing bilateral financing. It also fails to take into account multilateral assistance that already amounts to $247 million: The GEF's Adaptation Program has allocated $139 million for climate-resilient coastal zone management; the World Bank's Pilot Program for Climate Resilience has

ILLUSTRATION: G. GRULLÓN/*SCIENCE*

Downloaded from www.sciencemag.org on October 17, 2014

Published by AAAS

approved $73 million; and the Adaptation Fund under the Kyoto Protocol, $35 million.

Barbier notes that developing economies would benefit from assistance for institutional capacity-building. There already have been substantial efforts in that direction. Fifty least-developed countries have already completed their National Adaptation Programs of Action (*2*), a list of national priority adaptation needs, as a result of the UNFCCC process and financed by the GEF's Adaptation Program. Country parties to the UNFCCC further agreed that, as a next step, so-called National Adaptation Plans will be developed that will mainstream climate change adaptation into broader development frameworks in developing countries (*3*).

Dustin S. Schinn

The Global Environment Facility, 1818 H Steeet, NW, Washington, DC 20433, USA. E-mail: dschinn@thegef.org

REFERENCES

1. Global Environment Facility, *GEF Programming Strategy on Adaptation to Climate Change for the Least-Developed Countries Fund and the Special Climate Change Fund* (Global Environment Facility, Washington, DC, 2014).
2. Global Environment Facility, *Progress Report of the Least-Developed Countries Fund and the Special Climate Change Fund* (Global Environment Facility, Washington, DC, 2014).
3. United Nations Framework Convention on Climate Change, *The Cancun Agreements: Outcome of the Work of the Ad Hoc Working Group on Long-term Cooperative Action under the Convention* (Decision 1/CP.16, 2010).

Science and religion: Think local

IN THE 19 SEPTEMBER issue, M. McNutt's Editorial "The Pope tackles sustainability" (p. 1429) and P. Dasgupta and V. Ramanathan's Policy Forum "Pursuit of the common good" (p. 1457) highlighted the important role that religious communities and institutions can have in efforts to mitigate the impacts of anthropogenic climate change. On a global scale, Pope Francis can uniquely engage and orient the minds of many people to the problem of climate change, but a gulf still exists between the scientific and religious communities that cannot be bridged solely by macro-scale efforts.

At smaller scales and within particular religious communities, a general distrust of the scientific community predisposes people to doubt the scientific evidence for anthropogenic climate change. This predisposition must be addressed in order for some people to support the individual and collective socioeconomic changes that are necessary for mitigation. Given that this predisposition likely transcends denominational and theological lines, a unique voice is needed that can simultaneously build trust in these diverse communities and inform about the details of climate change.

I contend that scientists within religious communities are positioned to be this voice. Such scientists have existing relationships with non-scientists in their religious communities that are built on direct lines of communication and trust, making them well-suited for this task. Thankfully, there are already scientists who are leading this effort and providing a model for others to do the same (*1*).

Jonathan M. Hanes

Department of Geography, University of Wisconsin, Milwaukee, Milwaukee, WI 53211, USA. E-mail: jmhanes@uwm.edu

REFERENCE

1. K. Hayhoe, A. Farley, *A Climate for Change: Global Warming Facts for Faith-Based Decisions* (FaithWords, New York, 2009).

RESEARCH

Phenylalanine reveals it's electronic secrets
Calegari et al., *p. 336*

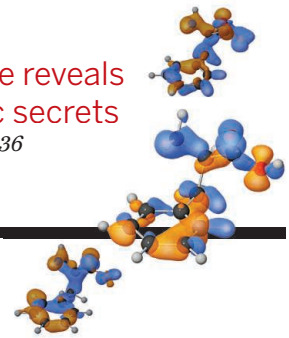

IN *SCIENCE* JOURNALS

Edited by **Stella Hurtley**

Tornado traveling across a plain

CLIMATE CHANGE

Tornadoes clustering in greater numbers

Will global warming cause more tornadoes? If so, that has not happened yet. Brooks *et al.* compiled data on the occurrence of tornadoes in the United States between 1954 and 2013 to determine if and how tornado numbers have changed. Although the authors saw no clear trend in the annual number of tornadoes, they did see more clusters of tornadoes since the 1970s. In other words, there has been a decrease in the number of days per year with tornadoes but an increase in the number of days with multiple tornadoes. Why this clustering effect has occurred is not clear. — HJS

Science, this issue p. 349

PLANETARY GEOLOGY

What's inside Saturn's tiniest moon?

The icy body Mimas is the smallest of Saturn's main moons, only slightly wider than Switzerland. Like our own Moon, Mimas is tidally locked in its orbit and shows nearly the same face to Saturn at all times. The rotational and orbital periods continually overtake each other slightly, however, so that the moon would appear to rock back and forth as viewed from Saturn. Tajeddine *et al.* measured these movements with the Cassini spacecraft to see what they reveal about the moon's interior. Surprisingly, the data are consistent with models for a subsurface ocean or an elongated core. — MMM

Science, this issue p. 322

NANOMEDICINE

Detoxing drug overdoses with nanoparticles

Quick action can save lives from drug overdoses. But what if the right antidote for the toxic drug or poison is not at hand? A new twist on peritoneal dialysis—an older method for replacing the function of failing kidneys—may provide the answer. Forster *et al.* injected nanosized lipid vesicles into the peritoneal cavity of rats. Charged toxins such as ammonia were driven inside the acidic vesicles by the pH gradient. Peritoneal dialysis with these loaded liposomes also rescued rats suffering from deadly amounts of verapamil, a heart drug that can cause lethal overdoses. The approach also worked for other drugs. Such liposomes may thus provide an all-purpose antidote. — MLF

Sci. Transl. Med. **6**, 258ra141 (2014).

DEVELOPMENTAL BIOLOGY

Ensuring a one-way flow of lymph

Without lymphatic vessels and valves to ensure unidirectional flow, fluid and immune cells that have gone into tissues from the blood—lymph—would build up and cause swelling. Liu *et al.* noted that the regions of developing lymphatic vessels destined to become valves had high levels of the receptor VEGFR3 but low levels of epsin 1 and 2, proteins involved in endocytosis. Epsin 1 and 2 suppressed VEGFR3 signaling in collecting lymphatic trunks by triggering the endocytosis and breakdown of VEGFR3. Mice lacking epsin 1 and 2 in the endothelial cells lining lymphatic vessels had defective lymphatic valves and impaired drainage. — WW

Sci. Signal. **7**, ra97 (2014).

TROPHIC CASCADES

A thorny defense keeps grazers at bay

Fear and avoidance of predators are known to influence how and where herbivore prey species, such as impala, forage. This in turn has cascading effects on plant morphologies and communities. Plants, however, have their own defenses, and so may not just be hapless victims of the predator-prey "dance." Ford

Downloaded from www.sciencemag.org on October 17, 2014

CREDITS: (TOP TO BOTTOM) NICOLETTA CALEGARI; JOHN LUNG/GETTY IMAGES

Published by AAAS

et al. found that thorny *Acacia* trees are more common in areas where impala experience a low risk of predation by wild dogs. A related *Acacia*, without thorns, is most abundant in areas where risk of predation is high, and so the number of hungry impala is low. — SNV

Science, this issue p. 346

QUANTUM ELECTRONICS

Complex light and matter interactions

When electrons are confined to a plane, lowered in temperature, and subjected to a magnetic field, they can interact and organize themselves into so-called many-body states and exhibit complex quantum electronic behavior. However, discerning the underlying interactions can be difficult. Adding light to the mix, Smolka *et al.* now show that these self-organized electronic states can be controlled and manipulated to unravel the details of the exotic electronic behavior. — ISO

Science, this issue p. 332

STRATEGIC REASONING

Smart monkeys can outwit a computer

What happens in the brain when we are learning to compete against an opponent? Seo *et al*. observed monkeys competing against a computer that can adapt to the monkey's behavior. The monkeys switched their learning strategies when they worked out that their opponent was reacting to their behavior. The responses of the dorsomedial prefrontal cortex cells in the monkey brains predicted their choices and switches in strategies. – PRS

Science, this issue p. 340

ION CHANNELS

Ions knock each other across the membrane

Potassium channels play a key role in regulating a cell's membrane potential, which in turn affects diverse processes. The channels contain four potassium binding sites that are thought to be alternately occupied by potassium and water. Starting from high-resolution crystal structures, Köpfer *et al.* simulated over a thousand potassium ions crossing the channel (see the Perspective by Hummer). They found that ions are in direct contact rather than being separated by water as previously assumed. It seems that repulsion between the ions is the key to their efficient movement through the channel. — VV

Science, this issue p. 352; see also p. 303

AUTOIMMUNITY

Finding the targets of T cells gone bad

Autoimmune diseases such as rheumatoid arthritis can result when the immune system attacks its own body. If we could identify the specific proteins targeted by autoimmune T cells, we might then be able to block this interaction, which might be useful therapeutically. Ito *et al*. identified one such target in mice that develop a disease similar to rheumatoid arthritis. Disease-causing T cells recognized a protein that is part of the ribosome, a large protein complex that catalyzes protein synthesis. They also found T cells specific for this protein in people with rheumatoid arthritis. — KLM

Science, this issue p. 363

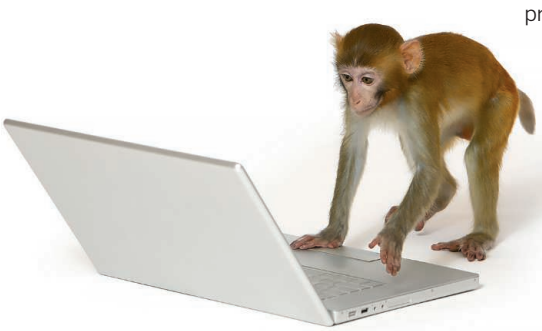

CREDITS: (LEFT TO RIGHT) © D. HURST/ALAMY; JAMES CAVALLINI/SCIENCE SOURCE

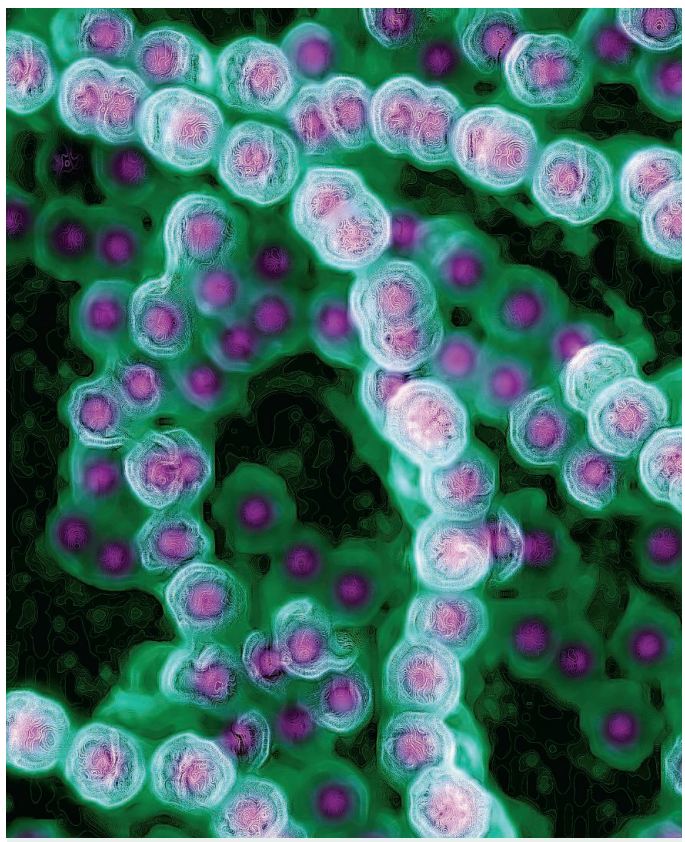

ANTIBIOTICS

Charting the course of antibiotic failure

Bacterial resistance to antibiotics is a major public health problem. To better understand this in a clinical setting, Currie *et al.* analyzed a 20-year prescribing history of antibiotics by UK primary care practitioners and report a 12% increase in treatment failure (when a specific antibiotic fails to cure an infection). The authors found only small decreases in the ability of frontline drugs, such as penicillins and macrolides, to control respiratory tract and soft tissue infections. More worryingly, however, second-line antibiotics, such as cephalosporins and quinolones, often used to treat elderly and frail patients with pneumonia, showed higher failure rates since 1991. — CA

BMJ 10.1136/bmj.g5493 (2014).

MAMMAL DIGIT NUMBER

Protein sorting sets digit number

Like human fingers and toes, mice have five digits on their front and back paws. To better understand the molecular mechanism behind this, Handschuh *et al.* studied mice with extra or fused digits caused by a mutation that leads to reduced expression of the protein Vps25. Vps25 helps to sort proteins at the cell surface in a process called endosomal protein trafficking. Such sorting ensures that cells express just

Published by AAAS

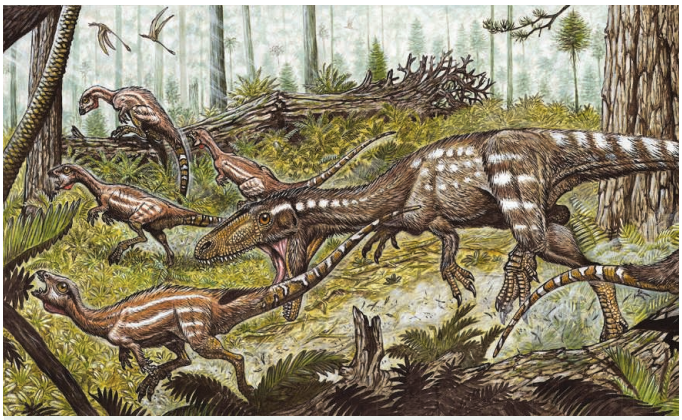

PALEONTOLOGY

Meat-eater lived in extinction's wake

A newly described dinosaur unearthed in Venezuela is a close relative of creatures that later evolved into giant meat-eaters such as *Allosaurus* and *Tyrannosaurus rex*. Langer *et al.* examined two lower leg bones from two different individuals of *Tachiraptor admirabilis.* The two bones were different enough from those of known species to mark the creature as new. *T. admirabilis* was a theropod, measuring 1.5 meters from nose to tail. The bones were found in an ancient flood plain, in sediments deposited 200.7 million years ago—less than 1 million years after the mass extinction that marked the end of the Triassic period and the beginning of the Jurassic. — SP

Roy. Soc. Open Sci. 10.1098/rsos.140184(2014).

the right amount of particular proteins, so things such as tissue development go off without a hitch. In Vps25 mutant mice, cells divided more in hindlimbs, and fewer cells in the spaces between digits died, which suggests that digit development requires that cells sort their proteins properly. — BAP

Cell Reports
10.1016/j.celrep.2014.09.019 (2014).

MINERAL PHYSICS

Unraveling ringwoodite hydration in mantle

Certain high-pressure minerals in Earth's mantle are likely to contain oceans' worth of water dissolved into their crystal structures. Exactly how water dissolves into ringwoodite, an important mineral in the mantle transition zone, influences our ability to detect mantle water using geophysical tools. Purevjav *et al.* tackle this problem by using a powerful beam of neutrons to determine the location of hydrogen atoms in the ringwoodite structure. They found that hydrogen substitutes for any of the major cations, dramatically lowering the speed of seismic waves in the mineral. This discovery may make it possible to map important water content variations in the transition zone of Earth's mantle. — BG

Geophys. Res. Lett.
10.1002/2014GL0614488 (2014).

BEHAVIORAL SCIENCE

A costly reluctance to speak out

Decision-making in groups depends not only on whether any of the group members knows the right answer but also on whether the most informed members actually speak up. Coffman examined the propensity to contribute one's ideas in a pared-down laboratory knowledge test in which other factors, such as discrimination and argumentativeness, do not play a role by design. She found that undergraduate women contribute their answer to the group less often than undergraduate men. The authors observed that this was subject area–dependent: women showed the least amount of reluctance for the most female-stereotyped subject area, arts, and the greatest amount for the most male-stereotyped subject, sports. — GJC

Quart. J. Econ. **129**, 10.1093/qje/qju023 (2014).

LIMNOLOGY

How many lakes are there on Earth?

Most maps or databases of global lakes either omit small lakes or estimate their numbers, leaving accurate calculations of their net subaerial coverage uncertain. This makes it difficult to determine the role of lakes in Earth's carbon cycle. Verpoorter *et al.* use high-resolution satellite images to create a database of all lakes with surface areas greater than 2000 square meters. The interpretation of satellite images can be hampered by the presence of features such as dark forests or mountain shadows, so the authors developed a special algorithm to overcome these problems. They conclude that there are 117 million lakes, covering 3.7% of Earth's land area not covered by ice. They conclude that there are fewer lakes, but that those lakes cover more area, than previous estimates have indicated. — JFU

Geophys. Res. Lett.
10.1002/2014GL060641 (2014).

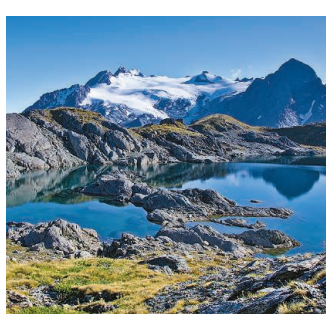

INFECTIOUS DISEASE

Taking the temperature of virulence

Cholera kills more than 100,000 people yearly and results from consuming food or water contaminated with *Vibrio cholerae*. The bacterium only expresses virulence factors, proteins that cause disease, when it infects people. Weber *et al.* investigated how this occurs at a molecular level and discovered that the bacteria possess an "RNA thermometer," which turns on expression of these virulence factors. At low temperatures, as found in water inhabited by the bacteria, a sequence from the bacterium's *toxT* messenger RNA (*toxT* encodes a protein that turns on virulence gene expression) folds into a structure that prevents its translation. However, at human body temperature, the structure opens up and the bacterium can express its virulence factor genes. — BJ

Proc. Natl. Acad. Sci. U.S.A. 10.1073/pnas.1411570111 (2014).

THEORETICAL BIOLOGY

Finding ways to reach the right endpoint

Most complex systems have an element of randomness: Even if we can describe them exactly at one point in time, we don't know for certain where they will be next. Scientists use stochastic equations to compute the many possible trajectories these systems can take. If we constrain both end points of such trajectories, the usual approach of calculating all trajectories and rejecting those that do not end at the desired final point can be very inefficient. Zhao *et al.* introduced an approach in which they modified the probabilities for moving from one state to the next, so that the system was guaranteed to reach the set final state. The authors used examples from population genetics to illustrate the power of the method. — JS

J. Theor. Biol. **363**, 419 (2014).

CREDITS: (TOP TO BOTTOM) MAURÍLIO OLIVEIRA; TOMAS SOBEK/FLICKR

Published by AAAS

REVIEW SUMMARY

APPLIED EVOLUTION

Applying evolutionary biology to address global challenges

Scott P. Carroll,* Peter Søgaard Jørgensen,* Michael T. Kinnison, Carl T. Bergstrom, R. Ford Denison, Peter Gluckman, Thomas B. Smith, Sharon Y. Strauss, Bruce E. Tabashnik

BACKGROUND: Differences among species in their ability to adapt to environmental change threaten biodiversity, human health, food security, and natural resource availability. Pathogens, pests, and cancers often quickly evolve resistance to control measures, whereas crops, livestock, wild species, and human beings often do not adapt fast enough to cope with climate change, habitat loss, toxicants, and lifestyle change. To address these challenges, practices based on evolutionary biology can promote sustainable outcomes via strategic manipulation of genetic, developmental, and environmental factors. Successful strategies effectively slow unwanted evolution and reduce fitness in costly species or improve performance of valued organisms by reducing phenotype-environment mismatch or increasing group productivity. Tactics of applied evolutionary biology range broadly, from common policies that promote public health or preserve habitat for threatened species—but are easily overlooked as having an evolutionary rationale, to the engineering of new genomes.

ADVANCES: The scope and development of current tactics vary widely. In particular, genetic engineering attracts much attention (and controversy) but now is used mainly for traits under simple genetic control. Human gene therapy, which mainly involves more complex controls, has yet to be applied successfully at large scales. In contrast, other methods to alter complex traits are improving. These include artificial selection for drought- and flood-tolerant crops through bioinformatics, and application of "life course" approaches in medicine to reduce human metabolic disorders.

Successful control of unwanted evolution depends on governance initiatives that address challenges arising from both natural and social factors. Principal among these challenges are (i) global transfer of genes and selection agents; (ii) interlinked evolution across traditional sectors of society (environment, food, and health); and (iii) conflicts between individual and group incentives that threaten regulation of antibiotic use and crop refuges. Evolutionarily informed practices are a newer prospect in some fields and require more systematic research, as well as ethical consideration—for example, in attempts to protect wild species through assisted migration, in the choice of source populations for restoration, or in genetic engineering.

OUTLOOK: A more unified platform will better convey the value of evolutionary methods to the public, scientists, and decision-makers. For researchers and practitioners, applications may be expanded to other disciplines, such as in the transfer of refuge strategies that slow resistance evolution in agriculture to slow unwanted evolution elsewhere (for example, cancer resistance or harvest-induced evolution). For policymakers, adoption of practices that minimize unwanted evolution and reduce phenotype-environment mismatch in valued species is likely essential to achieve the forthcoming Sustainable Development Goals and the 2020 Aichi Biodiversity Targets. ■

ON OUR WEB SITE

Read the full article at http://dx.doi.org/10.1126/science.1245993

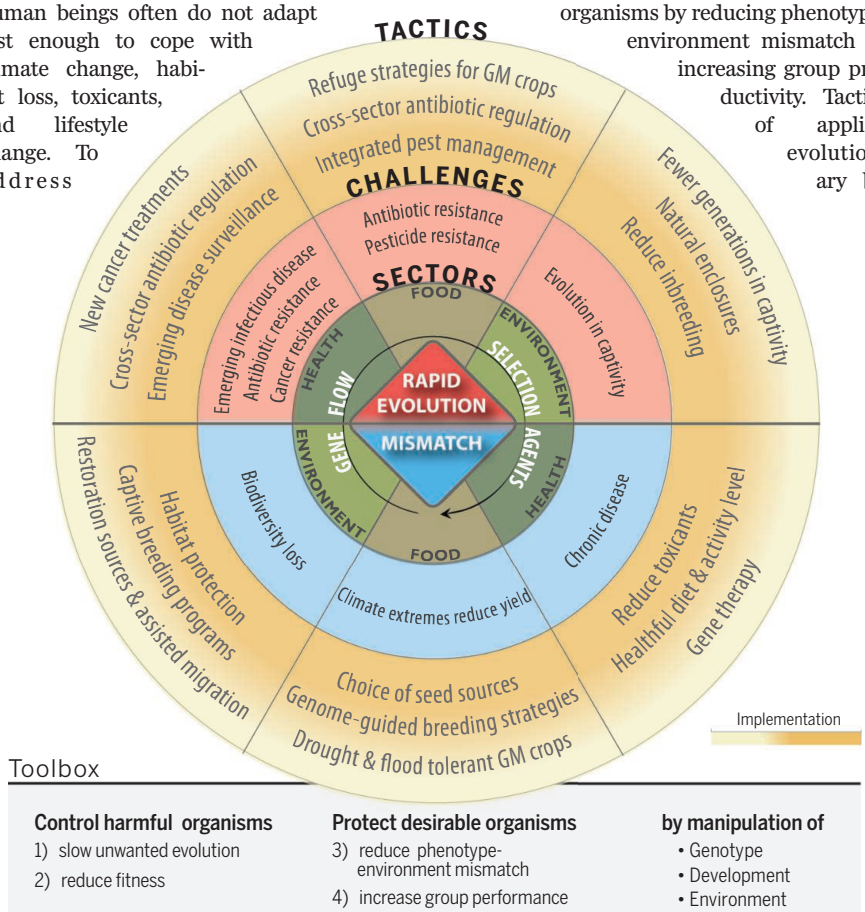

Tactics and tools of applied evolutionary biology. (**Top**) Evolutionary tactics to address the major societal challenges treated in the present study are shown as a wheel. Challenges in the food, health, and environment sectors are caused by rapid contemporary evolution or, in more slowly reproducing or threatened species, phenotype-environment mismatch. Gene flow and selection agents make challenges in one sector dependent on actions in others. Current progress in implementing tactics of applied evolutionary biology to address challenges varies widely. (**Bottom**) Many of these tactics use a common toolbox of strategies to prevent unwanted evolution or to reduce fitness in harmful organisms, as well as to reduce mismatch between organisms and human-altered environments or to increase group performance in desired organisms. Each of these strategies uses a combination of manipulations of the organismal genotype, phenotypic plasticity (development), or environmental conditions.

The list of author affiliations is available in the full article online.
*Corresponding author. E-mail: spcarroll@ucdavis.edu (S.P.C.); psjorgensen@bio.ku.dk (P.S.J.)
Cite this Review as Scott P. Carroll *et al.*, *Science* 346, 1245993 (2014). DOI: 10.1126/science.1245993

Published by AAAS

REVIEW

APPLIED EVOLUTION

Applying evolutionary biology to address global challenges

Scott P. Carroll,[1,2]*† Peter Søgaard Jørgensen,[3,4]*† Michael T. Kinnison,[5] Carl T. Bergstrom,[6] R. Ford Denison,[7] Peter Gluckman,[8] Thomas B. Smith,[9,10] Sharon Y. Strauss,[11] Bruce E. Tabashnik[12]

Two categories of evolutionary challenges result from escalating human impacts on the planet. The first arises from cancers, pathogens, and pests that evolve too quickly and the second, from the inability of many valued species to adapt quickly enough. Applied evolutionary biology provides a suite of strategies to address these global challenges that threaten human health, food security, and biodiversity. This Review highlights both progress and gaps in genetic, developmental, and environmental manipulations across the life sciences that either target the rate and direction of evolution or reduce the mismatch between organisms and human-altered environments. Increased development and application of these underused tools will be vital in meeting current and future targets for sustainable development.

Human influence on the biosphere (*1*, *2*) has profound consequences for both the rate and direction of evolution (*3*). Among the consequences are the challenges billions of people face from the effects of cancers, pests, and pathogens that adapt quickly to our interventions against them. At the same time, humans and other organisms that we value for economic, ecological, or aesthetic reasons are often not able to adapt quickly enough to keep pace with human alterations of the environment. These contemporary dilemmas increasingly threaten human health, food security, and biological diversity (*4*–*12*). For example, the World Health Organization (WHO) warns that microbial resistance to antimicrobial drugs threatens the achievements of modern medicine (*13*). Likewise, more than 11,000 documented cases of pesticide resistance in nearly 1000 species of insects, weeds, and plant pathogens jeopardize agricultural economies and food supplies worldwide (*14*). Failure to adapt may be equally dire and costly, as in the prevalent mismatch between modern human nutritional and lifestyle behaviors and those of our evolutionary past, which is generally considered a major contributing factor to the high incidence of obesity and associated illnesses such as type 2 diabetes mellitus and cardiovascular disease (*15*). Meanwhile, the prospect of Earth's sixth mass extinction of species becomes imminent as species are unable to adapt quickly enough to environmental change (*16*). A growing application of principles from evolutionary biology to challenges such as these may improve our ability to meet many of the most pressing problems of the 21st century (*12*, *17*–*19*).

Here, we review current and prospective applications of evolutionary biology that may provide solutions for major societal challenges. We examine management approaches that attempt either to improve or to undermine adaptation to modern environments by manipulating the relations between the traits of organisms and the patterns of selection imposed by their environments. These manipulations include tools that may be widely considered evolutionary, such as selective breeding and emerging technologies in genetics, as well as manipulations that are often overlooked as evolutionary, specifically manipulations of development that modify traits independent of genetic change and the altering of environments in ways that can modulate selection itself. A conceptual framework linking all of these genetic, developmental, and environmental manipulations is likely to lead to greater implementation and cross-disciplinary integration of applied evolutionary methods. We highlight how evolutionary strategies may be used to achieve policy targets of sustainable development for improved human health, food production, natural resource use, and biodiversity conservation, including how stakeholder conflicts may be reduced to achieve desired outcomes. Throughout, we underscore the merits of building a more unified and integrated field of applied evolutionary biology to address global challenges.

Core evolutionary concepts and their relevance to global challenges

Evolution, defined as the change in genetic makeup of a population over successive generations, requires genetic variation, which arises from mutation and recombination (*20*). Most important for adaptation is genetic variation that affects variation in functional traits (*21*), such that alternate genotypes produce alternate phenotypes. Selection increases the frequency of genes that improve fitness—the ability to survive and reproduce. The specific genetic basis for most traits is not known, but trait differences among individuals typically have a significant heritable (genotypic) basis. This basis includes heritable aspects of development, which also may evolve and give rise to adaptive phenotypic plasticity (*22*). A population with low fitness may experience strong natural selection that favors better-adapted genotypes. However, strong selection will not necessarily "rescue" a population if there are too few adapted individuals or suitable genes for the population to persist (*23*). Movement of genes between populations (gene flow) and random changes in gene frequency in small populations (genetic drift) can also cause evolution and influence the outcome of natural selection (*20*). These concepts apply not only to organisms from bacteria to humans but also to viruses and cancer cells (*24*).

The core concepts of evolutionary biology are best known for explaining the unity, diversity, and adaptive characteristics of organisms (*17*). Phylogenetic methods that establish the relatedness of organisms are central to understanding the patterns and processes of evolution underlying the function and diversity of living systems (*25*). The practical applications of phylogenetic methods have been thoroughly reviewed by others and include such diverse objectives as reconstructing invasion routes of harmful organisms, conservation planning, and combating crime (*17*, *26*). Here, we focus on the manipulation of processes that determine the adaptedness of individuals, populations, and other biological systems in order to meet management objectives (Fig. 1).

Agriculture, medicine, and conservation address different challenges but, nonetheless, share common strategies to manage phenotype-environment mismatch and the associated risks to populations experiencing strong selection (Fig. 2). Those strategies can be classified as genotypic, developmental, or those related to environmental manipulations. The potential sustainability of such practices may be assessed by comparing the intensity of selection with the adaptive capacity of a target population (*27*). For example, the widespread use of antibiotics that exert strong selection on

[1]Department of Entomology, University of California, Davis, One Shields Avenue, Davis, CA 95616, USA. [2]Institute for Contemporary Evolution, Davis, CA 95616, USA. [3]Center for Macroecology, Evolution and Climate, Department of Biology, University of Copenhagen, 2100 Copenhagen, Denmark. [4]Center for Macroecology, Evolution and Climate, Natural History Museum of Denmark, University of Copenhagen, 2100 Copenhagen, Denmark. [5]School of Biology and Ecology, University of Maine, Orono, ME 04469, USA. [6]Department of Biology, University of Washington, Seattle, WA 98195, USA. [7]Department of Ecology, Evolution, and Behavior, University of Minnesota, Minneapolis, MN 55108, USA. [8]Centre for Human Evolution, Adaptation and Disease, Liggins Institute, University of Auckland, Auckland, New Zealand. [9]Department of Ecology and Evolutionary Biology, University of California, Los Angeles, CA 90095, USA. [10]Center for Tropical Research, Institute of the Environment and Sustainability, University of California, Los Angeles, 619 Charles E. Young Drive East, Los Angeles, 90095-1496, CA. [11]Department of Evolution and Ecology and Center for Population Biology, University of California, Davis, One Shields Avenue, CA 95616, USA. [12]Department of Entomology, University of Arizona, Tucson, AZ 85721, USA.
*These authors contributed equally to this work. †Corresponding author. E-mail: spcarroll@ucdavis.edu (S.P.C.); psjorgensen@bio.ku.dk (P.S.J.)

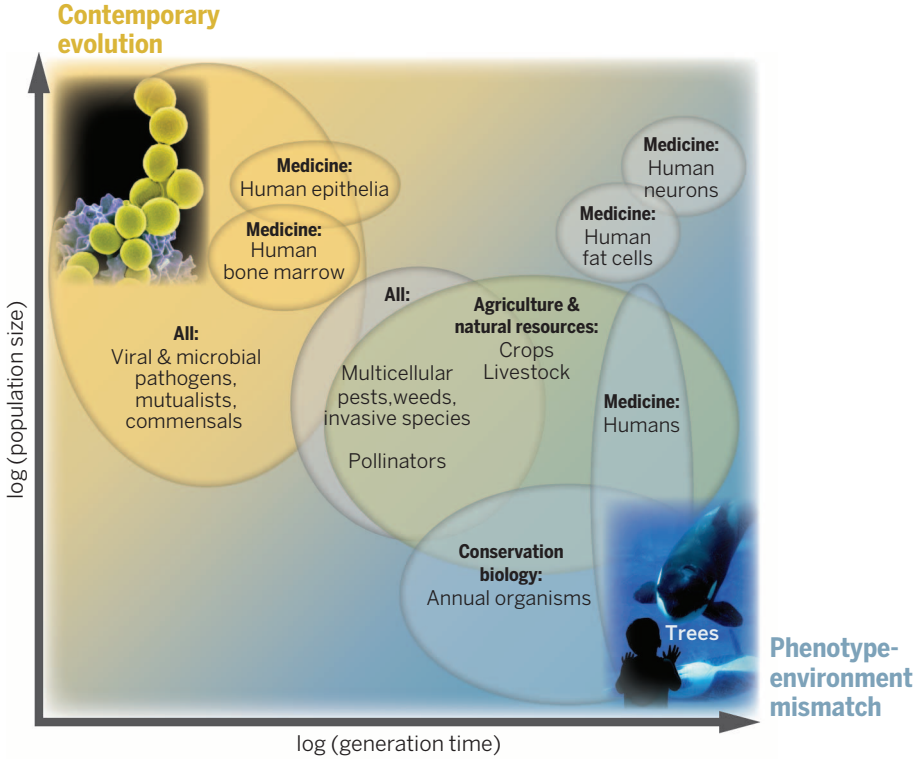

Fig. 1. The two central paradigms of applied evolution are managing contemporary evolution and phenotype-environment mismatch. Managing contemporary evolution is critical for rapidly reproducing organisms with large population sizes, such as the methicillin-resistant *Staphylococcus aureus* (MRSA), pictured top left. Altering phenotype-environment mismatch is most relevant for organisms with relatively long generation times and low population sizes, such as the large mammals shown lower right. Labels in ovals refer to example organisms, viruses, or cell types in specified management sectors. "All" indicates relevance to all management sectors (food, health, and environment). References are provided in table S1.

bacteria is typically not sustainable for controlling highly adaptable microbe populations, because they rapidly evolve resistance (*28*). Accordingly, the sustainability of antibiotic use can be increased by either reducing selection, for example, through regulated use of particularly strong antibiotics, or by attempts to surpass the adaptive capacity of microbes through drug combinations (*29*). Below, we review successes and emerging methods in applied evolutionary biology, highlighting commonalities across the sectors of health, food, and environmental management (Fig. 3).

Successes and prospects in applied evolutionary biology

Applied evolutionary biology encompasses widely different manipulations that may together achieve a broad range of goals. From protecting biodiversity with conventional environmental management that increases fitness in wild environments to medical recommendations for traditional diets, some methods of applied evolutionary biology have a long history of use, even if they are not often seen as evolutionary in nature. In contrast, the synthesis of wholly novel genomes with emerging technologies represents obvious evolutionary manipulation that deliberately adds new organisms to the tree of life, but with little history of application, it involves unknown risks and public controversy. Here, we review some of the most recent successes and leading prospects for the application of evolutionary biology, in a progression from relatively well established methods to underexplored strategies. We first consider manipulations of selection to improve population productivity and individual health and to delay the emergence of resistance (Fig. 2). We then examine less developed methods for the cultivation of populations inherently preadapted to impending environmental changes and for innovative applications of group selection in crops and wildlife. We end this section with urgent considerations for managing evolutionary factors that span disciplinary boundaries, as in cases of emerging zoonotic disease.

Environmental alignment to secure biodiversity and human health

A common application of evolutionary principles is to manage current environments to be more like the historical habitats in which selection shaped the genetic makeup of humans and other species. Conventional habitat protection and restoration recognize that threatened species often adapt poorly to changing environments in the wild (*26*, *30*). Conversely, rapid adaptation to captive rearing programs used to rebuild populations of rare species contributes to a 50 to 90% failure rate of reintroductions (*31*). Reintroduction success has been improved with enclosures and rearing methods that mimic wild conditions and by limiting the number of captive generations to minimize adaptation to artificial conditions (*32*).

Some of the most serious noncommunicable diseases in humans may be prevented by better aligning current environments with those in which our hunter-gatherer ancestors evolved (*33*). Sedentary modern lifestyles and diets with high–glycemic index processed foods are increasingly implicated in the rapidly rising rates of obesity, diabetes, and cardiovascular disorders (*34*). These disorders are estimated to contribute to about two-thirds of all deaths in Western societies (*35*) and to a growing proportion of deaths in developing countries (*36*, *37*). In 2012, the economic burden of type 2 diabetes alone was estimated at $500 billion globally, nearly 1% of world Gross Domestic Product (*38*). To restore conditions to which people are better adapted physiologically, while retaining the desired elements of a modern lifestyle (*35*), public health scientists recommend greater physical activity (*39*) with reduced consumption of refined carbohydrates (*36*), that is, diets and activity levels closer to those of the past, to which we are better adapted. More generally, a number of evolutionarily based tools are available to prevent chronic noncommunicable diseases, including the 19% of global cancer incidents that WHO attributes to environmental exposure (*40*). These tools include life-course approaches, which manage the timing and duration of environmental exposures to minimize risks of subsequent chronic disease (*41*). From a public health standpoint, environmental approaches to disease prevention may often be most cost-effective when applied outside of health care settings and when simultaneously targeting groups of people rather one individual at a time, such as through price regulation on goods or public information campaigns (*42*). Further, systematic population scans that associate disease phenotypes with human genotypes (*43*, *44*) are an important tool for determining the genetic basis of lifestyle diseases and, therefore, in assessing heritable risk and treatment options. Such assessments, however, run the risk of identifying false-positives and underestimating the complexity of genetic and epigenetic regulation (*45*, *46*). For example, it is estimated that 90% of chronic disease risk cannot currently be directly linked to genetic factors but is more likely to be understood in the context of human environmental exposures, such as diet and toxicants (*47*). Thus, future prevention and treatment of chronic diseases will combine enhanced genotype-phenotype association scans with improved monitoring of toxic compounds in the surrounding environment and in human tissues (*47*). Such genotype-phenotype association studies search simultaneously for associations across the hundreds of disease phenotypes included in electronic medical registers (*45*). This

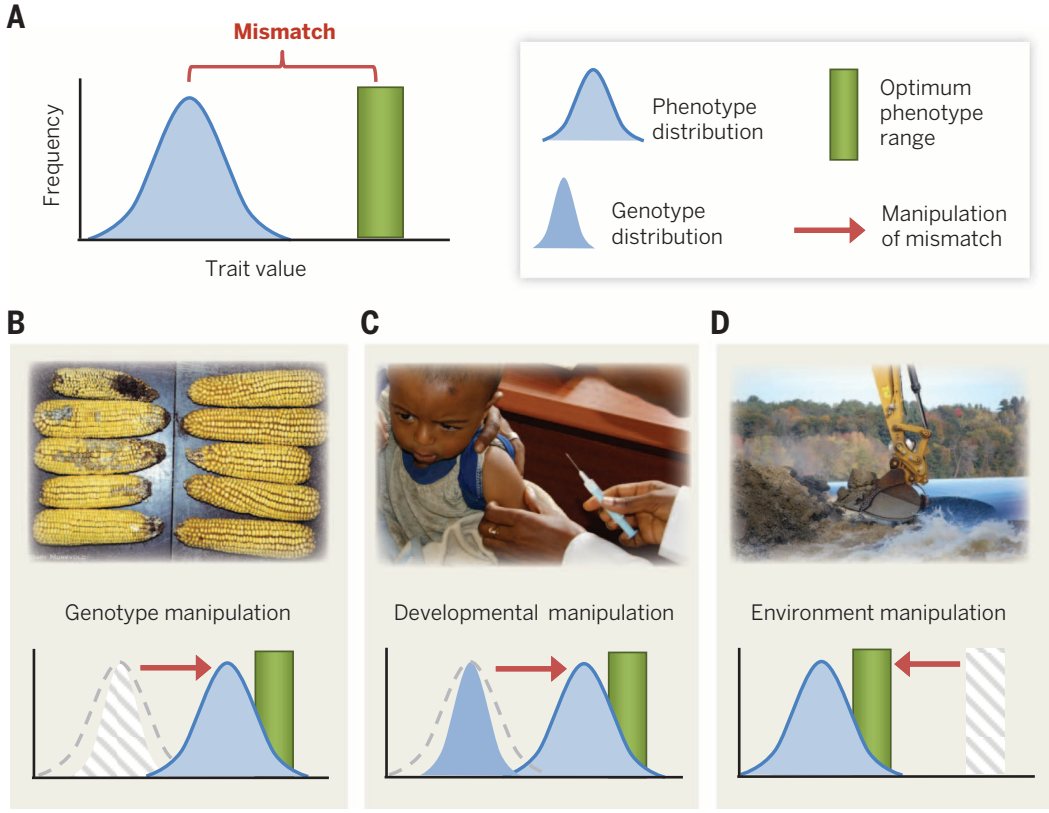

Fig. 2. Phenotype-environment mismatch. (**A**) Mismatch between phenotypes and an environment occurs when a population's phenotypic trait distribution differs from the optimum; greater mismatch increases selection for adaptation but also implies greater costs through reduced survival and reproduction. (**B**) Genotypic manipulations reduce mismatch by managing existing genetic variation or introducing new genes. For example, conventional corn is damaged by insect pests (left) that are killed by bacterial proteins produced by GE Bt corn (right). Alternatively, evolutionary mismatch can also be managed by (**C**) developmental manipulations of phenotypes, such as vaccination to enhance immunity against pathogens, or (**D**) environmental manipulations, such as habitat restoration. These examples demonstrate methods to reduce mismatch, but these same tactics can be reversed to impose greater mismatch where beneficial to human interests (e.g., pest eradication).

expanded approach reduces the rate of false-positives and helps to identify genetic factors that contribute to multiple diseases, as well as diseases controlled by multiple genes.

Altering genomes for improved food security and human health

Climate change and environmental degradation compromise the productivity of agricultural systems that must feed a rapidly growing human population (*48*). Genetic modification of crops, through enhanced artificial selection methods and perhaps genetic engineering, will likely be important in meeting these challenges. Genetically engineered (GE) crops were first grown on a large scale in 1996, and during 2013, 18 million farmers in 27 countries planted GE crops on ~10% of the world's cultivated land (175 million hectares) (*49*). More than 99% of this area was planted with soybean, corn, cotton, or canola into which genes were inserted to confer tolerance to herbicides, protection against insects, or both (*50*). These engineered varieties are extreme examples of apparently effective genotypic manipulations to reduce mismatch to specific environments. However, societal acceptance is an important factor, and GE crops remain controversial (*51*, *52*). They have not been adopted widely in some regions, including Europe, where alternative manipulations of evolutionary mismatch, such as use of non-GE lines with some degree of tolerance, pesticide applications, and integrated pest management serve as alternative genotypic and environmental manipulations (*53*).

An alternative to genetic engineering is enhanced artificial selection and hybridization of superior cultivated varieties with molecular genetic tools that identify individuals and gene regions conveying preferred traits (*54*). A priority application, where genetic engineering has until now been less successful (*55*), is to improve abiotic tolerance because of more frequent weather extremes under climate change. For example, flood-tolerant rice, which is grown by two million farmers in Bangladesh and India (*49*), was developed with marker-assisted breeding by using molecular markers of quantitative traits to identify targets for hybridization and selection (*56*). At the same time, candidate drought-tolerance genes for GE crops have also recently been identified in rice, as well as corn (*57*, *58*), with corn hybrids putatively tolerant to both drought and herbicides brought to market in 2013 (*55*, *59*). Regardless, whether produced via artificial selection or genetic engineering, the potential to improve food security by reducing mismatch may be greatest when technology allows growers to select or customize crop varieties for adaptation in their local agroecosystems (*60*).

In contrast to the advances in agriculture, genetic modification to treat human disease is in a trial phase. Gene therapy is under development mainly for diseases with high heritability and simple genetic control, in which replacing or complementing parts of a patient's genome can improve their health (*61*–*63*). Therapies in advanced trial stages include the targeting of retinal cells to prevent expression of heritable blindness (*64*, *65*), and oral administration of p53 gene for tumor suppression (*66*). However, even as targeted DNA analysis and whole-genome sequencing of patients becomes increasingly routine (*67*), few efforts have met the promise of their preclinical and clinical trials to reach final approval phase of "postmarketing" surveillance trials (*68*, *69*).

Using environmental heterogeneity to delay the evolution of resistance

One of the most costly and widespread outcomes of efforts to control populations is the rapid evolution of resistance to control measures in insect pests (*14*), weeds (*70*), pathogens, and cancers (*71*). For example, intensive use of the systemic herbicide glyphosate [*N*-(phosphonomethyl)glycine] by farmers, particularly those who grow glyphosate-tolerant GE crops, has selected for resistance in 24 weed species in 18 countries since 1996 (*72*, *73*). In contrast, strategies that vary selection in space or time have delayed the evolution of resistance in some pests (Fig. 3). For example, scientists and farmers have proactively developed and implemented strategies to slow pest adaptation to GE crops that produce insecticidal proteins from *Bacillus thuringiensis* (Bt) (*74*, *75*). The primary strategy employs "refuges" of host plants that do not produce Bt toxins to promote survival of susceptible pests (*74*). In principle, the rare resistant pests that survive on Bt crops are more likely to mate with the comparatively abundant, susceptible pests from the nearby refuges. If resistance is inherited as a recessive trait, the heterozygous offspring from such matings will be susceptible and will die on the transgenic plants. The U.S. Environmental Protection Agency (EPA) and regulatory agencies in many other countries

	Strategy	Tactic	Food and fiber	Health	Environment
A	**Control pests, pathogens and invaders by . . .**				
	. . . slowing unwanted evolution				
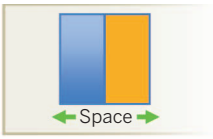	Spatial variation in selection	Protect some susceptible forms	Nontoxic plantings save treatable pests	Favor susceptible pathogens, cell lines	Maintain genotypes vulnerable to control
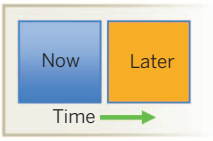	Temporal variation in selection	Switch treatments to slow adaptation	Rotate crops, pesticides	Cycle treatments of pathogens, cancers	Stress invader's weak points sequentially
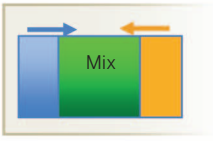	Diversified selection	Apply stressors together	Integrate multiple tactics, pyramiding	Multitarget vaccines; reduce transmission	Integrated control of invasive species
	Trait-based selection	Favor benign genotypes	Mow to select weeds to shade less	Favor survival of benign strains	Target mobile forms to reduce dispersal
	. . . reducing adversary fitness				
	Add mutational load	Transgenic mutation	Reduce pest fitness	Mutate viruses; eliminate vectors	Reduce invader fitness
B	**Protect desirable populations by . . .**				
	. . . reducing phenotype environment mismatch				
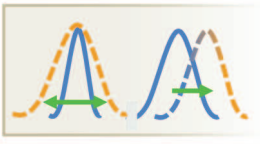	Reduce selection	Modify environment, or move	Adopt crops suited to current environment	Alter lifestyle for health, offspring	Alter local conditions or assist migration
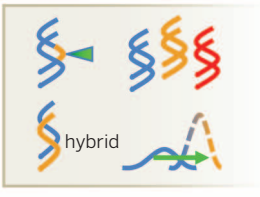	Improve fit to environment	Modify genotypes	Wild crop relatives; molecular breeding	Recombinant drugs; gene therapy	Selected, hybridized or GE genotypes
	. . . increasing group performance				
	Group selection, cooperation	Select emergent group traits	Favor efficiency, weed suppression	Internalize public costs and benefits	Limit competition, protect in reserves

Fig. 3. Two management intervention categories of applied evolutionary biology: (A) Controlling adversaries and (B) Protecting valued populations. Together they are enabled by four strategies (headings). A core set of eight evolutionary principles guides the execution of these strategies and underlies tactics (left columns) used to meet management objectives in the food and fiber production, health, and environmental sectors (right columns). Colored squares show different treatments; curves show frequency distributions of phenotypes; double helices are genomes; green arrows show change through space or time; green wedges show point interventions using selection or genetic engineering. Semicolons separate multiple management examples. Hypothetical applications are given in two cases that lack empirical examples. Expanded treatments for each cell and references are provided in table S2.

have mandated refuges since Bt crops were first commercialized (*76*, *77*). Retrospective analysis, after more than a decade of monitoring, indicates that refuges do indeed delay resistance, particularly when resistance is a recessive trait (*77*, *78*).

The success of refuge tactics in agriculture is now drawing attention in other management sectors, including fisheries, where refuges may impede costly life-history evolution and body-size evolution resulting from harvest selection (*79*). Likewise, in cancer management, portions of tumors with low vascularization and, consequently, low delivery of chemotoxins may serve as refuges that sustain chemosensitive tumor genotypes (*80*, *81*) and slow the evolution of resistance to chemotherapy in metastatic cancer (*82*, *83*). Such resistance accounts for a large proportion of current treatment failures (*84*). Compared with typical failures when oncologists try to eradicate a patient's cancer with high drug doses, lower doses could be more successful if they favor survival of chemosensitive cell lines that can outcompete chemoresistant lines (*85*). Increasingly sophisticated models of tumor evolution may eventually support implementation of such noneradication therapies (*86*).

Whereas refuges delay resistance by swamping resistant lineages with susceptible lineages, another strategy attempts to curb resistance through selection that combines multiple modes of action (also known as "stacking" or "pyramiding"). In many human diseases—including HIV, tuberculosis, malaria, and cancer—resistance frequently evolves under selection from individual drugs (*87*). Combination therapies are based on the evolutionary principle that, if genes conferring resistance to each selection pressure are rare and inherited independently, individuals with all of the genes required for full resistance will be rare or even absent in target populations (*4*, *14*, *88*, *89*). For example, resistance evolved rapidly to potent antiretroviral drugs administered singly in patients with HIV, but combinations of three such drugs have provided long-term efficacy and have become the standard of care (*90*, *91*). The potential tradeoffs associated with combining two or more drugs or pesticides to delay resistance include short-term increases in costs (*92*) and negative side effects (*93*), as well as the concern that such combinations will also ultimately favor the evolution of multiple resistance (*87*, *94*, *95*). For example, incorporating two or more toxins together in GE varieties slows resistance evolution (*96*, *97*), but this advantage may diminish when less-resistant single-toxin varieties are planted in the same area as multitoxin varieties and provide stepping stones for multiple-resistance evolution (*98*). Combined selection pressures are most likely to be durable when implemented as a facet of more broadly integrated systems, such as integrated pest management (IPM). IPM combines selection pressures from a diverse suite of tactics for pest suppression, including various forms of biological control and optimized spatiotemporal cropping schemes (*99*). By increasing treatment durability, combinatorial strategies are among the most important instruments for the control of highly adaptable pests, pathogens, and cancers (Fig. 3).

Choosing population sources to anticipate climate change

Although some strategies of applied evolutionary biology are established or rapidly increasing, other rarely used strategies are of interest because of their underexplored potential to replace or complement longstanding management practices. These include using nonlocal seeding sources for replanting in environmental restoration and forestry, as well as the exploitation of group selection-based designs in crop and livestock breeding.

The mismatch of valued plants to new climates is an overarching challenge in forestry, agriculture, and conservation biology. A widespread debate concerns whether to use local versus external sources of genetic material for replanting to best anticipate climate change in forestry, agriculture, wildlife, and environmental restoration. The massive scale of many replanting efforts—400,000 ha of production forest is planted each year in Canada alone (*100*)—plus the long intervals between plantings for many perennial species and restoration projects, means that these choices may have broad economic and ecological consequences. Traditionally, resident stocks have been favored to capture locally valuable adaptations. In forestry this approach is exemplified by established bioclimatic "seed-transfer zones" that guide seed sourcing for planting of some of the world's largest production systems (*101*, *102*). Evidence from wild-plant restoration programs indicates, however, that local sources are not always best, particularly in altered environments (*103*–*108*). This may arise when nearby sources share some of the vulnerabilities responsible for the declines of the original populations (*102*). In these situations, climate mismatches may be better relieved by translocating genotypes that are preadapted to expected conditions (*109*, *110*), for example, more tolerant to heat, drought, or pest stresses (*111*). When single sources do not show the range of adaptations required at a given site, reintroduction may be improved with propagules pooled from a diversity of sources to increase overall genetic variation and, thus, the odds that some individuals will be suited for changing conditions (*103*, *104*, *112*). A recent meta-analysis in restoration ecology underscores shortcomings of the "local-is-best" dictum (*108*), and comparable analyses of sourcing successes and failures in forestry and perennial agriculture are needed to find ways to sustain productivity under climate change.

Exploiting group versus individual performance in crops and livestock

In most agriculture and aquaculture, productivity is measured at the level of groups (e.g., field or herd) rather than in individual performance. More attention to traits that improve group performance may thus offer a broader suite of tactics to increase production while demanding fewer resources, including pesticides, to meet basic human needs (*113*) (Fig. 3). In the majority of natural systems, group selection is considered weak relative to selection among individuals (*114*). Consequently, past natural selection in the ancestors of domesticated species may have favored traits that promote individual performance but are costly to group productivity. One important consequence may be greater current opportunities for artificial selection of individual traits that improve group performance while avoiding inadvertent evolution of "uncooperative" individuals (*8*), such as those with competitive root structures in dryland field crops (*115*). Artificial selection for group yield in maize has produced lines with reduced male function and that bear more-vertical leaves, which reduce the shading of neighbors. Both of these traits decrease individual plant performance while enhancing group productivity (*116*, *117*), but in the absence of strategic breeding to favor these changes directly, they have evolved only slowly, requiring 60 years to appear as unplanned responses to selection on group yield alone (*118*). Weiner and colleagues (*119*) have proposed a proactive design for wheat production that selects for traits that increase collective shading of weeds within specific planting configurations, in order to increase overall crop yield while reducing herbicide use. Similar group-based perspectives apply in animal husbandry, where traits like reduced aggressiveness favor group productivity under domestication, but might have been selected against in the wild (*120*). By combining agronomy and environmental physiology with evolutionary modeling, group-based agricultural systems may offer new and more sustainable paths to meet global production goals.

Addressing evolution across management sectors

One of the most significant outcomes of the scale of human activity is that evolutionary concerns in one management sector often spill over into, or depend on, others (Fig. 4). These connections result from novel biotic interactions because of natural, intentional, or inadvertent transport of organisms and their genes by trade, infrastructure, and waste streams (*121*, *122*). Further coordination of prevention, control, and monitoring will be required to address growing interdependencies among management sectors. Increased exchange of emerging pathogens between health, agricultural, and natural systems is a key case in point (*123*–*126*). For example, although domestic pigs are the principal reservoir of "swine influenza" (H1N1), they simultaneously host other influenza strains, including those associated with human hosts and domestic and migratory avian hosts (*127*). The intensive communal raising of pigs and poultry for food therefore encourages virus strains to exchange genes and adapt to more host species (*128*). One overarching concern is that pigs hosting highly pathogenic wild avian strains (H5N1) could contribute to selection for

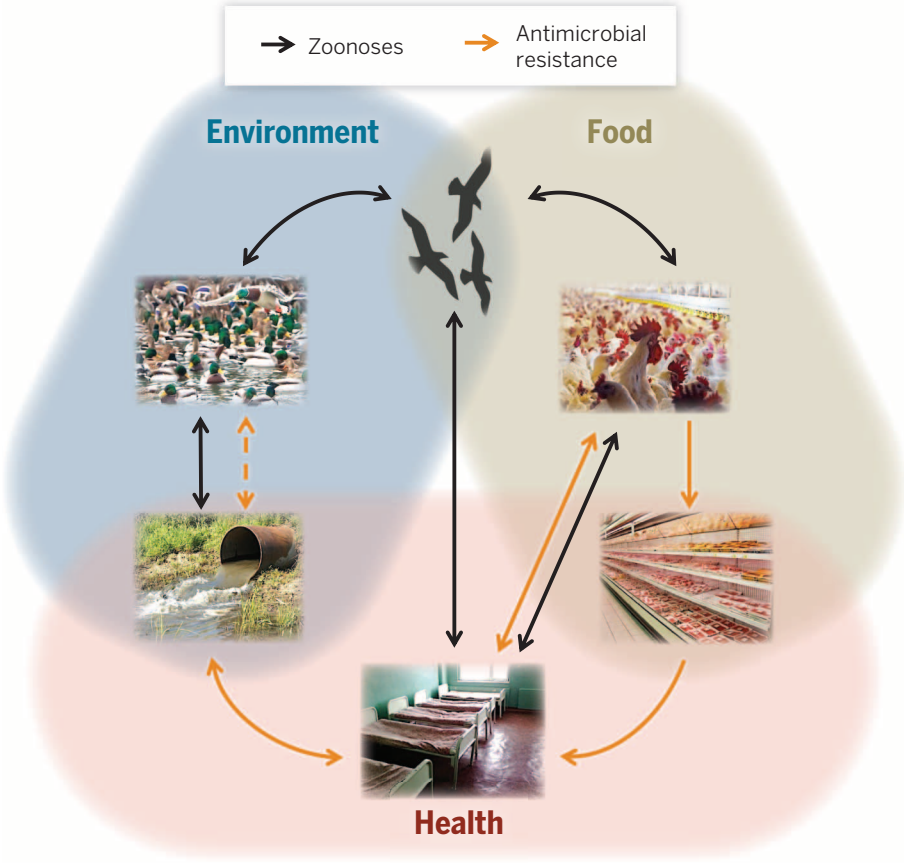

Fig. 4. Emerging pathogens such as zoonoses (black arrows) and resistant bacteria (orange arrows) illustrate interdependencies generated by gene flow among the economic sectors of food, health, and the environment. In zoonoses, vertebrates, such as birds, act as reservoirs for pathogens that can infect humans. Through direct transmission or via domesticated animals, zoonoses are passed to humans and cause regular local and rare global epidemics (such as the flu outbreaks of H5N1-2004 and H1N1-2009). "Reverse zoonoses" are transmitted from infected humans to wildlife (*177*). Antimicrobial resistance in bacterial stains associated with livestock evolves in response to widespread use of antibiotics in agriculture and to a lesser degree because of treatment in humans. Via food items, industry workers, and waste disposal, resistant strains enter other human contexts. In a public health context, resistant strains constitute a growing extra risk during treatment of illnesses, for example, in hospitals. Antibiotics in human effluent cause widespread resistance selection in natural and seminatural environments, which, together with resistance reservoirs in natural environments, further increase the risks of resistant pathogens in humans. In the figure, the dashed line indicates a variety of poorly known interactions among wild species.

the direct mammal-to-mammal transmission that underlies human epidemics. The consequences of such evolution (*129*) are foreshadowed by the recent global outbreaks of H5N1 in 2004 and H1N1 in 2009 (*130*). These events underscore the need for initiatives in prevention and control that cross traditional disciplinary boundaries, including coordinated surveillance of viral evolution and the monitoring of pathogen reservoir species across the food, health, and environment spectrum (*125*, *131*).

The unresolved problem of rapidly evolving antimicrobial resistance is another pressing example of interdependence among management sectors, particularly between systems managed for food production and human health. Annual estimated costs of combatting multidrug-resistant microbes in the United States alone total $35 billion (*132*, *133*), and the failure to produce new antimicrobials as quickly as their predecessors lose efficacy (*134*, *135*) places a premium on stewardship of the few drugs that remain broadly effective (*136*, *137*). Although overprescribing of antibiotics for human treatment is a very real concern, the major use of antimicrobial drugs in many parts of the world is to promote the health and growth of livestock (*138*, *139*). This use selects for antimicrobial-resistant microbes that may infect humans (Fig. 4) (*139*, *140*). For example, antibiotic-treated animals that are raised as food for people are now implicated in the origins of the most extensively resistant *Escherichia coli* encountered in human sepsis (*141*). Particularly worrisome is that, once free in the environment, resistance genes do not dissipate with distance like many abiotic environmental pollutants. Resistance genes can replicate, and thus, they can transfer horizontally among bacterial taxa, travel intact over great distances via hosts, and rise to new abundances in the presence of antimicrobials with similar modes of action. As pools of resistance genes become more prevalent and disseminated through human activities, they are likely to become increasingly important in new regions and management sectors (*142*). Because coupled evolutionary dynamics operate over such large spatial scales and multiple management sectors, their management requires political coordination, as exemplified by the Transatlantic Taskforce on Antimicrobial Resistance (*143*). Regulatory bodies have also taken the first steps to restrict use of some antibiotics to single management sectors (*144*, *145*). Broader and more rigorous implementation of such restrictions will be needed to sustain the most critical public benefits of our modern antibiotic era.

Next steps

Applied evolutionary biology in international policy

Applied evolutionary biology addresses both the rapidly evolving and the mismatched biological systems that underlie many global challenges (*146*). Meeting international objectives for sustainable development [Millennium Development Goals and the anticipated Sustainable Development Goals (*147*)] and biodiversity conservation [the Convention for Biological Diversity's 2020 "Aichi" Biodiversity Targets (*148*)] will require much greater integration of evolutionary principles into policy than has been widely acknowledged. The potential policy contributions of cases reviewed here are summarized in Box 1. For example, we must implement resistance-management strategies for pesticides and antibiotics to meet newly proposed Sustainable Development Goals for human health, food, and water security (*147*). Likewise, choices of adaptable source populations will improve the resilience of restored habitats (Aichi Target 15: "restore 15 percent of degraded habitats before 2020") and increase the reliability of crop supplies. Further, sustainable harvest strategies (*149*, *150*) and early warning signs of unsustainable harvest (*151*) will help to achieve lasting stocks of fish and aquatic invertebrates (Aichi Target 6: all stocks should be harvested sustainably). The identification and protection of diverse genotypes is also critical to the future of crop improvement and for the discovery of chemical compounds such as new therapeutics. In this realm, the international Nagoya Protocol on Access and Benefit-Sharing of genetic resources (*152*) may assist in securing public access to resources for adaptation to local conditions, while coordinating with global research and development efforts (*153*–*155*).

The extensive and targeted genetic manipulations permitted through recent advances in biotechnology are setting the stage for novel biological functions for which we either lack an understanding of potential risks, or knowledge of how best to assess them (*156*). There is a need

Box 1: Recommended contributions of applied evolutionary biology to proposed themes of new international sustainable development goals (*147*), based on examples presented in this review. For the currently negotiated draft of the sustainable development goals, go to http://sustainabledevelopment.un.org/focussdgs.html.

Goal 1: Thriving lives and livelihoods

- Reduce chronic lifestyle disease through environmental alignment of human lifestyle.
- Reduce environmental levels of human toxicants through application of reduced selection response techniques* to biocides.
- Apply reduced selection response techniques to maintain long-term efficacy of antimicrobials and to avert the antibiotics crisis.
- Reconcile individual and group incentives in health systems to reduce virulence and resistance of emerging and reemerging pathogens.

Goal 2: Sustainable food security

- Increase crop yield through continued selection of varieties and improved access to these.
- Prolong efficacy of pesticides and artificially selected or GE crops through reduced selection–response techniques.
- Improve yields through integration of group selection in production of novel crop varieties.
- Reduce climate change impact by choosing crop varieties resilient to drought, flooding, and other extremes.

Goal 3: Secure sustainable water

- Increase water security through use of reduced selection–response techniques to water-polluting pesticides and/or biocides
- Use genetic manipulation to produce crop varieties with improved water economy.

Goal 4: Universal clean energy

- Improve biofuels through genetic manipulation with the aim to reduce CO_2 emissions and land area for energy production.
- Assess risks and benefits of synthetic organisms for biofuel production while taking gene flow, land use, and property rights issues into account.

Goal 5: Healthy and productive ecosystems

- Reduce biodiversity extinction rates through environmental alignment and genetic manipulation of fitness.
- Retain naturalness of captive biodiversity through environmental alignment.
- Choose preadapted or high-diversity sources for increased habitat restoration success.
- Avoid collapse and protect genetic diversity of aquatic resources through nonselective harvesting strategies informed by early warning signals.

Goal 6: Governance for sustainable societies

- Incorporate externalities from rapid evolution, as well as the loss of evolutionary history and evolutionary potential, into green accounting for sustainable governance of the Earth system.
- Coordinate strategies of sustainable development goals in a coupled-systems framework to reduce conflicts from inadvertent contemporary evolution and phenotype-environment mismatch.

*"Reduced selection–response techniques" refer to the four tactics in Fig. 3 that slow evolution by varying selection in space and time, diversifying selection, and targeting of specific traits, as well as adoption of alternatives to strong selection agents, such as toxins.

for an overarching international framework to regulate synthetic (*156*, *157*), as well as conventional and advanced, GM organisms (*158*)–a framework that also would reduce conflict between existing frameworks (*159*). Perhaps the area of applied evolutionary biology where development of international policy is most urgent is the area of synthetic biology. Synthesizing wholly or partially novel organisms offers tremendous opportunities in many areas such as biofuels, medicine, environmental restoration, and conservation (*160*–*162*), but national and international guidelines are needed to avert potentially harmful outcomes (*156*, *163*). Segments of medicine and agriculture include social scientists and economists in systematic risk assessment (*76*, *164*). Similar practices would benefit conservation biology and natural resource management, as increasingly proactive and intensive manipulations appear on the horizon. These prospects include resurrected species and wild populations genetically engineered for resistance to lethal diseases such as chytrid fungus in frogs and white-nose syndrome in bats (*161*, *162*).

Implementing applied evolutionary biology locally and globally

Reconciliation of individual and group stakeholder interests plays a central role in the effort to achieve sustainability through applied evolutionary biology (*165*–*168*). Anthropogenic evolutionary change often has consequences that extend beyond the immediate vicinity of the causal agents and pose dilemmas in achieving cooperation from local to global scales (*169*). Thus, in some applied evolutionary strategies, individuals must exchange their private short-term gains for the long-term public good. In managing pest resistance to transgenic Bt crops, farmers who plant refuges of conventional crops contribute to the long-term public good of sustained pest susceptibility to Bt toxin but may incur the short-term private cost of pest damage to their refuges. However, farmers in five midwestern states of the United States accrued nearly two-thirds of the estimated $6.8 billion in Bt corn benefits between 1996 and 2009 from land planted with non-Bt corn refuges (*170*). This benefit arose because widespread adoption of Bt corn caused regional suppression of the major target pest and non-Bt corn seed was less expensive than Bt corn (*170*). Despite this benefit, farmer compliance with the refuge strategy for Bt corn in the United States has steadily declined and threatens the sustainability of resistance management (*171*). Farmers are increasingly planting Bt seeds alone, which may reflect their efforts to reduce the perceived risk of short-term losses from pest damage to refuges. Such conflicts between individual and public good may be the rule rather than the exception in the implementation of applied evolutionary biology.

The economic theories of public choice provide tools for reconciling individual and group conflicts (*169*) (Box 1). Governments can tax undesirable actions, subsidize desirable ones, regulate activities (*144*, *145*), and create tradable property rights. For example, subsidies and regulated access to public schools can increase participation in vaccination programs that benefit public health but may increase risks to unvaccinated individuals (*170*). Theoretical modeling suggests that an unregulated vaccination market will yield too little advance vaccination and too much vaccination at the time of infection, which could select for increased virulence (*164*). With pathogen resistance, both the relative fitness of resistant genotypes in untreated environments

(*174*, *175*) and the prevalence of resistance in natural environments (*176*) may increase the cost of lost susceptibility to a drug. Improved policies that reduce public costs may emerge from better accounting of the causes and consequences of such evolutionary externalities (*154*, *177*).

Toward a unified discipline

As demonstrated by many of the examples above, applied evolutionary biology uses principles common to all areas of biology, and because of this, progress in one area may often enable solutions in others. New approaches in this developing field may best be generated and assessed through collaborations that span disciplinary boundaries (*178*) (Fig. 3). Promoting greater adoption and consistency in the use of evolutionary terminology, which is currently inconsistent across disciplines (*179*), will therefore be an important first step toward a more unified field of applied evolutionary biology.

The global scale of human impacts is now more widely appreciated than ever before. Successful governance of living systems requires understanding evolutionary history, as well as contemporary and future evolutionary dynamics. Our current scientific capacity for evolutionarily informed management does not match the need, but it can be increased through new and more widespread training and collaboration, monitored experimentation, and context-sensitive implementation. Like engineering, which is a multifaceted applied science with common core principles, shared vocabulary, and coordinated methods, applied evolutionary biology has the potential to serve society as a predictive and integrative framework for addressing practical concerns in applied biology that share at their core the basic evolutionary principles governing life.

REFERENCES AND NOTES

1. Millennium Ecosystem Assessment, *Ecosystems and Human Well-Being: Synthesis*. (Island Press, Washington, DC, 2005).
2. E. C. Ellis *et al*., Used planet: A global history. *Proc. Natl. Acad. Sci. U.S.A.* **110**, 7978–7985 (2013). doi: 10.1073/pnas.1217241110; pmid: 23630271
3. R. G. Latta, Conservation genetics as applied evolution: From genetic pattern to evolutionary process. *Evol. Appl.* **1**, 84–94 (2008). doi: 10.1111/j.1752-4571.2007.00008.x
4. S. R. Palumbi, Humans as the world's greatest evolutionary force. *Science* **293**, 1786–1790 (2001). doi: 10.1126/science.293.5536.1786; pmid: 11546863
5. P. D. Gluckman, C. T. Bergstrom, Evolutionary biology within medicine: A perspective of growing value. *BMJ* **343** (dec19 suppl.1), d7671 (2011). doi: 10.1136/bmj.d7671; pmid: 22184558
6. F. Gould, Broadening the application of evolutionarily based genetic pest management. *Evolution* **62**, 500–510 (2008). doi: 10.1111/j.1558-5646.2007.00298.x; pmid: 17999722
7. P. H. Thrall *et al*., Evolution in agriculture: The application of evolutionary approaches to the management of biotic interactions in agro-ecosystems. *Evol. Appl.* **4**, 200–215 (2011). doi: 10.1111/j.1752-4571.2010.00179.x
8. R. F. Denison, *Darwinian Agriculture: How Understanding Evolution Can Improve Agriculture* (Princeton Univ. Press, Princeton, NJ, 2012).
9. D. W. Hollomon, Do we have the tools to manage resistance in the future? *Pest Manag. Sci.* **68**, 149–154 (2012). doi: 10.1002/ps.2291; pmid: 22223198
10. C. A. Stockwell, A. P. Hendry, M. K. Kinnison, Contemporary evolution meets conservation biology. *Trends Ecol. Evol.* **18**, 94–101 (2003). doi: 10.1016/S0169-5347(02)00044-7
11. A. P. Hendry *et al*., Evolutionary biology in biodiversity science, conservation, and policy: A call to action. *Evolution* **64**, 1517–1528 (2010). pmid: 20067518
12. A. P. Hendry *et al*., Evolutionary principles and their practical application. *Evol. Appl.* **4**, 159–183 (2011). doi: 10.1111/j.1752-4571.2010.00165.x
13. WHO, Antimicrobial resistance: Global report on surveillance (2014); www.who.int/drugresistance/documents/surveillancereport/en/.
14. B. E. Tabashnik, D. Mota-Sanchez, M. E. Whalon, R. M. Hollingworth, Y. Carrière, Defining terms for proactive management of resistance to Bt crops and pesticides. *J. Econ. Entomol.* **107**, 496–507 (2014). doi: 10.1603/EC13458; pmid: 24772527
15. P. D. Gluckman, M. A. Hanson, *Mismatch: Why Our World No Longer Fits Our Bodies* (Oxford Univ. Press, Oxford, 2006).
16. A. D. Barnosky *et al*., Has the Earth's sixth mass extinction already arrived? *Nature* **471**, 51–57 (2011). doi: 10.1038/nature09678; pmid: 21368823
17. J. J. Bull, H. A. Wichman, Applied evolution. *Annu. Rev. Ecol. Syst.* **32**, 183–217 (2001). doi: 10.1146/annurev.ecolsys.32.081501.114020
18. S. P. Carroll, C. W. Fox, *Conservation Biology: Evolution in Action* (Oxford Univ. Press, Oxford, 2008).
19. P. D. Gluckman, M. A. Hanson, T. Buklijas, F. M. Low, A. S. Beedle, Epigenetic mechanisms that underpin metabolic and cardiovascular diseases. *Nat. Rev. Endocrinol.* **5**, 401–408 (2009). doi: 10.1038/nrendo.2009.102; pmid: 19488075
20. D. Hartl, *A Primer of Population Genetics* (Sinauer Associates, Inc., Sunderland, MA, 1988).
21. P. A. Abrams, Modelling the adaptive dynamics of traits involved in inter- and intraspecific interactions: An assessment of three methods. *Ecol. Lett.* **4**, 166–175 (2001). doi: 10.1046/j.1461-0248.2001.00199.x
22. C. K. Ghalambor, J. K. McKay, S. P. Carroll, D. N. Reznick, Adaptive versus non-adaptive phenotypic plasticity and the potential for contemporary adaptation in new environments. *Funct. Ecol.* **21**, 394–407 (2007). doi: 10.1111/j.1365-2435.2007.01283.x
23. M. T. Kinnison, N. G. Hairston, Eco-evolutionary conservation biology: Contemporary evolution and the dynamics of persistence. *Funct. Ecol.* **21**, 444–454 (2007). doi: 10.1111/j.1365-2435.2007.01278.x
24. C. A. Aktipis, V. S. Kwan, K. A. Johnson, S. L. Neuberg, C. C. Maley, Overlooking evolution: A systematic analysis of cancer relapse and therapeutic resistance research. *PLoS ONE* **6**, e26100 (2011). doi: 10.1371/journal.pone.0026100; pmid: 22125594
25. N. Mouquet *et al*., Ecophylogenetics: Advances and perspectives. *Biol. Rev. Camb. Philos. Soc.* **87**, 769–785 (2012). doi: 10.1111/j.1469-185X.2012.00224.x; pmid: 22432924
26. G. M. Mace, A. Purvis, Evolutionary biology and practical conservation: Bridging a widening gap. *Mol. Ecol.* **17**, 9–19 (2008). doi: 10.1111/j.1365-294X.2007.03455.x; pmid: 17696991
27. L.-M. Chevin, R. Gallet, R. Gomulkiewicz, R. D. Holt, S. Fellous, Phenotypic plasticity in evolutionary rescue experiments. *Philos. Trans. R. Soc. Lond. B Biol. Sci.* **368**, 20120089 (2013). doi: 10.1098/rstb.2012.0089; pmid: 23209170
28. A. F. Read, S. Huijben, Evolutionary biology and the avoidance of antimicrobial resistance. *Evol. Appl.* **2**, 40–51 (2009). doi: 10.1111/j.1752-4571.2008.00066.x
29. A. F. Read, T. Day, S. Huijben, The evolution of drug resistance and the curious orthodoxy of aggressive chemotherapy. *Proc. Natl. Acad. Sci. U.S.A.* **108** (suppl. 2), 10871–10877 (2011). doi: 10.1073/pnas.1100299108; pmid: 21690376
30. M. V. Ashley *et al*., Evolutionarily enlightened management. *Biol. Conserv.* **111**, 115–123 (2003). doi: 10.1016/S0006-3207(02)00279-3
31. S. E. Williams, E. A. Hoffman, Minimizing genetic adaptation in captive breeding programs: A review. *Biol. Conserv.* **142**, 2388–2400 (2009). doi: 10.1016/j.biocon.2009.05.034
32. K. Leus, K. Traylor-Holzer, R. C. Lacy, Genetic and demographic population management in zoos and aquariums: Recent developments, future challenges and opportunities for scientific research. *Int. Zoo Yearb.* **45**, 213–225 (2011). doi: 10.1111/j.1748-1090.2011.00138.x
33. P. D. Gluckman, F. M. Low, T. Buklijas, M. Hanson, A. S. Beedle, How evolutionary principles improve the understanding of human health and disease. *Evol. Appl.* **4**, 249–263 (2011). doi: 10.1111/j.1752-4571.2010.00164.x
34. L. Cordain *et al*., Origins and evolution of the Western diet: Health implications for the 21st century. *Am. J. Clin. Nutr.* **81**, 341–354 (2005). pmid: 15699220
35. R. C. Brownson, D. Haire-Joshu, D. A. Luke, Shaping the context of health: A review of environmental and policy approaches in the prevention of chronic diseases. *Annu. Rev. Public Health* **27**, 341–370 (2006). doi: 10.1146/annurev.publhealth.27.021405.102137; pmid: 16533121
36. T. A. Gaziano, N. Pagidipati, Scaling up chronic disease prevention interventions in lower- and middle-income countries. *Annu. Rev. Public Health* **34**, 317–335 (2013). doi: 10.1146/annurev-publhealth-031912-114402; pmid: 23297660
37. C. D. Mathers, D. Loncar, Projections of global mortality and burden of disease from 2002 to 2030. *PLoS Med.* **3**, e442 (2006). doi: 10.1371/journal.pmed.0030442; pmid: 17132052
38. D. E. Bloom *et al*., "The global economic burden of noncommunicable diseases" (Working paper no. 87, Program on the Global Demography of Aging, Harvard School of Public Health; World Economic Forum, Geneva, 2012).
39. J. Woodcock, O. H. Franco, N. Orsini, I. Roberts, Non-vigorous physical activity and all-cause mortality: Systematic review and meta-analysis of cohort studies. *Int. J. Epidemiol.* **40**, 121–138 (2011). doi: 10.1093/ije/dyq104; pmid: 20630992
40. WHO, Environmental and occupational cancers. www.who.int/mediacentre/factsheets/fs350/en/.
41. J. Lynch, G. D. Smith, A life course approach to chronic disease epidemiology. *Annu. Rev. Public Health* **26**, 1–35 (2005). doi: 10.1146/annurev.publhealth.26.021304.144505; pmid: 15760279
42. D. A. Chokshi, T. A. Farley, The cost-effectiveness of environmental approaches to disease prevention. *N. Engl. J. Med.* **367**, 295–297 (2012). doi: 10.1056/NEJMp1206268; pmid: 22830461
43. J. Flannick *et al*., Go-T2D ConsortiumT2D-GENES Consortium, Loss-of-function mutations in *SLC30A8* protect against type 2 diabetes. *Nat. Genet.* **46**, 357–363 (2014). doi: 10.1038/ng.2915; pmid: 24584071
44. G. S. Omenn, Evolution in health and medicine Sackler colloquium: Evolution and public health. *Proc. Natl. Acad. Sci. U.S.A.* **107** (suppl. 1), 1702–1709 (2010). doi: 10.1073/pnas.0906198106; pmid: 19966311
45. J. C. Denny *et al*., Systematic comparison of phenome-wide association study of electronic medical record data and genome-wide association study data. *Nat. Biotechnol.* **31**, 1102–1111 (2013). doi: 10.1038/nbt.2749; pmid: 24270849
46. M. Travisano, R. G. Shaw, Lost in the map. *Evolution* **67**, 305–314 (2013). doi: 10.1111/j.1558-5646.2012.01802.x; pmid: 23356605
47. S. M. Rappaport, Implications of the exposome for exposure science. *J. Expo. Sci. Environ. Epidemiol.* **21**, 5–9 (2011). doi: 10.1038/jes.2010.50; pmid: 21081972
48. H. C. J. Godfray *et al*., Food security: The challenge of feeding 9 billion people. *Science* **327**, 812–818 (2010). doi: 10.1126/science.1185383; pmid: 20110467
49. C. James, "Executive summary. Global status of commercialized biotech/GM crops" (ISAAA Brief 46, International Service for the Acquisitions of Agri-Biotech Applications, New York, 2013).
50. M. Ashraf, Inducing drought tolerance in plants: Recent advances. *Biotechnol. Adv.* **28**, 169–183 (2010). doi: 10.1016/j.biotechadv.2009.11.005; pmid: 19914371
51. E. Pauwels, Public understanding of synthetic biology. *Bioscience* **63**, 79–89 (2013). doi: 10.1525/bio.2013.63.2.4
52. P. Aerni, Resistance to agricultural biotechnology: The importance of distinguishing between weak and strong public attitudes. *Biotechnol. J.* **8**, 1129–1132 (2013). pmid: 23857924
53. S.-E. Jacobsen, M. Sørensen, S. M. Pedersen, J. Weiner, Feeding the world: Genetically modified crops versus agricultural biodiversity. *Agron. Sustain. Dev.* **33**, 651–662 (2013). doi: 10.1007/s13593-013-0138-9
54. R. K. Varshney, K. C. Bansal, P. K. Aggarwal, S. K. Datta, P. Q. Craufurd, Agricultural biotechnology for crop improvement in a variable climate: Hope or hype? *Trends Plant Sci.* **16**, 363–371 (2011). doi: 10.1016/j.tplants.2011.03.004; pmid: 21497543
55. A. Marshall, Drought-tolerant varieties begin global march. *Nat. Biotechnol.* **32**, 308–308 (2014). doi: 10.1038/nbt.2875
56. R. K. Varshney *et al*., Can genomics boost productivity of orphan crops? *Nat. Biotechnol.* **30**, 1172–1176 (2012). doi: 10.1038/nbt.2440; pmid: 23222781
57. S. Yang, B. Vanderbeld, J. Wan, Y. Huang, Narrowing down the targets: Towards successful genetic engineering of drought-tolerant crops. *Mol. Plant* **3**, 469–490 (2010). doi: 10.1093/mp/ssq016; pmid: 20507936

58. A. C. M. Gaudin, A. Henry, A. H. Sparks, I. H. Slamet-Loedin, Taking transgenic rice drought screening to the field. *J. Exp. Bot.* **64**, 109–117 (2013). doi: 10.1093/jxb/ers313; pmid: 23202133
59. International Service for the Acquisition of Agri-Biotech Applications, Approval database 2013, http://www.isaaa.org/gmapprovaldatabase/default.asp (2013).
60. K. L. Mercer, H. R. Perales, J. D. Wainwright, Climate change and the transgenic adaptation strategy: Smallholder livelihoods, climate justice, and maize landraces in Mexico. *Glob. Environ. Change* **22**, 495–504 (2012). doi: 10.1016/j.gloenvcha.2012.01.003
61. M. Tachibana *et al*., Towards germline gene therapy of inherited mitochondrial diseases. *Nature* **493**, 627–631 (2013). doi: 10.1038/nature11647; pmid: 23103867
62. J. H. Kordower, D. Kirik, Introduction. *Neurobiol. Dis.* **48**, 151–152 (2012). doi: 10.1016/j.nbd.2012.07.014; pmid: 22841531
63. I.-K. Choi, C.-O. Yun, Recent developments in oncolytic adenovirus-based immunotherapeutic agents for use against metastatic cancers. *Cancer Gene Ther.* **20**, 70–76 (2013). doi: 10.1038/cgt.2012.95; pmid: 23306610
64. D. M. Lipinski, M. Thake, R. E. MacLaren, Clinical applications of retinal gene therapy. *Prog. Retin. Eye Res.* **32**, 22–47 (2013). doi: 10.1016/j.preteyeres.2012.09.001; pmid: 22995954
65. K. J. Wert, R. J. Davis, J. Sancho-Pelluz, P. M. Nishina, S. H. Tsang, Gene therapy provides long-term visual function in a pre-clinical model of retinitis pigmentosa. *Hum. Mol. Genet.* **22**, 558–567 (2013). doi: 10.1093/hmg/dds466; pmid: 23108158
66. K. Suzuki, H. Matsubara, Recent advances in p53 research and cancer treatment. *J. Biomed. Biotechnol.* **2011**, 978312 (2011). doi: 10.1155/2011/978312; pmid: 21765642
67. O. Kilpivaara, L. A. Aaltonen, Diagnostic cancer genome sequencing and the contribution of germline variants. *Science* **339**, 1559–1562 (2013). doi: 10.1126/science.1233899; pmid: 23539595
68. P. R. Lowenstein, M. G. Castro, Uncertainty in the translation of preclinical experiments to clinical trials. Why do most phase III clinical trials fail? *Curr. Gene Ther.* **9**, 368–374 (2009). doi: 10.2174/156652309789753392; pmid: 19860651
69. M. Edelstein, Gene therapy clinical trials worldwide. *J. Gene Medicine* database (2014); http://www.abedia.com/wiley/index.html.
70. C. C. Vigueira, K. M. Olsen, A. L. Caicedo, The red queen in the corn: Agricultural weeds as models of rapid adaptive evolution. *Heredity* **110**, 303–311 (2013). doi: 10.1038/hdy.2012.104; pmid: 23188175
71. S. E. Greene, A. Reid, *Moving Targets: Fighting the Evolution of Resistance in Infections, Pests, and Cancer* (American Society of Microbiology, Washington, DC, 2013); http://bit.ly/YeNhoS.
72. S. B. Powles, Q. Yu, Evolution in action: Plants resistant to herbicides. *Annu. Rev. Plant Biol.* **61**, 317–347 (2010). doi: 10.1146/annurev-arplant-042809-112119; pmid: 20192743
73. I. HeapThe International Survey of Herbicide Resistant Weeds, (2013); www.weedscience.com/summary/home.aspx.
74. B. E. Tabashnik, Evolution of resistance to *Bacillus thuringiensis*. *Annu. Rev. Entomol.* **39**, 47–79 (1994). doi: 10.1146/annurev.en.39.010194.000403
75. F. Gould, Sustainability of transgenic insecticidal cultivars: Integrating pest genetics and ecology. *Annu. Rev. Entomol.* **43**, 701–726 (1998). doi: 10.1146/annurev.ento.43.1.701; pmid: 15012402
76. EPA, "The Environmental Protection Agency's White Paper on *Bacillus thuringiensis* plant-pesticide resistance management" (EPA, Washington, DC, 1998).
77. B. E. Tabashnik, T. Brévault, Y. Carrière, Insect resistance to Bt crops: Lessons from the first billion acres. *Nat. Biotechnol.* **31**, 510–521 (2013). doi: 10.1038/nbt.2597; pmid: 23752438
78. B. E. Tabashnik, A. J. Gassmann, D. W. Crowder, Y. Carrière, Insect resistance to Bt crops: Evidence versus theory. *Nat. Biotechnol.* **26**, 199–202 (2008). doi: 10.1038/nbt1382; pmid: 18259177
79. E. S. Dunlop, M. L. Baskett, M. Heino, U. Dieckmann, The propensity of marine reserves to reduce the evolutionary effects of fishing in a migratory species. *Evol. Appl.* **2**, 371–393 (2009). doi: 10.1111/j.1752-4571.2009.00089.x
80. R. A. Gatenby, J. Brown, T. Vincent, Lessons from applied ecology: Cancer control using an evolutionary double bind. *Cancer Res.* **69**, 7499–7502 (2009). doi: 10.1158/0008-5472.CAN-09-1354; pmid: 19752088
81. A. S. Silva, R. A. Gatenby, A theoretical quantitative model for evolution of cancer chemotherapy resistance. *Biol. Direct* **5**, 25 (2010). doi: 10.1186/1745-6150-5-25; pmid: 20406443
82. R. J. Gillies, D. Verduzco, R. A. Gatenby, Evolutionary dynamics of carcinogenesis and why targeted therapy does not work. *Nat. Rev. Cancer* **12**, 487–493 (2012). doi: 10.1038/nrc3298; pmid: 22695393
83. M. Greaves, C. C. Maley, Clonal evolution in cancer. *Nature* **481**, 306–313 (2012). doi: 10.1038/nature10762; pmid: 22258609
84. D. B. Longley, P. G. Johnston, Molecular mechanisms of drug resistance. *J. Pathol.* **205**, 275–292 (2005). doi: 10.1002/path.1706; pmid: 15641020
85. R. A. Gatenby, A change of strategy in the war on cancer. *Nature* **459**, 508–509 (2009). doi: 10.1038/459508a; pmid: 19478766
86. V. Almendro *et al*., Inference of tumor evolution during chemotherapy by computational modeling and in situ analysis of genetic and phenotypic cellular diversity. *Cell Rep.* **6**, 514–527 (2014). doi: 10.1016/j.celrep.2013.12.041; pmid: 24462293
87. J.-B. Michel, P. J. Yeh, R. Chait, R. C. Moellering Jr., R. Kishony, Drug interactions modulate the potential for evolution of resistance. *Proc. Natl. Acad. Sci. U.S.A.* **105**, 14918–14923 (2008). doi: 10.1073/pnas.0800944105; pmid: 18815368
88. REX Consortium, Heterogeneity of selection and the evolution of resistance. *Trends Ecol. Evol.* **28**, 110–118 (2013). doi: 10.1016/j.tree.2012.09.001; pmid: 23040463
89. J. J. Cunningham, R. A. Gatenby, J. S. Brown, Evolutionary dynamics in cancer therapy. *Mol. Pharm.* **8**, 2094–2100 (2011). doi: 10.1021/mp2002279; pmid: 21815657
90. R. M. Gulick, Antiretroviral treatment 2010: Progress and controversies. *J. Acquir. Immune Defic. Syndr.* **55** (suppl. 1), S43–S48 (2010). doi: 10.1097/QAI.0b013e3181f9c09e; pmid: 21045599
91. R. K. Gupta, D. A. Van de Vijver, S. Manicklal, M. A. Wainberg, Evolving uses of oral reverse transcriptase inhibitors in the HIV-1 epidemic: From treatment to prevention. *Retrovirology* **10**, 82 (2013). doi: 10.1186/1742-4690-10-82; pmid: 23902855
92. H. Brun *et al*., Quantitative resistance increases the durability of qualitative resistance to *Leptosphaeria maculans* in *Brassica napus*. *New Phytol.* **185**, 285–299 (2010). doi: 10.1111/j.1469-8137.2009.03049.x; pmid: 19814776
93. B. E. Tabashnik, Managing resistance with multiple pesticide tactics: theory, evidence, and recommendations. *J. Econ. Entomol.* **82**, 1263–1269 (1989). pmid: 2689487
94. C. T. Bergstrom, M. Lo, M. Lipsitch, Ecological theory suggests that antimicrobial cycling will not reduce antimicrobial resistance in hospitals. *Proc. Natl. Acad. Sci. U.S.A.* **101**, 13285–13290 (2004). doi: 10.1073/pnas.0402298101; pmid: 15308772
95. J. P. Torella, R. Chait, R. Kishony, Optimal drug synergy in antimicrobial treatments. *PLOS Comput. Biol.* **6**, e1000796 (2010). doi: 10.1371/journal.pcbi.1000796; pmid: 20532210
96. B. Jacquemin, J. Gasquez, X. Reboud, Modelling binary mixtures of herbicides in populations resistant to one of the components: Evaluation for resistance management. *Pest Manag. Sci.* **65**, 113–121 (2009). doi: 10.1002/ps.1647; pmid: 18798178
97. R. T. Roush, Two–toxin strategies for management of insecticidal transgenic crops: Can pyramiding succeed where pesticide mixtures have not? *Philos. Trans. R. Soc. Lond. B Biol. Sci.* **353**, 1777–1786 (1998). doi: 10.1098/rstb.1998.0330
98. J.-Z. Zhao *et al*., Concurrent use of transgenic plants expressing a single and two *Bacillus thuringiensis* genes speeds insect adaptation to pyramided plants. *Proc. Natl. Acad. Sci. U.S.A.* **102**, 8426–8430 (2005). doi: 10.1073/pnas.0409324102; pmid: 15939892
99. A. M. Shelton *et al*., in *Field Manual of Techniques in Invertebrate Pathology* (Springer Amsterdam, 2007), pp. 793–811.
100. J. H. Pedlar *et al*., Placing forestry in the assisted migration debate. *Bioscience* **62**, 835–842 (2012). doi: 10.1525/bio.2012.62.9.10
101. L. K. Gray, T. Gylander, M. S. Mbogga, P.-Y. Chen, A. Hamann, Assisted migration to address climate change: Recommendations for aspen reforestation in western Canada. *Ecol. Appl.* **21**, 1591–1603 (2011). doi: 10.1890/10-1054.1; pmid: 21830704
102. K. M. Potter, W. W. Hargrove, Determining suitable locations for seed transfer under climate change: A global quantitative method. *New For.* **43**, 581–599 (2012). doi: 10.1007/s11056-012-9322-z
103. S. Godefroid *et al*., How successful are plant species reintroductions? *Biol. Conserv.* **144**, 672–682 (2011). doi: 10.1016/j.biocon.2010.10.003
104. L. M. Broadhurst *et al*., Seed supply for broadscale restoration: Maximizing evolutionary potential. *Evol. Appl.* **1**, 587–597 (2008).
105. A. R. Weeks *et al*., Assessing the benefits and risks of translocations in changing environments: A genetic perspective. *Evol. Appl.* **4**, 709–725 (2011). doi: 10.1111/j.1752-4571.2011.00192.x; pmid: 22287981
106. M. Byrne, L. Stone, M. A. Millar, Assessing genetic risk in revegetation. *J. Appl. Ecol.* **48**, 1365–1373 (2011). doi: 10.1111/j.1365-2664.2011.02045.x
107. K. Vander Mijnsbrugge, A. Bischoff, B. Smith, A question of origin: Where and how to collect seed for ecological restoration. *Basic Appl. Ecol.* **11**, 300–311 (2010). doi: 10.1016/j.baae.2009.09.002
108. S. Godefroid, T. Vanderborght, Plant reintroductions: The need for a global database. *Biodivers. Conserv.* **20**, 3683–3688 (2011). doi: 10.1007/s10531-011-0120-2
109. D. J. Merritt, K. W. Dixon, Conservation. Restoration seed banks—a matter of scale. *Science* **332**, 424–425 (2011). doi: 10.1126/science.1203083; pmid: 21512021
110. AdapTRee website; http://adaptree.sites.olt.ubc.ca/.
111. J. A. Hicke, J. C. Jenkins, Mapping lodgepole pine stand structure susceptibility to mountain pine beetle attack across the western United States. *For. Ecol. Manage.* **255**, 1536–1547 (2008). doi: 10.1016/j.foreco.2007.11.027
112. C. Moritz, Conservation units and translocations: Strategies for conserving evolutionary processes. *Hereditas* **130**, 217–228 (1999). doi: 10.1111/j.1601-5223.1999.00217.x
113. C. M. Donald, The breeding of crop ideotypes. *Euphytica* **17**, 385–403 (1968). doi: 10.1007/BF00056241
114. A. Gardner, A. Grafen, Capturing the superorganism: A formal theory of group adaptation. *J. Evol. Biol.* **22**, 659–671 (2009). doi: 10.1111/j.1420-9101.2008.01681.x; pmid: 19210588
115. A. Kumar, N. C. Turner, D. P. Singh, P. Singh, M. Barr, Diurnal and seasonal patterns of water potential, photosynthesis, evapotranspiration and water use efficiency of clusterbean. *Photosynthetica* **37**, 601–607 (2000). doi: 10.1023/A:1007127726207
116. P. R. Jennings, Plant type as a rice breeding objective. *Crop Sci.* **4**, 13–15 (1964). doi: 10.2135/cropsci1964.0011183X000400010005x
117. W. G. Duncan, W. A. Williams, R. S. Loomis, Tassels and productivity of maize. *Crop Sci.* **7**, 37–39 (1967). doi: 10.2135/cropsci1967.0011183X000700010013x
118. D. N. Duvick, K. G. Cassman, Post-green-revolution trends in yield potential of temperate maize in the north-central United States. *Crop Sci.* **39**, 1622–1630 (1999). doi: 10.2135/cropsci1999.3961622x
119. J. Weiner, S. B. Andersen, W. K. M. Wille, H. W. Griepentrog, J. M. Olsen, Evolutionary Agroecology: The potential for cooperative, high density, weed-suppressing cereals. *Evol. Appl.* **3**, 473–479 (2010). doi: 10.1111/j.1752-4571.2010.00144.x
120. M. J. Wade, P. Bijma, E. D. Ellen, W. Muir, Group selection and social evolution in domesticated animals. *Evol. Appl.* **3**, 453–465 (2010). doi: 10.1111/j.1752-4571.2010.00147.x
121. J. Liu *et al*., Coupled human and natural systems. *Ambio* **36**, 639–649 (2007). doi: 10.1579/0044-7447(2007)36[639:CHANS]2.0.CO;2; pmid: 18240679
122. P. Rabinowitz, L. Conti, Links among human health, animal health, and ecosystem health. *Annu. Rev. Public Health* **34**, 189–204 (2013). doi: 10.1146/annurev-publhealth-031912-114426; pmid: 23330700
123. M. E. J. Woolhouse, S. Gowtage-Sequeria, Host range and emerging and reemerging pathogens. *Emerg. Infect. Dis.* **11**, 1842–1847 (2005). doi: 10.3201/eid1112.050997; pmid: 16485468
124. B. Olsen *et al*., Global patterns of influenza a virus in wild birds. *Science* **312**, 384–388 (2006). doi: 10.1126/science.1122438; pmid: 16627734
125. G. J. D. Smith *et al*., Origins and evolutionary genomics of the 2009 swine-origin H1N1 influenza A epidemic. *Nature* **459**, 1122–1125 (2009). doi: 10.1038/nature08182; pmid: 19516283
126. K. E. Jones *et al*., Global trends in emerging infectious diseases. *Nature* **451**, 990–993 (2008). doi: 10.1038/nature06536; pmid: 18288193
127. W. Ma, R. E. Kahn, J. A. Richt, The pig as a mixing vessel for influenza viruses: Human and veterinary implications. *J. Mol. Genet. Med.* **3**, 158–166 (2008). pmid: 19565018
128. H. M. Yassine, C. W. Lee, Y. M. Saif, Interspecies transmission of influenza A viruses between swine and poultry. *Curr. Top. Microbiol. Immunol.* **370**, 227–240 (2011). doi: 10.1007/82_2011_180; pmid: 22167468

129. S. Altizer, R. Bartel, B. A. Han, Animal migration and infectious disease risk. *Science* **331**, 296–302 (2011). doi: 10.1126/science.1194694; pmid: 21252339
130. K. R. Ríos-Soto, B. Song, C. Castillo-Chavez, Epidemic spread of influenza viruses: The impact of transient populations on disease dynamics. *Math. Biosci. Eng.* **8**, 199–222 (2011). doi: 10.3934/mbe.2011.8.199; pmid: 21361408
131. K. M. Pepin, S. Lass, J. R. Pulliam, A. F. Read, J. O. Lloyd-Smith, Identifying genetic markers of adaptation for surveillance of viral host jumps. *Nat. Rev. Microbiol.* **8**, 802–813 (2010). doi: 10.1038/nrmicro2440; pmid: 20938453
132. European Center for Disease Prevention and Control and European Medicines Agency, *The Bacterial Challenge: Time to React* (ECDC/EMEA Joint Technical Report, EMEA/576176/2009, Stockholm, 2009).
133. Alliance for the Prudent Use of Antibiotics, *The Cost of Antibiotic Resistance to U.S. Families and the Healthcare System* (APUA, Boston, MA, 2010).
134. M. A. Cooper, D. Shlaes, Fix the antibiotics pipeline. *Nature* **472**, 32–32 (2011). doi: 10.1038/472032a; pmid: 21475175
135. M. S. Butler, M. A. Blaskovich, M. A. Cooper, Antibiotics in the clinical pipeline in 2013. *J. Antibiot. (Tokyo)* **66**, 571–591 (2013). doi: 10.1038/ja.2013.86; pmid: 24002361
136. A. M. Bal, I. M. Gould, Antibiotic stewardship: Overcoming implementation barriers. *Curr. Opin. Infect. Dis.* **24**, 357–362 (2011). doi: 10.1097/QCO.0b013e3283483262; pmid: 21587070
137. C. MacDougall, R. E. Polk, Antimicrobial stewardship programs in health care systems. *Clin. Microbiol. Rev.* **18**, 638–656 (2005). doi: 10.1128/CMR.18.4.638-656.2005; pmid: 16223951
138. US Food and Drug Administration, "2009 Summary report on antimicrobials sold or distributed for use in food-producing animals" (FDA, Washington, DC, 2010).
139. E. K. Silbergeld, J. Graham, L. B. Price, Industrial food animal production, antimicrobial resistance, and human health. *Annu. Rev. Public Health* **29**, 151–169 (2008). doi: 10.1146/annurev.publhealth.29.020907.090904; pmid: 18348709
140. M. E. J. Woolhouse, M. J. W. Ward, Sources of antimicrobial resistance. *Science* **341**, 1460–1461 (2013). doi: 10.1126/science.1243444; pmid: 24030495
141. A. R. Manges, J. R. Johnson, Food-borne origins of *Escherichia coli* causing extraintestinal infections. *Clin. Infect. Dis.* **55**, 712–719 (2012). doi: 10.1093/cid/cis502; pmid: 22615330
142. J. L. Martinez, J. Olivares, in *Antimicrobial Resistance in the Environment*, P. L. Keen, M. H. M. M. Montforts (Wiley-Blackwell, Hoboken, NJ, 2011), chap. 9, pp. 157–172.
143. Transatlantic Taskforce on Antimicrobial Resistance, *Recommendations for future collaboration between the U.S. and EU* (TATFAR Report, 2011); http://www.ecdc.europa.eu/en/activities/diseaseprogrammes/TATFAR/Documents/210911_TATFAR_Report.pdf.
144. European Commission, *Communication from the Commission to the European Parliament and the Council: Action plan against the rising threats from Antibmicrobial Resistance*, COM 748 (2011); http://ec.europa.eu/dgs/health_consumer/docs/communication_amr_2011_748_en.pdf.
145. FDA, New animal drugs; cephalosporin drugs; extralabel animal drug use; order of prohibition. *Fed. Regist.* **77**, 735 http://federalregister.gov/a/2012-35 (2012).
146. S. P. Carroll, M. T. Kinnison, L. Bernatchez, In light of evolution: Interdisciplinary challenges in food, health, and the environment. *Evol. Appl.* **4**, 155–158 (2011). doi: 10.1111/j.1752-4571.2011.00182.x
147. D. Griggs *et al*., Policy: Sustainable development goals for people and planet. *Nature* **495**, 305–307 (2013). doi: 10.1038/495305a; pmid: 23518546
148. Convention of Biological Diversity, Aichi Biodiversity Targets, Strategic Plan for Biodiversity 2011–2020, (2010); www.cbd.int/sp/targets/.
149. C. Jørgensen *et al*., Managing evolving fish stocks. *Science* **318**, 1247–1248 (2007). doi: 10.1126/science.1148089; pmid: 18033868
150. A. T. Laugen *et al*., Evolutionary impact assessment: Accounting for evolutionary consequences of fishing in an ecosystem approach to fisheries management. *Fish Fish.* **15**, 1–32 (2012).
151. M. L. Baskett, R. S. Waples, Evaluating alternative strategies for minimizing unintended fitness consequences of cultured individuals on wild populations. *Conserv. Biol.* **27**, 83–94 (2013). doi: 10.1111/j.1523-1739.2012.01949.x; pmid: 23082984
152. Convention on Biological Diversity, The Nagoya Protocol on Access and Benefit-Sharing, (2013); www.cbd.int/abs/.
153. L. Santamaría, P. F. Méndez, Evolution in biodiversity policy - current gaps and future needs. *Evol. Appl.* **5**, 202–218 (2012). doi: 10.1111/j.1752-4571.2011.00229.x
154. E. W. Welch, Potential implications of the Nagoya Protocol for the livestock sector. *J. Anim. Breed. Genet.* **129**, 423–424 (2012). pmid: 23148966
155. J. A. Jackson, L. Laikre, C. S. Baker, K. C. Kendall, Guidelines for collecting and maintaining archives for genetic monitoring. *Conserv. Genet. Resour.* **4**, 527–536 (2012). doi: 10.1007/s12686-011-9545-x
156. G. V. Dana, T. Kuiken, D. Rejeski, A. A. Snow, Synthetic biology: Four steps to avoid a synthetic-biology disaster. *Nature* **483**, 29–29 (2012). doi: 10.1038/483029a; pmid: 22382962
157. Convention on Biological Diversity Conference of the Parties, COP 11 Decision XI/11: New and emerging issues relating to the conservation and sustainable use of biodiversity (2012); www.cbd.int/decision/cop/default.shtml?id=13172.
158. K. A. Oye *et al*., Regulating gene drives. *Science* **345**, 626–628 (2014). doi: 10.1126/science.1254287
159. S. Oberthür, T. Gehring, Institutional interaction in global environmental governance: The case of the Cartagena Protocol and the World Trade Organization. *Global Environ. Polit.* **6**, 1–31 (2006). doi: doi:10.1162/glep.2006.6.2.1
160. A. A. Snow, V. H. Smith, Genetically engineered algae for biofuels: A key role for ecologists. *Bioscience* **62**, 765–768 (2012). doi: 10.1525/bio.2012.62.8.9
161. P. Mali *et al*., RNA-guided human genome engineering via Cas9. *Science* **339**, 823–826 (2013). doi: 10.1126/science.1232033; pmid: 23287722
162. M. A. Thomas *et al*., Ecology: Gene tweaking for conservation. *Nature* **501**, 485–486 (2013). doi: 10.1038/501485a; pmid: 24073449
163. K. H. Redford, W. Adams, G. M. Mace, Synthetic biology and conservation of nature: Wicked problems and wicked solutions. *PLoS Biol.* **11**, e1001530 (2013). doi: 10.1371/journal.pbio.1001530; pmid: 23565062
164. B. M. Althouse, T. C. Bergstrom, C. T. Bergstrom, Evolution in health and medicine Sackler colloquium: A public choice framework for controlling transmissible and evolving diseases. *Proc. Natl. Acad. Sci. U.S.A.* **107** (suppl. 1), 1696–1701 (2010). doi: 10.1073/pnas.0906078107; pmid: 20018681
165. J. Liu *et al*., Complexity of coupled human and natural systems. *Science* **317**, 1513–1516 (2007). doi: 10.1126/science.1144004; pmid: 17872436
166. E. Ostrom, A general framework for analyzing sustainability of social-ecological systems. *Science* **325**, 419–422 (2009). doi: 10.1126/science.1172133; pmid: 19628857
167. E. Ostrom, A diagnostic approach for going beyond panaceas. *Proc. Natl. Acad. Sci. U.S.A.* **104**, 15181–15187 (2007). doi: 10.1073/pnas.0702288104; pmid: 17881578
168. G. Hardin, The tragedy of the commons. *Science* **162**, 1243–1248 (1968). pmid: 5699198
169. F. Baquero, J. Campos, The tragedy of the commons in antimicrobial chemotherapy. *Rev. Esp. Quimioter.* **16**, 11–13 (2003) [Editorial]. pmid: 12750754
170. W. D. Hutchison *et al*., Areawide suppression of European corn borer with Bt maize reaps savings to non-Bt maize growers. *Science* **330**, 222–225 (2010). doi: 10.1126/science.1190242; pmid: 20929774
171. G. Jaffe, *Complacency on the Farm: Significant Noncompliance with EPA's Refuge Requirements Threatens the Future Effectiveness of Genetically Engineered Pest-Protected Corn* (Center for Science in the Public Interest, Washington, DC, 2009).
172. P. A. Samuelson, The pure theory of public expenditure. *Rev. Econ. Stat.* **36**, 387–389 (1954). doi: 10.2307/1925895
173. D. J. Nokes, R. M. Anderson, Vaccine safety versus vaccine efficacy in mass immunisation programmes. *Lancet* **338**, 1309–1312 (1991). doi: 10.1016/0140-6736(91)92601-W; pmid: 1682694
174. K. Kaier, U. Frank, Measuring the externality of antibacterial use from promoting antimicrobial resistance. *Pharmacoeconomics* **28**, 1123–1128 (2010). doi: 10.2165/11535640-000000000-00000; pmid: 21108531
175. K. Kaier, Economic modeling of the persistence of antimicrobial resistance. *Nat. Resour. Model.* **25**, 388–402 (2012). doi: 10.1111/j.1939-7445.2011.00114.x
176. G. D. Wright, Antibiotic resistance in the environment: A link to the clinic? *Curr. Opin. Microbiol.* **13**, 589–594 (2010). doi: 10.1016/j.mib.2010.08.005; pmid: 20850375
177. M. Herrmann, R. Laxminarayan, Antibiotic effectiveness: New challenges in natural resource management. *Annu. Rev. Resour. Econom.* **2**, 125–138 (2010). doi: 10.1146/annurev.resource.050708.144125
178. C. N. Cook, M. B. Mascia, M. W. Schwartz, H. P. Possingham, R. A. Fuller, Achieving conservation science that bridges the knowledge-action boundary. *Conserv. Biol.* **27**, 669–678 (2013). doi: 10.1111/cobi.12050; pmid: 23574343
179. J. Antonovics *et al*., Evolution by any other name: Antibiotic resistance and avoidance of the E-word. *PLoS Biol.* **5**, e30 (2007). doi: 10.1371/journal.pbio.0050030; pmid: 17298172

ACKNOWLEDGMENTS

M.T.K., R.F.D., S.P.C., S.Y.S., and T.B.S. were supported by grants from NSF. C.T.B. is supported by National Institute of General Medical Sciences, NIH, grant number U54GM088558. M.T.K., is supported by Maine Agricultural and Forest Experiment Station; P.D.G. by the National Research Centre for Growth and Development; S.P.C. by Commonwealth Scientific and Industrial Research Organization (Australia) and the Australian-American Fulbright Commission; S.Y.S. by grants from the College of Biological Sciences, University of California Davis; T.B.S. by grants from NIH, and B.E.T. by U.S. Department of Agriculture Biotechnology Risk Assessment grant 2011-33522-30729. P.S.J. acknowledges the Danish National Research Foundation for support to the Center for Macroecology, Evolution, and Climate and the American-Scandinavian Foundation. S. Singhal, J. Boomsma, C. Rahbek, N. Strange, and T. Fuller provided useful comments on previous versions of the manuscript. G. Reygondeau provided advice for the summary figure.

SUPPLEMENTARY MATERIALS

www.sciencemag.org/content/346/6207/1245993/suppl/DC1
Materials and Methods
Supplementary Text
Tables S1 to S2
References (*180*–*246*)

10.1126/science.1245993

REVIEW SUMMARY

SOCIAL EVOLUTION

Evolution of responses to (un)fairness

Sarah F. Brosnan[1]* *and* Frans B. M. de Waal[2]

BACKGROUND: The human sense of fairness presents an evolutionary puzzle because it appears to run counter to the short-term interests of at least some parties. We not only react negatively to getting less than a partner but sometimes also to getting more, which seems illogical. Following an ideal of impartiality, we seek appropriate outcomes for everyone within the community, not just a few individuals, and, in particular, not just ourselves. Why do we react this way? Are we the only species to do so? Here, we consider the evidence with regard to nonhuman primates and other animals to illuminate the evolution of the sense of fairness. Because social ideals escape measurement, we focus on behavioral responses to equal versus unequal reward division. Moreover, a true sense of fairness includes taking account of receiving both less than a partner and more than a partner. Therefore, we consider the evidence for both of these in other species and how this informs our understanding of the evolution of fairness in humans.

ADVANCES: There is widespread evidence for sensitivity to receiving less than a partner, or "first-order inequity aversion" (IA), in species that cooperate outside mating bonds and kinship. In these studies, animals are paired with a social partner who receives a preferred reward for completing a task. Subjects may respond by refusing to participate or refusing to accept the food reward, and such reactions are compared with those following control tests in which both subjects receive the same reward for the same effort. Increased responses when the partner receives a preferred reward are indicative of a sensitivity to inequity.

Thus far, passive and active protest against unfavorable outcomes has been documented in monkeys, apes, dogs, and birds. It is thought that these species compare their outcomes with those of others so as to judge the merit of their partnerships. They may turn away from partners that appropriate more than their fair share of the yields of cooperation.

A complete sense of fairness also includes second-order IA, however, which seeks to equalize outcomes even at a short-term cost to the self. This requires individuals to give up an immediate benefit to stabilize a long-term valuable cooperative relationship. Second-order IA reactions have thus far been found only in humans and apes. We hypothesize that second-order IA requires anticipation of first-order IA in the partner and its negative impact on the relationship. To forestall these consequences, and ensure continued cooperation, outcomes are equalized between partners.

OUTLOOK: Thus, humans and other species seem to share basic reactions to inequity, which serves to sustain cooperation. We postulate that the basic emotional reactions and calculations underlying our sense of fairness are rooted in our primate background and offer a model that places these reactions in the context of cooperative relationships.

Future research should more explicitly investigate the key variables underlying IA, such as the degree of dependence on cooperation, anticipation of the way resource division affects relationships, and the freedom to choose among and change partners. A cross-species investigation with a standardized paradigm, including both first- and second-order IA, may further illuminate the factors involved and help verify or falsify the model proposed. ■

ON OUR WEB SITE

Read the full article at http://dx.doi.org/10.1126/science.1251776

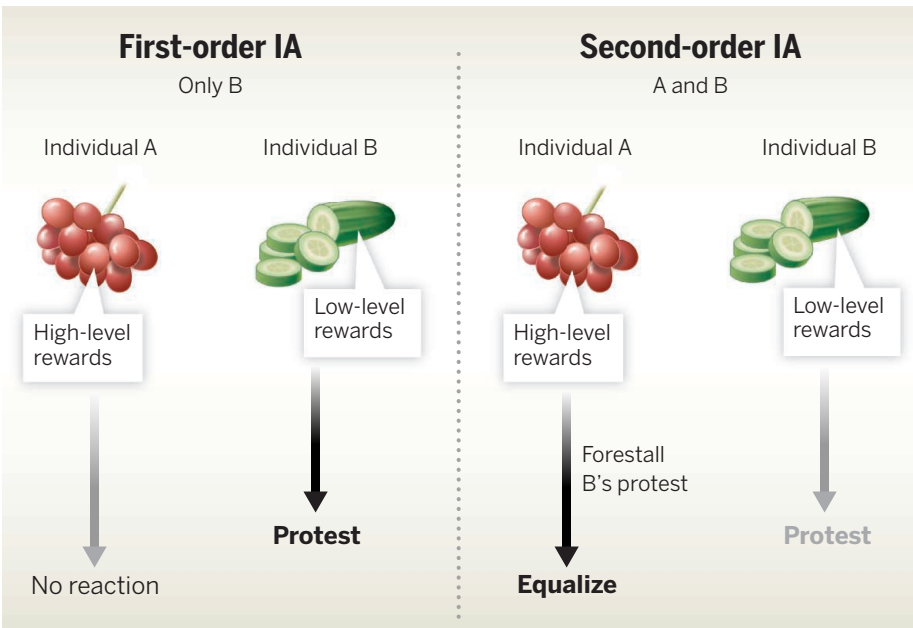

A diagram of the relationship between first-order IA and second-order IA. Individual A received high-level rewards, and individual B received low-level rewards. Individuals who recognize when they receive less than another may react against this situation—for instance, by finding a new cooperative partner. As reliance on cooperation increases, individuals also benefit from recognizing when they receive more, as this allows them to forestall first-order IA reactions in their partners and thereby maintain a successful cooperative relationship. This is the foundation of the full-blown human sense of fairness.

[1]Departments of Psychology and Philosophy, Neuroscience Institute and Language Research Center, Georgia State University, Atlanta, GA, USA. [2]Living Links, Yerkes National Primate Research Center and Psychology Department, Emory University, Atlanta, GA, USA.
*Corresponding author. E-mail: sarah.brosnan@gmail.com
Cite this article as S. F. Brosnan and F. B. M. de Waal, *Science* **346**, 1251776 (2014); DOI: 10.1126/science.1251776

Published by AAAS

REVIEW

SOCIAL EVOLUTION

Evolution of responses to (un)fairness

Sarah F. Brosnan[1]* and Frans B. M. de Waal[2]

The human sense of fairness is an evolutionary puzzle. To study this, we can look to other species, in which this can be translated empirically into responses to reward distribution. Passive and active protest against receiving less than a partner for the same task is widespread in species that cooperate outside kinship and mating bonds. There is less evidence that nonhuman species seek to equalize outcomes to their own detriment, yet the latter has been documented in our closest relatives, the apes. This reaction probably reflects an attempt to forestall partner dissatisfaction with obtained outcomes and its negative impact on future cooperation. We hypothesize that it is the evolution of this response that allowed the development of a complete sense of fairness in humans, which aims not at equality for its own sake but for the sake of continued cooperation.

Cooperation could not have evolved without mechanisms to ensure the sharing of payoffs. For an individual to cooperate with an unrelated partner to achieve goals that it cannot achieve alone or to exchange favors over time requires an ability to compare payoffs with investments. Given the ample evidence for mutualistic cooperation and reciprocal altruism (*1*, *2*) in humans as well as other species (hereafter, animals), we therefore expect well-developed capacities for payoff evaluation in species that flexibly cooperate with individually known partners. We also expect negative reactions to excessive payoff imbalances, because such imbalances undermine cooperation among nonrelatives, which requires proportionality between effort and gain so that gains among parties jointly contributing to a given enterprise are shared.

Along with the human sense of fairness and justice, responses to inequity have enjoyed a long history of scholarship in philosophy, law, economics, and psychology. Yet the evolution of these responses and possible parallels in other species have only recently come into focus. Even though "contrast effects," which describe how animals respond to unanticipated individual reward outcomes, have been known for nearly a century (*3*), the first study to measure reactions to interindividual outcome contrasts was published only in 2003 (*4*). In this study, brown capuchin monkeys (*Cebus apella*) became agitated and refused to perform a task for which a companion received superior rewards [see (*5*) for a video]. The monkeys' protest was not due to the mere sight of unavailable superior rewards, because they showed it only if these rewards actually went to their partner. If superior rewards were merely visible, they were mostly ignored (*4*, *6*). Since this early study, inequity responses have been explored in a number of species and found to be most pronounced in animals that cooperate outside of the bonds of mating and kinship.

We propose that sensitivity to (in)equity offers several evolutionary benefits. First, animals need to recognize when they receive less than a partner, because this tells them that the benefits of cooperation may be in danger. By protesting against this situation, they show a response known as inequity aversion (IA). Evidence indicates that this behavior is widespread in cooperative species under many circumstances. As the reliance on cooperation increases, individuals also benefit from sensitivity to receiving more than another, which risks undermining cooperative partnerships. This behavior is likely taxonomically restricted, because it requires prediction of the partner's reaction to getting less and its effect on the relationship. It also requires restraint to refrain from an immediately advantageous outcome. The pressure for increased cooperation combined with advanced cognitive abilities and emotional control allowed humans to evolve a complete sense of fairness. Here, we review the literature on IA in humans and other animals within an evolutionary framework of cooperation, social reciprocity, and conflict resolution. Our main conclusion is that the sense of fairness did not evolve for the sake of fairness per se but in order to reap the benefits of continued cooperation.

Responses to inequity

IA has been defined as a negative reaction to unequal outcomes (*7*). It is further subdivided into "disadvantageous IA," or reactions to inequity to the detriment of the actor, and "advantageous IA," also known as overcompensation, or reactions to inequity that benefits the actor (*7*). Responses to the first kind of IA offer a clear advantage if they help increase one's own share. Not surprisingly, human studies indicate that disadvantageous IA emerges earlier (*8*) and is more pronounced than advantageous IA (*9*). Young children may even pay a cost to maintain their advantage (*10*), although advantageous IA may have a more explicitly social focus (*11*). Disadvantageous IA is also the most common type in animals (see below). However, responses to overcompensation are also expected, as they, too, provide a long-term benefit (*12*). We have called disadvantageous IA "first-order inequity aversion" to indicate that it is the primary reaction, using "second-order inequity aversion" for the less common and less pronounced advantageous IA (Fig. 1) (*13*).

The connection between IA and fairness is not straightforward. The hallmark of the human sense of fairness is the idea of impartiality; that is, human fairness or justice is based on the idea of appropriate outcomes applied to everyone within the community, not just a few individuals, and, in particular, not just oneself. Thus, outcomes are judged against a standard, or an ideal. There is variation in this ideal across cultures or situations, but there is consistency within a given context. This complete sense of fairness likely requires abstraction at the community level as well as language (to establish a consistent set of ideals), both of which capacities may be restricted to our species (*14*). Community concern is not wholly absent in other primates, however, and neither is impartiality, such as when policing males break up fights (*15*).

Inasmuch as social ideals escape measurement, a sense of fairness is impossible to prove or disprove in animals. Reactions to inequity, on the other hand, are open to empirical investigation by creating situations in which one individual receives more or less than another. These reactions typically manifest as a rejection of a received reward or an unwillingness to participate in the interaction (Fig. 2A). In most experiments, subjects must complete a simple task to receive a reward (Table 1). To control for the social aspect of the interaction, these experiments often combine with ones on contrast effects that measure how subjects respond to a lesser reward after having just received a better reward (contrast) or another lesser one (control). It has been found that the mere visibility of better rewards is not the issue, because primates reliably perform tasks for lesser rewards regardless of whether or not better ones are immediately in front of them (*6*, *16*). Experiments on IA have shown that there is substantial variation among species in this response, even within the primates; some species respond more strongly to contrast effects (*17*), others more strongly to disadvantageous inequity (*4*, *16*); some respond to both (*18*), and some seem indifferent to either condition (*19*, *20*).

There are also important individual differences in response that hint at the situations in which inequity responses provide an advantage. For instance, merely feeding unequal foods fails to generate the same reaction; hence, an effortful task is essential (*6*, *16*, *20*) (Table 1), even though the nature of the task may be irrelevant (*20*). A second methodological issue emerges when we consider all reported studies regardless of species. Animals tested with an effortful task respond to inequity almost exclusively when seated closely side-by-side, compared with tests in which

[1]Departments of Psychology and Philosophy, Neuroscience Institute and Language Research Center, Georgia State University, Atlanta, GA, USA. [2]Living Links, Yerkes National Primate Research Center and Psychology Department, Emory University, Atlanta, GA, USA.
*Corresponding author. E-mail: sarah.brosnan@gmail.com

they sat far apart or across from each other, in which few IA responses were observed (Table 1). This suggests that physical proximity may be integral to IA outcomes, possibly because of the relationship between proximity and cooperation and the way proximity facilitates information gathering about the partner (*21*). Finally, individual differences have been found in some species, notably chimpanzees, who show substantial variation even within the same experiment (*16*, *22*, *23*). Responses also seem influenced by dominance rank, sex, and relationship quality. This is the case in humans as well, where factors such as relationship quality (*24*), personality (*25*), and the scale of competition (*26*) influence responses to unfair outcomes. Additional work to determine the influence of these and other factors on animal IA responses will provide additional nuance in our understanding of the evolution of IA (Table 1).

First-order IA has been documented in controlled experiments in capuchin monkeys [(*4*, *6*, *27*–*29*), but see also (*30*)], macaques (*18*, *31*), chimpanzees [(*16*, *22*), but see also (*32*, *23*)], dogs (*33*–*35*), and crows (*36*), and it has been implied in rodents (*37*). These animals refuse lesser rewards if a partner receives better ones and/or stop performing after multiple exposures to such outcomes. At first sight, this response is counterintuitive, as it reduces absolute outcome (the subject passes up a less-preferred, but still beneficial, reward) while increasing inequity (the partner still receives the preferred reward versus the other receiving nothing). If the goal of IA is to minimize current inequity (*7*), these animals show the wrong response.

New lines of evidence, however, have led to a reassessment of this evaluation. First, humans, too, respond in this way. The workhorse of inequity studies has been the ultimatum game (UG), in which one individual, the proposer, must decide how to divide a set sum of money. The second individual, the responder, then must decide whether to accept this division—in which case both individuals receive the money as allocated—or refuse it, in which case neither party receives anything (*38*). Decades of research demonstrate that, while there is variation among cultures (*39*), human proposers tend to make higher offers than the minimum required and responders tend to reject offers that are skewed (*40*), showing that humans, too, meet the first criterion, turning down net positive outcomes.

In most situations of unfairness, we have no recourse, however. How do humans respond when a refusal punishes only themselves? The impunity game (IG) is a related game for which a refusal by the responder still allows the proposer their allocated sum, whereas the responder receives nothing. This situation is similar to most inequity tasks applied to animals, in which subjects have the option to refuse but their refusal does not alter the other's outcome (*41*). Recent studies show refusals at about half the levels seen in the UG (*42*), bringing the human reaction close to that of animals refusing poorer rewards even if doing so decreases absolute gains and increases inequity.

The game context cannot include all possible outcomes that exist in natural social interactions, however. In the standard inequity task, refusals only hurt the actor, whereas in a natural social context, protest against inequity may lead to the actor either receiving a larger share or seeking out a better partner to work with. Despite the

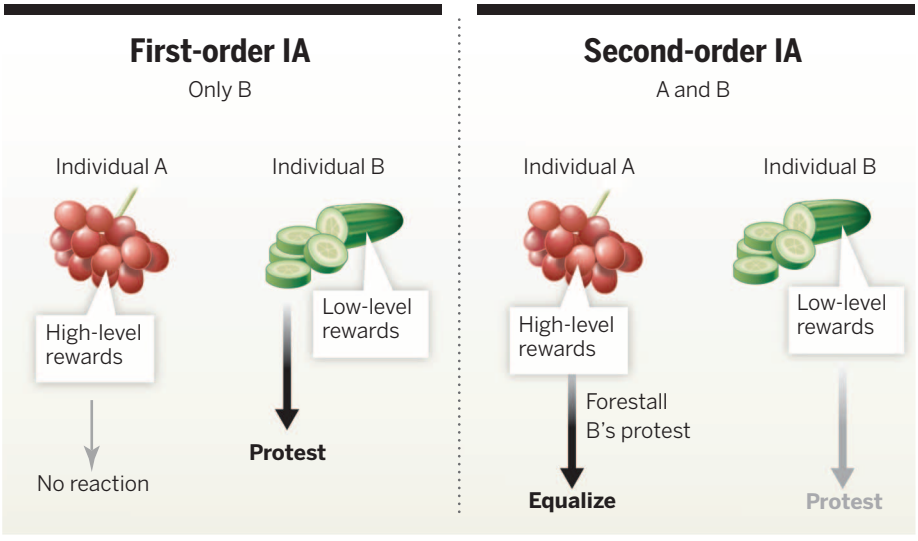

Fig. 1. A diagram of the relationship between first-order IA and second-order IA. Individual A received high-level rewards, and individual B received low-level rewards. Individuals who recognize when they receive less than another may react against this situation so as to maintain beneficial outcomes of cooperation, for instance, by finding a new cooperative partner. As reliance on cooperation increases, individuals also benefit from recognizing when they receive more, as this allows them to forestall first-order IA reactions in their partners and thereby maintain a successful cooperative relationship. Second-order IA requires advanced cognition and emotional control and thus far has only been seen in chimpanzees and humans. This is the foundation of the full-blown human sense of fairness.

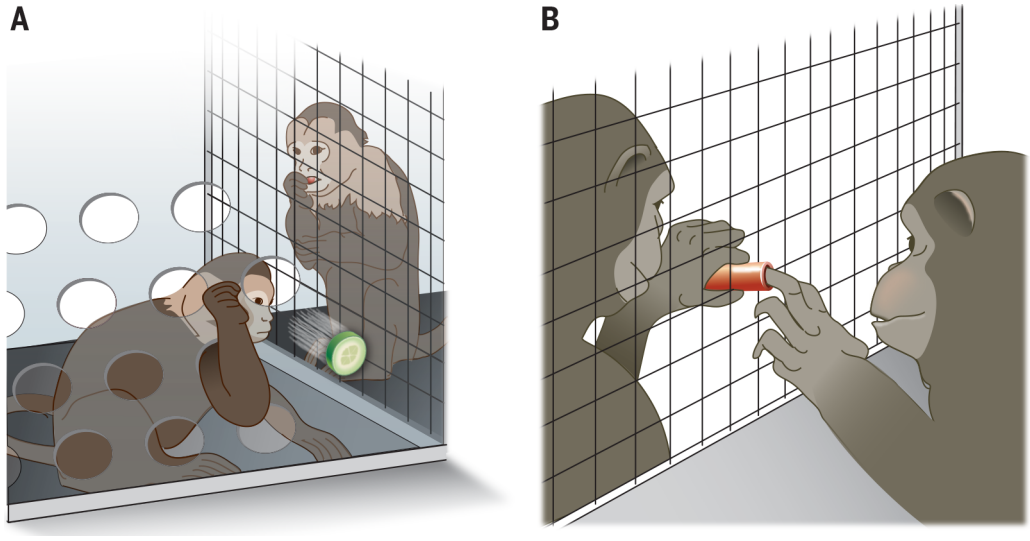

Fig. 2. Subjects' responses in the standard inequity task and the UG. (**A**) Capuchin monkeys during the original "monkeys reject unequal pay" experiment (*4*). The monkey on the left is rejecting the lesser reward, a cucumber slice, after viewing the partner receive a more preferred grape for the same amount of work. See video (*5*). (**B**) Chimpanzees during the UG (*81*). The chimpanzee who has just made the token choice (right) hands the token to her partner, who needs to accept and hand it over to the experimenter in order for both of them to receive the rewards corresponding with the token choice.

short-term costs, rejection of inequity may produce long-term gains by signaling to the partner that a relationship is about to end or by leading the actor to exit the relationship and replace it with a better one.

First-order IA and cooperation

The evolution of cooperation requires that its benefits reach all contributing parties in roughly similar amounts. Natural selection works on every individual's relative advantage compared with others; hence, gaining an absolute benefit is insufficient. If individuals were satisfied with any absolute benefit, they might still face negative fitness consequences if they were doing less well than competing others. It makes sense, therefore, to compare one's gains with those of others (*43*). Additionally, individuals must base decisions to cooperate on the entire history of interaction with a particular partner, not just any single interaction. Reciprocity requires a long-term evaluation of effort versus payoff balance.

The above perspective applies only to species with extensive cooperation outside of kinship relationships. The absence of flexible partner choice in the hymenoptera, for example, eliminates the need to compare efforts with payoffs. Our closest relatives, bonobos and chimpanzees, on the other hand, frequently cooperate with nonkin. Chimpanzees hunt together (*44*), form political coalitions and other reciprocal relations (*45*), collectively defend territories (*46*) and mates (*47*), and actively share food [e.g., (*48*)]. DNA collected in the field shows that most long-term male-male partnerships lack kinship ties (*49*). Bonobos show the same pattern. Females frequently share food and maintain a cooperative network that allows them to dominate males despite the fact that females are the migratory sex, hence largely unrelated within each community (*50*). In captive settings, bonobos even share food with outsiders (*51*).

Experimental studies of cooperation in primates began in 1936 with an experiment on cooperatively pulling chimpanzees (*52*). Since then,

Table 1. Publications since 2003 on IA in a variety of nonhuman species. The studies are divided into those using an effortful task and those that merely fed unequal foods. Tasks include exchange, in which the subject returns a token to the experimenter and subsequently receives a food reward; pulling, in which subjects must pull in a tray to bring themselves and/or others food rewards; target, in which the subject most hold on to a token for a specified period of time to receive a food reward; and none, in which the subject (and/or partner) receives food for "free," without completing a task. The "shake paw" and "sit on command" tasks were specific to domestic dogs (because they are in their behavioral repertoire already). The UG requires a proposer to choose one of two reward divisions, which then must be accepted by the responder, who can either accept the proposal, in which case both subjects get the food as proposed, or reject it, in which case neither subject gets anything. The table also notes the nature of the task and whether individuals were sitting near each other or not.

Species	Task	Side-by-side and near	Evidence of		Contrast effect	Other effects
			1st-order IA	2nd-order IA		
			Food rewards for task			
Chimpanzees	Exchange (*22*)	Yes	Yes	–	No	Social tie
	Exchange (*16*)	Yes	Yes	Yes	Yes	Rank, sex, task
	Exchange (*92*)	Yes	Yes	–	No	Sex
	Exchange (*23*)	No	No	–	–	
	UG (*79*)	No	–	No	–	
	UG (*80*)	No	No	No	–	
	UG (*81*)	Yes	–	Yes	–	
Bonobo	Exchange (*23*)	No	Maybe	–	–	
	UG (*80*)	No	No	No	–	
Orangutan	Exchange (*23*)	No	No	–	–	
	Exchange (*19*)	Yes	No	No	No	
Long-tailed macaque	Pulling (*31*)	Yes	Yes			Rank, social tie
Rhesus macaque	Target (*18*)	Yes	Yes	No	Yes	Ontogeny
Capuchin monkey	Exchange (*4*)	Yes	Yes	–	No	
	Exchange (*6*)	Yes	Yes	–	No	Task, effort
	Pulling (*27*)	Yes	Yes	–	No	
	Pulling (*28*)	No	Yes	Yes	–	Rank, visual access
	Exchange (*30*)	Yes	No	–	No	
	Exchange (*93*)	No	No	–	–	
Squirrel monkey	Exchange (*17*)	Yes	No	No	Yes	Sex, task
	Target (*20*)	Yes	No	No	Yes	Sex
Owl monkey	Target (*20*)	Yes	No	No	No	
Common marmoset	Target (*20*)	Yes	No	No	No	
Tamarin	Exchange (*74*)	Yes	No	No	Yes	Task
Domestic dog	Shake paw (*33*)	Yes	Yes	–	No	
	Various (*34*)	Yes	Yes	–	–	
	Sit on command (*35*)	Yes	Yes/No	No	–	Age, ownership history, training history
Crow	Exchange (*36*)	Yes	Yes	–	–	Effort
Raven	Exchange (*36*)	Yes	Yes	–	–	Effort
			Feeding without task			
Chimpanzee	None (*32*)	No	No	–	No	Rank
Bonobo	None (*32*)	No	No	–	No	
Gorilla	None (*32*)	No	No	–	No	
Capuchin monkey	None (*94*)	Yes	No	–	Yes	
	None (*95*)	Yes	No	–	–	
	None [(*93*), study 2]	Yes	No	–	–	

mutualistic cooperation has been demonstrated experimentally in most of the great apes, many monkey species, and also in nonprimates, including elephants, hyenas, and birds (*53*). Thus, we might expect that members of these species are sensitive to their own outcomes relative to those of a social partner. This would be in line with early work on IA in economics, which linked responses to inequity and cooperation (*7*). Individuals who perceive unequal outcomes may use this information to cease cooperation and find a new partner. If outcomes are sufficiently unequal, by chance alone cooperating with other partners will likely result in better outcomes (*43*). Research in other species supports a connection with cooperation in three different ways: (i) responses to inequity in the context of cooperation, (ii) phylogenetic comparisons, and (iii) responses in species facing partner-choice restrictions.

Reward distribution in cooperation experiments

Capuchin monkeys have been widely tested on the classical barpull paradigm in which two individuals work together (*52*). They produce mutual food rewards and appear to grasp the need for a partner (*54*). However, when individuals cooperate for unequal rewards, their behavior becomes more contingent upon their partner's, reflecting sensitivity to reward distribution. These monkeys show "payment for labor" in that they share more easily with partners who have helped them obtain food than with partners who did not. Conversely, partners quit helping if rewards are not shared (*55*). This sensitivity to payoffs is not limited to situations in which rewards are preassigned by the experimenter. It extends to those in which the monkeys themselves decide the reward division. Monkeys are less likely to pull for clumped rewards that their partner can monopolize than for distributed rewards that are easily divided. They make this distinction on the very first trial, indicating that it is not a conditioning effect, and the distinction varies with the level of tolerance between both partners (*56*).

Moreover, although these monkeys cooperate to the same degree for distributed rewards that are either equal or unequal, partnerships that alternated each individual's access to a preferred reward when rewards were unequal were almost three times as likely to cooperate successfully (*57*). The reluctance to cooperate with a monopolizing partner suggests that it is not inequity per se but the way partner attitude combines with inequity that impedes cooperation. This is reminiscent of children's focus on partiality over inequity (*58*) and moreover has implications for human cooperation, whereby individuals are not likely to forget the past and cooperate just because the payoff structure is now in their favor. In these experiments, monkeys did not respond with refusal to an isolated instance of inequity but required multiple instances before cooperation broke down (different thresholds for ceasing cooperation may be one cause of the individual variation in these responses). Even if rewards even out over time, in any given interaction one individual will usually do better than another. The monkeys appeared to integrate outcomes over multiple trials, allowing for cooperation in a wide range of situations.

Chimpanzees, too, are sensitive to reward distribution. They cooperate more successfully with a partner who, in other contexts, shares more tolerantly (*59*). Given a choice between potential partners, they prefer partners with whom they have a tolerant relationship (*60*). When goals conflict, such as when two individuals have the option to cooperate for equal (5 versus 5 rewards) or unequal (10 versus 1) payoffs, chimpanzees still manage to obtain food on the majority of trials. Even though dominant individuals prefer the possibility of 10 rewards, on almost half the trials the pair negotiate to work for the equal division (*61*). On the other hand, given a choice, chimpanzees prefer to work alone rather than collaborate (*62*) and, unlike capuchin monkeys (*55*), may not share more with a helper than a nonhelper (*63*). The latter result needs further testing, however, given indications that wild chimpanzees that contributed to a group hunt are given preferential access to the resulting meat (*44*).

Phylogeny: Cooperative versus noncooperative species

Another way to explore the interplay between cooperation and inequity is to look across species. Pronounced first-order IA has been observed in chimpanzees and brown capuchin monkeys (*4*, *6*, *16*, *22*, *27*, *28*), two species that are highly cooperative—for example, they hunt in groups for prey that is hard to capture by a single hunter (*48*, *64*). Moreover, chimpanzees seem attentive to their partner's rewards, even if they are inferior to their own (*16*), and both species behave prosocially in at least some experimental tests [(*65*–*67*), but see (*68*, *69*)], thus having the potential for second-order IA. Beyond these two primates, recent evidence indicates that bonobos (*23*) and several macaque species (*Macaca* spp.) (*18*, *31*) also respond negatively to getting a reward inferior to that of a partner. These primates, too, are highly cooperative. There are observations of group hunting in bonobos (*70*) and, although macaques do not show such behavior, they have an extensive alliance network among both kin and nonkin (*71*).

On the other hand, primates less likely to cooperate with nonkin, including orangutans (*Pongo* spp.) (*19*, *23*) and squirrel monkeys (*Saimiri* spp.) (*17*, *20*), have thus far failed to show IA. Neither taxonomic relations among the primates nor brain size, relative brain size, or social organization predict the known distribution of IA as well, it appears, as does the tendency to cooperate with individuals who are neither kin nor mates (*41*). Beyond the primates, IA has also been documented in domestic dogs (*Canis lupus familiaris*) (*33*, *34*), a species derived

Table 2. Studies on a variety of animals thus far have indicated five domains that help explain the variation in IA.

Comparison	IA is facilitated when subjects can easily perceive each other's pay for a task (i.e. sit side-by-side and in full view), which facilitates comparison.	
Phylogeny		Species with extensive cooperation among nonkin and nonmates show more pronounced IA.
Cooperation	Individuals who equalize outcomes by sharing or alternating between high-level rewards cooperate more successfully.	
Partner choice		IA is most likely to evolve in situations with relatively unconstrained partner choice. This may influence coalition and alliance formation. In contrast, cooperative breeders, with constrained kin-based partner choice, show no IA.
Cognition	Second-order IA (aversion to overcompensation) is a form of conflict resolution resting on anticipation of negative consequences in first-order IA. In the UG, chimpanzees anticipate partner's reactions and choose an equal token (black bar) more often than a selfish one (gray bar) when the partner has a choice (UG) than when it has not (No choice).	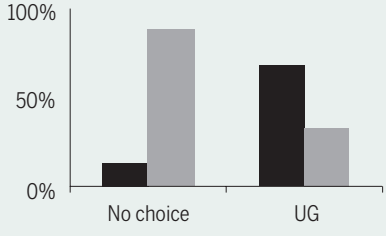

from a long line of cooperative hunters (*72*). Like monkeys, dogs are sensitive only to whether their outcomes are wanting as compared with those of others (*35*). Corvids are cooperative birds (*73*), and some species have shown IA in experiments. They may be more sensitive to inequities in effort than in reward, however (*36*).

Future research is needed to determine the degree to which the hypothesis of coevolution of IA and cooperation (*41*) extends beyond these species. For instance, do other animals with frequent nonkin cooperation, such as elephants, cetaceans, and noncanine social carnivores, also respond negatively to situations of inequity? We also need more research on noncooperative species. For example, a comparison between domestic cats and dogs may be useful, where we would predict cats (solitary hunters) to be less sensitive to reward distribution than dogs.

Constrained partner choice

Not all cooperative animals can easily find new partners. For example, the *Callithrichidae* (marmosets and tamarins) are cooperative breeders, a social system in which both parents and adult offspring are essential for offspring care. For obvious reasons, the cost of partner switching is high. Of the two callithrichid species tested on IA, neither responded negatively to receiving a lesser reward than their social partner (*20*, *74*). Even though not classified as cooperative breeders, owl monkeys (*Aotus spp.*), too, show pair-bonding and dual parental care and also fail to respond to inequity (*20*).

Even without cooperative breeding, in species with relationships developed over many years of play, grooming, mutual support, and other services, responses to inequity should wear off since replacement of long-term partners becomes too costly. There is indeed evidence that IA is less pronounced in well-established human friendships compared with relationships among acquaintances and colleagues (*24*), and the same has been reported for chimpanzees. A group of captive chimpanzees that grew up and lived together in the same space for more than 30 years showed far less IA than a similarly housed group of chimpanzees with a much shorter history (*22*).

Future research is needed to explore the degree to which both relationship quality and the costs of partner switching influence responses to inequity. One might predict, for instance, that if the evolution of IA requires cooperation under relatively unconstrained partner choice, hunting parties may be a prime example. Hunting parties change composition from one occasion to the next, whereas long-term friendships and pair-bonding may not be as conducive to pronounced IA. In the laboratory, we might anticipate that individuals show different responses in newly formed partnerships as compared with longer-term ones, particularly in the case of biparental care or cooperatively breeding species in which long-term relationships have produced offspring. For species for whom the costs of partner switching are too high, we may expect to see other partner-control mechanisms, such as punishment, play a greater role (*75*). Understanding the situations in which partner choice influences inequity responses will be critical for understanding the formation of coalitions and alliances (*76*).

Second-order inequity aversion

Until recently, second-order IA was unreported for nonhuman animals. Its explanation is more complex than that of first-order IA, which simply requires that one individual responds to an unequal outcome to avoid being taken advantage of. For second-order IA, in contrast, the advantages are less obvious, because this reaction occurs when the actor enjoys an advantage. Apart from humans, evidence for second-order IA is thus far restricted to chimpanzees. The first sign came from a study in which the apes reacted negatively not only to a lesser reward but also when they received a better one. In other words, subjects responded to any inequity, not just the disadvantageous kind (*16*). Subsequently, chimpanzees were tested on the UG, considered the gold standard of the human sense of fairness (see "Responses to inequity" above). In most cultures, humans typically offer a 50/50 split (*77*, *78*). In contrast, one UG study on chimpanzees found them to share the smallest possible amount with their partner [(*79*); see also (*80*)]. However, because the methodology of this experiment deviated substantially from the typical human UG, Proctor *et al.* (Fig. 2B) (*81*) applied a more intuitive UG for both apes and 3- to 5-year-old human children.

Proposers were presented with a choice of two differently colored tokens that could be exchanged for food. The tokens represented equal versus unequal reward divisions, and the partner needed to agree and participate in the exchange (Fig. 2B), an element similar to the typical human UG. Token choices in this situation were compared with choices when the partner's agreement was not needed. Similar to humans in the UG, the chimpanzees more often split the rewards equally if they needed their partner than if they did not. Because children behaved similarly in this token-exchange game, the study suggests shared patterns of proactive decision-making in relation to fair outcomes in both species (*81*).

Even though neither the apes nor the children in this study actively refused offers, behavioral protest did occur. Subjects occasionally reacted to selfish offers by spitting water at the other or hitting the mesh partition (apes) or saying "you got more than me" (children). Acceptance of offers despite behavioral protest is typical of young children (*82*). Strategic choices in the UG may be tied to emotional control rather than to social preferences, knowledge of norms, or perspective-taking abilities. In one study, 85% of the younger children claimed to reject unfair offers, but only 12.5% of them actually did. Only after 7 years of age do children resist the temptation of rewards and begin to refuse low offers for strategic reasons (*83*).

Reasons to refuse unfair offers in the UG are obvious enough. Refusals punish the actor, which may lead to better outcomes in the future. The individual making the offer, on the other hand, may anticipate negative reactions and strive for an equitable outcome to forestall them. This would amount to anticipatory conflict resolution, which may be the main rationale for second-order IA if those who divide the rewards try to eliminate reasons for frustration in their partners (Fig. 1). The better the anticipatory capacities of a species, the better it will be able to avoid first-order IA in others by showing second-order IA. Planning ahead has been demonstrated in apes in relation to tool use (*84*), as has anticipatory conflict resolution. Captive bonobos and chimpanzees show a grooming and play peak right before feeding time and engage in high levels of appeasing and sociosexual body contact upon food arrival (*85*, *86*). These primates thus anticipate competition and actively seek to reduce it. Second-order IA in chimpanzees may serve the same goal. Given the need to anticipate the partner's reactions as well as forgo short-term positive outcomes to gain long-term ones, individuals must have some emotional control. Although there are no studies linking self-control and IA in other species, in human children self-control is a limiting factor. Perhaps not surprisingly, the species with strong IA responses also delay gratification in experimental tests [e.g., (*87*, *88*)].

Finally, second-order IA may directly benefit an individual by enhancing its reputation, which may increase that individual's long-term access to beneficial relationships (*12*). Humans are much more likely to donate in a public goods game when they are recognizable (*89*) and cooperate more when they have the feeling of being watched (*90*), indicating that being nice only occurs when positive fitness gains are expected from a second-order IA reaction. To what degree this explanation may apply to species other than our own is as yet unclear, although there is evidence that apes pay attention to the generosity of others without necessarily having directly experienced it (*91*).

The evolution of fairness

Not only are signs of first-order IA evident in several cooperative species, in the form of a negative reaction to disadvantageous unequal outcomes, but also our closest relatives, the anthropoid apes, show evidence of second-order IA, an essential component of human fairness because it seeks to equalize outcomes. Thus, humans and other species seem to share basic reactions to inequity, which serve the need for sustained cooperation (Table 2). Humans' unprecedented brain enlargement allows for greater understanding of the benefits of self-control in the context of resource division. Additionally, the development of language enabled communication about third parties, which may have enhanced the role of reputation building. Despite these differences, many of the basic emotional reactions and calculations underlying our sense of fairness seem rooted in our primate background. We suggest that future research more explicitly investigate what we consider the key variables underlying IA, including dependence on cooperation, anticipation of the way resource division affects relationships, and

the freedom to choose and change partners, as well as the relative roles of first- and second-order IA. A cross-species investigation with a standardized paradigm may further illuminate the factors involved and help verify or falsify the model proposed.

REFERENCES AND NOTES

1. L. A. Dugatkin, *Cooperation Among Animals: An Evolutionary Perspective* (Oxford University Press, New York, 1997), *Oxford Series in Ecology and Evolution*.
2. P. M. Kappeler, C. P. Van Schaik, *Cooperation in Primates and Humans: Mechanisms and Evolution* (Springer, 2005).
3. O. L. Tinklepaugh, An experimental study of representative factors in monkeys. *J. Comp. Psychol.* **8**, 197–236 (1928). doi: 10.1037/h0075798
4. S. F. Brosnan, F. B. M. De Waal, Monkeys reject unequal pay. *Nature* **425**, 297–299 (2003). doi: 10.1038/nature01963; pmid: 13679918
5. Two monkeys were paid unequally: Excerpt from Frans de Waal's TED Talk (2013); www.youtube.com/watch?v=meiU6TxysCg.
6. M. van Wolkenten, S. F. Brosnan, F. B. M. de Waal, Inequity responses of monkeys modified by effort. *Proc. Natl. Acad. Sci. U.S.A.* **104**, 18854–18859 (2007). doi: 10.1073/pnas.0707182104; pmid: 18000045
7. E. Fehr, K. M. Schmidt, A theory of fairness, competition, and cooperation. *Q. J. Econ.* **114**, 817–868 (1999). doi: 10.1162/003355399556151
8. P. R. Blake, K. McAuliffe, "I had so much it didn't seem fair": Eight-year-olds reject two forms of inequity. *Cognition* **120**, 215–224 (2011). doi: 10.1016/j.cognition.2011.04.006; pmid: 21616483
9. G. F. Loewenstein, L. Thompson, M. H. Bazerman, Social utility and decision making in interpersonal contexts. *J. Pers. Soc. Psychol.* **57**, 426–441 (1989). doi: 10.1037/0022-3514.57.3.426
10. M. Sheskin, P. Bloom, K. Wynn, Anti-equality: Social comparison in young children. *Cognition* **130**, 152–156 (2014). doi: 10.1016/j.cognition.2013.10.008; pmid: 24291266
11. K. McAuliffe, P. R. Blake, G. Kim, R. W. Wrangham, F. Warneken, Social influences on inequity aversion in children. *PLOS ONE* **8**, e80966 (2013). doi: 10.1371/journal.pone.0080966; pmid: 24312509
12. R. H. Frank, in *Evolution and the Capacity for Commitment*, R. M. Nesse, Ed. (Russell Sage Foundation, New York, 2001), pp. 57–76.
13. S. F. Brosnan, F. B. M. de Waal, Fairness in animals: Where to from here?. *Soc. Justice Res.* **25**, 336–351 (2012). doi: 10.1007/s11211-012-0165-8
14. F. de Waal, *The Bonobo and the Atheist: In Search of Humanism Among the Primates* (W.W. Norton, New York, 2013).
15. F. B. M. de Waal, in *Coalitions and Alliances in Humans and Other Animals*, A. H. Harcourt, F. B. M. de Waal, Eds. (Oxford Univ. Press, Oxford, 1992), pp. 233–258.
16. S. F. Brosnan, C. Talbot, M. Ahlgren, S. P. Lambeth, S. J. Schapiro, Mechanisms underlying responses to inequitable outcomes in chimpanzees, *Pan troglodytes*. *Anim. Behav.* **79**, 1229–1237 (2010). doi: 10.1016/j.anbehav.2010.02.019
17. C. F. Talbot, H. D. Freeman, L. E. Williams, S. F. Brosnan, Squirrel monkeys' response to inequitable outcomes indicates a behavioural convergence within the primates. *Biol. Lett.* **7**, 680–682 (2011). doi: 10.1098/rsbl.2011.0211; pmid: 21508022
18. L. M. Hopper, S. P. Lambeth, S. J. Schapiro, B. J. Bernacky, S. F. Brosnan, The ontogeny of social comparisons in rhesus macaques (*Macaca mulatta*). *J. Primatol.* **2**, 109 (2013).
19. S. F. Brosnan, T. E. Flemming, C. Talbot, L. Mayo, T. S. Stoinski, Orangutans (*Pongo pygmaeus*) do not form expectations based on their partner's outcomes. *Folia Primatol.* **82**, 56–70 (2011). doi: 10.1159/000328142; pmid: 21625145
20. H. D. Freeman *et al*., Different responses to reward comparisons by three primate species. *PLOS ONE* **8**, e76297 (2013). doi: 10.1371/journal.pone.0076297; pmid: 24130767
21. R. Sommer, Small group ecology. *Psychol. Bull.* **67**, 145–152 (1967). doi: 10.1037/h0024201; pmid: 5343340
22. S. F. Brosnan, H. C. Schiff, F. B. M. de Waal, Tolerance for inequity may increase with social closeness in chimpanzees. *Proc. Biol. Sci.* **272**, 253–258 (2005). doi: 10.1098/rspb.2004.2947; pmid: 15705549
23. J. Bräuer, J. Call, M. Tomasello, Are apes inequity averse? New data on the token-exchange paradigm. *Am. J. Primatol.* **71**, 175–181 (2009). doi: 10.1002/ajp.20639; pmid: 19021260
24. M. S. Clark, N. K. Grote, in *Handbook of Psychology: Personality and Social Psychology*, T. Millon, M. J. Lerner, I. B. Weiner, Eds. (Wiley, New York, 2003), vol. 5, pp. 447–461.
25. H. Brandstätter, M. Königstein, Personality influences on ultimatum bargaining decisions. *Eur. J. Pers.* **15**, S53–S70 (2001). doi: 10.1002/per.424
26. P. Barclay, B. Stoller, Local competition sparks concerns for fairness in the ultimatum game. *Biol. Lett.* **10**, 20140213–20140213 (2014). doi: 10.1098/rsbl.2014.0213; pmid: 24850897
27. G. E. Fletcher, Attending to the outcome of others: Disadvantageous inequity aversion in male capuchin monkeys (*Cebus apella*). *Am. J. Primatol.* **70**, 901–905 (2008). doi: 10.1002/ajp.20576; pmid: 18521838
28. A. Takimoto, H. Kuroshima, K. Fujita, Capuchin monkeys (*Cebus apella*) are sensitive to others' reward: An experimental analysis of food-choice for conspecifics. *Anim. Cogn.* **13**, 249–261 (2010). doi: 10.1007/s10071-009-0262-8; pmid: 19609580
29. A. Takimoto, K. Fujita, I acknowledge your help: Capuchin monkeys' sensitivity to others' labor. *Anim. Cogn.* **14**, 715–725 (2011). doi: 10.1007/s10071-011-0406-5; pmid: 21519900
30. A. Silberberg, L. Crescimbene, E. Addessi, J. R. Anderson, E. Visalberghi, Does inequity aversion depend on a frustration effect? A test with capuchin monkeys (*Cebus apella*). *Anim. Cogn.* **12**, 505–509 (2009). doi: 10.1007/s10071-009-0211-6; pmid: 19184138
31. J. J. M. Massen, L. M. Van Den Berg, B. M. Spruijt, E. H. M. Sterck, Inequity aversion in relation to effort and relationship quality in long-tailed Macaques (*Macaca fascicularis*). *Am. J. Primatol.* **74**, 145–156 (2012). doi: 10.1002/ajp.21014; pmid: 22038902
32. J. Bräuer, J. Call, M. Tomasello, Are apes really inequity averse? *Proc. Biol. Sci.* **273**, 3123–3128 (2006). doi: 10.1098/rspb.2006.3693; pmid: 17015338
33. F. Range, L. Horn, Z. Viranyi, L. Huber, The absence of reward induces inequity aversion in dogs. *Proc. Natl. Acad. Sci. U.S.A.* **106**, 340–345 (2009). doi: 10.1073/pnas.0810957105; pmid: 19064923
34. F. Range, K. Leitner, Z. Virányi, The influence of the relationship and motivation on inequity aversion in dogs. *Soc. Justice Res.* **25**, 170–194 (2012). doi: 10.1007/s11211-012-0155-x
35. A. Horowitz, Fair is fine, but more is better: Limits to inequity aversion in the domestic dog. *Soc. Justice Res.* **25**, 195–212 (2012). doi: 10.1007/s11211-012-0158-7
36. C. A. F. Wascher, T. Bugnyar, Behavioral responses to inequity in reward distribution and working effort in crows and ravens. *PLOS ONE* **8**, e56885 (2013). doi: 10.1371/journal.pone.0056885; pmid: 23437262
37. F. Heidary *et al*., Food inequality negatively impacts cardiac health in rabbits. *PLOS ONE* **3**, e3705 (2008). doi: 10.1371/journal.pone.0003705; pmid: 19002245
38. W. Güth, R. Schmittberger, B. Schwartze, An experimental analysis of ultimatum bargaining. *J. Econ. Behav. Organ.* **3**, 367–388 (1982). doi: 10.1016/0167-2681(82)90011-7
39. J. Henrich, E. Fehr, S. Bowles, R. Boyd, C. Camerer, *Foundations of Human Sociality: Economic Experiments and Ethnographic Evidence from Fifteen Small-Scale Societies* (Oxford Univ. Press, Oxford, 2004).
40. C. Camerer, *Behavioral Game Theory: Experiments in Strategic Interaction* (Russell Sage Foundation, Princeton Univ. Press, Princeton, NJ, 2003).
41. S. F. Brosnan, A hypothesis of the co-evolution of cooperation and responses to inequity. *Front. Decis. Neurosci.* **5**, 43 (2011). pmid: 21519380
42. T. Yamagishi *et al*., The private rejection of unfair offers and emotional commitment. *Proc. Natl. Acad. Sci. U.S.A.* **106**, 11520–11523 (2009). doi: 10.1073/pnas.0900636106; pmid: 19564602
43. S. F. Brosnan, Nonhuman species' reactions to inequity and their implications for fairness. *Soc. Justice Res.* **19**, 153–185 (2006). doi: 10.1007/s11211-006-0002-z
44. C. Boesch, Cooperative hunting in wild chimpanzees. *Anim. Behav.* **48**, 653–667 (1994). doi: 10.1006/anbe.1994.1285
45. J. C. Mitani, in *Cooperation in Primates and Humans: Evolution and Mechanisms*, P. Kapeller, C. P. van Schaik, Eds. (Springer, Berlin, 2006), pp. 101–113.
46. M. L. Wilson, M. D. Hauser, R. W. Wrangham, Does participation in intergroup conflict depend on numerical assessment, range location, or rank for wild chimpanzees? *Anim. Behav.* **61**, 1203–1216 (2001). doi: 10.1006/anbe.2000.1706
47. D. P. Watts, Coalitionary mate guarding by male chimpanzees at Ngogo, Kibale National Park, Uganda. *Behav. Ecol. Sociobiol.* **44**, 43–55 (1998). doi: 10.1007/s002650050513
48. C. Boesch, H. Boesch, Hunting behavior of wild chimpanzees in the Taï National Park. *Am. J. Phys. Anthropol.* **78**, 547–573 (1989). doi: 10.1002/ajpa.1330780410; pmid: 2540662
49. K. E. Langergraber, J. C. Mitani, L. Vigilant, The limited impact of kinship on cooperation in wild chimpanzees. *Proc. Natl. Acad. Sci. U.S.A.* **104**, 7786–7790 (2007). doi: 10.1073/pnas.0611449104; pmid: 17456600
50. T. Furuichi, Female contributions to the peaceful nature of bonobo society. *Evol. Anthropol.* **20**, 131–142 (2011). doi: 10.1002/evan.20308; pmid: 22038769
51. J. Tan, B. Hare, Bonobos share with strangers. *PLOS ONE* **8**, e51922 (2013). doi: 10.1371/journal.pone.0051922; pmid: 23300956
52. H. W. Nissen, M. P. Crawford, A preliminary study of food-sharing behavior in young chimpanzees. *J. Comp. Psychol.* **22**, 383–419 (1936). doi: 10.1037/h0062234
53. S. F. Brosnan, R. Bshary, Cooperation and deception: From evolution to mechanisms. *Philos. Trans. R. Soc. Lond. B Biol. Sci.* **365**, 2593–2598 (2010). doi: 10.1098/rstb.2010.0155; pmid: 20679104
54. K. A. Mendres, F. B. M. de Waal, Capuchins do cooperate: The advantage of an intuitive task. *Anim. Behav.* **60**, 523–529 (2000). doi: 10.1006/anbe.2000.1512; pmid: 11032655
55. F. B. M. de Waal, M. L. Berger, Payment for labour in monkeys. *Nature* **404**, 563 (2000). doi: 10.1038/35007138; pmid: 10766228
56. F. B. de Waal, J. M. Davis, Capuchin cognitive ecology: Cooperation based on projected returns. *Neuropsychologia* **41**, 221–228 (2003). doi: 10.1016/S0028-3932(02)00152-5; pmid: 12459220
57. S. F. Brosnan, C. Freeman, F. B. M. De Waal, Partner's behavior, not reward distribution, determines success in an unequal cooperative task in capuchin monkeys. *Am. J. Primatol.* **68**, 713–724 (2006). doi: 10.1002/ajp.20261; pmid: 16786518
58. A. Shaw, K. Olson, Fairness as partiality aversion: The development of procedural justice. *J. Exp. Child Psychol.* **119**, 40–53 (2014). doi: 10.1016/j.jecp.2013.10.007; pmid: 24291349
59. A. P. Melis, B. Hare, M. Tomasello, Engineering cooperation in chimpanzees: Tolerance constraints on cooperation. *Anim. Behav.* **72**, 275–286 (2006). doi: 10.1016/j.anbehav.2005.09.018
60. A. P. Melis, B. Hare, M. Tomasello, Chimpanzees recruit the best collaborators. *Science* **311**, 1297–1300 (2006). doi: 10.1126/science.1123007; pmid: 16513985
61. A. P. Melis, B. Hare, M. Tomasello, Chimpanzees coordinate in a negotiation game. *Evol. Hum. Behav.* **30**, 381–392 (2009). doi: 10.1016/j.evolhumbehav.2009.05.003
62. A. F. Bullinger, A. P. Melis, M. Tomasello, Chimpanzees, *Pan troglodytes*, prefer individual over collaborative strategies towards goals. *Anim. Behav.* **82**, 1135–1141 (2011). doi: 10.1016/j.anbehav.2011.08.008
63. A. P. Melis, A.-C. Schneider, M. Tomasello, Chimpanzees, *Pan troglodytes*, share food in the same way after collaborative and individual food acquisition. *Anim. Behav.* (2011). doi: 10.1016/j.anbehav.2011.05.024
64. L. M. Rose, Vertebrate predation and food-sharing in *Cebus* and *Pan*. *Int. J. Primatol.* **18**, 727–765 (1997). doi: 10.1023/A:1026343812980
65. V. Horner, J. D. Carter, M. Suchak, F. B. M. de Waal, Spontaneous prosocial choice by chimpanzees. *Proc. Natl. Acad. Sci. U.S.A.* **108**, 13847–13851 (2011). doi: 10.1073/pnas.1111088108; pmid: 21825175
66. V. R. Lakshminarayanan, L. R. Santos, Capuchin monkeys are sensitive to others' welfare. *Curr. Biol.* **18**, R999–R1000 (2008). doi: 10.1016/j.cub.2008.08.057; pmid: 19000809
67. F. B. M. de Waal, K. Leimgruber, A. R. Greenberg, Giving is self-rewarding for monkeys. *Proc. Natl. Acad. Sci. U.S.A.* **105**, 13685–13689 (2008).
68. J. B. Silk *et al*., Chimpanzees are indifferent to the welfare of unrelated group members. *Nature* **437**, 1357–1359 (2005). doi: 10.1038/nature04243; pmid: 16251965
69. L. Drayton, L. Santos, Insights into intraspecies variation in primate prosocial behavior: Capuchins (*Cebus apella*) fail to show prosociality on a touchscreen task. *Behav. Sci.* **4**, 87–101 (2014). doi: 10.3390/bs4020087
70. M. Surbeck, G. Hohmann, Primate hunting by bonobos at LuiKotale, Salonga National Park. *Curr. Biol.* **18**, R906–R907 (2008). doi: 10.1016/j.cub.2008.08.040; pmid: 18957233
71. B. Chapais, C. M. Berman, *Kinship and Behavior in Primates* (Oxford University Press, Oxford, 2004).
72. M. Gácsi, P. McGreevy, E. Kara, A. Miklósi, Effects of selection for cooperation and attention in dogs. *Behav. Brain Funct.* **5**, 31 (2009). doi: 10.1186/1744-9081-5-31; pmid: 19630939

73. A. M. Seed, N. S. Clayton, N. J. Emery, Cooperative problem solving in rooks (*Corvus frugilegus*). *Proc. Biol. Sci.* **275**, 1421–1429 (2008). doi: 10.1098/rspb.2008.0111; pmid: 18364318
74. J. J. Neiworth, E. T. Johnson, K. Whillock, J. Greenberg, V. Brown, Is a sense of inequity an ancestral primate trait? Testing social inequity in cotton top tamarins (*Saguinus oedipus*). *J. Comp. Psychol.* **123**, 10–17 (2009). doi: 10.1037/a0012662; pmid: 19236140
75. N. J. Raihani, A. Thornton, R. Bshary, Punishment and cooperation in nature. *Trends Ecol. Evol.* **27**, 288–295 (2012). doi: 10.1016/j.tree.2011.12.004; pmid: 22284810
76. M. Mesterton-Gibbons, S. Gavrilets, J. Gravner, E. Akçay, Models of coalition or alliance formation. *J. Theor. Biol.* **274**, 187–204 (2011). doi: 10.1016/j.jtbi.2010.12.031; pmid: 21195717
77. J. Henrich *et al*., In search of Homo Economicus: Behavioral experiments in 15 small-scale societies. *Am. Econ. Rev.* **91**, 73–78 (2001). doi: 10.1257/aer.91.2.73
78. C. F. Camerer, G. Loewenstein, in *Advances in Behavioral Economics*, C. F. Camerer, G. Loewenstein, M. Rabin, Eds. (Princeton Univ. Press, Princeton, N. J., 2004), pp. 3–52.
79. K. Jensen, J. Call, M. Tomasello, Chimpanzees are rational maximizers in an ultimatum game. *Science* **318**, 107–109 (2007). doi: 10.1126/science.1145850; pmid: 17916736
80. I. Kaiser, K. Jensen, J. Call, M. Tomasello, Theft in an ultimatum game: Chimpanzees and bonobos are insensitive to unfairness. *Biol. Lett.* **8**, 942–945 (2012). doi: 10.1098/rsbl.2012.0519; pmid: 22896269
81. D. Proctor, R. A. Williamson, F. B. M. de Waal, S. F. Brosnan, Chimpanzees play the ultimatum game. *Proc. Natl. Acad. Sci. U.S.A.* **110**, 2070–2075 (2013). doi: 10.1073/pnas.1220806110; pmid: 23319633
82. V. LoBue, T. Nishida, C. Chiong, J. S. DeLoache, J. Haidt, When getting something good is bad: Even three-year-olds react to inequality. *Soc. Dev.* **20**, 154–170 (2011). doi: 10.1111/j.1467-9507.2009.00560.x
83. N. Steinbeis, B. C. Bernhardt, T. Singer, Impulse control and underlying functions of the left DLPFC mediate age-related and age-independent individual differences in strategic social behavior. *Neuron* **73**, 1040–1051 (2012). doi: 10.1016/j.neuron.2011.12.027; pmid: 22405212
84. M. Osvath, H. Osvath, Chimpanzee (*Pan troglodytes*) and orangutan (*Pongo abelii*) forethought: Self-control and pre-experience in the face of future tool use. *Anim. Cogn.* **11**, 661–674 (2008). doi: 10.1007/s10071-008-0157-0; pmid: 18553113
85. F. B. M. de Waal, in *Topics in Primatology, Vol. 1, Human Origins* (University of Tokyo Press, Tokyo, 1992), pp. 37–50.
86. N. Koyama, R. Dunbar, Anticipation of conflict by chimpanzees. *Primates* **37**, 79–86 (1996). doi: 10.1007/BF02382923
87. T. A. Evans, M. J. Beran, Delay of gratification and delay maintenance by rhesus macaques (*Macaca mulatta*). *J. Gen. Psychol.* **134**, 199–216 (2007). doi: 10.3200/GENP.134.2.199-216; pmid: 17503695
88. T. A. Evans, G. C. Westergaard, Self-control and tool use in tufted capuchin monkeys (*Cebus apella*). *J. Comp. Psychol.* **120**, 163–166 (2006). doi: 10.1037/0735-7036.120.2.163; pmid: 16719595
89. D. Semmann, H.-J. Krambeck, M. Milinski, Strategic investment in reputation. *Behav. Ecol. Sociobiol.* **56**, 248–252 (2004). doi: 10.1007/s00265-004-0782-9
90. M. Bateson, D. Nettle, G. Roberts, Cues of being watched enhance cooperation in a real-world setting. *Biol. Lett.* **2**, 412–414 (2006). doi: 10.1098/rsbl.2006.0509; pmid: 17148417
91. F. Subiaul, J. Vonk, S. Okamoto-Barth, J. Barth, Do chimpanzees learn reputation by observation? Evidence from direct and indirect experience with generous and selfish strangers. *Anim. Cogn.* **11**, 611–623 (2008). doi: 10.1007/s10071-008-0151-6; pmid: 18357476
92. L. M. Hopper, S. P. Lambeth, S. J. Schapiro, S. F. Brosnan, Social comparison mediates chimpanzees' responses to loss, not frustration. *Anim. Cogn.*, in press (2014). doi: 10.1007/s10071-014-0765-9; pmid: 24880642
93. M. B. Fontenot, S. L. Watson, K. A. Roberts, R. W. Miller, Effects of food preferences on token exchange and behavioural responses to inequality in tufted capuchin monkeys, *Cebus apella*. *Anim. Behav.* **74**, 487–496 (2007). doi: 10.1016/j.anbehav.2007.01.015
94. P. G. Roma, A. Silberberg, A. M. Ruggiero, S. J. Suomi, Capuchin monkeys, inequity aversion, and the frustration effect. *J. Comp. Psychol.* **120**, 67–73 (2006). doi: 10.1037/0735-7036.120.1.67; pmid: 16551166
95. M. Dindo, F. B. M. De Waal, Partner effects on food consumption in brown capuchin monkeys. *Am. J. Primatol.* **69**, 448–456 (2007). doi: 10.1002/ajp.20362; pmid: 17146793

ACKNOWLEDGMENTS

S.F.B. was funded by NSF CAREER grant SES 0847351 and NSF SES 1123897.

Published online 18 September 2014;
10.1126/science.1251776

ALSO IN *SCIENCE* JOURNALS

Edited by **Stella Hurtley**

APPLIED EVOLUTION

Exploiting evolution for humanity's sake

Using artificial selection, humans have tapped into evolutionary processes for thousands of years. The results of this process we see all around us, from the dogs we share our homes with to the food we put on our table. Carroll *et al.* review the ways that a more intentional harnessing of evolution may be able to help us meet some of Earth's most pressing challenges, including disease, climate change, and food security. — SNV

Science, this issue p. 313

SKILL DEVELOPMENT

Learning requires the brain to change

We may be leveraging change in our brains more than we have thought. Ohayon *et al.* knocked out cells responsible for laying down insulating myelin along neuronal axons in the brains of otherwise normal adult mice (see the Perspective by Long and Corfas). The mice lacking the myelin-forming cells were less able to learn a new motor skill involving running on a wheel with unevenly spaced bars. Although we may not run on a wheel, when trying to master new motor skills such as juggling, we too may well rely on similar myelin-producing cells. — PJH

Science, this issue p. 318; see also p. 298

SOCIAL EVOLUTION

The evolutionary benefits of behaving fairly

Humans have a deep and innate sense of fairness. Humans, however, are not the only species to react to apparent inequities. Brosnan and de Waal propose that inequity aversion can be broken down into two levels. At the most basic level, individuals react to immediate unequal distribution of a reward for equal effort expended, whereas at the second, they show the ability to accept a current unequal distribution with the expectation that over time distribution will equalize. This second level facilitates cooperation over time and requires the cognitive abilities both to assess current distribution and envision future opportunities for equalization. As cognitive abilities advanced across the primate lineage, this more complex accounting of equal distribution and cooperation may have developed into the complete sense of fairness we see in humans today. — SNV

Science, this issue p. 314

LAB ASTROPHYSICS

Stellar outflows replicated in miniature

Astronomers observe tight bright jets beaming from the poles of many celestial objects. But what focuses them so well? Albertazzi *et al.* recreated a scaled-down plasma jet in a laboratory setting to match the behavior of those in young stellar objects. The experiments show that the jets are collimated by a poloidal magnetic field aligned with the same axis. A conelike shock also emerges, as the expanding plasma is abruptly confined by the magnetic field. — MMM

Science, this issue p. 325

OPTICS

Achieving gain despite increasing loss

When energy is pumped into an optically active material, the buildup (or gain) of excitations within the material can reach a critical point where the emission of coherent light, or lasing, can occur. In many systems, however, the buildup of the excitations is suppressed by losses within the material. Overturning conventional wisdom that loss is bad and should be minimized, Peng *et al.* show that carefully tweaking the coupling strength between the various components of a coupled optical system can actually result in an enhancement of the optical properties by adding more loss into the system (see the Perspective by Schwefel). The results may provide a clever design approach to counteract loss in optical devices. — ISO

Science, this issue p. 328; see also p. 304

ATTOSECOND DYNAMICS

A very quick look at phenylalanine

Over the past decade, laser technology has pushed back the fastest directly observable time scale from femtoseconds (quadrillionths of a second) to attoseconds (quintillionths of a second). For the most part, attosecond studies so far have probed very simple molecules such as H_2 and O_2. Calegari *et al.* now look at a more elaborate molecule—the amino acid phenylalanine. They tracked changes in the electronic structure of the compound after absorption of an ultrafast pulse, before the onset of conventional vibrational motion. — JSY

Science, this issue p. 336

NITROGEN UPTAKE

Getting to the root of a root problem

Although a plant's root system reaches through the soil in search of nutrients, its search is not indiscriminate. If some section of the root is unable to deliver the amount of nitrogen that the rest of the plant demands, other sections of the root compensate and ramp up their delivery of nitrogen. Tabata *et al*. have now found a small peptide that delivers a signal involved in this process (see the Perspective by Bisseling and Scheres). Only with perception of the signal by the matching receptor in the shoot can the root system compensate for unproductive members. — PJH

Science, this issue p. 343; see also p. 300

ION CHANNELS

Insight into a retinal degeneration disease

Human bestrophin 1 (hBest1) is a membrane protein that forms a chloride channel in the retinal pigment epithelium. Mutations in hBest1 can lead to a retinal degeneration disease known as Best disease. Yang *et al*. describe the structure of KpBest, a bacterial homolog of hBest1. KpBest forms a pentamer with an ion channel at its center. In contrast to hBest1, KpBest1 is a sodium channel. The structure suggests a mechanism for ion selectivity that was confirmed by mutagenesis of KpBest and hBest1. A model of the hBest1 channel structure based on the KpBest structure reveals how mutations cause disease. — VV

Science, this issue p. 355

AGING

Cytoskeleton protects from stress and aging

The transcription factor HSF-1 has an unexpected second function that allows it to extend longevity in worms. Baird *et al.* expressed a modified form of HSF-1 in nematodes. The modified protein could not activate genes encoding protein chaperones. Such chaperones are thought to protect many cellular proteins from heat shock and other damage during aging However, the modified protein still extended the worm life span by regulating the transcription of other genes. One gene it regulated was *pat-10*, which encodes a troponin-like calcium binding protein. Overexpression of PAT-10 also extended worm life span, apparently by changing the stability of the actin cytoskeleton. — LBR

Science, this issue p. 360

Published by AAAS

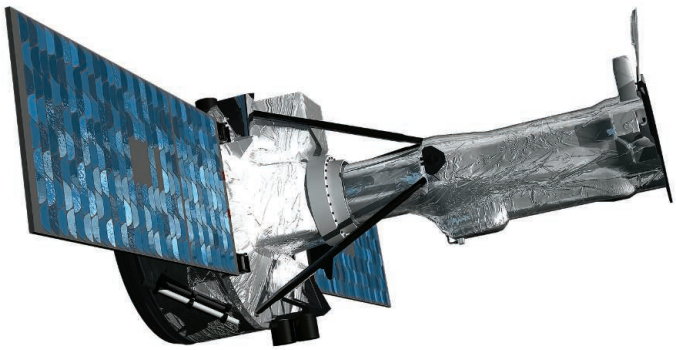

NASA/GSFC/CI LAB

PROBING THE solar interface region

By **Bart De Pontieu,[1] Alan Title,[1] and Mats Carlsson[2]**

The Sun has been the subject of human curiosity since the dawn of time. It provides the energy that makes Earth habitable and is also the closest star to Earth. The Sun thus acts as a laboratory that provides detailed views of physical processes that occur in other, much more distant, astrophysical objects. Much progress has been made in understanding how nuclear fusion powers the Sun's 15-million-degree core and the mechanisms that transport this energy to the visible surface, where most of the light that reaches Earth is released. However, major unresolved questions linger about how the heliosphere, the Sun's outer atmosphere in which we live, is shaped and powered. We do not understand the counter-intuitive rise of temperature from the 6000-K surface to millions of degrees in the Sun's outer atmosphere or corona. Equally puzzling is the solar wind, a high-speed continuous stream of particles that permeates space around Earth. These are not academic problems: Violent explosions such as flares and coronal mass ejections cause bouts of bad space weather that threaten power grids, satellites, and astronauts. These eruptions originate in and travel through this poorly understood solar atmosphere and wind. An important step in our quest to better understand such violent events is then to explore what drives the quiescent state of the solar atmosphere.

In June 2013, NASA launched the Interface Region Imaging Spectrograph (IRIS), an Earth-orbiting small explorer satellite with a 20-cm telescope onboard. IRIS uses gratings to split the Sun's near- and far-ultraviolet light into its constituent wavelengths, in order to remotely probe the physical conditions in the interface region that consists of the chromosphere and transition region. Recent research suggested that it is here, at the interface between surface and corona, that answers to some of the more vexing unresolved questions in solar physics might be found. In this special section of *Science*, five Reports exploit the high-resolution images and spectra obtained with IRIS to present major advances toward a comprehensive understanding of how the solar atmosphere is energized (sciencemag.org/special/iris).

Testa *et al.* find compelling evidence for the presence of high-energy particles generated during coronal nanoflares, small-scale heating events long hypothesized to drive coronal heating through the release of energy when magnetic field lines reconnect. These results provide constraints for models of the poorly understood mechanism that accelerates these electrons to such high energies and that probably acts under many other astrophysical conditions.

Hansteen *et al.* reveal the presence of small-scale magnetic loops in high-resolution images of IRIS and advanced three-dimensional numerical models, resolving a long-standing debate about the nature of the transition region emission. These results vindicate the view that much of this emission does not originate in the "classical" transition region between the surface and the hot loops. Rather, the emission occurs in "unresolved fine structure" that has now been spatially resolved, thereby removing a major impediment to the modeling of coronal loops.

Peter *et al.* exploit the power of high-resolution spectroscopy to reveal a solar atmosphere turned upside down: Hot plasma at 100,000 K is found closer to the solar surface than previously imagined, sandwiched by cool plasma both below and above. The hot plasma is heated by "bombs" in which the reconnection of magnetic fields leads to rapid heating. These unexpected results will likely lead to a reassessment of other phenomena in the low solar atmosphere, such as the mysterious Ellerman bombs discovered almost a century ago.

De Pontieu *et al.* describe a chromosphere that is replete with twisting motions on very small scales that are associated with the heating of plasma to transition region temperatures. They are the signature of propagating Alfven wave pulses and provide support for recently developed models of atmospheric heating and dynamics and insight into the transport of helicity in the solar atmosphere.

Tian *et al.* find evidence of high-speed jets at the root of the solar wind, fountains of plasma that appear to undergo rapid heating from chromospheric to transition region temperatures. These observations provide support for recent suggestions that the solar wind does not necessarily originate only from gentle evaporation in funnels rooted in strong field regions.

Together, these results provide critical pieces in the still-unsolved puzzle of fully understanding of how the Sun shapes and affects the heliosphere. With solar activity at high levels, more advances from the imaging spectrograph onboard IRIS can be expected, especially with respect to flares and coronal mass ejections.

10.1126/science.346.6207.315

[1]*Lockheed Martin Solar & Astrophysics Laboratory, Palo Alto, CA, USA,* [2]*Institute of Theoretical Astrophysics, University of Oslo, Norway.*

Published by AAAS

Downloaded from www.sciencemag.org on October 17, 2014

On the prevalence of small-scale twist in the solar chromosphere and transition region

B. De Pontieu,* L. Rouppe van der Voort, S. W. McIntosh, T. M. D. Pereira, M. Carlsson, V. Hansteen, H. Skogsrud, J. Lemen, A. Title, P. Boerner, N. Hurlburt, T. D. Tarbell, J. P. Wuelser, E. E. De Luca, L. Golub, S. McKillop, K. Reeves, S. Saar, P. Testa, H. Tian, C. Kankelborg, S. Jaeggli, L. Kleint, J. Martinez-Sykora

The solar chromosphere and transition region (TR) form an interface between the Sun's surface and its hot outer atmosphere. There, most of the nonthermal energy that powers the solar atmosphere is transformed into heat, although the detailed mechanism remains elusive. High-resolution (0.33–arc second) observations with NASA's Interface Region Imaging Spectrograph reveal a chromosphere and TR that are replete with twist or torsional motions on sub–arc second scales, occurring in active regions, quiet Sun regions, and coronal holes alike. We coordinated observations with the Swedish 1-meter Solar Telescope (SST) to quantify these twisting motions and their association with rapid heating to at least TR temperatures. This view of the interface region provides insight into what heats the low solar atmosphere.

The list of author affiliations is available in the full article online. * **Corresponding author:** **E-mail: bdp@lmsal.com** Read the full article at http:// dx.doi.org/10.1126/science.1255732

Prevalence of small-scale jets from the networks of the solar transition region and chromosphere

H. Tian,* E. E. DeLuca, S. R. Cranmer, B. De Pontieu, H. Peter, J. Martínez-Sykora, L. Golub, S. McKillop, K. K. Reeves, M. P. Miralles, P. McCauley, S. Saar, P. Testa, M. Weber, N. Murphy, J. Lemen, A. Title, P. Boerner, N. Hurlburt, T. D. Tarbell, J. P. Wuelser, L. Kleint, C. Kankelborg, S. Jaeggli, M. Carlsson, V. Hansteen, S. W. McIntosh

As the interface between the Sun's photosphere and corona, the chromosphere and transition region play a key role in the formation and acceleration of the solar wind. Observations from the Interface Region Imaging Spectrograph reveal the prevalence of intermittent small-scale jets with speeds of 80 to 250 kilometers per second from the narrow bright network lanes of this interface region. These jets have lifetimes of 20 to 80 seconds and widths of ≤300 kilometers. They originate from small-scale bright regions, often preceded by footpoint brightenings and accompanied by transverse waves with amplitudes of ~20 kilometers per second. Many jets reach temperatures of at least ~105 kelvin and constitute an important element of the transition region structures. They are likely an intermittent but persistent source of mass and energy for the solar wind.

The list of author affiliations is available in the full article online. *Corresponding author: **E-mail: hui.tian@cfa.harvard.edu** Read the full article at http://dx.doi.org/10.1126/science.1255711

Evidence of nonthermal particles in coronal loops heated impulsively by nanoflares

P. Testa,* B. De Pontieu, J. Allred, M. Carlsson, F. Reale, A. Daw, V. Hansteen, J. Martinez-Sykora, W. Liu, E. E. DeLuca, L. Golub, S. McKillop, K. Reeves, S. Saar, H. Tian, J. Lemen, A. Title, P. Boerner, N. Hurlburt, T. D. Tarbell, J. P. Wuelser, L. Kleint, C. Kankelborg, S. Jaeggli

The physical processes causing energy exchange between the Sun's hot corona and its cool lower atmosphere remain poorly understood. The chromosphere and transition region (TR) form an interface region between the surface and the corona that is highly sensitive to the coronal heating mechanism. High-resolution

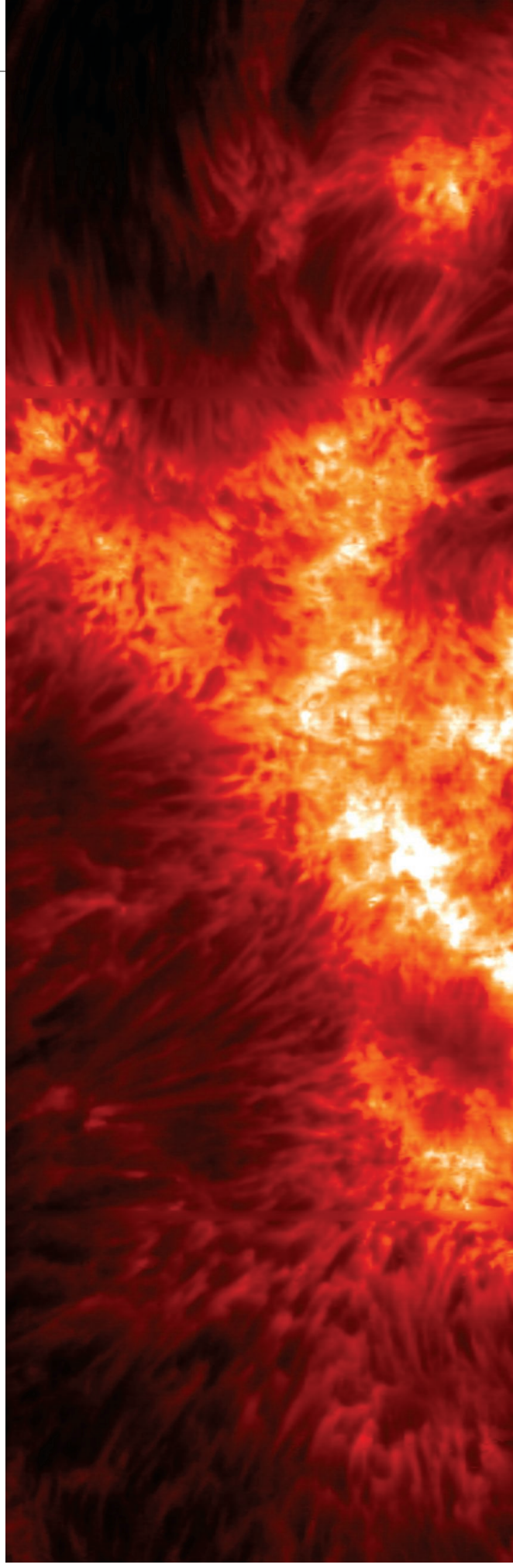

Published by AAAS

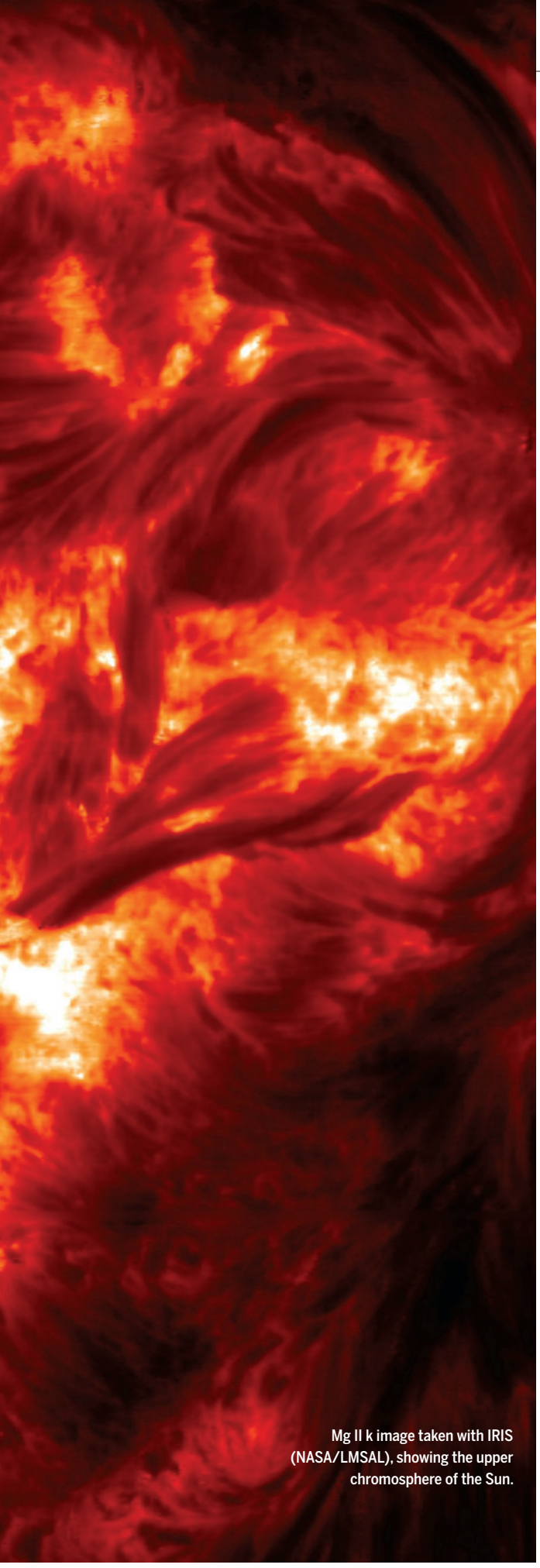

Mg II k image taken with IRIS (NASA/LMSAL), showing the upper chromosphere of the Sun.

PHOTO: TIAGO PEREIRA, UNIVERSITY OF OSLO, NORWAY

observations with the Interface Region Imaging Spectrograph reveal rapid variability (~20 to 60 seconds) of intensity and velocity on small spatial scales (≲500 kilometers) at the footpoints of hot and dynamic coronal loops. The observations are consistent with numerical simulations of heating by beams of nonthermal electrons, which are generated in small impulsive (≲30 seconds) heating events called "coronal nanoflares." The accelerated electrons deposit a sizable fraction of their energy (≲1025 erg) in the chromosphere and TR. Our analysis provides tight constraints on the properties of such electron beams and new diagnostics for their presence in the nonflaring corona.

The list of author affiliations is available in the full article online. *Corresponding author:
E-mail: ptesta@cfa.harvard.edu Read the full article at http://dx.doi.org/10.1126/science.1255724

Hot explosions in the cool atmosphere of the Sun

H. Peter,* H. Tian, W. Curdt, D. Schmit, D. Innes, B. De Pontieu, J. Lemen, A. Title, P. Boerner, N. Hurlburt, T. D. Tarbell, J. P. Wuelser, Juan Martínez-Sykora, L. Kleint, L. Golub, S. McKillop, K. K. Reeves, S. Saar, P. Testa, C. Kankelborg, S. Jaeggli, M. Carlsson, V. Hansteen

The solar atmosphere was traditionally represented with a simple one-dimensional model. Over the past few decades, this paradigm shifted for the chromosphere and corona that constitute the outer atmosphere, which is now considered a dynamic structured envelope. Recent observations by the Interface Region Imaging Spectrograph (IRIS) reveal that it is difficult to determine what is up and down, even in the cool 6000-kelvin photosphere just above the solar surface: This region hosts pockets of hot plasma transiently heated to almost 100,000 kelvin. The energy to heat and accelerate the plasma requires a considerable fraction of the energy from flares, the largest solar disruptions. These IRIS observations not only confirm that the photosphere is more complex than conventionally thought, but also provide insight into the energy conversion in the process of magnetic reconnection.

The list of author affiliations is available in the full article online. *Corresponding author:
E-mail: peter@mps.mpg.de Read the full article at http://dx.doi.org/10.1126/science.1255726

The unresolved fine structure resolved: IRIS observations of the solar transition region

V. Hansteen,* B. De Pontieu, M. Carlsson, J. Lemen, A. Title, P. Boerner, N. Hurlburt, T. D. Tarbell, J. P. Wuelser, T. M. D. Pereira, E. E. De Luca, L. Golub, S. McKillop, K. Reeves, S. Saar, P. Testa, H. Tian, C. Kankelborg, S. Jaeggli, L. Kleint, J. Martínez-Sykora

The heating of the outer solar atmospheric layers, i.e., the transition region and corona, to high temperatures is a long-standing problem in solar (and stellar) physics. Solutions have been hampered by an incomplete understanding of the magnetically controlled structure of these regions. The high spatial- and temporal-resolution observations with the Interface Region Imaging Spectrograph (IRIS) at the solar limb reveal a plethora of short, low-lying loops or loop segments at transition-region temperatures that vary rapidly, on the time scale of minutes. We argue that the existence of these loops solves a long-standing observational mystery. At the same time, based on comparison with numerical models, this detection sheds light on a critical piece of the coronal heating puzzle.

The list of author affiliations is available in the full article online. *Corresponding author:
E-mail: viggoh@astro.uio.no Read the full article at http://dx.doi.org/10.1126/science.1255757

Published by AAAS

SOLAR PHYSICS

Prevalence of small-scale jets from the networks of the solar transition region and chromosphere

H. Tian,[1]* E. E. DeLuca,[1] S. R. Cranmer,[1] B. De Pontieu,[2] H. Peter,[3] J. Martínez-Sykora,[2,4] L. Golub,[1] S. McKillop,[1] K. K. Reeves,[1] M. P. Miralles,[1] P. McCauley,[1] S. Saar,[1] P. Testa,[1] M. Weber,[1] N. Murphy,[1] J. Lemen,[2] A. Title,[2] P. Boerner,[2] N. Hurlburt,[2] T. D. Tarbell,[2] J. P. Wuelser,[2] L. Kleint,[2,4] C. Kankelborg,[5] S. Jaeggli,[5] M. Carlsson,[6] V. Hansteen,[6] S. W. McIntosh[7]

As the interface between the Sun's photosphere and corona, the chromosphere and transition region play a key role in the formation and acceleration of the solar wind. Observations from the Interface Region Imaging Spectrograph reveal the prevalence of intermittent small-scale jets with speeds of 80 to 250 kilometers per second from the narrow bright network lanes of this interface region. These jets have lifetimes of 20 to 80 seconds and widths of ≤300 kilometers. They originate from small-scale bright regions, often preceded by footpoint brightenings and accompanied by transverse waves with amplitudes of ~20 kilometers per second. Many jets reach temperatures of at least ~10^5 kelvin and constitute an important element of the transition region structures. They are likely an intermittent but persistent source of mass and energy for the solar wind.

The Sun continuously emits ionized particles into interplanetary space in the form of the solar wind. A challenging investigation has now carried on for almost 50 years to understand where the solar wind originates and how it is accelerated (*1*, *2*). Dark regions in coronal images indicate the coronal holes that are the commonly accepted large-scale source regions of the high-speed solar wind. However, identifying precise origin sites within coronal holes requires high-resolution observations of the chromosphere and transition region (TR), a complex interface between the relatively cool photosphere (~6 × 10^3 K) and hot corona (~10^6 K). The mass and energy that ultimately feed the solar wind must pass through this region.

The dominant emission features in this interface region are the network structures that appear as narrow bright lanes enclosing dark cells, with sizes of ~20,000 km in radiance images of emission lines (*3*). The network lanes (networks thereafter) are believed to be locations of strong magnetic fluxes originating from the boundaries of convection cells with similar sizes in the photosphere. Previous observations of coronal holes with the Solar Ultraviolet Measurements of Emitted Radiation (SUMER) instrument (*4*) onboard the Solar and Heliospheric Observatory (SOHO) revealed Doppler blue shifts of 5 to 10 km s^{-1} for emission lines formed in the upper TR (*5*). They were interpreted as signatures of the nascent solar wind guided by funnellike magnetic structures originating from the networks (*6*).

Recent analyses revealed weak blue wing enhancements in profiles of emission lines formed in the TR (*7*, *8*). These weak enhancements indicate the possible presence of a plasma component flowing upward with speeds of 50 to 100 km s^{-1}, which may provide heated mass to the solar wind (*8*). It has been difficult to test this proposed idea without direct imaging of such TR upflows on the solar disk, although moderate-resolution observations have revealed signatures

[1]Harvard-Smithsonian Center for Astrophysics, 60 Garden Street, Cambridge, MA 02138, USA. [2]Lockheed Martin Solar and Astrophysics Laboratory, 3251 Hanover Street, Organization A021S, Building 252, Palo Alto, CA 94304, USA. [3]Max Planck Institute for Solar System Research, Justus-von-Liebig-Weg 3, 37077 Göttingen, Germany. [4]Bay Area Environmental Research Institute, 596 1st Street West, Sonoma, CA 95476, USA. [5]Department of Physics, Montana State University, Post Office Box 173840, Bozeman, MT 59717, USA. [6]Institute of Theoretical Astrophysics, University of Oslo, Post Office Box 1029, Blindern, 0315 Oslo, Norway. [7]High Altitude Observatory, National Center for Atmospheric Research, Post Office Box 3000, Boulder, CO 80307, USA.
*Corresponding author. E-mail: hui.tian@cfa.harvard.edu

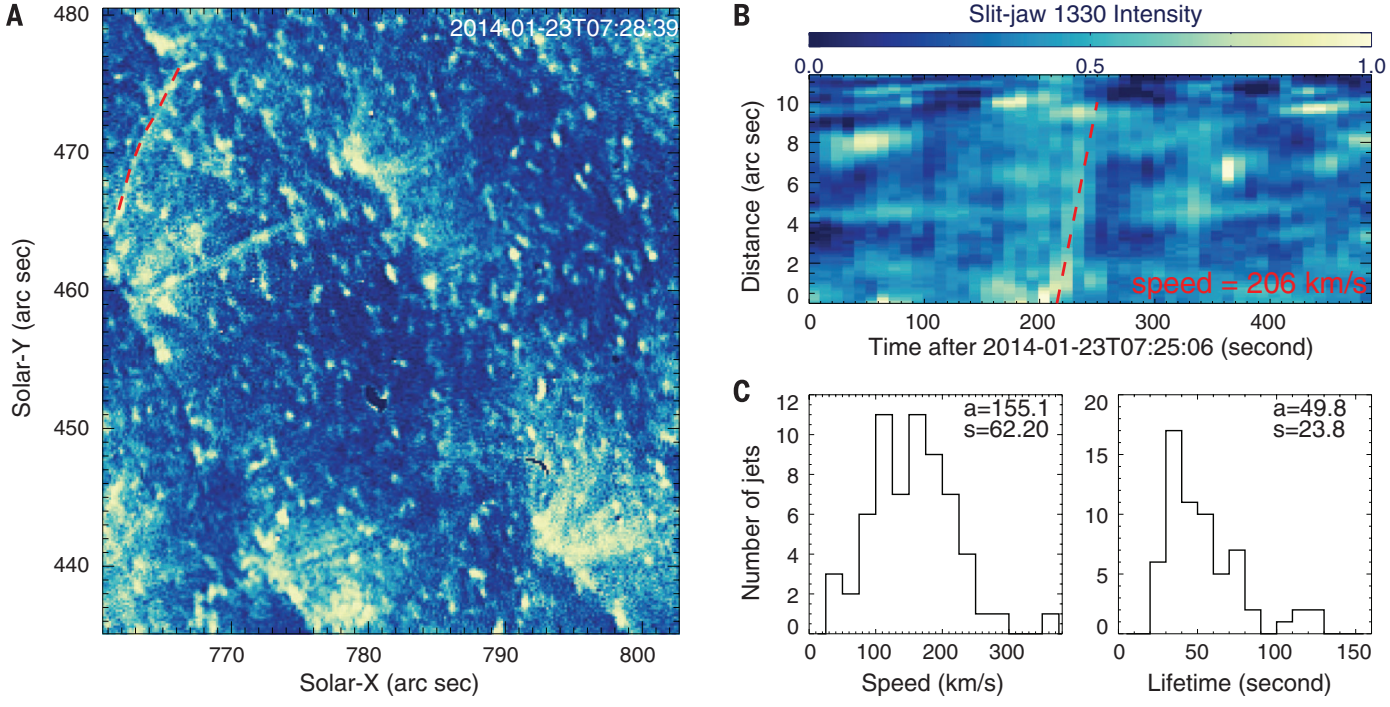

Fig. 1. Examples of network jets. (**A**) An unsharp masked (SM) 1330 Å slit-jaw image (movie S3). The dashed line marks the path of a jet. (**B**) Space-time plot for the jet marked in (A). (**C**) Distributions of the apparent speeds and lifetimes for 63 jets. The average (a) and standard deviation (s) values are also shown.

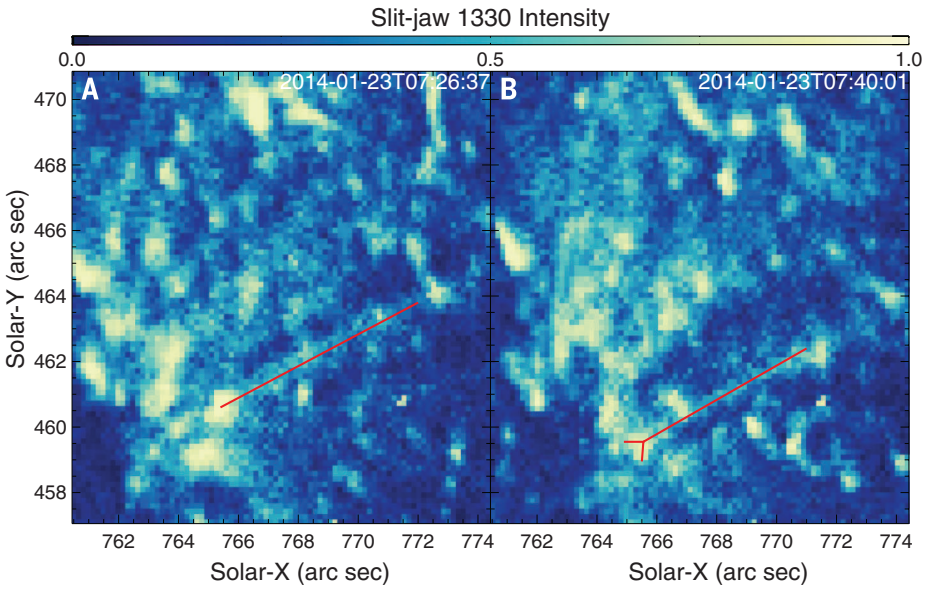

Fig. 2. (A and B) Two unsharp masked 1330 Å slit-jaw images showing the origin of network jets from small-scale bright regions in the network (movie S4). The red lines outline two jets.

of chromospheric upflows being heated to TR temperatures at the solar limb in a coronal hole (*9*).

Using observations from the Interface Region Imaging Spectrograph (IRIS) (*10*), we report results from direct imaging on the solar disk of high-speed upflows with apparent speeds of 80 to 250 km s^{-1}. Thanks to the high resolution (~250 km) in new wavelength windows, IRIS slit-jaw imaging observations with the 1400, 1330, and 2796 Å filters [see the supplementary materials (SM)] unambiguously reveal the prevalence of small-scale jetlike emission features from the bright networks (figs. S1 to S3 and movies S1 and S2). These three filters sample emission from the Si IV, C II, and Mg II ions, which are formed at temperatures of ~10^5 K, ~3×10^4 K, and ~10^4 K, respectively. These network jets usually show fast upward motion with no obvious downward component. Although these jets are more easily seen in coronal holes located near the solar limb (movies S1 to S5), they are clearly detected at any location on the solar disk outside active regions (movie S6).

These network jets are best seen in 1330 Å images. The jet widths are usually around ~300 km and approach the instrument resolution limit,

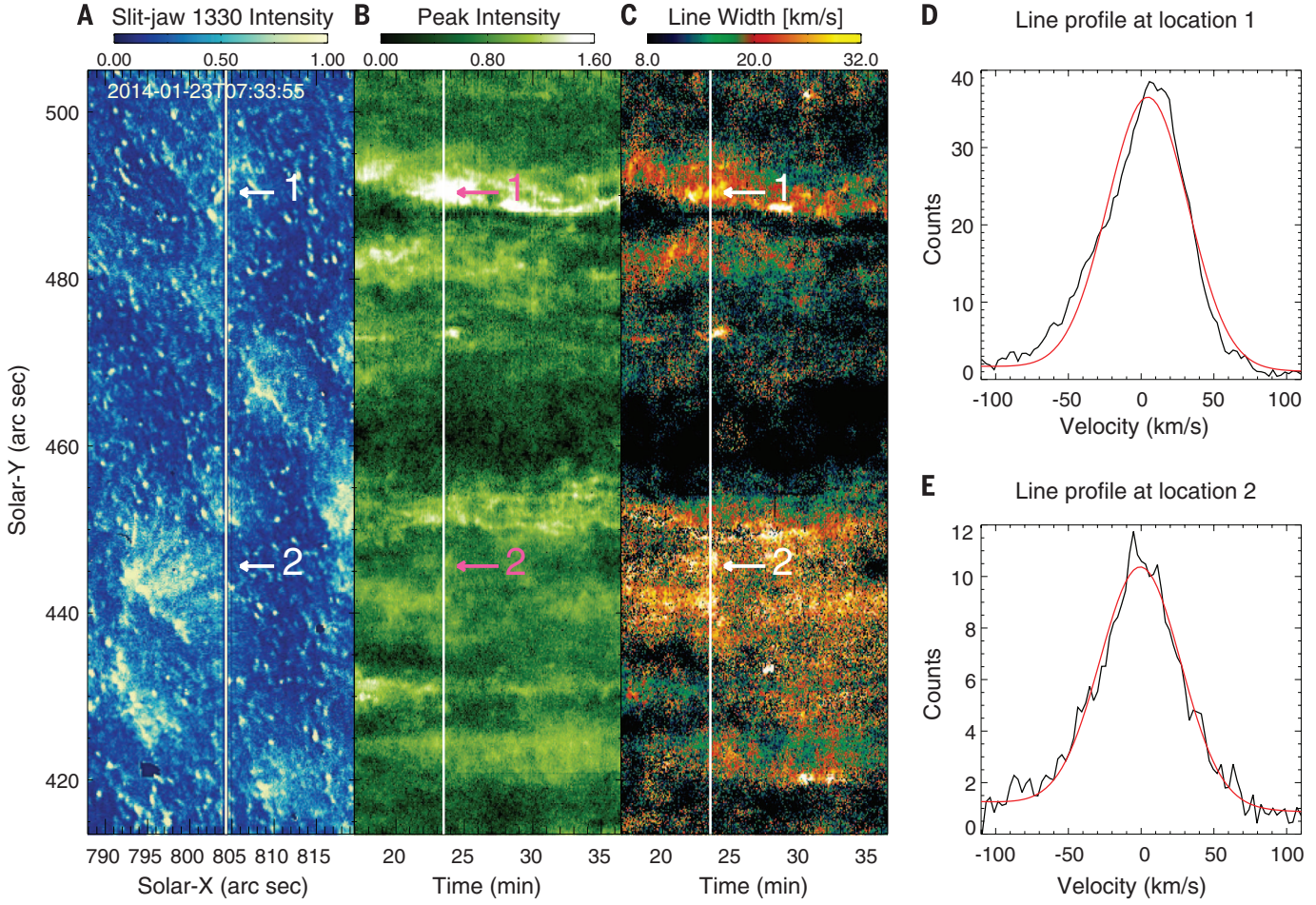

Fig. 3. Signatures of network jets in Si IV 1393.77 Å line profiles (movie S5). (**A**) Unsharp masked 1330 Å slit-jaw image taken at 07:33:55 UT on 23 January 2014. (**B** and **C**) Temporal evolution of the intensity and line width along the slit from a Gaussian fit of Si IV line profiles. The vertical line indicates the slit location in (A) and time of 07:33:55 UT in (B) and (C). (**D** and **E**) Observed line profiles (black) at the two locations indicated by the arrows. Red lines are the Gaussian fits.

suggesting that the actual widths of many jets may be even smaller. By applying the space-time technique (SM) to the 1330 Å image sequence obtained on 23 January 2014 (table S1 and movie S2), we have quantified the apparent speeds and lifetimes for 63 randomly selected jets (Fig. 1). The speeds fall mostly in the range of 80 to 250 km s^{-1}, which is much larger than the sound speed and close to the Alfvén speed in the chromosphere (*11*) and TR. These velocities are significantly larger than previously reported jet velocities in the chromosphere and TR (*12*–*16*). Some jets also show signatures of acceleration. Their lifetimes range mainly from 20 to 80 s. Most jets extend to lengths of 4 to 10 Mm (1 Mm = 10^6 m), although some clearly reach ~15 Mm.

Many network jets also exhibit obvious motions transverse to their propagation direction, indicating that they carry transverse magnetohydrodynamic waves known as Alfvén waves (*11*, *17*). The wave magnitudes are difficult to measure from slit-jaw images, because strong emission from other features complicates the quantification of the transverse displacement, and the jet lifetimes are usually too short to allow the detection of a full wave cycle. Instead, we use spectroscopic observations to estimate the approximate velocity amplitudes of Alfvén waves. The root-mean-square value of the fluctuating Doppler shift of the Si IV 1393.77 Å line is ~5 km s^{-1}, which can be regarded as the resolved wave amplitude (SM and fig. S5).

Many of these network jets are likely the on-disk counterparts and TR manifestation of type II spicules (SM), which are jetlike features moving upward with speeds of 50 to 110 km s^{-1} in the chromosphere above the solar limb (*15*, *16*). Our direct imaging of flows along these jets on the solar disk is almost unaffected by line-of-sight superposition, thus providing further support for the debated existence of high-speed jetlike features (*16*, *18*). IRIS observations also reveal their origin in the networks, which off-limb observations cannot determine. Yet we notice that network jet velocities are generally twice those of type II spicules, suggesting that the network jets sampled by the TR passbands are those being heated and accelerated in the upper chromosphere and TR (*19*) and/or that the apparent speeds we observe here are not all caused by mass flows. Additional absorbing components at the blue wings of some chromospheric absorption lines were previously claimed to be on-disk counterparts of type II spicules (*13*). These features with speeds of 20 to 50 km s^{-1} are probably the lower-temperature parts and/or less-accelerated phase of the network jets.

Many network jets tend to recur at roughly the same locations on time scales of ~2 to 15 min. Our on-disk observations show that these jets originate from localized bright regions in the networks (Fig. 2 and movie S4). Sometimes we see obvious brightening at the footpoints of these jets. A few jets appear to reveal the characteristic inverted Y-shape morphology (Fig. 2B) that is associated with a bipolar magnetic field line reconnecting with a unipolar large-scale field (*12*). These characteristics, together with the high speeds, suggest that some of these intermittent jets may result from repeated magnetic reconnection (*20*) between small magnetic loops and the background open flux in the networks. It is also possible that the source regions of these jets are too small to be resolved by IRIS, or that other mechanisms (SM) such as flux emergence and the associated Lorentz force are responsible for the acceleration of the jets (*21*).

Spectroscopic observations from IRIS reveal that many jets reach temperatures of at least ~10^5 K, the formation temperature of the Si IV 1393.77 Å line under ionization equilibrium. The most prominent signature of network jets in Si IV line profiles is a significant increase of the line broadening, which could be a consequence of field-aligned flows (*22*) or unresolved transverse motions such as Alfvén waves (*23*) and twists (*24*). Combined imaging and spectral observations of IRIS can help evaluate the contribution from field-aligned flows and transverse motions.

Greatly enhanced widths of the Si IV line are found around two locations of network jets (Fig. 3). The slit crosses the lower part of a recurring jet complex at location 1. There the obvious enhancement of the line profile at the blue wing (Fig. 3D and SM) indicates an association with the network jets visible in the slit-jaw images (movie S5). Thus, the enhanced line broadening here is largely caused by the superposition of the field-aligned flows (jets) on the network background.

Location 2 corresponds to the upper part of some swaying network jets (movie S5). Given the nearly symmetric line profile and that this region is close to the limb, these jets are likely propagating largely in the plane perpendicular to the line of sight. So the line broadening appears to be largely caused by unresolved Alfvén waves, or small-scale twists that are often associated with unresolved torsional Alfvén waves (*25*). If we

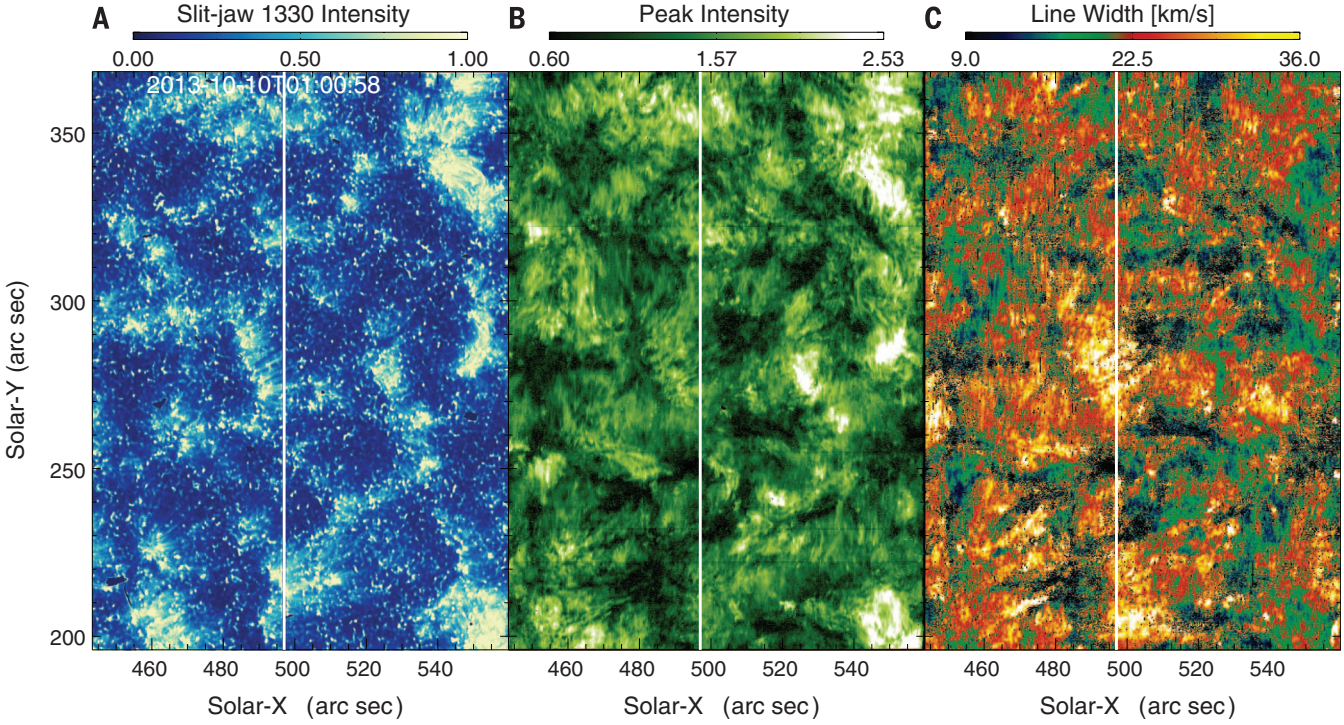

Fig. 4. TR filamentary structures caused by network jets (movie S6). (**A**) An unsharp masked 1330 Å slit-jaw image. (**B** and **C**) Maps of intensity and line width from a Gaussian fit of Si IV 1393.77 Å line profiles. The vertical line indicates the slit location.

attribute the nonthermal width (SM and fig. S5) to these unresolved waves, the wave amplitude is estimated to be ~21 km s^{-1}.

Intensity and linewidth maps of Si IV (Fig. 4) reveal details of the TR structures. One prominent feature of these maps is the presence of filamentary or elongated structures. Comparing these maps with the slit-jaw images (movie S6) reveals an association of many such features with network jets. Depending on viewing angles, enhanced line widths in these filamentary structures could be caused by either the superposition of jet emission on the network background, or unresolved transverse motions, or both. This association reveals that network jets constitute an important element of TR structures (SM).

These jets are likely to be an intermittent but continual source of mass and energy for the solar wind. We find a total mass loss rate of (2.8 to 36.4) × 10^{12} g s^{-1} for these jets if we assume that all jet plasma contributes to the solar wind (SM). This value is about 2 to 24 times larger than the total mass loss rate of the solar wind, yet we have to remember that it is difficult to determine the true contribution to the solar wind without sufficiently sensitive coronal observations. With a wave amplitude of ~20 km s^{-1}, the energy flux of Alfvén waves carried by the jets should be 4 to 24 kW m^{-2} (SM). This is much larger than that required to drive the solar wind (~700 W m^{-2}), yet we do not know how much of this energy is dissipated.

The prevalence of these network jets may challenge current solar wind models. Most time-steady descriptions of the solar wind (*1*, *26*) rely on mass flux driven by evaporation from the upper TR, induced by a combination of downward heat conduction from the corona and local radiative losses (*27*). Although successfully predicting the coronal heating and wind properties at Earth, these models usually produce steady flows of only a few kilometers per second in the chromosphere and TR. Such steady low-speed outflows have never been imaged.

In contrast, our IRIS observations reveal the presence of intermittent high-speed upflows from the networks. If the mass in these jets actually is lost in the solar wind, then models must be updated to account for this highly intermittent component. A proposed reconnection-driven solar wind model (*6*) may be consistent with our observations. This scenario, which involves reconnection between open field lines in the network and surrounding low-lying loops, has been simulated numerically (*28*). However, the maximum outflow velocities produced by this model are only ~30 km s^{-1}, and it is unclear whether the entire mass and energy flux of the wind can be produced in this way (*29*).

If these jets are not the nascent solar wind, at least their interaction with the wind should be considered in solar wind models, because they are the most prominent TR features in the networks where the wind is believed to originate. One recent model does include some upward and downward motions of the TR plasma (*30*). However, these motions have speeds of ~60 km s^{-1} at most, and the jets we observe show much faster upward motions. Obviously, a successful solar wind model must carefully evaluate the mass and energy contributions from these network jets.

REFERENCES AND NOTES

1. S. R. Cranmer, Coronal holes. *Living Rev. Sol. Phys* **6**, 3 (2009). doi: 10.12942/lrsp-2009-3
2. V. H. Hansteen, M. Velli, Solar wind models from the chromosphere to 1 AU. *Space Sci. Rev.* **172**, 89–121 (2012). doi: 10.1007/s11214-012-9887-z
3. E. M. Reeves, The EUV chromospheric network in the quiet Sun. *Sol. Phys.* **46**, 53–72 (1976). doi: 10.1007/BF00157554
4. K. Wilhelm *et al*., SUMER - Solar Ultraviolet Measurements of Emitted Radiation. *Sol. Phys.* **162**, 189–231 (1995). doi: 10.1007/BF00733430
5. D. M. Hassler *et al*., Solar wind outflow and the chromospheric magnetic network. *Science* **283**, 810–813 (1999). doi: 10.1126/science.283.5403.810; pmid: 9933156
6. C.-Y. Tu *et al*., Solar wind origin in coronal funnels. *Science* **308**, 519–523 (2005). doi: 10.1126/science.1109447; pmid: 15845846
7. B. De Pontieu, S. W. McIntosh, V. H. Hansteen, C. J. Schrijver, Observing the roots of solar coronal heating—in the chromosphere. *Astrophys. J.* **701**, L1–L6 (2009). doi: 10.1088/0004-637X/701/1/L1
8. S. W. McIntosh, R. J. Leamon, B. De Pontieu, The spectroscopic footprint of the fast solar wind. *Astrophys. J.* **727**, 7 (2011). doi: 10.1088/0004-637X/727/1/7
9. B. De Pontieu *et al*., The origins of hot plasma in the solar corona. *Science* **331**, 55–58 (2011). doi: 10.1126/science.1197738; pmid: 21212351
10. B. De Pontieu *et al*., The Interface Region Imaging Spectrograph (IRIS). *Sol. Phys.* **289**, 2733–2779 (2014). doi: 10.1007/s11207-014-0485-y
11. B. De Pontieu *et al*., Chromospheric alfvenic waves strong enough to power the solar wind. *Science* **318**, 1574–1577 (2007). doi: 10.1126/science.1151747; pmid: 18063784
12. K. Shibata *et al*., Chromospheric anemone jets as evidence of ubiquitous reconnection. *Science* **318**, 1591–1594 (2007). doi: 10.1126/science.1146708; pmid: 18063790
13. L. Rouppe van der Voort, J. Leenaarts, B. de Pontieu, M. Carlsson, G. Vissers, On-disk counterparts of type ii spicules in the Ca II 854.2 nm and Hα lines. *Astrophys. J.* **705**, 272–284 (2009). doi: 10.1088/0004-637X/705/1/272
14. H.-S. Ji, W.-D. Cao, P. Goode, Observation of ultrafine channels of solar corona heating. *Astrophys. J.* **750**, L25 (2012). doi: 10.1088/2041-8205/750/1/L25
15. B. De Pontieu *et al*., *Pub. Astron. Soc. Japan* **59**, S655 (2007).
16. T. M. D. Pereira, B. De Pontieu, M. Carlsson, Quantifying spicules. *Astrophys. J.* **759**, 18 (2012). doi: 10.1088/0004-637X/759/1/18
17. S. W. McIntosh *et al*., Alfvénic waves with sufficient energy to power the quiet solar corona and fast solar wind. *Nature* **475**, 477–480 (2011). doi: 10.1038/nature10235; pmid: 21796206
18. Y. Z. Zhang *et al*., Revision of solar spicule classification. *Astrophys. J.* **750**, 16 (2012). doi: 10.1088/0004-637X/750/1/16
19. J. Martínez-Sykora, V. Hansteen, F. Moreno-Insertis, On the origin of the type II spicules: Dynamic three-dimensional mhd simulations. *Astrophys. J.* **736**, 9 (2011). doi: 10.1088/0004-637X/736/1/9
20. V. Archontis, K. Tsinganos, C. Gontikakis, Recurrent solar jets in active regions. *Astron. Astrophys.* **512**, L2 (2010). doi: 10.1051/0004-6361/200913752
21. M. L. Goodman, Acceleration of type 2 spicules in the solar chromosphere. II. Viscous braking and upper bounds on coronal energy input. *Astrophys. J.* **785**, 87 (2014). doi: 10.1088/0004-637X/785/2/87
22. B. De Pontieu, S. W. McIntosh, Quasi-periodic propagating signals in the solar corona: The signature of magnetoacoustic waves or high-velocity upflows? *Astrophys. J.* **722**, 1013–1029 (2010). doi: 10.1088/0004-637X/722/2/1013
23. J. Chae, U. Schuhle, P. Lemaire, SUMER measurements of nonthermal motions: Constraints on coronal heating mechanisms. *Astrophys. J.* **505**, 957–973 (1998). doi: 10.1086/306179
24. B. De Pontieu *et al*., *Science* **346**, 1255732 (2014).
25. A. A. van Ballegooijen, M. Asgari-Targhi, S. R. Cranmer, E. E. DeLuca, Heating of the solar chromosphere and corona by Alfvén wave turbulence. *Astrophys. J.* **736**, 3 (2011). doi: 10.1088/0004-637X/736/1/3
26. B. Chandran, T. J. Dennis, E. Quataert, S. D. Bale, Incorporating kinetic physics into a two-fluid solar-wind model with temperature anisotropy and low-frequency Alfvén-wave turbulence. *Astrophys. J.* **743**, 197 (2011). doi: 10.1088/0004-637X/743/2/197
27. R. Hammer, Energy balance of stellar coronae. I - Methods and examples. II - Effect of coronal heating. *Astrophys. J.* **259**, 767 (1982). doi: 10.1086/160213
28. L.-P. Yang *et al*., Injection of plasma into the nascent solar wind via reconnection driven by supergranular advection. *Astrophys. J.* **770**, 6 (2013). doi: 10.1088/0004-637X/770/1/6
29. S. R. Cranmer, A. A. van Ballegooijen, Can the solar wind be driven by magnetic reconnection in the Sun's magnetic carpet? *Astrophys. J.* **720**, 824–847 (2010). doi: 10.1088/0004-637X/720/1/824
30. T. Matsumoto, T. K. Suzuki, Connecting the Sun and the solar wind: The first 2.5-dimensional self-consistent mhd simulation under the Alfvén wave scenario. *Astrophys. J.* **749**, 8 (2012). doi: 10.1088/0004-637X/749/1/8

ACKNOWLEDGMENTS

IRIS is a NASA Small Explorer mission developed and operated by the Lockheed Martin Solar and Astrophysics Laboratory (LMSAL), with mission operations executed at the NASA Ames Research Center and major contributions to downlink communications funded by the Norwegian Space Center (Norway) through a European Space Agency PRODEX contract. This work is supported by NASA contract NNG09FA40C (IRIS), the Lockheed Martin Independent Research Program, European Research Council grant agreement no. 291058, contract 8100002705 from LMSAL to the Smithsonian Astrophysical Observatory, and NASA grant NNX11AO98G. The publicly available IRIS data (including the data used in this study) are archived at http://iris.lmsal.com/data.html.

SUPPLEMENTARY MATERIALS

www.sciencemag.org/content/346/6207/1255711/suppl/DC1
Supplementary Text S1 to S11
Figs. S1 to S5
Table S1
References (*31*–*64*)
Captions for Movies S1 to S6
Movies S1 to S6

6 May 2014; accepted 22 September 2014
10.1126/science.1255711

SOLAR PHYSICS

Evidence of nonthermal particles in coronal loops heated impulsively by nanoflares

P. Testa,[1]* B. De Pontieu,[2,3] J. Allred,[4] M. Carlsson,[3] F. Reale,[5] A. Daw,[4] V. Hansteen,[3] J. Martinez-Sykora,[6] W. Liu,[2,7] E. E. DeLuca,[1] L. Golub,[1] S. McKillop,[1] K. Reeves,[1] S. Saar,[1] H. Tian,[1] J. Lemen,[2] A. Title,[2] P. Boerner,[2] N. Hurlburt,[2] T. D. Tarbell,[2] J. P. Wuelser,[2] L. Kleint,[2,6] C. Kankelborg,[8] S. Jaeggli[8]

The physical processes causing energy exchange between the Sun's hot corona and its cool lower atmosphere remain poorly understood. The chromosphere and transition region (TR) form an interface region between the surface and the corona that is highly sensitive to the coronal heating mechanism. High-resolution observations with the Interface Region Imaging Spectrograph (IRIS) reveal rapid variability (~20 to 60 seconds) of intensity and velocity on small spatial scales (≲500 kilometers) at the footpoints of hot and dynamic coronal loops. The observations are consistent with numerical simulations of heating by beams of nonthermal electrons, which are generated in small impulsive (≲30 seconds) heating events called "coronal nanoflares." The accelerated electrons deposit a sizable fraction of their energy (≲10^{25} erg) in the chromosphere and TR. Our analysis provides tight constraints on the properties of such electron beams and new diagnostics for their presence in the nonflaring corona.

Though it is established that the magnetic field plays a major role in the energetics of the bright corona, determining the details of the physical mechanisms that heat the solar corona remains one of the outstanding open issues in astrophysics. Several physical processes are candidates for heating the corona, including dissipation of magnetic stresses via reconnection and dissipation of magnetohydrodynamic waves (*1*–*3*). In many heating models, the energy release is characterized by small spatial and temporal scales. For instance, in the "nanoflare" model, random photospheric motions lead to braiding or shearing of magnetic field lines and to reconnection, which yields impulse-driven heating of the coronal plasma (*4*, *5*). Several statistical studies of large numbers of solar flares (*6*–*8*) have suggested that the energy-release mechanism that produces flares is likely similar within a large range from micro- to X-class flares. If nanoflares behave as a scaled-down version of larger flares, then particles accelerated in the corona by reconnection processes could play an important role in the heating of plasma even in the absence of large flares. Hard x-ray observations of microflares (E ~ 10^{27} erg) in active regions reveal the presence of nonthermal particles (*8*, *9*), but nanoflare-size events (E ~ 10^{24} erg) are not currently accessible to hard x-ray studies, owing to the limited sensitivity of existing facilities. As a result, the properties and generation of nonthermal particles in the solar atmosphere and their role in quiescent coronal heating remain poorly known.

The observational tracers of the coronal heating are elusive because the corona is highly conductive, washing out the signatures of heating release. However, the emission of the transition region (TR), where the temperature steeply increases to million degree values (MK) in a narrow layer (~1 × 10^8 to 3 × 10^8 cm), is instead highly responsive to heating because its density, temperature gradients, and spatial dimensions change rapidly during heating events (*10*–*12*). This is also the case for coronal heating events where nonthermal electrons are produced that lose most of their energy through collisions with dense chromospheric and transition-region plasma (thick-target model) (*13*, *14*).

Recently, the High-resolution Coronal Imager (Hi-C) rocket experiment (*15*) provided high-cadence ~5 s) extreme ultraviolet (EUV) imaging observations of the corona at the highest spatial (~200 km) resolution to date. Hi-C observations of the upper TR at the footpoints (i.e., the lower portion of the loop that connects it to the lower atmosphere) of hot (>4 MK) coronal loops (the "moss") have

[1]Harvard-Smithsonian Center for Astrophysics, 60 Garden Street, Cambridge, MA 02138, USA. [2]Lockheed Martin Solar and Astrophysics Laboratory, 3251 Hanover Street, Org. A021S, Building 252, Palo Alto, CA 94304, USA. [3]Institute of Theoretical Astrophysics, University of Oslo, Post Office Box 1029, Blindern, N-0315, Oslo, Norway. [4]NASA Goddard Space Flight Center, Greenbelt, MD 20771, USA. [5]Dipartimento di Fisica e Chimica, Universita' di Palermo and Istituto Nazionale di Astrofisica (INAF)/Osservatorio Astronomico di Palermo, Piazza del Parlamento 1, 90134 Palermo, Italy. [6]Bay Area Environmental Research Institute 596 1st Street West, Sonoma, CA 95476, USA. [7]W. W. Hansen Experimental Physics Laboratory, Stanford University, Stanford, CA 94305, USA. [8]Department of Physics, Montana State University, Bozeman, Post Office Box 173840, Bozeman, MT 59717, USA.
*Corresponding author. E-mail: ptesta@cfa.harvard.edu

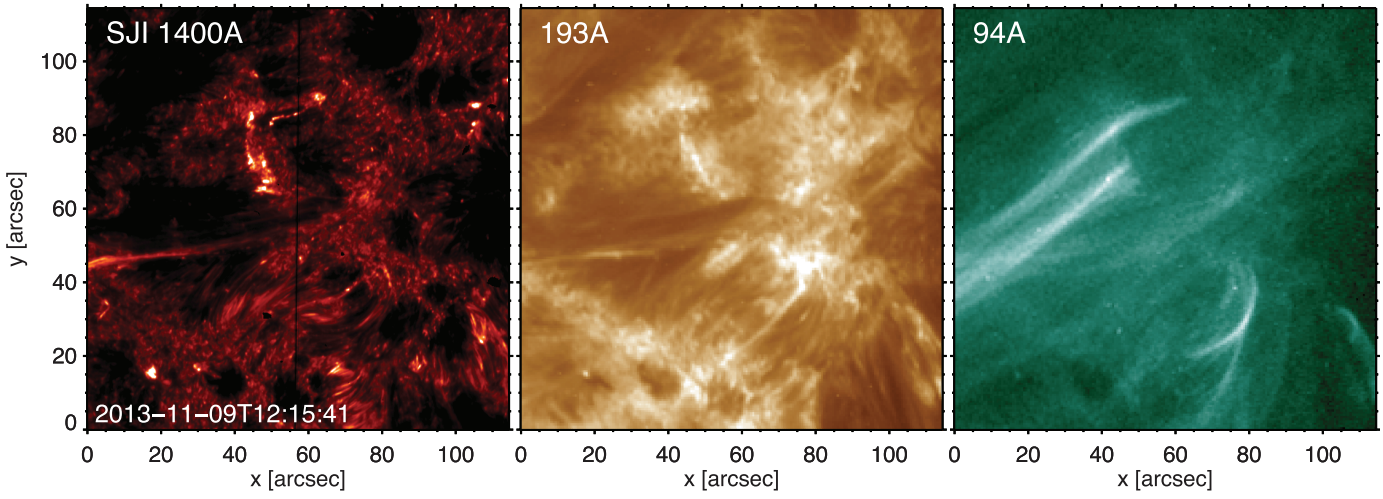

Fig. 1. Imaging observations of moss brightenings associated with coronal loop heating. Coronal and TR images of active region 11890, on 2013-11-09. The IRIS slit-jaw image (SJI) in the 1400 Å passband, and the AIA/SDO 193 Å image are dominated by TR emission, whereas the 94 Å images is dominated by hot coronal emission (*19*). The brightenings that we focus on occur around x = 40 to 65 and y = 60 to 90 [see also movies S1 and S2; in (*19*), we also discuss brightenings that occur around x ~ 55 and y = 20 to 25].

revealed rapidly variable emission, consistent with coronal nanoflares caused by slipping reconnection (*12*). However, the lack of spectral information in Hi-C data precludes an accurate determination of the plasma properties (e.g., plasma flows at different temperatures) and therefore prevents a detailed study of the physical processes at work.

The Interface Region Imaging Spectrograph (IRIS) (*16*), launched in June 2013, is exceptionally well suited to investigate the response of the lower atmosphere to heating events, as it provides

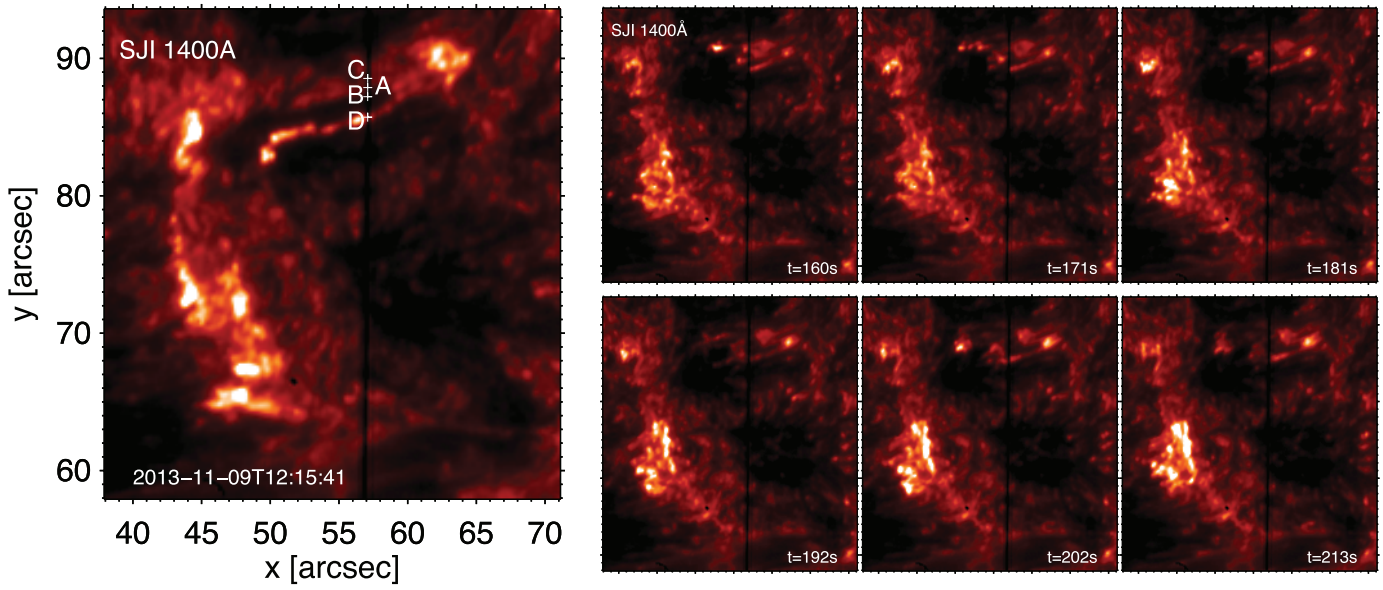

Fig. 2. Temporal evolution of TR emission for observed brightenings is dominated by time scales on the order of 10 to 30 s. Left: IRIS 1400 Å SJI of a region where most of the footpoint chromospheric and TR brightenings occur. A few locations are marked for which the temporal evolution of the chromospheric, TR, and coronal emission is shown in Fig. 3. Right: IRIS SJI observations of the same subregion shown in the left panel, at different times [see also (*19*) and figs. S1 and S2]. Times are in seconds from the start of the IRIS observations, 2013-11-09 12:04:16UT.

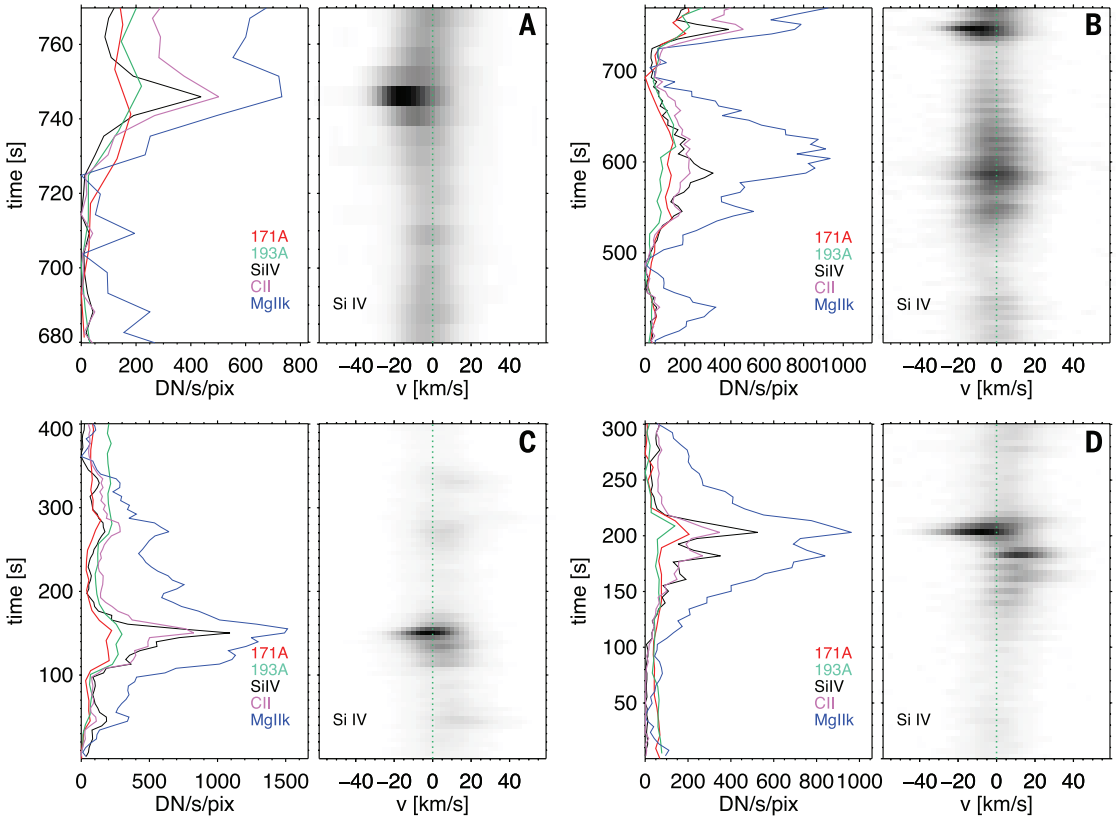

Fig. 3. Temporal evolution for observed brightenings of line and passband intensities and Si IV spectra shows a wide range of upper- and lower-TR response. (**A** to **D**) For the locations marked (A) to (D) in Fig. 2, we show (left panel) the intensities versus time (with the minimum value of the time series subtracted) of FUV and NUV emission lines (Si IV 1402.77 Å, C II 1335.71 Å, Mg II k 2796.4 Å) observed with IRIS, and in AIA EUV narrow bands (171 Å, 193 Å); also shown are the Si IV spectra versus time (right panel), where the wavelengths have been converted to Doppler velocities (the dotted line marks $v = 0$). Negative velocity values (i.e., blueshifts) correspond to upflows, positive velocities (i.e., redshifts) to downflows.

imaging and spectral observations of chromospheric and TR emission at high spatial, temporal, and spectral resolution. We analyze IRIS observations of short-lived brightenings at the footpoints of hot dynamic loops (Figs. 1 and 2 and movies S1 and S2), together with coronal observations from the Atmospheric Imaging Assembly (AIA) (*17*) onboard the Solar Dynamics Observatory (SDO) (*18*). We couple the data analysis to advanced numerical modeling of impulsively heated loops, to diagnose the properties of the heating, the mechanisms of energy transport, and the dynamic plasma processes. We show that the interaction of the lower atmosphere with nonthermal electrons accelerated in small ($E \lesssim 10^{25}$ erg) heating events can reproduce the IRIS observations.

We observe footpoint brightenings in IRIS chromospheric and TR lines {e.g., MgII k 2796.4 Å, CII 1335.78 Å, Si IV 1402.77 Å, formed around log[T_{max} (K)] ~ 4.0, 4.5, and 4.9, respectively; (*19*)}, as well as in upper TR lines with AIA [e.g., 171 Å, 193 Å passbands, which are mostly sensitive to 0.7 to 1.5 MK emission; (*19*)]. The moss brightenings are clearly associated with heating of the overlying loops, which become brighter minutes later (movie S2). The brightenings show a typical duration of 20 to 60 s (Fig. 2), and their intensity variations span more than two orders of magnitude, especially for Si IV (Fig. 3 and figs. S2 and S3). For a few brightenings occurring at the location of the IRIS spectrograph slit, we also obtained far-ultraviolet (FUV) and near-ultraviolet (NUV) spectra. The Si IV spectra (Fig. 3) indicate that many of the brightenings are associated with modest upflows (blueshifts, i.e., $v < 0$) with typical velocities of ~15 km/s.

State-of-the-art physical models are necessary to interpret the observed spectral and temporal evolution of the chromospheric and TR plasma. We use the radiative hydrodynamic model (RADYN) (*20*, *21*) of plasma confined in a loop, which includes non–local thermodynamic equilibrium (non-LTE) radiative transfer and also allows us to model heating by nonthermal electron beams (*19*). We simulate the chromospheric and TR response to impulsive (10 to 30 s duration) heating with total energy ~10^{24} to 10^{25} erg. As estimated from the observations (*19*), we assume the loop to be of half-length and cross section of 10^{10} cm and 5×10^{14} cm^2, respectively, and initially of low coronal density {log [n_e (cm^{-3})] ~ 7.5} and temperature {log (T_{max} (K)] ~ 6}. We consider two different heating mechanisms: (i) a power-law distribution of high-energy nonthermal particles, and (ii) localized coronal heating without accelerated particles, resulting in thermal conduction as the primary mechanism of energy transport from the corona to the lower atmospheric layers. For the simulations with nonthermal electron beams, we explored the effects of the energy flux and of the low-energy cutoff value E_c (*19*).

The synthetic IRIS and AIA observable parameters from the model show that the duration of the chromospheric and TR brightenings is generally very similar to the duration of the heating event (Fig. 4) (*19*). Therefore, the temporal variability of the TR and chromospheric emission is an excellent direct diagnostic of the temporal properties of the heating for short events.

The observable that discriminates most efficiently between the beam-heating models and the conduction models is the Doppler shift in the Si IV emission. Models with beam heating generally predict blueshifts in Si IV, with typical associated velocities analogous to the observed ones. The blue shifts are due to the energetic particles initially depositing a large fraction of

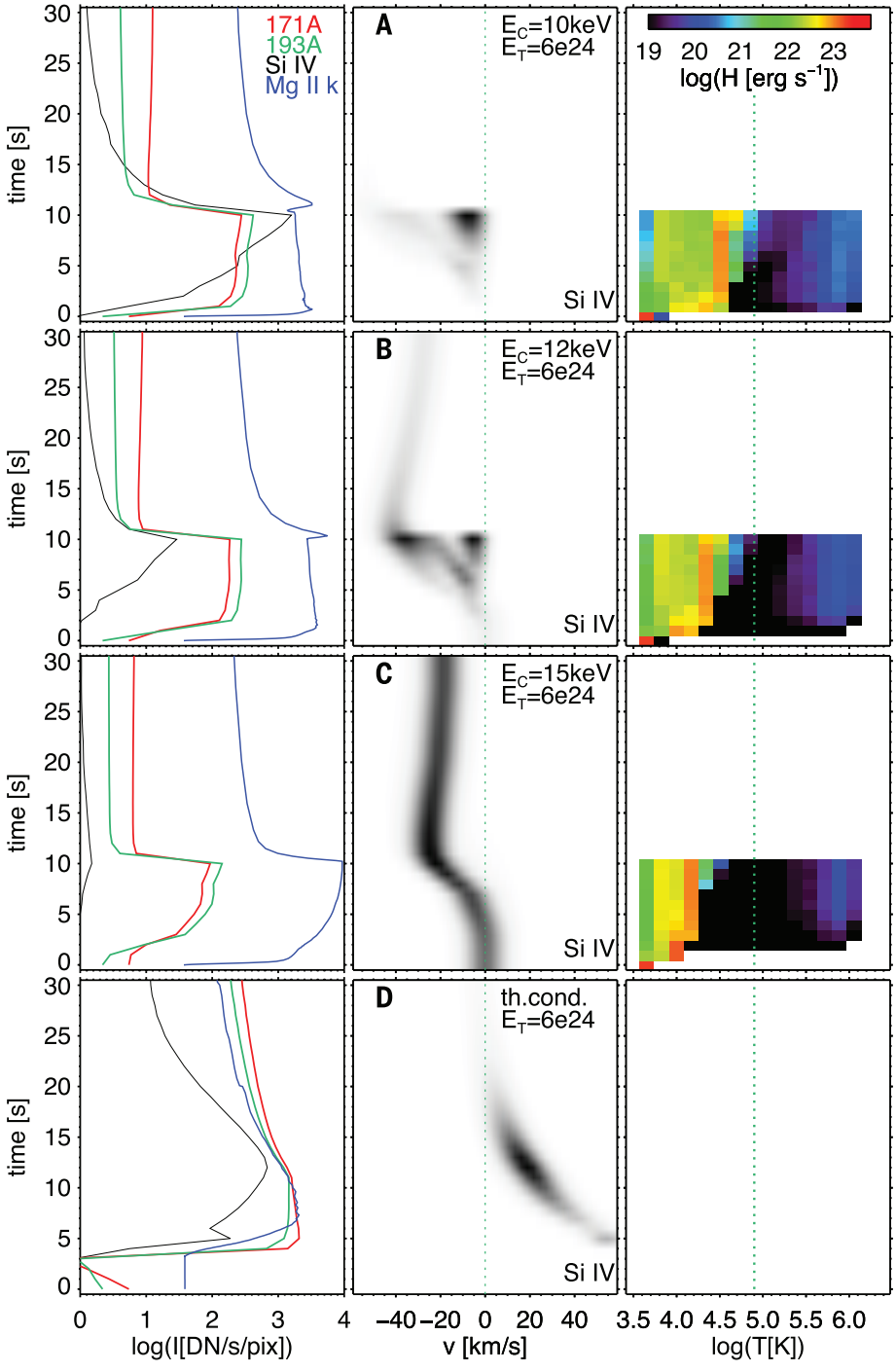

Fig. 4. Loop models with impulsive heating from nonthermal electron beams reproduce properties of observed loop footpoint brightenings. We show synthetic IRIS and AIA emission from RADYN simulations with heating duration of 10 s, total energy $E_T = 6 \times 10^{24}$ erg, and energy cutoff E_c equal to 10 keV (**A**), 12 keV (**B**), and 15 keV (**C**); (**D**) shows a model without accelerated particles. For each model, we show IRIS and AIA emission lightcurves (left), Si IV spectra versus time (middle), and, for beam models, the heating rate as a function of temperature and time (right; the dotted line marks the temperature of maximum formation of the Si IV line), due to the interaction of the energetic particles with the dense plasma in the lower atmosphere.

their energy in the chromosphere, locally heating it, with the subsequent pressure pulse triggering both upflows for the hotter plasma above this layer and downflows for the cooler plasma below. The depth of the layer where most of the beam energy is deposited depends sensitively on E_c (*19*, *22*). In the absence of accelerated particles, thermal conduction transports the energy, originally deposited in the corona, to the lower atmosphere, and the TR and chromospheric plasma are pushed down, leading only to redshifted emission in the initial impulsive phase.

Therefore, the blueshifts observed in Si IV for many footpoint brightenings are incompatible with heating transported by thermal conduction or by Alfven waves (*19*, *23*), but are compatible with beams of nonthermal electrons depositing energy directly in the chromosphere and lower transition region.

The models with electron beams also naturally reproduce a larger range of brightening intensities observed in Mg II, Si IV, AIA 171 Å, and 193 Å. In particular, the Si IV emission is formed at heights where these nanoflare-sized beams naturally deposit most of their energy: Large brightenings are observed when the combination of electron energy cutoff and total energy flux results in high densities at temperatures that contribute to the Si IV lines. In the conductive case, the brightenings in layers that range from the chromosphere to the upper TR are more tightly coupled, as they are produced as a direct consequence of the energy conducted down from the corona (*19*). In the beam-heating models, the heating of the lower chromospheric layers is partially decoupled from the heating of the higher TR layers, because nonthermal particles of different energies will deposit energy in different layers. In the cases of a hard distribution (E_c ~15 to 20 keV), for the considered total energies (which are much lower than in larger flares), the energy is deposited in the low chromosphere and does not produce observable transient brightenings in the TR emission (*19*). Softer distributions with $E_c < 10$ keV generally deposit much of their energy in the corona, thus leading to results analogous to heating by conduction (*19*).

The combination of IRIS observations and modeling can thus provide a novel diagnostic of nonthermal particle heating in small coronal heating events or nanoflares. The high sensitivity of the TR emission to the beam parameters implies that IRIS observations help constrain the cutoff value E_c of the nonthermal electron distribution. Determining E_c from observations is critical to derive the nonthermal energy content (because most of the beam energy is found around E_c) and to constrain mechanisms of particle acceleration (*22*, *24*, *25*). Hard x-ray observations are the main diagnostic tool to study nonthermal electron distributions (*26*), because the bremsstrahlung process is well understood (*27*). However, they are intrinsically limited in their ability to constrain E_c, mainly because the thermal emission typically dominates the emission at lower energies [$\lesssim$20 keV; (*13*)]. Our IRIS spectral observations of footpoint brightenings show that the heating occurs on small time scales ($\lesssim$30s), that each event is characterized by total energy of $\lesssim 10^{25}$ erg, and that E_c ~10 keV. A few brightenings also show redshifts or no shifts and might be explained by either conduction or by beams with a low E_c value (*19*).

IRIS chromospheric and TR observations offer a unique opportunity to investigate nonthermal electron beams, as an alternative to hard x-ray observations. The IRIS beam diagnostics have higher sensitivity than hard–x-ray observations, allowing us to study nanoflare-size heating events at high spatial resolution and to constrain the low-energy tail of the beam distribution. Systematic studies of IRIS and AIA observations alongside numerical models will help determine the prevalence of beam heating in active regions, as well as its role in the energetics of nonflaring plasma. Our results are also relevant for space physics and astrophysics, where particle acceleration is thought to play a major role in many phenomena [e.g., (*28*–*30*)].

REFERENCES AND NOTES

1. J. Klimchuk, On solving the coronal heating problem. *Sol. Phys.* **234**, 41–77 (2006). doi: 10.1007/s11207-006-0055-z
2. F. Reale, Coronal Loops: Observations and modeling of confined plasma. *Living Rev. Sol. Phys* **7**, 5 (2010). doi: 10.12942/lrsp-2010-5
3. A. van Ballegooijen, M. Asgari-Targhi, S. R. Cranmer, E. E. DeLuca, Heating of the solar chromosphere and corona by Alfvén wave turbulence. *Astrophys. J.* **736**, 3 (2011). doi: 10.1088/0004-637X/736/1/3
4. E. N. Parker, Nanoflares and the solar X-ray corona. *Astrophys. J.* **330**, 474 (1988). doi: 10.1086/166485
5. E. R. Priest, J. F. Heyvaerts, A. M. Title, A flux-tube tectonics model for solar coronal heating driven by the magnetic carpet. *Astrophys. J.* **576**, 533–551 (2002). doi: 10.1086/341539
6. N. Crosby, M. Aschwanden, B. Dennis, Frequency distributions and correlations of solar X-ray flare parameters. *Sol. Phys.* **143**, 275–299 (1993). doi: 10.1007/BF00646488
7. U. Feldman, G. A. Doschek, W. E. Behring, K. J. H. Phillips, Electron temperature, emission measure, and X-ray flux in A2 to X2 X-ray class solar flares. *Astrophys. J.* **460**, 1034 (1996). doi: 10.1086/177030
8. S. Christe, I. G. Hannah, S. Krucker, J. McTiernan, R. P. Lin, *RHESSI* microflare statistics. I. Flare-finding and frequency distributions. *Astrophys. J.* **677**, 1385–1394 (2008). doi: 10.1086/529011
9. I. Hannah *et al.*, Microflares and the statistics of X-ray flares. *Space Sci. Rev.* **159**, 263–300 (2011). doi: 10.1007/s11214-010-9705-4
10. L. Fletcher, B. De Pontieu, Plasma diagnostics of transition region "moss" using *SOHO*/CDS and *TRACE*. *Astrophys. J.* **520**, L135 (1999). doi: 10.1086/312157
11. P. C. H. Martens, C. C. Kankelborg, T. E. Berger, On the nature of the "moss" observed by *TRACE*. *Astrophys. J.* **537**, 471–480 (2000). doi: 10.1086/309000
12. P. Testa *et al.*, Observing coronal nanoflares in active region moss. *Astrophys. J.* **770**, L1 (2013). doi: 10.1088/2041-8205/770/1/L1
13. J. Brown, R. Turkmani, E. P. Kontar, A. L. MacKinnon, L. Vlahos, Local re-acceleration and a modified thick target model of solar flare electrons. *Astron. Astrophys.* **508**, 993–1000 (2009). doi: 10.1051/0004-6361/200913145
14. M. Varady, M. Karlický, Z. Moravec, J. Kašparová, Modifications of thick-target model: Re-acceleration of electron beams by static and stochastic electric fields. *Astron. Astrophys.* **563**, A51 (2014). doi: 10.1051/0004-6361/201322391
15. J. W. Cirtain *et al.*, Energy release in the solar corona from spatially resolved magnetic braids. *Nature* **493**, 501–503 (2013). doi: 10.1038/nature11772; pmid: 23344359
16. B. De Pontieu *et al.*, The Interface Region Imaging Spectrograph (IRIS). *Sol. Phys.* **289**, 2733–2779 (2014). doi: 10.1007/s11207-014-0485-y
17. J. Lemen *et al.*, The Atmospheric Imaging Assembly (AIA) on the Solar Dynamics Observatory (SDO). *Sol. Phys.* **275**, 17–40 (2012). doi: 10.1007/s11207-011-9776-8
18. D. Pesnell, B. J. Thompson, P. C. Chamberlin, The Solar Dynamics Observatory (SDO). *Sol. Phys.* **275**, 3–15 (2012). doi: 10.1007/s11207-011-9841-3
19. Supplementary material is available on *Science* Online.
20. M. Carlsson, R. Stein, Formation of solar calcium H and K bright grains. *Astrophys. J.* **481**, 500–514 (1997). doi: 10.1086/304043
21. J. Allred, S. L. Hawley, W. P. Abbett, M. Carlsson, Radiative hydrodynamic models of optical and ultraviolet emission from M dwarf flares. *Astrophys. J.* **644**, 484–496 (2006). doi: 10.1086/503314
22. G. Holman *et al.*, Implications of X-ray observations for electron acceleration and propagation in solar flares. *Space Sci. Rev.* **159**, 107–166 (2011). doi: 10.1007/s11214-010-9680-9
23. L. Fletcher, H. Hudson, Impulsive phase flare energy transport by large-scale Alfvén waves and the electron acceleration problem. *Astrophys. J.* **675**, 1645 (2008). doi: 10.1086/527044
24. V. Zharkova *et al.*, Recent advances in understanding particle acceleration processes in solar flares. *Space Sci. Rev.* **159**, 357–420 (2011). doi: 10.1007/s11214-011-9803-y
25. V. Petrosian, S. Liu, Stochastic acceleration of electrons and protons. I. Acceleration by parallel-propagating waves. *Astrophys. J.* **610**, 550–571 (2004). doi: 10.1086/421486
26. E. Kontar *et al.*, Deducing electron properties from hard X-ray observations. *Space Sci. Rev.* **159**, 301–355 (2011). doi: 10.1007/s11214-011-9804-x
27. H. Koch, J. Motz, Bremsstrahlung cross-section formulas and related data. *Rev. Mod. Phys.* **31**, 920–955 (1959). doi: 10.1103/RevModPhys.31.920
28. R. Blandford, J. Ostriker, Particle acceleration by astrophysical shocks. *Astrophys. J.* **221**, 29 (1978). doi: 10.1086/182658
29. A. Bell, Turbulent amplification of magnetic field and diffusive shock acceleration of cosmic rays. *Mon. Not. R. Astron. Soc.* **353**, 550–558 (2004). doi: 10.1111/j.1365-2966.2004.08097.x
30. V. Petrosian, A. Bykov, Particle acceleration mechanisms. *Space Sci. Rev.* **134**, 207–227 (2008). doi: 10.1007/s11214-008-9315-6

ACKNOWLEDGMENTS

IRIS is a NASA Small Explorer mission developed and operated by Lockheed Martin Solar and Astrophysics Laboratory with mission operations executed at NASA Ames Research Center and major contributions to downlink communications funded by the Norwegian Space Center (NSC, Norway) through an European Space Agency PRODEX contract. The IRIS data can be accessed at http://iris.lmsal.com/search/, and the AIA data at www.lmsal.com/get_aia_data/. This work is supported by NASA under contract NNG09FA40C (IRIS) and the Lockheed Martin Independent Research Program, the European Research Council grant agreement no.291058, and contract 8100002705 from Lockheed-Martin to the Smithsonian Astrophysical Observatory. M.C. acknowledges funding from the Research Council of Norway. W.L. is supported by NASA Living with a Star–Targeted Research and Technology grant NNX13AF79G.

SUPPLEMENTARY MATERIALS

www.sciencemag.org/content/346/6207/1255724/suppl/DC1
Materials and Methods
Supplementary text
Figs. S1 to S6
References (*31*–*76*)
Movies S1 to S10

7 May 2014; accepted 4 September 2014
10.1126/science.1255724

SOLAR PHYSICS

Hot explosions in the cool atmosphere of the Sun

H. Peter,[1]* H. Tian,[2] W. Curdt,[1] D. Schmit,[1] D. Innes,[1] B. De Pontieu,[3,7] J. Lemen,[3] A. Title,[3] P. Boerner,[3] N. Hurlburt,[3] T. D. Tarbell,[3] J. P. Wuelser,[3] Juan Martínez-Sykora,[3,4] L. Kleint,[3,4,5] L. Golub,[2] S. McKillop,[2] K. K. Reeves,[2] S. Saar,[2] P. Testa,[2] C. Kankelborg,[6] S. Jaeggli,[6] M. Carlsson,[7] V. Hansteen[7]

The solar atmosphere was traditionally represented with a simple one-dimensional model. Over the past few decades, this paradigm shifted for the chromosphere and corona that constitute the outer atmosphere, which is now considered a dynamic structured envelope. Recent observations by the Interface Region Imaging Spectrograph (IRIS) reveal that it is difficult to determine what is up and down, even in the cool 6000-kelvin photosphere just above the solar surface: This region hosts pockets of hot plasma transiently heated to almost 100,000 kelvin. The energy to heat and accelerate the plasma requires a considerable fraction of the energy from flares, the largest solar disruptions. These IRIS observations not only confirm that the photosphere is more complex than conventionally thought, but also provide insight into the energy conversion in the process of magnetic reconnection.

The energy produced in the core of the Sun by the fusion of hydrogen into helium is transported toward the surface first by radiation and then by convection. The layer where the photons become free to escape defines the visible surface of the Sun. The atmosphere of the Sun above the surface was traditionally described as one-dimensionally stratified. Moving outward from the photosphere, the innermost layer, the temperature drops before rising again slightly in the middle layer, the chromosphere. When the outgoing energy, which is transported by a heating mechanism that is not yet fully understood, can no longer be buffered by radiative loss and hydrogen ionization, the temperature rises steeply. This transition marks the boundary of the corona, the outermost layer, which is brilliantly visible to the naked eye in a total solar eclipse. Semi-empirical models represent this simplified one-dimensional (1D) stratification well (*1*). However, more advanced observations and models have established that the outer atmosphere (chromosphere and corona) is highly structured and dynamic (*2*–*4*). Modern models of the solar atmosphere also take into account its 3D dynamic nature (*5*–*7*). In the photosphere, these models deviate only mildly from the average temperature and density stratification in the semi-empirical models, typically by a factor of 2 or less (*8*). In particular, no evidence has been found so far, either in models or observations, for pockets of hot gas in the cool photosphere; that is, an inversion of the temperature structure. Here we exploit the extensive temperature coverage of the Interface Region Imaging Spectrograph (IRIS) spectra (*9*) to show that very marked deviations of the temperature structure exist, even in the dense (upper) photosphere: Small pockets of plasma that reach temperatures of almost 100,000 K appear to be embedded in the 4000-K (or cooler) photosphere. This finding has consequences for our understanding of the structure and energetics close to the solar surface and sheds new light on the conversion of magnetic energy into heat and flows in plasma physics in general. This underlines the value of the low solar atmosphere as a laboratory, in particular for partly ionized collisional plasmas. Such conditions are common in astrophysics, such as in molecular clouds or protoplanetary discs.

The observations presented here concentrate on an emerging active region (see supplementary text S1). In such a region, new sunspots that host magnetic fields up to 0.3 T appear in the solar photosphere. The magnetic flux that emerges through the surface gives rise to magnetic activity in which magnetic energy is converted into other forms, most noticeably internal energy (i.e., heating the plasma) and kinetic energy through the acceleration of plasma. This results in heating and mass loading of coronal loop structures, which follow magnetic field lines. These can be seen in the emerging active region (Fig. 1) connecting regions of opposite magnetic polarities. Small round brightenings are also visible in a spectral line image (Si IV; Fig. 1A) that samples gas at ~80,000-K equilibrium temperatures; these features are the pockets of hot gas in the cool photosphere.

The temporal evolution in the IRIS slit-jaw images shows that these roundish features are transient and have a lifetime of ~5 min. This is long enough for Si IV to reach ionization equilibrium (supplementary text S2). To some extent, these brightenings share properties of Ellerman bombs (*10*, *11*), which manifest themselves as brightenings in the wings of the Hα line at 6563 Å and in ultraviolet continua (*11*). Ellerman bombs are found in emerging active regions and are believed to occur in the photosphere (*12*, *13*) in response to reconnection (*14*, *15*), with no signature in coronal emission (above 10^6 K) (*16*). Like Ellerman bombs, the events we report occur in regions on the surface where magnetic flux of opposite polarities converges and cancels (Fig. 1 and supplementary text S2). However, observations and models show that temperatures in Ellerman bombs are well below 10,000 K (*17*–*19*), which is in contrast to the hot pockets we find. As yet, there are insufficient IRIS data overlapping with ground-based Hα measurements to determine whether the events we report here are identical to or different from the well-studied Ellerman bombs. Because of this missing observational link and the difference in temperature, we refer to these simply as bombs (and in Fig. 1A, as bombs 1 to 4).

The principal tool for analyzing the thermal structure of the upper atmosphere is spectroscopy at ultraviolet wavelengths, where IRIS provides unprecedented spatial, temporal, and spectral resolution. We first show an average spectrum for the quiet plage region surrounding the emerging active region with the main lines of C II, Si IV, Fe XII, Cl I, O IV, and Mg II (Fig. 2; see supplementary text S1 and table S1 for a complete list of lines). The line profiles generally conform to a single Gaussian, where they form under optically thin conditions. The lines of Mg II (and, to a lesser degree, those of C II) show self-absorption in the center due to large opacity.

In contrast to the average spectrum, the spectra from the bombs are very peculiar—they are fundamentally different from any other individual spectrum from the active region and surrounding plage area outside the bomb regions (Fig. 3; other cases described in supplementary text S3). The line profiles of the Si IV doublets at 1394 and 1403 Å are notable for their clear double-peaked appearance. The ratio of these lines under optically thin conditions should be 2; here it is 1.95. Thus, the dip in the middle is not caused by self-absorption. The profiles therefore indicate a bidirectional flow with a speed of about ±75 km/s toward and away from the observer (corresponding to the Doppler shifts of the two components). This observation was acquired close to the center of the solar disk, which indicates a predominantly vertical bidirectional flow.

The simple fact that Si IV is visible and remains visible for longer than the ionization and recombination times shows that the plasma is heated to (at least) ~80,000 K, the line-formation temperature of Si IV (supplementary text S2). Our IRIS observations reveal that absorption lines from singly ionized species (Fe II and Ni II) are found in these Si IV profiles (Fig. 3). These

[1]Max Planck Institute for Solar System Research, 37077 Göttingen, Germany. [2]Harvard-Smithsonian Center for Astrophysics, 60 Garden Street, Cambridge, MA 02138, USA. [3]Lockheed Martin Solar and Astrophysics Laboratory (LMSAL), 3251 Hanover Street, Building 252, Palo Alto, CA 94304, USA. [4]Bay Area Environmental Research Institute, 596 1st Street West, Sonoma, CA 95476, USA. [5]NASA Ames Research Center, Moffett Field, CA 94305, USA. [6]Department of Physics, Montana State University, Bozeman, Post Office Box 173840, Bozeman, MT 59717, USA. [7]Institute of Theoretical Astrophysics, University of Oslo, Post Office Box 1029, Blindern, NO-0315 Oslo, Norway.
*Corresponding author. E-mail: peter@mps.mpg.de

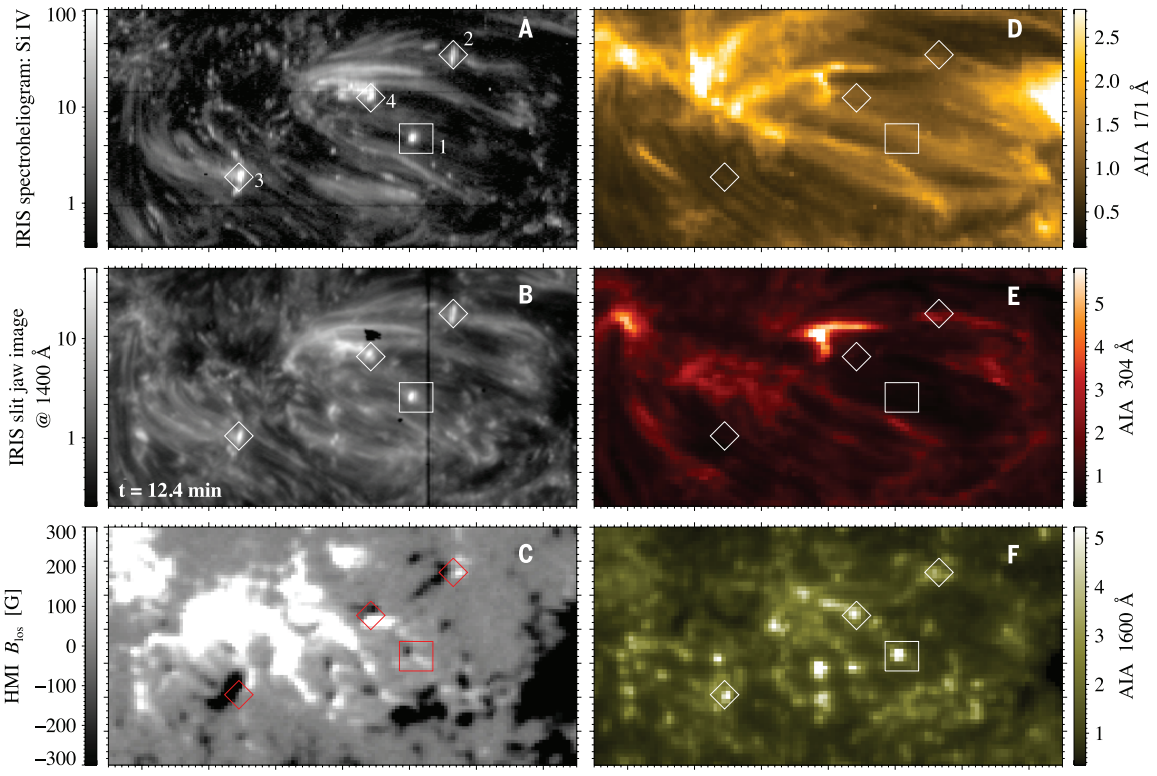

Fig. 1. Hot explosions, or bombs, in an emerging active region. Overview of the observations with IRIS and with other instruments providing context from the photosphere into the corona. The field of view is 70 arcsec by 35 arcsec. (**A**) The raster map in Si IV 1394 Å (80,000 K). The diamonds and the rectangle indicate the bomb locations. (**B**) IRIS 1400 Å slit-jaw image dominated by Si IV. The vertical black line is the slit. (**C**) The line-of-sight magnetic field, B_{los}, at the surface obtained with the Helioseismic and Magnetic Imager (HMI). The right panels show different channels of the Atmospheric Imaging Assembly (AIA) with emission from (**D**) the corona at 10^6 K. (**E**) The transition region at 10^5 K. (**F**) The chromosphere below 10^4 K. The intensity images are normalized to the median intensity. A movie showing the temporal evolution over 20 min is available online (movie S1).

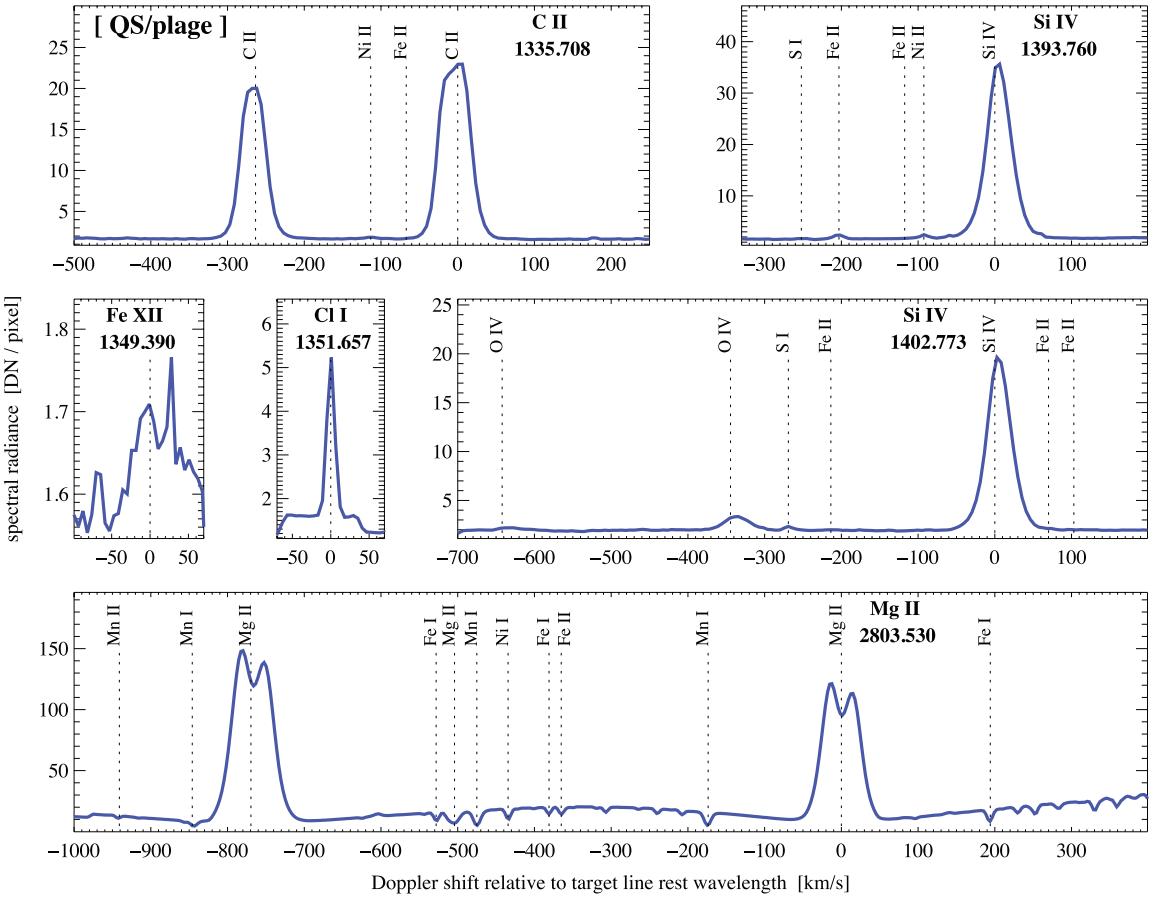

Fig. 2. Spectrum in the quiet Sun (QS) and plage area. This displays an average of the region surrounding the emerging active region, showing spectral lines covering temperatures from 4000 to 80,000 K (region marked in fig. S1). The wavelength in each window is plotted in Doppler-shift units relative to the rest wavelength of the respective main target line (shown in bold). The Doppler-shift scale is the same in all panels. The vertical dotted lines indicate the rest wavelengths for the (main) spectral lines (see table S1). This spectrum is averaged over a total area of about 37 arcsec by 110 arcsec and comprises ~75,000 individual spectra. The spectral radiance is given in data numbers (DN) per pixel.

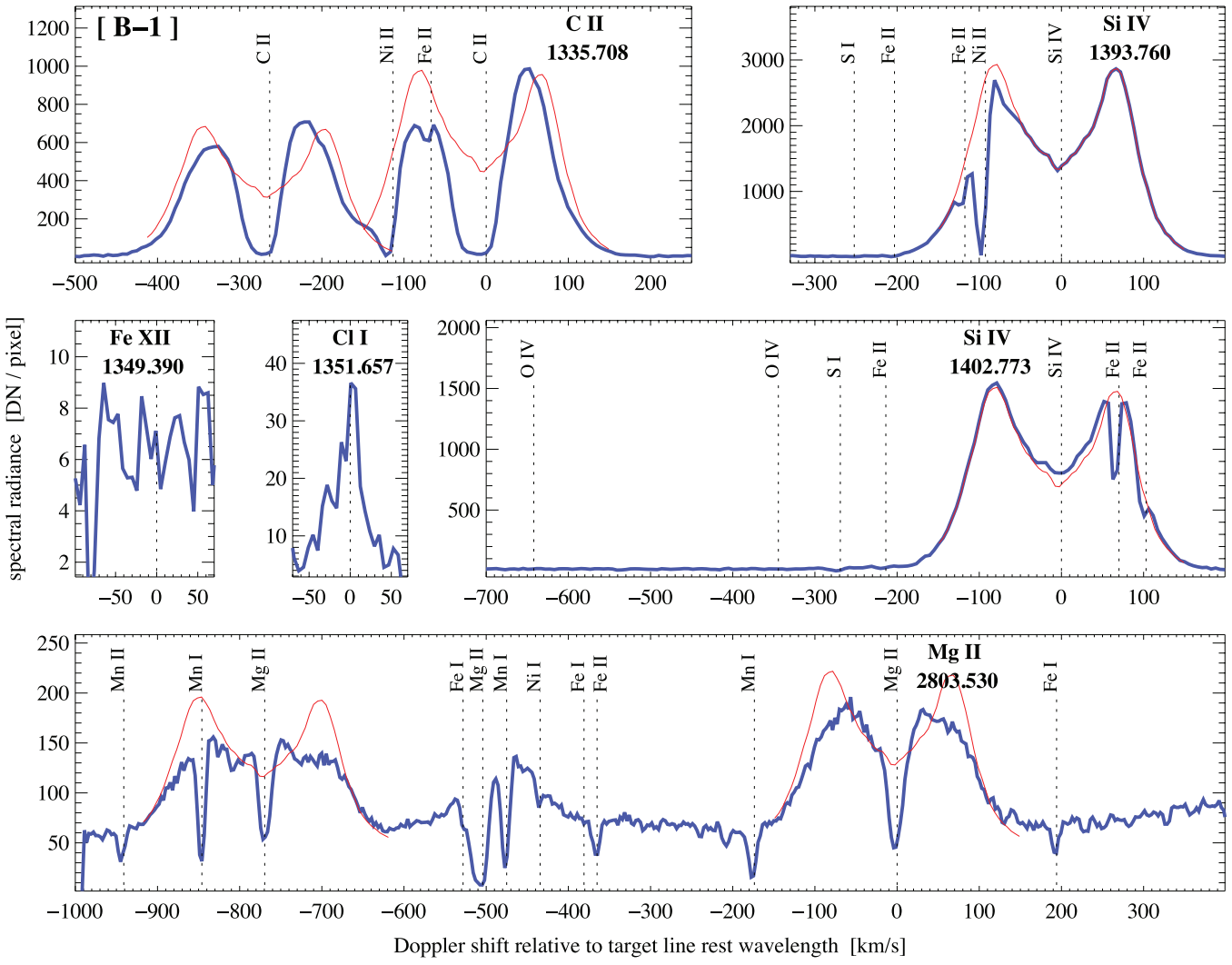

Fig. 3. Spectrum of a hot explosion. High-up and downward velocities and cool overlying plasma can be seen in the spectrum of bomb 1 (in a single spatial pixel in the middle of the diamond marked "1" in Fig. 1). Wavelengths and labeling are identical to those in Fig. 2. The thin red lines show a Si IV composite spectrum plotted over the C II, Si IV, and Mg II lines (shifted to the respective rest wavelength and scaled in radiance to roughly match the C II and Mg II lines). The statistical errors in spectral radiance are 0.5 × (DN per pixel)$^{1/2}$ in the far ultraviolet channels (top and middle row) and 0.24 × (DN per pixel)$^{1/2}$ in the near ultraviolet channel (bottom row).

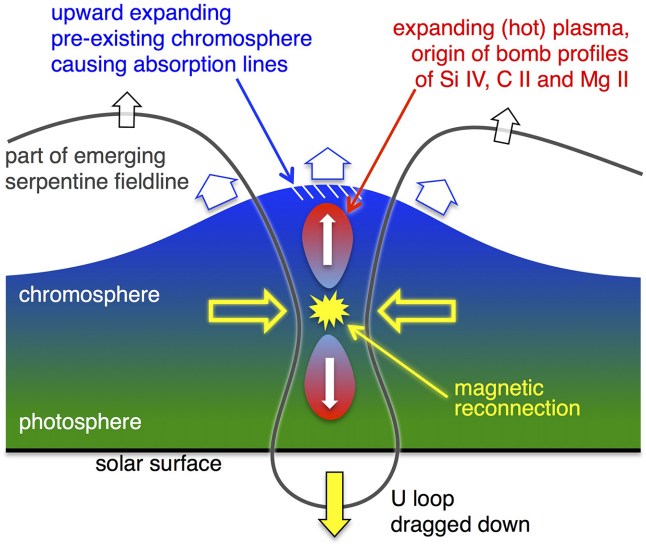

Fig. 4. Scenario for the hot explosions, or bombs. Cartoon of the bomb scenario. An undulating magnetic field line emerges, and the resulting U-loop gets dragged down. Being squeezed together, the magnetic field reconnects, and plasma is heated and accelerated deep in the atmosphere. The bidirectional outflow from the reconnection region causes the double-humped line profiles of Si IV, C II, and Mg II, whereas the cool material above (white hashed area) causes the absorption lines.

absorption features are typically blueshifted by ~5 km/s (table S1). The presence of absorption features superimposed on emission lines implies that cool material is stacked on top of hot material.

These observations are compatible with the following scenario (Fig. 4): Similar to another observationally motivated scenario (*17*) and 3D models for Ellerman bombs (*18*, *19*), serpentine magnetic field lines form in the process of flux emergence, which produce magnetic dips in the photosphere (*20*, *21*). The corresponding opposite polarities at the bomb locations are clear (Fig. 1 and movie S1; see also supplementary text S2). The resulting U-loop is dragged down by the mass it accumulated (*22*, *23*), and in the upper part of the U shape, the magnetic field reconnects. In response to the explosion caused by reconnection, the plasma in the photosphere is heated to almost 100,000 K, and a bidirectional flow channeled by the magnetic field is

initiated. A density analysis based on the IRIS observations of O IV and Si IV shows that the bombs form in the photosphere (supplementary text S4). The overlying (preexisting) cool chromosphere is slowly shifted upwards by the flux emergence (*24*, *25*), which explains the slight blueshift of the absorption lines from the overlying cool layer. In this scenario, the presence of hot dense pockets of gas deep in the atmosphere implies that the normal temperature stratification (hot transition region gas above the chromosphere) is turned upside down. Because the density in these bombs is so high, it might be that the ionization equilibrium is closer to a Saha-Boltzman local thermodynamic equilibrium. This would imply that the temperature in the bombs is lower than the 80,000 K quoted above. Further aspects of this scenario are discussed in supplementary text S3 and fig. S7. In supplementary text S5, we show that the absorption features indeed belong directly to the bombs.

The similarity of the profiles of C II, Si IV, and Mg II in the bomb is marked. Normally, these lines show quite different shapes because of their different opacities and formation temperatures (Fig. 2). In the bombs, however, a Si IV composite spectrum plotted over the C II and Mg II spectra shows a surprisingly similar overall shape (Fig. 3). Of course, C II and Mg II show strong self-absorption features in the line center. The self-absorption is slightly blueshifted because it originates from the overlying expanding chromosphere. But both the C II and the Mg II lines show a structure similar to Si IV farther away from the self-absorption center. Therefore, it is reasonable to assume that the plasma ejected in the explosion covers temperatures from 6000 to 100,000 K. The high speeds exceeding 70 km/s are supersonic and close to or higher than the Alfvén speed. This supports the conclusion that we observe a multithermal reconnection outflow.

Energy is needed to accelerate, heat, and ionize the plasma when the bomb explodes. A rough estimate sets a lower limit for the required energy at 10^{22} J (= 10^{29} ergs), which must be dumped within, at most, a couple of minutes (supplementary text S6). Thus, for the brightest of our bombs, the required energy exceeds estimates for traditional Ellerman bombs by one order of magnitude or more (*17*) and is a fraction of 0.1% to 1% of what is needed for a full-blown flare on the Sun that can reach up to 10^{32} ergs (*26*, *27*); therefore, the energy requirements for the bombs are substantial. The magnetic field strength near the surface in the regions where the bombs occur is almost 0.1 T, which means that drawing in the magnetic field from the surrounding volume and converting the magnetic energy in a reconnection process should deliver sufficient energy to power the bombs (*19*).

Because an observational link to Ellerman bombs could not be established yet, we cannot conclude if the bombs we report here are identical or different to the well-studied Ellerman bombs. Either they are a new class of energy-release phenomena, or they change our view of Ellerman bombs by showing that these reach much higher temperatures. Given current energy estimations, both models and observations indicate temperature enhancements in Ellerman bombs of only a few thousand K (*16*, *19*). Both conclusions mean that we have to revise our understanding of the dynamics and structure of the photosphere because dense material deep in the 6000-K cool near-surface regions can be heated to almost 100,000 K within minutes, which creates a temperature inversion in the solar atmosphere. Even modern 3D time-dependent models fail to predict energetic events in which the dense plasma is heated to such high temperatures and accelerated to several times the speed of sound (*19*). These IRIS observations challenge our current view of the photospheric structure and dynamics and should stimulate further observational and theoretical research to investigate this interesting phenomenon.

REFERENCES AND NOTES

1. J. E. Vernazza, E. H. Avrett, R. Loeser, Structure of the solar chromosphere. III - Models of the EUV brightness components of the quiet-sun. *Astrophys. J. Suppl. Ser.* **45**, 635–725 (1981). doi: 10.1086/190731
2. M. Carlsson, R. F. Stein, Formation of solar calcium H and K bright grains. *Astrophys. J.* **481**, 500–514 (1997). doi: 10.1086/304043
3. C. J. Schrijver, The coronae of the Sun and solar-type stars. *ASP Conf. Ser.* **223**, 131–144 (2001).
4. S. Wedemeyer-Böhm, A. Lagg, Å. Nordlund, Coupling from the photosphere to the chromosphere and the corona. *Space Sci. Rev.* **144**, 317–350 (2009). doi: 10.1007/s11214-008-9447-8
5. M. Rempel, M. Schussler, R. H. Cameron, M. Knolker, Penumbral structure and outflows in simulated sunspots. *Science* **325**, 171–174 (2009). doi: 10.1126/science.1173798
6. M. Asplund, N. Grevesse, A. J. Sauval, C. Allende Prieto, D. Kiselman, Line formation in solar granulation. *Astron. Astrophys.* **417**, 751–768 (2004). doi: 10.1051/0004-6361:20034328
7. F. Chen, H. Peter, S. Bingert, M. C. M. Cheung, A model for the formation of the active region corona driven by magnetic flux emergence. *Astron. Astrophys.* **564**, A12 (2014). doi: 10.1051/0004-6361/201322859
8. Å. Nordlund, R. F. Stein, M. Asplund, Solar surface convection. *Living Rev. Sol. Phys* **6**, 2 (2009). doi: 10.12942/lrsp-2009-2
9. B. De Pontieu *et al*., The Interface Region Imaging Spectrograph (IRIS). *Sol. Phys.* **289**, 2733–2779 (2014). doi: 10.1007/s11207-014-0485-y
10. F. Ellerman, Solar hydrogen "bombs". *Astrophys. J.* **46**, 298–300 (1917). doi: 10.1086/142366
11. R. J. Rutten, G. J. M. Vissers, L. H. M. R. van der Voort, P. Sütterlin, N. Vitas, Ellerman bombs: Fallacies, fads, usage. *J. Phys. Conf. Ser.* **440**, 012007 (2013). doi: 10.1088/1742-6596/440/1/012007
12. H. Watanabe, G. Vissers, R. Kitai, L. Rouppe van der Voort, R. J. Rutten, Ellerman bombs at high resolution. I. Morphological evidence for photospheric reconnection. *Astrophys. J.* **736**, 71 (2011). doi: 10.1088/0004-637X/736/1/71
13. G. J. M. Vissers, L. H. M. Rouppe van der Voort, R. J. Rutten, Ellerman bombs at high resolution. II. Triggering, visibility, and effect on upper atmosphere. *Astrophys. J.* **774**, 32 (2013). doi: 10.1088/0004-637X/774/1/32
14. E. Pariat *et al*., Spectrophotometric analysis of Ellerman bombs in the Ca II, Hα, and UV range. *Astron. Astrophys.* **473**, 279–289 (2007). doi: 10.1051/0004-6361:20067011
15. N. Bello González, S. Danilovic, F. Kneer, On the structure and dynamics of Ellerman bombs. *Astron. Astrophys.* **557**, A102 (2013). doi: 10.1051/0004-6361/201321632
16. B. Schmieder, D. M. Rust, M. K. Georgoulis, P. Demoulin, P. N. Bernasconi, Emerging flux and the heating of coronal loops. *Astrophys. J.* **601**, 530–545 (2004). doi: 10.1086/380199
17. M. K. Georgoulis, D. M. Rust, P. N. Bernasconi, B. Schmieder, Statistics, morphology, and energetics of Ellerman bombs. *Astrophys. J.* **575**, 506–528 (2002). doi: 10.1086/341195
18. E. Pariat *et al*., Resistive emergence of undulatory flux tubes. *Astrophys. J.* **614**, 1099–1112 (2004). doi: 10.1086/423891
19. V. Archontis, A. W. Hood, Formation of Ellerman bombs due to 3D flux emergence. *Astron. Astrophys.* **508**, 1469–1483 (2009). doi: 10.1051/0004-6361/200912455
20. G. Aulanier, P. Démoulin, 3-D magnetic configurations supporting prominences. I. The natural presence of lateral feet. *Astron. Astrophys.* **329**, 1125–1137 (1998).
21. A. López Ariste, G. Aulanier, B. Schmieder, A. Sainz Dalda, First observation of bald patches in a filament channel and at a barb endpoint. *Astron. Astrophys.* **456**, 725–735 (2006). doi: 10.1051/0004-6361:20064923
22. T. Magara, Dynamic and topological features of photospheric and coronal activities produced by flux emergence in the Sun. *Astrophys. J.* **653**, 1499–1509 (2006). doi: 10.1086/508926
23. M. C. M. Cheung, M. Rempel, A. M. Title, M. Schüssler, Simulation of the formation of a solar active region. *Astrophys. J.* **720**, 233–244 (2010). doi: 10.1088/0004-637X/720/1/233
24. S. K. Solanki, A. Lagg, J. Woch, N. Krupp, M. Collados, Three-dimensional magnetic field topology in a region of solar coronal heating. *Nature* **425**, 692–695 (2003). doi: 10.1038/nature02035; pmid: 14562096
25. J. Martínez-Sykora, V. Hansteen, M. Carlsson, Twisted flux tube emergence from the convection zone to the corona. II. Later states. *Astrophys. J.* **702**, 129–140 (2009). doi: 10.1088/0004-637X/702/1/129
26. C. J. Schrijver *et al*., Estimating the frequency of extremely energetic solar events, based on solar, stellar, lunar, and terrestrial records. *J. Geophys. Res.* **117**, A08103 (2012). doi: 10.1029/2012JA017706
27. G. Aulanier *et al*., The standard flare model in three dimensions. *Astron. Astrophys.* **549**, A66 (2013). doi: 10.1051/0004-6361/201220406

ACKNOWLEDGMENTS

H.P. thanks LMSAL for hospitality during his visit. We thank R. Rutten for countless comments and good discussions and two anonymous referees for valuable comments. IRIS is a NASA Small Explorer mission developed and operated by LMSAL, with mission operations executed at NASA Ames Research Center and major contributions to downlink communications funded by the Norwegian Space Centre through a European Space Agency PRODEX contract. This work is supported by NASA contract NNG09FA40C (IRIS), the Lockheed Martin Independent Research Program, European Research Council grant agreement 291058, and NASA grant NNX11AO98G. The Solar Dynamics Observatory (SDO) data that we used are provided courtesy of NASA/SDO and the Atmospheric Imaging Assembly and Helioseismic and Magnetic Imager science teams. All data used in this study are publicly available through the Virtual Solar Observatory (http://sdac.virtualsolar.org). The IRIS data are archived at http://iris.lmsal.com/data.html, where manuals for data reduction are also available.

SUPPLEMENTARY MATERIALS

www.sciencemag.org/content/346/6207/1255726/suppl/DC1
Supplementary Text
Figs. S1 to S9
Tables S1 and S2
References (*28*–*41*)
Movie S1

7 May 2014; accepted 22 September 2014
10.1126/science.1255726

SOLAR PHYSICS

On the prevalence of small-scale twist in the solar chromosphere and transition region

B. De Pontieu,[1,2]* L. Rouppe van der Voort,[2] S. W. McIntosh,[3] T. M. D. Pereira,[2] M. Carlsson,[2] V. Hansteen,[2] H. Skogsrud,[2] J. Lemen,[1] A. Title,[1] P. Boerner,[1] N. Hurlburt,[1] T. D. Tarbell,[1] J. P. Wuelser,[1] E. E. De Luca,[4] L. Golub,[4] S. McKillop,[4] K. Reeves,[4] S. Saar,[4] P. Testa,[4] H. Tian,[4] C. Kankelborg,[5] S. Jaeggli,[5] L. Kleint,[6] J. Martinez-Sykora[6]

The solar chromosphere and transition region (TR) form an interface between the Sun's surface and its hot outer atmosphere. There, most of the nonthermal energy that powers the solar atmosphere is transformed into heat, although the detailed mechanism remains elusive. High-resolution (0.33–arc second) observations with NASA's Interface Region Imaging Spectrograph (IRIS) reveal a chromosphere and TR that are replete with twist or torsional motions on sub–arc second scales, occurring in active regions, quiet Sun regions, and coronal holes alike. We coordinated observations with the Swedish 1-meter Solar Telescope (SST) to quantify these twisting motions and their association with rapid heating to at least TR temperatures. This view of the interface region provides insight into what heats the low solar atmosphere.

The physical mechanism that is predominantly responsible for the heating of the solar outer atmosphere remains unknown. A variety of mechanisms are still under investigation, the most important ones being dissipation of magnetic waves (*1*–*4*) or braiding and reconnection of magnetic fields and subsequent energy release (*5*–*7*). One mechanism that has recently received attention is the effect of vorticity (*8*), assumed to be generated by magneto-convective motions at or below the surface, within the outer atmosphere. Theoretical models predict that vorticity may be a signature of reconnection or magnetic waves or may be associated with strong electrical currents, all of which can lead to substantial heating (*8*). However, observational support in the solar atmosphere for vortical motions and associated heating has been (i) limited to the chromosphere, that is, lacking a heating component (*9*, *10*); (ii) limited to quiet Sun regions (i.e., away from active regions) (*10*); or (iii) isolated in incidence and on larger spatial scales (*11*, *12*) than predicted by models (*13*, *14*).

We report observations of twisting or torsional motions that are much more prevalent than previously reported (*12*), permeate both the chromosphere and the transition region (TR) of the Sun, and sometimes appear to be associated with vigorous heating of chromospheric plasma. We exploited the multithermal chromospheric (<20,000 K) and TR (20,000 to 80,000 K) coverage of the high spatial (0.33 arc sec) and spectral (3 km/s per pixel) resolution near-ultraviolet and far-ultraviolet spectra and slit-jaw images (SJIs) taken with the 20-cm telescope on board the Interface Region Imaging Spectrograph (IRIS) (*15*), which was launched in June 2013. These data reveal the strong torsional motions (10 to 30 km/s) that imply significant twist in the chromospheric and TR magnetic field.

We analyzed spectroheliograms, that is, raster scans in which the IRIS slit is scanned across the solar surface to build up a three-dimensional view (two spatial and one spectral dimension) in the Mg II h 2803-Å and Si IV 1402-Å spectral lines, which are formed, respectively, in the chromosphere (5000 to 15,000 K) and TR (80,000 K, under ionization equilibrium conditions) (*12*). From that data, we constructed dopplergrams (*12*), in which we subtracted the intensities in the blue- and red-shifted wings of a spectral line (at fixed offset velocities from the rest wavelength, e.g., ±30 km/s). The dopplergrams reveal a large number of elongated looplike structures that contain regions of strongly blue- and red-shifted plasma that are in close proximity to one another and that are part of the same dynamic structure (Figs. 1 and 2, figs. S7 and S8, and movies S1 to S20). Most of the plasma imaged in these spectral lines occurs at heights where the magnetic field dominates the plasma dynamics (plasma $\beta << 1$) (*15*–*19*). Thus, the elongated structures most likely trace the magnetic field and the observed plasma motions are compatible with torsional flows, that is, flows along twisted magnetic field lines; alternative interpretations have been considered but deemed less likely (*12*). Figure 1 shows the ubiquity of these twisted features in active regions and quiet Sun on the disk and at the limb. The prevalence of these twisted features is actually higher than observed here for several reasons (*12*). The torsional motions are only visible if the viewing angle is significantly inclined with respect to the magnetic field direction, which is not the case over the whole field of view. In addition, both field-aligned flows and the significant swaying motions in the solar atmosphere (*2*, *4*, *10*, *20*) render it less likely to see the "ideal" blue-and-red appearance of a twisted feature.

Despite these limitations, twist occurs throughout much of the field of view within a variety of structures (Figs. 1 and 2, figs. S7 and S8, and movies S5 to S21). In quiet Sun regions, many of these features appear to be spicules (*20*), rapidly evolving jets that appear to propel plasma upward and on which torsional motions have been reported before in chromospheric lines (*10*, *21*). However, the IRIS observations now reveal the heating associated with the twisting motions (Fig. 1): The hotter Si IV emission occurs toward the tops of the spicules, both at the limb and more clearly on the disk (where there is less superposition). Moreover, IRIS now reveals prevalent twist also in active region loops that appear to be low-lying and highly dynamic, with both chromospheric and TR plasma involved in the torsional motions (Fig. 1B and movies S5 to S7 and S21). We also see twist in some of the small-scale loops that appear to continuously form in quiet Sun regions (*22*) and that are visible at the limb.

The amplitude of the torsional motions was estimated from a detailed study of the spectra across the twisted features. Several examples shown in Fig. 2 (and fig. S8) indicate that velocities of order 10 to 30 km/s (over a cross-field distance of 1 arc sec or less) appear to be typical, with one side of the feature more red-shifted and the other side more blue-shifted, leading to a tilted appearance in wavelength-space plots. Such tilted features are ubiquitous, especially toward the limb, where the viewing angle combined with the mostly radial magnetic field provide optimal visibility. There are indications that there may even be more locations with significant twist that are not resolved by IRIS. For example, many locations show spectra that do not appear to be tilted but are instead very broad. Such broad profiles could also be caused by bidirectional field-aligned flows or other sources of nonthermal broadening, such as small-scale turbulence. Our observations suggest that at least a significant subset of these broad profiles is likely caused by torsional motions (*12*).

The temporal and thermal evolution of these twisted features is brought to light more clearly with simultaneous IRIS SJIs (*12*) and rapid scans in the chromospheric Hα spectral line (Fig. 3) taken with the Crisp Imaging Spectropolarimeter Fabry-Pérot interferometer (*23*) at the SST (*24*). Chromospheric dopplergrams show that the twisted features are highly dynamic (Fig. 3 and movies S5 to S19) with evidence of rapid propagation of the torsional motions along

[1]Lockheed Martin Solar and Astrophysics Laboratory (LMSAL), 3251 Hanover Street, Organization A021S, Building 252, Palo Alto, CA 94304, USA. [2]Institute of Theoretical Astrophysics, University of Oslo, Post Office Box 1029, Blindern, N-0315 Oslo, Norway. [3]High Altitude Observatory, National Center for Atmospheric Research, Post Office Box 3000, Boulder, CO 80307, USA. [4]Harvard-Smithsonian Center for Astrophysics, 60 Garden Street, Cambridge, MA 02138, USA. [5]Department of Physics, Montana State University, Bozeman, Post Office Box 173840, Bozeman, MT 59717, USA. [6]Bay Area Environmental Research Institute, 596 1st Street West, Sonoma, CA 95476, USA.
*Corresponding author. E-mail: bdp@lmsal.com

the features, typically 30 to 100 km/s (Fig. 4 and fig. S6). This speed is compatible with the value expected for Alfvén waves in the upper chromosphere and low TR. Typical time scales for the torsional motions are of the order of 1 min (Fig. 2, C and D) with short-lived excursions in the far blue and red wings of the Mg II h 2803-Å line predominant in regions where the line of sight is more perpendicular to the magnetic field.

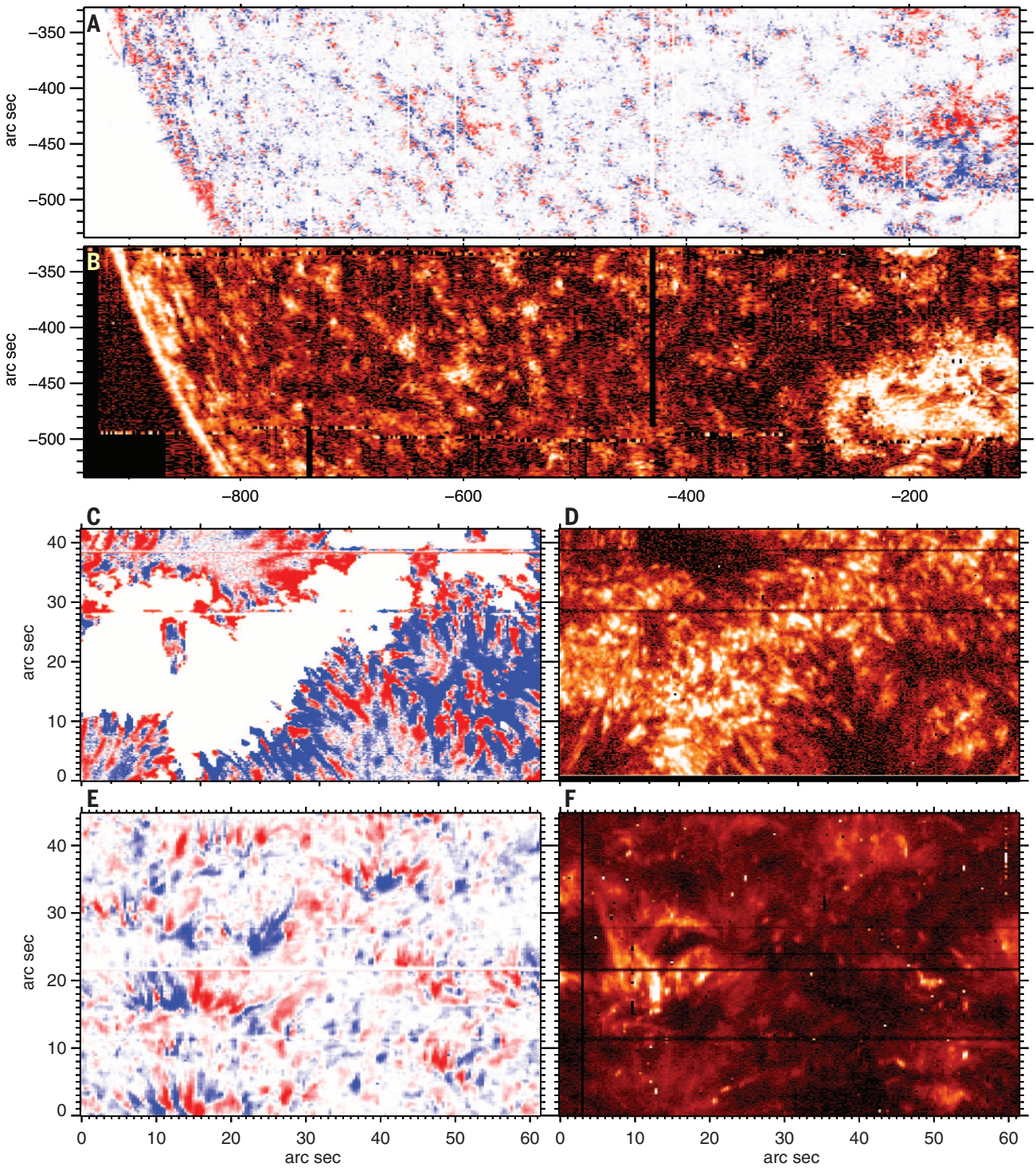

Fig. 1. Prevalence of twist in quiet Sun and active regions. Dopplergrams (**A**, **C**, and **E**) of the chromospheric (~10,000 K) Mg II h 2803-Å line (at 30 km/s from line center) show a multitude of elongated features in which strongly red- and blue-shifted features are parallel and adjacent to each other. These features illustrate that twist is predominant: at the solar limb associated in so-called spicules [(A) and (E)] but also in active regions [(C) and around −250″,−475″ in (A)], both regions where the line of sight is likely more perpendicular to the local magnetic field. Twist is often associated with significant brightening in the transition region (80,000 K), as illustrated with the Si IV 1403-Å integrated brightness maps (**B**, **D**, and **F**). When looking straight down plage regions, the line of sight is aligned with the magnetic field, severely reducing or eliminating the visibility of twist. This is why the plage regions have been removed from the active-region dopplergram. See fig. S7 for a larger field of view.

The torsional time scales stand in sharp contrast to the longer time scales (several minutes) and smaller line-of-sight velocities in plage regions (Fig. 2B), where the line of sight is more aligned with the magnetic field and the line profiles are dominated by magnetoacoustic shocks (*25*).

SJIs taken with IRIS (Fig. 3 and movies S8 to S10) also show how the propagating torsional motions are often associated with bright, highly dynamic linear features (C II 1335 Å and Si IV 1402 Å); this emission indicates heating to at least TR temperatures (20,000 to 80,000 K). In quiet Sun regions, these SJI features appear to be the TR counterparts of so-called rapid-blue-shifted and rapid-red-shifted events in the chromosphere, the disk counterparts of spicules (*26*). Many of the TR features IRIS observes in quiet Sun regions are associated with twisted features, indicating that the heating we observed is substantial. Some of these events are also visible in coronal passbands (movie S7), although it is not yet clear how much plasma is heated to coronal temperatures in association with these heating events (*12*).

Our observations of twist that permeates the chromosphere and the TR of the Sun expand on a picture that has recently emerged that draws together disparate observations of twist in the

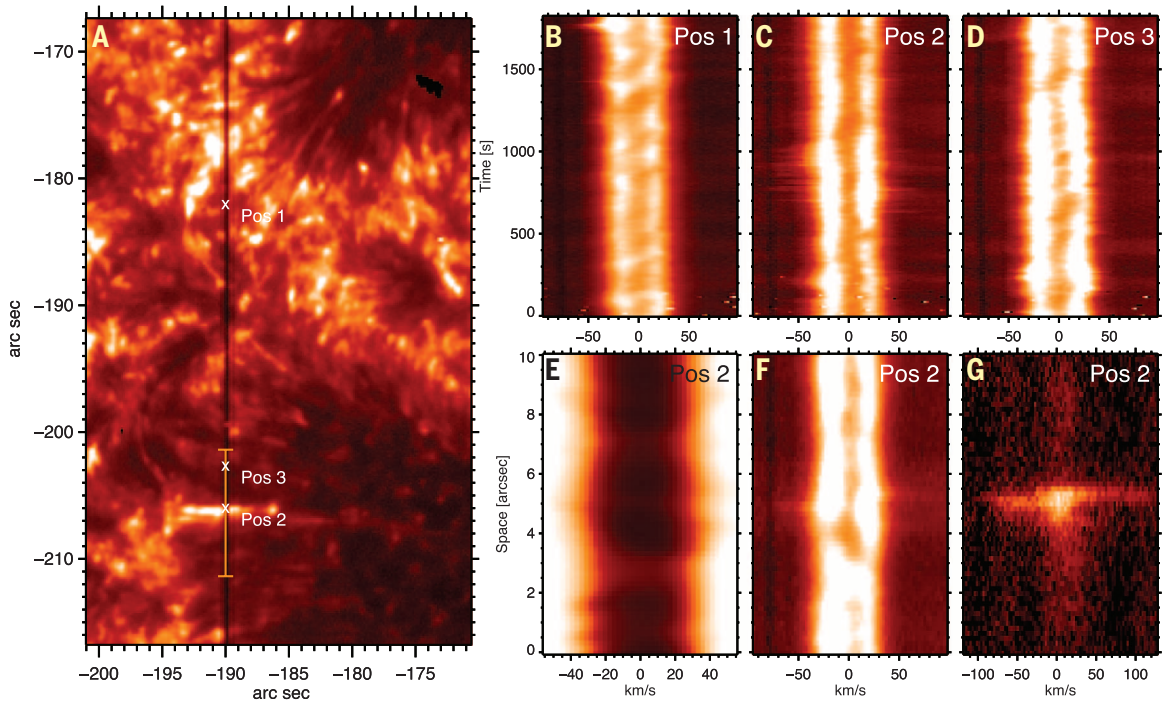

Fig. 2. Spatiotemporal properties of twist. Rapidly evolving twisting motions are apparent as short-lived, bright features in the blue and red wings (e.g., around ±50 km/s) of the chromospheric Mg II h 2803-Å spectral line (**C** and **D**) in regions of inclined field [positions 2 and 3 shown in (**A**), Si IV 1403-Å SJI]. These motions are in contrast to the acoustic shock–dominated spectral profiles (**B**) in position 1 in plage (where field and line of sight are more aligned, preventing visibility of twist) that evolve on time scales of several minutes (*25*). The spatial pattern of the bright Si IV feature around –190″, –207″ [position 2 in (A)] is associated with short-lived twisting motions that are visible in Si IV [80,000 K (**G**)], in Mg II h [10,000 K (**F**)], and faintly in Hα [<10,000 K (**E**); see movies S5 to S7]. Velocities of order 50 km/s are reached in this twisting feature. Typical velocities are lower (10 to 30 km/s) with visibility in these various passbands variable; Mg II h showed excellent visibility in most cases. See supplementary materials for other examples (figs. S7 and S8) and movies S5 to S19 and S21.

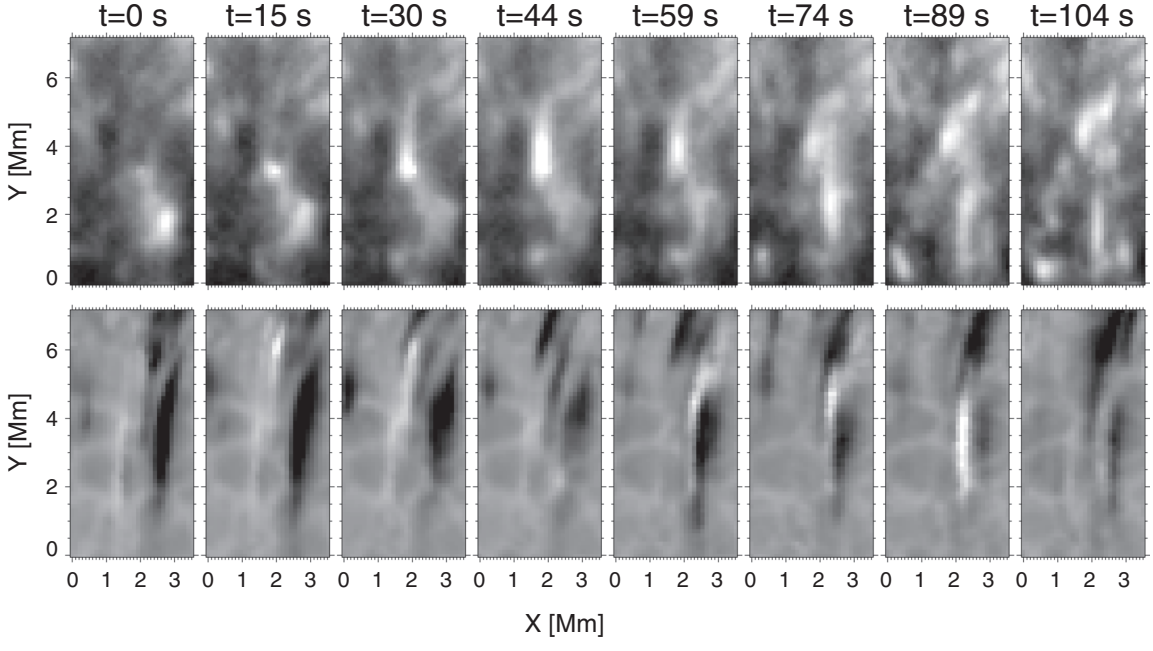

Fig. 3. Temporal evolution of twist and associated heating. SST Hα dopplergrams at ±46 km/s (**bottom**; black is blue-shifted; white is red-shifted) show how quickly chromospheric twist propagates along elongated features on time scales of less than 1 min. Several of these twisted features are associated with TR signals (**top**) as observed with the IRIS SJIs that are dominated by Si IV lines (~80,000 K). Movies S8 to S10 provide further examples of the dynamic nature of the twist and associated heating. *t* indicates time.

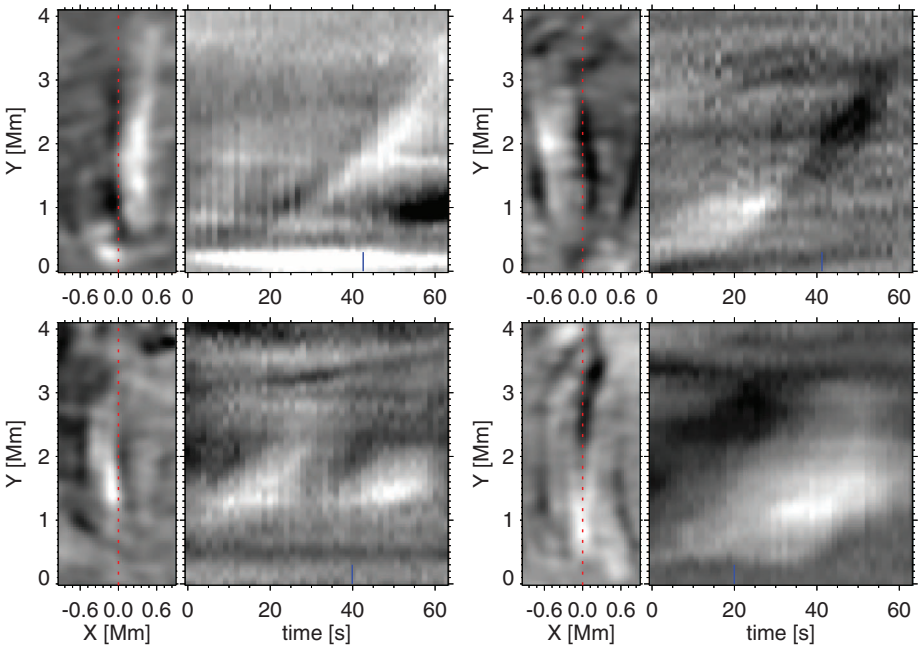

Fig. 4. Propagation speed of twisting motions near the limb. Chromospheric Ca II 8542-Å dopplergrams at ±25 km/s of twisted features (**left**) from high-cadence observations at the SST show rapid propagation (~30 to 100 km/s). These speeds are derived from time-distance plots (**right**) of the Doppler signal along the long axis of the features (red dashed line) and are consistent with Alfvén speeds at chromospheric heights.

solar atmosphere: in macrospicules (*27*, *28*), explosive events (*28*), spicules (*10*, *26*), and so-called swirls (*11*, *12*). The powerful combination of SST and IRIS observations indicate that, as higher spatial resolutions become available, the apparent prevalence of twist increases. In addition, the unique TR coverage of IRIS shows that the presence of twist is not limited to the chromosphere, but extends into higher temperature regimes and indicates that substantial heating often occurs in twisted features.

The occurrence of this twist and the associated heating likely has several causes. It seems possible that the strong photospheric vortical flows that have been observed (*29*) and that occur in advanced numerical models (*8*) play an important role. In such models, the vortical flows are often associated with strong currents, and it thus seems plausible that significant heating could result. Some of the observed twist, for example, in the small-scale loops observed with IRIS (*22*), likely originates from twist in flux tubes that emerge into the atmosphere. Although more advanced modeling and further coronal observations are required, the observed heating is also compatible with recent numerical models that predict significant chromospheric and coronal heating from dissipation of torsional Alfvén waves generated by very small-scale photospheric vortices (*13*, *14*). The prevalent twist and associated heating are also compatible with dissipation of torsional modes that arise from resonant absorption of swaying motions on flux-tube–like features in the atmosphere (*30*).Last, torsional motions and heating could also be expected if they result from the reconnection of field lines, for example, as a result of flux emergence (*16*). Thus, detailed studies of the origin of twist and extent of the heating will open a new window on several proposed heating mechanisms for the lower solar atmosphere. Such studies should also help elucidate the impact of the ubiquitous propagation of small-scale twist on the helicity budget of the solar atmosphere, which may play a role in solar eruptions.

REFERENCES AND NOTES

1. J. Hollweg, Alfvén waves in the solar atmosphere. *Sol. Phys.* **70**, 25–66 (1981). doi: 10.1007/BF00154391
2. B. De Pontieu *et al*., Chromospheric alfvenic waves strong enough to power the solar wind. *Science* **318**, 1574–1577 (2007). doi: 10.1126/science.1151747; pmid: 18063784
3. J. A. McLaughlin, I. De Moortel, A. W. Hood, Phase mixing of nonlinear visco-resistive Alfvén waves. *Astron. Astrophys.* **527**, A149 (2011). doi: 10.1051/0004-6361/201015552
4. S. W. McIntosh *et al*., Alfvénic waves with sufficient energy to power the quiet solar corona and fast solar wind. *Nature* **475**, 477–480 (2011). doi: 10.1038/nature10235; pmid: 21796206
5. E. N. Parker, Nanoflares and the solar X-ray corona. *Astrophys. J.* **330**, 474 (1988). doi: 10.1086/166485
6. J. Klimchuk, On solving the coronal heating problem. *Sol. Phys.* **234**, 41–77 (2006). doi: 10.1007/s11207-006-0055-z
7. J. W. Cirtain *et al*., Energy release in the solar corona from spatially resolved magnetic braids. *Nature* **493**, 501–503 (2013). doi: 10.1038/nature11772; pmid: 23344359
8. R. Moll, R. H. Cameron, M. Schüssler, Vortices in simulations of solar surface convection. *Astron. Astrophys.* **533**, A126 (2011). doi: 10.1051/0004-6361/201117441
9. D. B. Jess *et al*., Alfvén waves in the lower solar atmosphere. *Science* **323**, 1582–1585 (2009). doi: 10.1126/science.1168680; pmid: 19299614
10. B. De Pontieu *et al*., Ubiquitous torsional motions in type ii spicules. *Astrophys. J.* **752**, L12 (2012). doi: 10.1088/2041-8205/752/1/L12
11. S. Wedemeyer-Böhm *et al*., Magnetic tornadoes as energy channels into the solar corona. *Nature* **486**, 505–508 (2012). doi: 10.1038/nature11202; pmid: 22739314
12. See supplementary materials.
13. A. van Ballegooijen, M. Asgari-Targhi, S. R. Cranmer, E. E. DeLuca, Heating of the solar chromosphere and corona by alfvén wave turbulence. *Astrophys. J.* **736**, 3 (2011). doi: 10.1088/0004-637X/736/1/3
14. M. Asgari-Targhi, A. van Ballegooijen, Model for Alfvén wave turbulence in solar coronal loops: Heating rate profiles and temperature fluctuations. *Astrophys. J.* **746**, 81 (2012). doi: 10.1088/0004-637X/746/1/81
15. B. De Pontieu *et al*., The Interface Region Imaging Spectrograph (IRIS). *Sol. Phys.* **289**, 2733–2779 (2014). doi: 10.1007/s11207-014-0485-y
16. J. Martínez-Sykora *et al*., A detailed comparison between the observed and synthesized properties of a simulated type ii spicule. *Astrophys. J.* **771**, 66 (2013). doi: 10.1088/0004-637X/771/1/66
17. J. Leenaarts, T. M. D. Pereira, M. Carlsson, H. Uitenbroek, B. De Pontieu, The formation of *IRIS* diagnostics. I. A quintessential model atom of Mg II and general formation properties of the Mg II h&k lines. *Astrophys. J.* **772**, 89 (2013). doi: 10.1088/0004-637X/772/2/89
18. J. Leenaarts, T. M. D. Pereira, M. Carlsson, H. Uitenbroek, B. De Pontieu, The formation of *IRIS* diagnostics. II. The formation of the Mg II h&k lines in the solar atmosphere. *Astrophys. J.* **772**, 90 (2013). doi: 10.1088/0004-637X/772/2/90
19. T. M. D. Pereira, J. Leenaarts, B. De Pontieu, M. Carlsson, H. Uitenbroek, The formation of *IRIS* diagnostics. III. Near-ultraviolet spectra and images. *Astrophys. J.* **778**, 143 (2013). doi: 10.1088/0004-637X/778/2/143
20. B. De Pontieu *et al*., *Publ. Astron. Soc. Jpn.* **59**, 655 (2007).
21. L. Rouppe van der Voort, J. Leenaarts, B. De Pontieu, M. Carlsson, G. Vissers, On-disk counterparts of type II spicules in the Ca II 854.2 nm and Hα lines. *Astrophys. J.* **705**, 272–284 (2009). doi: 10.1088/0004-637X/705/1/272
22. V. Hansteen *et al*., The unresolved fine structure resolved: IRIS observations of the Solar Transition Region. *Science* **346**, 1255757 (2014).
23. G. Scharmer *et al*., CRISP Spectropolarimetric Imaging of Penumbral Fine Structure. *Astrophys. J.* **689**, L69–L72 (2008). doi: 10.1086/595744
24. G. Scharmer, K. Bjelksjo, T. K. Korhonen, B. Lindberg, B. Petterson, *Proc. SPIE* **4853**, 341–350 (2003). doi: 10.1117/12.460377
25. V. Hansteen, B. De Pontieu, L. Rouppe van der Voort, M. van Noort, M. Carlsson, Dynamic fibrils are driven by magnetoacoustic shocks. *Astrophys. J.* **647**, L73–L76 (2006). doi: 10.1086/507452
26. D. Sekse, L. Rouppe van der Voort, B. De Pontieu, Statistical properties of the disk counterparts of type II spicules from simultaneous observations of rapid blueshifted excursions in Ca II 8542 and Hα. *Astrophys. J.* **752**, 108 (2012). doi: 10.1088/0004-637X/752/2/108
27. D. Pike, H. Mason, Rotating transition region features observed with the SOHO Coronal Diagnostic Spectrometer. *Sol. Phys.* **182**, 333–348 (1998). doi: 10.1023/A:1005065704108
28. W. Curdt, H. Tian, Spectroscopic evidence for helicity in explosive events. *Astron. Astrophys.* **532**, L9 (2011). doi: 10.1051/0004-6361/201117116
29. J. Bonet, I. Márquez, J. Sánchez Almeida, I. Cabello, V. Domingo, Convectively driven vortex flows in the Sun. *Astrophys. J.* **687**, L131–L134 (2008). doi: 10.1086/593329
30. D. Pascoe, A. N. Wright, I. De Moortel, Propagating coupled Alfvén and kink oscillations in an arbitrary inhomogeneous corona. *Astrophys. J.* **731**, 73 (2011). doi: 10.1088/0004-637X/731/1/73

ACKNOWLEDGMENTS

We thank A. Ortiz, E. Scullion, and A. Sainz-Dalda for assistance with SST observations. IRIS is a NASA Small Explorer developed and operated by LMSAL with mission operations executed at NASA Ames research center and major contributions to downlink communications funded by the Norwegian Space Center through a European Space Agency PRODEX contract. IRIS data can be downloaded from iris.lmsal.com. This work is supported by NASA contract NNG09FA40C (IRIS), the Lockheed Martin Independent Research Program, and European Research Council grant no. 291058. The SST is operated on the island of La Palma by the Institute for Solar Physics of Stockholm University in the Observatorio del Roque de los Muchachos of the Instituto de Astrofísica de Canarias.

SUPPLEMENTARY MATERIALS

www.sciencemag.org/content/346/6207/1255732/suppl/DC1
Materials and Methods
Supplementary Text
Figs. S1 to S8
References (*31*–*45*)
Movies S1 to S22

7 May 2014; accepted 24 September 2014
10.1126/science.1255732

SOLAR PHYSICS

The unresolved fine structure resolved: IRIS observations of the solar transition region

V. Hansteen,[1*] B. De Pontieu,[1,2] M. Carlsson,[1] J. Lemen,[2] A. Title,[2] P. Boerner,[2] N. Hurlburt,[2] T. D. Tarbell,[2] J. P. Wuelser,[2] T. M. D. Pereira,[1] E. E. De Luca,[3] L. Golub,[3] S. McKillop,[3] K. Reeves,[3] S. Saar,[3] P. Testa,[3] H. Tian,[3] C. Kankelborg,[4] S. Jaeggli,[4] L. Kleint,[5,2] J. Martínez-Sykora[5,2]

The heating of the outer solar atmospheric layers, i.e., the transition region and corona, to high temperatures is a long-standing problem in solar (and stellar) physics. Solutions have been hampered by an incomplete understanding of the magnetically controlled structure of these regions. The high spatial and temporal resolution observations with the Interface Region Imaging Spectrograph (IRIS) at the solar limb reveal a plethora of short, low-lying loops or loop segments at transition-region temperatures that vary rapidly, on the time scales of minutes. We argue that the existence of these loops solves a long-standing observational mystery. At the same time, based on comparison with numerical models, this detection sheds light on a critical piece of the coronal heating puzzle.

The outer solar atmosphere between the 10^4 K chromosphere and the 10^6 K corona, the so-called transition region, has long puzzled solar physicists (*1*). It has been difficult to reconcile measured intensities and motions, either directly observed or inferred from spectra, with models of the energy and mass exchange between the cooler chromosphere and hot corona. For one, the observed intensities of lower transition-region lines are much greater than can be accounted for by thermal conductive flux flowing back from the corona. Furthermore, lower transition-region lines show, on average, Doppler redshifts on the order of 10 km/s (*1*), one-third the speed of sound. Based on indirect spectroscopic evidence from High-Resolution Telescope Spectrograph (HRTS) and Skylab spectra, it was already postulated in 1983 that the dominant emission from lines formed in the transition region occurs in structures magnetically isolated from the corona called the "unresolved fine structure" (UFS) (*2*–*5*). However, the following decades have not brought consensus that the UFS has been directly observed, nor indeed that it contributes to an important extent to transition-region emission (*6*–*10*). As a result, our understanding of coronal heating has not advanced substantially.

We exploit the high spatial and temporal resolution of the recently launched Interface Region Imaging Spectrograph (IRIS) satellite to reveal structures remarkably similar to those postulated to comprise the UFS. Images of the lower transition region at the solar limb with the IRIS slit-jaw camera (*11*) in the Si IV 1400 Å filter or in the C II 1330 Å filter invariably show bright low-lying loops or loop segments in quiet Sun regions (Fig. 1 and movies S1 and S2). In addition to these bright structures, a much fainter component forms a background that extends up to 10 arcsec above the limb. The background includes a large number of linear structures, with properties similar to the well-known spicules observed from the ground in the Hα 656.3-nm line. Here, we concentrate on the brighter loop-shaped objects that appear to be magnetically isolated from the corona and are at transition-region temperatures.

Viewing the same limb with the Solar Dynamics Observatory Atmospheric Imaging Assembly (SDO/AIA) instrument (*12*) in the 304 Å channel (which is dominated by He II, at 100,000 K) and the coronal 171 Å (Fe IX/X at ~10^6) and 193 Å (Fe XII at ~1.5 10^6 K) channels (*13*), we do not clearly observe UFS-related structures (Fig. 1 and movie S3). This is for two reasons: (i) the AIA spatial resolution is insufficient to resolve the structures discussed here, and (ii) bound-free absorption by neutral hydrogen and singly ionized helium renders the AIA opaque to extreme ultraviolet emission, thereby shielding the lower transition region and making the UFS nearly invisible.

One of the most striking features of UFS loops is temporal variability. Isolated UFS loops light up, either partially or wholly, and show large

[1]Institute of Theoretical Astrophysics, University of Oslo, Post Office Box 1029, Blindern, NO-0315, Oslo, Norway. [2]Lockheed Martin Solar and Astrophysics Laboratory, 3251 Hanover Street, Org. A021S, Building 252, Palo Alto, CA 94304, USA. [3]Harvard-Smithsonian Center for Astrophysics, 60 Garden Street, Cambridge, MA 02138, USA. [4]Department of Physics, Montana State University, Bozeman, Post Office Box 173840, Bozeman, MT 59717, USA. [5]Bay Area Environmental Research Institute, 596 1st Street West, Sonoma, CA 95476, USA.
*Corresponding author. E-mail: viggoh@astro.uio.no

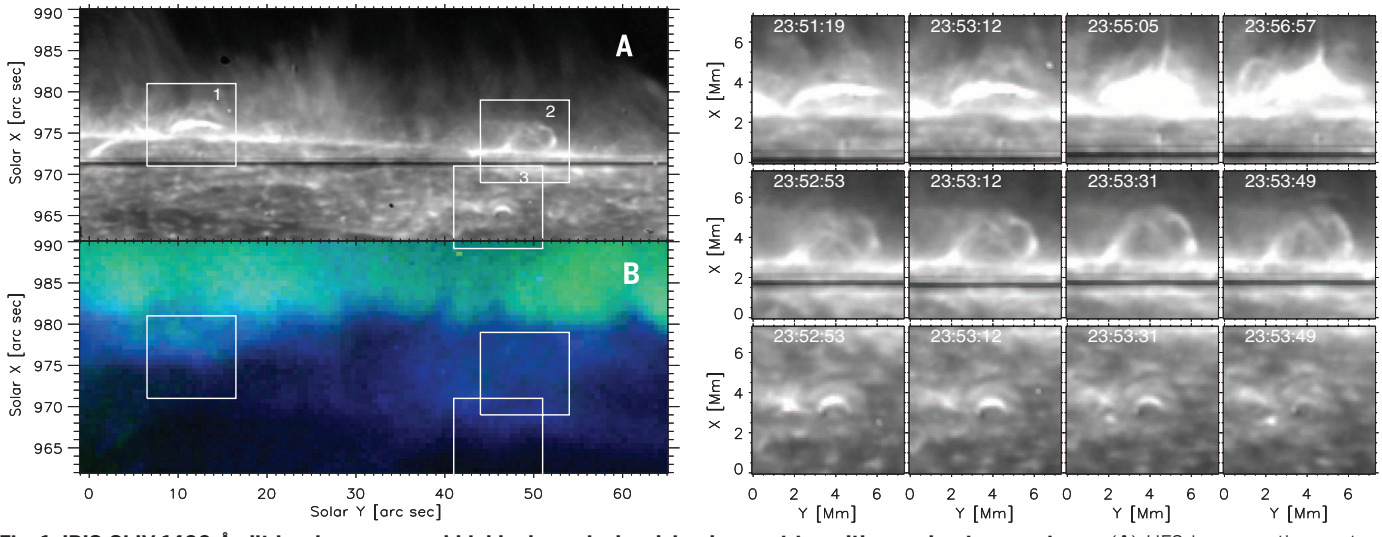

Fig. 1. IRIS Si IV 1400 Å slit jaw images reveal highly dynamic, low-lying loops at transition-region temperatures. (**A**) UFS loops on the western solar limb. The slit is evident as a dark line near solar-x = 971 arcsec. (**B**) The same field of view is shown, but with SDO/AIA images: the coronal 171 Å (blue) and 193 Å (green) filters (movie S3 shows the same field of view, but with the AIA He II 304 Å filter). The rapid evolution of the UFS in three ROIs is demonstrated in the small panels on the right side of the figure. The time of each exposure (hour:minute:second) is indicated at the top of the panels.

changes on scales down to the shortest cadence data inspected so far (every 4 s), examples of which are shown in region of interest (ROI) 2 and ROI 3 of Fig. 1. On the other hand, a system of loops, in which individual loops vary from exposure to exposure, can remain recognizable as a system over periods extending to several tens of minutes. The temporal evolution of the three regions of interest are shown in Fig. 1 (more loops are displayed in fig. S1). ROI 1 was observed with a cadence of 54 s and is an example of a fairly long-lived "nest" of loops that remains active during the entire 40-min span that the observations lasted. Movies S1, S2, and S3 show these nests to be composed of many loops with more or less cospatial footpoints that light up and darken episodically.

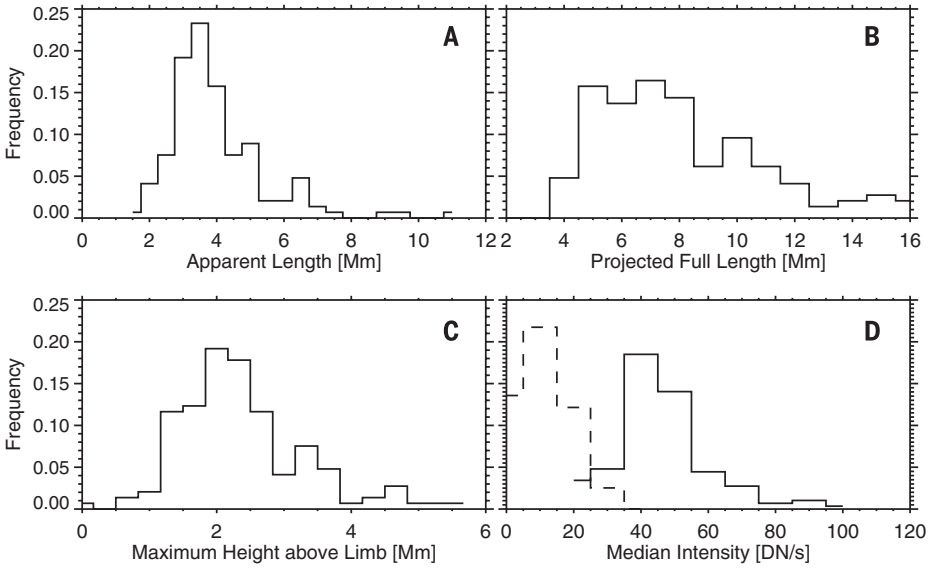

Fig. 2. UFS loops are short, bright, and low-lying. Properties of 85 UFS loops taken from a limb observation data set: (**A**) apparent length of the visible loop segments, (**B**) projected full length along loop, (**C**) maximum height, and (**D**) median intensity of the visible loop segments. The intensity measured for the dimmer "spicular" background is shown with a dashed line.

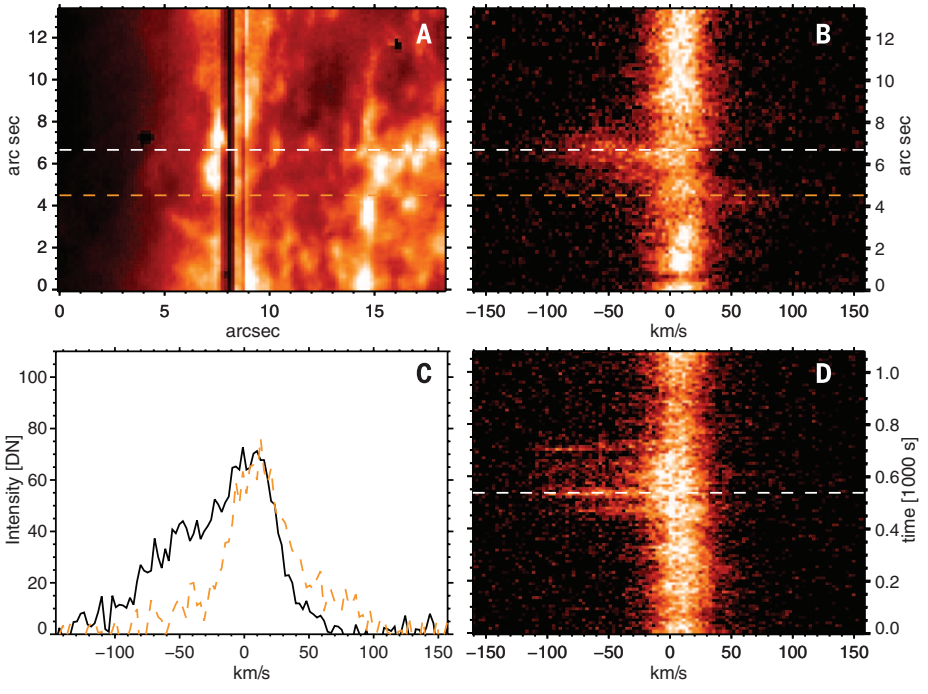

Fig. 3. UFS loops display large, rapidly evolving Doppler shifts and nonthermal velocities. (**A**) The slit position along the limb (SJI 1400 Å). (**B**) The corresponding spectral scans of the Si IV 1393 Å line are shown as a function of position along the slit and as a function of time at the location of the UFS loop footpoint (**D**) located at 6.6 arcsec. In (B) and (D), the dashed white and orange lines show the locations of the footpoints. (**C**) The corresponding line profiles at these footpoint locations (540 s) are shown in solid and gold dashed curves, respectively.

Fully formed loops are seldom seen. Rather, loops appear to be lit up in segments, with each segment only being visible for roughly a minute. There is also a tendency for the UFS loops to appear to rise with time, as can be seen in ROI 2 (Fig. 1).

We find that the UFS loops have a full length of 4 to 12 Mm (10^6 meters), a maximum height of 1 to 4.5 Mm with an average of 2.5 Mm, and a median intensity in data numbers per second of 40 to 50 DN/s (Figs. 2) (*14*). This intensity is larger than the measured intensity of the background "spicules"—longer nearly radial features—of 15 DN/s, which is also apparent from visual inspection of Fig. 1. Although the detailed filling factor of either component is not well known (given the superposition at the limb and their limited visibility on the disk), it is clear that both resolved components have an important role in the lower transition-region emission, with the relative contribution dependent on the local magnetic field topology.

By aligning the slit along the limb, IRIS also allows one to gather spectral data of the UFS (example in Fig. 3). The spectrum shows large excursions as a function of position along the loop, implying large plasma velocities, toward the red as well as toward the blue. We find extreme line profiles at the upper loop footpoint—the portion of the loop that meets the underlying atmosphere—during the entire 200-s lifetime of the UFS loop, with redward excursions of 70 to 80 km/s. This is two to three times the speed of sound in a 80,000 to 100,000 K plasma. We observed the spectral properties of several UFS loops and find that such high velocities occur often, although not always. This indicates that the UFS loops are locations of episodic and violent heating.

How can we put these observations into the context of coronal heating models and the structure of the upper solar atmosphere? Models that assume most transition-region emission stems from loops connected to the corona, and therefore whose temperature structure is maintained by thermal conduction, lead to predicted intensities much smaller than those observed. Alternative models propose the existence of low-lying cool loops (*15*–*17*), but these static models cannot be reconciled with the highly dynamic loops we observe here. Guidance comes from three-dimensional (3D) modeling: Low-lying, episodically heated loops that seldom or never reach coronal temperatures naturally arise in 3D models and predict (*18*–*20*) highly dynamic spectral lines originating in the lower transition region. Thus, several properties of UFS loops are remarkably similar to those found in recent realistic 3D models spanning the convection zone to the corona.

The typical loop height of the brightest cool loops that spontaneously arise in 3D simulations

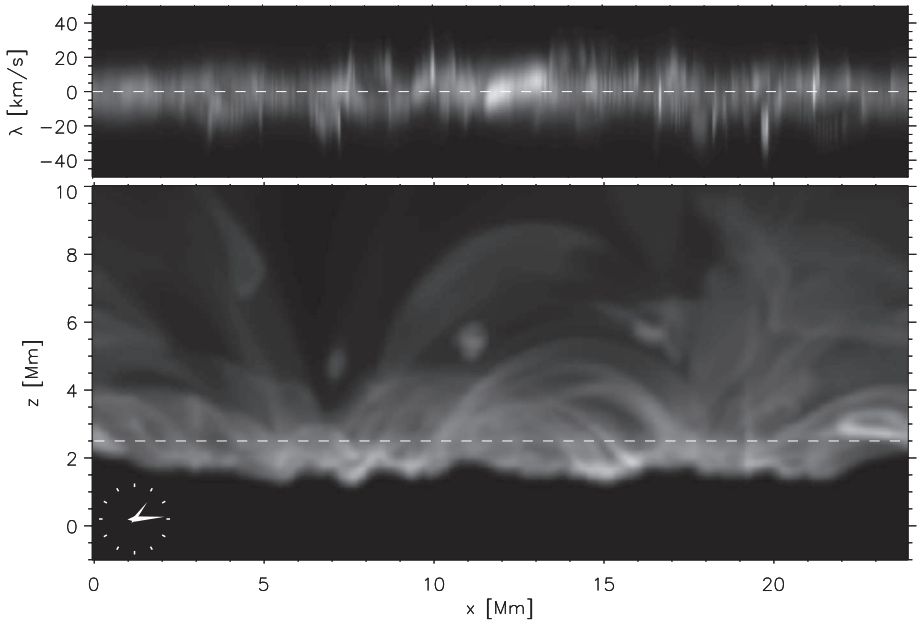

Fig. 4. Episodic structures with properties similar to UFS loops arise in advanced 3D numerical simulations. The synthetic line profile of the Si IV 1393 Å line (**top**) and the corresponding synthetic intensity images of the solar limb (**bottom**) are shown. The dashed white line in the lower panel shows the location sampled for the synthetic spectrum. The resolution of the intensity images has been degraded to the IRIS spatial resolution of 0.33 arcsec. Movie S4 shows the temporal evolution of this simulation.

(Fig. 4) is less than 4 Mm above the photosphere. The lifetime of individual "strands," or loops, that maintain plasma in the temperature range required for emission in the Si IV line is a few hundred seconds or less. Both of these properties are very similar to what is observed. However, Doppler velocities measured at the origin of the line profile show line-of-sight velocities on the order of 20 to 30 km/s, which is less than that reported for our observations.

Why do these loops form? Heating in the upper chromosphere and corona will proceed along and be guided by the loop magnetic field. This could occur either through the dissipation of waves or through the dissipation of stresses built up as a result of footpoint motions (*21*). Whereas long loops lose energy through thermal conduction, shorter loops are denser at their apices and will therefore lose energy efficiently through radiative losses, which scale as the density squared [e.g., (*18*, *19*, *20*)]. The cooling time of low-lying loops is short (a few minutes or less), and a reduction in the heating rate ensures rapid cooling. At heights of 5 Mm or less above the photosphere, these models therefore predict short low-lying loops that are episodically heated to ~500,000 K or less. The loops cool rapidly thereafter rather than being heated to coronal temperatures.

The discrepancy between observed and modeled velocities could be an indication that the models correctly predict the spatial distribution and episodic nature of the heating in the corona, but the detailed nature of the heating mechanism may not be exactly reproduced. The spatial distribution of loops is largely independent of the heating mechanism and is instead set by the structure of the field. We thus expect low-lying loops to occur in any realistic 3D model. However, the temporal properties of the loop emission or Doppler velocities are a direct result of the heating process, and comparison of synthesized and observed data could validate a given model.

What sets the low height of the observed loops? It is likely that these dynamic small-scale loops in the low solar atmosphere are associated with ubiquitous weak magnetic field in the solar photosphere (*22*–*24*). These continuously emerging weak fields occur on granular scales, with opposite polarities separated by a few Mm. Our observations of the low loop heights and the sometimes persistent "nests" of loops are fully compatible with theoretical predictions. If such weak fields are present, they should form a multitude of dynamic low-lying loops (*16*), especially when they interact with the strong magnetic field in the quiet Sun network (*25*). The apparent rise of some of the observed loops is likely caused by the emergence of the loops into the atmosphere (*26*).

Based on their properties, and in comparison with 3D models, we conclude that the short low-lying loops observed with IRIS constitute a set of low-lying magnetic structures whose plasma is episodically heated. The thermal properties of these loops are determined by their high density, which causes efficient radiative cooling and thus prevents the occurrence of coronal temperatures. Higher-lying loops are presumably heated in much the same way, but with radiative losses that are much less efficient at lower densities, and temperatures must rise to > 1 MK to balance heating with losses due to thermal conduction. By revealing the existence and properties of these previously unresolved fine-structured loops, we have obtained direct insight into the otherwise difficult to observe coronal heating mechanism. The episodic nature, height distribution, and high velocities of UFS loops provide strict constraints on recent 3D models of the coronal heating problem. Further observations and more advanced modeling of these loops are critical for determining the relation between the topology of the magnetic field in the photosphere and vigorous heating in the outer atmosphere.

REFERENCES AND NOTES

1. J. Mariska, *The Solar Transition Region*, Cambridge Astrophysics Series (Cambridge Univ. Press, New York, 1992).
2. U. Feldman, On the unresolved fine structures of the solar atmosphere in the 30,000-200,000 K temperature region. *Astrophys. J.* **275**, 367 (1983). doi: 10.1086/161539
3. U. Feldman, On the unresolved fine structures of the solar atmosphere. II. The temperature region 200,000 - 500,000 K. *Astrophys. J.* **320**, 426 (1987). doi: 10.1086/165556
4. U. Feldman, K. G. Widing, H. P. Warren, Morphology of the quiet solar upper atmosphere in the $4 \times 10^4 < T_e < 1.4 \times 10^6$ K temperature regime. *Astrophys. J.* **522**, 1133–1147 (1999). doi: 10.1086/307682
5. U. Feldman, I. E. Dammasch, K. Wilhelm, On the unresolved fine structures of the solar upper atmosphere. IV. The interface with the chromosphere. *Astrophys. J.* **558**, 423–427 (2001). doi: 10.1086/322471
6. J. Dowdy, Observational evidence for hotter transition region loops within the supergranular network. *Astrophys. J.* **411**, 406 (1993). doi: 10.1086/172842
7. Ø. Wikstøl, P. Judge, V. Hansteen, On inferring the properties of dynamic plasmas from their emitted spectra: The case of the solar transition region. *Astrophys. J.* **501**, 895–910 (1998). doi: 10.1086/305854
8. H. P. Warren, A. Winebarger, Small scale structure in the solar transition region. *Astrophys. J.* **535**, L63 (2000). doi: 10.1086/312690
9. H. Oluseyi, M. Carpio, J. Sheung, Implausibility of hydrostatic funnels constituting the Sun's upper transition region. *Sol. Phys.* **245**, 69–85 (2007). doi: 10.1007/s11207-007-9023-5
10. S. Patsourakos, P. Gouttebroze, A. Vourlidas, The quiet sun network at subarcsecond resolution: VAULT observations and radiative transfer modeling of cool loops. *Astrophys. J.* **664**, 1214–1220 (2007). doi: 10.1086/518645
11. B. De Pontieu *et al.*, The Interface Region Imaging Spectrograph (IRIS). *Sol. Phys.* **289**, 2733–2779 (2014). doi: 10.1007/s11207-014-0485-y
12. J. R. Lemen *et al.*, The Atmospheric Imaging Assembly (AIA) on the Solar Dynamics Observatory (SDO). *Sol. Phys.* **275**, 17–40 (2012). doi: 10.1007/s11207-011-9776-8
13. J. Martínez-Sykora, B. De Pontieu, P. Testa, V. Hansteen, Forward modeling of emission in Solar Dynamics Observatory/atmospheric imaging assembly passbands from dynamic three-dimensional simulations. *Astrophys. J.* **743**, 23 (2011). doi: 10.1088/0004-637X/743/1/23
14. Materials and Methods are available as supplementary materials on *Science* Online.
15. S. Antiochos, G. Noci, The structure of the static corona and transition region. *Astrophys. J.* **301**, 440 (1986). doi: 10.1086/163912
16. J. Dowdy Jr., D. Rabin, R. Moore, On the magnetic structure of the quiet transition region. *Sol. Phys.* **105**, 35–45 (1986). doi: 10.1007/BF00156374
17. J. A. Klimchuk, S. K. Antiochos, J. T. Mariska, A numerical study of the nonlinear thermal stability of solar loops. *Astrophys. J.* **320**, 409 (1987). doi: 10.1086/165554
18. V. Hansteen, H. Hara, B. De Pontieu, M. Carlsson, On redshifts and blueshifts in the transition region and corona. *Astrophys. J.* **718**, 1070–1078 (2010). doi: 10.1088/0004-637X/718/2/1070
19. N. Guerreiro, V. Hansteen, B. De Pontieu, The cycling of material between the solar corona and chromosphere. *Astrophys. J.* **769**, 47 (2013). doi: 10.1088/0004-637X/769/1/47
20. D. Spadaro, A. F. Lanza, J. T. Karpen, S. K. Antiochos, A transient heating model for the structure and dynamics of the solar transition region. *Astrophys. J.* **642**, 579–583 (2006). doi: 10.1086/500963
21. J. Klimchuk, On solving the coronal heating problem. *Sol. Phys.* **234**, 41–77 (2006). doi: 10.1007/s11207-006-0055-z
22. B. Lites *et al.*, The horizontal magnetic flux of the quiet-sun internetwork as observed with the Hinode spectro-polarimeter. *Astrophys. J.* **672**, 1237–1253 (2008). doi: 10.1086/522922

23. M. J. Martínez González, M. Collados, B. Ruiz Cobo, S. K. Solanki, Low-lying magnetic loops in the solar internetwork. *Astron. Astrophys.* **469**, L39–L42 (2007). doi: 10.1051/0004-6361:20077505
24. J. Sánchez Almeida *et al*., Search for photospheric footpoints of quiet Sun transition region loops. *Astron. Astrophys.* **475**, 1101–1109 (2007). doi: 10.1051/0004-6361:20078124
25. C. J. Schrijver, A. M. Title, The magnetic connection between the solar photosphere and the corona. *Astrophys. J.* **597**, L165–L168 (2003). doi: 10.1086/379870
26. J. Martínez-Sykora, V. Hansteen, M. Carlsson, Twisted flux tube emergence from the convection zone to the corona. II. Later states. *Astrophys. J.* **702**, 129–140 (2009). doi: 10.1088/0004-637X/702/1/129

ACKNOWLEDGMENTS

IRIS is a NASA Small Explorer mission developed and operated by the Lockheed Martin Solar and Astrophysics Laboratory (LMSAL), with mission operations executed at NASA Ames Research Center and major contributions to downlink communications funded by the Norwegian Space Center (NSC, Norway) through a European Space Agency PRODEX contract. This research was supported by the Research Council of Norway through the grant "Solar Atmospheric Modelling" and through grants of computing time from the Programme for Supercomputing. This work is supported by NASA contract NNG09FA40C (IRIS), the Lockheed Martin Independent Research Program, and European Research Council grant agreement no. 291058. Authors from the Smithsonian Astrophysical Observatory are supported by LMSAL contract 8100002705. The data presented in this paper may be found on the Hinode Science Data Centre Europe (www.sdc.uio.no).

SUPPLEMENTARY MATERIALS

www.sciencemag.org/content/346/6207/1255757/suppl/DC1
Materials and Methods
Supplementary Text
Fig. S1
Table S1
Movies S1 to S6
References (*27*–*31*)

7 May 2014; accepted 12 September 2014
10.1126/science.1255757

RESEARCH ARTICLE

SKILL DEVELOPMENT

Motor skill learning requires active central myelination

Ian A. McKenzie,[1]* David Ohayon,[1]* Huiliang Li,[1] Joana Paes de Faria,[1]† Ben Emery,[2] Koujiro Tohyama,[3] William D. Richardson[1]‡

Myelin-forming oligodendrocytes (OLs) are formed continuously in the healthy adult brain. In this work, we study the function of these late-forming cells and the myelin they produce. Learning a new motor skill (such as juggling) alters the structure of the brain's white matter, which contains many OLs, suggesting that late-born OLs might contribute to motor learning. Consistent with this idea, we show that production of newly formed OLs is briefly accelerated in mice that learn a new skill (running on a "complex wheel" with irregularly spaced rungs). By genetically manipulating the transcription factor myelin regulatory factor in OL precursors, we blocked production of new OLs during adulthood without affecting preexisting OLs or myelin. This prevented the mice from mastering the complex wheel. Thus, generation of new OLs and myelin is important for learning motor skills.

Myelin is the spirally wrapped cell membrane that surrounds and insulates axons in the central and peripheral nervous systems (CNS and PNS, respectively). Myelin greatly increases the speed of electrical communication among neurons and, hence, the brain's computational power. CNS myelin is synthesized by oligodendrocytes (OLs), the majority of which develop in the first 6 postnatal weeks in rodents, from proliferating OL precursors [(OPs), also known as NG2 glia] (*1*, *2*). However, many OPs persist in the adult mouse CNS (~5% of all neural cells) and continue to divide and differentiate into myelinating OLs throughout life (*1*–*3*). For example, nearly 30% of OLs in the 8-month-old corpus callosum are formed after 8 weeks of age (*2*). What is the function of adult-born OLs and myelin? Magnetic resonance imaging (MRI) has detected changes in the structure of white matter in people trained in complex sensorimotor tasks such as playing the piano, juggling, or abacus use (*4*–*6*). Analogous MRI changes are observed in rats during motor training (*7*). The histological basis of the MRI change is not known, but one possibility is that newly generated myelin is laid down preferentially in circuits that are engaged during motor learning. Here we show that active myelination during adulthood is required for motor skill learning and that motor learning increases OL production.

[1]The Wolfson Institute for Biomedical Research, University College London, Gower Street, London WC1E 6BT, UK. [2]Department of Anatomy and Neuroscience and the Florey Institute for Neuroscience and Mental Health, University of Melbourne, Melbourne, Victoria 3010, Australia. [3]The Center for Electron Microscopy and Bio-Imaging Research, Iwate Medical University, 19-1 Uchimuru, Morioka, Iwate 020-8505, Japan. *These authors contributed equally to this work. †Present address: Instituto de Biologia Molecular e Celular, Rua do Campo Alegre 823, 4150-180 Porto, Portugal. ‡Corresponding author. E-mail: w.richardson@ucl.ac.uk

Preventing adult myelination by conditional deletion of myelin regulatory factor

Myelin regulatory factor (MyRF) is a transcription factor required in OLs to initiate and maintain their myelination program (*8*–*10*). It is not expressed in OPs, in other CNS cells, or in Schwann cells, which myelinate PNS axons. We have a mouse line that carries a "floxed" allele of *Myrf* (*10*). By breeding (see supplementary materials and methods), we obtained *Myrf*$^{(+/flox)}$ and *Myrf*$^{(flox/flox)}$ littermates on a *Pdgfra-CreER*^{T2}:*Rosa-YFP* background (*2*, *11*); we refer to these as *P-Myrf*$^{(+/flox)}$ and *P-Myrf*$^{(flox/flox)}$, respectively. Administering tamoxifen induces Cre-mediated recombination, inactivating one or both alleles of *Myrf* in *Pdgfra*-expressing OPs while simultaneously labeling the OPs with yellow fluorescent protein (YFP) (see supplementary materials and methods). We refer to the tamoxifen-treated mice as *P-Myrf*$^{(+/-)}$ and *P-Myrf*$^{(-/-)}$. Recombination at the *Myrf* locus was confirmed by reverse transcription polymerase chain reaction (fig. S1).

We inactivated *Myrf* in OPs by tamoxifen administration on postnatal day 60 (P60) or P90. Subsequently, we identified YFP$^+$ OPs and newly differentiated YFP$^+$ OLs by triple-immunolabeling with anti-YFP, anti-Pdgfra (for OPs), and the CC1 monoclonal antibody (for OLs). In *P-Myrf*$^{(+/-)}$ mice, YFP$^+$,CC1$^+$,Pdgfra$^-$ OLs accumulated in the anterior corpus callosum (beneath the motor cortex) after the administration of tamoxifen (post-tamoxifen) (arrows in Fig. 1A). In *P-Myrf*$^{(-/-)}$ mice, production of YFP$^+$,CC1$^+$ OLs was decreased to ~10% of control (Fig. 1, A and B); at 1 month post-tamoxifen, we counted 301 ± 59 YFP$^+$,CC1$^+$ cells/mm^2 in 20-μm sections of *P-Myrf*$^{(+/-)}$ corpus

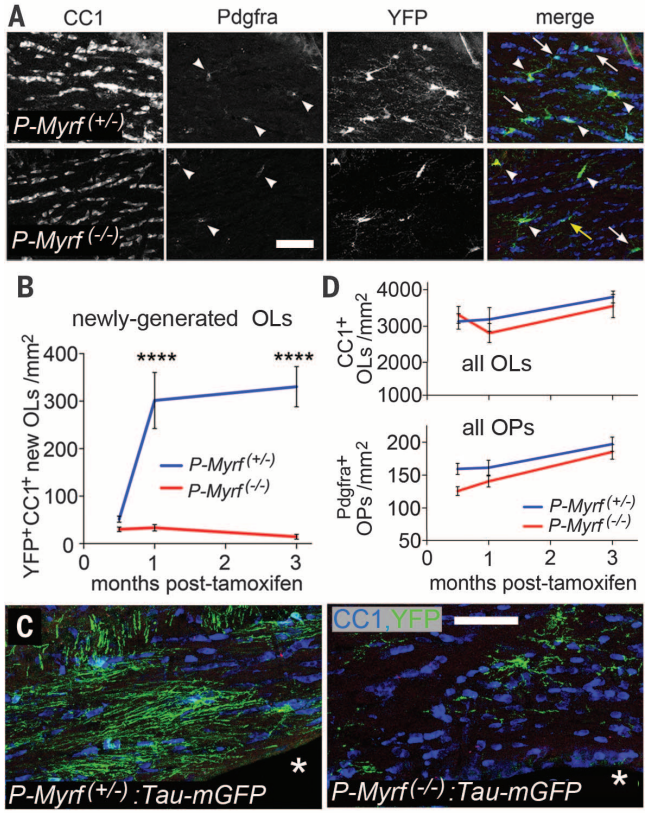

Fig. 1. Deleting *Myrf* in OPs prevents new myelination. (**A**) Many YFP$^+$ (newly formed) cells accumulated 1 month after tamoxifen treatment in the *P-Myrf*$^{(+/-)}$ corpus callosum, including Pdgfra$^+$,CC1$^-$ OPs (arrowheads) and CC1$^+$, Pdgfra$^-$ OLs (arrows). In contrast, the *P-Myrf*$^{(-/-)}$ corpus callosum contained few YFP$^+$ cells, mainly Pdgfra$^+$ OPs. Some YFP$^+$,CC1$^+$ cells appeared fragmented, presumably because they are apoptotic (yellow arrow). (**B**) Numbers of YFP$^+$,CC1$^+$ OLs in the *P-Myrf*$^{(-/-)}$ versus *P-Myrf*$^{(+/-)}$ corpus callosum (****P < 0.0001). Error bars indicate SEM. (**C**) Very few GFP$^+$ (newly formed) myelin sheaths are present in the *P-Myrf*$^{(-/-)}$:*Tau-mGFP* corpus callosum 1 month post-tamoxifen relative to *P-Myrf*$^{(+/-)}$ siblings. Asterisk indicates third ventricle. (**D**) The number densities of Pdgfra$^+$ OPs or CC1$^+$,YFP$^-$ (preexisting) OLs did not change between P60 and P150. Error bars indicate SEM. Scale bars: 50 μm, (A) and (C).

callosum but only 33 ± 7 cells/mm^2 in *P-Myrf*$^{(-/-)}$ (means ± SEM; six fields of view in three sections of three mice of each genotype). There was a comparable reduction in other regions of the *P-Myrf*$^{(-/-)}$ brain, including the cerebral cortex, striatum, midbrain, and cerebellum. In the motor cortex, for example, we counted 123 ± 15 YFP$^+$,CC1$^+$ cells/mm^2 in *P-Myrf*$^{(+/-)}$ and 10 ± 3 cells/mm^2 in *P-Myrf*$^{(-/-)}$. There was no recovery of OL production over at least 3 months (Fig. 1B). Loss of newly formed OLs was confirmed visually using a different reporter line, *Tau-mGFP* (GFP, green fluorescent protein), that expresses a membrane-bound green fluorescent protein, revealing whole-cell morphology including the myelin sheaths (*3*, *12*). One month post-tamoxifen, *P-Myrf*$^{(-/-)}$*:Tau-mGFP* corpus callosum was almost devoid of GFP-positive myelin sheaths, in contrast to their *Myrf*$^{(+/-)}$ littermates, which had many (Fig. 1C).

To quantify new OL production in *P-Myrf*$^{(-/-)}$ versus *P-Myrf*$^{(+/-)}$ mice, we administered 5-ethynyl-2′-deoxyuridine (EdU) to P60 mice for 1 week, after tamoxifen treatment. One month later, 5.7% ± 0.7% of CC1$^+$ OLs in *P-Myrf*$^{(+/-)}$ corpus callosum were positive for EdU (i.e., recently formed from cycling OPs), compared with only 0.20% ± 0.07% in *P-Myrf*$^{(-/-)}$ littermates (means ± SEM; six fields, >250 OLs per field in three sections of three mice of each genotype) (fig. S2). Therefore, *Myrf* was deleted in >90% of all OPs, whether or not they recombined the *Rosa-YFP* reporter. Over the same period, we detected no significant changes in the number density of Pdgfra$^+$ OPs or CC1$^+$,YFP$^-$ (i.e., preexisting) OLs in *P-Myrf*$^{(-/-)}$ versus *P-Myrf*$^{(+/-)}$ corpus callosum (Fig. 1D). Therefore, our strategy prevents the formation of new OLs without affecting preexisting OLs.

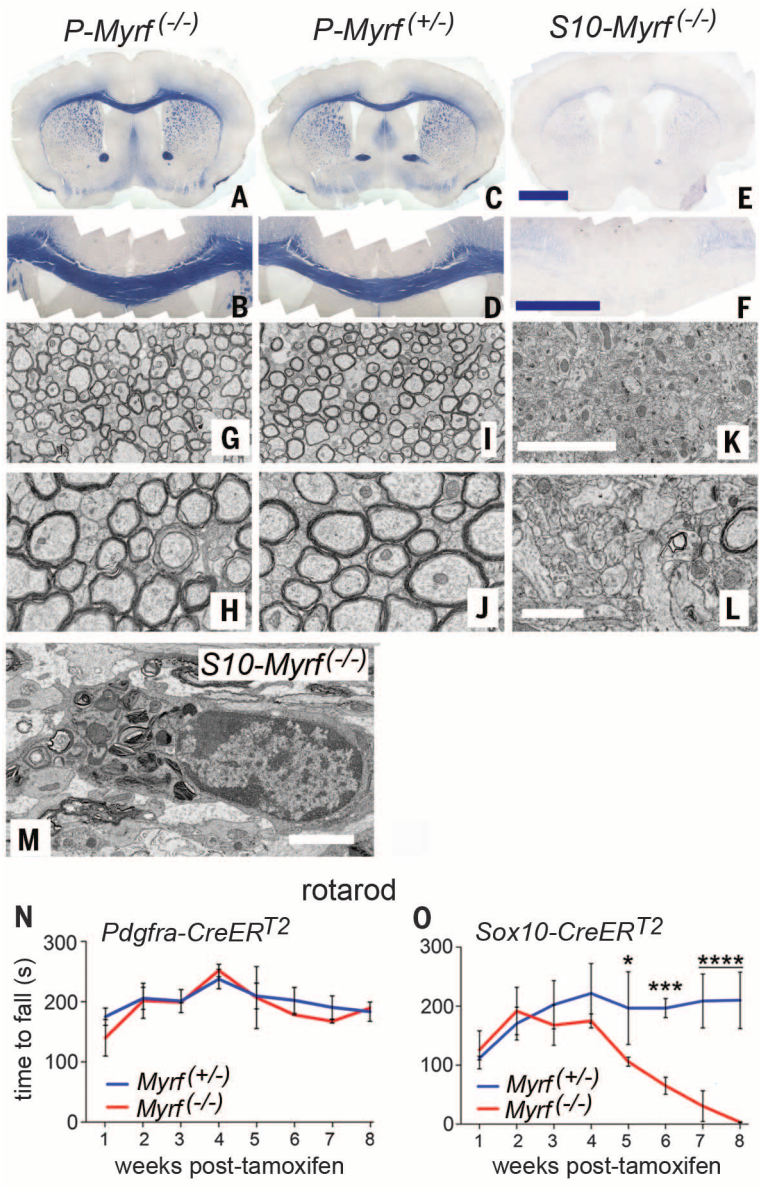

Fig. 2. Deleting *Myrf* in OPs does not trigger demyelination. Tamoxifen was administered to P60 mice and, 5 weeks later, their brains were examined by Eri-C histochemistry (**A** to **F**) or electron microscopy (**G** to **M**). There was no visible loss of myelin in *P-Myrf*$^{(-/-)}$ [(A), (B), (G), and (H)] or *P-Myrf*$^{(+/-)}$ [(C), (D), (I), and (J)] brains, but there was marked demyelination in *S10-Myrf*$^{(-/-)}$ [(E), (F), (K), and (L)]. In *S10-Myrf*$^{(-/-)}$ white matter, phagocytic cells containing membrane debris were present (M). Performance on an accelerating rotarod was not impaired in *P-Myrf*$^{(-/-)}$ mice for at least 8 weeks post-tamoxifen compared with their *P-Myrf*$^{(+/-)}$ littermates (**N**), whereas *S10-Myrf*$^{(-/-)}$ mice were seriously impaired after 4 to 5 weeks (**O**). Error bars indicate SEM. *$P < 0.05$; ***$P < 0.001$; ****$P < 0.0001$. Scale bars: 2 mm, (A), (C), and (E); 1 mm, (B), (D), and (F); 5 μm, (G), (I), and (K); 1 μm, (H), (J), and (L); and 2 μm (M).

Preventing new OL production does not trigger demyelination

Myelin histochemistry with Eriochrome cyanine (Life Technologies) showed that *P-Myrf*$^{(-/-)}$ mice had normal-appearing white matter (Fig. 2, A and B), indistinguishable from their *P-Myrf*$^{(+/-)}$ littermates (Fig. 2, C and D). In contrast, when *Myrf*$^{(flox/flox)}$ was deleted conditionally in both OLs and OPs using *Sox10-CreER*^{T2} mice [*S10-Myrf*$^{(-/-)}$] (see supplementary materials and methods and fig. S3), there was dramatic loss of myelin (Fig. 2, E and F). Electron microscopy (EM) revealed compact myelin sheaths in *P-Myrf*$^{(-/-)}$ mice (Fig. 2, G and H) that were indistinguishable from *P-Myrf*$^{(+/-)}$ controls (Fig. 2, I and J), whereas *S10-Myrf*$^{(-/-)}$ mice were severely demyelinated (Fig. 2, K and L). Phagocytic cells (macrophages or activated microglia) containing cell debris were observed by EM in *S10-Myrf*$^{(-/-)}$ corpus callosum (34 cells counted in four fields from two P90 mice 5 weeks post-tamoxifen; mean cell density ~220 cells/mm^2) (Fig. 2M); such cells were much less frequent in *P-Myrf*$^{(-/-)}$ (7 cells; ~44 cells/mm^2) or in *P-Myrf*$^{(+/-)}$ controls (10 cells; ~55 cells/mm^2). For comparison, the density of OPs in the healthy CNS is ~150 cells/mm^2. There was no evidence of inflammation or blood-brain barrier breakdown marked by invasion of immune cells (e.g., neutrophils or T cells), loss of tight junctions between endothelial cells, or retraction of astrocyte processes from blood vessels, even in the severely demyelinated *S10-Myrf*$^{(-/-)}$ brain.

Consistent with the myelin histology, *P-Myrf*$^{(-/-)}$ mice showed no outward signs of demyelination (e.g., tremors) and were indistinguishable from their *P-Myrf*$^{(+/-)}$ littermates on an accelerating rotarod, a test for motor coordination and balance (Fig. 2N). In contrast, *S10-Myrf*$^{(-/-)}$ mice developed severe tremors around 1 month post-tamoxifen (movie S1), and their performance on the rotarod was seriously impaired (Fig. 2O), similar to when *Myrf* deletion was targeted to mature OLs using *Plp-CreER* (*9*).

The complex running wheel

We assessed motor learning ability using a running wheel with irregularly spaced rungs ("complex wheel") (Fig. 3) (*13*, *14*). Mice run on the wheel spontaneously and, when skilled, can run the equivalent of 5 to 7 km per night. When wild-type (WT) (C57B6/CBA hybrid) mice accustomed

to a regular wheel with equally spaced rungs are switched to the complex wheel, they experience great difficulty at first but persevere and after about a week can run as fast on the complex wheel as they can on the regular wheel (movies S2 and S3). High-speed filming reveals that on the regular wheel mice adopt a symmetrical "running walk" with an eight-gap stride, out of phase by four gaps left to right (*15*) (Fig. 3A). They bring their hindpaws up to the rung immediately behind their forepaws. On the complex wheel, they break step, adopting an asymmetrical gait with six- to nine-gap strides out of phase by two to six gaps between sides. A critical adaptation is that the mice bring their hindpaws forward to grasp the same rung as their forepaws (Fig. 3, B to E). Thus, their hindpaws always find a rung, whatever the pattern of gaps. They also prefer rungs preceded by a one- or two-rung gap (Fig. 3, B to D); presumably, they reach forward into a gap and "pull back" to grasp the nearest rung, a second adaptation that is transferable to other rung patterns. Therefore, mice do not memorize specific stepping patterns but develop general strategies for running on wheels with unequal gaps; mastering one rung pattern primes them to master a different pattern more easily (fig. S4).

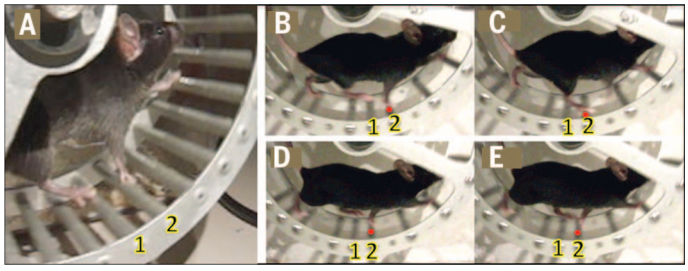

Fig. 3. Mice learn general strategies for coping with even rung spacing. (**A**) On the regular running wheel, WT mice place fore- and hindpaws on consecutive rungs while reaching forward with the contralateral forepaw. (**B** to **E**) On the complex wheel, they grasp the same rung with fore- and hindpaws (red dots), selecting rungs preceded by a one- or two-rung gap [e.g., (B) and (D)]. These strategies are transferable to other rung patterns. (B) and (C) and (D) and (E) are consecutive video frames (240 frames/s).

Active myelination is required for motor skill learning

Learning to run on the complex wheel presumably engages motor control circuits in addition to those required for normal symmetrical gait, involving the basal ganglia, cerebellum, motor cortex, and connecting pathways including the corpus callosum, but independent of the hippocampus (*16*–*18*). We introduced *P-Myrf*$^{(-/-)}$ and *P-Myrf*$^{(+/-)}$ littermates (mixed C57B6/CBA/129 background, predominantly C57B6; see supplementary materials and methods) to the complex wheel 3 weeks after tamoxifen treatment beginning on P60 (four experiments) or P90 (one experiment) (Fig. 4, A and B). The P90 experiment is

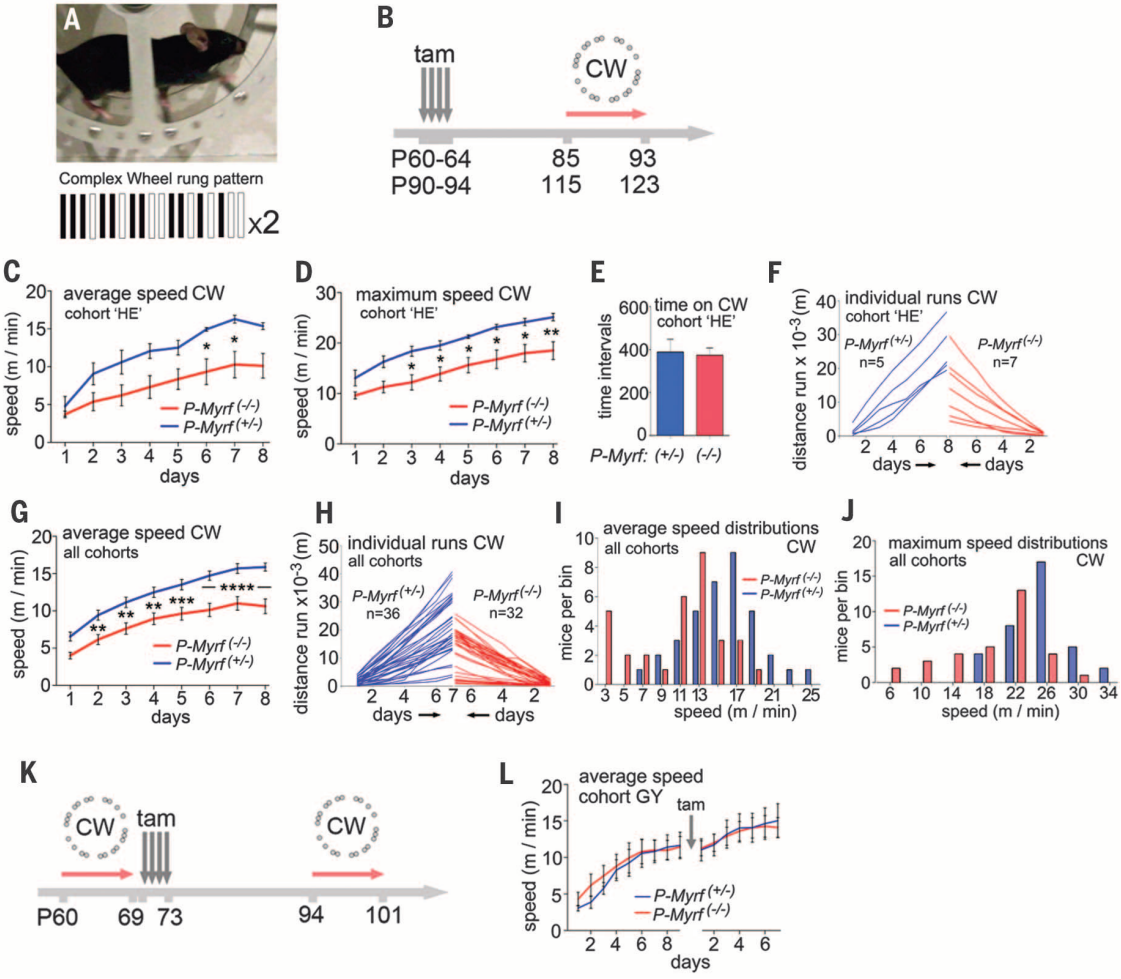

Fig. 4. Active CNS myelination is required for motor skill learning. (**A**) The complex wheel pattern. (**B**) Experimental design. *P-Myrf*$^{(-/-)}$ and *P-Myrf*$^{(+/-)}$ mice were housed singly, and tamoxifen was administered from P60 or P90. Three weeks later, they were introduced to the complex wheel (CW). (**C** and **D**) On the wheel, *P-Myrf*$^{(-/-)}$ mice were impaired relative to *P-Myrf*$^{(+/-)}$ [tamoxifen on P90; means ± SEM (error bars), n = 7 and 5, respectively]. (**E**) Time on wheel at >1 m/min was not different between cohorts. Error bars denote SEM. (**F**) Individual performances, distance versus time. (**G** to **J**) Five pooled experiments confirm divergence between *P-Myrf*$^{(+/-)}$ and *P-Myrf*$^{(-/-)}$ mice [P = 0.0063 for accumulated distances, P = 0.0003 for average speeds; K-S test, n = 36 (20 males) and 32 (17 males), respectively]. Error bars in (G) denote SEM. (**K** and **L**) *P-Myrf*$^{(+/flox)}$ and *P-Myrf*$^{(flox/flox)}$ mice were introduced to the complex wheel before tamoxifen exposure and reintroduced 3 weeks after treatment. Both before and after, there was no difference between cohorts (n = 7 and 8, respectively). Error bars in (L) denote SEM. *P < 0.05; **P < 0.01; ***P < 10^{-3}; ****P < 10^{-4}. Also see fig. S6.

shown (Fig. 4, C to F). Both cohorts improved their performance during the first week on the complex wheel, but the daily average and maximum speeds attained by the *P-Myrf*$^{(-/-)}$ group were always less than their *P-Myrf*$^{(+/-)}$ siblings (Fig. 4, C and D). Time spent turning the wheel >1 m/min was the same for both genotypes, arguing against a difference in motivation (Fig. 4E). Individual performances varied widely, and there was substantial overlap between genotypes (Fig. 4F). Pooled data for all five experiments confirmed significant differences in the average speeds attained by *P-Myrf*$^{(-/-)}$ versus *P-Myrf*$^{(+/-)}$ animals (Fig. 4G), as well as their individual performances (Fig. 4H) [$P = 0.0063$, Kolgomorov-Smirnov (K-S) nonparametric test; $n = 32$ and 36 mice, respectively]. One-third (12 of 36) of *P-Myrf*$^{(+/-)}$ mice ran further in 1 week than the best-performing of their *P-Myrf*$^{(-/-)}$ counterparts (Fig. 4H). High-speed filming showed that *P-Myrf*$^{(-/-)}$ mice ran less rhythmically and sometimes appeared to propel the wheel with their rear ankle or lower leg rather than their hindpaw (movies S4 and S5). The average speeds of *P-Myrf*$^{(+/-)}$ mice (on the seventh day) had an approximately normal distribution ($P = 0.2$, K-S test), whereas the average speeds of *P-Myrf*$^{(-/-)}$ mice were bimodal and skewed toward lower speeds (different distributions, $P = 0.007$) (Fig. 4I), possibly reflecting multistage learning (Fig. 3). The maximum speed distribution of *P-Myrf*$^{(-/-)}$ mice was also shifted to lower speeds ($P < 0.0001$) (Fig. 4J). When retested 1 month later, the difference between *P-Myrf*$^{(-/-)}$ and *P-Myrf*$^{(+/-)}$ animals persisted (fig. S4). There were no significant differences between males and females (fig. S5).

Active myelination is not required to recall a prelearned skill

Despite the lack of a general locomotor defect on the rotarod, *Myrf* deletion could have caused some subtle neural or physical impairment unrelated to learning. To control for this, we introduced P60 *P-Myrf*$^{(flox/flox)}$ and *P-Myrf*$^{(+/flox)}$ littermates to the complex wheel before tamoxifen treatment (Fig. 4K). As expected, the two cohorts were indistinguishable before tamoxifen (Fig. 4L and fig. S6). We administered tamoxifen, housed the mice singly for 3 weeks without a wheel, and then reintroduced them to the complex wheel (Fig. 4K). Both *P-Myrf*$^{(-/-)}$ and *P-Myrf*$^{(+/-)}$ groups were immediately able to run at speed (Fig. 4L and fig. S6). We conclude that (i) *P-Myrf*$^{(-/-)}$ mice are inherently able to run at speed on the complex wheel (i.e., they are physically capable) and (ii) myelin formation is not required to perform a prelearned skill.

Running stimulates OP proliferation and OL production

To relate motor learning to cell dynamics, we introduced P60 WT mice to the complex wheel while administering EdU via their drinking water, and we counted EdU$^+$ cells in the corpus callosum after various periods. At 4 days, there was a transient increase (~40%, $P = 0.006$, $n = 4$) in the fraction of Pdgfra$^+$ OPs that was EdU-labeled ("labeling index") in runners relative to control mice housed without a wheel, indicating that running had accelerated the G_1-to-S transition (Fig. 5A). This was followed 2 days later by a spike in the absolute number of Pdgfra$^+$ OPs as they completed the cell cycle (~40% increase, $P = 0.04$, $n = 3$) (Fig. 5B), then 5 days after that (11 days running) by an increase (~40%, $P = 0.003$, $n = 3$) in the number of EdU$^+$,Pdgfra$^-$ cells—a mixture of CC1$^+$ and CC1$^-$ OLs (Fig. 5C). At 11 days, almost all (94% ± 4%) EdU$^+$ cells were Sox10$^+$ OL lineage cells. After 3 weeks, there were many newly formed EdU$^+$,CC1$^+$ OLs in control animals housed without a wheel, as expected (*2*, *3*), but a ~50% greater number of those cells in runners (Fig. 5D).

The transient increase in EdU labeling index was not observed a second time when the complex wheel was removed from the cage and reintroduced 1 week later (Fig. 5, E and F), suggesting that it was triggered by novel experience (e.g., learning), not exercise per se. OP division and differentiation was increased by running on the regular wheel (fig. S7) as well as the complex wheel, suggesting that the region of corpus callosum we examined is involved in skills common to both (e.g., grasping or general bilateral coordination).

The cellular events described above occurred on a similar time scale as the improvement in running performance and, together with our data from *Myrf* knockout mice, support an important role for newly formed OLs in motor skill acquisition. How might new myelinating cells contribute to skill learning? It is likely that new neuronal connections are formed, or existing connections strengthened, in response to repetitive firing of neural circuits that elicit a particular sequence of movements (*18*). The increased activity in these circuits might then stimulate myelination of their axons, or myelin remodeling, making the circuit more efficient. There might even be a reserve of preformed, parallel circuits in the brain, and motor training selects the best of these by stimulating myelination in the most active circuits. The fact that most axons in the mouse corpus callosum and cerebral cortex remain incompletely myelinated into adulthood could be consistent with this idea (*19*, *20*). The existence of an activity-driven myelination mechanism has been postulated, based on the fact that OPs express various neurotransmitter receptors, form synapses with naked axons, and display transmembrane ion currents in response to action potentials in the axons that they contact (*21*–*25*). There is evidence that activity or experience can regulate OP division and differentiation in vivo [(*26*–*32*) and this paper] and also MRI evidence of structural changes in the white matter of individuals learning sensorimotor skills (*4*–*7*), undertaking working memory training (*33*), or learning a second language (*34*). We have now provided experimental evidence that OL genesis and myelin formation are important for motor learning and, therefore, are likely to contribute

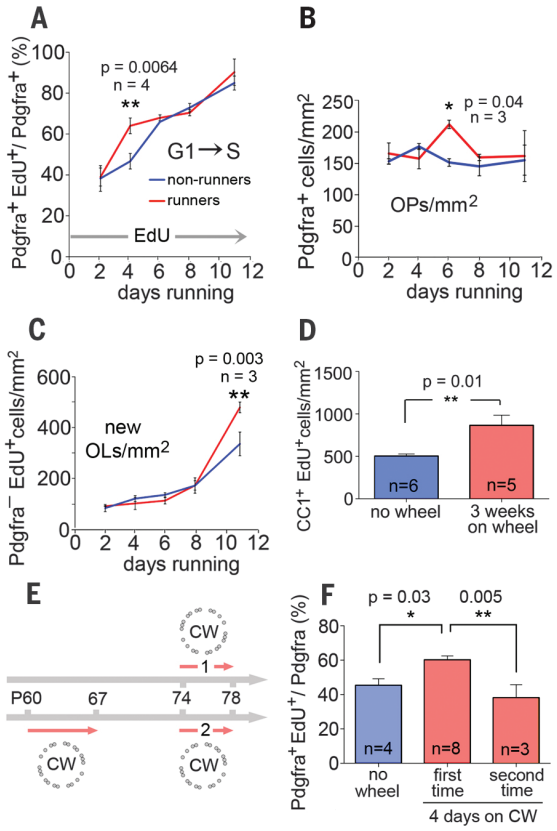

Fig. 5. Running stimulates OP proliferation and OL production. Running on the complex wheel (CW) caused (**A**) a transient increase in the EdU labeling index of Pdgfra$^+$ OPs in the corpus callosum after 2 days, (**B**) an increase in the number density of OPs at 6 days, and (**C**) increased production of OLs (EdU$^+$,Pdgfra$^-$) by 11 days. The latter were a mixture of mature CC1$^+$ and immature CC1$^-$ OLs. The numbers of both cell types were greater in runners than nonrunners at 11 days, although individually the increases did not reach significance ($P = 0.15$ and 0.06, respectively). (**D**) After 3 weeks running, there were ~50% more EdU$^+$,CC1$^+$ OLs in runners than nonrunners. (**E**) Experimental design. EdU was administered in the drinking water for 4 days during running, as indicated (arrows 1 and 2). (**F**) The EdU labeling index was increased by the first but not the second encounter with the wheel. Each data point represents multiple fields from at least three sections from three or more mice. Error bars in (A) to (D) and (F) represent SEM. Also see fig. S7.

to the changes observed by MRI. Future experiments can assess whether new myelinating cells are required for other types of learning as well.

REFERENCES AND NOTES

1. W. D. Richardson, K. M. Young, R. B. Tripathi, I. McKenzie, *Neuron* **70**, 661–673 (2011).
2. L. E. Rivers *et al.*, *Nat. Neurosci.* **11**, 1392–1401 (2008).
3. K. M. Young *et al.*, *Neuron* **77**, 873–885 (2013).
4. S. L. Bengtsson *et al.*, *Nat. Neurosci.* **8**, 1148–1150 (2005).
5. J. Scholz, M. C. Klein, T. E. Behrens, H. Johansen-Berg, *Nat. Neurosci.* **12**, 1370–1371 (2009).
6. Y. Hu *et al.*, *Hum. Brain Mapp.* **32**, 10–21 (2011).
7. C. Sampaio-Baptista *et al.*, *J. Neurosci.* **33**, 19499–19503 (2013).
8. B. Emery *et al.*, *Cell* **138**, 172–185 (2009).
9. M. Koenning *et al.*, *J. Neurosci.* **32**, 12528–12542 (2012).
10. H. Bujalka *et al.*, *PLOS Biol.* **11**, e1001625 (2013).
11. S. Srinivas *et al.*, *BMC Dev. Biol.* **1**, 4 (2001).
12. S. Hippenmeyer *et al.*, *PLOS Biol.* **3**, e159 (2005).
13. D. Liebetanz *et al.*, *Exp. Neurol.* **205**, 207–213 (2007).
14. N. Hibbits, R. Pannu, T. J. Wu, R. C. Armstrong, *ASN Neuro* **1**, 153–164 (2009).
15. M. Hildebrand, *Bioscience* **39**, 766–775 (1989).
16. S. Grillner, *Neuron* **52**, 751–766 (2006).
17. P. M. Schalomon, D. Wahlsten, *Brain Res. Bull.* **57**, 27–33 (2002).
18. B. Milner, L. R. Squire, E. R. Kandel, *Neuron* **20**, 445–468 (1998).
19. R. R. Sturrock, *Neuropathol. Appl. Neurobiol.* **6**, 415–420 (1980).
20. G. S. Tomassy *et al.*, *Science* **344**, 319–324 (2014).
21. Y. Bakiri *et al.*, *Neuroscience* **158**, 266–274 (2009).
22. D. E. Bergles, R. Jabs, C. Steinhäuser, *Brain Res. Rev.* **63**, 130–137 (2010).
23. V. Gallo, J. M. Mangin, M. Kukley, D. Dietrich, *J. Physiol.* **586**, 3767–3781 (2008).
24. P. P. Maldonado, M. Vélez-Fort, M. C. Angulo, *J. Anat.* **219**, 8–17 (2011).
25. R. D. Fields, *Semin. Cell Dev. Biol.* **22**, 214–219 (2011).
26. C. Simon, M. Götz, L. Dimou, *Glia* **59**, 869–881 (2011).
27. E. M. Gibson *et al.*, *Science* **344**, 1252304 (2014).
28. B. A. Barres, M. C. Raff, *Nature* **361**, 258–260 (1993).
29. Q. Li, M. Brus-Ramer, J. H. Martin, J. W. McDonald, *Neurosci. Lett.* **479**, 128–133 (2010).
30. M. Makinodan, K. M. Rosen, S. Ito, G. Corfas, *Science* **337**, 1357–1360 (2012).
31. J. M. Mangin, P. Li, J. Scafidi, V. Gallo, *Nat. Neurosci.* **15**, 1192–1194 (2012).
32. H. Wake, P. R. Lee, R. D. Fields, *Science* **333**, 1647–1651 (2011).
33. H. Takeuchi *et al.*, *J. Neurosci.* **30**, 3297–3303 (2010).
34. A. A. Schlegel, J. J. Rudelson, P. U. Tse, *J. Cogn. Neurosci.* **24**, 1664–1670 (2012).

ACKNOWLEDGMENTS

We thank the staff of the Center for Electron Microscopy and Bio-Imaging Research, Iwate Medical University, and U. Dennehy and M. Grist (University College London) for technical help and our colleagues in the Wolfson Institute for Biomedical Research for encouragement and suggestions. W.D.R. thanks T. Richardson for stimulating discussions. The study was supported by the European Research Council (grant agreement 293544), the UK Medical Research Council, the Wellcome Trust, and Grants-in-Aid from the Japanese Ministry of Education, Culture, Sports, Science and Technology. W.D.R. and K.T. acknowledge an Invitation Fellowship from the Japan Society for Promotion of Science. I.M. was supported by a Royal Society USA/Canada Exchange Fellowship, J.P.d.F. by a fellowship from the Portuguese Fundação para a Ciência e a Tecnologia, and B.E. by a Career Development Fellowship from the Australian National Health and Medical Research Council. *Pdgfra-CreER^{T2}* and *Sox10-CreER^{T2}* mice can be obtained by request through www.e-lucid.com/ with a material transfer agreement. *Myrf(flox)* mice can be obtained from Jackson Laboratories, strain 010607. The supplementary materials include additional data.

SUPPLEMENTARY MATERIALS

www.sciencemag.org/content/346/6207/318/suppl/DC1
Materials and Methods
Supplementary Text
Figs. S1 to S7
References (*35*, *36*)
Movies S1 to S5

17 April 2014; accepted 14 August 2014
10.1126/science.1254960

REPORTS

PLANETARY GEOLOGY

Constraints on Mimas' interior from Cassini ISS libration measurements

R. Tajeddine,[1,2,3]* N. Rambaux,[2,3] V. Lainey,[2] S. Charnoz,[4] A. Richard,[2] A. Rivoldini,[5] B. Noyelles[6]

Like our Moon, the majority of the solar system's satellites are locked in a 1:1 spin-orbit resonance; on average, these satellites show the same face toward the planet at a constant rotation rate equal to the satellite's orbital rate. In addition to the uniform rotational motion, physical librations (oscillations about an equilibrium) also occur. The librations may contain signatures of the satellite's internal properties. Using stereophotogrammetry on Cassini Image Science Subsystem (ISS) images, we measured longitudinal physical forced librations of Saturn's moon Mimas. Our measurements confirm all the libration amplitudes calculated from the orbital dynamics, with one exception. This amplitude depends mainly on Mimas' internal structure and has an observed value of twice the predicted one, assuming hydrostatic equilibrium. After considering various possible interior models of Mimas, we argue that the satellite has either a large nonhydrostatic interior, or a hydrostatic one with an internal ocean beneath a thick icy shell.

Among Saturn's inner main moons, Mimas is the smallest (radius ~198 km) and closest to the planet (semimajor axis ~189,000 km). Along with Enceladus, Tethys, Dione, and Rhea, it is classified as a mid-sized icy moon; the origin of these moons is still being debated. The classical model describes their formation by accretion in the protoplanetary subnebula (*1*–*6*) or by collision between two large satellites and reaccretion of the impact ejecta (*7*, *8*), but does not explain the satellites' masses, sizes, and radial locations. A new model reconciles these parameters by forming the satellites in the rings (*9*–*11*). However, this model assumes that the primordial rings were massive and contained silicate; furthermore, Saturn must have been tidally very dissipative (*12*) to move all the mid-sized moons to their current locations.

We measured Mimas' forced librations using Cassini's ISS Narrow Angle Camera (NAC) images, using methods previously applied to Phobos (*13*, *14*), to gain insights into Mimas' interior. The measurements of rotational parameters have been proven to be a powerful tool to investigate the interior state of celestial bodies (*15*). The absence of evident geological activity on Mimas' surface (*16*) suggests that it may have a cold interior that may have helped in conserving a "fossil" record of structures within its interior. This encouraged us to investigate Mimas' rotational variations, which are directly linked to its internal structure and may inform us about its origin.

First, we developed a control point network across Mimas' surface by applying the method of stereophotogrammetry, where (*X*, *Y*, *Z*) coordinates of a surface point in the satellite's frame are projected in an image as sample (*x*) and line (*y*) coordinates in pixels. For the 3D reconstruction, each point has been observed at least twice and from two different viewing angles (*17*). After selecting recognizable landmarks from Mimas' map (*18*), a least-squares method was applied comparing the (*X*, *Y*, *Z*) coordinates of each projected point in the image to the observed ones. From this, a topographic map of 260 surface points was built (Fig. 1A), based on 2135 point measurements from 40 Cassini images with resolutions ranging from 360 to 1450 m per pixel (see table S2 for a full list of images). The mean uncertainties on a point's coordinates are estimated as ±599 m, ±731 m, and ±395 m on *X*, *Y*, and *Z* coordinates, respectively. To test our method, we rebuilt and confirmed the satellite's triaxial shape using these points (*17*, *19*).

In the photogrammetric reconstruction method described above, a rotational model of Mimas is used (*17*). The better this model describes Mimas' rotation, the smaller the χ^2 errors from the topographic reconstruction. Hence, we repeatedly built Mimas' control point network by varying its forced libration amplitudes and phases until the total value of χ^2 was minimized. The measurements (Table 1) (*17*) confirm all the theoretical values (*20*) except for the amplitude corresponding to the 0.945-day period, which is almost twice the predicted one (Fig. 1B). The uncertainty on this libration amplitude has been

[1]Department of Astronomy, Cornell University, Ithaca, NY 14853, USA. [2]IMCCE–Observatoire de Paris, UMR 8028 du CNRS, UPMC, Université Lille 1, 77 Av. Denfert-Rochereau, 75014 Paris, France. [3]Université Pierre et Marie Curie, UPMC – Paris VI, 4 Place Jussieu, 75005 Paris, France. [4]Laboratoire AIM, UMR 7158, Université Paris Diderot/CEA IRFU/CNRS, Centre de l'Orme les Merisiers, 91191 Gif-sur-Yvette Cedex, France. [5]Royal Observatory of Belgium, Avenue Circulaire 3, B-1180 Brussels, Belgium. [6]Department of Mathematics and Namur Center for Complex Systems, Université de Namur, 5000 Namur, Belgium.
*Corresponding author. E-mail: tajeddine@astro.cornell.edu

estimated by adding Gaussian noise (taking into account all the sources of error) to the control points, and by repeatedly measuring the libration amplitude (Fig. 1C) (*17*). The final value of the libration amplitude (Table 1) is the result of a Gaussian fit to the histogram. Here, all the sources of error were considered random; by accounting for systematic errors, the highest value of uncertainty on the libration amplitude for the 0.945-day signal is ~1.5 arc min (*17*).

The mathematical expression for the physical forced libration is

$$\gamma = \sum_i \frac{H_i}{1-(\omega_i/\omega_0)^2}\cos(\omega_i t + \varphi_i) \qquad (1)$$

where ω_i and φ_i are the ith libration frequency and phase, respectively (*17*, *21*). H_i depends on the satellite's orbital dynamics and ω_0 is the system's free libration frequency, which for a solid body can be written, to the first order in eccentricity, as

$$\omega_0 = n\sqrt{3\left(\frac{B-A}{C}\right)} \qquad (2)$$

where A, B, and C are the satellite's principal moments of inertia and n is the satellite's mean motion. When the ratio $(\omega_i/\omega_0)^2$ is non-negligible in front of 1, the libration amplitude is dominated by the satellite's internal structure (*21*). Otherwise, the libration amplitude depends mainly on its orbital dynamics. The periods in Table 1 are the outcome of Mimas' orbital dynamics, creating effects of the longitudinal librations through Saturn's external gravitational torque. The strongest libration periods of ~70 and ~23 years are created by the Mimas-Tethys mean motion resonance. The period of 0.945 days is the anomalistic orbital period (perigee to perigee), which is slightly longer than the orbital period of 0.942 days; it is due to the precession of the pericenter, and the last three periods are directly linked to the precession of Mimas' pericenter. Using a triaxiality of $(B - A)/C = 0.06$ (*22*), the only amplitude that depends on the interior is the one with a period of 0.945 days (Table 1), which has been computed (*20*) assuming that Mimas is in hydrostatic equilibrium. The measured libration amplitude of 50.3 ± 1 arc min corresponds to a solid Mimas of triaxiality $(B-A)/C = 0.091 \pm 0.001$, which is surprisingly high.

To better understand such a large measured libration amplitude, we investigated five possible interior models of Mimas (*17*) to assess whether they could reproduce the observed libration: a homogeneous distribution of mass, a two-layer body in hydrostatic equilibrium, a mass anomaly under crater Herschel, a nonhydrostatic core, and an internal ocean. The results show that the cases of a homogeneous and a two-layer equilibrium body (*17*) can be discarded because the libration amplitude for these models is much smaller that our measured value (between 25.5 and 29 arc min).

Herschel, the largest crater on Mimas, is located at a longitude of 111.76°W, near Mimas' equator, and is 140 km wide and 10 km deep. The missing material from the impact basin modifies the satellite's moments of inertia. Moreover, as a consequence of the impact, a large subsurface mass anomaly could have formed below the crater. As in analyses of the effect of the Stickney crater on the libration of Phobos (*23*, *24*), we computed Mimas' libration amplitude by considering the presence of a large volume with porosity up to 45% (*25*) at depths as much as 70 km under Herschel (*17*). The effect of the basin increases the libration amplitude by ~1 arc min, which is not enough to explain the observed libration amplitude. On the other hand, the macroporosity increases the libration amplitude up to 46 arc min, for which the mass anomaly is so big that (if currently present) it would cause a reorientation of Mimas about the polar axis by 8°. Such reorientation is inconsistent with the present-day location of Herschel.

We also tested a model of Mimas with a nonhydrostatic shaped core. Any change in the core's shape must maintain the configuration of the satellite's principal moments of inertia where $A \leq B \leq C$. This can only be done by increasing the core's axis a_c, yielding a decrease in the b_c and/or c_c axes in order to conserve the core's total mass. In this model, we varied the densities of the shell and the core between 700 kg/m^3 and 950 kg/m^3 and between 1200 kg/m^3 and 3300 kg/m^3, respectively. Our calculations show that in order to explain the observed libration, the core should be elongated (compared to an equivalent model in hydrostatic equilibrium), between 20 and 60 km, on each side of the core's longest axis, increasing proportionally with the shell and core densities (*17*). Our calculations show that the suggested excess in topography for a silicate body such as Mimas' suggested core is supportable (*17*). Although this interior model seems simplistic (as an unlimited number of models with core deformations could be developed), it quantifies the

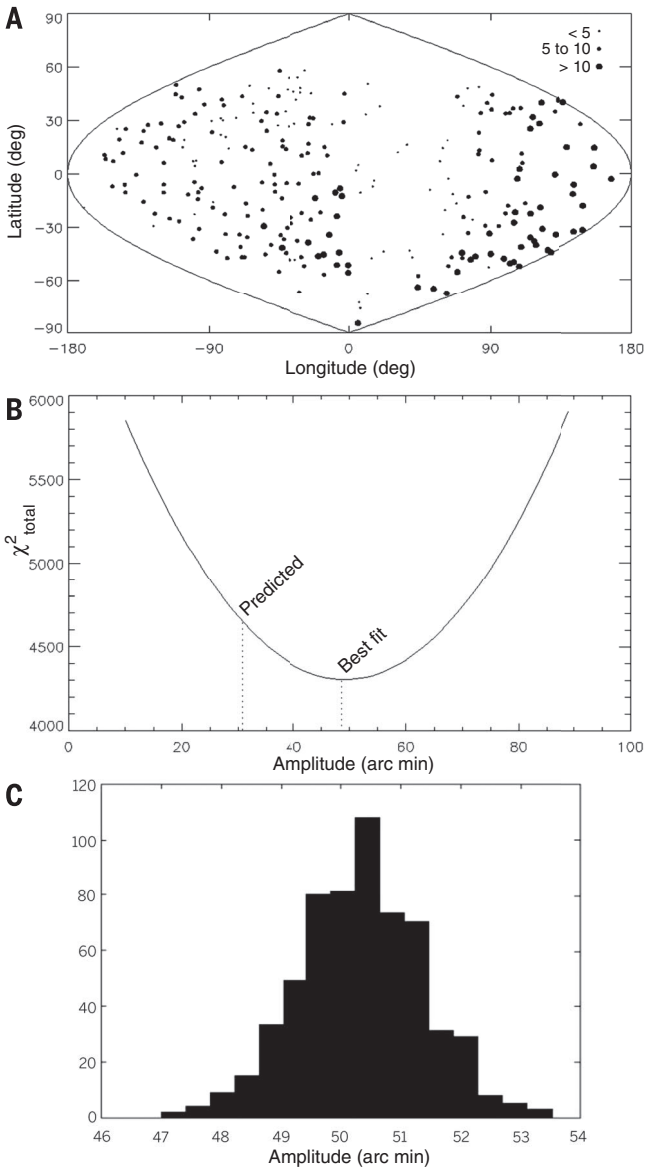

Fig. 1. Mimas' control point network and libration measurement. (**A**) A map of the used control point network of Mimas, where size represents the number of times a point has been observed. The map has poor coverage at low longitudes but good coverage around the Herschel crater (longitude 111.76°W, latitude –1.38°). Mimas' north pole has been observed only once, preventing access to any topographic information about this area. (**B**) A plot of the non-normalized total χ^2 (obtained from the map reconstruction) as a function of the libration amplitude of the period, 0.945 days. The number of degrees of freedom is 4269, as each point measurement provides one data point in sample and one in line. However, this plot is the result of only one fit. (**C**) Histogram of 600 solutions for the libration amplitude, when adding 1σ (of the estimated uncertainties on points) of Gaussian noise to the control points' positions. The Gaussian fit to the histogram gives the final solution for the libration amplitude (with its estimated uncertainty) as shown in Table 1.

required excess in the core's topography in order to explain the high libration amplitude. One question is whether such core should have effects on the satellite's global shape. Assuming that the shell is fully relaxed (which may not be necessarily the case), the effect of the core's shape on the global geoid (*17*) is not consistent with the satellite's observed shape (*19*). The mean offsets to the observations are about 2 km, –1.5 km, and –1.4 km in *a*, *b*, and *c* axes, respectively. Hence, the satellite should be more elongated. In fact, any anomaly in Mimas' interior should ultimately have an effect on Mimas' global geoid. However, in the models we developed, the densities in the layers were assumed constant. A low-gravity body like Mimas could generate and maintain large porosity in both ice and silicates. Large lateral variations in density could result, which may not correlate with the surface topography. In fact, it has been argued (*26*) that small bodies like Enceladus or Mimas may retain oddly shaped cores as a result of their original accretion and collisional evolution.

For a body with an internal global ocean, the calculation of the libration amplitude depends mainly on the shell thickness. It depends to a lesser extent on the core-shell couplings and periodic tidal deformation (*27*, *28*) that decrease the satellite's libration amplitude (*17*). An ocean at 24 km below a viscoelastic shell (assuming a Maxwell rheology), or at 31 km below a rigid shell, is in agreement with the observed libration amplitude (Fig. 2). We considered two end-member cases for the viscosity of water ice. The low viscosity value of 10^{12} Pa·s induces the largest deformations and with it the strongest reduction of the libration amplitude. In contrast, for the high viscosity value of 10^{21} Pa·s, the deformations are small and the libration amplitude is close to the rigid case. Therefore, the ice layer has a thickness between 24 km and 31 km, depending on the value of the viscosity.

The ocean hypothesis sounds unlikely because, contrary to the findings on Enceladus, Mimas' heavily cratered surface has shown no evidence of liquid water, thermal heating, or geological activities. Radiogenic heating alone could not sustain such an ocean, because the heat produced by the core escapes through the satellite's icy shell and any ocean would freeze very quickly. One explanation could be found in Mimas' high eccentricity (~0.02), whose origin remains unexplained and may have been higher in the past. As a consequence, an ocean could have been formed and sustained by tidal heating.

We tested only few possible interior models in this work in an attempt to explain the observed libration amplitude, and many others could be developed. Among those that we suggested, only two are consistent with our observations: a non-hydrostatic core and a subsurface ocean. An ocean could have plausible explanations. However, the discrimination between the suggested models could be done by mapping of Mimas' gravity field that could reveal any possible mass anomalies, measuring the tidal dissipation in Mimas using Cassini's accurate astrometry (*29*), or measuring the heat flux at its surface. In any case, the measurement of the physical forced librations using Cassini ISS images shows surprising evidence that Mimas is more complex than we thought.

Table 1. Comparison of the measured forced libration's amplitudes and phases to theoretical ones (*19*). The phases corresponding to signals at 225.04, 227.02, and 223.09 days have not been measured because of their close periods and low amplitudes. The last column shows how the libration amplitude depends on the satellite's internal structure. All amplitudes here are positive, and the phase of the 0.945-day libration is out of phase by π with respect to the forcing one.

Period (days)	Theoretical amplitude (arc min)	Measured amplitude (arc min)	Theoretical phase at J2000 (deg)	Measured phase at J2000 (deg)	$(\omega_i/\omega_O)^2$
25772.62	2616.6	2631.6 ± 3.0	51.35	52.9 ± 0.9	7×10^{-9}
8590.87	43.26	44.5 ± 1.1	–25.91	–18 ± 3.2	6×10^{-8}
0.945	26.07	50.3 ± 1.0	101.35	107.7 ± 0.8	5.52
225.04	7.82	7.5 ± 0.8	–157.74	—	9×10^{-5}
227.02	3.65	2.9 ± 0.9	–119.03	—	9×10^{-5}
223.09	3.53	3.3 ± 0.8	–16.31	—	9×10^{-5}

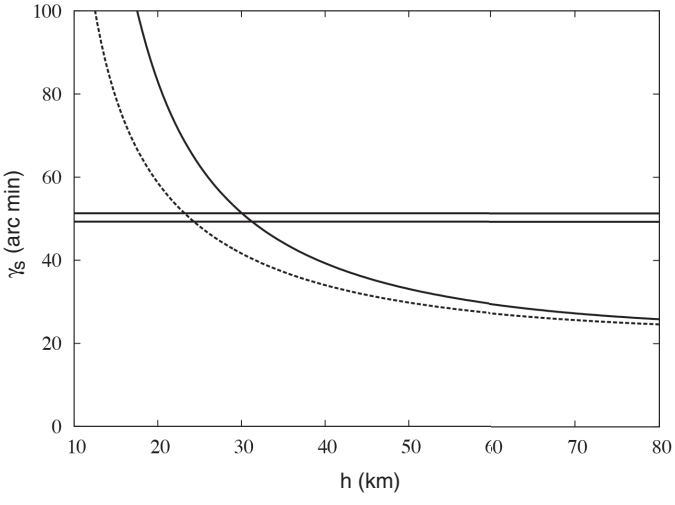

Fig. 2. Libration amplitude (γ_s) as a function of the icy shell thickness (h) for Mimas with a subsurface global ocean. The solid line represents a model with rigid solid layers, pressure, and internal gravitational coupling. The dashed line represents the same model that includes viscoelastic deformations. Horizontal lines represent 1σ range of the observed libration amplitude, 50.3 ± 1.0 arc min.

REFERENCES AND NOTES

1. R. M. Canup, W. R. Ward, *Astron. J.* **124**, 3404–3423 (2002).
2. R. M. Canup, W. R. Ward, *Nature* **441**, 834–839 (2006).
3. I. Mosqueira, P. R. Estrada, *Icarus* **163**, 198–231 (2003).
4. I. Mosqueira, P. R. Estrada, *Icarus* **163**, 232–255 (2003).
5. M. Ogihara, S. Ida, *Astrophys. J.* **753**, 60 (2012).
6. T. Sasaki, G. R. Stewart, S. Ida, *Astrophys. J.* **714**, 1052–1064 (2010).
7. Y. Sekine, H. Genda, *Planet. Space Sci.* **63–64**, 133–138 (2012).
8. E. Asphaug, A. Reufer, *Icarus* **233**, 544 (2012).
9. S. Charnoz, J. Salmon, A. Crida, *Nature* **465**, 752–754 (2010).
10. S. Charnoz *et al.*, *Icarus* **216**, 535–550 (2011).
11. A. Crida, S. Charnoz, *Science* **338**, 1196–1199 (2012).
12. V. Lainey *et al.*, *Astrophys. J.* **752**, 14 (2012).
13. T. C. Duxbury, J. D. Callahan, *Icarus* **77**, 275–286 (1989).
14. K. Willner *et al.*, *Earth Planet. Sci. Lett.* **294**, 541–546 (2010).
15. J. L. Margot, S. J. Peale, R. F. Jurgens, M. A. Slade, I. V. Holin, *Science* **316**, 710–714 (2007).
16. P. M. Schenk, *Lunar Planet. Sci. Conf.* **42**, 2729 (2011).
17. See supplementary materials on *Science* Online.
18. T. Roatsch *et al.*, *Planet. Space Sci.* **57**, 83–92 (2009).
19. P. C. Thomas, *Icarus* **208**, 395–401 (2010).
20. B. Noyelles, Ö. Karatekin, N. Rambaux, *Astron. Astrophys.* **536**, A61 (2011).
21. N. Rambaux, J. C. Castillo-Rogez, J. G. Williams, Ö. Karatekin, *Geophys. Res. Lett.* **37**, 4202 (2010).
22. S. F. Dermott, P. C. Thomas, *Icarus* **73**, 25–65 (1988).
23. N. Rambaux, J. C. Castillo-Rogez, S. Le Maistre, P. Rosenblatt, *Astron. Astrophys.* **548**, A14 (2012).
24. E. Asphaug, H. J. Melosh, *Icarus* **101**, 144–164 (1993).
25. W. B. Durham, W. B. McKinnon, L. A. Stern, *Geophys. Res. Lett.* **32**, L18202 (2005).
26. W. B. McKinnon, *J. Geophys. Res.* **118**, 1775–1788 (2013).
27. T. Van Hoolst, R. M. Baland, A. Trinh, *Icarus* **226**, 299–315 (2013).
28. A. Richard, N. Rambaux, B. Charnay, *Planet. Space Sci.* **93–94**, 22–34 (2014).
29. R. Tajeddine, N. J. Cooper, V. Lainey, S. Charnoz, C. D. Murray, *Astron. Astrophys.* **551**, A129 (2013).

ACKNOWLEDGMENTS

We thank the "ENCELADE" working group, J. A. Burns, N. J. Cooper, K. Degiorgio, M. M. Hedman, C. D. Murray, P. D. Nicholson, and T. Van Hooslt for fruitful discussions and suggestions; and the anonymous reviewers for their suggestions that improved the quality of the paper. The Cassini images that were used to obtain this paper's results are available on the Planetary Data System website, pds.nasa.gov. Supported by UPMC-EMERGENCE (contract EME0911), the Cassini mission (R.T.), the European Community's Seventh Framework Program (FP7/2007-2013) under grant agreement 263466 for the FP7-ESPaCE project (R.T., N.R., and V.L.), the UnivEarthS Labex program at Sorbonne Paris Cité (ANR-10-LABX-0023 and ANR-11-IDEX-0005-02), RS/CNRS (2011/R1 ref. IE110421) (S.C.), the European Space Agency in collaboration with the Belgian Federal Science Policy Office (A.Riv.), and an FRS-FNRS postdoctoral research fellowship (B.N.).

SUPPLEMENTARY MATERIALS

www.sciencemag.org/content/346/6207/322/suppl/DC1
Materials and Methods
Figs. S1 to S11
Tables S1 to S3
References (*30*–*47*)

28 April 2014; accepted 15 September 2014
10.1126/science.1255299

LAB ASTROPHYSICS

Laboratory formation of a scaled protostellar jet by coaligned poloidal magnetic field

B. Albertazzi,[1,2,20] A. Ciardi,[3,4] M. Nakatsutsumi,[1] T. Vinci,[1] J. Béard,[5] R. Bonito,[6,7] J. Billette,[5] M. Borghesi,[8,9] Z. Burkley,[1] S. N. Chen,[1] T. E. Cowan,[10,11] T. Herrmannsdörfer,[11] D. P. Higginson,[1] F. Kroll,[10,11] S. A. Pikuz,[12,13] K. Naughton,[8] L. Romagnani,[1] C. Riconda,[14] G. Revet,[1] R. Riquier,[1,15] H.-P. Schlenvoigt,[11] I. Yu. Skobelev,[12] A.Ya. Faenov,[12,16] A. Soloviev,[17] M. Huarte-Espinosa,[18,19] A. Frank,[18] O. Portugall,[5] H. Pépin,[2] J. Fuchs[1,17]*

Although bipolar jets are seen emerging from a wide variety of astrophysical systems, the issue of their formation and morphology beyond their launching is still under study. Our scaled laboratory experiments, representative of young stellar object outflows, reveal that stable and narrow collimation of the entire flow can result from the presence of a poloidal magnetic field whose strength is consistent with observations. The laboratory plasma becomes focused with an interior cavity. This gives rise to a standing conical shock from which the jet emerges. Following simulations of the process at the full astrophysical scale, we conclude that it can also explain recently discovered x-ray emission features observed in low-density regions at the base of protostellar jets, such as the well-studied jet HH 154.

Narrow bipolar jets are often spectacular and are commonly observed in the universe along the axis of rotation of varied objects, such as young stellar objects (YSOs) surrounded by an accretion disk. Jets are also thought to play a key role in the evolution of these objects. Hence, understanding their formation is key to understanding the mass, energy, and angular momentum redistribution between the dense core and the parent cloud. Once formed, these jets can continue ballistically over large distances (*1*). However, it is important to know how the narrow jet forms and what its characteristics are. The accepted standard model (*2*, *3*) of matter extraction and launching involves a poloidal magnetic field anchored in the disk. Here, poloidal means generally axial with respect to the jet flow, as opposed to the toroidal component that winds around the jet. In the model, matter is magneto-centrifugally accelerated into wide-angle conical winds (*4*). As the magnetic field lines become twisted by the inertia of the initially corotating plasma, the toroidal component of the magnetic field leads to self-collimation of the wind. Nonetheless, this process alone cannot explain collimation of the flow into narrow, jetlike form. First, self-collimation cannot account for the confinement of the whole outflow structure. Indeed, the winds in these models formally extend to infinity and cannot explain the observed jet widths (*5*). Furthermore, jets dominated by a toroidal magnetic field are prone to current and pressure-driven instabilities, which can disrupt the jet (*6*). Efforts to improve the model have led to studies of truncated disk winds where, to collimate the flow, the whole outflow structure has to rely on the thermal pressure of a surrounding medium (*7*), the presence of which has yet to be established.

Alternatively, outflow confinement by a large-scale poloidal magnetic field (*8*) has been explored in numerical simulations (*9*). Although evidence for such fields near the jet source is mostly indirect so far (*10*), they are well established on larger scales (*11*) and observed to be aligned (within ~35°) with the bipolar outflow axes of YSOs. These earlier numerical studies showed that such poloidal fields could convert ejected matter from being weakly collimated to streamlined. However, the simulations lacked a proper treatment of plasma cooling and were constrained by computing limitations to simulate the flow over only small distances from the source. More recently, we revisited the poloidal confinement scenario using large-scale, high-resolution three-dimensional (3D) magneto-hydrodynamic (MHD) simulations (*12*), which included cooling, and we showed that the whole outflow could be constrained. Notably, we predicted a particular morphology for the outflow with a shock-bounded cavity followed by a narrow jet. Such a mechanism does not exclude magneto-centrifugal self-collimation: Even if poloidal collimation can act on its own, it can also be complementary to self-collimation by stabilizing and further collimating the jets produced by the latter.

We report here on scaled laboratory experiments that exploit coupling of a high-amplitude and large-scale magnetic field to high-velocity plasma flows, to create conditions representative of a YSO. Our measurements conclusively demonstrate that stable jets can indeed be collimated from a wide-angle star/disk wind embedded in a coaligned, large-scale poloidal magnetic field. This is notably obtained without having to rely on the collimation by an external medium. We also show that the stable collimation of the whole flow into a narrow jet can be obtained even in the case of an angular offset (up to 40°) between the magnetic field and the outflow axis. The transition (Fig. 1A) from a divergent to a narrowly collimated flow results from the plasma being redirected toward the axis by a shock structure, which is induced by the compression of the magnetic field lines under the action of the expanding plasma. Consequently, a standing conical shock feature forms at the converging point where the plasma becomes reheated. We performed full-scale astrophysical simulations of an isotropic wind embedded in a large-scale magnetic field under conditions typical of YSOs, which appear consistent with the laboratory observations. By calculating the x-ray emission from the simulated plasma, we determine that the shock-focused region generates an x-ray source whose luminosity and location are in agreement with the Chandra observations of the puzzling x-ray emission from HH 154, one of the best-studied astrophysical jets emerging from a YSO (*13*).

The laboratory plasma, mimicking a YSO flow, is produced by short (0.5-ns), high-power laser irradiation of massive solid (plastic) targets (see methods). The plasma is a highly conductive and superfast-magnetosonic flow. The plasma is thermally launched from a region on the target on the order of the laser spot diameter (0.75 mm), and this wide-angle flow is, as it is in a YSO, initially dominated by its kinetic energy. The scaling between the laboratory plasma and a YSO outflow allows us also to scale a time span of 20 ns

[1]Laboratoire d'Utilisation des Lasers Intenses (LULI), École Polytechnique, CNRS, Commissariat à l'Energie atomique et aux énergies alternatives (CEA), Université Pierre et Marie Curie (UPMC), F-91128 Palaiseau, France. [2]Institut National de la Recherche Scientifique–Energie, Matériaux, Télécommunications (INRS-EMT), Varennes, Québec, Canada. [3]Sorbonne Universités, UPMC Université. Paris 06, UMR 8112, Laboratoire d'Etudes du Rayonnement et de la Matière en Astrophysique (LERMA), F-75005 Paris, France. [4]Observatoire de Paris and CNRS, UMR 8112, LERMA, Paris, France. [5]Laboratoire National des Champs magnétiques Intenses (LNCMI), UPR 3228, CNRS-Université Joseph Fourier (UJF)-Université Paul Sabatier (UPS)-Institut National des Sciences Appliquées (INSA), F-31400 Toulouse, France. [6]Dipartimento di Fisica e Chimica, Università di Palermo, Piazza del Parlamento, I-1 90134 Palermo, Italy. [7]National Institute for Astrophysics (INAF)–Osservatorio Astronomico di Palermo, Piazza del Parlamento, I-1 90134 Palermo, Italy. [8]School of Mathematics and Physics, The Queen's University of Belfast, Belfast BT7 1NN, UK. [9]Institute of Physics of the Academy of Science of the Czech Republic (ASCR), Extreme Light Infrastructure (ELI)-Beamlines Project, Na Slovance 2, 18221 Prague, Czech Republic. [10]Technische Universität Dresden, D-01062 Dresden, Germany. [11]Helmholtz-Zentrum Dresden-Rossendorf, Bautzner Landstrasse 400, D-01328 Dresden, Germany. [12]Joint Institute for High Temperatures Russian Academy of Science (RAS), Moscow 125412, Russia. [13]National Research Nuclear University MEPhI, Moscow 115409, Russia. [14]Sorbonne Universités, UPMC Université Paris 06, UMR 7605, LULI, F-75005 Paris, France. [15]CEA–Bruyères le Chatel, F-91297 Arpajon, France. [16]Institute for Academic Initiatives, Osaka University, Suita, Osaka 565-0871, Japan. [17]Institute of Applied Physics, 46 Ulyanov Street, 603950 Nizhny Novgorod, Russia. [18]Department of Physics and Astronomy, University of Rochester, Rochester, NY, USA. [19]Center for Advanced Computing and Data Systems, University of Houston, Houston, TX 77204, USA. [20]Graduate School of Engineering, Osaka University, Suita 565-0871, Japan.
*Corresponding author. E-mail: julien.fuchs@polytechnique.fr

in the laboratory to an equivalent ~6 years in the natural environment, during which it propagates over ~600 astronomical units (AU). Hence, even over short time scales (<100 ns), the experiment has the ability to sample the stationary morphology of an astrophysical outflow. Toroidal magnetic fields, which are self-generated in the plasma outflow owing to crossed density and temperature gradients (*14*), have a low amplitude in our study, because of the low laser intensity that we used (see methods). At the same time, they are limited to zones close (<0.5 mm) to the target surface and thus are not able to confine the flow beyond that (Fig. 1D): The plasma then freely expands at a wide angle. In short, this experimental configuration mimics well the expansion of one hemisphere of a naturally occurring YSO spherical wind that emerges at large distances from the disk, where acceleration is complete and gravitational effects are unimportant.

A steady (i.e., with duration >5 μs) and homogeneous axial magnetic field can be applied to the laboratory plasma (see methods). The magnetic field extends over a large volume (3 cm in length and 1 cm in diameter) with a strength of up to 0.4 MG (*15*). The plasma flow in this case is well approximated by ideal MHD (*16*), ensuring its relevance as a scaled astrophysical plasma. Indeed, the dimensionless Reynolds (*Re*), magnetic Reynolds (*ReM*), and Peclet (*Pe*) numbers are much larger than unity ($Re \sim 10^4$ to 10^5; *ReM* ~50; *Pe* ~ 3 to 5). This implies that the advective transport of momentum, magnetic field, and thermal energy dominates over diffusive transport, as expected in a YSO outflow. The strength of the magnetic field in which the plasma is embedded is much larger than in the astrophysical environment (on the order of milligauss) (*10*), to compensate for the shortness of the space and the time scales of the experiment. This means that the ratio of the plasma's kinetic ram pressure to magnetic pressure will transition from >>1 to <<1 over a few millimeters, while it does the same over a few tens of astronomical units in a YSO.

The typical morphology of our laboratory plasma, when applying the axial magnetic field to it, is shown in Fig. 1B. We present a measurement of the integrated electron density along the line of sight of the expanding plasma obtained through transverse optical laser probing. The axial magnetic field has a profound effect on the collimation of the laser-produced plasma flow, thus leading to the emergence of a narrow jet with an aspect ratio of >10 that is maintained over the entire homogeneous magnetic field region with little variation in density. Such tight collimation is also observed when imaging the x-ray emission in the kilo–electronvolt range originating from the plasma (see methods) and is in excellent agreement with our earlier MHD numerical investigations (*12*). We emphasize that even laser experiments specifically designed to produce jets from radiatively cooled, unmagnetized plasmas do not exhibit such morphology and have in fact much lower aspect ratios (*17*–*19*). The mechanism leading to the tight magnetic collimation of the plasma plume is illustrated in Fig. 1, C and D. We also present 3D resistive MHD numerical simulations using the parameters of the experiment (Fig. 2; see methods). When the laboratory plasma expands in the presence of a magnetic field (Fig. 1C), one clearly observes the formation of a converging cavity with an outer shell of higher electron density. We stress that neither the cavity nor the jet is observed when no magnetic field is applied (Fig. 1D). The formation of this shell is the consequence of the accumulation and heating of

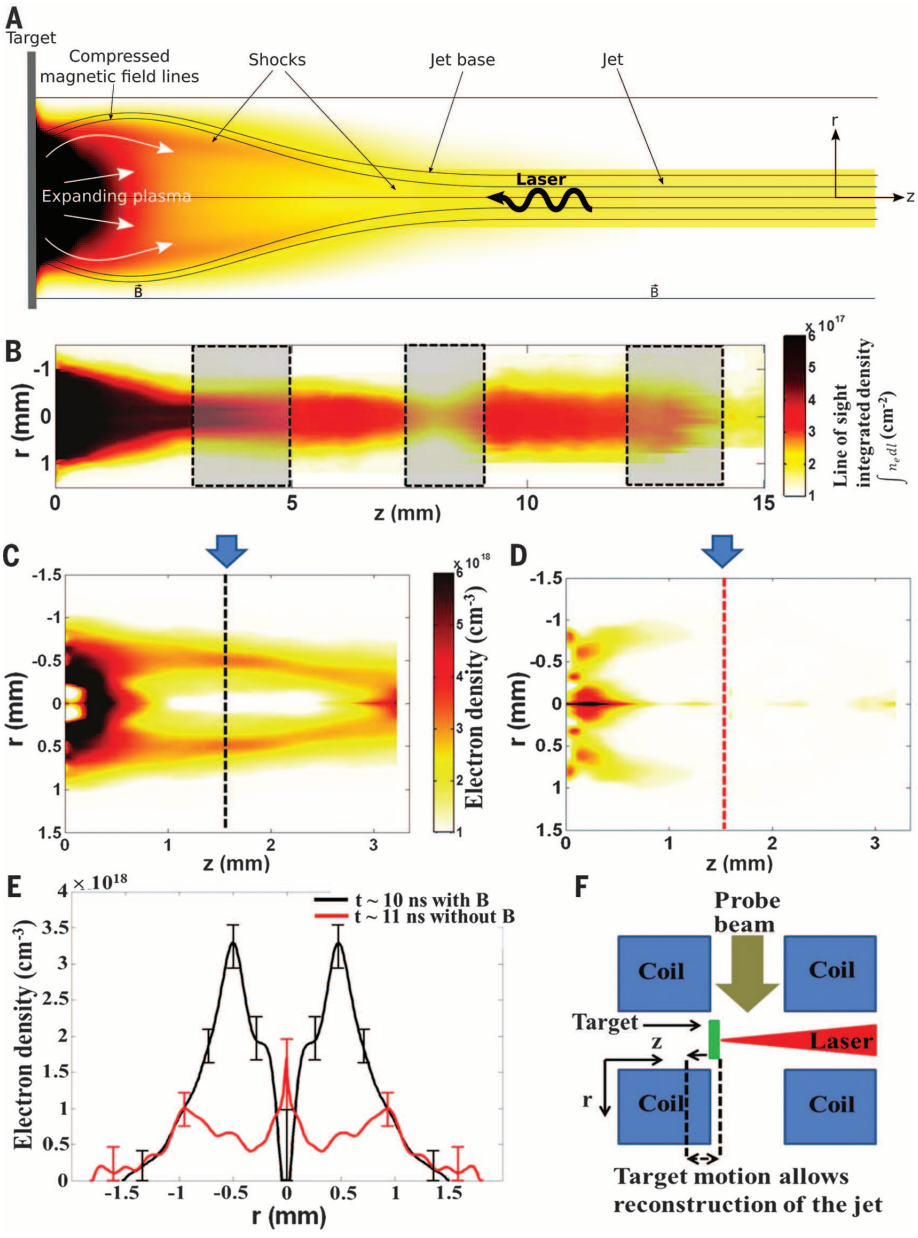

Fig. 1. Laboratory demonstration of jet formation by axial magnetic field. (**A**) Cartoon of the experiment and of the jet-formation mechanism. (**B**) Integrated plasma density measured 20 ns after the laser irradiation (from the right) of a plastic (CH) target (left) immersed in the *z*-oriented [see (A)] 0.2-MG magnetic field. Four images obtained with different target positions are used [see (F)]. Shaded areas indicate linear interpolation in between observed sections of the jet (in the middle section, flow gradients, converging on the left and diverging on the right, indicate the presence of a refocusing intermediate point). (**C** and **D**) Abel inverted density maps (the color map applies to both images) with (C) and without (D) a magnetic field; and (**E**) profiles [along the dashed lines shown in (C) and (D)] show the cavity region, and plasma convergence on-axis that is induced by the magnetic field. The error bars in (E) represent the difference in the plasma density retrieved by Abel inversion from the upper and lower measured phase maps (see methods). (**F**) Target and magnetic field arrangement used in the experiment.

plasma in a fast-mode oblique shock generated by the external magnetic field halting the radial expansion of the flow. Because the plasma is of high temperature and has a superfast-magnetosonic expansion speed (200 to 500 km/s, similar to the outflow velocity measured in YSO), the magnetic field lines are bent and compressed past this shocked envelope (Fig. 2).

The expanding plasma from the target is refracted across this oblique shock and slides along the walls of the cavity, which has been curved toward the axis by the magnetic forces. When the flow reaches a convergence point, it stagnates and forms a conical shock, which focuses the flow along the polar axis and generates a narrow jet ahead of the convergence point. This convergence of plasma toward the axis (at z ~3 mm) is visible in the experimental images (Fig. 1, B and C), and our simulations reveal that the plasma becomes heated to ~70 eV by this shock. When applying the external magnetic field, substantial plasma heating (compared to what is observed in the freely expanding plasma) is also seen by our spectrally resolved diagnostic that images the x-ray emission (see methods) (*20*). This mechanism of jet formation is similar to astrophysical models of hydrodynamic collimation of a wind by the inertia of a dense, torus-like circumstellar envelope (*21*). However, we demonstrate here that it can operate even in the absence of a surrounding medium.

The overall jet-formation process illustrated here for a particular set of laser and target conditions was repeatable and effective over a wide variety of different experimental conditions. The jets were always found to be in agreement with MHD modeling, hence validating the physical mechanism described above. Notably, when the laser intensity on the target was increased, we could increase the kinetic pressure at the target surface. This produced a wider cavity and moved the shock convergence region further away along the jet axis. Similarly, we could also move the distance of the shock with respect to the plasma source by varying the magnetic field strength. Contrary to what takes place in the experiment, if the deposition of energy was continuous, the location of the shock convergence region of the jet would be stationary. Finally, when we tilted the target and likewise the axis of the plasma expansion with respect to the magnetic field axis, we still observed the cavity formation and plasma focusing on-axis, even for angular offsets up to 40°, showing that the mechanism is robust.

We find the same morphology of the wind tightly focusing into a convergence point and forming a jet in the same direction in full-scale

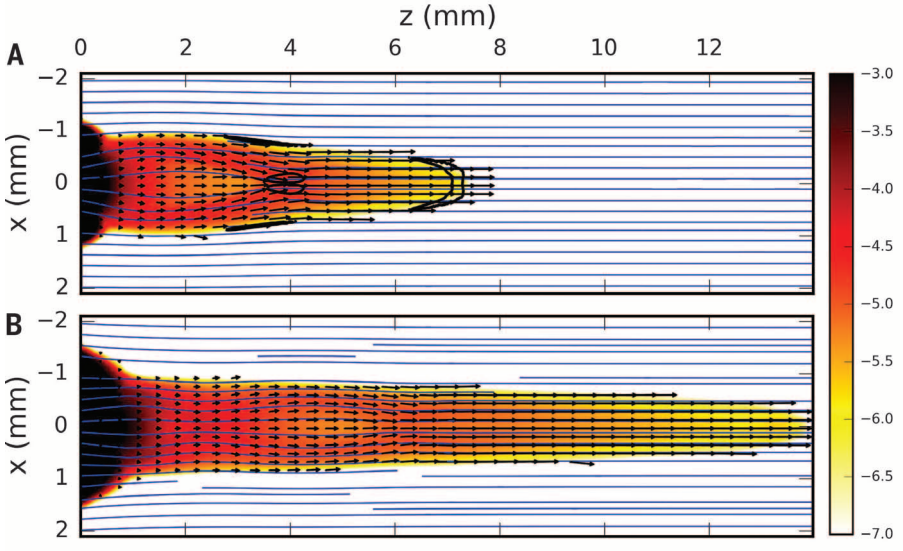

Fig. 2. Three-dimensional MHD modeling of the experiment. The maps show two snapshots [(**A**) 10 ns and (**B**) 20 ns from the end of the laser pulse] of the density ($\log_{10}$ ρ in g cm^{-3}) of the carbon plasma along the *x*-*z* plane. The arrows represent velocity vectors, and the lines represent the magnetic field. The black contour line shows plasma heated to a temperature above 70 eV.

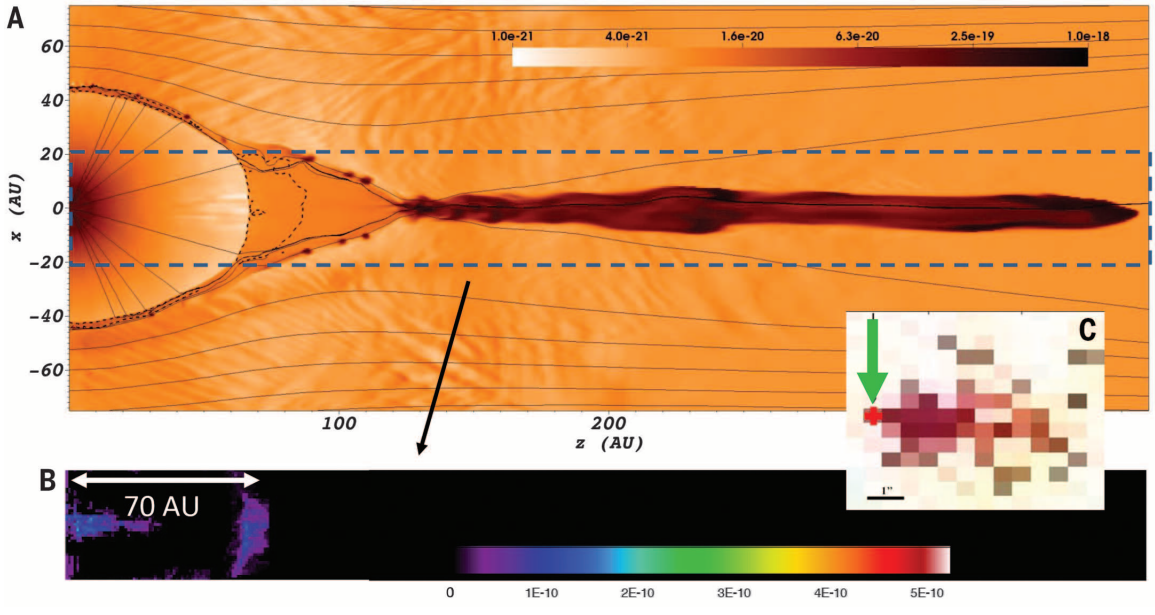

Fig. 3. Three-dimensional simulation of jet formation and collimation in a young star system embedded in a 5-mG axial magnetic field. An isotropic wind of H from the combined star–disk system with a mass ejection rate of 10^{-8} $M_\odot$/year and velocity 200 km/s is embedded in an initially axial (z) magnetic field. (**A**) (*x*-*z*) mass density ($\log_{10}$ ρ in g cm^{-3}) at time 20 years. Black lines: magnetic field lines; dashed contour: plasma of temperature ≥70 eV. (**B**) X-ray emission synthesized (see methods) from the simulated plasma of (A) (counts/s in each pixel with size of 1 AU). (**C**) X-ray emission image of HH154 as detected by the Chandra telescope. The color map ranges from white (no emission) to red. The stationary emission feature that is the brightest zone in the image, and that is located ~60 to 80 AU away from the star (located by the red dot at the tip of the green arrow), has a luminosity and a distance to the source that is consistent with the simulated bright region located at 70 AU in (B).

astrophysical simulations (Fig. 3A; see methods), performed with mass-ejection rates (*22*) and magnetic field strengths (*10*) typical of YSOs. We further verified that the range of density and temperature conditions found along the jet implies that the material within covers the full range of ionization fraction, with most of the jet part being only weakly ionized, consistent with observations (*23*). We see the principal dynamics and features of the laboratory flows also in the simulation results, which support the scalability of the laboratory experiment. We varied the wind and field parameters extensively with detailed numerical simulations to verify that the poloidal-field–induced jet collimation mechanism was a very robust process.

An interesting outcome of our study is that typical YSOs should then have a stationary region of shock-heated plasma that forms within a few tens to 100 AU from the wind source (see Fig. 3A). This numerical prediction can be directly compared to the analysis of observations made over more than one decade using x-ray satellites that have revealed (see Fig. 3C) bright sources of stationary x-ray emission zones located at the base of jets (~100 AU from the source) emerging from a YSO (*24*–*26*) and distinct from it. They have not been explained so far by self-collimation models of jet formation but are still consistent with the process revealed here (Fig. 3B).

We have therefore proposed a simple and plausible scenario for the collimation of a narrow stable jet past its launching phase (*1*, *2*) that is consistent with recent astrophysical observations (*10*, *24*, *25*). In addition to helping to advance the understanding of jet–core interaction in YSOs, our work enables studying and/or modeling important aspects of jet physics in the laboratory. These include, e.g., transverse instabilities that can affect the jet structure, or episodic ejections, i.e., multicomponent and time-dependent interacting winds, which can be easily simulated in the laboratory by using multiple laser pulses separated by a few nanoseconds. Producing such magnetized narrow plasma columns and letting them strike a solid will also uniquely allow the study of plasma dynamics in accretion columns in young stars; that is, one can model magnetic arches that are loaded with disk material that free-falls toward the star. Beyond these aspects, adapting the present experimental work to other configurations will permit advances in resolving pending questions about a wide range of astrophysical and plasma physics systems where magnetic fields are thought to play an important role.

REFERENCES AND NOTES

1. A. Frank, T. P. Ray, S. Cabrit, P. Hartigan, H. G. Arce, F. Bacciotti, J. Bally, M. Benisty, J. Eislöffel, M. Güdel, S. Lebedev, B. Nisini, A. Raga, *Jets and Outflows From Star to Cloud: Observations Confront Theory, in Protostars and Planets VI*, H. Beuther, R. Klessen, C. Dullemond, Th. Henning, Eds. (Univ. of Arizona Press, Tucson, 2014).
2. R. D. Blandford, D. G. Payne, *Mon. Not. R. Astron. Soc.* **199**, 883–903 (1982).
3. J. Ferreira, *Astron. Astrophys.* **319**, 340–359 (1997).
4. R. E. Ainsworth, T. P. Ray, A. M. M. Scaife, J. S. Greaves, R. J. Beswick, *Mon. Not. R. Astron. Soc.* **436**, L64–L68 (2013).
5. M. Stute, J. Gracia, K. Tsinganos, N. Vlahakis, *Astron. Astrophys.* **516**, A6 (2010).
6. R. Moll, H. C. Spruit, M. Obergaulinger, *Astron. Astrophys.* **492**, 621–630 (2008).
7. T. Matsakos *et al.*, *Astron. Astrophys.* **502**, 217–229 (2009).
8. H. C. Spruit, T. Foglizzo, R. Stehle, *Mon. Not. R. Astron. Soc.* **288**, 333–342 (1997).
9. S. Matt, R. Winglee, K.-H. Böhm, *Mon. Not. R. Astron. Soc.* **345**, 660–670 (2003).
10. P. Hartigan, A. Frank, P. Varniére, E. G. Blackman, *Astrophys. J.* **661**, 910–918 (2007).
11. N. L. Chapman *et al.*, *Astrophys. J.* **770**, 151 (2013).
12. A. Ciardi *et al.*, *Phys. Rev. Lett.* **110**, 025002 (2013).
13. F. Favata *et al.*, *Astron. Astrophys.* **450**, L17–L20 (2006).
14. J. A. Stamper, *Laser Part. Beams* **9**, 841–862 (1991).
15. B. Albertazzi *et al.*, *Rev. Sci. Instrum.* **84**, 043505 (2013).
16. D. D. Ryutov, R. P. Drake, B. A. Remington, *Astrophys. J. Suppl. Ser.* **127**, 465–468 (2000).
17. D. Farley *et al.*, *Phys. Rev. Lett.* **83**, 1982–1985 (1999).
18. B. Loupias *et al.*, *Phys. Rev. Lett.* **99**, 265001 (2007).
19. Ph. Nicolaï *et al.*, *Phys. Plasmas* **15**, 082701 (2008).
20. A. Faenov *et al.*, *Phys. Scr.* **53**, 591–596 (1996).
21. B. Balick, A. Frank, *Annu. Rev. Astron. Astrophys.* **40**, 439–486 (2002).
22. S. Cabrit, in *Star-Disk Interaction in Young Stars*, Proceedings IAU Symp. no. 243, J. Bouvier, I. Appenzeller, Eds. (Cambridge Univ. Press, Cambridge, 2007), pp. 203–214.
23. L. Maurri *et al.*, *Astron. Astrophys.* **565**, A110 (2014).
24. M. Güdel, S. L. Skinner, M. Audard, K. R. Briggs, S. Cabrit, *Astron. Astrophys.* **478**, 797–807 (2008).
25. P. C. Schneider, H. M. Günther, J. H. M. M. Schmitt, *Astron. Astrophys.* **530**, A123 (2011).
26. R. Bonito *et al.*, *Astrophys. J.* **737**, 54 (2011).

ACKNOWLEDGMENTS

We acknowledge the support of the LULI teams and of S. Dittrich and S. Nitsche (Helmholtz–Zentrum Dresden–Rossendorf) and discussions with P. Audebert. This work was supported by grant E1127 from Région Ile-de-France, Agence Nationale de la recherche (ANR) white grant 12-BS09-025-01 SILAMPA, grant ELAM from Réseau thématique de recherche avancé (RTRA)-Saclay, a grant from RTRA–Triangle de la Physique, grants Engineering and Physical Sciences Research Council (EPSRC) EP/I029206/1 and EP/J500094/1, and the Natural Sciences and Engineering Research Council of Canada (NSERC) Discovery grant 26558-2007 RGPIN. This work was partly done within the LABEX Plas@Par project and received financial state aid managed by the Agence Nationale de la Recherche, as part of the program "Investissements d'avenir" under the reference ANR-11-IDEX-0004-02. This work was supported in part by the Ministry of Education and Science of the Russian Federation under contract no. 14.Z50.31.0007. S.N.C. acknowledges the support received during this work by NSF grant 1064468. Experimental data and simulations are, respectively, archived on servers at LULI and LERMA laboratories and can be consulted upon demand. Part of the experimental system is covered by a patent (1000183285, 2013, Institut National de la Propriété Industrielle–France).

SUPPLEMENTARY MATERIALS

www.sciencemag.org/content/346/6207/325/suppl/DC1
Materials and Methods
References (*27*–*32*)

6 August 2014; accepted 17 September 2014
10.1126/science.1259694

OPTICS

Loss-induced suppression and revival of lasing

B. Peng,[1]* Ş. K. Özdemir,[1]*† S. Rotter,[2] H. Yilmaz,[1] M. Liertzer,[2] F. Monifi,[1] C. M. Bender,[3] F. Nori,[4,5] L. Yang[1]†

Controlling and reversing the effects of loss are major challenges in optical systems. For lasers, losses need to be overcome by a sufficient amount of gain to reach the lasing threshold. In this work, we show how to turn losses into gain by steering the parameters of a system to the vicinity of an exceptional point (EP), which occurs when the eigenvalues and the corresponding eigenstates of a system coalesce. In our system of coupled microresonators, EPs are manifested as the loss-induced suppression and revival of lasing. Below a critical value, adding loss annihilates an existing Raman laser. Beyond this critical threshold, lasing recovers despite the increasing loss, in stark contrast to what would be expected from conventional laser theory. Our results exemplify the counterintuitive features of EPs and present an innovative method for reversing the effect of loss.

Dissipation is ubiquitous in nature; the states of essentially all physical systems thus have a finite decay time. A proper description of this situation requires a departure from conventional Hermitian models with real eigenvalues and orthogonal eigenstates to non-Hermitian models featuring complex eigenvalues and nonorthogonal eigenstates (*1*–*3*). When tuning the parameters of such a dissipative system, its complex eigenvalues and the corresponding eigenstates may coalesce, giving rise to a non-Hermitian degeneracy, also called an exceptional point (EP) (*4*). The presence of such an EP has a dramatic effect on the system, leading to nontrivial physics with interesting counterintuitive features such as resonance trapping (*5*), a mode exchange when encircling an EP (*6*), and a singular topology in the parameter landscape (*7*). These characteristics can control the flow of light in optical devices with both loss and gain. In particular, waveguides with parity-time symmetry (*8*), where loss and gain are balanced, have attracted enormous attention (*9*, *10*), with effects

[1]Department of Electrical and Systems Engineering, Washington University, St. Louis, MO 63130, USA. [2]Institute for Theoretical Physics, Vienna University of Technology, A-1040 Vienna, Austria. [3]Department of Physics, Washington University, St. Louis, MO 63130, USA. [4]Center for Emergent Matter Science, RIKEN, Wako-shi, Saitama 351-0198, Japan. [5]Department of Physics, University of Michigan, Ann Arbor, MI 48109, USA.
*These authors contributed equally to this work. **†Corresponding author. E-mail: ozdemir@ese.wustl.edu (S.K.O.); yang@ese.wustl.edu (L.Y.)**

such as loss-induced transparency (*11*), unidirectional invisibility (*12*), and reflectionless scattering (*13*, *14*) having already been observed.

Theoretical work indicates that EPs give rise to many more intriguing effects when they occur near the lasing regime; for example, enhancement of the laser linewidth (*15*, *16*), fast self-pulsations (*15*), and a pump-induced lasing death (*17*). Realizing such anomalous phenomena, however, requires moving from waveguides to resonators, which can trap and amplify light resonantly beyond the lasing threshold. With the availability of such devices (*18*, *19*), we discuss here the most counterintuitive aspect, namely, that close to an exceptional point, lasing should be inducible solely by adding loss to a resonator.

Our experimental system (*20*) consists of two directly coupled silica whispering-gallery-mode resonators (WGMRs), μR_1 and μR_2, each coupled to a different fiber-taper, WG1 and WG2 (Fig. 1A and supplementary text S1). The resonance frequencies of the WGMRs were tuned to be the same via the thermo-optic effect, and a controllable coupling strength κ was achieved between the WGMRs by adjusting the interresonator distance. To observe its behavior in the vicinity of an EP, the system was steered parametrically via κ and an additional loss γ_{tip} induced on μR_2 by a chromium (Cr)–coated silica-nanofiber tip (Fig. 1, B and C), which features strong absorption in the 1550-nm band. The strength of γ_{tip} was increased by enlarging the volume of the nanotip within the μR_2 mode field, resulting in a broadened resonance linewidth with no observable change in resonance frequency (Fig. 1D). A small fraction of the scattered light from the nanotip coupled back into μR_2 in the counter-propagating (backward) direction and led to a resonance peak whose linewidth broadened as the loss increased (Fig. 1E). The resonance peak in the backward direction was ~$1/10^4$ of the input field, confirming that the linewidth broadening and the decrease of the resonance depth in the forward direction were due to γ_{tip} via absorption and scattering losses, but not due to backscattering into the resonator.

In the first set of experiments, WG2 was moved away from μR_2 to eliminate the coupling between them. We investigated the evolution of the eigenfrequencies and the transmission spectra $T_{1\to2}$ from input port 1 to output port 2 by continuously increasing γ_{tip} while keeping κ fixed. In this configuration, losses experienced by μR_1 and μR_2 were $\gamma_1' = \gamma_1 + \gamma_{c1}$ and $\gamma_2' = \gamma_2 + \gamma_{tip}$, where γ_{c1} is the WG1-μR_1 coupling loss, and γ_1 and γ_2 include material absorption, scattering, and radiation losses of μR_1 and μR_2. The coupling between the WGMRs led to the formation of two supermodes with complex eigenfrequencies $\omega_\mp = \omega_0 - i\chi \mp \beta$ whose real and imaginary parts are respectively denoted by $\omega_\mp'$ and $\omega_\mp''$ (*20*). Here, ω_0 is the resonance frequency of the solitary WGMRs; $\chi = (\gamma_1' + \gamma_2')/4$ and $\Gamma = (\gamma_1' - \gamma_2')/4$, respectively, quantify the total loss and the loss contrast of the WGMRs; and $\beta = \sqrt{\kappa^2 - \Gamma^2}$ reflects the transition between the strong and the weak intermode coupling regimes due to an interplay of the interresonator coupling strength κ and the loss contrast Γ (supplementary text S1). In the strong-coupling regime, quantified by $\kappa > |\Gamma|$ and real β, the supermodes had different resonance frequencies (mode splitting of 2β) but the same linewidths quantified by χ. This was reflected as two spectrally separated resonance modes in $T_{1\to2}$ [Fig. 2A (i)] and in the corresponding eigenfrequencies [Fig. 2B (i)]. Because our system satisfied $\gamma_1 + \gamma_{c1} > \gamma_2$, introducing γ_{tip} to μR_2 increased the amount of splitting until $\gamma_1 + \gamma_{c1} = \gamma_2 + \gamma_{tip}$ (that is, $\gamma_1' = \gamma_2'$) was satisfied [Fig. 2, A (ii) and B (ii)]. Increasing γ_{tip} beyond this point gradually led to an overlap of the supermode resonances [Fig. 2A (iii)], such as to necessitate a fit to a theoretical model to extract the complex resonance parameters (supplementary text S1 and S2) (*20*). At $\gamma_{tip} = \gamma_{tip}^{EP}$ where $\kappa = |\Gamma|$, the supermodes coalesced at the EP. With a further increase of γ_{tip}, the system entered the weak-coupling regime, quantified by $\kappa < |\Gamma|$ and imaginary β, which led to two supermodes with the same resonance frequency but different linewidths [Fig. 2, A (iv) and B (iv)]. The resulting resonance trajectories in the complex plane clearly displayed a reversal of eigenvalue evolution (Fig. 2B): The real parts of the eigenfrequencies of the system approached each other while their imaginary parts remained equal until the EP. After passing the EP, their imaginary parts were repelled, which resulted in an increasing imaginary part for one of the eigenfrequencies and a decreasing imaginary part for the other. As a result, one of the modes became less lossy, whereas the other became more lossy (supplementary text S4).

By repeating the experiments for different κ and γ_{tip}, we obtained the eigenfrequency surfaces $\omega_\mp(\kappa, \gamma_2')$, whose real and imaginary parts are shown in Fig. 2, C and D. The resulting surfaces exhibit a complex square root–function topology with the special feature that a coalescence of the eigenfrequencies can be realized by varying either κ or γ_{tip} alone, which leads to a continuous thread of EPs along what may be

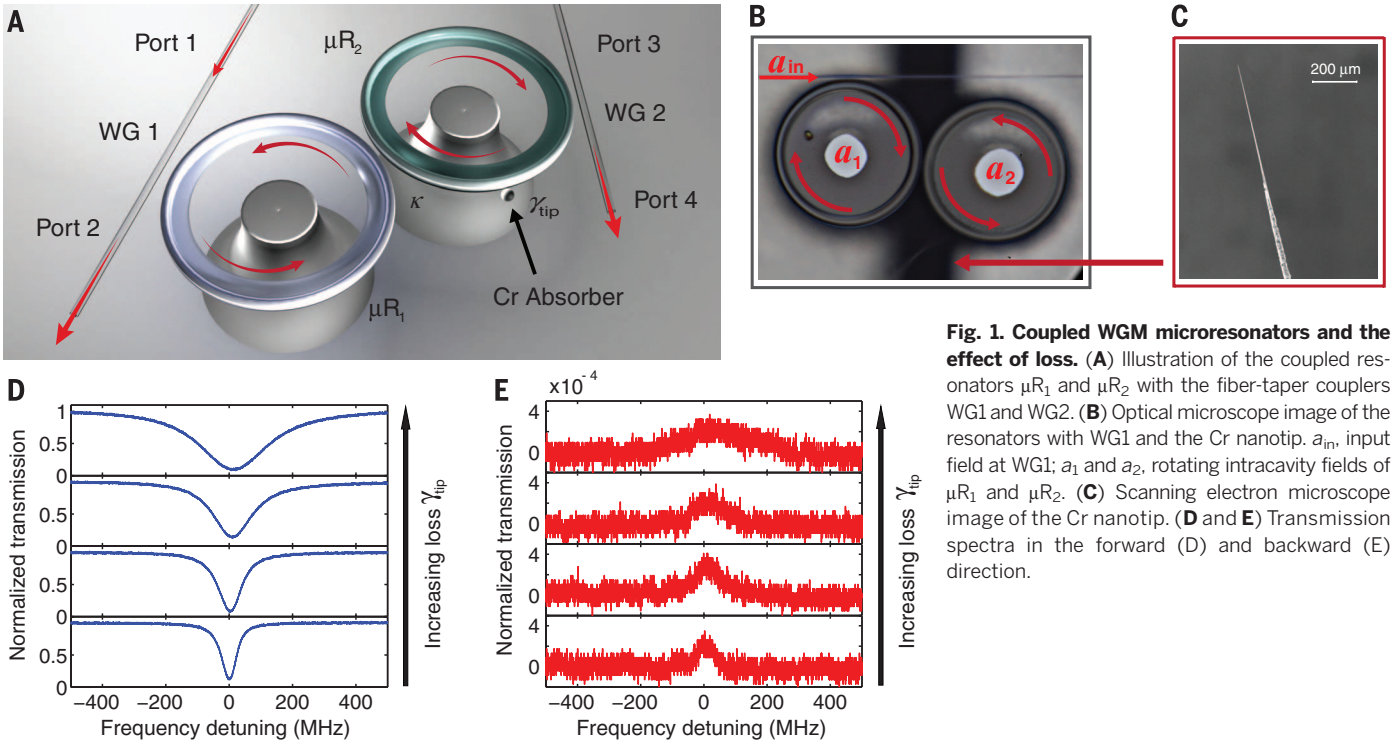

Fig. 1. Coupled WGM microresonators and the effect of loss. (**A**) Illustration of the coupled resonators μR_1 and μR_2 with the fiber-taper couplers WG1 and WG2. (**B**) Optical microscope image of the resonators with WG1 and the Cr nanotip. a_{in}, input field at WG1; a_1 and a_2, rotating intracavity fields of μR_1 and μR_2. (**C**) Scanning electron microscope image of the Cr nanotip. (**D** and **E**) Transmission spectra in the forward (D) and backward (E) direction.

called an exceptional line. As expected, the slope of this line is such that stronger κ requires higher γ_{tip} to reach the EP (supplementary text S4).

Our second set of experiments was designed to elucidate the effect of the EP on the intracavity field intensities. For this we used both WG1 and WG2, introducing an additional coupling loss γ_{c2} to μR_2 (that is, $\gamma_2' = \gamma_2 + \gamma_{tip} + \gamma_{c2}$). We tested two different cases by choosing different mode

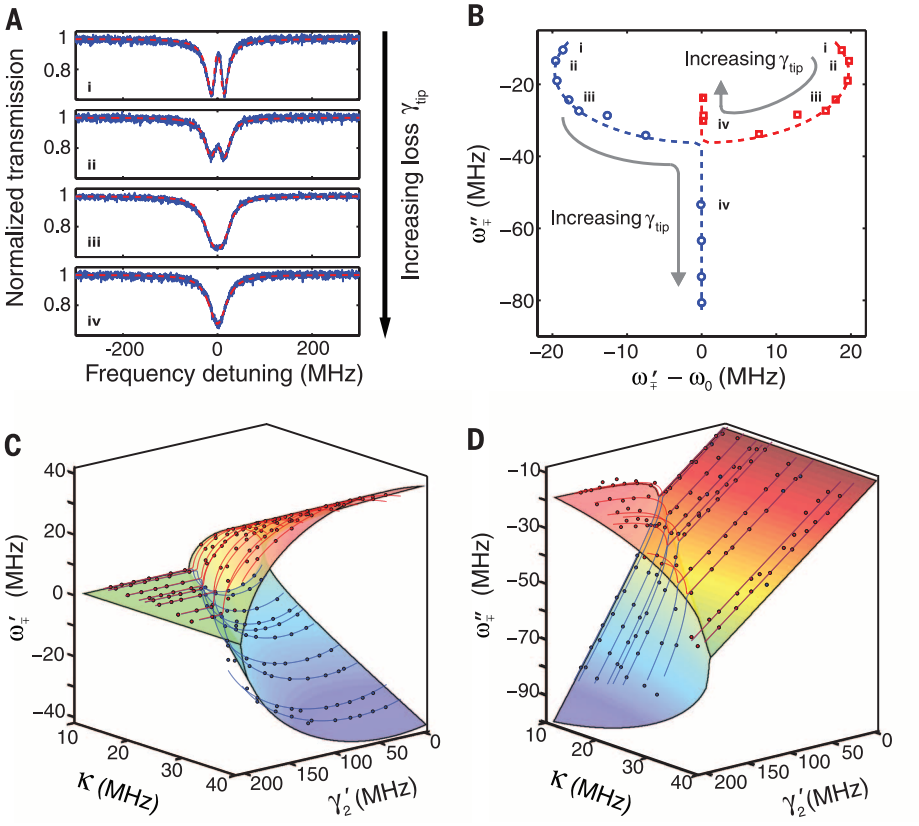

Fig. 2. Evolution of the transmission spectra and the eigenfrequencies as a function of loss γ_{tip} and interresonator coupling strength κ. (**A**) Transmission spectra $T_{1\to2}$ showing the effect of loss on the supermodes. Blue and red curves denote the experimental data and the best fit using a theoretical model (supplementary text S1 and S2), respectively. (**B**) Evolution of the eigenfrequencies of the supermodes in the complex plane as γ_{tip} was increased. Open circles and squares are the eigenfrequencies estimated from the measured $T_{1\to2}$. Dashed red and blue lines denote the best theoretical fit to the experimental data. (**C** and **D**) Eigenfrequency surfaces in the (κ,γ_2') parameter space (supplementary text S4).

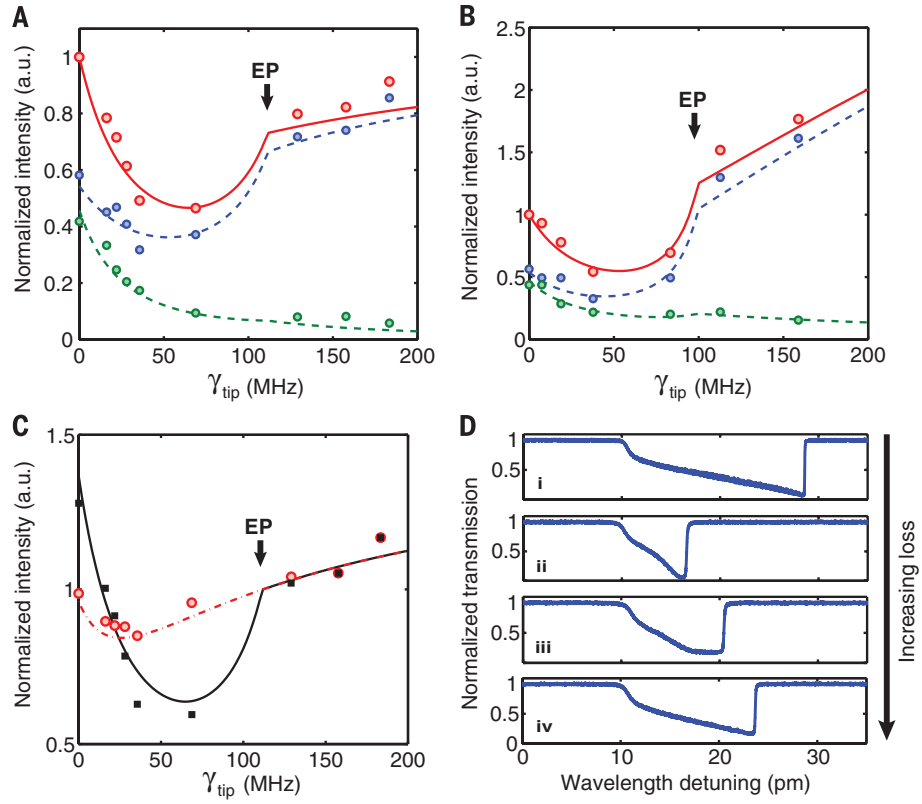

Fig. 3. Loss-induced enhancement of intracavity field intensities and thermal nonlinearity in the vicinity of an exceptional point. (**A** and **B**) Intracavity field intensities of the resonators at $\omega_{\mp}$ (blue, I_1 of μR_1; green, I_2 of μR_2; red, total I_T) for (A) case 1 and (B) case 2. Normalization was done with respect to the total intensity at $\gamma_{tip} = 0$. a.u., arbitrary units. (**C**) Total intracavity field intensities I_T at eigenfrequencies $\omega_{\mp}$ (black) and ω_0 (red) for case 1 (see supplementary text S5 for case 2). Normalization was done with respect to the intensity at the EP. (**D**) Effect of loss on nonlinear thermal response of coupled resonators (supplementary text S8): (i) solitary resonator, (ii) coupled resonators with $\gamma_{tip} = 0$, and (iii and iv) coupled resonators with increasing γ_{tip} (*20*). Circles in (A) to (C) and squares in (C) were calculated from experimentally obtained transmissions $T_{1\to2}$ and $T_{1\to4}$, whereas solid and dashed curves are from the theoretical model (supplementary text S1 to S3).

pairs in the resonators (*20*). In case 1, the mode in μR_1 had a higher loss than the mode in μR_2 ($\gamma_1 + \gamma_{c1} > \gamma_2 + \gamma_{c2}$); in case 2, the mode in μR_2 had a higher loss ($\gamma_1 + \gamma_{c1} < \gamma_2 + \gamma_{c2}$). The system was adjusted so that two spectrally separated supermodes were observed in the transmission spectra $T_{1\to2}$ and $T_{1\to4}$ as resonance dipped and peaked (supplementary text S3). No resonance dip or peak was observed at port 3. Using experimentally obtained $T_{1\to2}$ and $T_{1\to4}$, we estimated the intracavity fields I_1 and I_2 and the total intensity $I_T = I_1 + I_2$ as a function of γ_{tip} (Fig. 3, A to C, and supplementary text S1, S2, S5, and S6). As γ_{tip} was increased, I_T first decreased and then started to increase despite increasing loss. This loss-induced recovery of the intensity is in contrast to the expectation that the intensity would decrease with increasing loss and is a direct manifestation of the EP.

The effect of increasing γ_{tip} on I_1 and I_2 at $\omega_\mp$ is depicted in Fig. 3, A and B. When $\gamma_{tip} = 0$ and the system was set in the strong-coupling regime, the light input at μR_1 was freely exchanged between the resonators, establishing evenly distributed supermodes. As a result, the intracavity field intensities were almost equal. As γ_{tip} was increased, I_1 and I_2 decreased continuously at different rates until I_1 reached a minimum at $\gamma_{tip} = \gamma_{tip}^{min}$. The rate of decrease was higher for I_2 because of increasingly higher loss of μR_2. Beyond γ_{tip}^{min}, until the EP was reached at $\gamma_{tip} = \gamma_{tip}^{EP}$, the system remained in the strong-coupling regime, but the supermode distributions were strongly affected by γ_{tip}, which led to an increase of I_1 and, hence, of I_T, whereas no appreciable change was observed for I_2 (*20*). Increasing γ_{tip} further pushed the system beyond the EP, thereby completing the transition from the strong-coupling to the weak-coupling regime during which I_1 increased and kept increasing, whereas I_2 continued decreasing. This behavior is a manifestation of the progressive localization of one of the supermodes in the less lossy μR_1 and of the other supermode in the more lossy μR_2. We conclude that the nonmonotonic evolution of I_T for increasing values of γ_{tip} is the result of a transition from a symmetric to an asymmetric distribution of the supermodes in the two resonators (supplementary text S5 and S7).

The data shown in Fig. 3, A and B, also demonstrate that the initial loss contrast of the resonators affects both the amount of γ_{tip} required to bring the system to the EP and the intensity values themselves (*20*): Increasing γ_{tip} in case 2 increased I_T to a higher value than that at $\gamma_{tip} = 0$; in case 1, on the other hand, I_T stayed below its initial value at $\gamma_{tip} = 0$. Finally, Fig. 3C shows that the intracavity field intensities at $\omega_\mp$ and ω_0 coincide when $\gamma_{tip} \geq \gamma_{tip}^{EP}$; that is, after the EP transition to the weak coupling regime (*20*). This is a direct consequence of the coalescence of eigenfrequencies $\omega_\mp$ at ω_0 (supplementary text S5).

Whispering-gallery-mode microresonators (*21*) combine high-quality factor Q (long photon storage time, narrow linewidth) and high-finesse F (strong resonant power build-up) with microscale mode volume V (tight spatial confinement, enhanced resonant field intensity) and are thus ideal for studying quantum electrodynamics (*22*), optomechanics (*23*), lasing (*24*), and sensing (*25*–*27*). The ability of WGMRs to provide high intracavity field intensity and long interaction time reduces thresholds for nonlinear processes. Therefore, loss-induced reduction and the recovery of intracavity field intensities should have a direct effect on the thermal nonlinearity (*28*) and the Raman lasing (*24*, *29*) in WGMRs.

Thermal nonlinearity in WGMRs is due to the temperature-dependent resonance-frequency shifts caused by material absorption of the intracavity field and the resultant heating (*20*, *28*). In silica WGMRs, this is manifested as thermal broadening (or narrowing) of the resonance line when the wavelength of a probe laser is scanned from shorter to longer (or longer to shorter) wavelengths. In our system, thermal nonlinearity was observed in $T_{1\to2}$ as a shark-fin feature (Fig. 3D). With an input power of 600 μW, thermal broadening kicked in and made it impossible to resolve the individual supermodes [Fig. 3D (i and ii)]. When γ_{tip} was introduced and gradually increased, thermal nonlinearity and the associated linewidth broadening decreased at first but then gradually recovered [Fig. 3D (iii and iv)]. This aligns well with the evolution of the total intracavity field as a function of loss (supplementary text S8).

Finally, we tested the effect of the loss-induced recovery of the intracavity field intensity on Raman lasing in silica microtoroids (*29*, *30*). The threshold for Raman lasing scales as $P_{Raman\text{-}threshold} \propto V/g_R Q^2$ (where g_R is the Raman gain coefficient), implying the importance of the pump intracavity field intensity in the process. With a pump in the 1550-nm band, Raman lasing in the silica WGMR takes place in the 1650-nm band. Figure 4 depicts the spectrum and the efficiency of Raman lasing in our system. The lasing threshold for μR_1 was ~150 μW (Fig. 4B, blue curve). Keeping the pump power fixed, we introduced μR_2, which had a much larger loss than μR_1. This effectively increased the total loss of the system and annihilated the laser (Fig. 4A, gray curve). Introducing γ_{tip} to μR_2 helped to recover the Raman laser, whose intensity increased with increasing γ_{tip} (Fig. 4A). We also checked the lasing threshold of

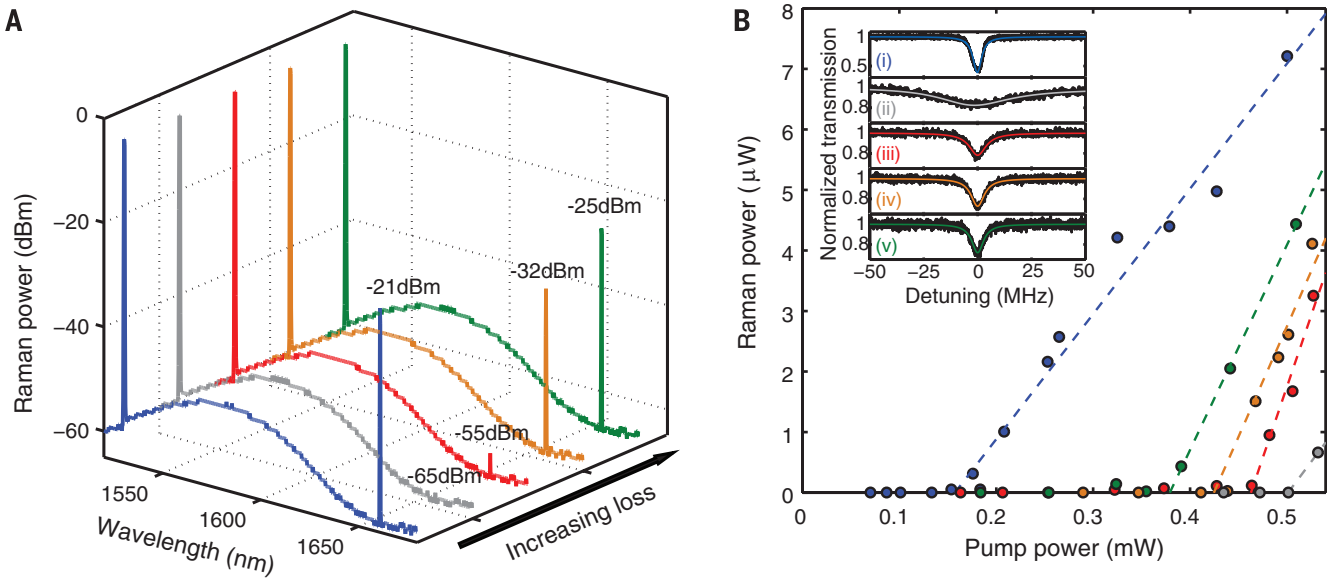

Fig. 4. Loss-induced suppression and revival of Raman lasing in silica microcavities. (**A**) Raman lasing spectra of coupled silica microtoroid resonators as a function of increasing loss. dBm, decibel-milliwatts. (**B**) Effect of loss on the threshold of Raman laser and its output power. The inset shows the normalized transmission spectra $T_{1\to2}$ in the pump band obtained at very weak powers for different amounts of additional loss. Loss increases from top to bottom. The curves with the same color code in (A), (B), and the inset of (B) are obtained at the same value of additionally introduced loss.

each of the cases depicted in Fig. 4A and observed that as γ_{tip} was increased, the $P_{Raman\text{-}threshold}$ increased at first but then decreased (Fig. 4B).

These observations are in stark contrast with what one would expect in conventional systems, where the higher the loss, the higher the lasing threshold. Surprisingly, in the vicinity of an EP, less loss is detrimental and annihilates the process of interest; more loss is good because it helps to recover the process. This counterintuitive effect happens because the supermodes of the coupled system readjust themselves as loss is gradually increased. When the loss exceeds a critical value, one supermode is mostly located in the subsystem with less loss and, thus, the total field can build up more strongly (*20*). As our results demonstrate, this behavior also affects nonlinear processes, such as thermal broadening and Raman lasing, that rely on intracavity field intensity.

Our system provides a comprehensive platform for further studies of EPs and opens up new avenues of research on non-Hermitian systems and their behavior. Our findings may also lead to new schemes and techniques for controlling and reversing the effects of loss in other physical systems, such as in photonic crystal cavities, plasmonic structures, and metamaterials.

REFERENCES AND NOTES

1. C. M. Bender, *Rep. Prog. Phys.* **70**, 947–1018 (2007).
2. I. Rotter, *J. Phys. Math. Theor.* **42**, 153001 (2009).
3. N. Moiseyev, *Non-Hermitian Quantum Mechanics* (Cambridge Univ. Press, Cambridge, 2011).
4. W. D. Heiss, *J. Phys. A* **37**, 2455–2464 (2004).
5. E. Persson, I. Rotter, H. Stöckmann, M. Barth, *Phys. Rev. Lett.* **85**, 2478–2481 (2000).
6. C. Dembowski *et al.*, *Phys. Rev. Lett.* **86**, 787–790 (2001).
7. S. B. Lee *et al.*, *Phys. Rev. Lett.* **103**, 134101 (2009).
8. C. M. Bender, S. Boettcher, *Phys. Rev. Lett.* **80**, 5243–5246 (1998).
9. R. El-Ganainy, K. G. Makris, D. N. Christodoulides, Z. H. Musslimani, *Opt. Lett.* **32**, 2632–2634 (2007).
10. C. E. Rüter *et al.*, *Nat. Phys.* **6**, 192–195 (2010).
11. A. Guo *et al.*, *Phys. Rev. Lett.* **103**, 093902 (2009).
12. A. Regensburger *et al.*, *Nature* **488**, 167–171 (2012).
13. L. Feng *et al.*, *Nat. Mater.* **12**, 108–113 (2013).
14. L. Feng *et al.*, *Opt. Express* **22**, 1760–1767 (2014).
15. H. Wenzel, U. Bandelow, H.-J. Wünsche, J. Rehberg, *IEEE J. Quantum Electron.* **32**, 69–78 (1996).
16. M. V. Berry, *J. Mod. Opt.* **50**, 63–81 (2003).
17. M. Liertzer *et al.*, *Phys. Rev. Lett.* **108**, 173901 (2012).
18. B. Peng *et al.*, *Nat. Phys.* **10**, 394–398 (2014).
19. M. Brandstetter *et al.*, *Nat. Commun.* **5**, 4034 (2014).
20. Supplementary materials are available on *Science* Online.
21. K. J. Vahala, *Nature* **424**, 839–846 (2003).
22. D. O'Shea, C. Junge, J. Volz, A. Rauschenbeutel, *Phys. Rev. Lett.* **111**, 193601 (2013).
23. T. J. Kippenberg, K. J. Vahala, *Science* **321**, 1172–1176 (2008).
24. L. He, S. K. Ozdemir, L. Yang, *Laser & Photon. Rev.* **7**, 60–82 (2013).
25. X. Fan *et al.*, *Anal. Chim. Acta* **620**, 8–26 (2008).
26. F. Vollmer, S. Arnold, *Nat. Methods* **5**, 591–596 (2008).
27. J. Zhu *et al.*, *Nat. Photonics* **4**, 46–49 (2010).
28. T. Carmon, L. Yang, K. Vahala, *Opt. Express* **12**, 4742–4750 (2004).
29. S. M. Spillane, T. J. Kippenberg, K. J. Vahala, *Nature* **415**, 621–623 (2002).
30. S. K. Ozdemir *et al.*, *Proc. Natl. Acad. Sci. U.S.A.* **111**, E3836–E3844 (2014).

ACKNOWLEDGMENTS

Ş.K.O. and L.Y. conceived the idea and designed the experiments. B.P. and Ş.K.O. performed the experiments with help from H.Y. and F.M. Theoretical background and simulations were provided by B.P., Ş.K.O., S.R., M.L., C.M.B., and F.N. All authors discussed the results, and Ş.K.O., S.R., and L.Y. wrote the manuscript with input from all authors. This work was supported by Army Research Office (ARO) grant no. W911NF-12-1-0026. C.M.B. was supported by U.S. Department of Energy grant no. DE-FG02-91ER40628. F.N. is partially supported by the RIKEN iTHES Project, Multidisciplinary University Research Initiatives (MURI) Center for Dynamic Magneto-Optics, Grant-in-Aid for Scientific Research (S). S.R. and M.L. are supported by the Vienna Science and Technology Fund (WWTF) project no. MA09-030 and by the Austrian Science Fund (FWF) project no. SFB-IR-ON F25-P14, SFB-NextLite F49-P10.

SUPPLEMENTARY MATERIALS

www.sciencemag.org/content/346/6207/328/suppl/DC1
Supplementary Text
Figs. S1 to S16
Table S1
References (*31*–*34*)

27 June 2014; accepted 11 September 2014
10.1126/science.1258004

QUANTUM ELECTRONICS

Cavity quantum electrodynamics with many-body states of a two-dimensional electron gas

Stephan Smolka,[1]* Wolf Wuester,[1,2]* Florian Haupt,[1] Stefan Faelt,[1,2] Werner Wegscheider,[2] Ataç Imamoglu[1]†

Light-matter interaction has played a central role in understanding as well as engineering new states of matter. Reversible coupling of excitons and photons enabled groundbreaking results in condensation and superfluidity of nonequilibrium quasiparticles with a photonic component. We investigated such cavity-polaritons in the presence of a high-mobility two-dimensional electron gas, exhibiting strongly correlated phases. When the cavity was on resonance with the Fermi level, we observed previously unknown many-body physics associated with a dynamical hole-scattering potential. In finite magnetic fields, polaritons show distinct signatures of integer and fractional quantum Hall ground states. Our results lay the groundwork for probing nonequilibrium dynamics of quantum Hall states and exploiting the electron density dependence of polariton splitting so as to obtain ultrastrong optical nonlinearities.

Strong electric-dipole coupling of excitons in an intrinsic semiconductor quantum well (QW) to microcavity photons leads to the formation of mixed light-matter quasiparticles called cavity-polaritons (*1*, *2*). In contrast to excitons, optical excitations from a two-dimensional electron gas (2DEG) show many-body effects associated with the abrupt turn-on of a valence-band hole-scattering potential. The resulting absorption spectrum exhibits a power-law divergence, stemming from final-state interaction effects that lead to orthogonal initial and final many-body wave functions, and is referred to as Fermi-edge singularity (*3*). Despite initial attempts (*4*–*6*), the nature of strong coupling of a Fermi-edge singularity, rather than an exciton, to a microcavity mode remained largely unexplored.

We investigated a 2DEG in a modulation-doped GaAs QW embedded in a distributed Bragg reflector (DBR) microcavity (Fig. 1A). We used this system to analyze two distinct problems: In the absence of an external magnetic field (B_z = 0), optical excitations from a 2DEG are simultaneously subject to Coulomb interactions and strong cavity coupling, which lead to the formation of Fermi-edge polaritons—a many-body excitation with a dynamical valence-hole scattering potential (*7*). In the $B_z \neq 0$ limit, we establish cavity quantum electrodynamics (QED) as a new paradigm for investigating integer and fractional quantum Hall (QH) states (*8*) in which information about a strongly correlated electronic ground state is transcribed onto the reflection and transmission amplitudes of a single-cavity photon.

The dispersion of the relevant electronic states when B_z = 0 is shown in Fig. 1B, left. The Fermi energy E_F is tuned by applying a gate voltage (V_g) between a p-doped GaAs top layer and the 2DEG. When $B_z \neq 0$, the electronic states form discrete Landau levels (LLs) (Fig. 1B, right). Each (spin-resolved) LL has a degeneracy $e\,B_z/h$; the filling factor $\nu = n_e\,h/(e\,B_z)$ determines the number of filled LLs at a given electron density n_e. We studied two different samples with gate-tunable n_e: sample *A* exhibits an electron mobility of $\mu = 2 \times 10^5$ cm^2(V s)$^{-1}$ at $n_e = 1.0 \times 10^{11}$ cm^{-2} (*9*). Sample *B* exhibits an order-of-magnitude-higher mobility of $\mu = 2.5 \times 10^6$ cm^2(V s)$^{-1}$ at $n_e = 2.3 \times 10^{11}$ cm^{-2}.

The differential reflectivity (dR) (*9*) spectra of sample *A* (blue) is shown in Fig. 1D as the electron density n_e in the 2DEG is varied from $n_e < 2 \times 10^{10}$ cm^{-2} to $n_e = 8 \times 10^{10}$ cm^{-2}. The cavity mode is visible as a dR peak at 1521 meV. Changing n_e modifies the nature of elementary optical excitations: At low electron densities

[1]Institute of Quantum Electronics, Eidgenössische Technische Hochschule (ETH) Zurich, 8093 Zurich, Switzerland. [2]Solid State Physics Laboratory, ETH Zurich, 8093 Zurich, Switzerland.
*These authors contributed equally to this work. †Corresponding author. E-mail: imamoglu@phys.ethz.ch

($n_e < 2 \times 10^{10}$ cm^{-2}), the QW spectrum is dominated by the heavy-hole exciton X^0_{hh} peak. The weak resonance on the red side of X^0_{hh} stems from the excitation of a bound state of two electrons and one hole (X^-, trion). For 2×10^{10} cm$^{-2} \leq n_e < 8 \times 10^{10}$ cm^{-2}, the trion transition emerges as the dominant feature in the spectrum. Increasing n_e leads to an asymmetry in the X^- line shape and a blue-shift of its center frequency (*10*). Last, for $n_e > 8 \times 10^{10}$ cm^{-2} the absorption spectrum is dominated by an asymmetric resonance at the Fermi edge (*11*). Photoluminescence (PL) spectra, obtained after tuning the cavity mode to 1531 meV, is shown with dR in Fig. 1D in orange. For $n_e > 6 \times 10^{10}$ cm^{-2}, the PL spectrum (*12*) exhibits a double-peaked structure with a total width that agrees well with E_F, which was estimated by using independently determined n_e (*9*).

We first address the confluence of Fermi-edge singularity and nonperturbative light-matter coupling (Fig. 2). In stark contrast to earlier work on edge singularity physics, our system exhibits a dynamical hole-scattering potential due to vacuum Rabi oscillations in the final state of the optical transition, and a finite hole recoil induced modification of the cavity-2DEG coupling. Prior work—based on a fixed n_e 2DEG embedded in a microcavity—demonstrated normal-mode splitting at a relatively high temperature of 2 K and used single-particle transfer-matrix calculations to obtain a fit to the data (*5*). However, we show that only by measuring the polariton dispersion as well as the n_e, mobility, and temperature dependence of the vacuum Rabi coupling is it possible to develop a consistent picture of the underlying many-body physics.

To demonstrate nonperturbative light-matter coupling, we fixed n_e to 1.2×10^{11} cm^{-2} in sample *A* and tuned the cavity mode across the absorption edge at E_F. When the cavity frequency E_c is resonant with E_F (Fig. 2A), we observe normal-mode splitting of $2g = (2.0 \pm 0.1)$ meV, with g denoting the dipole-coupling strength. Because $2g$ is larger than the bare-cavity linewidth $\Gamma_c = 1$ meV, it is concluded that the system is in the strong coupling regime of cavity-QED, where the elementary optical excitations could be described as trion/Fermi-edge polaritons (*5*, *13*). In contrast to the exciton-polariton excitations observed in undoped QWs coupled to microcavities (*1*), in our case the upper polariton is substantially broader than the lower polariton. This broadening and the asymmetry stem from the shake-up of the Fermi sea that accompanies bound-trion or Fermi-edge resonance formation (*6*).

The dispersion of Fermi-edge polaritons is shown in Fig. 2B. The data were obtained by measuring angle-resolved dR spectra (*14*) for a cavity detuning that yields minimal normal-mode splitting at normal incidence (Fig. 2A). We observed two split branches, each with an ultra-small effective polariton mass, which is approximately twice as large as that of the bare cavity-photon mass (*9*).

In order to study the density and mobility dependence of the Fermi-edge polaritons, we recorded the polariton excitations versus detuning from the Fermi edge at $n_e = 1.6 \times 10^{11}$ cm^{-2} on the high-mobility sample *B* (Fig. 2C). The data shows a significantly smaller normal-mode splitting as compared with that of sample *A* (Fig. 2A), which is a consequence of weaker hole confinement owing to higher n_e and mobility. A detailed study of the normal-mode splitting at resonance as a function of n_e is presented in Fig. 2D, showing a clear decrease from $2g = (2.0 \pm 0.1)$ meV to $2g = (1.3 \pm 0.2)$ meV as the density is increased from $n_e = 0.8 \times 10^{11}$ cm^{-2} to $n_e = 1.6 \times 10^{11}$ cm^{-2} (*9*). The scattering of an electron with momentum $\sim k_F$ on the Fermi surface is accompanied by a hole momentum kick, leading to a hole recoil energy E_r (*15*). A larger hole recoil partially inhibits the formation of the electron screening cloud as $n_e(k_F)$ is increased, resulting in the observed reduction of the normal-mode splitting.

Remarkably, polariton excitations depend strongly on temperature as well. When we compare the $n_e = 0.9 \times 10^{11}$ cm^{-2} dR spectrum at $T = 0.2$ K with the one at $T = 4$ K (Fig. 2D, inset), we observe that the normal-mode splitting disappears at $T = 4$ K. This observation is striking because the corresponding splitting at $T = 0.2$ K ($2g = 1.3 \pm 0.2$ meV) is larger than the thermal energy $E_T = 345$ μeV at $T = 4$ K.

Our experimental findings point to a scenario in which the nonperturbative cavity-QW coupling leads to the formation of Fermi-edge polaritons for $n_e > 8 \times 10^{10}$ cm^{-2}. In contrast to the Fermi-edge singularity associated with screening of a localized hole by the Fermi sea (*4*, *6*), these new many-body optical excitations are delocalized as demonstrated by the polariton dispersion (Fig. 2B). A key requirement for the observation of Fermi-edge polaritons is that the cavity-QW coupling strength exceeds E_r: in this limit, the enhancement of the 2DEG-cavity coupling by optical excitations with energy $\geq E_F + E_r$ ensures strong coupling, albeit with reduced normal-mode splitting. This conclusion is supported by the reduction of normal-mode splitting (Fig. 2D) with increasing n_e, or equivalently, increasing E_r observed in the high-mobility

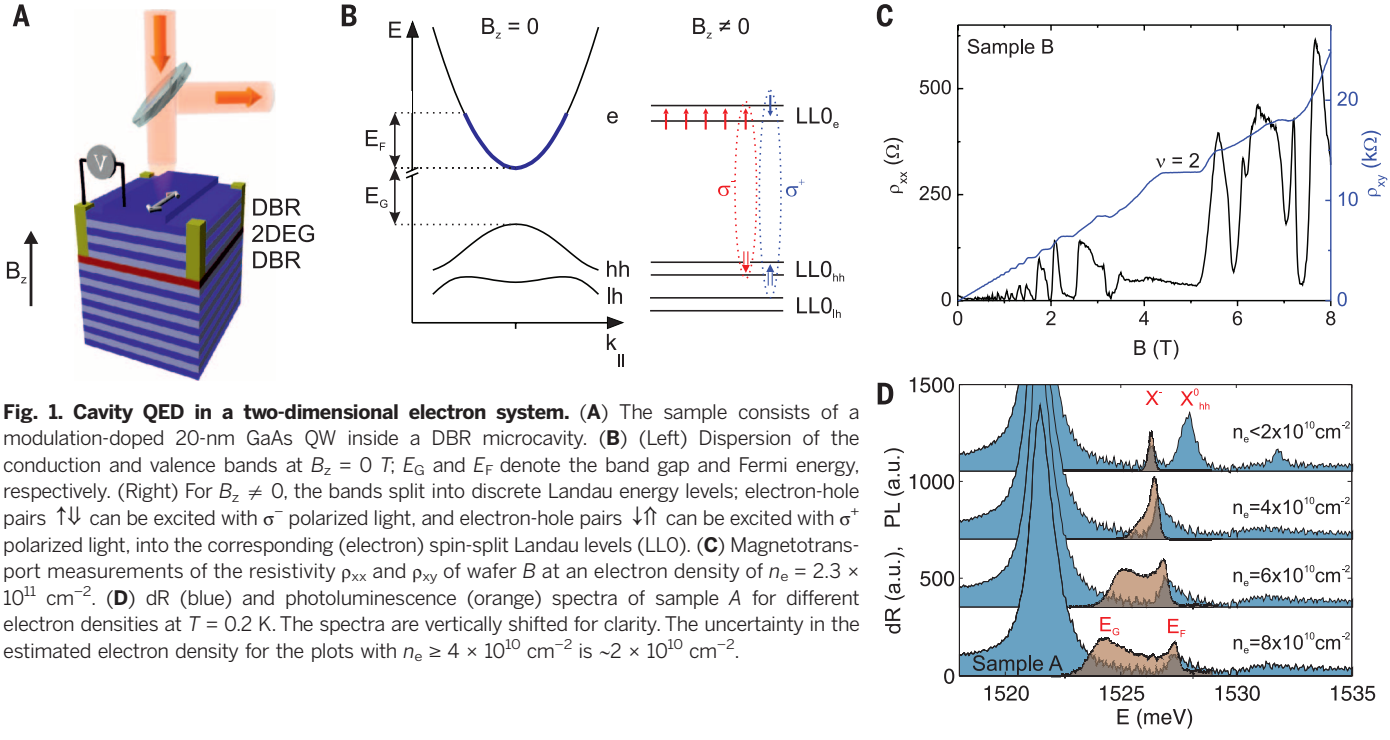

Fig. 1. Cavity QED in a two-dimensional electron system. (**A**) The sample consists of a modulation-doped 20-nm GaAs QW inside a DBR microcavity. (**B**) (Left) Dispersion of the conduction and valence bands at $B_z = 0$ *T*; E_G and E_F denote the band gap and Fermi energy, respectively. (Right) For $B_z \neq 0$, the bands split into discrete Landau energy levels; electron-hole pairs ↑⇓ can be excited with σ^- polarized light, and electron-hole pairs ↓⇑ can be excited with σ^+ polarized light, into the corresponding (electron) spin-split Landau levels (LL0). (**C**) Magnetotransport measurements of the resistivity ρ_{xx} and ρ_{xy} of wafer *B* at an electron density of $n_e = 2.3 \times 10^{11}$ cm^{-2}. (**D**) dR (blue) and photoluminescence (orange) spectra of sample *A* for different electron densities at $T = 0.2$ K. The spectra are vertically shifted for clarity. The uncertainty in the estimated electron density for the plots with $n_e \geq 4 \times 10^{10}$ cm^{-2} is ~2×10^{10} cm^{-2}.

sample *B*. Conversely, the persistence of polariton splitting implies that the hole population in the QW exhibits Rabi oscillations, leading to a time-dependent scattering potential.

In contrast to the $B_z = 0$ limit at which the initial state of the optical transition is a Fermi sea without interaction-induced correlations, the electronic states for $B_z \neq 0$ in the absence of photonic excitations are QH states. We analyzed polariton excitations out of these many-body states by performing polarization-resolved dR measurements. Because the absorption of right-hand circularly polarized σ^+ light generates a spin-down $|\downarrow\rangle$ electron and a $|\Uparrow\rangle$ heavy-hole, and absorption of left-hand circularly polarized σ^- light generates a spin-up $|\uparrow\rangle$ electron and a $|\Downarrow\rangle$ heavy-hole, the observed spectrum is highly sensitive to spin polarization-dependent phase-space-filling. When the magnetic field is increased, the filling factor ν is reduced, allowing optical absorption into LLs that are no longer (completely) filled. In Fig. 3, A and B, the cavity resonance on sample *B* is tuned to $E = 1523.8$ meV. In the low field range ($B_z = 0 - 2$ T), absorption into higher lying empty LLs ($\nu \geq 2$), enabled by the weak off-resonant coupling of these resonances to the cavity mode, is visible.

The reflection spectrum from the lowest LL (LL0) at $n_e = 1.4 \times 10^{11}$ cm^{-2} (Fig. 3, A and B) shows that a finite polariton splitting emerges at $B_z \sim 3$ T ($\nu \sim 2$). To study the resonant interaction between the cavity mode and the optical excitations of QH states, we fixed $B_z = 3$ T, tuned the cavity to resonance with the LL0 spin-up (σ^-) transition at $\nu = 2$, and varied n_e through V_g. For both light polarizations, only the bare cavity resonance is visible for $\nu \geq 2$ because phase-space-filling blocks all 2DEG optical excitations at E_c (Fig. 3, C and D). In contrast, a normal-mode splitting appears for $\nu < 2$; the splitting grows monotonically as n_e is reduced because the number of available final states is thereby increased. The normal-mode splitting of σ^+ polarization starts at higher ν than the one of σ^-, suggesting that 2DEG electrons remain spin-polarized for $1.7 \leq \nu < 2.0$.

Unlike the $B_z = 0$ case, the normal-mode splitting at $B_z \neq 0$ is comparable with that of a heavy-hole exciton polariton in the limit $n_e \rightarrow 0$, pointing to a reduced screening of electron-hole attraction. The dominant optical excitations into LL0 for $1 < \nu < 2$ can be described as heavy-hole singlet trions (*16*) because the strongest binding energy and the highest optical oscillator strength would be obtained for a complex of two electrons of opposite spin in the same electronic orbital *m* of size $\cong a_m = \sqrt{\hbar/eB_z}$ and a heavy-hole with a strong spatial overlap. Such a trion could have an absorption strength comparable with that obtained for an exciton because the magnetic length a_m is comparable with the exciton Bohr radius for $B_z \sim 5$T.

By increasing the magnetic field to $B_z = 4.9$ T, we explored polariton excitations around $\nu = 1$. In Fig. 3, E and F, we see a drastic change in the optical response: Whereas the normal-mode splitting collapses for σ^- light, it increases sharply for σ^+. This feature shows the emergence of a high degree of spin polarization, which we associate with the $\nu = 1$ integer QH state (*17*, *18*). In case of full spin polarization, the oscillator strength ($\propto g^2$) of the σ^+ polariton excitations is maximum because no $|\downarrow\rangle$ states are occupied. For $\nu = 1$, the degree of spin polarization, $P = (g^2_{\sigma^+} - g^2_{\sigma^-})/(g^2_{\sigma^+} + g^2_{\sigma^-})$, is determined from the measured minimum normal-mode splittings and found to be $P = 90 \pm 10\%$. The error arises primarily from the measurement uncertainty of the individual splittings and simultaneous coupling to higher lying optical transitions. As we moved away to both sides from $\nu = 1$ by changing either V_g or B_z, we observed a symmetric decrease of the normal-mode splitting for the σ^- polariton excitations and a symmetric increase of the normal-mode splitting for the σ^+ polariton excitations, which we attribute to spin-depolarization due to skyrmion excitations (*19*).

In order to investigate fractional QH states, we tuned E_c into resonance with the $|\downarrow\rangle$-transition of LL0 at $\nu = 2/3$. dR spectra at $B_z = 6$ T as a function of n_e is presented in Fig. 4, A and B. For $\nu \cong 2/3$, we observed a small decrease in the normal-mode splitting for the σ^- polariton modes and a small increase in the normal-mode splitting for the σ^+ polariton modes, which points to enhanced spin polarization associated with the $\nu = 2/3$ fractional QH state (*20*, *21*). The small change in the splitting stems from the sizeable degree of spin polarization that persists for $\forall \nu < 1$ and the fact that even for complete spin polarization at $\nu = 2/3$, one third of the states in the spin-up LL0 are available for excitonic excitations. To highlight the variations in the normal-mode splitting, we plot in Fig. 4C the energy difference ΔE_{LP} between the dR peaks of the σ^+ and σ^- lower polariton branches as a function of ν at $B_z = 6$ T (blue circles): A local maximum in ΔE_{LP} around the fractional QH state $\nu = 2/3$ signifies spin polarization (*22*–*25*). To confirm that the peak in ΔE_{LP} at $\nu = 2/3$ does not have an auxiliary origin, we spatially tuned the cavity mode to $E_{\nu=1}$ (Fig. 4C, red squares) and found that the local maximum in ΔE_{LP} at $\nu = 2/3$ persists.

It has been previously established that a phase transition from an unpolarized $\nu = 2/3$ to a polarized $\nu = 2/3$ QH ground state takes place at a critical magnetic field B_c that depends strongly on the effective width of the electron wave function (*26*, *27*). At a lower magnetic field of $B_z = 4.9$ T (Figs. 3, E and F), we did not observe a local maximum in ΔE_{LP} at $\nu = 2/3$ (Fig. 4C), suggesting that the excess spin polarization is lost; this observation is consistent with a phase transition from an unpolarized to a polarized $\nu = 2/3$ state.

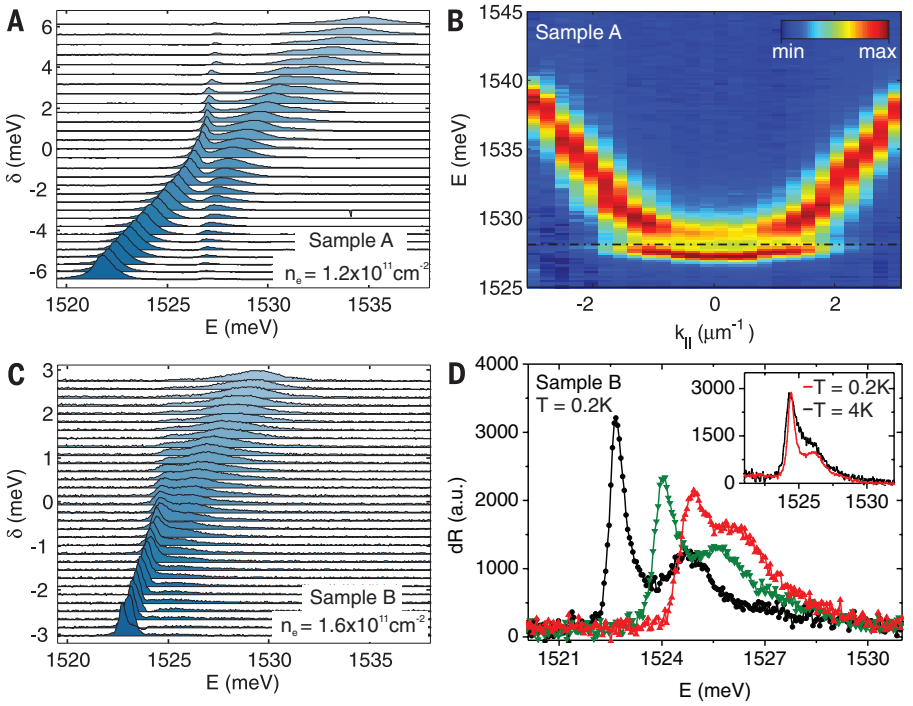

Fig. 2. Experimental signatures of Fermi-edge polaritons. (**A**) dR spectra taken from sample *A* as a function of cavity detuning δ from the Fermi edge at $T = 0.2$ K and $n_e = 1.2 \times 10^{11}$ cm^{-2}. (**B**) Fermi-edge polariton energy dispersion obtained at $T = 1.6$ K, $n_e = 1.2 \times 10^{11}$ cm^{-2}, and $\delta = 0$. The dashed straight line depicts the Fermi energy. The blue color-coded area displays low dR signal, and the red color-coded area displays high dR signal. (**C**) dR spectra measured on sample *B* versus cavity detuning at $T = 0.2$ K and $n_e = 1.6 \times 10^{11}$ cm^{-2}. (**D**) dR spectra for different densities from sample *B* at $\delta = 0$ and $T = 0.2$ K for $n_e = 0.8 \times 10^{11}$ cm^{-2} (black), $n_e = 1.2 \times 10^{11}$ cm^{-2} (green), and $n_e = 1.6 \times 10^{11}$ cm^{-2} (red). The spectra shift to higher energies as the density increases due to the increasing E_F. (Inset) dR spectra for two different temperatures of $T = 0.2$ K (red) and $T = 4$ K (black) at $\delta = 0$. In both cases, we have $n_e = 0.9 \times 10^{11}$ cm^{-2}.

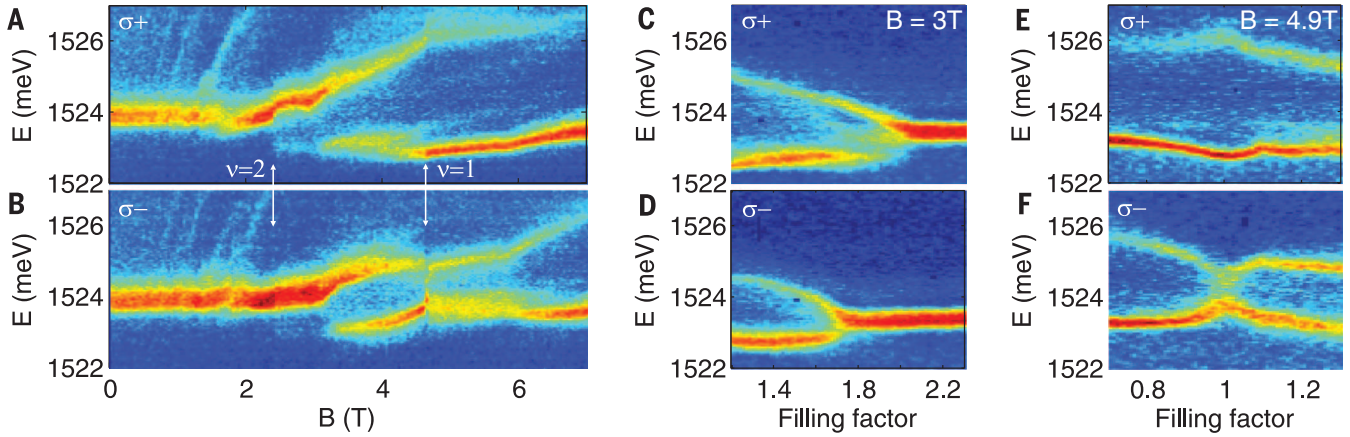

Fig. 3. Integer QH polariton excitations. (**A** and **B**) Polarization-resolved dR measurements versus magnetic field of sample *B* at a constant cavity energy of E_c = 1523.8 meV and an electron density of $n_e = 1.4 \times 10^{11}$ cm^{-2} (V_g = −4 V). (**C** and **D**) Polarization-resolved dR measurements versus V_g around ν = 2 when the cavity energy is on resonance with the lowest Landau level (B_z = 3 T). The blue color-code represents low dR signal, and the red color-code represents high dR signal. σ^+ corresponds to right-hand circularly polarized light, and σ^- corresponds to left-hand circularly polarized light. (**E** and **F**) Polarization-resolved dR measurements as a function of the filling factor obtained by changing V_g around ν = 1 at a magnetic field of B_z = 4.9 T for σ^+- in (E) and σ^--polarized light in (F). The spectral white light power in (A) and (B) is $P \approx 15$ pW nm^{-1}. In (C) to (F), we used a spectral power $P \approx 0.2$ pW nm^{-1}; the plotted data are an average over 150 measurements.

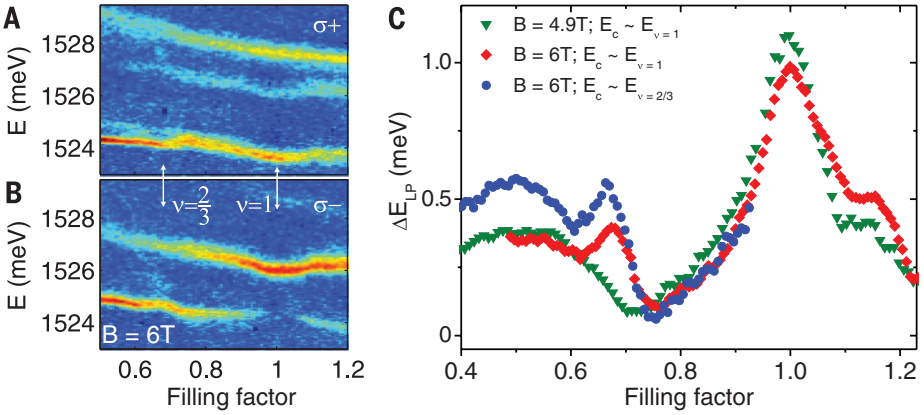

Fig. 4. Fractional QH polariton excitations. (**A** and **B**) Polarization-resolved dR measurements versus V_g performed on sample *B* when the cavity energy is on resonance with the lowest Landau level (B_z = 6 T). The color-code is the same as in Fig. 3. (**C**) The energy difference, $\Delta E_{LP} = E(LP_{\sigma-}) - E(LP_{\sigma+})$, of the σ^- and σ^+ lower polariton branches versus filling factor for different magnetic fields and resonance conditions. Blue circles (B_z = 6 T) correspond to data obtained when the cavity is tuned into resonance with LL0 around ν = 2/3; red squares (B_z = 6 T) and green triangles (B_z = 4.9 T) show data obtained when the cavity is tuned into resonance with LL0 around ν = 1 (data were analyzed from the same scan as in Fig. 3, E and F).

Our B_z = 0 experiments reveal a previously unknown cavity excitation–induced strongly correlated state that requires a new theoretical framework to describe a mobile 2DEG impurity in a cavity-QED setting. Furthermore, $B_z \neq 0$ experiments establish cavity-QED as an invaluable spectroscopic tool for investigating and manipulating properties of many-body states in a 2DEG. By increasing the cavity lifetime, it should be possible to enhance the measurement sensitivity and to observe the incompressibility-induced modification of the polariton splitting. Semi-integrated cavity structures not only allow for a factor of 20 increase in lifetime but also enable tuning the electric-dipole coupling strength (*28*). More intriguing possibilities raised by our observations include observation of nonequilibrium dynamics after an optical quench into a fractional QH state. Last, the system we consider in the B_z = 0 limit could also be viewed as a new nonlinear optical system in which n_e of the 2DEG can be used to change the effective Bohr radius and consequently the strength of polariton-polariton interactions (*29*).

REFERENCES AND NOTES

1. C. Weisbuch, M. Nishioka, A. Ishikawa, Y. Arakawa, *Phys. Rev. Lett.* **69**, 3314–3317 (1992).
2. H. Deng, H. Haug, Y. Yamamoto, *Rev. Mod. Phys.* **82**, 1489–1537 (2010).
3. K. Ohtaka, Y. Tanabe, *Rev. Mod. Phys.* **62**, 929–991 (1990).
4. N. S. Averkiev, M. M. Glazov, *Phys. Rev. B* **76**, 045320 (2007).
5. A. Gabbay, Y. Preezant, E. Cohen, B. M. Ashkinadze, L. N. Pfeiffer, *Phys. Rev. Lett.* **99**, 157402 (2007).
6. M. Baeten, M. Wouters, http://arxiv.org/abs/1404.2048 (2014).
7. B. Sbierski *et al.*, *Phys. Rev. Lett.* **111**, 157402 (2013).
8. S. Das Sarma, A. Pinczuk, Eds., *Perspectives on Quantum Hall Effects* (Wiley, New York, 1996).
9. Materials and methods are available as supplementary materials on *Science* Online.
10. B. R. Bennett, R. A. Soref, J. A. del Alamo, *IEEE J. Quantum Electron.* **26**, 113–122 (1990).
11. P. W. Anderson, *Phys. Rev. Lett.* **18**, 1049–1051 (1967).
12. M. S. Skolnick *et al.*, *Phys. Rev. Lett.* **58**, 2130–2133 (1987).
13. M. Perrin, P. Senellart, A. Lemaître, J. Bloch, *Phys. Rev. B* **72**, 075340 (2005).
14. R. Houdré *et al.*, *Phys. Rev. Lett.* **73**, 2043–2046 (1994).
15. A. Rosch, T. Kopp, *Phys. Rev. Lett.* **75**, 1988–1991 (1995).
16. I. Bar-Joseph, *Semicond. Sci. Technol.* **20**, R29–R39 (2005).
17. P. Plochocka *et al.*, *Phys. Rev. Lett.* **102**, 126806 (2009).
18. L. Tiemann, G. Gamez, N. Kumada, K. Muraki, *Science* **335**, 828–831 (2012).
19. E. H. Aifer, B. B. Goldberg, D. A. Broido, *Phys. Rev. Lett.* **76**, 680–683 (1996).
20. B. I. Halperin, *Hel. Phys. Acta* **56**, 75–102 (1983).
21. J. P. Eisenstein, H. L. Stormer, L. N. Pfeiffer, K. W. West, *Phys. Rev. B* **41**, 7910–7913 (1990).
22. I. V. Kukushkin, K. von Klitzing, K. Eberl, *Phys. Rev. Lett.* **82**, 3665–3668 (1999).
23. J. H. Smet *et al.*, *Nature* **415**, 281–286 (2002).
24. B. Verdene *et al.*, *Nat. Phys.* **3**, 392–396 (2007).
25. J. Hayakawa, K. Muraki, G. Yusa, *Nat. Nanotechnol.* **8**, 31–35 (2013).
26. T. Chakraborty, *Surf. Sci.* **229**, 16–20 (1990).
27. N. Kumada *et al.*, *Phys. Rev. Lett.* **89**, 116802 (2002).
28. B. Besga *et al.*, http://arxiv.org/abs/1312.0819 (2013).
29. I. Carusotto, C. Ciuti, *Rev. Mod. Phys.* **85**, 299–366 (2013).

ACKNOWLEDGMENTS

The authors acknowledge insightful discussions with L. Glazman, M. Goldstein, A. Rosch, A. Srivastava, and J. von Delft. This work is supported by Swiss National Center of Competence in Research Quantum Photonics (NCCR QP), research instrument of the Swiss National Science Foundation (SNSF).

SUPPLEMENTARY MATERIALS

www.sciencemag.org/content/346/6207/332/suppl/DC1
Materials and Methods
Supplementary Text
Figs. S1 to S8
References (*30*–*35*)

10 July 2014; accepted 17 September 2014
Published online 2 October 2014;
10.1126/science.1258595

ATTOSECOND DYNAMICS

Ultrafast electron dynamics in phenylalanine initiated by attosecond pulses

F. Calegari,[1] D. Ayuso,[2] A. Trabattoni,[3] L. Belshaw,[4] S. De Camillis,[4] S. Anumula,[3] F. Frassetto,[5] L. Poletto,[5] A. Palacios,[2] P. Decleva,[6] J. B. Greenwood,[4] F. Martín,[2,7]* M. Nisoli[1,3]*

In the past decade, attosecond technology has opened up the investigation of ultrafast electronic processes in atoms, simple molecules, and solids. Here, we report the application of isolated attosecond pulses to prompt ionization of the amino acid phenylalanine and the subsequent detection of ultrafast dynamics on a sub–4.5-femtosecond temporal scale, which is shorter than the vibrational response of the molecule. The ability to initiate and observe such electronic dynamics in polyatomic molecules represents a crucial step forward in attosecond science, which is progressively moving toward the investigation of more and more complex systems.

The investigation of ultrafast processes in atoms received a major stimulus with the introduction of attosecond pulses in the extreme ultraviolet (XUV) spectral region (*1*). Real-time observation of the femtosecond Auger decay in krypton was the first application of isolated attosecond pulses in 2002 (*2*). This demonstration was then followed by other important experimental results in the field of ultrafast atomic physics, such as the real-time observation of electron tunneling (*3*) and the measurement of temporal delays of the order of a few tens of attoseconds in the photoemission of electrons from different atomic orbitals of neon (*4*) and argon (*5*). The unprecedented time resolution offered by attosecond pulses has also allowed quantum mechanical electron motion and its degree of coherence to be measured in atoms by using attosecond transient absorption spectroscopy (*6*). Attosecond techniques have been applied in the field of ultrafast solid-state physics, with the measurement of delays in electron photoemission from crystalline solids (*7*) and the investigation of the ultrafast field-induced insulator-to-conductor state transition in a dielectric (*8*). In the past few years, attosecond pulses have also been used to measure ultrafast electronic processes in simple molecules (*9*). Subfemtosecond electron localization after attosecond excitation has been observed in H_2 and D_2 molecules (*10*), and control of photo-ionization of D_2 and O_2 molecules has been achieved by using attosecond pulse trains (APTs) (*11*, *12*). More recently, an APT, in combination with two near-infrared fields, was used to coherently excite and control the outcome of a simple chemical reaction in a D_2 molecule (*13*). Although the study of more complex molecules is challenging, a formative measurement of the amino acid phenylalanine has shown that ionization by a short APT leads to dynamics on a temporal scale of a few tens of femtoseconds. This has been interpreted as the possible signature of ultrafast electron transfer inside the molecule (*14*).

The application of attosecond techniques to molecules offers the possibility of investigating primary relaxation processes, which involve electronic and nuclear degrees of freedom and their coupling. In the case of large molecules (e.g., biologically relevant molecules), prompt ionization by attosecond pulses may produce ultrafast charge migration along the molecular skeleton, which can precede nuclear rearrangement. This behavior has been predicted in theoretical calculations by various authors (*15*–*19*), whose work was stimulated by pioneering experiments performed by Weinkauf, Schlag, and co-workers on fragmentation of peptide chains (*20*, *21*). This electron dynamics, evolving on an attosecond or few-femtosecond temporal scale, can determine the subsequent relaxation pathways of the molecule (*9*). The process is induced by sudden generation of an electronic wave packet, which moves across the molecular chain and induces a site-selective reactivity, which is related to charge localization in a particular site of the molecule (*15*). Although picosecond and femtosecond pulses are suitable for the investigation of nuclear dynamics, the study of electronic dynamics with these pulses has been made possible by slowing down the dynamics through the use of Rydberg electron wave packets (*22*). However, in order to study the electron wave-packet dynamics in the outer-valence molecular orbitals relevant to most chemical and biological systems, attosecond pulses are required.

Here, we present experimental evidence of ultrafast charge dynamics in the amino acid phenylalanine after prompt ionization induced by isolated attosecond pulses. A probe pulse then produced a doubly charged molecular fragment by ejection of a second electron, and charge migration manifested itself as a sub-4.5-fs oscillation in the yield of this fragment as a function of pump-probe delay. Numerical simulations of the temporal evolution of the electronic wave packet created by the attosecond pulse strongly support the interpretation of the experimental data in terms of charge migration resulting from ultrafast electron dynamics preceding nuclear rearrangement.

The α-amino acids consist of a central carbon atom (α carbon) linked to an amine (-NH_2) group, a carboxylic group (-COOH), a hydrogen

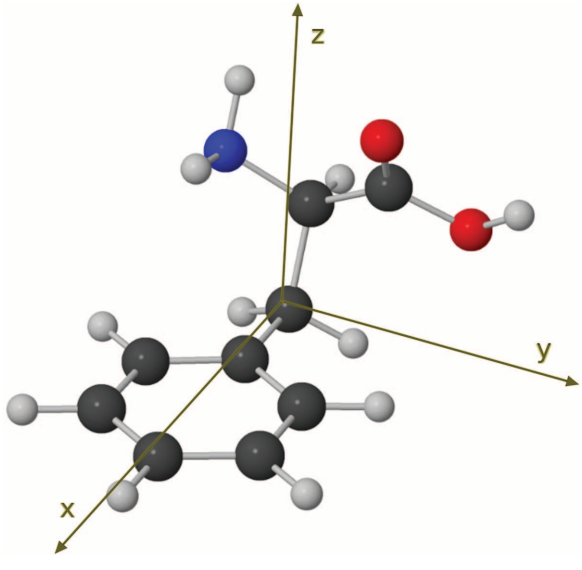

Fig. 1. Three-dimensional structure of phenylalanine. Molecular structure of the most abundant conformer of the aromatic amino acid phenylalanine. Dark gray spheres represent carbon atoms; light gray spheres, hydrogen atoms; blue sphere, nitrogen; and red spheres, oxygen. The molecular geometry has been optimized by using density functional theory (DFT) with a B3LYP functional.

[1]Institute of Photonics and Nanotechnologies (IFN)–Consiglio Nazionale delle Ricerche (CNR), Piazza Leonardo da Vinci 32, 20133 Milano, Italy. [2]Departamento de Química, Modulo 13, Universidad Autónoma de Madrid, Cantoblanco 28049 Madrid, Spain. [3]Department of Physics, Politecnico di Milano, Piazza Leonardo da Vinci 32, 20133 Milano, Italy. [4]Centre for Plasma Physics, School of Maths and Physics, Queen's University, Belfast BT7 1NN, UK. [5]IFN-CNR, Via Trasea 7, 35131 Padova, Italy. [6]Dipartimento di Scienze Chimiche e Farmaceutiche, Università di Trieste and CNR–Istituto Officina dei Materiali, 34127 Trieste, Italy. [7]Instituto Madrileño de Estudios Avanzados en Nanociencia, Cantoblanco, 28049 Madrid, Spain.
*Corresponding author. E-mail: fernando.martin@uam.es (F.M.); mauro.nisoli@polimi.it (M.N.)

atom, and a side chain (R), which in the case of phenylalanine is a benzyl group (Fig. 1). In our experiments, we used a two-color, pump-probe technique. Charge dynamics were initiated by isolated XUV sub-300-as pulses, with photon energy in the spectral range between 15 and 35 eV and probed by 4-fs, waveform-controlled visible/near infrared (VIS/NIR, central photon energy of 1.77 eV) pulses (see supplementary materials). A clean plume of isolated and neutral molecules was generated by evaporation of the amino acid from a thin metallic foil heated by a continuous wave (CW) laser. The parent and fragment ions produced by the interaction of the molecules with the pump and probe pulses were then collected by a linear time-of-flight device for mass analysis, where the metallic foil was integrated into the repeller electrode (*23*). Ionization induced by the attosecond pulse occured in a sufficiently short time interval to exclude substantial electron rearrangement during the excitation process.

We measured the yield for the production of doubly charged immonium ions as a function of the time delay between the attosecond pump pulse and the VIS/NIR probe pulse (the structure of the immonium dication is $^{++}NH_2$÷CH-R). Figure 2A shows the results on a 100-fs time scale. The experimental data display a rise time of 10 ± 2 fs and an exponential decay with time constant of 25 ± 2 fs [this longer relaxation time constant is in agreement with earlier experimental results reported in (*14*)]. Figure 2B shows a 25-fs-wide zoom of the pump-probe dynamics, obtained by reducing the delay step between pump and probe pulses from 3 to 0.5 fs. An oscillation of the dication yield is clearly visible. For a better visualization, Fig. 2C shows the same yield after subtraction of an exponential fitting curve. The data have been fitted with a sinusoidal function of frequency 0.234 PHz (corresponding to an oscillation period of 4.3 fs), with lower and upper confidence bounds of 0.229 and 0.238 PHz, respectively (see supplementary materials). The experimental data have been also analyzed by using a sliding-window Fourier transform, which, at the expense of frequency resolution, shows frequency and time information on the same plot. The result is shown in Fig. 3A. At short pump-probe delays, two frequency components are present, around 0.14 and 0.3 PHz. A strong and broad peak around 0.24 PHz forms in about 15 fs and vanishes after about 35 fs, with a spectral width that slightly increases upon increasing the pump-probe delay, in agreement with the frequency values obtained from best fitting of the data reported in Fig. 2C.

From these results, we can draw the following conclusions: (i) the ultrafast oscillations in the temporal evolution of the dication yield cannot be related to nuclear dynamics, which usually come into play on a longer temporal scale, ultimately leading to charge localization in a particular molecular fragment. Indeed, standard quantum chemistry calculations in phenylalanine (see supplementary materials) show that the highest vibrational frequency is 0.11 PHz, which corresponds to a period of 9 fs, associated with X-H stretching modes, whereas skeleton vibrations are even slower, so that one can rule out that the observed beatings are due to vibrational motion. In any case, some influence of the nuclear motion cannot be completely excluded, because, for example, stretching of the order of a few picometers of carbon bonds can occur in a few femtoseconds, and this could modify the charge dynamics (*24*, *25*). (ii) Clear oscillatory evolution of the dication yield is observed even without any conformer selection. It is well known that amino acids exist in many conformations as a result of their structural flexibility. Typically, the energy barrier to interconversion between different conformers is small, of the order of a few kcal/mol, so that, even at room temperature, thermal energy is sufficient to induce conformational changes. Theoretical investigations have shown that such changes can affect the charge migration process (*26*). In the case of phenylalanine, 37 conformers have been found by ab initio calculations (*27*), with a conformational distribution that depends on temperature. In our experiment, at an average temperature of about 430 K, only the six most stable conformers are substantially present, as discussed in the supplementary materials, with the most abundant configuration shown in Fig. 1.

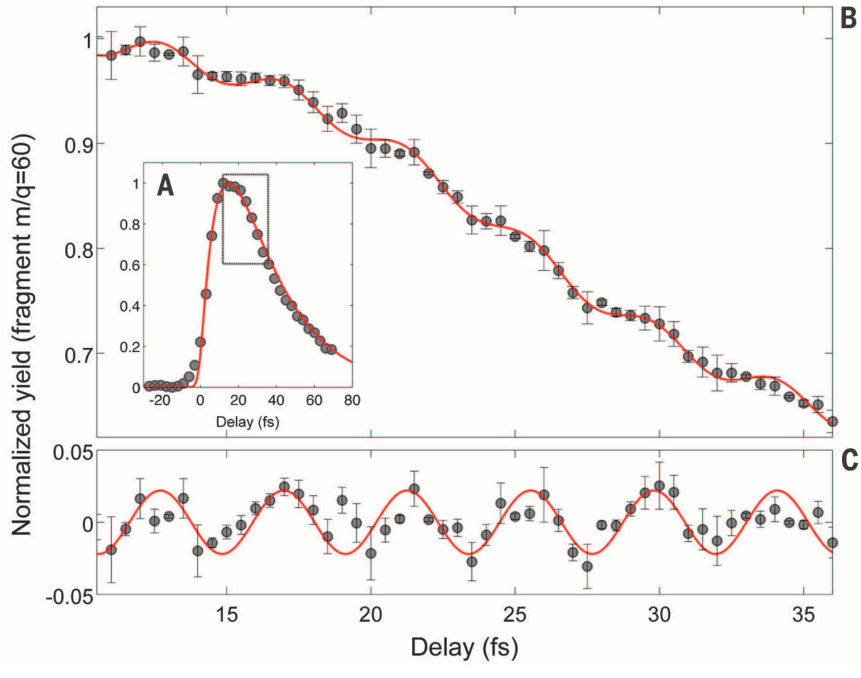

Fig. 2. Pump-probe measurements. (**A**) Yield of doubly charged immonium ion (mass/charge = 60) as a function of pump-probe delay, measured with 3-fs temporal steps. The red line is a fitting curve with an exponential rise time of 10 fs and an exponential relaxation time of 25 fs. (**B**) Yield of doubly charged immonium ion versus pump-probe delay measured with 0.5-fs temporal steps, within the temporal window shown as dotted box in (A). Error bars show the standard error of the results of four measurements. The red line is the fitting curve given by the sum of the fitting curve shown in (A) and a sinusoidal function of frequency 0.234 PHz (4.3-fs period). (**C**) Difference between the experimental data and the exponential fitting curve displayed in (A). Red curve is a sinusoidal function of frequency 0.234 PHz.

To further investigate the measured dynamics, we also varied the photon energy and spectral width of the attosecond pump pulse by inserting an indium foil in the XUV beam path. The new XUV spectrum was characterized by a 3-eV (full width at half maximum) peak centered around 15 eV, followed by a broad and weak spectral component extending up to 25 eV. In this case, doubly charged immonium fragments were barely visible, suggesting that the dication formation involves relatively highly excited states of the cation. We have calculated the energy level diagram with all the states of singly charged phenylalanine generated by the XUV pump pulse and all the states of the dication (see supplementary materials). A number of transitions from excited states of the cation to the lowest states of the dication are possible, which involve the absorption of just a few VIS/NIR photons. These states cannot be accessed by low-energy excitation, as in the case of XUV pulses transmitted by the indium foil. In this case, transitions from cation states to the lowest dication states would require the less probable absorption of many VIS/NIR photons.

We also performed theoretical calculations to describe the hole dynamics induced by an attosecond pulse similar to that used in the experiment. Details of the method can be found in the supplementary materials. Because of the high central frequency and large spectral width of the pulse, a manifold of ionization channels is open, thus leading to a superposition of many one-hole (1h) cationic states, i.e., to an electronic wave packet. Ionization amplitudes for all 1h

open channels (32 for a single conformer) were quantitatively determined by means of the static-exchange density functional theory (*28*–*30*), which has been thoroughly tested in systems of similar complexity, and first-order time-dependent perturbation theory. A calculated photoelectron spectrum at 45-eV photon energy is in very good agreement with that obtained at 100 eV in a synchrotron radiation experiment (*31*). From the ionization amplitudes, the actual electronic wave packet was calculated by using the experimental frequency spectrum of the attosecond pulse. The evolution of the electronic wave packet was then evaluated by using a standard time-dependent density matrix formalism (*6*), in which the system is described by a sum of single-particle Hamiltonians. This is a reasonable approximation when, as in the present case, changes in electronic density are mostly due to the coherent superposition of 1h cationic states induced by the XUV pulse (see supplementary materials). In other words, higher-order processes in which additional electrons are excited (e.g., correlation satellites) play a minor role in the observed dynamics. The hole-density was calculated as the difference between the electronic density of the neutral molecule, which does not depend on time, and the electronic density of the cation, from immediately after XUV excitation up to a 500-fs delay. Because, in the experiments, the molecules were not aligned, we calculated the charge dynamics resulting from excitation by pulses with the electric field polarized along three orthogonal directions (shown in Fig. 1). The results were then averaged assuming randomly oriented molecules. For a better analysis, we integrated the hole density around selected portions of the molecule: Beating frequencies were observed when the charge density was integrated around the amine group.

The six most populated conformers at 430 K were considered in the simulations. Although the precise frequencies of the relevant peaks in the calculated Fourier spectra depend on the particular conformer, the common characteristic is the presence of three dominant groups of Fourier peaks between 0.15 and 0.4 PHz. Our calculations show that the largest temporal modulation of the hole dynamics occurs around the amine group. Because of this fact, in Fig. 3C we only show the Fourier power spectrum of the calculated hole density around this group for the most abundant conformer. We have then analyzed the numerical results by using the same sliding-window Fourier transform procedure applied to the experimental data. Figure 3B shows the resulting spectrogram in a temporal window up to 45 fs, considering an experimental temporal resolution of about 3 fs. A dominant peak around 0.25 PHz is visible, which forms in about 15 fs and vanishes after about 35 fs, in close agreement with the results of the Fourier analysis of the experimental data. A higher frequency component is visible around 0.36 PHz in the delay intervals below ~15 fs and above ~30 fs. At short delays, this component favorably compares with the experimental observation of the

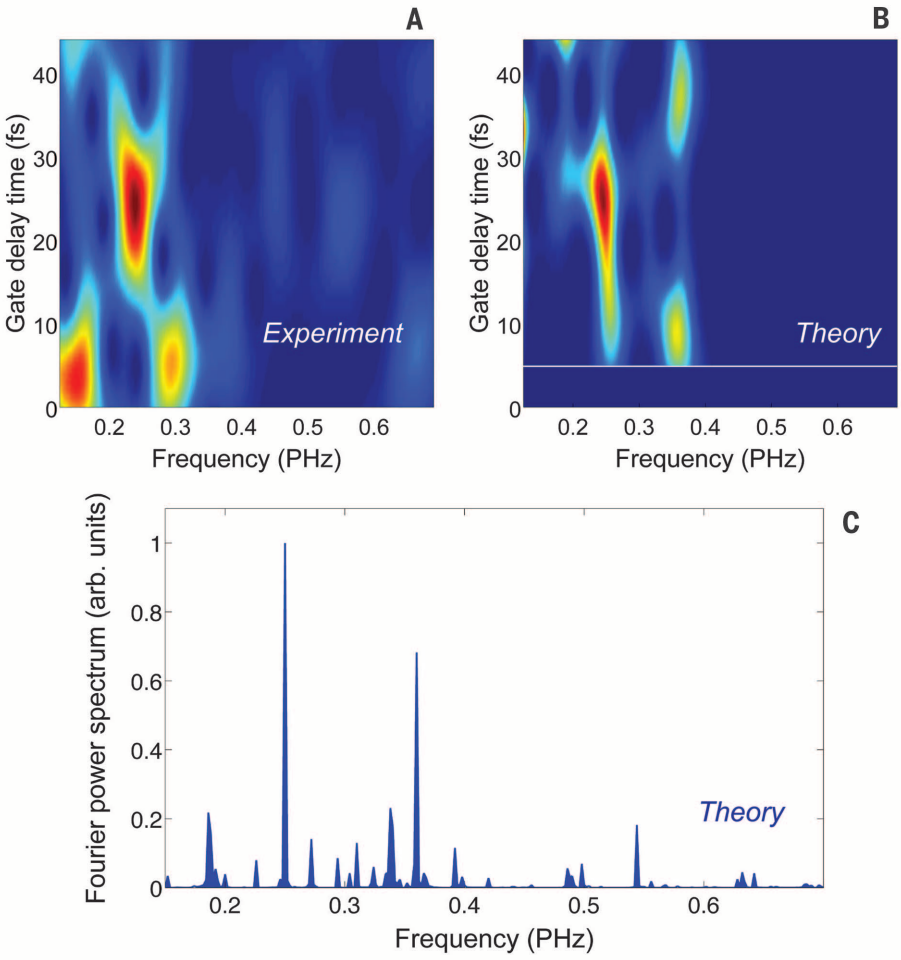

Fig. 3. Fourier analysis of charge dynamics. Spectrograms calculated for the measured data of Fig. 2C (**A**) and for the calculated hole density integrated over the amine group for the most abundant conformer (**B**). The sliding window Fourier transforms have been calculated by using a Gaussian window function $g(t - t_d) = \exp[-(t - t_d)^2/t_0^2]$, with t_0 = 10 fs and peak at t_d (gate delay time). The spectrogram (B) was calculated considering an experimental temporal resolution of about 3 fs. (**C**) Fourier power spectrum of the calculated hole density integrated over the amine group for the most abundant conformer.

frequency peak around 0.30 PHz in the same window of pump-probe delays. The temporal evolution of the main Fourier components is a consequence of the complex interplay among several beating processes initiated by the broadband excitation pulse. Despite the agreement with the experimental results, we cannot exclude that the nuclear dynamics, which are not included in the simulations, also play a role in the temporal evolution of the measured oscillation frequencies. The good agreement between simulations and experimental results is rather remarkable in light of the fact that simulations do not take into account the interaction of the VIS/NIR probe pulse. The fact that the effects of the probe pulse are not included in the simulations can explain why the calculated intensities of the different beatings differ from the experimental ones. We note that the beating frequencies have been observed experimentally even though the initial hole density is highly delocalized. An important result of the simulations is that the measured beating frequencies originate from charge dynamics around the amine group. This leads to the conclusion that the periodic modulations measured in the experiment are mainly related to the absorption of the probe pulse by the amine group. The mechanism that makes the probe pulse sensitive specifically to the charge density on this group is still not well understood, and therefore it will not be further discussed in the manuscript. Moreover, we observe that, in spite of the large number of potential frequency beatings associated to the wave packet motion induced by the attosecond pulse, only a few ones manifest in the experiment, thus reducing the impact of the modulations introduced by the probe pulse in the analysis of the wave packet motion. Figure 4 displays snapshots of the variation of the hole density with respect to the time-averaged hole density as a function of time for the most abundant conformer. In spite of the very delocalized nature of the hole-density resulting from the broadband XUV excitation, a

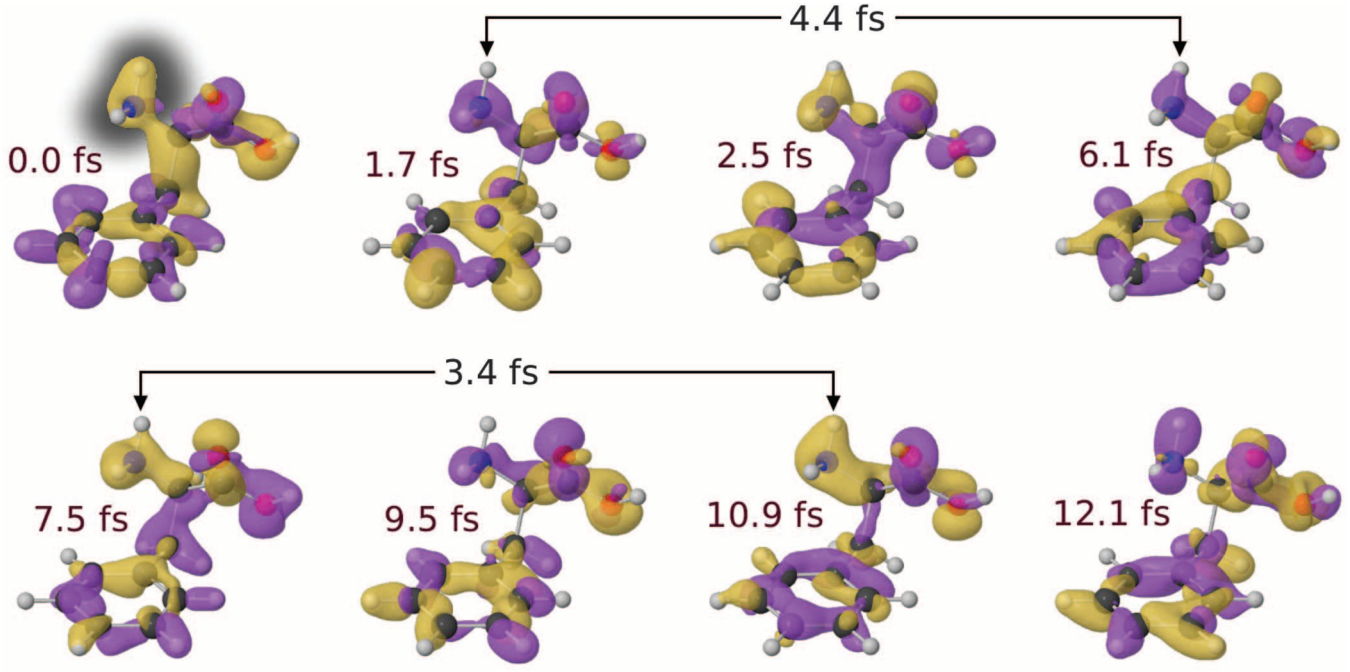

Fig. 4. Snapshots of hole dynamics. Relative variation of the hole density with respect to its time-averaged value as a function of time for the most abundant conformer. Isosurfaces of the relative hole density are shown for cutoff values of $+10^{-4}$ arbitrary units (yellow) and -10^{-4} (purple). Time is with reference to the end of the XUV pulse (first snapshot). To guide the eye, time intervals between snapshots showing a similar accumulated density over the amine group are indicated. These time intervals are close to the dominant periods associated with the electronic wave-packet motion shown in Fig. 3. The location of the amine group is highlighted in the first snapshot with a shaded contour.

substantial redistribution of this density is observed on a sub-femtosecond scale. These charge dynamics cannot be associated with a simple migration from one side of the molecule to the other. Despite the complexity of the charge configuration calculated in a realistic (i.e., experimentally accessible) situation, the concept of charge migration is still valid. In particular, the snapshots shown in Fig. 4 evidence a notable and periodic variation of the charge density around the amine group. This is because the dominant beatings always involve delocalized orbitals with substantial localization around the amine group (see supplementary materials), thus showing that evolution of the hole density around this functional group provides a highly selective interaction with the probe pulse.

Direct measurement of the ultrafast charge dynamics in an amino acid, initiated by attosecond pulses, represents a crucial benchmark for the extension of attosecond methodology to complex systems. We have demonstrated that charge fluctuations over large regions of a complex molecule such as phenylalanine can be induced by attosecond pulses on a temporal scale much shorter than the vibrational response of the system. This result was achieved in spite of the broad bandwidth of the attosecond pulses and, therefore, their low frequency selectivity, thus showing that attosecond science offers the possibility to elucidate processes ultimately leading to charge localization in complex molecules. The latter has already been achieved in hydrogen molecules, where, after attosecond excitation, charge localization was induced by the probe NIR pulse as a result of the coupling with the nuclear degrees of freedom at long time delays (*10*). A similar achievement can be envisaged in more complex molecules by performing more sophisticated experiments, e.g., as those of (*10*), combined with the extension of the existing theoretical methods to account for the nuclear motion.

REFERENCES AND NOTES

1. F. Krausz, M. Ivanov, *Rev. Mod. Phys.* **81**, 163–234 (2009).
2. M. Drescher *et al.*, *Nature* **419**, 803–807 (2002).
3. M. Uiberacker *et al.*, *Nature* **446**, 627–632 (2007).
4. M. Schultze *et al.*, *Science* **328**, 1658–1662 (2010).
5. K. Klünder *et al.*, *Phys. Rev. Lett.* **106**, 143002 (2011).
6. E. Goulielmakis *et al.*, *Nature* **466**, 739–743 (2010).
7. A. L. Cavalieri *et al.*, *Nature* **449**, 1029–1032 (2007).
8. A. Schiffrin *et al.*, *Nature* **493**, 70–74 (2013).
9. F. Lépine, M. Y. Ivanov, M. J. J. Vrakking, *Nat. Photonics* **8**, 195–204 (2014).
10. G. Sansone *et al.*, *Nature* **465**, 763–766 (2010).
11. F. Kelkensberg *et al.*, *Phys. Rev. Lett.* **107**, 043002 (2011).
12. W. Siu *et al.*, *Phys. Rev. A* **84**, 063412 (2011).
13. P. Ranitovic *et al.*, *Proc. Natl. Acad. Sci. U.S.A.* **111**, 912–917 (2014).
14. L. Belshaw *et al.*, *J. Phys. Chem. Lett.* **3**, 3751–3754 (2012).
15. F. Remacle, R. D. Levine, *Proc. Natl. Acad. Sci. U.S.A.* **103**, 6793–6798 (2006).
16. L. S. Cederbaum, J. Zobeley, *Chem. Phys. Lett.* **307**, 205–210 (1999).
17. H. Hennig, J. Breidbach, L. S. Cederbaum, *J. Phys. Chem. A* **109**, 409–414 (2005).
18. J. Breidbach, L. S. Cederbaum, *Phys. Rev. Lett.* **94**, 033901 (2005).
19. J. Breidbach, L. S. Cederbaum, *J. Chem. Phys.* **118**, 3983 (2003).
20. R. Weinkauf, P. Schanen, D. Yang, S. Soukara, E. W. Schlag, *J. Phys. Chem.* **99**, 11255–11265 (1995).
21. R. Weinkauf *et al.*, *J. Phys. Chem.* **100**, 18567–18585 (1996).
22. J. Wals *et al.*, *Phys. Rev. Lett.* **72**, 3783–3786 (1994).
23. C. R. Calvert *et al.*, *Phys. Chem. Chem. Phys.* **14**, 6289–6297 (2012).
24. S. Lünnemann, A. I. Kuleff, L. S. Cederbaum, *Chem. Phys. Lett.* **450**, 232–235 (2008).
25. D. Mendive-Tapia, M. Vacher, M. J. Bearpark, M. A. Robb, *J. Chem. Phys.* **139**, 044110 (2013).
26. A. I. Kuleff, L. S. Cederbaum, *Chem. Phys.* **338**, 320–328 (2007).
27. H. Z. Huang, W. Yu, Z. Lin, *J. Mol. Struct. THEOCHEM* **758**, 195–202 (2006).
28. D. Toffoli, M. Stener, G. Fronzoni, P. Decleva, *Chem. Phys.* **276**, 25–43 (2002).
29. E. Plésiat, P. Decleva, F. Martín, *Phys. Chem. Chem. Phys.* **14**, 10853–10871 (2012).
30. S. E. Canton *et al.*, *Proc. Natl. Acad. Sci. U.S.A.* **108**, 7302–7306 (2011).

ACKNOWLEDGMENTS

We acknowledge support from the European Research Council under ERC grant nos. 227355 ELYCHE and 290853 XCHEM, LASERLAB-EUROPE (grant agreement no. 284464, European Commission's Seventh Framework Programme), European COST Action CM1204 XLIC, the Ministerio de Ciencia e Innovación project FIS2010-15127, the ERA-Chemistry project PIM2010EEC-00751, European grants MC-ITN CORINF and MC-RG ATTOTREND 268284, UK's Science and Technology Facilities Council Laser Loan Scheme, the Engineering and Physical Sciences Research Council (grant EP/J007048/1), the Leverhulme Trust (grant RPG-2012-735), and the Northern Ireland Department of Employment and Learning.

SUPPLEMENTARY MATERIALS

www.sciencemag.org/content/346/6207/336/suppl/DC1
Materials and Methods
Supplementary Text
Figs. S1 to S11
Tables S1 and S2
References (*31*–*53*)
Movie S1

28 March 2014; accepted 16 September 2014
10.1126/science.1254061

STRATEGIC REASONING

Neural correlates of strategic reasoning during competitive games

Hyojung Seo,[1]* Xinying Cai,[1]† Christopher H. Donahue,[1]‡ Daeyeol Lee[1,2,3]*

Although human and animal behaviors are largely shaped by reinforcement and punishment, choices in social settings are also influenced by information about the knowledge and experience of other decision-makers. During competitive games, monkeys increased their payoffs by systematically deviating from a simple heuristic learning algorithm and thereby countering the predictable exploitation by their computer opponent. Neurons in the dorsomedial prefrontal cortex (dmPFC) signaled the animal's recent choice and reward history that reflected the computer's exploitative strategy. The strength of switching signals in the dmPFC also correlated with the animal's tendency to deviate from the heuristic learning algorithm. Therefore, the dmPFC might provide control signals for overriding simple heuristic learning algorithms based on the inferred strategies of the opponent.

Learning algorithms suffer from the curse of dimensionality, as the amount of data necessary for statistically robust learning increases with the complexity of the task (*1*). Simple heuristic learning algorithms can thus be more effective, even for complex tasks (*2*). A broad range of animal and human behaviors follows model-free reinforcement learning algorithms operating with a small number of discrete states (*3*–*5*). Nevertheless, more complex learning models can be advantageous when sufficient knowledge of the decision-maker's environment is available. In particular, inferences about the likely behaviors of other decision-makers often complement simple learning algorithms in social settings (*6*–*11*). However, the nature of control signals resulting from complex strategic inferences and how they are incorporated into the process of action selection remain unknown.

To investigate the nature of neural signals responsible for disengaging the animals from simple heuristic learning, we trained three rhesus monkeys to perform a token-based oculomotor decision-making task modeled after a biased matching pennies game against a computer opponent (Fig. 1A) (*12*). The outcome in each trial was jointly determined by the choices of the animal and the computer opponent according to the payoff matrix of the game (Fig. 1B), and the number of tokens shown on the computer screen was adjusted after each trial accordingly. The animal gained a token whenever it chose the same target as the computer. When the animal and computer chose different targets, the outcome was neutral for one target (referred to as safe) and loss for the other target (referred to as risky). The animal received a juice reward whenever it accumulated six tokens. The optimal strategy [known as Nash equilibrium (*13*)] for the animal was to choose the risky target with a probability of 1/3. If the animal chose the risky or safe target more frequently than predicted by the optimal strategy, this was exploited by the computer (*14*). The locations of risky and safe targets were fixed in a block of trials (mean = 47.6 ± 7.6 trials) and reversed between blocks. The computer used only the history of the animal's choices and outcomes in the current block to exploit the animal's biases.

The animals were more likely to choose the same target after receiving a token and to switch to the other target after losing a token, compared to when the outcome of their previous choice was neutral. The effects of gains and losses on subsequent choices decayed gradually (Fig. 1C). This is consistent with a model-free reinforcement learning algorithm in which the value functions for the two options are continually adjusted according to the outcome of the animal's choice (*3*–*5*). Such a simple learning algorithm during a competitive game might be disadvantageous because it leads to predictable choices. However, animals performed significantly better than the best-fitting model-free reinforcement learning algorithm and achieved payoffs indistinguishable from that of the Nash-equilibrium player (fig. S1). This suggests that the animals might have complemented a model-free reinforcement learning algorithm with more flexible strategies, potentially counter-exploiting the computer's algorithm.

The animal's choices systematically deviated from the predictions from a model-free reinforcement learning algorithm. For some animals (monkeys H and J), this was manifest as the attenuation in the immediate effect of losing a token on the animal's behaviors (Fig. 1C, arrows). More generally, the animal's choices and their outcomes in the previous two trials reliably predicted whether the animal would choose the safe or risky target more frequently than predicted by a model-free reinforcement learning algorithm (Fig. 2), and this relationship was consistent across sessions within each animal, as well as across animals (fig. S2). The computer opponent largely exploited the sequences of animal's choices and outcomes expected from simple reinforcement learning (fig. S3A). The animals tended to choose the safe target much more frequently than predicted by the reinforcement learning algorithm, following the same sequence of outcomes that strongly biased the computer to predict the opposite (fig. S3B). The computer's prediction for the animal's next choice was frequently exploited

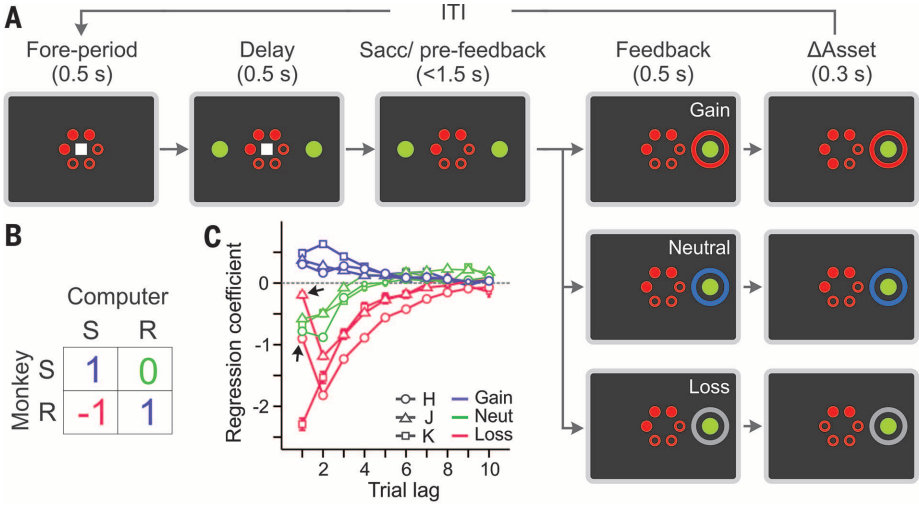

Fig. 1. Behavioral task and performance. Biased matching pennies (**A**) and its payoff matrix (**B**). R, risky target; S, safe target. (**C**) Behavioral effects of gains and losses. Average regression coefficients (ordinate) quantified the tendency for the animal to choose the same target that produced a particular outcome in each of the last 10 trials. Arrows indicate the attenuation in the immediate effect of loss. Error bars, SEM.

[1]Department of Neurobiology, Yale University School of Medicine, New Haven, CT 06510, USA. [2]Kavli Institute for Neuroscience, Yale University School of Medicine, New Haven, CT 06510, USA. [3]Department of Psychology, Yale University, New Haven, CT 06510, USA.
***Corresponding author. E-mail: hyojung.seo@yale.edu (H.S.); daeyeol.lee@yale.edu (D.L.)** †Present address: NYU-ECNU Joint Institute of Brain and Cognitive Sciences, NYU-Shanghai, Shanghai, China. ‡Present address: Gladstone Institute of Neurological Disease, San Francisco, CA 94158, USA.

by the animals when it was based on simple patterns, such as the win-stay-lose-switch strategy (fig. S3C). This increased the animal's expected payoff beyond the level predicted for the Nash-equilibrium strategy (Fig. 2).

We analyzed single-neuron activity recorded from the dorsolateral prefrontal cortex (dlPFC), dorsomedial prefrontal cortex (dmPFC), and dorsal anterior cingulate cortex (ACCd), as well as the dorsal (caudate nucleus, CN) and ventral striatum (VS; fig. S4). Signals related to the animal's previous choices and their outcomes have been found in all of these areas and can contribute to reinforcement learning (*15*–*23*). Because the animals tended to deviate from the model-free reinforcement learning frequently after specific sequences of choices and outcomes, we assumed that neurons involved in overriding the use of simple reinforcement learning algorithm might encode high-order conjunctive signals related to the animal's choices and their outcomes in multiple trials. Neurons encoding such high-order conjunctions were common in the dmPFC. During the 0.5-s delay period, 48.7% of the neurons in the dmPFC significantly modulated their activity according to such conjunctions (*14*), and this was significantly higher than in all other areas tested in this study (χ^2 test, $P < 0.001$; Fig. 3).

We hypothesized that dmPFC activity related to conjunctions of previous choices and outcomes might provide the information necessary for the animal's decision to deviate from a model-free reinforcement learning algorithm. We decoded the animal's choice in the current trial from the activity of each neuron during the delay period, separately for different sequences of choices and outcomes in the two preceding trials, and quantified how much the accuracy of this decoding changed depending on whether the animal made the same choice in the previous trial or not (i.e., stay versus switch; Fig. 4A) (*14*). We then tested whether this measure of switching activity was correlated with the frequency of deviations from model-free reinforcement learning across different outcome sequences (Fig. 4B). Significant correlation was found only for the dmPFC ($r = 0.14$, $P < 0.001$; Fig. 4, C and D, and figs. S5 and S6). Therefore, switching activity in the dmPFC might contribute to strategically deviating from a simple reinforcement learning algorithm.

As a further independent test of this hypothesis, we applied the same methods to analyze the activity of neurons previously recorded from four cortical areas [dmPFC (*23*), dlPFC (*21*), ACCd (*16*), and the lateral intaparietal area or LIP (*22*)] during an unbiased matching pennies task. Signals related to conjunctions of previous choices and outcomes were observed more frequently in the dmPFC than in other areas (χ^2 test, $P < 10^{-4}$; fig. S7). Switching activity was also significantly correlated across different outcome sequences with the deviations from model-free reinforcement learning only for the dmPFC ($r = 0.13$, $P < 10^{-6}$; Fig. 4D and fig. S8). These results suggest that activity in the dmPFC might be involved in multiple levels of switching, not only for switching between different motor responses (*24*–*26*), but also for switching between actions favored by simple reinforcement learning and more abstract strategic inferences.

For learning agents, the complexity of the optimal internal model for action selection not only depends on the complexity of the environment,

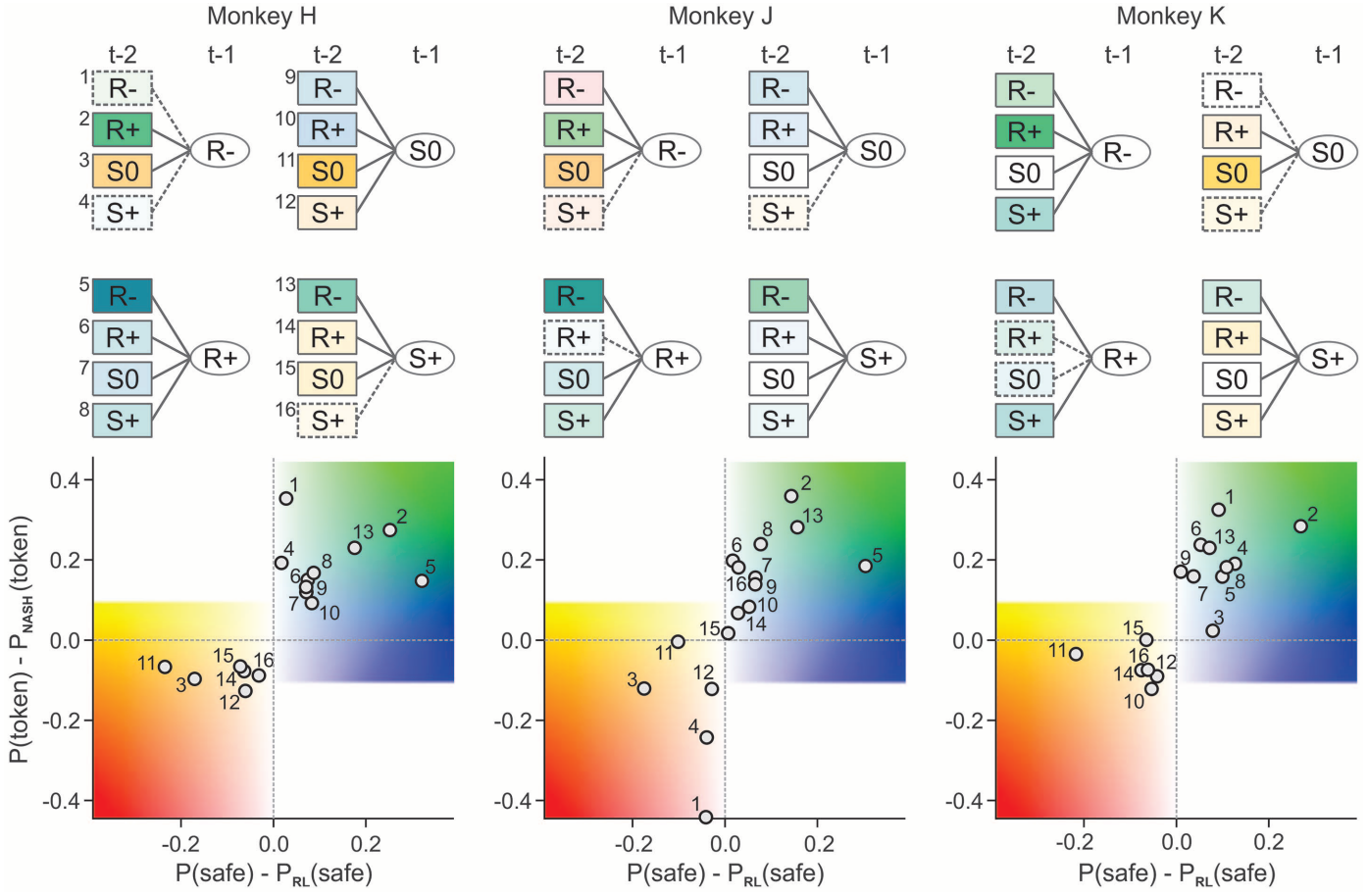

Fig. 2. Systematic deviations from reinforcement learning was beneficial. The color of each box in the decision trees (top) and the position of each circle in the scatter plots (bottom) indicate how much the probability of choosing the safe target deviated from the prediction of the best-fitting reinforcement learning model (abscissa in the bottom scatter plot) according to the choices and outcomes in the last two trials, and how this increased or decreased the probability of token compared to the Nash-equilibrium strategy (ordinate in the scatter plot). Numbers indicate different sequences of choices and outcomes in the two preceding trials. Solid boxes correspond to the sequences included in the best hybrid reinforcement learning model (*14*). R− and R+ denote loss and gain from the risky target, respectively, whereas S0 and S+ indicate neutral outcome and gain from the safe target.

but also increases with the amount of experience. Accordingly, animals learning in real time must apply multiple learning algorithms in parallel (*4*, *27*–*29*). Real or simulated social interactions provide an ideal platform to investigate the dynamics and neural mechanisms for arbitrating between multiple learning algorithms. We found that monkeys can complement the use of a simple reinforcement learning algorithm with strategic high-order reasoning to improve their choice outcomes during virtual competitive interaction. We also identified a neural signature of switching

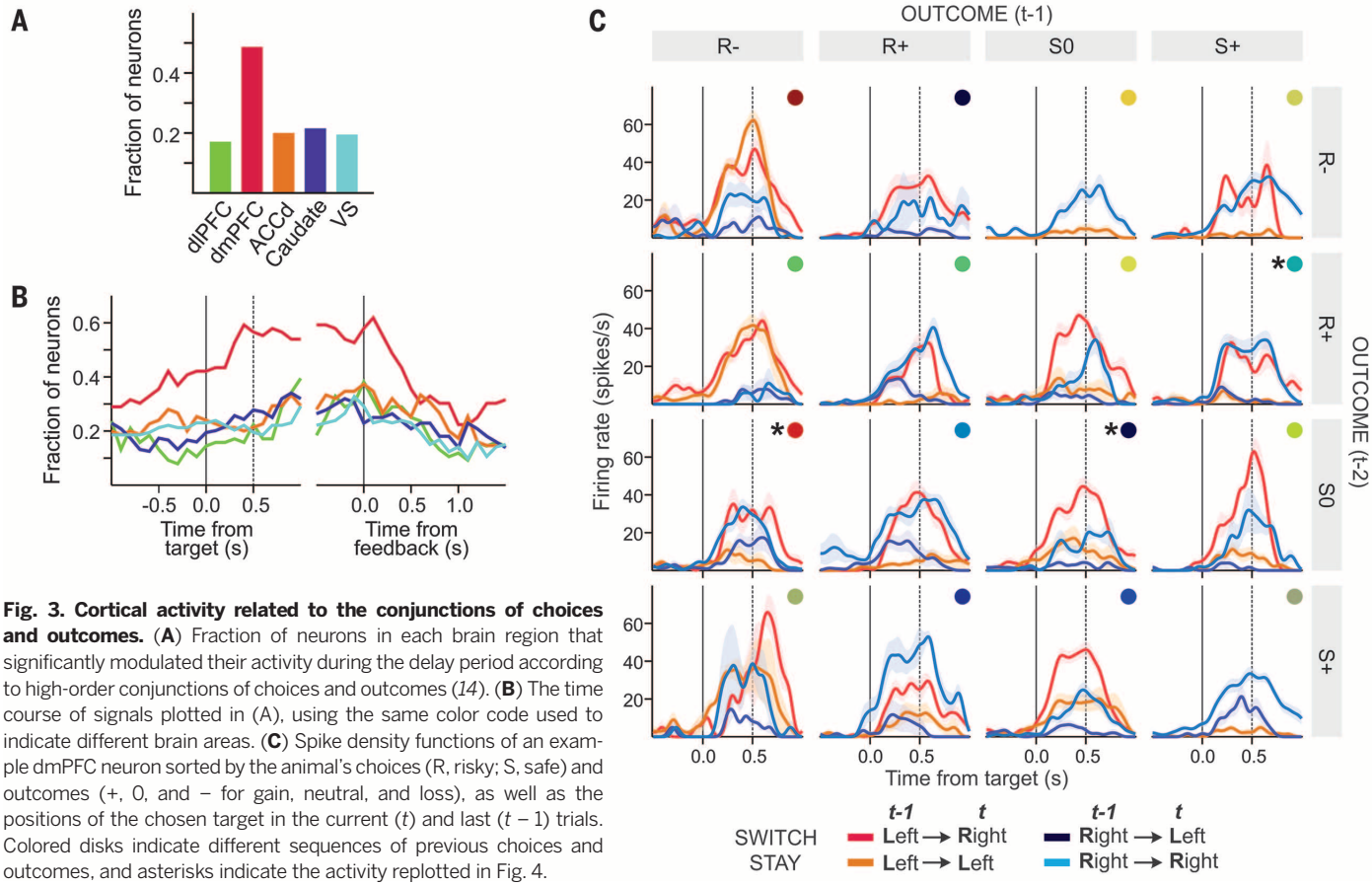

Fig. 3. Cortical activity related to the conjunctions of choices and outcomes. (**A**) Fraction of neurons in each brain region that significantly modulated their activity during the delay period according to high-order conjunctions of choices and outcomes (*14*). (**B**) The time course of signals plotted in (A), using the same color code used to indicate different brain areas. (**C**) Spike density functions of an example dmPFC neuron sorted by the animal's choices (R, risky; S, safe) and outcomes (+, 0, and − for gain, neutral, and loss), as well as the positions of the chosen target in the current (*t*) and last (*t* − 1) trials. Colored disks indicate different sequences of previous choices and outcomes, and asterisks indicate the activity replotted in Fig. 4.

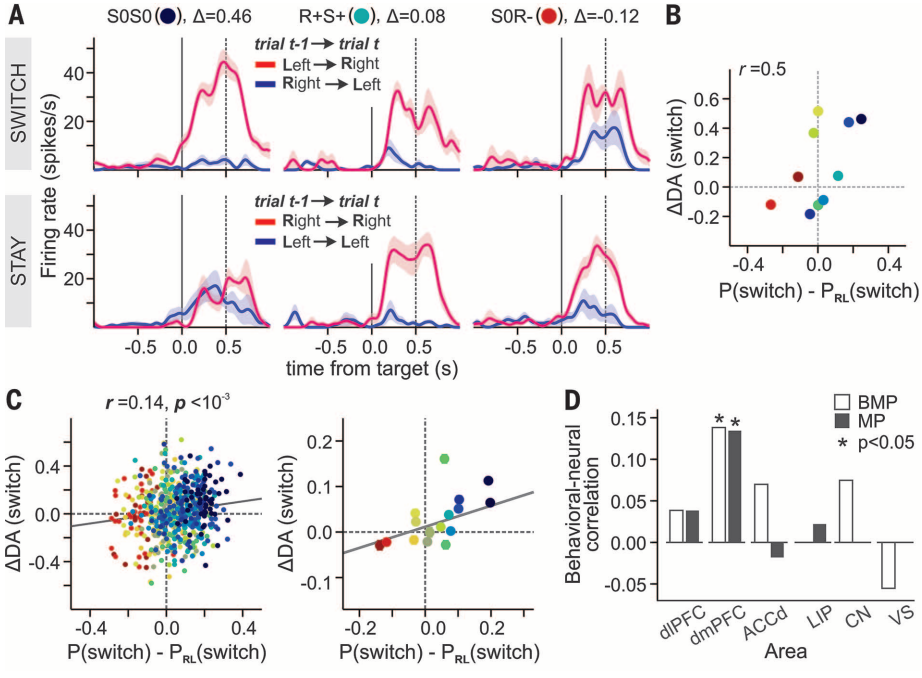

Fig. 4. Cortical signals for deviation from simple reinforcement learning. (**A**) Spike density functions from a dmPFC neuron (shown in Fig. 3C) sorted by the animal's choices in the current and previous trials for three different sequences of outcomes in the last two trials (indicated by the text label and color defined in Fig. 3C). Δ denotes the difference in the accuracy of decoding the animal's choice in switch versus stay trials. (**B**) The difference in the decoding accuracy, ΔDA (switch), plotted as a function of how much more often the animal switched its choices compared to the prediction from the simple reinforcement learning algorithm. (**C**) The same results shown in (B) for the entire population of dmPFC neurons (left) and averaged for each outcome sequence (identified by colors defined in Fig. 3C; right). Lines correspond to the best-fitting regression models. (**D**) The correlation coefficient between ΔDA and the deviation from reinforcement learning model for two different data sets (BMP, biased matching pennies; MP, matching pennies).

between different learning algorithms in the medial frontal cortex. Inabilities to choose appropriate learning algorithms are thought to underlie a number of psychiatric disorders and might arise from the disruption in the neural circuits investigated in the present study (*30*, *31*).

REFERENCES AND NOTES

1. T. Hastie, R. Tibshirani, J. Friedman, *The Elements of Statistical Learning* (Springer, New York, 2001).
2. G. Gigerenzer, H. Brighton, *Top. Cogn. Sci.* **1**, 107–143 (2009).
3. R. S. Sutton, A. G. Barto, *Reinforcement Learning: An Introduction* (MIT Press, Cambridge, MA, 1998).
4. M. Ito, K. Doya, *Curr. Opin. Neurobiol.* **21**, 368–373 (2011).
5. D. Lee, H. Seo, M. W. Jung, *Annu. Rev. Neurosci.* **35**, 287–308 (2012).
6. C. F. Camerer, *Behavioral Game Theory* (Princeton Univ. Press, Princeton, NJ, 2003).
7. H. L. Gallagher, C. D. Frith, *Trends Cogn. Sci.* **7**, 77–83 (2003).
8. A. N. Hampton, P. Bossaerts, J. P. O'Doherty, *Proc. Natl. Acad. Sci. U.S.A.* **105**, 6741–6746 (2008).
9. T. E. Behrens, L. T. Hunt, M. F. Rushworth, *Science* **324**, 1160–1164 (2009).
10. L. Zhu, K. E. Mathewson, M. Hsu, *Proc. Natl. Acad. Sci. U.S.A.* **109**, 1419–1424 (2012).
11. S. Suzuki *et al.*, *Neuron* **74**, 1125–1137 (2012).
12. H. Seo, D. Lee, *J. Neurosci.* **29**, 3627–3641 (2009).
13. J. F. Nash, *Proc. Natl. Acad. Sci. U.S.A.* **36**, 48–49 (1950).
14. Materials and methods are available as supplementary materials on *Science* Online.
15. A. Genovesio, P. J. Brasted, S. P. Wise, *J. Neurosci.* **26**, 7305–7316 (2006).
16. H. Seo, D. Lee, *J. Neurosci.* **27**, 8366–8377 (2007).
17. S. Tsujimoto, A. Genovesio, S. P. Wise, *Nat. Neurosci.* **13**, 120–126 (2010).
18. J. H. Sul, H. Kim, N. Huh, D. Lee, M. W. Jung, *Neuron* **66**, 449–460 (2010).
19. T. J. Vickery, M. M. Chun, D. Lee, *Neuron* **72**, 166–177 (2011).
20. H. Kim, D. Lee, M. W. Jung, *J. Neurosci.* **33**, 52–63 (2013).
21. D. J. Barraclough, M. L. Conroy, D. Lee, *Nat. Neurosci.* **7**, 404–410 (2004).
22. H. Seo, D. J. Barraclough, D. Lee, *J. Neurosci.* **29**, 7278–7289 (2009).
23. C. H. Donahue, H. Seo, D. Lee, *Neuron* **80**, 223–234 (2013).
24. K. Shima, H. Mushiake, N. Saito, J. Tanji, *Proc. Natl. Acad. Sci. U.S.A.* **93**, 8694–8698 (1996).
25. M. Isoda, O. Hikosaka, *Nat. Neurosci.* **10**, 240–248 (2007).
26. O. Hikosaka, M. Isoda, *Trends Cogn. Sci.* **14**, 154–161 (2010).
27. S. W. Lee, S. Shimojo, J. P. O'Doherty, *Neuron* **81**, 687–699 (2014).
28. A. Bernacchia, H. Seo, D. Lee, X. J. Wang, *Nat. Neurosci.* **14**, 366–372 (2011).
29. M. M. Botvinick, *Curr. Opin. Neurobiol.* **22**, 956–962 (2012).
30. T. V. Maia, M. J. Frank, *Nat. Neurosci.* **14**, 154–162 (2011).
31. D. Lee, *Neuron* **78**, 233–248 (2013).

ACKNOWLEDGMENTS

This study was supported by the grants from the National Institutes of Health (R01 MH 073246, R01 DA 029330, and T32 NS007224). All primary behavioral and neurophysiological data are archived in the Department of Neurobiology at Yale University School of Medicine.

SUPPLEMENTARY MATERIALS

www.sciencemag.org/content/346/6207/340/suppl/DC1
Materials and Methods
Figs. S1 to S8

19 May 2014; accepted 10 September 2014
Published online 18 September 2014;
10.1126/science.1256254

NITROGEN UPTAKE

Perception of root-derived peptides by shoot LRR-RKs mediates systemic N-demand signaling

Ryo Tabata,[1] Kumiko Sumida,[1] Tomoaki Yoshii,[2] Kentaro Ohyama,[2] Hidefumi Shinohara,[1] Yoshikatsu Matsubayashi[1]*

Nitrogen (N) is a critical nutrient for plants but is often distributed unevenly in the soil. Plants therefore have evolved a systemic mechanism by which N starvation on one side of the root system leads to a compensatory and increased nitrate uptake on the other side. Here, we study the molecular systems that support perception of N and the long-distance signaling needed to alter root development. Rootlets starved of N secrete small peptides that are translocated to the shoot and received by two leucine-rich repeat receptor kinases (LRR-RKs). *Arabidopsis* plants deficient in this pathway show growth retardation accompanied with N-deficiency symptoms. Thus, signaling from the root to the shoot helps the plant adapt to fluctuations in local N availability.

Nitrogen is an essential macronutrient in plants. Plants take up inorganic N directly from the soil in the form of nitrate or ammonium and assimilate these ions into amino acids. Most of the inorganic N in natural soils is, however, present as nitrate as a result of microbial nitrification. Additionally, there is spatial variation in soil nitrate distribution at scales relevant to individual plants due to uptake by plants or leaching by rain. Plants, therefore, have evolved sophisticated strategies allowing them to modulate the efficiency of root N acquisition in response to fluctuating external N availability and their own nutritional status.

Nitrate uptake systems are under control by both cell-autonomous local signaling triggered by nitrate itself and systemic long-distance signaling that transduces external and internal N status across spatially distant root compartments (*1*). N starvation on one side of the root system leads to an up-regulation of nitrate uptake on the other side of the root system (*2*–*4*). This compensatory N acquisition response is accompanied by the transcriptional up-regulation of nitrate transporter genes such as *NRT2.1* and is postulated to be mediated by a systemic signal, the N-demand signal (*2*–*4*).

Small molecules such as secreted peptides can mediate long-distance signaling, as exemplified by *Rhizobium*-induced CLAVATA3/ESR-related (CLE) peptides involved in autoregulation of nodulation (*5*). Similarly, peptide signaling may coordinate root development with needs for N. The genes that encode small peptide signals are often parts of large families of genes with overlapping and redundant functions (*6*). To overcome the experimental limitations associated with gene redundancy on signaling peptides, we explored the function of these peptides from the receptor side by a binding assay against an expression library of *Arabidopsis* leucine-rich repeat receptor kinases (LRR-RKs). Here, we clarify the functions of an *Arabidopsis*-secreted peptide family consisting of multiple functionally redundant members and identify peptide ligands and receptors mediating long-distance N-demand signaling.

The *Arabidopsis* C-terminally encoded peptide (CEP) family was identified by in silico screening for a family of secreted peptides that share short, conserved domains near the C terminus, a feature that is common to several posttranslationally modified small peptide signals in plants (*7*). CEP1 is secreted as a 15–amino acid peptide originating from a C-terminal conserved domain (the CEP domain) through posttranslational proline hydroxylation and proteolytic processing. A total of 15 *CEP* family genes (*CEP1* through *CEP15*) have been found in the *Arabidopsis* genome (*7*–*9*). Expression of *CEP1* through *CEP5* is mainly found in the basal region of the lateral roots, but minor expression has also been detected in the aboveground tissues. Overexpression of several *CEP* family genes leads to repression of root growth accompanied with morphological alterations of shoots and, conversely, loss-of-function mutation of *CEP3* promotes root development (*7*–*9*). However, genetic redundancy obscures the functions of *CEP*s.

To gain insight into the function of CEP family peptides, we prepared a CEP1 analog derivatized with ^{125}I-labeled photoreactive 4-azidosalicylic acid ([^{125}I]ASA-CEP1) (Fig. 1A). ASA-CEP1 exhibited biological activity comparable to that of CEP1 in a root growth assay (fig. S1A). We also generated an expression library of *Arabidopsis* LRR-RKs subfamily X and XI by overexpressing individual proteins in tobacco BY-2 cells. Photoaffinity labeling of *Arabidopsis* LRR-RKs by [^{125}I]ASA-CEP1 revealed that two related LRR-RKs, At5g49660 and At1g72180, in subfamily XI directly interact with

[1]Division of Biological Science, Graduate School of Science, Nagoya University, Chikusa, Nagoya 464-8602, Japan.
[2]Department of Applied Molecular Biosciences, Graduate School of Bio-Agricultural Sciences, Nagoya University, Chikusa, Nagoya 464-8601, Japan.
***Corresponding author. E-mail: matsu@bio.nagoya-u.ac.jp**

CEP1 (Fig. 1B and fig. S1B). This binding was competitively inhibited by excess unlabeled CEP1, supporting the specificity of this interaction. We confirmed that the double loss-of-function mutant of At5g49660 and At1g72180 was insensitive to CEP1 in a root growth assay (Fig. 1C and fig. S2A). We concluded that these two LRR-RKs function as CEP receptors and named them CEPR1 (At5g49660) and CEPR2 (At1g72180). At5g49660 has been characterized as XIP1, and a loss-of-function mutant displays anthocyanin accumulation in the leaves and ectopic lignification in phloem of inflorescence stems (*10*), although we did not observe the latter phenotype under our culture conditions.

Seedlings of *cepr1-1 cepr2-1* double mutants displayed a pleiotropic phenotype characterized by pale-green leaves and enhanced lateral root elongation (Fig. 1, D and E, and fig. S2B). At the adult stage, compared with wild type, the mutant developed smaller rosette leaves and shorter floral stems, accompanied by anthocyanin accumulation (fig. S2C). An enhanced lateral root elongation phenotype was also observed, albeit to a lesser degree, in the *cepr1-1* single mutant, but was absent in the *cepr2-1* single mutant, suggesting a major role of *CEPR1* and a minor but redundant role of *CEPR2* in the relevant signaling pathways (fig. S2D). Confirming this, a genomic fragment containing the 2.0-kb promoter and the entire *CEPR1*-coding region completely rescued the above phenotype when introduced in the *cepr1-1 cepr2-1* double mutant (fig. S2, C and D).

β-glucuronidase (GUS) reporter–aided histochemical analysis revealed *CEPR1* promoter activity in the vascular veins of cotyledons and mature leaves, primary roots, and lateral roots, except for the root tip region (Fig. 1F and fig. S3, A and B). *CEPR2* promoter activity was detected in mature leaves, primary roots, and the root tips of both primary roots and lateral roots.

Because enhanced lateral root elongation, pale-green leaves, dwarfism, and anthocyanin accumulation are typical responses to N starvation (*11*), we next analyzed whether *cepr1-1* and *cepr2-1* mutations affect expression of genes involved in N uptake and assimilation pathways. Using microarray profiling followed by quantitative reverse transcription polymerase chain reaction (qRT-PCR), we found that genes considerably down-regulated in the *cepr1-1 cepr2-1* mutant include *NRT2.1* (in the top 0.1% of all down-regulated genes), *NRT3.1* (in the top 1%), and *NRT1.1* (in the top 2%), which encode major components of the root nitrate transport system (table S1 and fig. S4A). These three genes are known to be targets for systemic N-demand signaling (*2*–*4*). Along with the decrease in expression of nitrate transporters, nitrate uptake activity of *cepr1-1 cepr2-1* mutant roots was considerably reduced compared with wild type, as indicated by analysis of $^{15}NO_3^-$ influx (Fig. 2A).

To confirm whether these *NRT* genes are indeed regulated by CEP, we treated roots of wild-type seedlings with 1 μM CEP1 for 6, 24, and 48 hours. qRT-PCR of transcripts in roots revealed that *NRT2.1* expression was up-regulated within 6 hours and transcripts accumulated over 5-fold after 24 hours, even under N-rich conditions (Fig. 2B). This stimulatory activity was dependent largely on *CEPR1* (Fig. 2C) and detectable at CEP1 concentrations as low as 100 nM when applied to wild-type plants (fig. S4B). CEP1 also induced other nitrate transporters such as *NRT3.1* and *NRT1.1* (Fig. 2B), but had lesser effects on expression of transporters for ammonium and other macronutrients (fig. S4C). These phenotypic and transcriptional analyses suggest that CEP signaling is likely to underlie N starvation responses and, accordingly, its overactivation or blockage leads to pleiotropic developmental effects in both roots and shoots.

The *Arabidopsis* genome includes 11 genes (*CEP1* through *CEP11*) encoding secreted polypeptides containing well-conserved 15–amino acid CEP domains and an additional 4 genes that may encode CEP-like peptides (*CEP12* through *CEP15*) (*7*–*9*). We selected *CEP1* through *CEP11* for deep analysis. qRT-PCR indicated that 10 of the 11 *CEP* genes are capable of inducing *NRT2.1* expression in roots when overexpressed in *Arabidopsis* seedlings (fig. S5). We confirmed that several of these CEPs—such as CEP3, CEP5, CEP6, and CEP9—are secreted as 15–amino acid peptides originating from conserved CEP domains (fig. S6, A to M) and that at least the CEP3 and CEP5 peptides interact with CEPR1 and induce *NRT2.1* expression at 1 μM (fig. S7, A and B).

In addition to the previously characterized *CEP1* through *CEP5* (*7*, *8*), we tested expression patterns of *CEP6* through *CEP11* by generating promoter-GUS reporter lines. We detected promoter activity of *CEP6*, *CEP8*, *CEP9*, and *CEP11* both in lateral root primordia and in lateral roots excluding the meristem region (fig. S8A). Promoter activity of *CEP6*, *CEP8*, and *CEP9* was also detected in the aerial tissues, such as leaf petioles and the shoot apex region (fig. S8B).

We then analyzed whether expression of CEP family peptides are under the control of external N status. When *Arabidopsis* seedlings cultured under N-rich conditions were transplanted to a medium devoid of N, we observed immediate induction of seven *CEP* genes (*CEP1*, *CEP3*, *CEP5*, *CEP6*, *CEP7*, *CEP8*, and *CEP9*) after 6 hours and further up-regulation for up to 24 hours (Fig. 2, D to F). Induction levels correlated well with external N status, being stronger at lower concentrations of nitrate, ammonium, and glutamine in the medium (Fig. 2G and fig. S9A). Deprivation of other macronutrients such as phosphate and potassium showed no effect on *CEP* expression (fig. S9B). These results indicate that the 7 *CEP* genes are up-regulated specifically in response to N starvation.

In a heterogeneous N environment, N starvation on one side of the roots can up-regulate nitrate transporter genes in a distant part of the roots exposed to a N-rich medium to compensate for N deficiency (*2*–*4*). This long-distance systemic response is postulated to be controlled by a N-demand signal emitted from the N-starved roots and is prominent when only nitrate is available

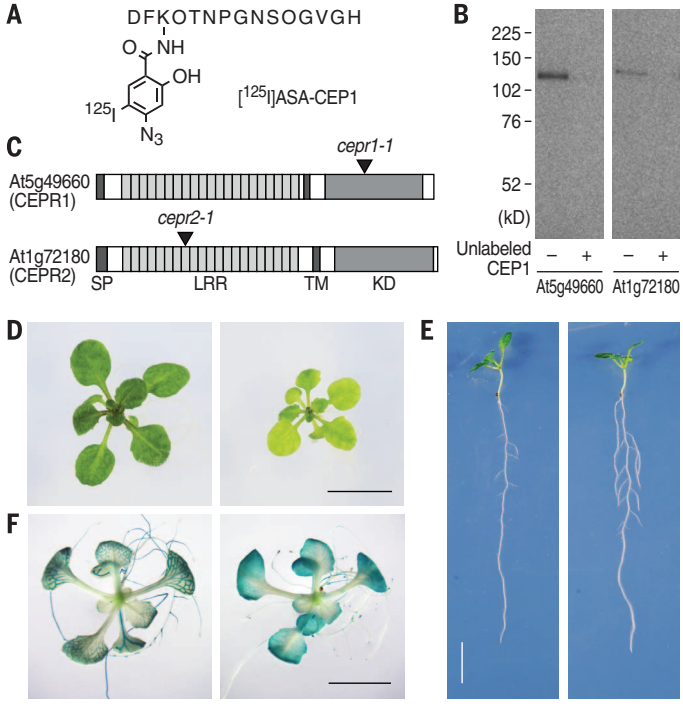

Fig. 1. Identification and functional characterization of *Arabidopsis* CEP receptors. (**A**) Structure of [^{125}I]ASA-CEP1 used for photoaffinity labeling. (**B**) Direct binding of 10 nM [^{125}I]ASA-CEP1 with LRR-RKs At5g49660 and At1g72180. This binding was competitively inhibited by 100-fold excess unlabeled CEP1. (**C**) Diagram of CEPR1 (At5g49660) and CEPR2 (At1g72180), showing the locations of the transferred DNA (T-DNA) insertions. The deduced primary structure of CEPR1 and CEPR2 includes an N-terminal signal peptide (SP), leucine-rich repeats (LRR), a transmembrane domain (TM), and an intracellular kinase domain (KD). (**D**) Shoot phenotype of 14-day-old wild-type (left) and *cepr1-1 cepr2-1* mutant (right) on the N-rich medium. Scale bar, 5 mm. (**E**) Root phenotypes of wild type (left) and *cepr1-1 cepr2-1* (right) vertically grown on the N-rich medium for 10 days. Scale bar, 1 cm. (**F**) Histochemical staining of *Arabidopsis* seedlings transformed with the *CEPR1pro:GUS* (left) and *CEPR2pro:GUS* (right) genes. Scale bar, 5 mm.

as a nitrogen source (*2*–*4*). If the CEP family peptides are involved in systemic N-demand signaling, we would expect the compensatory N acquisition response to be abolished in the *cepr1-1 cepr2-1* mutant. To test this possibility, we used a split-root culture system, in which the root system of a plant is separated into two parts exposed to different nutrient conditions (Fig. 3A).

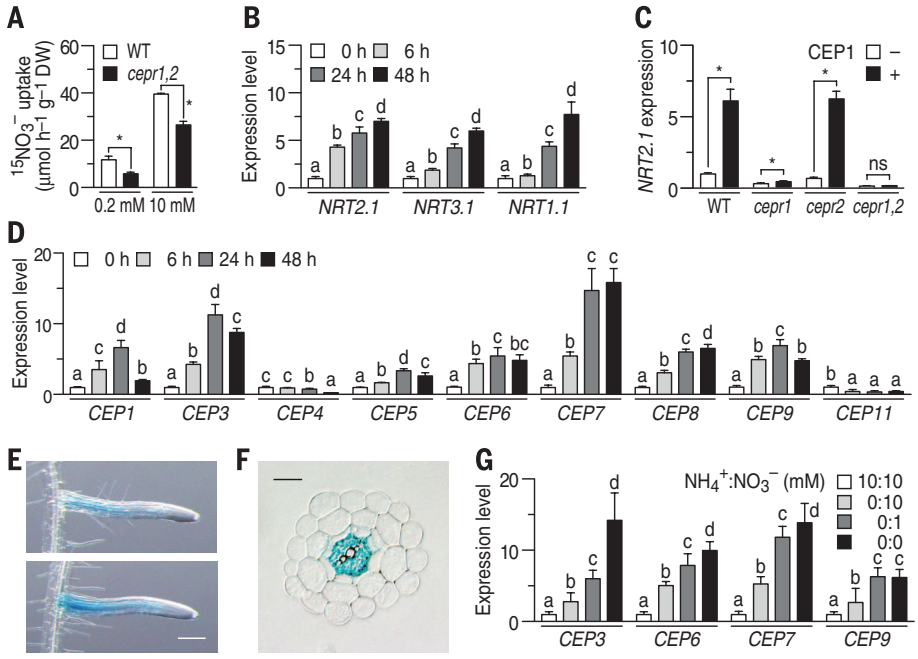

Fig. 2. CEP signaling underlies N-starvation response. (**A**) Nitrate uptake activity of wild-type and *cepr1-1 cepr2-1* roots, as determined by $^{15}NO_3^-$ influx at 0.2 mM and 10 mM (mean ± SD of triplicates, *$P <$ 0.05 by Student's *t* test. (**B**) qRT-PCR of *NRT* transcripts in the roots of wild-type *Arabidopsis* seedlings treated with 1 μM CEP1 for various periods of time. Significant differences between treatments are indicated with different letters ($P < 0.05$, one-way analysis of variance. (**C**) qRT-PCR of *NRT2.1* transcripts in roots of wild-type, *cepr1-1*, *cepr2-1*, and *cepr1-1 cepr2-1* seedlings treated with 1 μM CEP1 for 24 hours. (**D**) qRT-PCR of *CEP* transcripts in the roots of wild-type seedlings subjected to N starvation for various periods of time. *CEP2* transcripts were not detected. (**E**) Histochemical staining of roots of 10-day-old seedlings transformed with the *CEP6pro:GUS* gene before (top) and after (bottom) N starvation for 24 hours. Scale bar, 0.2 mm. (**F**) Cross section of N-starved lateral roots pictured in (E). Scale bar = 2 μm. (**G**) qRT-PCR of *CEP* transcripts in the wild-type roots subjected to various degrees of N deprivation for 24 hours.

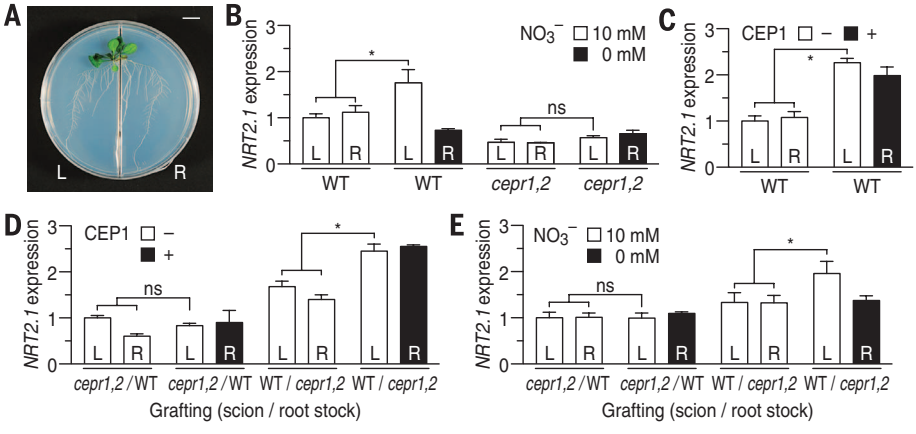

Fig. 3. Perception of root-derived CEP by CEPR in shoots mediates systemic N-demand signaling. (**A**) *Arabidopsis* split-root culture system in which the root system of a plant is separated into left (L) and right (R) parts that are exposed to different nutrient conditions. Scale bar, 1 cm. (**B**) qRT-PCR of *NRT2.1* transcripts on each side of the split-root system of wild-type and *cepr1-1 cepr2-1* plants, in which one side of the root system was starved for N for 24 hours (mean ± SD of triplicates). (**C**) qRT-PCR of *NRT2.1* transcripts on each side of a split-root system of wild-type plants, in which one side was treated with 1 μM CEP1 for 24 hours. (**D** and **E**) qRT-PCR of *NRT2.1* transcripts on each side of a split-root system of reciprocally grafted plants, in which one side was treated with 1 μM CEP1 for 48 hours (D) or starved for N for 48 hours (E).

We transferred one side of the split-root system to a medium lacking N, whereas the other side was kept in a medium containing 10 mM NO_3^-. In wild-type plants, we observed up-regulation of *NRT2.1*, *NRT3.1*, and *NRT1.1* in the roots exposed to the N-rich medium after 24 hours (Fig. 3B and fig. S10, A and B), accompanied by induction of *CEP* genes in the portion of the root system directly experiencing N starvation (fig. S10C). In contrast, no such systemic up-regulation of nitrate transporter genes was detected in the roots of the *cepr1-1 cepr2-1* mutant, despite local induction of *CEP* genes in the N-starved roots (Fig. 3B and fig. S10, A, B, and D). These results indicate that CEP family peptides are components for systemic N-demand signaling in roots.

We then analyzed whether systemic induction of nitrate transporter genes is observed in a split-root system in response to CEP1 treatment instead of N starvation. When both sides of a split-root system were cultured in the presence of 10 mM NO_3^- and one side was treated with 1 μM CEP1, we observed up-regulation of *NRT2.1* in the untreated distant roots as well as the treated roots (Fig. 3C). This systemic response was detectable as early as 6 hours after CEP1 treatment (fig. S10E). *NRT3.1* and *NRT1.1* also showed similar systemic responses (fig. S10, F and G). These results indicate that CEP1 mediates systemic up-regulation of nitrate transporter genes over long distances in roots. Our observation that, in contrast to N starvation, CEP1 treatment on one side in the presence of 10 mM NO_3^- causes up-regulation of *NRT2.1* on both sides of a split-root system suggests that CEP-mediated up-regulation of nitrate transporters may also reflect the balance of local external NO_3^- availability and nutritional status of the whole plant.

Finally, to analyze whether root-derived CEP1 is perceived directly in roots or perceived in shoots and then induces a descending secondary signal that up-regulates nitrate transporters, we performed split-root experiments combined with reciprocal grafting between *cepr1-1 cepr2-1* and wild-type plants. When *cepr1-1 cepr2-1* mutant scions were grafted onto wild-type rootstocks by hypocotyl-to-hypocotyl grafting followed by treating one side of the root system with CEP1, we observed no up-regulation of *NRT2.1* on either side of the root system (Fig. 3D). In contrast, when wild-type scions were grafted onto *cepr1-1 cepr2-1* mutant rootstocks, root-applied CEP1 caused substantial systemic up-regulation of *NRT2.1* on both sides of the root system, even though the rootstocks themselves expressed no CEP receptors (Fig. 3D). In split N-starvation experiments, we confirmed that systemic up-regulation of *NRT2.1* in roots was induced only when wild-type scions were grafted onto *cepr1-1 cepr2-1* mutant rootstocks (Fig. 3E). These results indicate that CEPRs expressed in the shoots are responsible for the CEP-mediated systemic up-regulation of nitrate transporters in roots and that root-derived CEP is graft-transmissible from roots to shoots. Further supporting the mobile nature of CEP family peptides, we detected endogenous CEPs in xylem sap collected from *Arabidopsis* plants (fig. S11, A to G). The levels in

xylem sap were high under N-starved conditions but lower under N-rich conditions.

Altogether, the available evidence from molecular and physiological analyses of CEP–CEPR ligand receptor pairs suggests that CEP acts as a root-derived ascending N-demand signal to the shoot, where its perception by CEPR leads to the production of a putative shoot-derived descending signal that up-regulates nitrate transporter genes in the roots. This mechanism supports N acquisition, especially when NO_3^- is unevenly distributed within the soil. CEP family peptides induced on one side of the roots by local N starvation mediate up-regulation of nitrate transporter genes in the distant part of the roots exposed to N-rich conditions to compensate for N deficiency.

The systemic mode of action of CEP family peptides in N-demand signaling is reminiscent of that of *Rhizobium*-induced, xylem-mobile CLE peptides that suppress excess nodulation in legume plants, although CEP plays a role opposite to that of CLE in terms of lateral organ formation (*5*, *12*, *13*). Plants, as sessile organisms, continuously face a complex array of environmental fluctuations and have evolved sophisticated responses to cope with them. Given that CEP family peptides are conserved throughout vascular plants except for ferns (*8*, *9*), peptide-mediated root-to-shoot-to-root long-distance signaling is likely to be a general strategy employed by all higher plants for environmental adaptation.

REFERENCES AND NOTES

1. B. G. Forde, *Annu. Rev. Plant Biol.* **53**, 203–224 (2002).
2. X. Gansel, S. Muños, P. Tillard, A. Gojon, *Plant J.* **26**, 143–155 (2001).
3. S. Ruffel *et al.*, *Plant Physiol.* **146**, 2020–2035 (2008).
4. S. Ruffel *et al.*, *Proc. Natl. Acad. Sci. U.S.A.* **108**, 18524–18529 (2011).
5. D. E. Reid, B. J. Ferguson, S. Hayashi, Y. H. Lin, P. M. Gresshoff, *Ann. Bot. (Lond.)* **108**, 789–795 (2011).
6. Y. Matsubayashi, *Annu. Rev. Plant Biol.* **65**, 385–413 (2014).
7. K. Ohyama, M. Ogawa, Y. Matsubayashi, *Plant J.* **55**, 152–160 (2008).
8. I. Roberts *et al.*, *J. Exp. Bot.* **64**, 5371–5381 (2013).
9. C. Delay, N. Imin, M. A. Djordjevic, *J. Exp. Bot.* **64**, 5383–5394 (2013).
10. A. C. Bryan, A. Obaidi, M. Wierzba, F. E. Tax, *Planta* **235**, 111–122 (2012).
11. E. A. Vidal, R. A. Gutiérrez, *Curr. Opin. Plant Biol.* **11**, 521–529 (2008).
12. N. Imin, N. A. Mohd-Radzman, H. A. Ogilvie, M. A. Djordjevic, *J. Exp. Bot.* **64**, 5395–5409 (2013).
13. S. Okamoto, H. Shinohara, T. Mori, Y. Matsubayashi, M. Kawaguchi, *Nat. Commun.* **4**, 2191 (2013).

ACKNOWLEDGMENTS

This research was supported by a Grant-in-Aid for Scientific Research (S) from the Ministry of Education, Culture, Sports, Science, and Technology (no. 25221105). The supplementary materials contain additional data.

SUPPLEMENTARY MATERIALS

www.sciencemag.org/content/346/6207/343/suppl/DC1
Materials and Methods
Figs. S1 to S11
Table S1
References (*14*–*18*)

23 June 2014; accepted 3 September 2014
10.1126/science.1257800

TROPHIC CASCADES

Large carnivores make savanna tree communities less thorny

Adam T. Ford,[1,2]* Jacob R. Goheen,[2,3] Tobias O. Otieno,[2] Laura Bidner,[2,4] Lynne A. Isbell,[2,4] Todd M. Palmer,[2,5] David Ward,[6] Rosie Woodroffe,[2,7] Robert M. Pringle[2,8]

Understanding how predation risk and plant defenses interactively shape plant distributions is a core challenge in ecology. By combining global positioning system telemetry of an abundant antelope (impala) and its main predators (leopards and wild dogs) with a series of manipulative field experiments, we showed that herbivores' risk-avoidance behavior and plants' antiherbivore defenses interact to determine tree distributions in an African savanna. Well-defended thorny *Acacia* trees (*A. etbaica*) were abundant in low-risk areas where impala aggregated but rare in high-risk areas that impala avoided. In contrast, poorly defended trees (*A. brevispica*) were more abundant in high- than in low-risk areas. Our results suggest that plants can persist in landscapes characterized by intense herbivory, either by defending themselves or by thriving in risky areas where carnivores hunt.

The observation that most ecosystems support abundant plant life, despite the existence of herbivores that eat plants, has motivated a great deal of research and debate in ecology. Two broad hypotheses have been advanced to explain this phenomenon. The green world hypothesis (*1*) posits that predators indirectly benefit plants by suppressing herbivory; such trophic cascades occur when carnivores consumptively reduce herbivore densities or trigger risk-avoidance behaviors (such as increased vigilance or refuge-seeking) that reduce plant consumption (*2*, *3*). In contrast, the plant defense hypothesis contends that the world is green because plants have evolved structural and chemical defenses that inhibit consumption (*4*, *5*), often at a cost to their growth and competitive ability (*6*, *7*). Although traditionally viewed as alternatives, these hypotheses are no longer thought to be mutually exclusive (*7*, *8*). A key challenge for contemporary ecology is to understand how plant defense and predation interact across landscapes to shape a green world (*8*).

We evaluated how the combination of plant defense and risk avoidance by a common African ungulate (impala, *Aepyceros melampus*) determined the outcome of a trophic cascade in an East African savanna. Impala consume a mixture of grasses and trees ("browse") (*9*) and are preyed upon by several carnivores, especially leopards (*Panthera pardus*) and African wild dogs (*Lycaon pictus*) (fig. S1). We tested three hypotheses (Fig. 1) to explain the structure of this food web: (i) Predation risk drives habitat selection by impala; (ii) impala prefer to eat less-thorny tree species, thereby suppressing their abundance; and (iii) predation risk thus differentially influences the distribution of thorny versus less-thorny *Acacia* trees (table S1).

To test our first hypothesis, we quantified habitat selection by impala, using resource selection functions, global positioning system (GPS) telemetry, and high-resolution (0.36-m^2) satellite imagery (*10*) (fig. S2). Specifically, we quantified the selection of woody cover, which represents forage for impala (*9*) but could also increase risk by concealing predators (*11*, *12*). We also tracked how impala used two discrete habitat features typified by low versus high woody cover (fig. S3): (i) "glades," which are ~0.5-ha clearings (with 8% mean tree cover) derived from abandoned cattle corrals, covered with nutrient-rich grasses, and maintained through grazing by wildlife (*13*, *14*); and (ii) "thickets," which are <100-m-wide strips of woody vegetation (with 25% cover) along the edges of dry channels. We then quantified the relationship between woody cover and two components of risk: (i) relative probability of encountering predators, assessed using resource-selection functions of leopards and wild dogs for woody cover; and (ii) per-capita risk of mortality from predation, measured as the spatial distribution of kill sites relative to the spatial distribution of impala (*10*).

Impala avoided woody cover (Fig. 2A) and aggregated in glades and other open habitats, especially during times of the day when their predators are most active (tables S2 and S3). Both the relative probability of encountering predators (Fig. 2A) and the per-capita risk of mortality from predation (Fig. 2B) increased with increasing woody cover. Leopards and wild dogs accounted for 83% of impala kills (52 and 31% respectively; fig. S1), and kill sites from all carnivore species occurred in areas with similar amounts of woody cover ($F_{2,51}$ = 0.765, P = 0.47).

[1]Department of Zoology, University of British Columbia, Vancouver, BC, Canada. [2]Mpala Research Centre, Post Office Box 555, Nanyuki, Kenya. [3]Department of Zoology and Physiology, University of Wyoming, Laramie, WY, USA. [4]Department of Anthropology, University of California, Davis, CA, USA. [5]Department of Biology, University of Florida, Gainesville, FL, USA. [6]School of Life Sciences, University of KwaZulu-Natal, Scottsville, South Africa. [7]Institute of Zoology, Zoological Society of London, Regent's Park, London, UK. [8]Department of Ecology and Evolutionary Biology, Princeton University, Princeton, NJ, USA.
*Corresponding author. E-mail: atford@zoology.ubc.ca

Thus, a single cue—woody cover—integrated two components of risk (encounters and mortalities) arising from the two major predators of impala.

Although impala avoided risky areas, this behavior might be explained by selection for the nutrient-rich grasses that characterize glades and open habitats (*14*). We tested this alternative hypothesis by experimentally removing all woody cover from five 0.5-ha plots, thereby

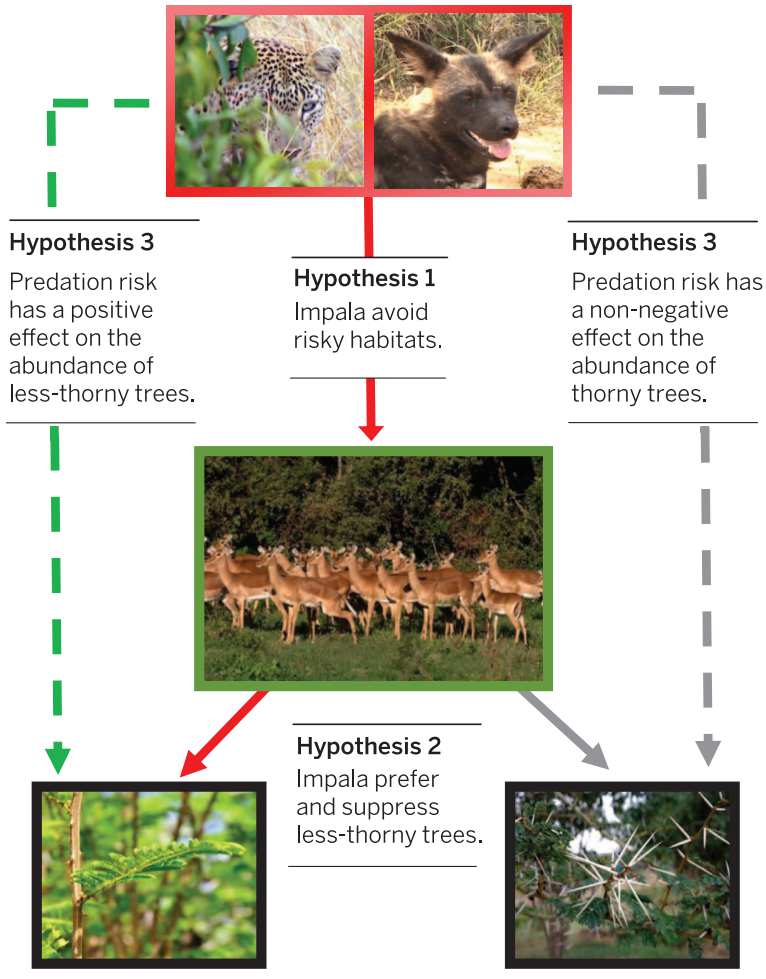

Fig. 1. Food web hypotheses tested in our study. Solid and dashed arrows represent direct and indirect effects, respectively. Red arrows represent negative effects, green arrows represent positive effects, and gray arrows represent either neutral or positive effects. Hypothesis 1: The risk of predation from large carnivores drives habitat selection of impala. Hypothesis 2: Impala both prefer and suppress the densities of poorly defended plants. Hypothesis 3: Predation risk increases the abundance of poorly defended trees in high-risk areas.

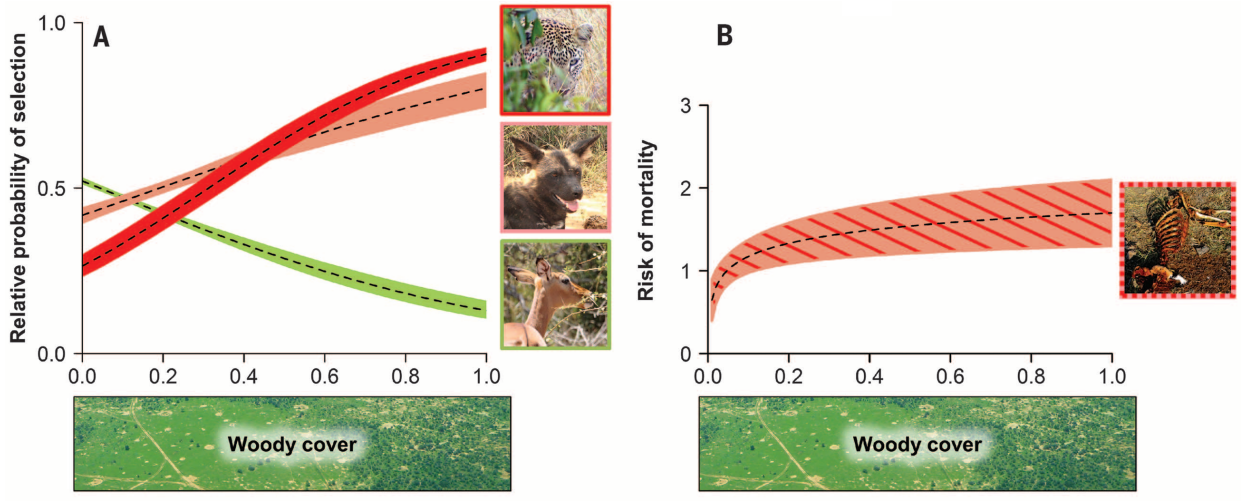

Fig. 2. Impala avoid risky areas, characterized by increasing woody cover. **(A)** Habitat selection by impala (green, β = –1.99 ± 0.14, n = 20 impala, P < 0.001), leopards (red, β = 3.42 ± 0.14, n = 4 leopards, P < 0.001), and wild dogs (pink, β = 1.64 ± 0.19, n = 5 wild dogs, P < 0.001), where the βs represent population-level coefficients from resource selection functions for woody cover. Positive and negative coefficients indicate selection and avoidance of woody cover, respectively. (**B**) The predicted per-capita risk of mortality from predation [1.70 + 0.228 × ln(woody cover)], coefficient of determination based on pooled kill sites from all large carnivores (fig. S2). Values <1 and >1 indicate that kill sites occur less or more than expected, respectively, relative to the spatial distribution of impala. Shading indicates 95% prediction intervals.

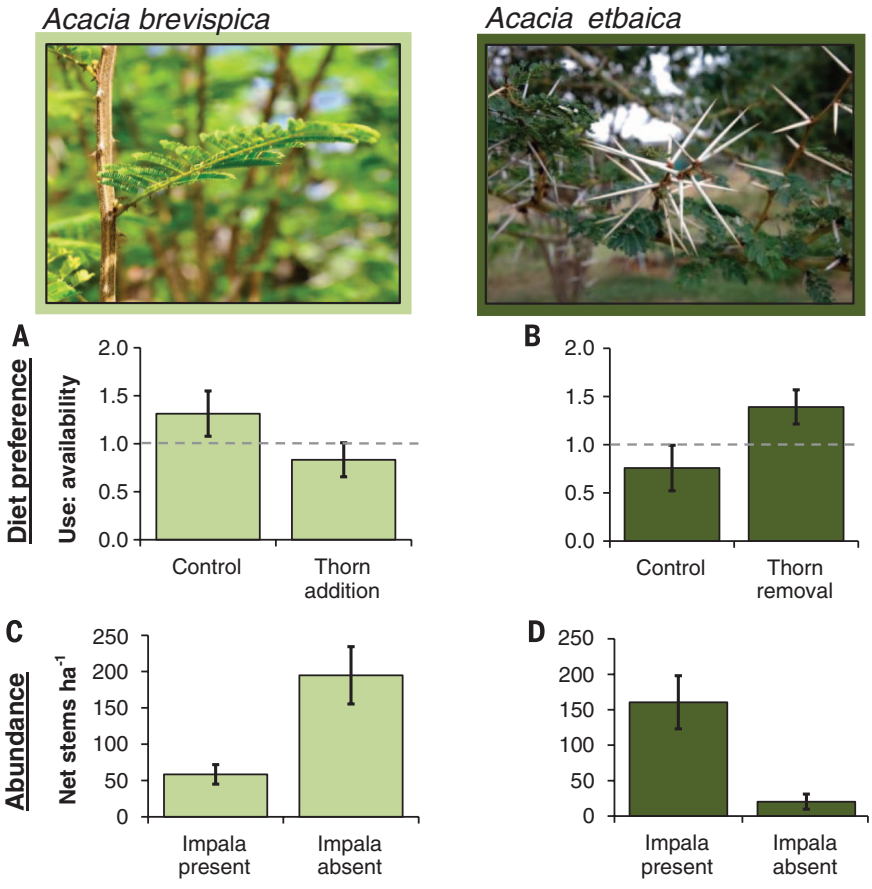

Fig. 3. Impala both preferentially consume and suppress *Acacia* spp. lacking large thorns. The presence of long thorns significantly reduced impala's preference for (**A**) *A. brevispica* and (**B**) *A. etbaica* in feeding experiments [likelihood ratio (*LR*) = 4.76, $P = 0.029$)]. The effects of species and species × thorns on preference were nonsignificant (*10*). A value of 1 (dashed line) indicates that diet preference (leaf consumption) occurred randomly among the four treatments, whereas values >1 indicate selection and values <1 indicate avoidance. Over a 5-year impala exclusion experiment, the net density (stems/ha) of (**C**) *A. brevispica*, which lacks long thorns, increased in plots where impala were absent (*LR*: $\chi^2_1 = 127.13$, $P < 0.001$); in contrast, (**D**) *A. etbaica* decreased in plots where impala were absent (*LR*: $\chi^2_1 = 158.88$, $P < 0.001$). Error bars indicate ±1 SEM.

mimicking the lowered risk of glades, but without potential confounds associated with forage quality. We monitored the movements of five GPS-collared impala herds for 60 days before and after creating these clearings. Impala's use of these areas increased by 160 to 576% after the removal of woody cover (table S4), indicating that forage quantity and quality cannot fully explain impala's selection of open areas. Additionally, impala typically increase their consumption of woody plants during the dry season when grass quality is poor (*9*), yet we detected no significant influence of season on their use of open habitat (tables S2 and S3). Hence, risk avoidance appears to drive habitat selection by impala.

We next tested our second hypothesis: that impala prefer and consequently reduce the abundance of poorly defended plants. We started by quantifying the effect of plant defenses on diet preference, focusing on two common *Acacia* species (*A. brevispica* and *A. etbaica*) that together constitute ~80% of trees in the study area (*13*) and differ in traits that may affect the diet preference of herbivores (*4*–*8*): *A. brevispica* has shorter thorns (≤0.6 cm versus ≤6.0 cm) but higher condensed-tannin concentrations than *A. etbaica* (table S5). To measure the impact of these traits on diet preference, we removed thorns from *A. etbaica* branches and attached them to *A. brevispica* branches; we then presented both types of manipulated branches alongside unmanipulated controls of each species to free-ranging impala in a cafeteria-style feeding experiment. Mean leaf selection by impala was 1.4 times greater for unmanipulated *A. brevispica* branches than for unmanipulated *A. etbaica* (Fig. 3, A and B). This preference for *A. brevispica* was due to differential thorniness: The removal of

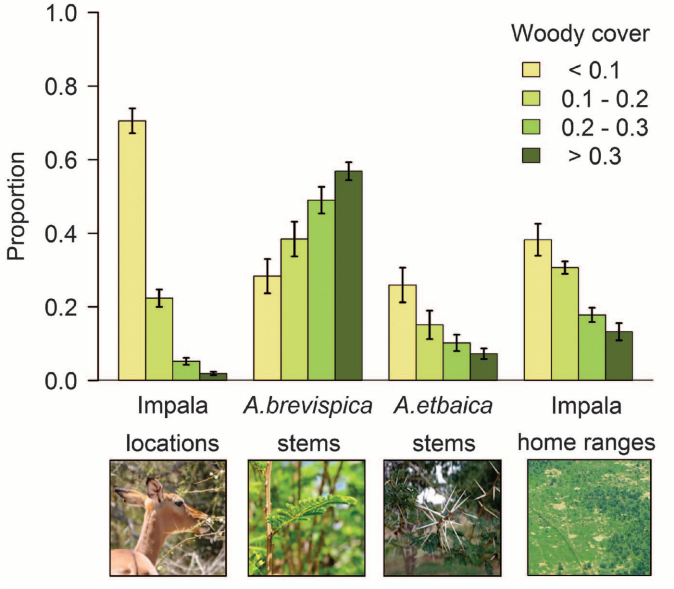

Fig. 4. Tree-community composition as a function of predation risk. Impala avoid woody cover because it increases the risk of predation (Fig. 1), thereby shifting tree communities toward dominance by the less thorny species (*A. brevispica*) as woody cover increases. Shown are (left) the mean proportions of GPS relocations per individual ($n = 20$ adult female impala located at 20-min intervals in 2011–2012) within each of four classes of woody cover; the proportions of poorly defended *A. brevispica* (middle left) and well-defended *A. etbaica* (middle right) among the total number of trees within 108 randomly located 200 m^2 transects; and (right) the availability of woody cover within impala home ranges. Additionally, in Poisson regressions, woody cover had a positive effect on the number of *A. brevispica* stems [1.96 + exp(3.74 × woody cover); $P < 0.001$] and a negative effect on the number *A. etbaica* stems [1.52 + exp(−1.03 × woody cover); $P = 0.011$]. Error bars indicate ±1 SEM.

A. etbaica's long thorns increased leaf selection to levels commensurate with that of unmanipulated *A. brevispica*, whereas selection for thorn-addition *A. brevispica* was roughly equal to that of unmanipulated *A. etbaica* (Fig. 3, A and B). Thus, we conclude that *A. brevispica* is preferred relative to *A. etbaica* and that this preference is determined by thorns rather than tannins or other species-specific attributes.

Next, we considered whether the diet preference of impala could alter the abundance of *Acacia* species. We therefore measured the net change in the density of tree stems from 2009–2014 within nine replicate sets of 1-ha herbivore exclosures that independently manipulated megaherbivores [elephants (*Loxodonta africana*) and giraffes (*Giraffa camelopardalis*)], mesoherbivores [impala and eland (*Taurotragus oryx*)], and small browsers [dik-dik (*Madoqua guentheri*)], using electrified wires at different heights (*15*). We isolated the effects of impala on *Acacia* species by comparing the megaherbivore and mesoherbivore-exclusion treatments; we attributed mesoherbivore-driven effects on tree density to impala because they account for ~87% of browser biomass in this size class (*9*). The exclusion of impala increased the net stem density of the preferred and poorly defended *A. brevispica* by 233% (Fig. 3C). Conversely, net stem density of well-defended *A. etbaica* increased by 692% in plots accessible to impala as compared to impala-exclusion plots (Fig. 3D). This increase in *A. etbaica* in plots where impala were present is perhaps due to reduced competition with *A. brevispica* (*15*, *16*). Thus, although impala consumed leaves from both *Acacia* species (Fig. 3, A and B), the long thorns of *A. etbaica* enabled them to avoid suppression by impala.

To evaluate our third and final hypothesis, we related spatial patterns in the abundance of these two *Acacia* species to satellite-derived estimates of woody cover. We counted all trees in 108 transects (200 m^2) located near randomly selected glades and thickets throughout our 140-km^2 study area. The abundance of *A. brevispica* increased monotonically with satellite-derived estimates of woody cover (i.e., risk) across these transects, whereas *A. etbaica* became scarcer as woody cover increased (Fig. 4 and fig. S4). Risk avoidance by impala (Fig. 2) was functionally analogous to impala exclusion by electrified fences (Fig. 3, C and D): Our results consistently showed that the absence of impala herbivory increased the prevalence of poorly defended trees but not the prevalence of well-defended trees. Thus, tree communities became less thorny as predation risk arising from large carnivores increased (Fig. 4).

Collectively, our results show that the nature of trophic control is contingent on biotic context: namely predation risk and plant defenses (Fig. 1). Both mechanisms enable plants to thrive in different parts of the landscape: Where risk is high, poorly defended trees are released from browsing, resulting in a trophic cascade; where risk is low, intense herbivory increases the benefit of defenses, creating communities dominated by thorny trees. Consequently, the thorniness of tree communities decreased across the landscape because of the way in which impala responded to spatial variation in predation risk, and also because of the way plant defenses affected impala's diet preference.

Human activities—both past and present—exert a major influence on the interactions between carnivores, impala, and the tree community. Glades represent the legacy of traditional livestock production (*17*), generating a constellation of refugia that has shaped the spatial distribution of impala herbivory. However, the loss of large carnivores will make landscapes less risky (*18*), decoupling the spatial interplay of risk avoidance and herbivory. The loss of carnivores will also render obsolete the need for pastoralists to corral their cattle nightly, eliminating the formation of glades. Consequently, human-driven extirpation of large carnivores from African savannas (*2*) will reduce spatial variation in plant communities, leading to a world that is thornier, but still green. As large-carnivore populations continue to decline globally, understanding the context in which predators shape key ecosystem processes is an urgent priority (*19*). Studies integrating risk of predation and plant defenses will constitute a major step toward this goal.

REFERENCES AND NOTES

1. N. G. Hairston, F. E. Smith, L. B. Slobodkin, *Am. Nat.* **94**, 421 (1960).
2. J. A. Estes *et al.*, *Science* **333**, 301–306 (2011).
3. E. L. Preisser, D. I. Bolnick, M. F. Benard, *Ecology* **86**, 501–509 (2005).
4. W. W. Murdoch, *Am. Nat.* **100**, 219 (1966).
5. S. L. Pimm, *The Balance of Nature?: Ecological Issues in the Conservation of Species and Communities* (Univ. of Chicago Press, Chicago, 1991).
6. O. J. Schmitz, *Proc. Natl. Acad. Sci. U.S.A.* **91**, 5364–5367 (1994).
7. K. A. Mooney, R. Halitschke, A. Kessler, A. A. Agrawal, *Science* **327**, 1642–1644 (2010).
8. O. J. Schmitz, *Resolving Ecosystem Complexity*, vol. 47 of *Monographs in Population Biology*, S. A. Levin, H. S. Horn, Eds. (Princeton Univ. Press, Princeton, NJ, 2010).
9. D. J. Augustine, *Afr. J. Ecol.* **48**, 1009–1020 (2010).
10. Materials and methods are available as supplementary materials on *Science* Online.
11. R. Underwood, *Behaviour* **79**, 81–107 1982).
12. M. Thaker *et al.*, *Ecology* **92**, 398–407 (2011).
13. T. P. Young, N. Patridge, A. Macrae, *Ecol. Appl.* **5**, 97 (1995).
14. D. J. Augustine, *J. Wildl. Manage.* **68**, 916–923 (2004).
15. J. R. Goheen *et al.*, *PLOS ONE* **8**, e55192 (2013).
16. J. L. Orrock, R. D. Holt, M. L. Baskett, *Ecol. Lett.* **13**, 11–20 (2010).
17. K. E. Veblen, *J. Arid Environ.* **78**, 119–127 (2012).
18. J. Berger, J. E. Swenson, I.-L. Persson, *Science* **291**, 1036–1039 (2001).
19. W. J. Ripple *et al.*, *Science* **343**, 1241484 (2014).

ACKNOWLEDGMENTS

This research was supported by grants from Canada's Natural Sciences and Engineering Research Council (A.T.F., J.R.G.), the University of British Columbia (A.T.F.), the University of Wyoming (J.R.G.), the American Society of Mammalogists (A.T.F.), Keren Keyemet I'Israel (D.W.), the U.S. National Science Foundation (L.A.I.), and the Wenner-Gren Foundation (L.B.). We thank S. Lima, M. Kinnaird, M. Littlewood, B. Agwanda, C. Forbes, J. Estes, M. Kauffman, R. Ostfeld, S. Buskirk, C. Martinez del Rio, C. Riginos, and the Kenya Wildlife Service. Comments from three anonymous reviewers greatly improved the manuscript.

SUPPLEMENTARY MATERIALS

www.sciencemag.org/content/346/6207/346/suppl/DC1
Materials and Methods
Figs. S1 to S4
Tables S1 to S5
References

28 February 2014; accepted 15 September 2014
10.1126/science.1252753

CLIMATE CHANGE

Increased variability of tornado occurrence in the United States

Harold E. Brooks,[1]* Gregory W. Carbin,[2] Patrick T. Marsh[2]

Whether or not climate change has had an impact on the occurrence of tornadoes in the United States has become a question of high public and scientific interest, but changes in how tornadoes are reported have made it difficult to answer it convincingly. We show that, excluding the weakest tornadoes, the mean annual number of tornadoes has remained relatively constant, but their variability of occurrence has increased since the 1970s. This is due to a decrease in the number of days per year with tornadoes combined with an increase in days with many tornadoes, leading to greater variability on annual and monthly time scales and changes in the timing of the start of the tornado season.

Separating nonmeteorological effects in the official database of tornadoes in the United States from actual meteorological ones has made interpreting the existence and causes of long-term physical changes in tornado occurrence extremely difficult (*1*). Nonmeteorological effects in the database result from changes in the emphasis on, and methodology of, collecting reports, and from how tornadoes are observed. The mean occurrence of well-reported aspects of the database, such as the mean annual

[1]National Oceanic and Atmospheric Administration (NOAA)/National Severe Storms Laboratory, Norman, OK 73072, USA. [2]NOAA/National Weather Service Storm Prediction Center, Norman, OK 73072, USA.
*Corresponding author. E-mail: harold.brooks@noaa.gov

number of all but the weakest tornadoes and their locations, has appeared to show little or no consistent trend (*2*). In light of the long-term warming of the globe and the United States, the apparent lack of relationship between large-scale temperature and tornadoes has led to questions about long-term changes in occurrence in the future (*3*, *4*).

As a result of the nonmeteorological effects on the tornado database, much of the research has focused on developing covariates that relate environmental conditions to the occurrence of tornadoes and looking at distributions of those covariates in time and space, mimicking a process seen in operational weather forecasting (*5*–*8*). Unfortunately, the approach of using covariates has produced more robust results for severe thunderstorms (including large hail and strong nontornadic winds) than for tornadoes themselves. Environments with large values of convective available potential energy (CAPE) favor severe thunderstorms because they support strong updrafts and large values of wind shear (the change of the environmental horizontal winds with height, over the lowest ~6 km of the atmosphere), a factor that leads to rotation of the storm. In general, the CAPE term is projected to increase in the United States with warming over the next century, and the shear term is projected to decrease, with the net effect being that the frequency of environments supportive of severe thunderstorms is projected to increase over the 21st century, but the fraction of those storms that are tornadic may decrease, so that it is difficult to have confidence in changes in mean tornado occurrence. (*7*, *8*).

Part of the problem with tornado discrimination has to do with the sample size and the strength of the statistical relationships between events and environments, and part to limitations of the descriptions of the environments, both from raw and processed observations, as well as from numerical prediction models. In particular, most of the variables associated with discriminating tornadic from nontornadic environments in forecasting are typically concentrated in the lowest 1 km of the atmosphere and, as such, require high-vertical-resolution data in that layer (*5*, *9*, *10*). Recent results from analysis of the higher-resolution climate simulations have suggested that the frequency of environments supportive of tornadoes will increase in a warming climate, particularly in springtime, based on an increase in the frequency of high values of wind shear in the lowest 1 km (*8*).

The long-term annual database of (E)F1 [F is for Fujita, and E is for Enhanced; the Fujita scale is used for damage ratings before March 2007, and the Enhanced Fujita Scale (*1*) for damage ratings since then, with 0 being the weakest and 5 the strongest] and stronger tornadoes from 1954 to 2013 shows much interannual variability but no long-term linear trend (Fig. 1). Despite the lack of a long-term annual trend, changes in the distribution of tornado occurrence are present at shorter time scales. In the past 15 years (1999–2013)—a quarter of the database—the largest number of (E)F1+ tornadoes occurring in a calendar month have been during the 6 months of January, February, April, May, September, and October (table S1). Only two of the monthly maxima are in the first half of the 1954–2013 period (March and December). On the other hand, records for the fewest number of (E)F1+ tornadoes in a calendar month have been set in 5 different months (February, May, June, July, and September) and tied in 2 other months (January and November) in 1999–2013. (There are seven Januarys, three Novembers, and four Decembers with no tornadoes.) The only calendar month with a nonzero record minimum for (E)F1+ tornado occurrence in the 1954 to 1983 period is March. Thus, 11 monthly records (of either sign) and two ties have occurred in the final quarter of the observational period. Excluding the zero-tornado months, there are more extreme months in the most recent 15 years of the database than in the first 45 years, and those extremes are essentially equally balanced between minima and maxima. A more complete picture of the increase in variability of monthly tornado occurrence can be seen by considering the variability of ranks of monthly tornado counts. For each calendar month, we have ranked the tornado count from 1 (fewest) to 60 (most), with ties being assigned the mean value of ranks for the ties. The standard deviation (SD) of ranks calculated over a 15-year period has increased from 15.1 in the first 15 years to 18.8 in the most recent 15 years of the database. The overall SD of the ranks is 17.3, with a 95% confidence interval (CI) for a 15-year period of (16.1, 18.4) (Fig. 2).

Another aspect of the tornado database that has shown increased variability is the timing of the beginning of the "tornado season." The definition of the beginning of the season is somewhat ambiguous and arbitrary. Any apparently objective definition will have the subjectivity of what the definition values as most important. One could consider what day was the first to have more than some threshold (such as any tornado, or 10 tornadoes, for example) or the date when some accumulated total of tornadoes or tornado days has been reached. Unlike tropical cyclones in the North Atlantic, which have a season from June to November, there are no times of the year in which conditions make it almost certain that the event will never occur. Tornadoes have occurred on every calendar day of the year in the United States in the past 60 years. Defining the beginning of the tornado season as the date of the first tornado leads to the possibility of a single event on 1 January making it appear that the season got off to an early start, even though there

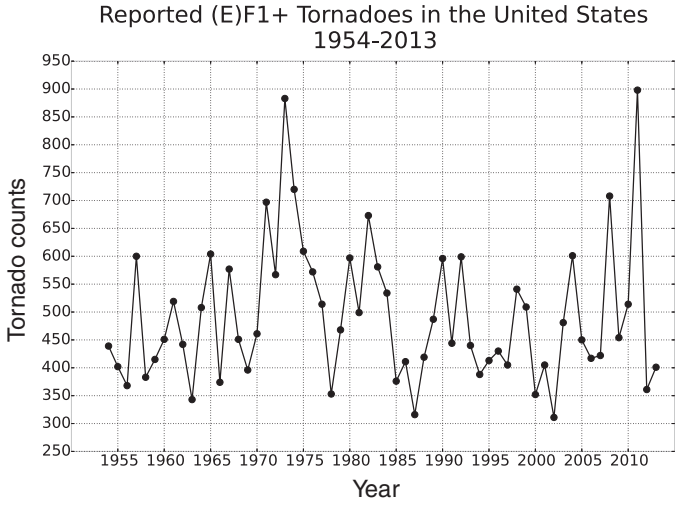

Fig. 1. Number of reported (E)F1+ tornadoes in United States by year, 1954–2013. These data have a mean of 495 and show a linear trend of −0.001 per year.

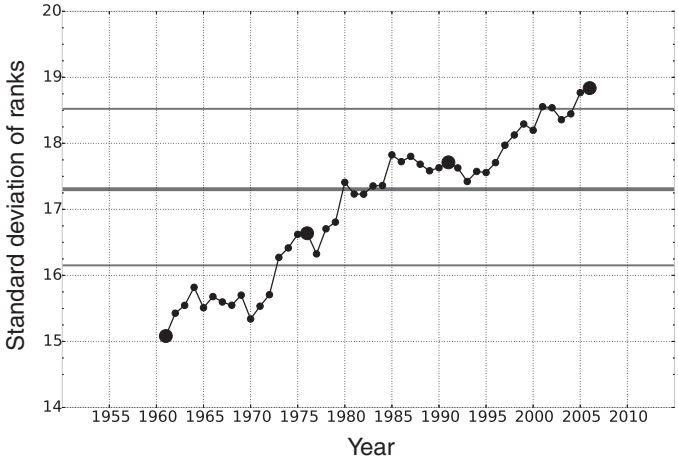

Fig. 2. Variability of SD of monthly ranks for tornado counts. Black line is mean value, gray lines are 95% CI. Large dots are associated with 15-year nonoverlapping periods.

might not be another tornado for many weeks. Here, we take advantage of the fact that the minimum probability of tornado occurrence in the United States is close to 1 January and start counting (E)F1+ tornadoes on that date. For simplicity, we have chosen to designate as the beginning of the season the Julian date on which the count of (E)F1+ tornadoes reaches 50, which is ~10% of the way to the long-term annual mean of 495 tornadoes (Fig. 3 and table S2). The long-term linear trend in the date of the 50th tornado is statistically insignificant (–0.07 days/year), with a mean of 22 March. The four latest starts to the season all have occurred in the 1999 to 2013 period. Five of the 10 earliest starts have occurred in that period, and 7 out of 10 if we look at the past 17 years. The date of the 50th (E)F1+ tornado occurs between 1 March and 10 April in only 6 of the past 17 years, but in 40 of the first 43 years in the database. Thus, despite a small change in the mean date of occurrence, the latter portion of the period has seen a dramatic increase in the years with early and late starts to the tornado season.

Additional indications of a change in variability are shown by examining the number of tornadoes on convective days. Since the early 1970s, the number of days with at least one (E)F1+ tornado in the United States has decreased from a mean of 150 to a mean of 100 (Fig. 4). Over the same period, the number of days with many tornadoes has increased dramatically. For example, the frequency of days with more than 30 (E)F1+ has increased from 0.5 to 1 days per year in the 1960s and 1970s to 3 days per year over the past decade. The most recent year with fewer than 2 days was 2002. The only 2 years with more than 750 (E)F1+ tornadoes were 2011 (897) and 1973 (888). The manner in which these 2 years accumulated large numbers of tornadoes was quite different. 1973 had the most days with (E)F1+ tornadoes, 187, in which only 2 days had more than 30. In contrast, 2011 had only 110 days with at least one (E)F1+ tornado, but 9 of those days had more than 30. 2011 had as many days with more than 30 as the entire period from 1961 to 1981, despite having fewer days with one or more tornado than that of any of the individual years from the earlier period.

The different characteristics of the "at least one" and "many" daily tornado categories is informative. The fact that the two series move in opposite directions is very difficult to explain as a result of changes in how they are reported. Increased likelihood of reporting should lead to an increase in both the probability that a day has at least one (E)F1+ tornado and that a large number occurs on any particular day. It still is possible that the observed changes are the result of some nonmeteorological factors, but that would require a complex set of influences acting in opposite directions, making it exceedingly unlikely. Unfortunately, the nature of the database makes it impossible to be absolutely certain.

The change in the distribution of number of tornadoes per day drives most of the results discussed earlier. In effect, there is a lower probability of a day having a tornado, but if a day does have a tornado, there is a much higher chance of having many tornadoes. As a result, tornadoes are "concentrated" into a smaller number of days in more recent years. Approximately 20% of the annual tornadoes in the most recent decade have occurred on the three "biggest" days of each year, in contrast to 10% in the earlier period. This concentration leads to the potential for short periods of time, such as months, to have extreme (both large and small) numbers of tornadoes. Thus, the large number of monthly records for most and fewest tornadoes in recent years would be predicted from the change in distribution. Similarly, the increased variability of the date of the 50th (E)F1+ tornado would be expected from the same process. When a day with many tornadoes occurs early in the year, it increases the likelihood of an early start to the season, but in the absence of days with tornadoes, implied by the lower probabilities of any tornado, the season will have a late start.

At this point, we cannot offer a physical hypothesis for the increased variability, but our analysis implies that a change in the areal distribution of favorable environmental conditions,

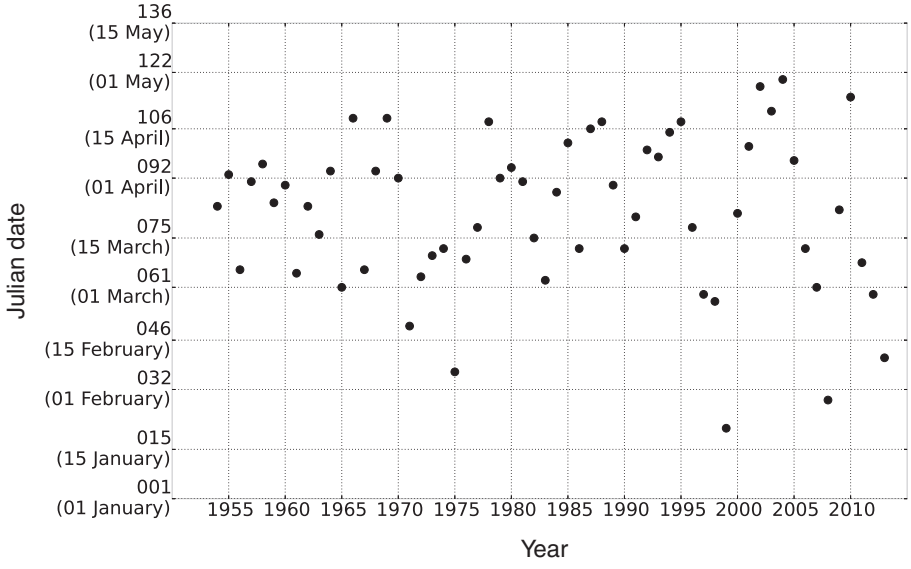

Fig. 3. Julian date of occurrence of 50th (E)F1+ tornado for each year, 1954–2013.

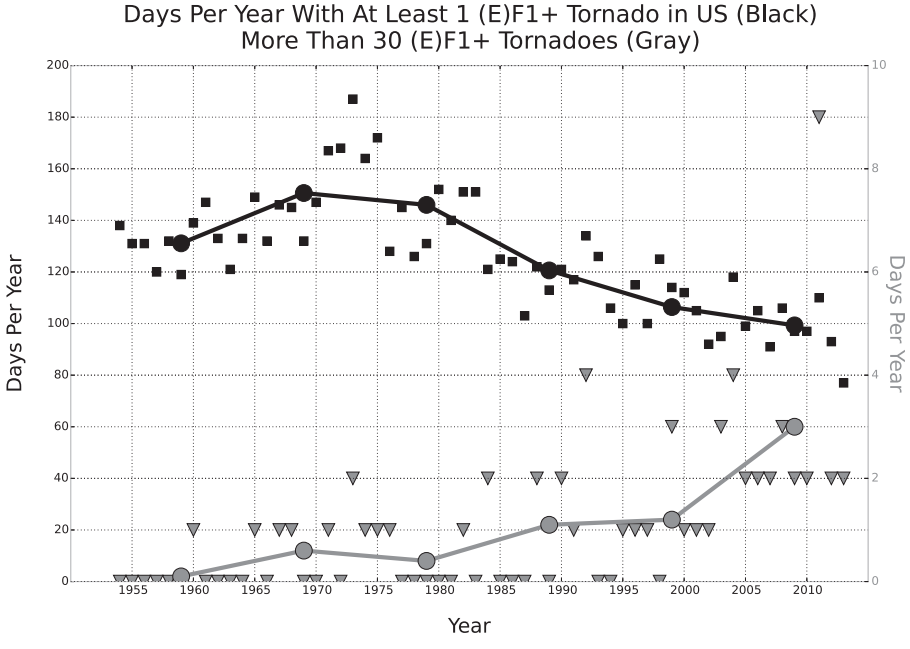

Fig. 4. Number of days per year with at least one and more than 30 (E)F1+ tornadoes. Black squares indicate one (E)F1+ tornado, and gray triangles indicate more than 30. Large dots and lines are decadal means.

or in the probability of a tornado given favorable environmental conditions, is involved. Determining the relative contribution will require the continued development of relationships between environments and events (*11*, *12*), which will depend on the quality of high-resolution reanalysis products of the atmosphere (*13*–*15*). How such a change would relate to the increase in global temperature, if it relates at all, is unknown at this time. Nevertheless, if the variability continues to increase, it could lead to an even greater concentration of tornadoes on fewer days.

REFERENCES AND NOTES

1. C. A. Doswell III, H. E. Brooks, N. Dotzek, *Atmos. Res.* **93**, 554–563 (2009).
2. S. M. Verbout, H. E. Brooks, L. M. Leslie, D. M. Schultz, *Wea. Forecast.* **21**, 86–93 (2006).
3. IPCC, *Climate Change 2013: The Physical Science Basis. Contribution of Working Group I to the Fifth Assessment Report of the Intergovernmental Panel on Climate Change*, T. F. Stocker *et al.*, Eds. (Cambridge Univ. Press, Cambridge, 2013).
4. H. E. Brooks, *Atmos. Res.* **123**, 129–138 (2013).
5. H. E. Brooks, J. W. Lee, J. P. Craven, *Atmos. Res.* **67-68**, 73–94 (2003).
6. R. J. Trapp *et al.*, *Proc. Natl. Acad. Sci. U.S.A.* **104**, 19719–19723 (2007).
7. R. J. Trapp, N. S. Diffenbaugh, A. Gluhovsky, *Geophys. Res. Lett.* **36**, L01703 (2009).
8. N. S. Diffenbaugh, M. Scherer, R. J. Trapp, *Proc. Natl. Acad. Sci. U.S.A.* **110**, 16361–16366 (2013).
9. E. N. Rasmussen, D. O. Blanchard, *Wea. Forecast.* **13**, 1148–1164 (1998).
10. J. P. Craven, H. E. Brooks, *Nat. Wea. Digest* **28**, 13–24 (2004).
11. C. M. Shafer, A. E. Mercer, C. A. Doswell III, M. B. Richman, L. M. Leslie, *Mon. Weather Rev.* **137**, 1250–1271 (2009).
12. C. M. Shafer, A. E. Mercer, M. B. Richman, L. M. Leslie, C. A. Doswell III, *Wea. Forecast.* **27**, 809–831 (2012).
13. E. N. Kalnay *et al.*, *Bull. Am. Meteorol. Soc.* **77**, 437–471 (1996).
14. S. M. Uppala *et al.*, *Q. J. R. Meteorol. Soc.* **131**, 2961–3012 (2005).
15. G. P. Compo, J. S. Whitaker, P. D. Sardeshmukh, *Bull. Am. Meteorol. Soc.* **87**, 175–190 (2006).

ACKNOWLEDGMENTS

The scientific results and conclusions, as well as any views or opinions expressed herein, are those of the authors and do not necessarily reflect the views of NOAA or the Department of Commerce. G.W.C. carried out quality control on the dataset, H.E.B. performed primary analyses, and P.T.M. performed additional analyses and prepared figures.

SUPPLEMENTARY MATERIALS

www.sciencemag.org/content/346/6207/349/suppl/DC1
Materials and Methods
SupplementaryText
Fig. S1
Table S1

16 June 2014; accepted 11 September 2014
10.1126/science.1257460

ION CHANNELS

Ion permeation in K^+ channels occurs by direct Coulomb knock-on

David A. Köpfer,[1]† Chen Song,[2]*† Tim Gruene,[3] George M. Sheldrick,[3] Ulrich Zachariae,[4,5]*‡ Bert L. de Groot[1]*‡

Potassium channels selectively conduct K^+ ions across cellular membranes with extraordinary efficiency. Their selectivity filter exhibits four binding sites with approximately equal electron density in crystal structures with high K^+ concentrations, previously thought to reflect a superposition of alternating ion- and water-occupied states. Consequently, cotranslocation of ions with water has become a widely accepted ion conduction mechanism for potassium channels. By analyzing more than 1300 permeation events from molecular dynamics simulations at physiological voltages, we observed instead that permeation occurs via ion-ion contacts between neighboring K^+ ions. Coulomb repulsion between adjacent ions is found to be the key to high-efficiency K^+ conduction. Crystallographic data are consistent with directly neighboring K^+ ions in the selectivity filter, and our model offers an intuitive explanation for the high throughput rates of K^+ channels.

Potassium (K^+) channels play fundamental roles in almost all cell types. They are essential elements in cellular electric excitability and help maintain the resting potential in non-excitable cells. Their universality is based on a unique combination of strong selectivity for K^+ ions and near–diffusion-limited permeation efficiency (*1*). Common to all K^+ channels is the highly conserved K^+ selectivity filter (SF), which underlies both their exquisite K^+ selectivity and high conduction rates. A wealth of K^+ channel structural information has been acquired since 1998 (*2*). The structures revealed that the SF is formed at the interface of four channel subunits, each contributing a linearly extended backbone of five or six residues (Fig. 1A, left), the carbonyl groups of which point into a four-fold symmetric narrow pore (*2*). This arrangement generates four equidistant K^+ binding sites (S_1 to S_4; Fig. 1A, right) (*2*–*5*).

Anomalous scattering data from the bacterial K^+ channel KcsA from *Streptomyces lividans*, in whose SF K^+ ions were replaced with Tl^+, had originally been interpreted as a superposition of two states, each displaying occupation with two alkali ions alternating with water (Fig. 1B) (*4*). This interpretation still forms the basis for the commonly accepted K^+ conduction mechanism, which suggests cotranslocation of ions with water (*4*, *6*–*9*) (fig. S1). Any possible closer grouping of K^+ ions had been excluded owing to the expectation that the electrostatic repulsion between the ions would prohibit such an arrangement (*4*, *9*), although it was noted that geometrically, the ions could fit in the filter side by side (*9*, *10*). The notion of K^+-water cotranslocation has been applied to other K^+ channels (*11*–*14*), and similar mechanisms have been reported in equilibrium (*10*, *15*–*18*) and non-equilibrium (*19*–*21*) simulation studies. In most of these, biasing restraints were applied on the filter and/or supraphysiological transmembrane voltages were applied to elicit ion transfer (*19*–*21*). However, alternative computational studies demonstrated that multiple pathways may exist, including mechanisms that exhibit close ionic contacts and display similar free energy barriers to K^+ permeation (*18*, *22*, *23*). It has thus remained unclear which mechanism of K^+ permeation predominates under physiological conditions.

Table 1. Occupancy refinement of Tl^+ in the KcsA structure (PDB ID 1r3j) and K^+ in the MthK structure (PDB ID 3ldc), respectively. The absolute occupancy was determined with SHELXL, which allowed for an estimation of the absolute error. Values greater than one are caused by the correlation between occupancies and *B* values. As an independent cross-validation, we calculated the relative occupancies based solely on the anomalous signal using SHELXD.

Binding site	KcsA, refinement of Tl^+			MthK, refinement of K^+	
	Residue ID	Absolute occupancy	Relative occupancy	Residue ID	Absolute occupancy
S_1	C401	1.02 ± 0.04	1.0	A1	0.92 ± 0.07
S_2	C402	0.93 ± 0.03	0.9	A2	0.80 ± 0.07
S_3	C403	0.92 ± 0.04	0.9	A3	1.00 ± 0.09
S_4	C404	0.99 ± 0.04	1.0	A4	1.00 ± 0.09

[1]Biomolecular Dynamics Group, Max Planck Institute for Biophysical Chemistry, 37077 Göttingen, Germany. [2]Department of Biochemistry, University of Oxford, Oxford OX1 3QU, UK. [3]Department of Structural Chemistry, University of Göttingen, 37077 Göttingen, Germany. [4]School of Engineering, Physics and Mathematics, University of Dundee, Dundee DD1 4HN, UK. [5]College of Life Sciences, University of Dundee, Dundee DD1 5EH, UK.
***Corresponding author. E-mail: sc3210@gmail.com (C.S.); u.zachariae@dundee.ac.uk (U.Z.); bgroot@gwdg.de (B.L.d.G.)**
†These authors contributed equally to this work. ‡These authors contributed equally to this work.

Enabled by the recent availability of K^+ crystal structures with an open gate (*24*) and methods to simulate ion flux driven by transmembrane ion gradients (*25*), we set out to investigate the molecular mechanism of ion transfer across the K^+ channel SF from first principles. We performed atomistic molecular dynamics (MD) simulations of KcsA [Protein Data Bank (PDB) IDs 3f5w, 3fb7, and 1k4c] under sustained transmembrane potentials, evoked by K^+ ion gradients, to study the molecular basis of K^+ conduction efficiency in the physiological voltage range (Fig. 1C). The simulations were repeated in the archaeal MthK channel from *Methanobacterium thermoautotrophicum* (PDB ID 3ldc) and the eukaryotic $K_v1.2$-$K_v2.1$ chimeric channel (PDB ID 2r9r) (fig. S4). In total, we recorded more than 1300 spontaneous K^+ permeation events within a simulation time of ~50 μs.

At KCl concentrations of 400 mM, 200 mM, and 10 mM, we recorded the number of permeating ions as a function of time, where the slope of the curves reflects ion current (Fig. 1D). The simulated currents under positive potentials are in good agreement with experimentally reported values (up to a factor of ~2, similar to the experimental range of variation). We found that sustained currents were restricted to states displaying adjacent K^+ ions in the SF. These invariably involved a K^+ ion pair at binding sites S_2 and S_3 in the SF. One ion bound near S_0, frequently exchanging with ions from the bulk solution (Fig. 1E), such that S_1 was left vacant. Individual outward permeation events were initiated by intracellular K^+ ions entering into the internal channel cavity at binding site S_{cav}. Translocation of the central ions in the SF at S_3 and S_2 started when a water molecule at S_4 left to generate a vacancy (Fig. 1, F and G).

At the core of the permeation mechanism is a fast, concerted motion of the three ions at binding sites S_{cav}, S_3, and S_2, triggered by positional fluctuations of the incoming K^+ ion between S_{cav} and S_4 (Fig. 1H). These motions repeatedly reduce its distance to the ion pair at S_3 and S_2. A subsequent "knock-on" between the ion at S_4 and the S_3-S_2 ion pair ultimately leads to a progression of the central ion pair to S_2 and S_1 (Fig. 1I) and to further ion transfers from S_1 to S_0 and from S_4 to S_3 (Fig. 1J). These final rearrangements complete the transition by reestablishing the initial occupancy pattern of the SF (Fig. 1E). We observed the direct knock-on mechanism in simulations of three KcsA crystal structures (PDB IDs 3f5w, 3fb7, and 1k4c), MthK (PDB ID 3ldc), and the voltage-gated channel chimera $K_v1.2$-$K_v2.1$ (PDB ID 2r9r), independently of the force fields and water models used (fig. S4 and tables S1 and S2).

Our finding that direct ion contacts underpin the most efficient K^+ permeation route in K^+ channels contrasts with the commonly accepted transport mechanism, which is based on alternating ion and water occupation inside the SF. Similar direct cation-cation contacts have so far mainly been detected in concentrated salt solutions (*26*). The accepted mechanism has predominantly been inferred from channel crystallographic data, among which the anomalous data of Tl^+ ions in the KcsA SF (PDB ID 1r3j) played a particularly important role (*4*). We were therefore interested in whether our simulation results were compatible with the experimental data. Because the original interpretation of the anomalous electron density map may contain potential drawbacks (such as a degree of dependence on the quality of the refined model from which phases are calculated), we used the program SHELXD (*27*) to determine Tl^+ occupancies in KcsA solely against anomalous data. This analysis established the relative occupancies to be equal among all four ions, within experimental error. The absolute occupancy was refined by SHELXL (*28*) (Table 1). In addition, K^+ occupancies

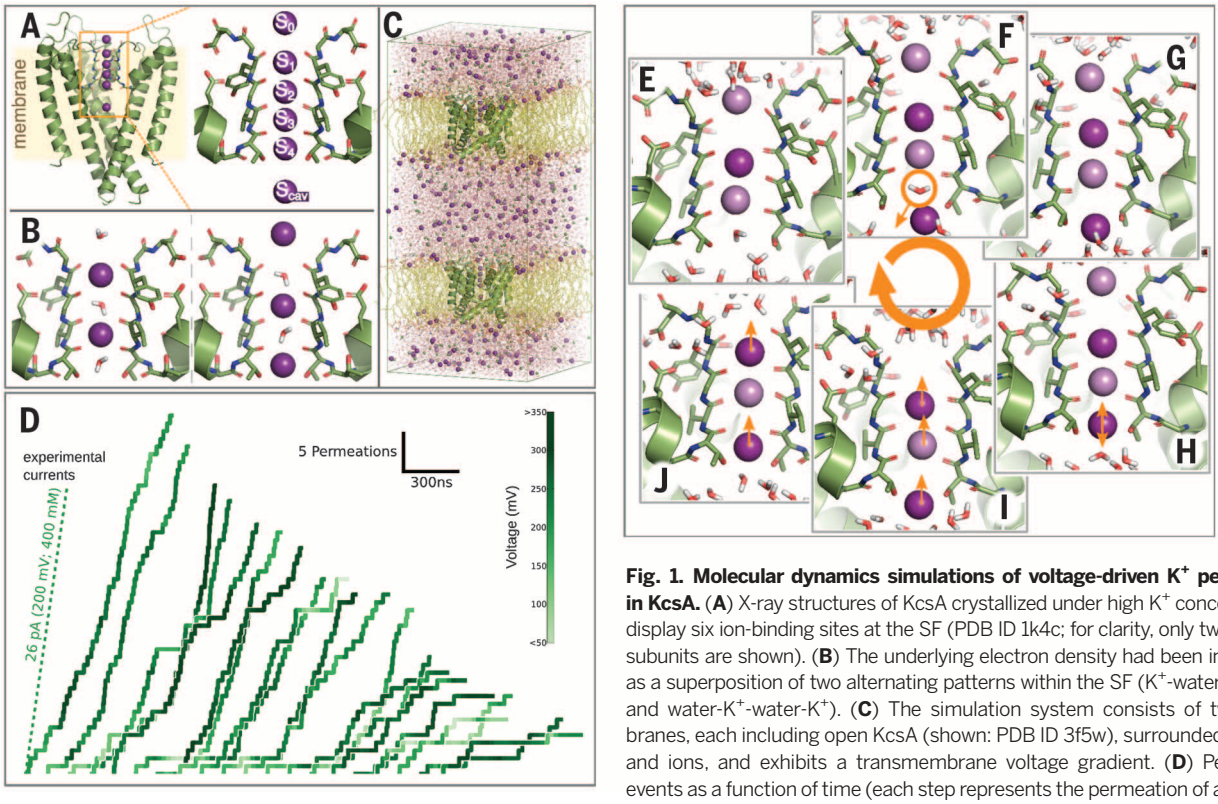

Fig. 1. Molecular dynamics simulations of voltage-driven K^+ permeation in KcsA. (**A**) X-ray structures of KcsA crystallized under high K^+ concentrations display six ion-binding sites at the SF (PDB ID 1k4c; for clarity, only two or three subunits are shown). (**B**) The underlying electron density had been interpreted as a superposition of two alternating patterns within the SF (K^+-water-K^+-water and water-K^+-water-K^+). (**C**) The simulation system consists of two membranes, each including open KcsA (shown: PDB ID 3f5w), surrounded by water and ions, and exhibits a transmembrane voltage gradient. (**D**) Permeation events as a function of time (each step represents the permeation of a single K^+ ion) over 20 individual simulations at 400 mM KCl (set I; see table S1) and in comparison with experimentally measured ion currents [dashed line, data from (*36*)]. The slope of each curve denotes computed or experimental current. The transmembrane voltage measured in experiments and simulations is color-coded from light to dark green. (**E** to **J**) Observed mechanism and sequence of events during K^+ translocation. The most frequent ion configuration under voltage contains two K^+ ions at S_2 and S_3 and a more loosely bound ion at S_0, leaving a vacancy at S_1 (E). Permeation starts when a K^+ ion enters the cavity and binds to S_{cav} (F). Upon displacement of a water molecule (G), translocation of the central ions is triggered by fluctuations of the incoming ion between S_{cav} and S_4, coinciding with release of K^+ from S_0 into the solution (H). Ions at S_3 and S_2 advance in a fast, concerted transition (I), followed by the movement of ions at S_4 and S_1 (J), reestablishing the initial configuration (E).

were refined for MthK (PDB ID 3ldc) (*29*) and Kir3.1 (PDB ID 2qks) (*30*) (Table 1 and tables S4 and S5). We consistently find high values close to unit occupancy that are consistent with the interpretation that close contacts between alkali ions occur in the SF. These contacts were identified as the key to efficient conduction in our MD simulations. Water molecules do not seem to be necessary to separate alkali ions in the filter in order to shield them from repulsion. As previously suggested, and as directly observed in our simulations under transmembrane voltage, ion conduction in K^+ channels "in action" relies on frequent transitions between substates of different ion occupation, whereas open-activated channel states under crystalline conditions are thought to be characterized by the presence of electron density at all four SF positions (*31*). Accordingly, without applied voltage and at reduced temperature, the SF occupancy seen in our simulations converges to that observed in the crystal structures (PDB IDs 1k4c and 3ldc) (fig. S2).

We next investigated whether the basic physical principles of ion translocation in single file predetermine close ion-ion contacts to drive efficient permeation. We modeled the fundamental ion translocation event as Brownian diffusion in a periodic one-dimensional potential, reflecting the sequence of ion-water binding sites in the SF (Fig. 2 and supplementary materials). By testing various occupation patterns and a range of membrane voltages, we found that configurations with direct contacts between ions consistently gave rise to markedly higher transfer rates than water-separated patterns in our Brownian dynamics simulations. These results were independent of the ion and water models used and of the details of the potential (fig. S6 and supplementary materials). Under physiologically relevant voltages, fully ion-occupied systems showed a conductance of ~80 pS, whereas those with alternating ion and water occupancy displayed only little permeation, further decreasing with increasing water content (Fig. 2). Hence, a simple physical model of ion transfer through a confined pore with multiple binding sites already predicts ion-ion contacts to enhance, and the presence of uncharged species to impede, ion permeation.

Together with the results from our MD simulations, the data suggest that water is not cotranslocated with K^+ to a large degree in open-activated KcsA. This is seemingly in conflict with the ion/water cotranslocation ratio derived from measurements of water translocation through KcsA (*32*–*35*). However, these experiments were based on the application of high osmotic gradients. Water permeation as a result of an applied osmotic pressure is likely to lead to ion-depleted SF states in which individual ions are only occasionally dragged along by permeating water molecules, whereas bound ions are reported to completely block water flux (*33*, *34*). Such ion-depleted, and water-permeable, filter states are therefore likely markedly different from the ion-conductive states at higher ion occupancy considered by crystallography and in our MD simulations.

The agreement among the multiple approaches we used to study ion flux in K^+ channels suggests a consensus mechanism of ion permeation across the SF. Figure 3 displays a schematic potential landscape in the SF according to the main observations made in our simulations (Fig. 3A, gray). In the resting state under physiological membrane voltage, two K^+ ions bind stably to S_2 and S_3 (Fig. 3A, purple). The height of the energy barrier (red) prevents transfer of K^+ from S_2 to S_1. As K^+ enters into S_{cav} and progresses to S_4, Coulomb repulsion with the central ions leads to their relative energetic destabilization (Fig. 3, B and C). This Coulomb interaction also lowers the permeation barrier between S_2 and S_1 (Fig. 3C). As a result, productive translocation of the ion at S_2 can occur (Fig. 3D). Subsequently, translocation from S_3 to S_2 lowers the potential energy of the ion at S_4, while simultaneously the energy of the ion at S_1 is increased (Fig. 3E, red arrows). Owing to the new potential energy surface, the initial ion configuration is then recovered by transfer from S_4 to S_3 and exit of the ion at S_1 from the SF (Fig. 3F). This cycle constitutes a full conduction

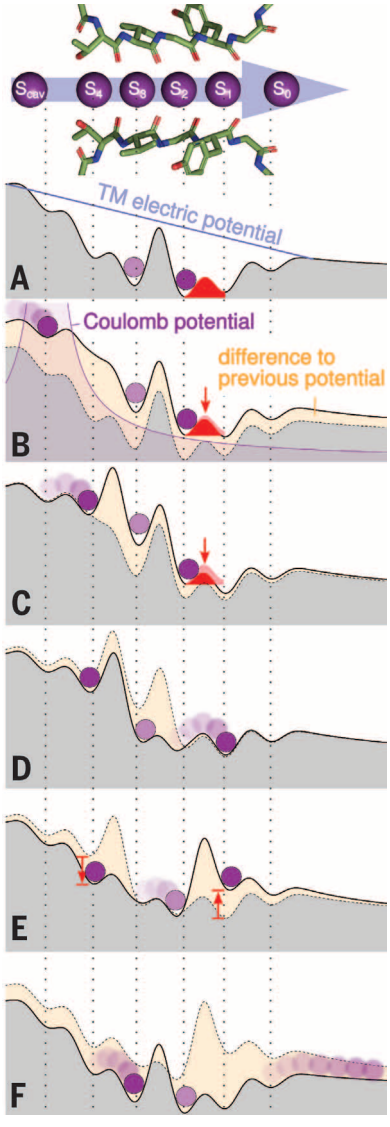

Fig. 3. Energetic basis and mechanism of ion permeation in the KcsA selectivity filter. (**A**) Potential landscape (gray) of the steady-state situation with K^+ simultaneously bound in S_2 and S_3 (purple) and a transmembrane (TM) electric potential attracting cations toward the extracellular face (blue). (**B**) An incoming K^+ ion binding to S_{cav} alters the potential of the ions at S_2 and S_3 as a result of Coulomb repulsion (magenta), raising their free energy with respect to the bulk and lowering the barrier for the ions at S_3 and S_2. (**C** and **D**) Subsequent binding of the incoming ion to S_4 (C) finally reduces the barrier sufficiently for the ion at S_2 to advance to S_1 (D). (**E**) The strong destabilization of the ion at S_1 is simultaneous with an increase in stabilization of the incoming ion at S_4 (red arrows), triggered by the transfer of the central ion to S_2. (**F**) In the last step, the ion at S_4 binds to S_3 while the ion at S_1 leaves the SF, thereby recovering the original state.

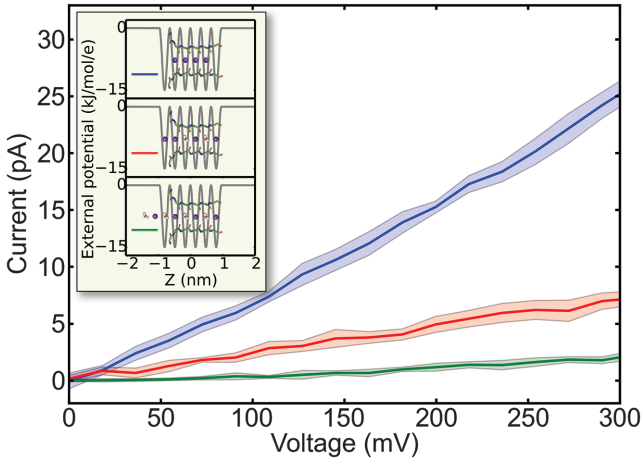

Fig. 2. Brownian dynamics simulations of K^+ ions and water across a repetitive well potential. Potential energy minima represent ion or water binding sites in the SF (insets). Approximately equal binding site affinity for each species, and hence potential depth, is implicitly assumed in the accepted ion-water cotranslocation model. An electric field was applied from left to right. The highest ionic current is seen when K^+ ions are bound in adjacent binding sites (blue line). When direct ion-ion contacts are only occasionally allowed (red line), the current decreases by ~70%. The canonical K^+-water-K^+-water pattern reduces the maximal current by an order of magnitude (green line).

step. Notably, the free energy required to destabilize binding at S_2 ultimately stems from the binding energy of the incoming ion, best seen during the transition of the central ion (Fig. 3E, red arrows).

The proposed mechanism predicts an important experimental characteristic of K^+ channels. Because the rate of K^+ ions leaving the SF at the extracellular side is determined by the rate with which incoming intracellular ions arrive at the filter (movie S1), our model inherently implies that K^+ channels are diffusion-limited as long as an ion pair occupies the inner SF binding sites. We therefore recorded the occupancy of the inner SF sites under varying K^+ concentrations. Indeed, we found that ions occupy these positions over a broad range of concentrations from 10 mM to 400 mM (fig. S3). Taken together, our model thus not only accounts for the diffusion control of K^+ channels, but also explains the wide linear regime of K^+ channel conductance above ~10 mM K^+ (*9*), which is a prerequisite for robust K^+ channel function under variable external conditions.

Our permeation model for ion transfer in K^+ channels at physiological voltages relies on repulsive Coulomb interactions between adjacent ions in the SF as the main driver for conduction near the diffusion limit (Fig. 3). In re-investigating several K^+ channel structures, we found direct ionic contacts to be compatible with the available crystallographic data. The results presented above demonstrate that these direct contacts are not energetically prohibitive. Rather, they serve to enhance ion flux to the maximum attainable speed over a broad range of concentrations.

REFERENCES AND NOTES

1. B. Hille, *Ion Channels of Excitable Membranes* (Sinauer, Sunderland, MA, ed. 3, 2001).
2. D. A. Doyle *et al.*, *Science* **280**, 69–77 (1998).
3. Y. Zhou, J. H. Morais-Cabral, A. Kaufman, R. MacKinnon, *Nature* **414**, 43–48 (2001).
4. Y. Zhou, R. MacKinnon, *J. Mol. Biol.* **333**, 965–975 (2003).
5. L. G. Cuello *et al.*, *Nature* **466**, 272–275 (2010).
6. C. Domene, M. S. P. Sansom, *Biophys. J.* **85**, 2787–2800 (2003).
7. A. L. Hodgkin, R. D. Keynes, *J. Physiol.* **128**, 61–88 (1955).
8. C. Miller, *Nature* **414**, 23–24 (2001).
9. J. H. Morais-Cabral, Y. Zhou, R. MacKinnon, *Nature* **414**, 37–42 (2001).
10. J. Åqvist, V. Luzhkov, *Nature* **404**, 881–884 (2000).
11. L. Ceccarini, M. Masetti, A. Cavalli, M. Recanatini, *PLOS ONE* **7**, e49017 (2012).
12. F. Khalili-Araghi, E. Tajkhorshid, K. Schulten, *Biophys. J.* **91**, L72–L74 (2006).
13. G. Yellen, *Nature* **419**, 35–42 (2002).
14. T. Lu *et al.*, *Nat. Neurosci.* **4**, 239–246 (2001).
15. S. Bernèche, B. Roux, *Biophys. J.* **78**, 2900–2917 (2000).
16. I. H. Shrivastava, M. S. P. Sansom, *Biophys. J.* **78**, 557–570 (2000).
17. T. Sumikama, S. Saito, I. Ohmine, *J. Phys. Chem. B* **110**, 20671–20677 (2006).
18. S. Bernèche, B. Roux, *Nature* **414**, 73–77 (2001).
19. M. Ø. Jensen *et al.*, *Proc. Natl. Acad. Sci. U.S.A.* **107**, 5833–5838 (2010).
20. M. Ø. Jensen, V. Jogini, M. P. Eastwood, D. E. Shaw, *J. Gen. Physiol.* **141**, 619–632 (2013).
21. K. Kasahara, M. Shirota, K. Kinoshita, *PLOS ONE* **8**, e56342 (2013).
22. S. Furini, C. Domene, *Proc. Natl. Acad. Sci. U.S.A.* **106**, 16074–16077 (2009).
23. P. W. Fowler, E. Abad, O. Beckstein, M. S. P. Sansom, *J. Chem. Theory Comput.* **9**, 5176–5189 (2013).
24. L. G. Cuello, V. Jogini, D. M. Cortes, E. Perozo, *Nature* **466**, 203–208 (2010).
25. C. Kutzner, H. Grubmüller, B. L. de Groot, U. Zachariae, *Biophys. J.* **101**, 809–817 (2011).
26. G. Hummer, D. M. Soumpasis, M. Neumann, *Mol. Phys.* **81**, 1155–1163 (1994).
27. C. B. Hübschle, G. M. Sheldrick, B. Dittrich, *J. Appl. Crystallogr.* **44**, 1281–1284 (2011).
28. G. M. Sheldrick, *Acta Crystallogr. A* **64**, 112–122 (2008).
29. S. Ye, Y. Li, Y. Jiang, *Nat. Struct. Mol. Biol.* **17**, 1019–1023 (2010).
30. M. Nishida, M. Cadene, B. T. Chait, R. MacKinnon, *EMBO J.* **26**, 4005–4015 (2007).
31. O. B. Clarke *et al.*, *Cell* **141**, 1018–1029 (2010).
32. M. Iwamoto, S. Oiki, *J. Neurosci.* **31**, 12180–12188 (2011).
33. T. Hoomann, N. Jahnke, A. Horner, S. Keller, P. Pohl, *Proc. Natl. Acad. Sci. U.S.A.* **110**, 10842–10847 (2013).
34. S. M. Saparov, P. Pohl, *Proc. Natl. Acad. Sci. U.S.A.* **101**, 4805–4809 (2004).
35. S. Imai, M. Osawa, K. Takeuchi, I. Shimada, *Proc. Natl. Acad. Sci. U.S.A.* **107**, 6216–6221 (2010).
36. M. LeMasurier, L. Heginbotham, C. Miller, *J. Gen. Physiol.* **118**, 303–314 (2001).

ACKNOWLEDGMENTS

We thank H. Sun and S. Wacker for simulations of $K_v1.2$, R. Sknepnek for assistance with HOOMD-blue, and H. Grubmüller, M.S.P. Sansom, P. Pohl, T. Graen, and K. Zeth for helpful discussions. Supported by the International Max Planck Research School for Biology and Complex Systems (D.A.K.), a Marie Curie Intra European Fellowship within the 7th European Community Framework Programme (C.S.), the Volkswagen Stiftung (via the Niedersachsenprofessur awarded to G.M.S.) (T.G.), the Scottish Universities' Physics Alliance (U.Z.), and the German research foundation DFG through SFB803 (B.L.d.G.).

SUPPLEMENTARY MATERIALS

www.sciencemag.org/content/346/6207/352/suppl/DC1
Materials and Methods
Figs. S1 to S6
Tables S1 to S14
Movie S1
References (*37*–*63*)

15 April 2014; accepted 27 August 2014
10.1126/science.1254840

ION CHANNELS

Structure and selectivity in bestrophin ion channels

Tingting Yang,[1] Qun Liu,[2] Brian Kloss,[3] Renato Bruni,[3] Ravi C. Kalathur,[3] Youzhong Guo,[1] Edda Kloppmann,[3,4] Burkhard Rost,[3,4] Henry M. Colecraft,[5] Wayne A. Hendrickson[1,2,3,5]*

Human bestrophin-1 (hBest1) is a calcium-activated chloride channel from the retinal pigment epithelium, where mutations are associated with vitelliform macular degeneration, or Best disease. We describe the structure of a bacterial homolog (KpBest) of hBest1 and functional characterizations of both channels. KpBest is a pentamer that forms a five-helix transmembrane pore, closed by three rings of conserved hydrophobic residues, and has a cytoplasmic cavern with a restricted exit. From electrophysiological analysis of structure-inspired mutations in KpBest and hBest1, we find a sensitive control of ion selectivity in the bestrophins, including reversal of anion/cation selectivity, and dramatic activation by mutations at the cytoplasmic exit. A homology model of hBest1 shows the locations of disease-causing mutations and suggests possible roles in regulation.

The human *BEST1* gene encodes a protein [human bestrophin-1 (hBest1)] that is highly expressed in retinal pigment epithelium (*1*–*4*). More than 120 distinct mutations in hBest1 have been identified that result in multiple retinal degeneration disorders (*5*–*11*), notably vitelliform macular degeneration or Best disease. Functionally, hBest1 was identified as a Cl^- channel that can be activated by Ca^{2+} (*8*, *12*, *13*), and most of the disease-causing mutations in hBest1 are point mutations that cause channel dysfunction (*8*, *12*, *14*–*16*). Thus, understanding the structure of the hBest1 channel holds value from both biological and biomedical perspectives.

The bestrophin family identified by hBest1 is distributed widely, with representatives in most metazoan animals, including four in humans, and also in other eukaryotes and in prokaryotes (*7*, *8*). The animal bestrophins are characterized by a highly conserved N-terminal domain that includes four predicted transmembrane helices (TMs) and diverse C-terminal domains that may be involved in protein-protein interactions (*8*, *12*, *15*, *17*). Bacterial bestrophins lack the variable C-terminal domain and are more divergent in the transmembrane portion. Using a structural genomics approach, we identified a homolog from *Klebsiella pneumoniae* (KpBest) that could be produced by recombinant expression for structural and functional characterization. The structure-based sequence alignment implies 14% identity between KpBest and hBest1 (fig. S1).

Initial crystals of detergent-solubilized KpBest diffracted poorly; however, constructs from a truncation series did yield suitable crystals. The initial structure was solved from one of these,

[1]Department of Biochemistry and Molecular Biophysics, Columbia University, New York, NY 10032, USA. [2]New York Structural Biology Center, Synchrotron Beamlines, Brookhaven National Laboratory, Upton, NY 11973, USA. [3]New York Consortium on Membrane Protein Structure, New York Structural Biology Center, 89 Convent Avenue, New York, NY 10027, USA. [4]Department of Informatics, Bioinformatics and Computational Biology, TUM (Technische Universität München), Garching 85748, Germany. [5]Department of Physiology and Cellular Biophysics, Columbia University, New York, NY 10032, USA.
***Corresponding author. E-mail: wayne@xtl.cumc.columbia.edu**

grown from a solution containing zinc acetate, at 2.9 Å resolution by single-wavelength anomalous diffraction (SAD) at the zinc K-edge resonance. Improved diffraction was obtained after further truncation, removing a total of 11 residues from the C terminus (fig. S1), and the structure was further refined to 2.3 Å resolution (tables S1 and S2). The building and refinement of the structural model were facilitated by five-fold noncrystallographic symmetry. The refined model comprises ordered residues from 22, 23, or 24 through 285 or 289 in different protomers, plus Zn^{2+} ions and water molecules.

Bestrophins have been predicted by different groups to form dimers, tetramers, or pentamers (*12*, *18*). Here, we found that KpBest forms a stable pentamer (Fig. 1, A and B, and fig. S2) with large intersubunit contacts (26,880 $Å^2$ total buried surface area). The electrostatic potential surface is largely negative on the extracellular surface, neutral in the transmembrane region, and positive at the cytoplasmic membrane surface (Fig. 1, C and D). Consistent with the experimentally determined topology of hBest1 (*19*), each protomer has four transmembrane helices and the N and C termini both reside on the cytoplasmic side (Fig. 1, E and F). Extracellular interhelix loops TM1-TM2 (12 residues) and TM3-TM4 (3 residues) are short, whereas the intracellular connection between TM2 and TM3 is long (105 residues), comprising five helices (α3 to α7) that form a separate cytoplasmic domain together with the C-terminal helix α10 (red in Fig. 1, E and F). Both the transmembrane and the cytoplasmic helical bundles appear to have novel folds: Dali searches find matches only to fragments of these structures.

The TM2 helices line the putative ion-conducting pore through the membrane, and they continue intracellularly as long and curved, but uninterrupted, helices α2 (light blue in Fig. 1, E and F). In contrast, TM3/α8 and TM4/α9 are connected to the cytoplasmic domain by extended segments (4 and 12 residues, respectively). The α9-α10 connection is a loop structure that corresponds to a conserved carboxylate-rich segment (EDDDDFE) in eukaryotes, possibly playing a role in Ca^{2+} regulation. This segment has fewer carboxylate residues in prokaryotic homologs, but it presents an electronegative surface patch in KpBest nevertheless (Fig. 1D). The α7 helices (light yellow in Fig. 1F) and cytoplasmic portions of α2 line a cytoplasmic cavern beneath the transmembrane pore.

An apparent ion conduction pathway is at the center of the KpBest pentamer. A funnel-shaped electronegative vestibule, penetrating midway into the membrane, precedes a hydrophobic five-helix transmembrane pore (Fig. 2A). The pore is followed by a cytoplasmic cavern with a restricted,

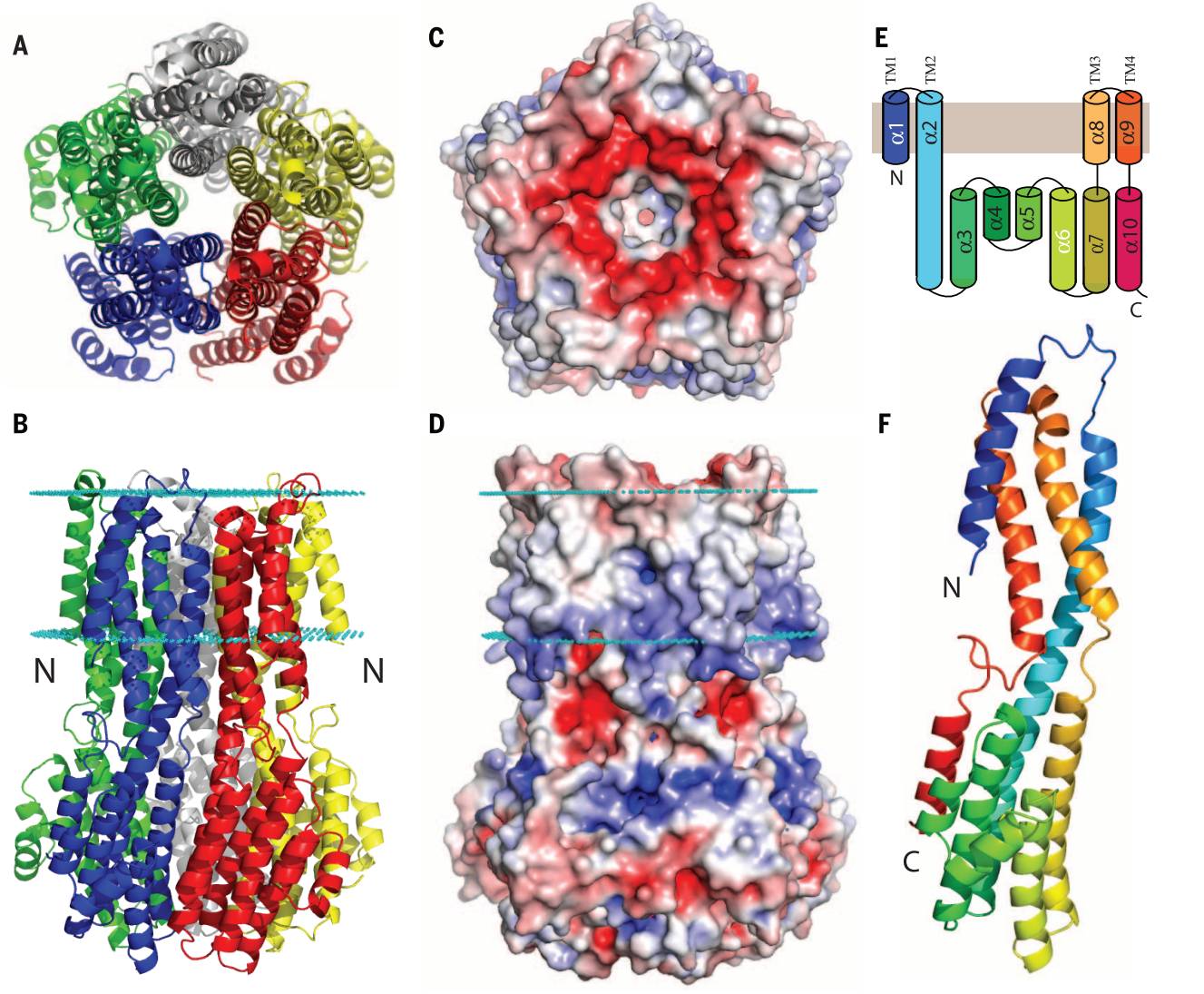

Fig. 1. Crystal structure of KpBest. (**A** and **B**) Ribbon diagram of the KpBest pentamer with each protomer colored differently: (A) as viewed from outside the membrane and (B) as viewed from the side (rotated 90° through the *x* axis). (**C** and **D**) Electrostatic potential at the molecular surface viewed as in (A) and (B), respectively. The contour level is at ±5 kT/e; red for negative potential and blue for positive potential. Membrane boundaries in (B) and (D) were calculated by OPM (Orientations of Proteins in Membranes) server. (**E**) 2D topology of a protomer, colored spectrally from dark blue at its N-terminal segment to red at its C-terminal segment. (**F**) Ribbon diagram of a protomer. Colored as in (E).

on-axis exit ~46 Å below the membrane. The pore and upper parts of the cavern are highly conserved, whereas outer surfaces and lower parts of the cytoplasmic domain are not (Fig. 2B). Overall, the ion permeation pathway has a flower-vase shape, with one restriction (radius < 2.0 Å) from three rings of TM2 residues (I62, I66, and F70) at the pore and another (I180, radius = 1.2 Å) at the start of cytoplasmic helix α7 (Fig. 2C). Therefore, the structure of KpBest predicts two distinct permeation restrictions in the ion passageway, providing a vital clue for the functional mechanism of bestrophin channels. Notably, all four residues located at the predicted restrictions are highly conserved and/or disease related in hBest1: I76, F84, and I205 (KpBest I62, F70, and I180, respectively) are identical (fig. S1), whereas point mutation of either F80 or I205 (KpBest I66 and I180, respectively) causes retinal disorders (*6*, *20*, *21*).

Although eukaryotic bestrophins are known as Ca^{2+}-activated Cl^- channels, the function of KpBest had not been previously examined. To test its function, purified KpBest was fused into a planar lipid bilayer with 150 mM of NaCl in both the trans (internal) and cis (external) solutions. Applying a range of transmembrane potentials resulted in well-resolved unitary currents with a linear single-channel I-V relationship (Fig. 3, A and B), confirming that KpBest is indeed an ion channel. Ca^{2+} was not required for KpBest activation, as might have been expected given that KpBest lacks the C-terminal domain that contains putative Ca^{2+} binding sites in eukaryotic bestrophins (*7*, *13*, *22*). Strikingly, with 150 mM of NaCl on the cis side and no NaCl on the trans side, inward single-channel currents were recorded (Fig. 3C) with mean amplitude of −5.3 pA (fig. S3A, left), demonstrating that KpBest is a cation channel that conducts Na^+, unlike Cl^--conducting eukaryotic bestrophins. To fully assess KpBest ion selectivity, reversal potentials under various bionic conditions were measured. KpBest is permeable to monovalent cations with rank order $Na^+ > K^+ \approx Cs^+$ but not to bivalent cations Mg^{2+}, Ca^{2+}, or Ba^{2+} (Fig. 3D). It is noteworthy that ion channels in the same family can have reversed charge selectivity, as exemplified by TMEM16 Ca^{2+}-activated channels: TMEM16A and 16B are anion channels, whereas TMEM16F may conduct cations (*23*).

Despite extensive studies on the ion-conducting pores of eukaryotic bestrophins, including hBest1 and mouse bestrophin-2 (mBest2) (*15*, *24*–*26*), the molecular basis for ion selection in these channels is not clear. Our KpBest model predicts three critical residues (I62, I66, and F70) at the first permeation restriction (Fig. 2C) that likely control ion selectivity. To test this hypothesis, we first examined I66, because it is the only residue among the three that is different in KpBest compared with anion-conducting bestrophin channels (where this residue is F) (Fig. 3F and fig. S1) (*12*, *15*, *24*–*27*). In bilayer experiments, KpBest I66F showed outward current with 150 mM of NaCl on the cis side and no NaCl on the trans side, indicating that this mutant channel conducts Cl^- rather than Na^+ (Figs. 3E, top, and fig. S4). To further test this premise in the eukaryotic counterpart, wild-type (WT) and F80I mutant hBest1 (corresponding to KpBest I66) were transfected into human embryonic kidney (HEK) 293 cells, and their reversal potentials were determined in whole-cell voltage clamp experiments. Consistent with the KpBest1 I66F results, hBest1 F80I was much less permeable to Cl^- compared with WT (P_{Na}/P_{Cl} = 0.39 for F80I, compared with P_{Na}/P_{Cl} = 0.03 for the WT) (Fig. 3G and fig. S5).

Inspired in part by selectivity-flipping changes made at F81 (equivalent to KpBest I66) in *Drosophila melanogaster* bestrophin-1 (dBest1) (*28*), we next examined whether KpBest ion selectivity could be altered by individually substituting each of the hydrophobic pore-lining residues with positively charged arginine (R), which in principle might favor negatively charged Cl^-. When purified KpBest I62R, I66R, and F70R mutants were tested in bilayer experiments, I62R (but not I66R or F70R) conducted Cl^- rather than Na^+ (Fig. 3E and fig. S4). These mutants showed perturbed conductance amplitudes (fig. S4), indicating effects on permeation at all of these sites. Following the same logic as for KpBest, the equivalent residues on hBest1 (I76, F80, and F84, respectively) were individually mutated to negatively charged glutamic acid (E). Consistent with the KpBest results, only I76E flipped the ion selectivity to Na^+ (P_{Na}/P_{Cl} = 1.54) (Fig. 3G and fig. S5B), although F80E and F84E were also less permeable to Cl^- than WT (P_{Na}/P_{Cl} = 0.33 and 0.46, respectively) (Fig. 3G). None of the hBest1 mutations significantly affected current density (fig. S6). Notably, our results are in accord with previous reports: The rectification of mBest2 could be altered in opposite directions by replacing F80 with either R or E (*26*), and the corresponding F81E mutation of dBest1 flipped the cation/anion selectivity (*28*). Taken together, using our KpBest model as a guide, we have identified three residues that sensitively affect ion selectivity in bestrophins.

The dramatic change in ion selectivity from substitutions at the first hydrophobic residue of the pore (I62R in KpBest and I76E in hBest1) suggests a particularly critical role for this position. Interestingly, the expression level of I62R in *E. coli* was much lower compared with that of WT KpBest (about 1/14) (fig. S7), suggesting that

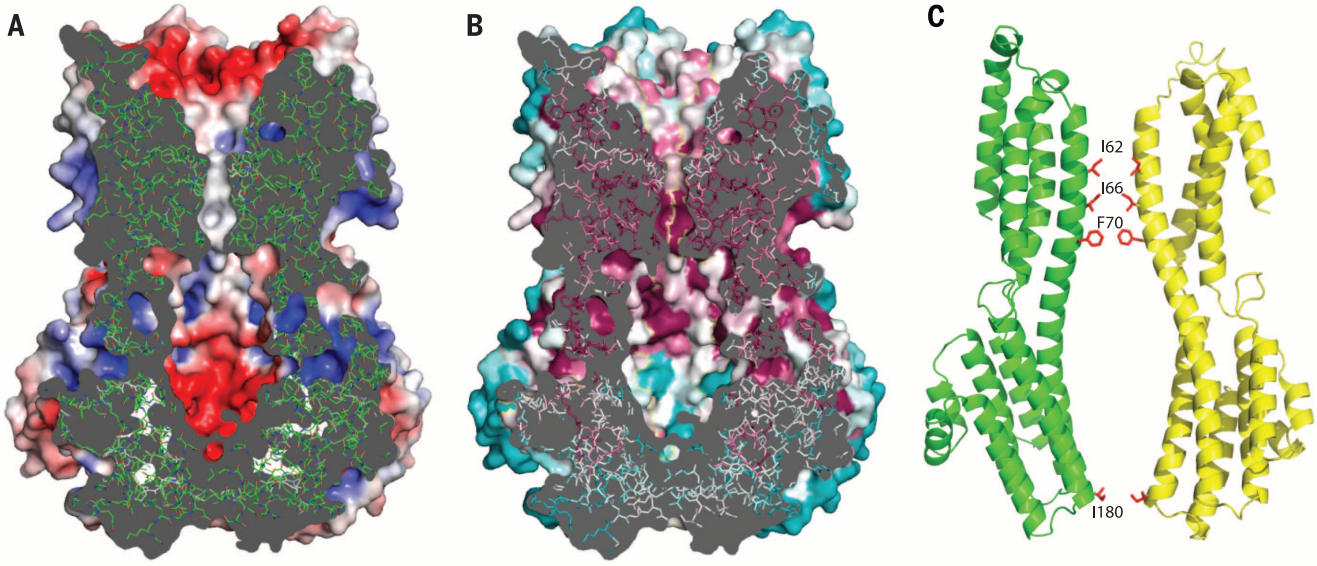

Fig. 2. Structure of the ion-conducting pathway through KpBest. (**A**) Cross section through the pore center. The model is viewed as in Fig. 1D, with the electrostatic potential shown on exposed surfaces of the molecular envelope. (**B**) Cross section as in (A), but colored by Consurf sequence conservation. Turquoise marks the most variable positions, and maroon marks those most conserved. The calculation used 150 prokaryotic homologs with 95% maximal and 35% minimal sequence identities compared with KpBest. (**C**) Ribbon diagram of two oppositely facing (144°) protomers of a KpBest pentamer are shown with the extracellular side on the top. The side chains of critical residues are red.

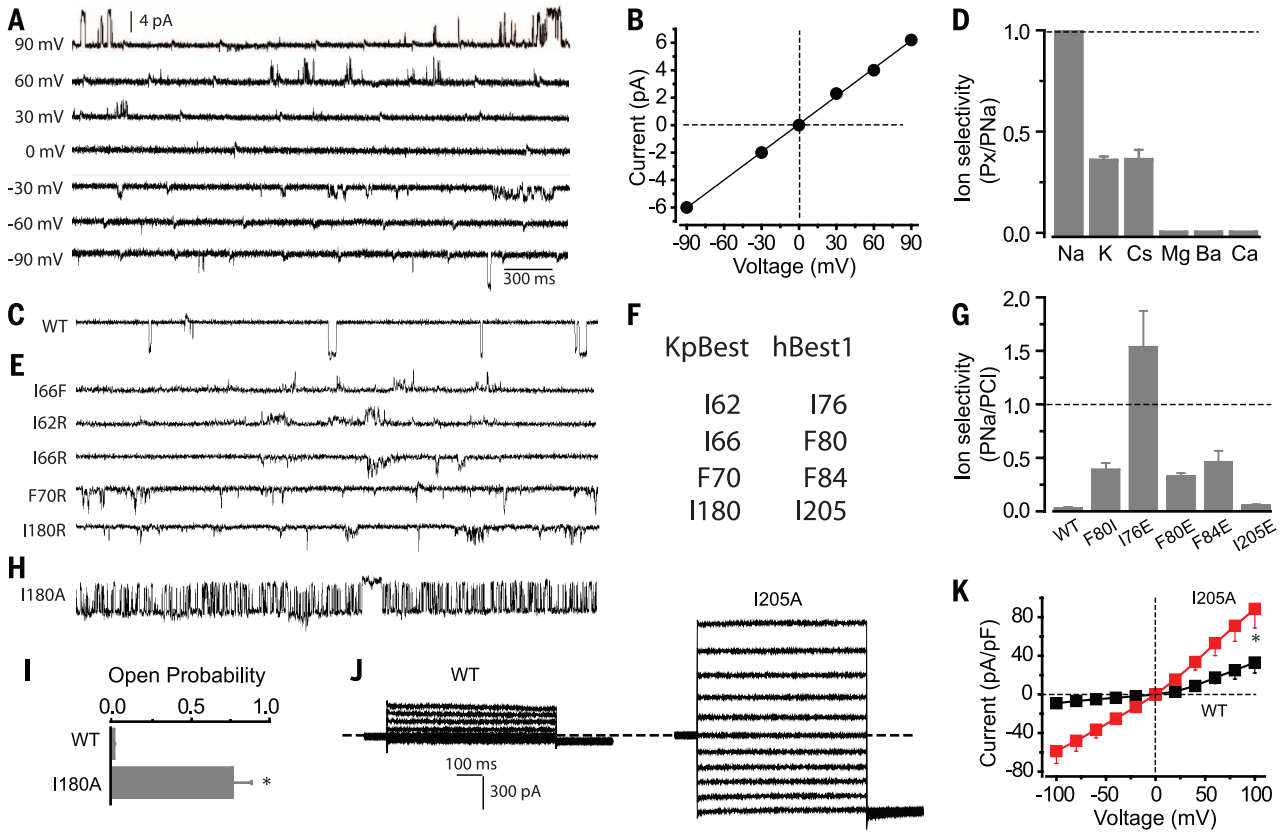

Fig. 3. Ionic conductance measurements of KpBest and hBest1. (**A**) Representative families of single KpBest currents recorded from planar lipid bilayers at different voltages (150 mM of NaCl in both trans and cis solutions). No current was recorded at −60 mV. (**B**) Single KpBest channel current-voltage relationship. (**C**) Current trace of WT single KpBest channels (150 mM of NaCl in cis and 0 NaCl in trans solutions). The voltage for recordings (C), (E), and (H) was 0 mV. (**D**) Relative cation permeability; $n = 3$ recordings in independent bilayers for each point. (**E**) Current traces of mutant KpBest channels [same condition as (C)]. (**F**) Critical residues in KpBest and hBest1. (**G**) Relative permeability (P_{Na}/P_{Cl}) of hBest1 WT and mutant variants; $n = 12$ to 15 cells for each bar. (**H**) Current trace of I180A single KpBest channels [same condition as (C)]. (**I**) WT and I180A single KpBest channel open probabilities. (**J**) Exemplar whole-cell currents of WT (left) and I205A (right) hBest1 in HEK 293 cells. (**K**) Population steady-state current-voltage relationships; $n = 3$ to 6 cells for each point. * $P < 0.05$ when compared with WT using two-tailed unpaired Student's t test. No Ca^{2+} was added for hBest1 recordings.

I62 is important for the expression or assembly of the channel. Consistent with this idea, mutating the equivalent mBest2 I76 to C/L/V resulted in no currents (*26*). Surprisingly, the simple swapping of the central hydrophobic pore residues (KpBest I66 and hBest1 F80) significantly altered ion selectivity without affecting expression levels. The hydrophobic character of the five-helix transmembrane pore of bestrophins is reminiscent of that in the SLAC1 channel (*29*), where the anion selectivity series, like that observed for mBest2 (*24*, *25*) and also for TMEM16A (*30*, *31*), is inversely related to the hydration energy of monovalent anions (*32*).

The second restriction in the permeation pathway of KpBest, at the base of the cytoplasmic cavity where I180 residues interact (Fig. 2C), suggests a possible permeation gate. To test this idea, we replaced the bulky isoleucine with alanine and tested the purified I180A mutant channels in bilayer experiments. Indeed, I180A channels conducted unitary currents with the same amplitude as for WT (fig. S3A); however, the open probability was markedly enhanced (Figs. 3, H and I, and fig. S3B). Substituting I180 on KpBest with R, which has a longer side chain than A, yielded mutant channels that still conducted Na^+ (Fig. 3E) with a low open probability similar to WT KpBest. To determine whether the equivalent residue in hBest1 also acts as an activation gate, the comparable I205A/E mutants were generated and subjected to a whole-cell voltage clamp. Phenocopying their respective KpBest counterparts, hBest I205A displayed significantly larger currents compared with WT and lost inward rectification, indicating a change in channel gating (Fig. 3, J and K), whereas I205E barely affected channel ion selectivity ($P_{Na}/P_{Cl} = 0.06$) (Fig. 3G). Thus, the gate predicted by our KpBest model (KpBest I180 and hBest1 I205) controls gating of the channels but not selectivity. Notably, hBest1 I205T is a disease-causing mutation with significantly decreased Cl^- conductance (*6*), reinforcing the functional importance of I205.

To understand characteristics of hBest1, including the disposition of disease-causing mutations, we generated a homology model for its transmembrane portion based on the KpBest structure (Fig. 4). Consistent with the anion selectivity, the transmembrane pore and the lower restriction of hBest1 are both positively charged (Fig. 4A), contrasting with the negative interior of the KpBest permeation pathway. The conservation pattern among eukaryotic bestrophins (Fig. 4B) is roughly similar to that of prokaryotic relatives (Fig. 2B), although the cytoplasmic exterior is less variable. Disease-causing mutations in hBest1 are abundant (www-huge.uni-regensburg.de/BEST1_database/home.php?select_db=BEST1) and have been clustered into hot spots in the sequence (fig. S1) (*8*, *33*). When plotted onto the three-dimensional (3D) model (Fig. 4C and fig. S8B), the hot spots segregate into a cavity-lining set from hot spot 2 along α2 and a juxtamembrane set from hot spots 3 and 4 at the top of α7 and at the α9-α10 carboxylate loop, which is even more negative in hBest1 (fig. S8A) than in KpBest (Fig. 1D). The carboxylate loop could conceivably play a role in regulation by Ca^{2+}. Hot spot 1 is along the N-terminal segment that is disordered in KpBest, but presumably it too would be alongside other hot spots in the juxtamembrane region in hBest1.

In summary, our structure of the bacterial homolog KpBest provides a solid basis for understanding human bestrophin activity and disease-causing mutations, and physiological tests on KpBest and hBest1 provide insights into the control of ion selectivity and activation in bestrophins generally.

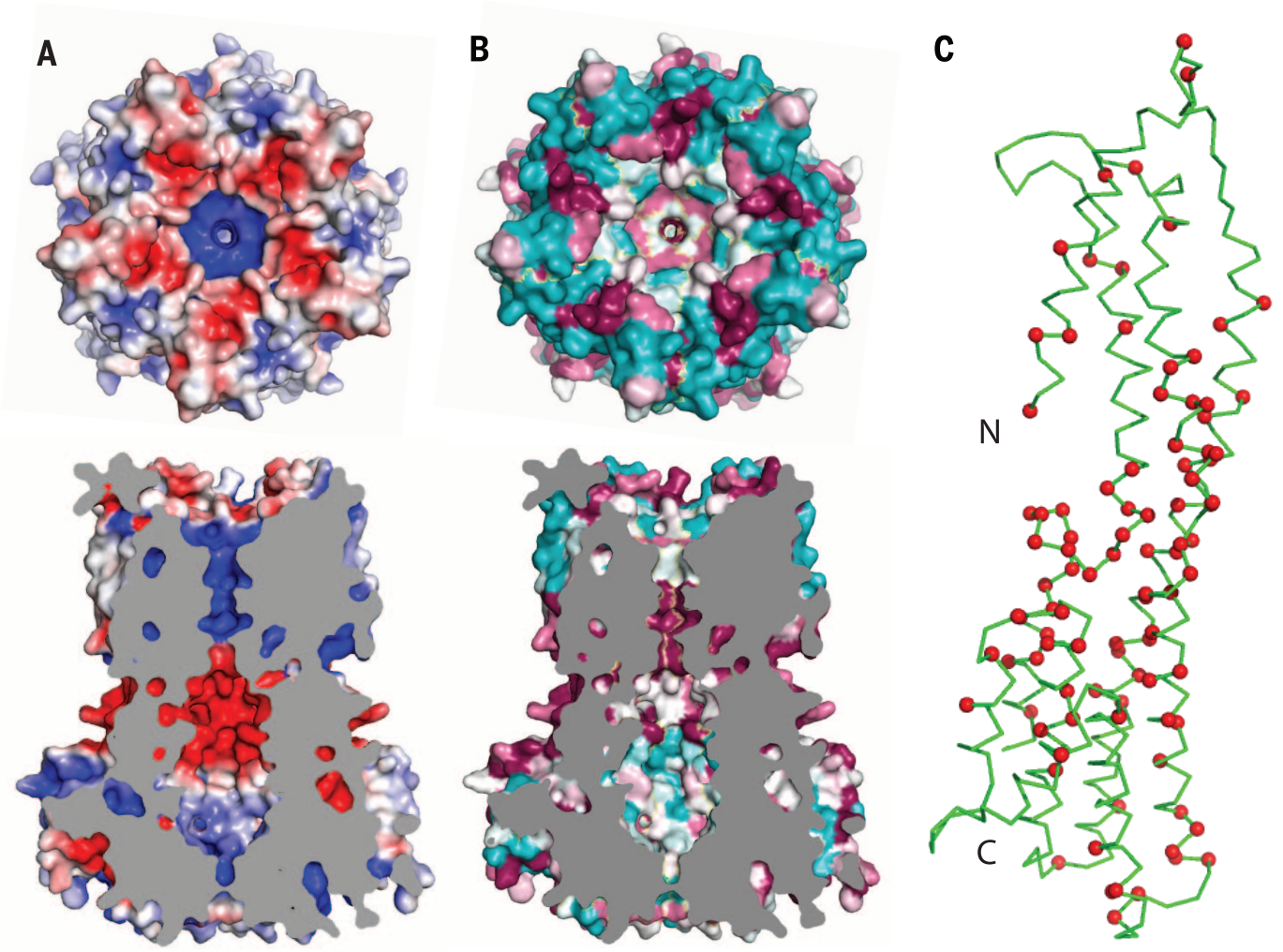

Fig. 4. Homology model of hBest1. (**A**) (Top) Electrostatic potential at the extracellular surface of the hBest1 homology model. Viewed and drawn as for Fig. 1C. (Bottom) Cross section through the homology model of hBest1. Viewed and drawn as for Fig. 2A, except that the cut surface is plain gray. (**B**) (Top) Top view as in (A), but colored by surface conservation. Turquoise marks the most variable positions, and maroon marks those most conserved. This calculation used 150 homologs with 95% maximal and 35% minimal sequence identities compared with hBest1. (Bottom) Cross section viewed and drawn as in Fig. 2B but having a plain gray cut surface. (**C**) Ribbon diagram of a protomer from the hBest1 homology pentamer. The Cα positions of residues that are sites of disease-causing point mutations are marked in red.

REFERENCES AND NOTES

1. A. D. Marmorstein *et al.*, *Proc. Natl. Acad. Sci. U.S.A.* **97**, 12758–12763 (2000).
2. A. Marquardt *et al.*, *Hum. Mol. Genet.* **7**, 1517–1525 (1998).
3. K. Petrukhin *et al.*, *Nat. Genet.* **19**, 241–247 (1998).
4. R. Neussert, C. Müller, V. M. Milenkovic, O. Strauss, *Pflugers Arch: Eur. J. Phys.* **460**, 163–175 (2010).
5. C. J. Boon *et al.*, *Prog. Retin. Eye Res.* **28**, 187–205 (2009).
6. A. E. Davidson *et al.*, *Am. J. Hum. Genet.* **85**, 581–592 (2009).
7. Q. Xiao, H. C. Hartzell, K. Yu, *Pflugers Arch: Eur. J. Phys.* **460**, 559–569 (2010).
8. H. C. Hartzell, Z. Qu, K. Yu, Q. Xiao, L. T. Chien, *Physiol. Rev.* **88**, 639–672 (2008).
9. F. Krämer, N. Mohr, U. Kellner, G. Rudolph, B. H. F. Weber, *Hum. Mutat.* **22**, 418 (2003).
10. F. Krämer *et al.*, *Eur. J. Hum. Genet.* **8**, 286–292 (2000).
11. R. Allikmets *et al.*, *Hum. Genet.* **104**, 449–453 (1999).
12. H. Sun, T. Tsunenari, K. W. Yau, J. Nathans, *Proc. Natl. Acad. Sci. U.S.A.* **99**, 4008–4013 (2002).
13. Q. Xiao, A. Prussia, K. Yu, Y. Y. Cui, H. C. Hartzell, *J. Gen. Physiol.* **132**, 681–692 (2008).
14. K. Yu, Z. Qu, Y. Cui, H. C. Hartzell, *Invest. Ophthalmol. Vis. Sci.* **48**, 4694–4705 (2007).
15. T. Tsunenari *et al.*, *J. Biol. Chem.* **278**, 41114–41125 (2003).
16. K. Yu, Y. Cui, H. C. Hartzell, *Invest. Ophthalmol. Vis. Sci.* **47**, 4956–4961 (2006).
17. A. D. Marmorstein, H. E. Cross, N. S. Peachey, *Prog. Retin. Eye Res.* **28**, 206–226 (2009).
18. J. B. Stanton, A. F. Goldberg, G. Hoppe, L. Y. Marmorstein, A. D. Marmorstein, *Biochim. Biophys. Acta* **1758**, 241–247 (2006).
19. V. M. Milenkovic, A. Rivera, F. Horling, B. H. Weber, *J. Biol. Chem.* **282**, 1313–1321 (2007).
20. A. J. Lotery *et al.*, *Invest. Ophthalmol. Vis. Sci.* **41**, 1291–1296 (2000).
21. S. Maia-Lopes *et al.*, *Hum. Genet.* **123**, 112 (2008).
22. A. Kranjc *et al.*, *PLOS ONE* **4**, e4672 (2009).
23. H. Yang *et al.*, *Cell* **151**, 111–122 (2012).
24. Z. Qu, R. Fischmeister, C. Hartzell, *J. Gen. Physiol.* **123**, 327–340 (2004).
25. Z. Qu, C. Hartzell, *J. Gen. Physiol.* **124**, 371–382 (2004).
26. Z. Qu, L. T. Chien, Y. Cui, H. C. Hartzell, *J. Neurosci.* **26**, 5411–5419 (2006).
27. T. Tsunenari, J. Nathans, K. W. Yau, *J. Gen. Physiol.* **127**, 749–754 (2006).
28. L. T. Chien, H. C. Hartzell, *J. Gen. Physiol.* **132**, 537–546 (2008).
29. Y. H. Chen *et al.*, *Nature* **467**, 1074–1080 (2010).
30. B. C. Schroeder, T. Cheng, Y. N. Jan, L. Y. Jan, *Cell* **134**, 1019–1029 (2008).
31. Y. D. Yang *et al.*, *Nature* **455**, 1210–1215 (2008).
32. E. M. Wright, J. M. Diamond, *Physiol. Rev.* **57**, 109–156 (1977).
33. A. D. Marmorstein, T. R. Kinnick, *Exp. Eye Res.* **85**, 423–424 (2007).

ACKNOWLEDGMENTS

We thank O. Clarke for help in the diffraction analysis; A. Marks for use of planar lipid instrumentation; W. Xie for help in planar lipid experiments; Q. Fan, Y. Geng, and members of the Hendrickson laboratory for discussions; and J. Schwanof and R. Abramowitz at National Synchrotron Light Source (NSLS) beamlines X4A and X4C and F. Murphy at the Advanced Photon Source beamline 24-ID-E for their assistance in data collection. This work was supported in part by NIH grants GM095315 and GM107462 to W.A.H. X4 beamlines are supported by the New York Structural Biology Center at the NSLS of Brookhaven National Laboratory, a Department of Energy facility. The data reported in this paper are tabulated in the supplementary materials and deposited to the Protein Data Bank with access codes listed in table S2. Author contributions: T.Y. and W.A.H. designed research, analyzed data, and wrote the paper; T.Y. performed experiments; Q.L. analyzed diffraction data; B.K., R.C.K., and R.B. performed expression tests; Y.G. advised on protein production and analyzed diffraction data; E.K. and B.R. performed bioinformatics analyses; and H.M.C. designed and analyzed electrophysiology experiments. The authors declare no conflicts of interest.

SUPPLEMENTARY MATERIALS

www.sciencemag.org/content/346/6207/355/suppl/DC1
Materials and Methods
Figs. S1 to S8
Table S1 and S2
References (*34*–*44*)

7 August 2014; accepted 17 September 2014
Published online 25 September 2014;
10.1126/science.1259723

AGING

HSF-1–mediated cytoskeletal integrity determines thermotolerance and life span

Nathan A. Baird,[1]* Peter M. Douglas,[1]* Milos S. Simic,[1] Ana R. Grant,[2] James J. Moresco,[3] Suzanne C. Wolff,[1] John R. Yates III,[3] Gerard Manning,[4] Andrew Dillin[1]†

The conserved heat shock transcription factor–1 (HSF-1) is essential to cellular stress resistance and life-span determination. The canonical function of HSF-1 is to regulate a network of genes encoding molecular chaperones that protect proteins from damage caused by extrinsic environmental stress or intrinsic age-related deterioration. In *Caenorhabditis elegans*, we engineered a modified HSF-1 strain that increased stress resistance and longevity without enhanced chaperone induction. This health assurance acted through the regulation of the calcium-binding protein PAT-10. Loss of *pat-10* caused a collapse of the actin cytoskeleton, stress resistance, and life span. Furthermore, overexpression of *pat-10* increased actin filament stability, thermotolerance, and longevity, indicating that in addition to chaperone regulation, HSF-1 has a prominent role in cytoskeletal integrity, ensuring cellular function during stress and aging.

The survival of an organism is intricately linked to its ability to maintain cellular quality control, including organelle integrity, lipid homeostasis, proper protein folding, and cellular communication. The organismal response to unpredictable environmental changes is critical to mitigate damages caused by stress. Genes encoding the heat shock protein (HSP) family of molecular chaperones show the largest transcriptional increase in response to thermal stress, suggesting that these proteins are part of a fundamental defense against proteotoxic stress. Consistent with this hypothesis, ectopic expression of the master transcriptional regulator of HSPs, HSF-1, is sufficient to confer resistance to thermal stress and increase life span in the nematode *Caenorhabditis elegans* (*1*). Furthermore, *hsf-1* overexpression can alleviate toxicity associated with diseases caused by misfolded or aggregated proteins (*2*).

However, chaperones may be dispensable for thermotolerance and longevity. Neither a hypomorphic mutation of *hsf-1*, nor preventing the up-regulation of HSPs affects thermotolerance of *C. elegans* (*3*, *4*). However, other studies using the same *hsf-1* mutant show decreased heat resistance (*5*). The conflicting data may result from differences in experimental design, but it is clear that HSF-1 function is not fully explained by chaperones mediating stress resistance and life-span determination.

To test for protective mechanisms independent of enhancing chaperone induction, we generated

[1]Howard Hughes Medical Institute, University of California Berkeley, Berkeley, CA 94720, USA. [2]Department of Computational Medicine and Bioinformatics, University of Michigan Medical School, Ann Arbor, MI 48109, USA. [3]Scripps Research Institute, La Jolla, CA 92037, USA. [4]Genentech, South San Francisco, CA 94080, USA. *These authors contributed equally to this work. †Corresponding author. E-mail: dillin@berkeley.edu

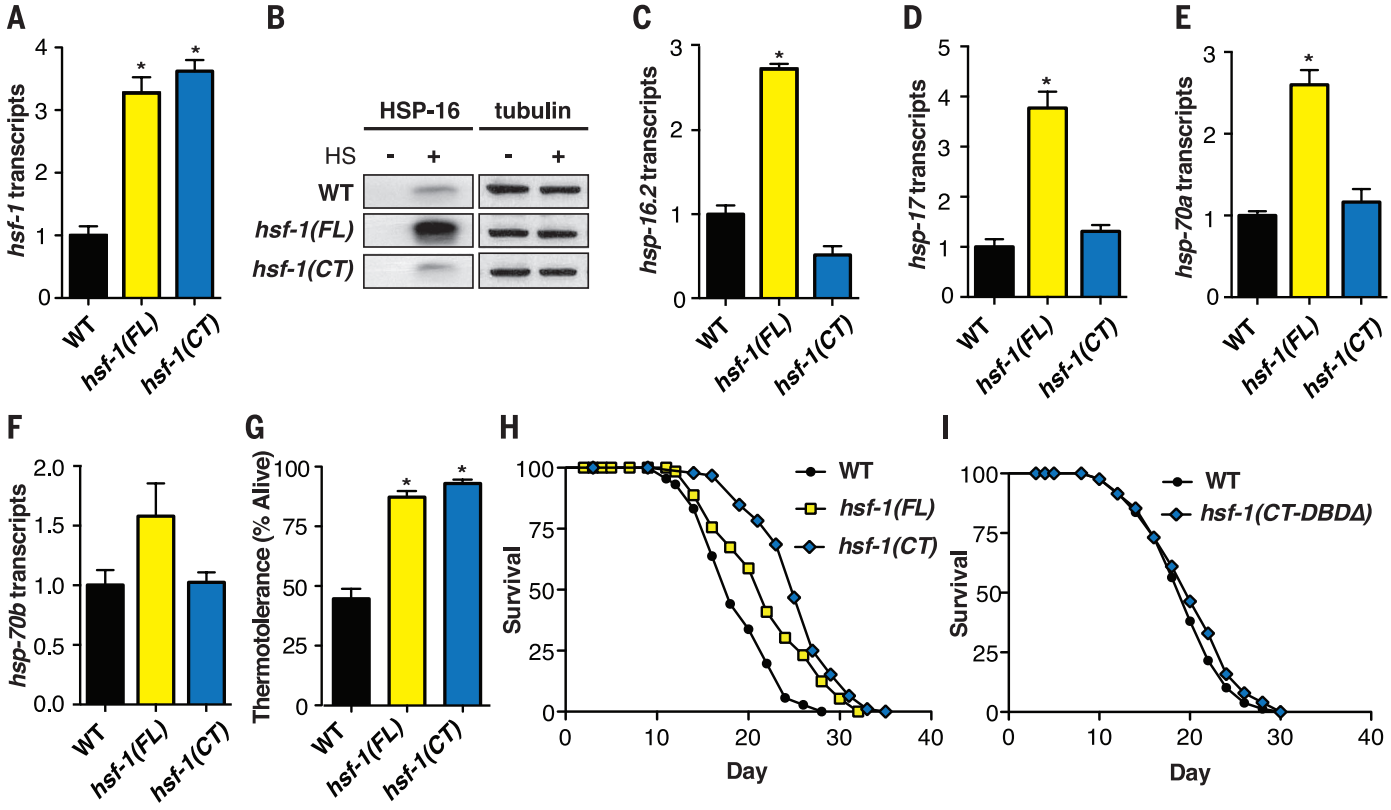

Fig. 1. *hsf-1(CT)* increases life span and thermotolerance without enhancing chaperone induction. (**A**) Equal overexpression of *hsf-1(FL)* and *hsf-1(CT)* determined by means of quantitative polymerase chain reaction (PCR). (**B**) Western blot of HSP-16 before and after heat shock (HS). (**C** to **F**) Quantitative PCR of (C) *hsp-16.2*, (D) *hsp-17*, (E) *hsp-70a* (C12C8.1), and (F) *hsp-70b* (F44E5.4) show enhanced induction in *hsf-1(FL)*. (**G**) Thermotolerance assay of WT, *hsf-1(FL)*, and *hsf-1(CT)* worms shifted from 20° to 34° for 13 hours. (**H**) Life-span survival curves of WT, *hsf-1(FL)*, and *hsf-1(CT)* strains. (**I**) Life-span survival curves of WT and *hsf-1(CT)* strains with the DNA-binding domain deleted (*CT-DBD*Δ). *$P < 0.005$; error bars indicate SEM.

transgenic nematodes overexpressing full-length *hsf-1* [*hsf-1(FL)*] or a *hsf-1* C-terminal truncation [*hsf-1(CT)*]. The *hsf-1(CT)* variant was designed to mimic the C-terminal missense mutation found in the *hsf-1(sy441)* mutant, a widely used allele that decreases stress-induced HSP transcription via the removal of a transactivation domain (*6*). *hsf-1(FL)* was overexpressed in the N2 wild-type (WT) background, and *hsf-1(CT)* was overexpressed in the *hsf-1(sy441)* mutant. Therefore, the *hsf-1(CT)* strain mirrored the overexpression of *hsf-1(FL)* but contained no endogenous copies of full-length *hsf-1* (fig. S1). Both transgenes were expressed threefold higher than endogenous *hsf-1* (Fig. 1A).

Analysis of protein and transcript abundance confirmed that overexpression of *hsf-1(FL)* enhanced heat-inducible expression of all HSPs tested, whereas *hsf-1(CT)* caused no difference from wild type (Fig. 1, B to F, and fig. S2). Yet, both *hsf-1(FL)* and *hsf-1(CT)* transgenic worms had increased thermotolerance and life span (Fig. 1, G and H). The life-span extension of *hsf-1(CT)* was unexpected, so we tested whether this phenotype was dependent on a functional DNA-binding domain. Increased longevity was abolished upon removal of the DNA binding domain (*hsf-1(CT-DBDΔ)* (Fig. 1I). Thus, increased life span and thermotolerance did not correlate with enhanced HSP transcription.

To find other cellular networks that contribute to HSF-1–mediated stress resistance and longevity assurance, we performed quantitative transcriptomic and proteomic analyses comparing *hsf-1(FL)* and *hsf-1(CT)* strains with WT and *hsf-1(sy441)* strains. We filtered for transcripts or proteins that showed increased abundance, under basal or heat-stressed conditions, exclusively in the heat-protected strains (fig. S3). The 98 genes that met our filtering criteria were enriched for functions in development, cytoskeleton organization, complex assembly, and immune defense response (fig. S4).

Reduced expression of genes essential to thermotolerance should lower survival under heat stress. Therefore, we performed a RNA interference (RNAi)–based thermotolerance screen on the genes that passed our filtering criteria (fig. S5 and table S1). From the screen, we identified a troponin-like calcium-binding protein, PAT-10, as essential for thermotolerance (Fig. 2A). Transcription of *pat-10* was heat-inducible in all strains (Fig. 2B). Furthermore, *hsf-1* overexpression strains showed an increase in *pat-10* transcripts under basal and heat-stress conditions (Fig. 2B). After examining the upstream promoter region of *pat-10*, a putative binding site for HSF-1 (*7*, *8*) was identified within 500 base pairs of the transcription start site (fig. S6). Additionally, *hsf-1* RNAi blocked the up-regulation of *pat-10* upon heat shock (Fig. 2C). Therefore, *pat-10* appears to be a direct target of HSF-1 transcriptional regulation.

Because loss of *pat-10* expression reduced thermotolerance, we tested whether ectopic overexpression of *pat-10* could render animals more thermotolerant. Twofold overexpression of *pat-10* (Fig. 2D) significantly increased heat protection (Fig. 2E) and extended life span (Fig. 2F). Furthermore, RNAi of *pat-10* eliminated the increased thermotolerance (Fig. 2E) and life span (Fig. 2F) of the *pat-10* overexpression strain. *pat-10* RNAi also abolished the extended life spans of the *hsf-1* overexpression strains (Fig. 2G). Thus, *pat-10* appears to be necessary and sufficient for increased thermotolerance and longevity. Additionally, the beneficial effects of *pat-10* overexpression were not due to increases in basal HSP transcription (fig. S7). One function of *pat-10* is its role in the troponin complex (*9*–*11*), which is necessary for the contraction of body wall muscles.

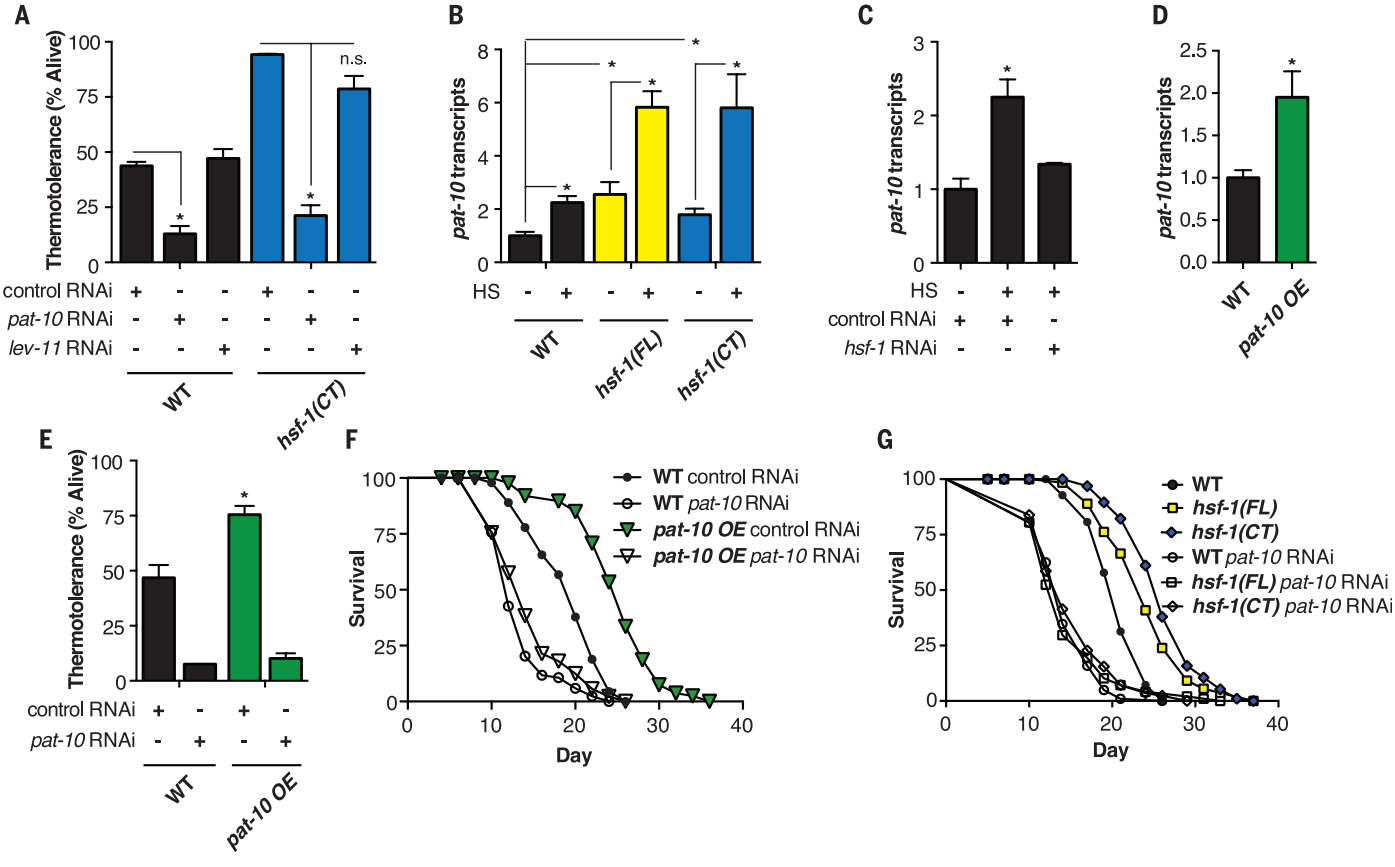

Fig. 2. *pat-10* is necessary and sufficient for thermotolerance and longevity. (**A**) Thermotolerance of WT and *hsf-1(CT)* strains treated with *pat-10* or *lev-11* RNAi. (**B**) Quantitative PCR of *pat-10* with and without heat shock (HS). (**C**) Effect of *hsf-1* RNAi on *pat-10* transcription upon heat shock. (**D**) Quantified expression of *pat-10* in the *pat-10 OE* strain. (**E**) Effect of *pat-10* overexpression or *pat-10* RNAi on thermotolerance. (**F**) Life-span survival curves for WT or *pat-10*–overexpressing strains treated with control or *pat-10* RNAi. (**G**) Life-span survival curves for WT or *hsf-1*–overexpressing strains treated with control or *pat-10* RNAi. *$P < 0.05$; error bars indicate SEM.

However, RNAi toward the worm homolog of tropomyosin—*lev-11*, a partner with *pat-10* in the troponin complex—did not affect heat resistance (Fig. 2A). This suggests that the role of *pat-10* in muscle contraction does not influence thermotolerance.

Loss of *pat-10* also disrupts actin cytoskeleton dynamics and endocytosis (*10*–*13*). To address these potential mechanisms of protection, we used green fluorescent protein (GFP)–labeled muscle filaments to assess actin organization (*14*). Upon heat shock, muscle filaments became unorganized and damaged, leading to impaired motility (Fig. 3, A and B). However, *pat-10* overexpression was sufficient to prevent heat-induced muscle and motility deterioration (Fig. 3, A and B). Furthermore, heat shock decreased the ratio of the filamentous (F) actin to globular (G) actin in WT worms, whereas the protected *pat-10* overexpression animals maintained F actin upon exposure to heat stress (Fig. 3C and fig. S8). With regard to aging, the ratio of F to G actin also decreased with age, and *pat-10* overexpression lessened this decline (Fig. 3D and fig. S8). Hence, under conditions of acute stress or gradual age-related deterioration, the integrity of the actin cytoskeleton is correlated with organismal survival, and overexpression of *pat-10* can abrogate the collapse of actin filaments.

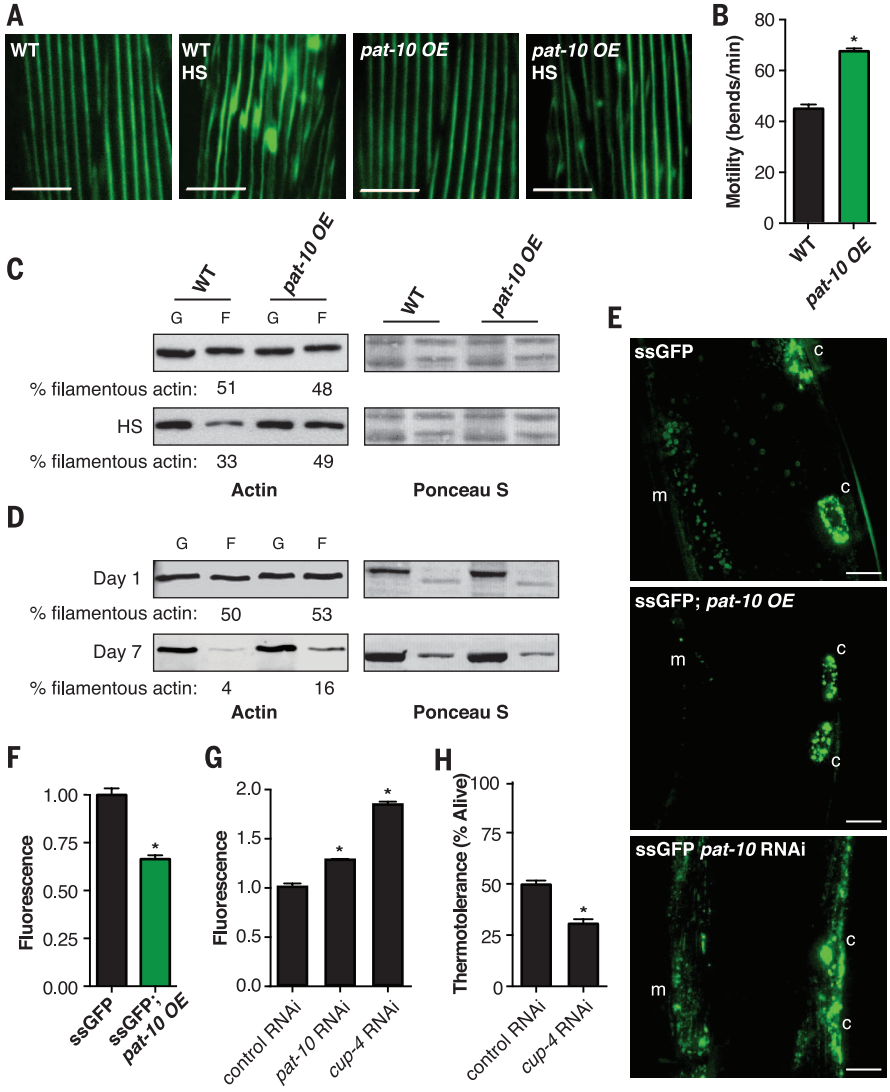

Fig. 3. *pat-10* overexpression improves actin cytoskeletal integrity and cellular trafficking. (**A**) GFP-tagged myosin heavy chain in muscle detected by means of fluorescent microscopy, before and after heat shock (HS). (**B**) Worm thrashes per minute in liquid to monitor motility after heat shock. (**C** and **D**) Abundance of filamentous (F) actin or globular (G) actin after (C) heat shock or (D) aging. Ponceau S staining shown as a loading control. (**E**) Microscopy showing ssGFP derived from muscle cells (m), endocytosed by coelomocytes (c) to be degraded. (**F**) Normalized ssGFP fluorescence quantification with and without *pat-10* overexpression. (**G**) Effect of blocking coelomocytic endocytosis on GFP fluorescence in the ssGFP reporter strain. (**H**) Thermotolerance after RNAi of *cup-4*. *$P < 0.05$; error bars indicate SEM. Scale bars, 10 μm.

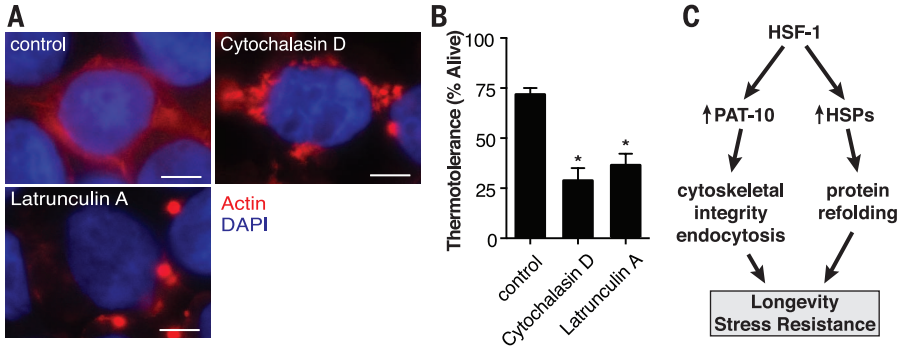

Fig. 4. Impairing actin dynamics decreases thermotolerance in mammalian cell culture. (**A**) Microscopy of HEK293T cells treated with cytochalasin D or latrunculin A [phalloidin stain of actin in red, 4′,6-diamidino-2-phenylindole (DAPI) stain of DNA in blue]. (**B**) Thermotolerance of HEK293T cells after a heat shock at 45°C for 2 hours treated with cytochalasin D or latrunculin A. (**C**) Proposed model of the dual pathways of HSF-1–mediated health assurance. *$P < 0.05$; error bars indicate SEM. Scale bars, 5 μm.

RNAi-induced loss of *pat-10* disrupts endocytosis through impairment of the actin cytoskeleton (*12*, *13*, *15*). To assay the role of *pat-10* in endocytosis, we used a secretion and endocytosis reporter designed to actively secrete GFP (ssGFP) from muscle cells into the pseudocoelomic fluid, where it is endocytosed by the coelomocyte cells and degraded (fig. S9A) (*16*). Therefore, the ssGFP reports upon effective muscular secretion and endocytosis by coelomocytes. Fitting the hypothesis that *pat-10* overexpression improves transport and cellular processing through improved subcellular scaffolding, the *pat-10 OE* strain had a decrease in overall ssGFP fluorescence (Fig. 3, E and F). The decrease in ssGFP resulted from improved secretion and uptake, as shown by the absence of fluorescence in the muscle and pseudocoelomic fluid (Fig. 3E). This decrease was not due to an overall decrease in expression of GFP (fig. S9B). Conversely, RNAi of *pat-10* increased overall fluorescence through decreased muscle secretion and coelomocytic endocytosis (Fig. 3, E and G). To fully block coelomocytic uptake and degradation of ssGFP, RNAi of *cup-4*, a ligand-gated ion channel required in endocytosis (*17*), showed an even higher increase in fluorescence (Fig. 3G) and also reduced thermotolerance in the wild type (Fig. 3H). Collectively, these data indicate *pat-10* has an active role in cytoskeletal maintenance, which is critical to cellular transport.

To test for conservation, we disrupted the actin cytoskeleton in human embryonic kidney (HEK) 293T cells using cytochalasin D, which blocks the addition of actin monomers to filaments (*18*), or latrunculin A, which binds actin monomers and prevents polymerization (Fig. 4A) (*19*). Inhibiting filamentous actin formation with either cytochalasin D or latrunculin A significantly reduced thermotolerance in human cells without causing death at permissive temperatures (Fig. 4B and fig. S10). Similar to our *C. elegans* data, these findings reiterate the importance of the actin cytoskeleton during times of cellular stress.

Elevated levels of *hsf-1* have been shown to benefit multiple organisms, yet its oncogenic properties are a major therapeutic drawback (*20*, *21*). Because the inducible chaperone network promotes survival and proliferation of metastasizing cells (*22*), the ability to harness protective, non-chaperone components within the HSF-1 signal transduction cascade appears essential for future drug development. Identification of *pat-10* as a modifier of thermotolerance and longevity may apply to mammalian systems without the typical oncogenic dangers associated with increased chaperone levels.

The *hsf-1(CT)* strain was still able to mount a transcriptional response to heat shock, albeit reduced in complexity of *hsf-1(FL)*. The molecular mechanism remains unclear by which *hsf-1(CT)* regulates transcription without the C-terminal activation domain, but possible explanations include HSF-1 containing multiple activation domains. Alternatively, the *hsf-1(CT)* modification may alter affinities to DNA-binding sites or different cofactors, which would modify the transcriptional profile.

Our findings underscore the importance of maintaining filamentous actin, as opposed to total levels of actin. We propose a model in which HSF-1 regulates chaperones and actin cytoskeletal genes in parallel to promote thermotolerance and longevity (Fig. 4C). In the absence of chaperone induction, stabilization of the actin cytoskeleton is sufficient to promote survival under conditions of cellular stress and aging.

REFERENCES AND NOTES

1. A.-L. Hsu, C. T. Murphy, C. Kenyon, *Science* **300**, 1142–1145 (2003).
2. M. Fujimoto *et al.*, *J. Biol. Chem.* **280**, 34908–34916 (2005).
3. G. McColl *et al.*, *Cell Metab.* **12**, 260–272 (2010).
4. N. Kourtis, V. Nikoletopoulou, N. Tavernarakis, *Nature* **490**, 213–218 (2012).
5. V. Prahlad, T. Cornelius, R. I. Morimoto, *Science* **320**, 811–814 (2008).
6. Y. M. Hajdu-Cronin, W. J. Chen, P. W. Sternberg, *Genetics* **168**, 1937–1949 (2004).
7. P. E. Kroeger, R. I. Morimoto, *Mol. Cell. Biol.* **14**, 7592–7603 (1994).
8. N. D. Trinklein, J. I. Murray, S. J. Hartman, D. Botstein, R. M. Myers, *Mol. Biol. Cell* **15**, 1254–1261 (2004).
9. H. Terami *et al.*, *J. Cell Biol.* **146**, 193–202 (1999).
10. K. Ono, S. Ono, *Mol. Biol. Cell* **15**, 2782–2793 (2004).
11. T. Obinata, K. Ono, S. Ono, *J. Cell Sci.* **123**, 1557–1566 (2010).
12. Z. Balklava, S. Pant, H. Fares, B. D. Grant, *Nat. Cell Biol.* **9**, 1066–1073 (2007).
13. T. Kuwahara *et al.*, *Hum. Mol. Genet.* **17**, 2997–3009 (2008).
14. L. A. Herndon *et al.*, *Nature* **419**, 808–814 (2002).
15. W. Greene, S.-J. Gao, *PLOS Pathog.* **5**, e1000512 (2009).
16. H. Fares, I. Greenwald, *Nat. Genet.* **28**, 64–68 (2001).
17. A. Patton *et al.*, *Curr. Biol.* **15**, 1045–1050 (2005).
18. J. F. Casella, M. D. Flanagan, S. Lin, *Nature* **293**, 302–305 (1981).
19. I. Spector, N. R. Shochet, Y. Kashman, A. Groweiss, *Science* **219**, 493–495 (1983).
20. L. Whitesell, S. Lindquist, *Expert Opin. Ther. Targets* **13**, 469–478 (2009).
21. C. H. Nguyen *et al.*, *Biochem. J.* **452**, 321–329 (2013).
22. D. R. Ciocca, A. P. Arrigo, S. K. Calderwood, *Arch. Toxicol.* **87**, 19–48 (2013).

ACKNOWLEDGMENTS

Bioinformatic analysis is included in the supplementary materials. The following funding sources supported this research: Howard Hughes Medical Institute, National Center for Research Resources (5P41RR011823-17), National Institute of General Medical Sciences (8 P41 GM103533-17), and National Institute on Aging (R01AG027463-04). N.A.B. was funded by a postdoctoral fellowship to the Salk Center for Nutritional Genomics from the Leona M. & Harry B. Helmsley Charitable Trust; P.M.D. was funded by George E. Hewitt Foundation for Medical Research and National Institute of Aging (1K99AG042495-01A1). We thank the laboratory of G. Lithgow for generously sharing the HSP-16 antibody and J. Durieux for helping design figure illustrations. Some of the nematode strains used in this work were provided by the *Caenorhabditis* Genetics Center (University of Minnesota), which is supported by the NIH–Office of Research Infrastructure Programs (P40 OD010440).

SUPPLEMENTARY MATERIALS

www.sciencemag.org/content/346/6207/360/suppl/DC1
Materials and Methods
Figs. S1 to S10
Tables S1
References (*23*–*40*)

10 March 2014; accepted 13 August 2014
10.1126/science.1253168

AUTOIMMUNITY

Detection of T cell responses to a ubiquitous cellular protein in autoimmune disease

Yoshinaga Ito,[1] Motomu Hashimoto,[1,2,3,4]* Keiji Hirota,[2]* Naganari Ohkura,[2,5] Hiromasa Morikawa,[2] Hiroyoshi Nishikawa,[2] Atsushi Tanaka,[2,5] Moritoshi Furu,[3,6] Hiromu Ito,[3,6] Takao Fujii,[3,4] Takashi Nomura,[1] Sayuri Yamazaki,[7] Akimichi Morita,[7] Dario A. A. Vignali,[8,9] John W. Kappler,[10,11] Shuichi Matsuda,[6] Tsuneyo Mimori,[4] Noriko Sakaguchi,[2] Shimon Sakaguchi[1,2,12]†

T cells that mediate autoimmune diseases such as rheumatoid arthritis (RA) are difficult to characterize because they are likely to be deleted or inactivated in the thymus if the self antigens they recognize are ubiquitously expressed. One way to obtain and analyze these autoimmune T cells is to alter T cell receptor (TCR) signaling in developing T cells to change their sensitivity to thymic negative selection, thereby allowing their thymic production. From mice thus engineered to generate T cells mediating autoimmune arthritis, we isolated arthritogenic TCRs and characterized the self antigens they recognized. One of them was the ubiquitously expressed 60S ribosomal protein L23a (RPL23A), with which T cells and autoantibodies from RA patients reacted. This strategy may improve our understanding of the underlying drivers of autoimmunity.

T cells mediate a variety of autoimmune diseases (*1*, *2*), likely through the recognition of self antigens. However, identification of the self antigens targeted by T cells in systemic autoimmune diseases such as rheumatoid arthritis (RA) has been technically difficult (*3*–*5*). This is because pathogenic T cells expressing high-affinity T cell receptors (TCRs) for ubiquitous self antigens may be largely deleted (i.e., negatively selected) in the thymus and

[1]Department of Experimental Pathology, Institute for Frontier Medical Sciences, Kyoto University, Kyoto 606-8507, Japan. [2]Department of Experimental Immunology, Immunology Frontier Research Center, Osaka University, Suita 565-0871, Japan. [3]Department of the Control for Rheumatic Diseases, Graduate School of Medicine, Kyoto University, Kyoto 606-8507, Japan. [4]Department of Rheumatology and Clinical Immunology, Graduate School of Medicine, Kyoto University, Kyoto 606-8507, Japan. [5]Department of Frontier Research in Tumor Immunology, Center of Medical Innovation and Translational Research, Osaka University, Osaka 565-0871, Japan. [6]Department of Orthopaedic Surgery, Graduate School of Medicine, Kyoto University, Kyoto 606-8507, Japan. [7]Department of Geriatric and Environmental Dermatology, Graduate School of Medical Sciences, Nagoya City University, Nagoya 467-8601, Japan. [8]Department of Immunology, St. Jude Children's Research Hospital, Memphis, TN 38105, USA. [9]Department of Immunology, University of Pittsburgh School of Medicine, Pittsburgh, PA 15261, USA. [10]Integrated Department of Immunology, National Jewish Health, Denver, CO 80206, USA. [11]Howard Hughes Medical Institute, National Jewish Health, Denver, CO 80206, USA. [12]Core Research for Evolutional Science and Technology (CREST), Japan Science and Technology Agency, Tokyo 102-0075, Japan. *These authors contributed equally to this work. **†Corresponding author. E-mail: shimon@ifrec.osaka-u.ac.jp**

scarcely detectable in the periphery or, if detected, in an inactivated state (*6*). This can be circumvented by altering TCR signaling, which changes the sensitivity of developing T cells to thymic selection and results in new dominant self-reactive TCR specificities that are causative of systemic autoimmune diseases (*7*–*11*). For example, a hypomorphic point mutation of ζ-associated protein 70 (ZAP-70), a TCR-proximal signaling molecule, causes T cell–mediated spontaneous autoimmune arthritis in mice, which resembles RA (*8*).

To identify ubiquitously expressed self antigens commonly targeted in mouse and human systemic autoimmune disease, we first examined whether the arthritogenic $CD4^+$ T helper (T_H) cells in BALB/c SKG mice, which develop autoimmune arthritis due to the ZAP-70 mutation, made use of a specific dominant TCR. We compared the arthritogenic capacity of SKG $CD4^+$ T cells expressing different TCR Vβ subfamilies (fig. S1). Transfer of SKG $CD4^+$ T cells expressing Vβ6, Vβ8.1/8.2, or Vβ10 into BALB/c *Rag2*$^{-/-}$ mice induced arthritis with similar severities. In addition, CDR3 gene segments of $V\beta6^+$ $CD4^+$ T cells in arthritic joints were diverse, with few common sequences among individual arthritic SKG mice (fig. S2 and tables S1 and S2). Thus, under the assumption that arthritogenic SKG $CD4^+$ T cells are highly polyclonal and make use of various Vα and Vβ TCR chains, we attempted to isolate a single arthritogenic $CD4^+$ T cell from a particular $CD4^+$ T cell subpopulation—for example, those expressing Vα2 and Vβ6, which constituted ~1% of joint-infiltrating $CD4^+$ T cells. To differentiate arthritogenic $CD4^+$ T cells from forkhead box P3 (Foxp3)–expressing $CD4^+$ regulatory T (T_{reg}) cells (*1*), we used SKG mice with knock-in of enhanced green fluorescent protein (EGFP)–Foxp3 fusion protein, designated eFOX SKG mice, which also spontaneously developed arthritis (fig. S3). We cloned a single TCR pair

A

Clone	Vα	Jα	CDR3	Vβ	Jβ	CDR3	Arthritogenic	Positive cells / Analyzed cells
1-23	14D-3/DV8*03	26*01	CAAS KG YAQGLTF	19*01	2-4*01	CASSI GGTGP SQNTLYF	No	1 / 12 (8.3%)
7-39	14D-3/DV8*03	40*01	CA AIY TGNYKYVF	19*01	2-1*01	CASS WRWGGER AEQFF	Yes	27 / 30 (90%)
6-39	14D-3/DV8*03	52*01	CAAS AA GANTGKLTF	19*01	2-7*01	CAS TPTF SYEQYF	Yes	2 / 26 (8%)

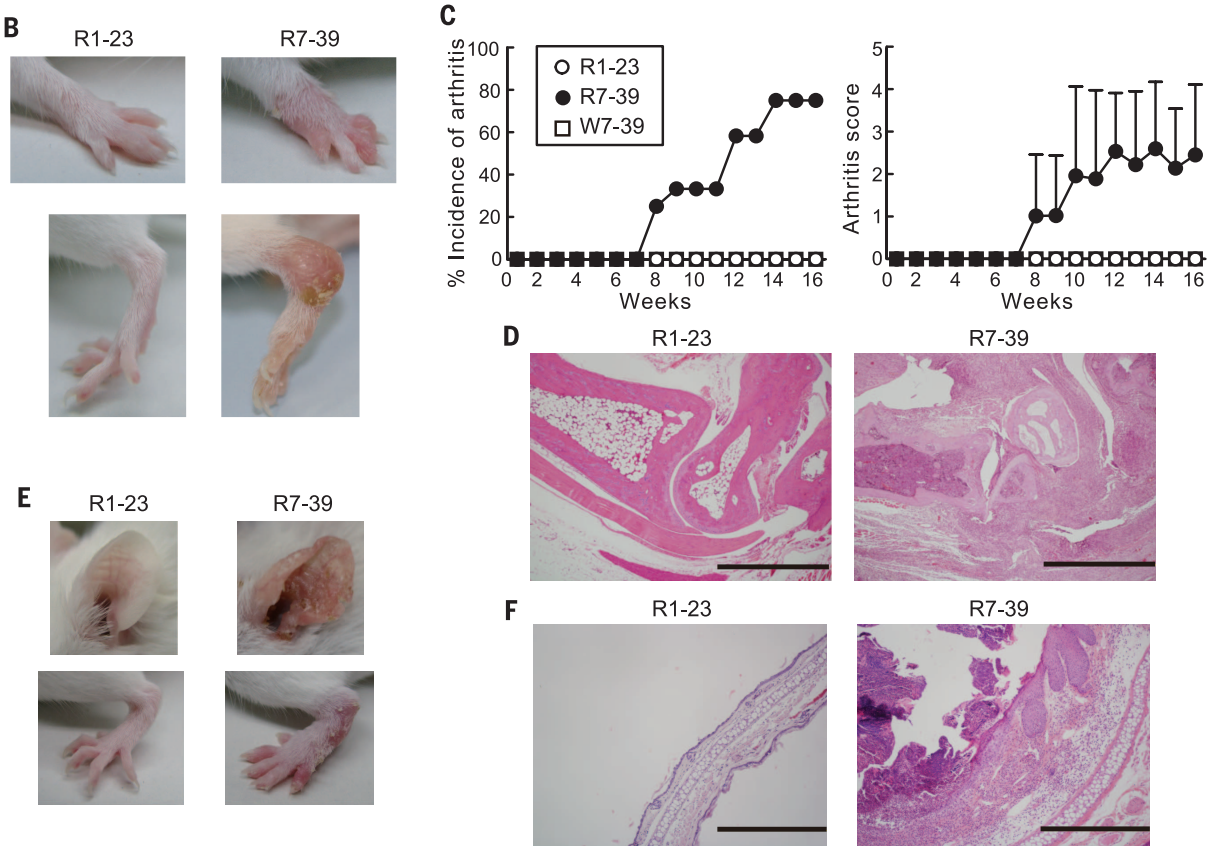

Fig. 1. Arthritis-inducing activity of two TCRs individually expressed in retrogenic mice. (**A**) Amino acid sequences and frequencies of two arthritogenic TCRs (7-39 and 6-39) and the nonarthritogenic 1-23 TCR. These three TCRs were obtained from three different mice. CDR, complementarity-determining region. Amino acid abbreviations: A, Ala; C, Cys; E, Glu; F, Phe; G, Gly; I, Ile; K, Lys; L, Leu; N, Asn; P, Pro; Q, Gln; R, Arg; S, Ser; T, Thr; V, Val; W, Trp; Y, Tyr. (**B**) Joint swelling in R7-39 retrogenic mice. (**C**) Incidence and scores of spontaneous arthritis in R7-39 (n = 11), R1-23 (n = 14), and W7-39 mice (n = 8). Error bars indicate means ± SD. (**D**) Hematoxylin and eosin (HE) staining of arthritic joints; scale bar, 1 mm. (**E**) Ears and hind paws of R7-39 and R1-23 mice. (**F**) HE staining of ears from R7-39 and R1-23 mice; scale bar, 500 μm. Results in (B) and in (D) to (F) represent three independent experiments.

from individual GFP$^-$ Vα2$^+$ Vβ6$^+$ CD4$^+$ T cells present in arthritic joints of eFOX SKG mice, transfected *Rag2*$^{-/-}$ SKG bone marrow (BM) cells with the TCR gene, and transferred the BM cells into *Rag2*$^{-/-}$ mice to construct retrogenic mice expressing the TCR pair in developing T cells (*12*–*15*). Among nine retrogenic strains each expressing a distinct TCR, those expressing 7-39 or 6-39 TCRs spontaneously developed arthritis at incidences of 80.0% and 27.3%, respectively (Fig. 1, A to C, and fig. S4, A to C). The two arthritogenic TCRs and a control nonarthritogenic 1-23 TCR used the same Vα and Vβ gene segments but different Jα and Jβ genes and CDR3 sequences (Fig. 1A). Arthritic joints in retrogenic 7-39 (R7-39) mice showed mononuclear cell infiltration, pannus formation, and cartilage destruction (Fig. 1D). Some (66.7%) of the R7-39, but not the R6-39, mice also developed chronic dermatitis, which exhibited hyperkeratosis and parakeratosis, histopathological features of human psoriasis (*16*) (Fig. 1, E and F, and fig. S5). Other organs were histologically intact (fig. S6).

In R7-39 mice, 7-39 TCR–transduced cells preferentially differentiated into monoclonal CD4$^+$ T cells with an activated and memory phenotype (fig. S7), and were able to transfer both arthritis and dermatitis into other *Rag2*$^{-/-}$ mice. Both arthritic R7-39 and nonarthritic R1-23 mice failed to develop Foxp3$^+$ T$_{reg}$ cells (fig. S8). In contrast to 7-39 TCR gene–transfected *Rag2*$^{-/-}$ BM cells with the SKG ZAP-70 mutation, 7-39 TCR gene–transfected ZAP-70–intact *Rag2*$^{-/-}$ BALB/c BM cells did not cause arthritis in retrogenic mice (designated W7-39 mice). In W7-39 mice, the majority of 7-39 TCR–expressing CD4$^+$ T cells were negatively selected in the thymus, and those that had escaped thymic negative selection exhibited a naïve nonactivated phenotype, indicating their dormant or anergic state (Fig. 1C and fig. S9).

Taken together, these results demonstrate that CD4$^+$ T cells with a specific TCR mediate autoimmune arthritis and also dermatitis, and that more than one TCR specificity is individually able to confer T cell arthritogenicity.

We next constructed T cell hybridomas expressing 7-39 or 6-39 TCRs and attempted to determine the self antigens recognized by these TCRs. The 7-39 hybridoma cells produced interleukin-2 (IL-2) when stimulated by cell extracts not only from SKG fibroblast-like synoviocytes (FLSs) but also from P3U1 cells, a BALB/c plasma cell–derived cell line (fig. S10). In contrast, syngeneic antigen-presenting cells (APCs) were sufficient to induce IL-2 production by 6-39 hybridoma cells, indicating that the 6-39 TCRs recognized a self antigen constitutively displayed by APCs (fig. S4D). To further characterize the self antigen recognized by 7-39 TCRs, we reconstituted *Rag2*$^{-/-}$ mice with a mixture of 7-39 TCR–transfected *Rag2*$^{-/-}$ SKG BM cells and *TCR*β$^{-/-}$ BALB/c BM cells on the assumption that the autoantibodies produced by B cells might specifically react with the self antigen recognized by 7-39 TCRs because T cell help came solely from 7-39 T$_H$ cells. The sera from these "B cell–reconstituted" mice specifically reacted with an 18-kD protein from the cell extract of P3U1 cells (Fig. 2A). Mass spectrometric analysis identified this protein as RPL23A, a component of the 60*S* subunit of ribosomes (*17*, *18*) (fig. S11). Various organs were found to express *RPL23A* mRNA at high levels (Fig. 2B). The amino acid sequence of RPL23A is 100% conserved between mice and humans (*18*). The sera from the B cell–reconstituted R7-39 mice indeed recognized recombinant RPL23A, but not histone H1.2 protein, another candidate protein indicated by the mass spectrometric analysis (Fig. 2C). In addition, recombinant RPL23A protein specifically stimulated the 7-39 hybridoma cells in a dose-dependent, class II major histocompatibility complex (MHC) I-A^d–dependent manner (Fig. 2D and fig. S12). Among 20–amino acid RPL23A peptides with consecutive overlapping of 5 amino acid residues, RPL23A$_{71\text{-}90}$ peptide stimulated 7-39 TCRs most potently (table S3 and fig. S13A).

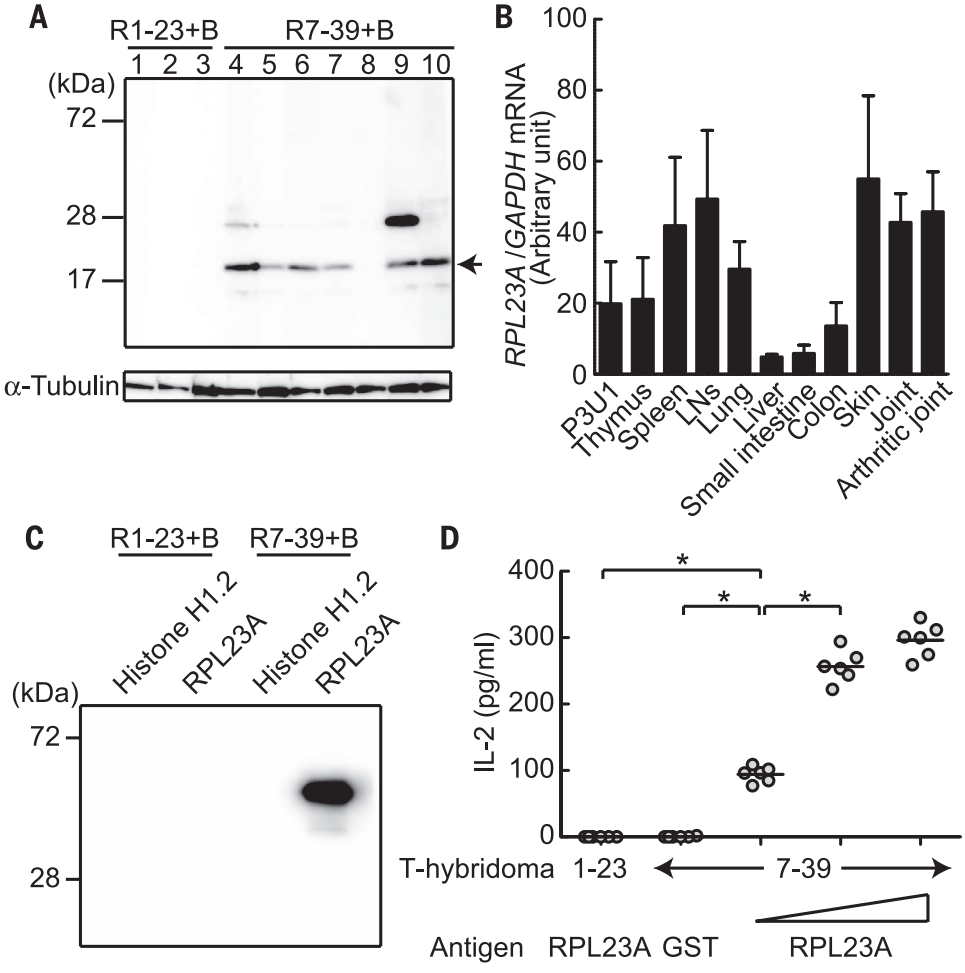

Fig. 2. Identification of the self antigen recognized by arthritogenic 7-39 TCRs. (**A**) Immunoblot analysis by sera from B cell–reconstituted R7-39 mice (n = 7) and B cell–reconstituted R1-23 mice (n = 3). Arrow indicates the commonly recognized protein. (**B**) Quantitative real-time polymerase chain reaction (qPCR) analysis for RPL23A gene expression in various tissues from SKG mice (n = 3). Error bars indicate means ± SD. (**C**) Recombinant RPL23A protein revealed by immunoblotting with sera from the indicated mice. (**D**) IL-2 production by 7-39 or 1-23 T cell hybridomas stimulated with the indicated recombinant proteins (n = 6). Horizontal bars indicate the means. *P < 0.05 (Kruskal-Wallis test followed by Steel-Dwass test). Results represent two [(A) to (C)] or three (D) independent experiments.

B cell–reconstituted R7-39 mice and arthritic SKG mice developed antibodies reacting with cyclic citrullinated peptides (CCP), as also observed in RA patients (*19*) (fig. S14A), yet there was no significant difference in titer of antibodies to RPL23A whether this was assessed with citrullinated or noncitrullinated RPL23A protein (fig. S14, B and C). In addition, the $RPL23A_{71\text{-}90}$ peptide recognized by 7-39 TCRs contained no arginine residue to be converted to citrulline (table S3).

Taken together, these results indicate that the ubiquitously expressed protein RPL23A can be a target antigen of both arthritis and dermatitis. Furthermore, more than one systemic antigen can be targeted for arthritis induction, because the 6-39 TCRs did not react to peptides derived from RPL23A (fig. S13B).

Upon transfer, $CD4^+$ T cells, but not sera, from B cell–reconstituted R7-39 mice induced arthritis in *Rag2*$^{-/-}$ mice (fig. S15). Indeed, $CD4^+$ T cells from arthritic joints or the regional lymph nodes of R7-39 mice produced inflammatory cytokines [including IL-17A, interferon-γ (IFN-γ), and granulocyte macrophage-colony stimulating factor (GM-CSF)] upon activation with phorbol 12-myristate 13-acetate (PMA) and ionomycin, RPL23A protein, or $RPL23A_{71\text{-}90}$ peptide (Fig. 3, A to D, fig. S16, A to D, and fig. S17). In addition, RPL23A stimulated nonarthritic SKG, but not BALB/c, $CD4^+$ T cells to produce IL-17A in vitro (Fig. 3E). It also augmented the production of IL-17A by $CD4^+$ T cells from SKG mice treated with mannan, which can trigger autoimmune arthritis in SKG mice by promoting T_H17 differentiation of arthritogenic $CD4^+$ T cells (*20*, *21*). An arthritic joint of SKG mice indeed harbored $CD4^+$ T cells possessing the Vβ CDR3 of 7-39 TCRs (table S2).

We next evaluated the contribution of T_{reg} cells to controlling arthritogenic $CD4^+$ T cells. T_{reg} cells

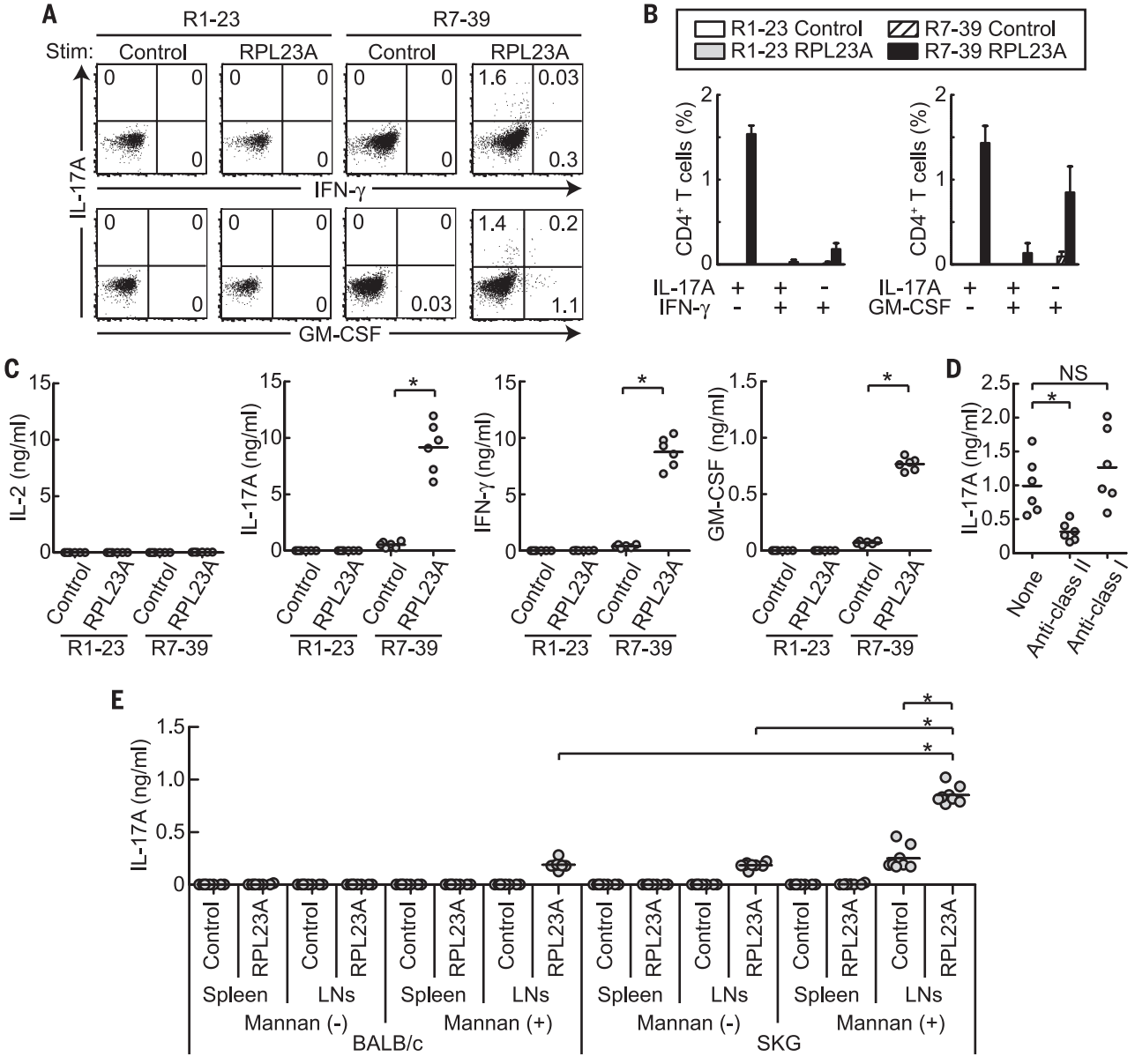

Fig. 3. RPL23A-reactive T_H cells in R7-39 mice. (**A**) Cytokine production by $CD4^+$ T cells from regional lymph nodes of R7-39 or R1-23 mice after in vitro stimulation with recombinant RPL23A or control glutathione *S*-transferase (GST) protein. Stim, stimulation. Data are representative of three independent experiments. (**B**) Percentages of cytokine-producing $CD4^+$ T cells in (A) (n = 3). (**C**) Cytokine amounts in culture supernatants in (A) (n = 6). (**D**) IL-17A production by RPL23A-stimulated lymphocytes from R7-39 mice in the presence or absence of blocking antibodies to MHC class I or class II (n = 6). (**E**) IL-17A production by lymphocytes stimulated with recombinant RPL23A or control GST proteins (n = 8). Lymphocytes were taken from SKG or BALB/c mice with or without mannan treatment. In (B), results are shown as means ± SD. In (C) to (E), horizontal bars indicate the means; *P < 0.05 (Kruskal-Wallis test followed by Steel-Dwass test); NS, not significant. Results represent two independent experiments in (B) and (C).

from either ZAP-70–intact BALB/c or ZAP-70–mutant SKG mice failed to suppress arthritis development in *Rag2*$^{-/-}$ mice when cotransferred with phenotypically activated or memory 7-39 TCR$^+$ CD4$^+$ T cells (figs. S7 and S18), although T_{reg} cells were capable of suppressing naïve arthritogenic T cells effectively (*9*).

These results collectively indicate that RPL23A is able to stimulate CD4$^+$ T cells in R7-39 mice via RPL23A-derived peptide–MHC class II complexes, driving them to differentiate into arthritogenic effector T_H cells (*20*), which are capable of mediating arthritis even in the presence of T_{reg} cells.

Lastly, we examined possible immune responses to RPL23A in RA patients. *RPL23A* mRNA was found to be ubiquitously expressed in healthy human tissues (Fig. 4A). In synovial tissues of RA patients and also in the apparently normal synovial tissues of osteoarthritis (OA) patients, RPL23A was detected in the cytoplasm of synovial cells, including CD55$^+$ FLSs (Fig. 4B). Relative to healthy controls (1.3%, n = 74), a significantly higher proportion of RA patients (16.8%, n = 374) were positive for serum immunoglobulin G–type autoantibodies to RPL23A (Fig. 4C). Two out of 23 psoriatic arthritis (PsA) patients (8.7%) were positive for the autoantibody, whereas all of the OA patients (n = 11), systemic lupus erythematosus (SLE) patients (n = 30), or

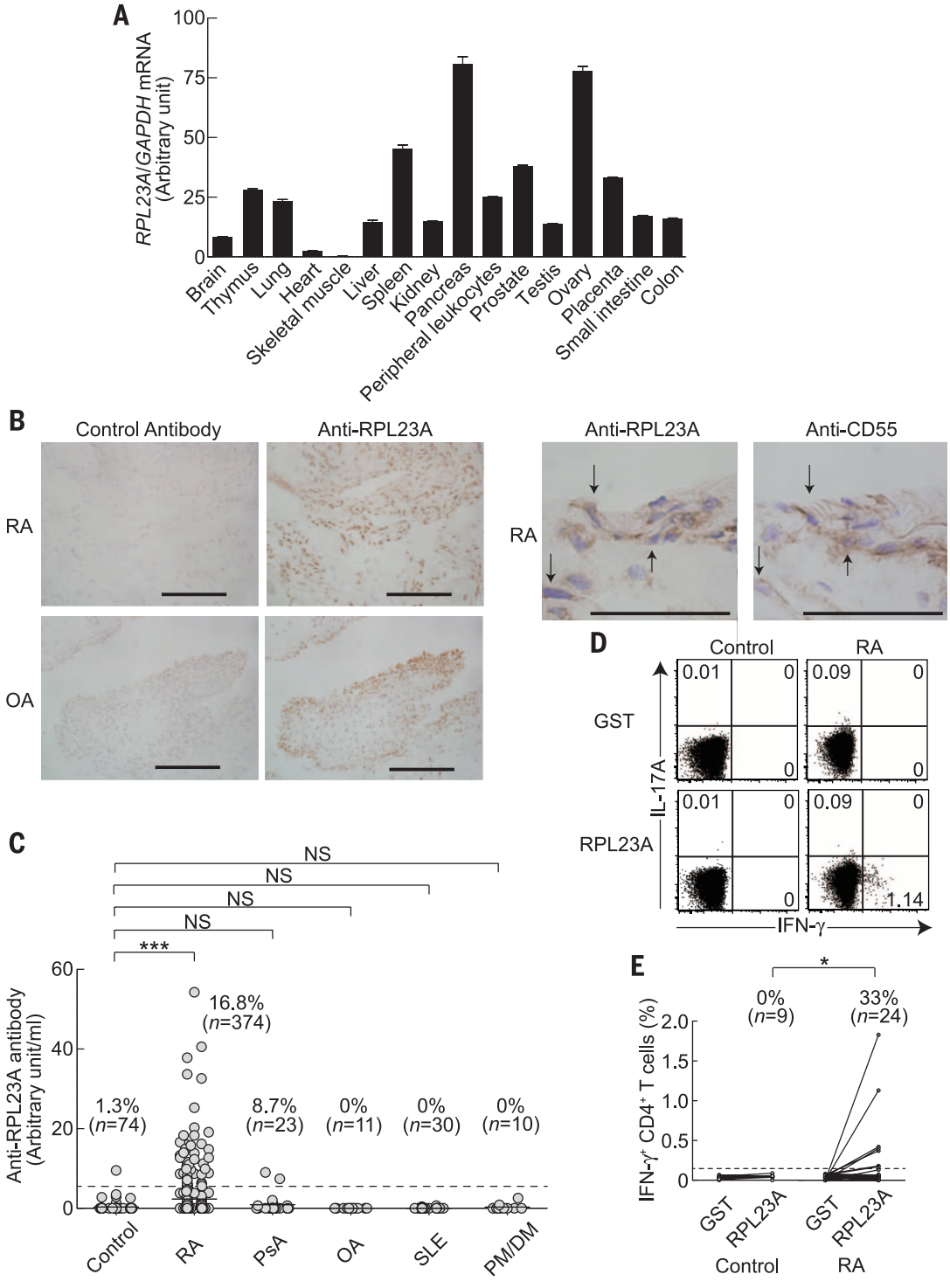

Fig. 4. Anti-RPL23A humoral and cellular immune responses in RA patients. (**A**) qPCR analysis of RPL23A gene expression in various tissues from healthy human subjects (n = 3). Results are shown as means ± SD and represent two independent experiments. (**B**) Immunohistochemical staining of synovial tissues from RA or OA patients for RPL23A or CD55 expression (scale bars, four images at left, 200 μm; two images at right, 50 μm). Serial sections were stained by anti-RPL23A, anti-CD55, or control antibody. Arrows indicate cells that are both RPL23A- and CD55-positive. Representative results from three patients are shown. (**C**) Serum levels of autoantibodies to RPL23A assessed by enzyme-linked immunosorbent assay (ELISA) in RA, PsA, OA, SLE, and PM/DM patients or healthy individuals. Horizontal bars indicate the medians. ***P < 0.001 (Kruskal-Wallis test followed by Dunn's multiple comparison test). (**D**) Cytokine production from CD4$^+$ T cells stimulated with recombinant RPL23A or GST protein. (**E**) Percentages of IFN-γ$^+$ cells in RPL23A- or GST-stimulated CD4$^+$ T cells in RA patients (n = 24) or healthy individuals (n = 9). *P < 0.05 (χ^2 test). Dashed lines indicate the threshold in (C) and (E).

polymyositis/dermatomyositis (PM/DM) patients (n = 10) were negative. In addition, in the synovial fluid of a subset of RA patients, we detected $CD4^+$ T cells producing IFN-γ upon stimulation with RPL23A (Fig. 4, D and E). These findings in humans, together with the key role of anti-RPL23A T cell responses for autoimmune arthritis and psoriasis-like dermatitis in mice, suggest that the responses may play a pathogenic role at least in a subset of patients with RA or PsA.

Our results show that by attenuating TCR signal intensity in developing T cells (hence reducing their sensitivity to thymic negative selection by natural self ligands), T cells reactive with ubiquitously expressed self antigens can be generated as dominant pathogenic clones causing systemic autoimmune disease. Because similar attenuation of TCR signaling at various degrees in conjunction with T_{reg} cell depletion is able to produce a variety of other autoimmune diseases in mice (*9*, *22*), this strategy of generating pathogenic T cells and characterizing the self antigens they recognize would facilitate our understanding of the mechanisms of other autoimmune diseases of currently unknown etiology. In addition, given that genetic polymorphism in a signaling molecule in T cells is a major determinant of genetic susceptibility to various human autoimmune diseases including RA (*23*), such a genetic variation might, at least in part, alter thymic selection, hence forming a TCR repertoire for causing autoimmune disease. Our approach may also be useful in deciphering how T cell autoimmunity to a ubiquitous self antigen triggers localized tissue damage in RA and other human autoimmune diseases, and in devising effective means of systemic or local intervention in the disease process.

REFERENCES AND NOTES

1. S. Sakaguchi, F. Powrie, R. M. Ransohoff, *Nat. Med.* **18**, 54–58 (2012).
2. P. Marrack, J. Kappler, B. L. Kotzin, *Nat. Med.* **7**, 899–905 (2001).
3. M. Feldmann, F. M. Brennan, R. N. Maini, *Cell* **85**, 307–310 (1996).
4. G. S. Firestein, *Nature* **423**, 356–361 (2003).
5. I. B. McInnes, G. Schett, *N. Engl. J. Med.* **365**, 2205–2219 (2011).
6. C. X. Chang *et al*., *Front. Biosci.* **16**, 3014–3035 (2011).
7. L. Y. Hsu, Y. X. Tan, Z. Xiao, M. Malissen, A. Weiss, *J. Exp. Med.* **206**, 2527–2541 (2009).
8. N. Sakaguchi *et al*., *Nature* **426**, 454–460 (2003).
9. S. Tanaka *et al*., *J. Immunol.* **185**, 2295–2305 (2010).
10. C. L. Sommers *et al*., *Science* **296**, 2040–2043 (2002).
11. O. M. Siggs *et al*., *Immunity* **27**, 912–926 (2007).
12. J. Holst *et al*., *Nat. Protoc.* **1**, 406–417 (2006).
13. G. P. Lennon *et al*., *Immunity* **31**, 643–653 (2009).
14. M. L. Bettini, M. Bettini, M. Nakayama, C. S. Guy, D. A. Vignali, *Nat. Protoc.* **8**, 1837–1840 (2013).
15. See supplementary materials on *Science* Online.
16. F. O. Nestle, D. H. Kaplan, J. Barker, *N. Engl. J. Med.* **361**, 496–509 (2009).
17. K. Suzuki, I. G. Wool, *J. Biol. Chem.* **268**, 2755–2761 (1993).
18. W. Fan, M. Christensen, E. Eichler, X. Zhang, G. Lennon, *Genomics* **46**, 234–239 (1997).
19. W. J. van Venrooij, J. J. van Beers, G. J. Pruijn, *Nat. Rev. Rheumatol.* **7**, 391–398 (2011).
20. K. Hirota *et al*., *J. Exp. Med.* **204**, 41–47 (2007).
21. M. Hashimoto *et al*., *J. Exp. Med.* **207**, 1135–1143 (2010).
22. M. Ono, J. Shimizu, Y. Miyachi, S. Sakaguchi, *J. Immunol.* **176**, 4748–4756 (2006).
23. N. Bottini, T. Vang, F. Cucca, T. Mustelin, *Semin. Immunol.* **18**, 207–213 (2006).

ACKNOWLEDGMENTS

We thank D. O. Adeegbe, Y. Kitagawa, and K. Chen for critical reading of the manuscript; E. Yamamoto, M. Matsuura, R. Ishii, Y. Tada, Y. Funabiki, the technical support team (Graduate School of Medicine, Kyoto University), and K. Saito of DNA-chip Development Center for Infectious Diseases (RIMD, Osaka University) for technical assistance; T. Matsushita for histology; T. Kitamura for gifts of the packaging cell line Plat-E; the members of the Department of Rheumatology and Clinical Immunology, Kyoto University, for providing us with patients' sera; and the members of our laboratories for comments. The data presented in this paper are tabulated in the main paper and in the supplementary materials. eFOX mice and plasmids for making retrogenic mice are subject to a material transfer agreement. A patent application related to the work in this paper has been filed (PCT/JP2014/069306: A way to diagnose autoimmune arthritis; Y.I. and S.S. as inventors). Supported by Grants-in-Aid for Specially Promoted Research 20002007 (S.S. and Y.I.),;for Young Scientists (B) 24790996 (Y.I.) from the Japan Society for the Promotion of Science; Core Research for Evolutional Science and Technology from the Japan Science and Technology Agency (S.S.); NIH grant R01 DK089125 (D.A.A.V.); and American Lebanese Syrian Associated Charities (D.A.A.V.). M.H., T.F., M.F., H.I., and T.M. are affiliated with a department that is supported financially by five pharmaceutical companies (Mitsubishi Tanabe Pharma Co., Bristol-Myers K.K., Chugai Pharmaceutical Co. Ltd., AbbVie GK., and Eisai Co. Ltd.). The sponsors were not involved in the study design; in the collection, analysis, or interpretation of data; in the writing of this manuscript; or in the decision to submit the article for publication.

SUPPLEMENTARY MATERIALS

www.sciencemag.org/content/346/6207/363/suppl/DC1
Materials and Methods
Supplementary Text
Figs. S1 to S18
Tables S1 to S3
References (*24*–*36*)

22 July 2014; accepted 16 September 2014
10.1126/science.1259077

This is the start of something big.

Science Advances
SIGNIFICANT RESEARCH, GLOBAL IMPACT

AAAS

Introducing *Science Advances* – the new, online-only, open-access journal from *Science* and AAAS. Find out how you can be among the first authors published at **scienceadvances.org.**

THE 2014–2015 KEYSTONE SYMPOSIA MEETINGS

The Modes of Action of Vaccine Adjuvants (S1)
October 8–13, 2014 | Seattle, Washington | USA

Cell Death Signaling in Cancer and the Immune System (S2)
October 28–November 2, 2014 | Guaruja, São Paulo | Brazil

Precision Genome Engineering and Synthetic Biology (A1)
January 11–16, 2015 | Big Sky, Montana | USA

Viral Immunity (A2)
January 11–16, 2015 | Breckenridge, Colorado | USA

The Biological Code of Signaling – A Tribute to Tony Pawson (F1)
January 11–16, 2015 | Steamboat Springs, Colorado | USA

Integrating Metabolism and Tumor Biology (J1)
joint with **PI 3-Kinase Signaling Pathways in Disease (J2)**
January 13–18, 2015 | Vancouver, British Columbia | Canada

Immunity to Veterinary Pathogens: Informing Vaccine Development (A3)
January 20–25, 2015 | Keystone, Colorado | USA

Host Response in Tuberculosis (J3)
joint with **Granulomas in Infectious and Non-Infectious Diseases (J4)**
January 22–27, 2015 | Santa Fe, New Mexico | USA

Epigenetics and Cancer (A4)
January 25–30, 2015 | Keystone, Colorado | USA

Neuroinflammation in Diseases of the Central Nervous System (A5)
January 25–30, 2015 | Taos, New Mexico | USA

Mitochondria, Metabolism and Heart Failure (J5)
joint with **Diabetes and Metabolic Dysfunction (J6)**
January 27–Feb 1, 2015 | Santa Fe, New Mexico | USA

Autoimmunity and Tolerance (B1)
February 3–8, 2015 | Keystone, Colorado | USA

Endoderm Lineages in Development and Disease (B2)
February 8–13, 2015 | Keystone, Colorado | USA

Plant Receptor Kinases: From Molecules to Environment (B3)
February 8–13, 2015 | Taos, New Mexico | USA

Tumor Immunology:
Multidisciplinary Science Driving Combination Therapy (J7)
joint with **Antibodies as Drugs: Immunological Scaffolds as Therapeutics (J8)**
February 8–13, 2015 | Banff, Alberta | Canada

Systems Biology of Lipid Metabolism (B4)
February 9–13, 2015 | Breckenridge, Colorado | USA

RNA Silencing in Plants (G1)
February 17–22, 2015 | Keystone, Colorado | USA

Neuroepigenetics (B5)
February 22–26, 2015 | Santa Fe, New Mexico | USA

Hematopoiesis (B6)
February 22–27, 2015 | Keystone, Colorado | USA

Gut Microbiota Modulation of Host Physiology:
The Search for Mechanism (C1)
March 1–6, 2015 | Keystone, Colorado | USA

Heart Disease and Regeneration: Insights from Development (X1)
joint with **Cell Biology of the Heart: Beyond the Myocyte-Centric View (X2)**
March 1–6, 2015 | Copper Mountain, Colorado | USA

DNA Replication and Recombination (X3)
joint with **Genomic Instability and DNA Repair (X4)**
March 1–6, 2015 | Whistler, British Columbia | Canada

Hybrid Methods in Structural Biology (C2)
March 4–8, 2015 | Tahoe City, California | USA

Biology of Sirtuins (C3)
March 8–12, 2015 | Santa Fe, New Mexico | USA

Dendritic Cells and Macrophages Reunited (C4)
March 8–13, 2015 | Montreal, Quebec | Canada

Optogenetics (C5)
March 12–16, 2015 | Denver, Colorado | USA

Co-Infection: A Global Challenge for Disease Control (C6)
March 15–20, 2015 | Ouro Preto, Minas Gerais | Brazil

Long Noncoding RNAs: From Evolution to Function (C7)
March 15–20, 2015 | Keystone, Colorado | USA

Pathways of Neurodevelopmental Disorders (C8)
March 16–20, 2015 | Tahoe City, California | USA

HIV Vaccines (X5)
joint with **The Golden Anniversary of B Cell Discovery (X6)**
March 22–27, 2015 | Banff, Alberta | Canada

Obesity and the Metabolic Syndrome:
Mitochondria and Energy Expenditure (X7)
joint with **Liver Metabolism and Nonalcoholic Fatty Liver Disease (NAFLD) (X8)**
March 22–27, 2015 | Whistler, British Columbia | Canada

Transcriptional and Epigenetic Influences on Stem Cell States (C9)
March 23–28, 2015 | Steamboat Springs, Colorado | USA

Gram-Negative Resistance (D1)
March 29–April 2, 2015 | Tahoe City, California | USA

Viruses and Human Cancer (D2)
March 29–April 3, 2015 | Big Sky, Montana | USA

T Cells: Regulation and Effector Function (D3)
March 29–April 3, 2015 | Snowbird, Utah | USA

DNA Methylation (Z1)
joint with **Epigenomics (Z2)**
March 29–April 3, 2015 | Keystone, Colorado | USA

Neural Control of Metabolic Physiology and Diseases (D4)
April 12–17, 2015 | Snowbird, Utah | USA

Beige and Brown Fat:
Basic Biology and Novel Therapeutics (D5)
April 17–22, 2015 | Snowbird, Utah | USA

The Crossroads of Lipid Metabolism and Diabetes (D6)
April 19–24, 2015 | Copenhagen | Denmark

Innate Immunity and Determinants of Microbial Pathogenesis (Z3)
joint with **Mechanisms of Pro-Inflammatory Diseases (Z4)**
April 19–24, 2015 | Olympic Valley, California | USA

The Human Proteome (D7)
April 24–29, 2015 | Stockholm | Sweden

Mechanisms of HIV Persistence: Implications for a Cure (E1)
April 26–May 1, 2015 | Boston, Massachusetts | USA

The Arthropod Vector: The Controller of Transmission (E2)
May 12–17, 2015 | Taos, New Mexico | USA

Hypoxia: From Basic Mechanisms to Therapeutics (E3)
May 12–17, 2015 | Dublin | Ireland

Hippo Pathway: Signaling, Development and Disease (E4)
May 17–21, 2015 | Taos, New Mexico | USA

MicroRNAs and Noncoding RNAs in Cancer (E5)
June 7–12, 2015 | Keystone, Colorado | USA

Autophagy (E6)
June 19–24, 2015 | Breckenridge, Colorado | USA

KEYSTONE SYMPOSIA™
on Molecular and Cellular Biology
Accelerating Life Science Discovery

*Discounted Abstract and Scholarship Deadlines precede meetings by four months and Discounted Registration Deadlines by two months. Visit keystonesymposia.org/meetings for more details. You can also view each meeting's program by adding 15 and then the program code (in parentheses after each meeting name) after keystonesymposia.org/ (e.g., **keystonesymposia.org/15A1**).*

Temperature-Controlled Polarimeters

ADP600 Series high-accuracy Peltier temperature-controlled polarimeters are available with single, dual, and multiple wavelength derivatives covering the visible spectrum. The series also features measurement in the highly sensitive ultraviolet region. This capability makes the instrument particularly suited for use by scientists wishing to measure chiral compounds, and other optically active substances in the chemical, pharmaceutical and food sectors as well as for use in academic research. Integral to operational simplicity is the full color high definition touchscreen graphical user interface. A simple menu structure, featuring a METHOD system is similar to the popular wide range RFM series of Peltier-controlled refractometers commonly found across the industry. ADP600 polarimeters have an extensive interfacing capability and may be configured to operate in secure environments in accordance with FDA regulation 21 CFR Part 11 and also meet the requirements of U.S., European, and Japanese pharmacopoeia.

Xylem Analytics
For info: 978-778-1010
www.xylemanalytics.com

Compact Ozone Sterilizer

The Ozilla is a new high quality, purpose-built ozone gas generator. Measuring just 13 x 11 x 5 inches (32 x 28 x 13 cm), it will fit in most standard laboratory cell culture incubators, air incubators, cell culture hoods, polymerase chain reaction hoods, or any other environment where a sterile atmosphere is critical. Following simple operational instructions the Ozilla is able to completely eliminate airborne as well as surface contaminants and germs including bacteria, phage, and fungus. Ozone is the most powerful oxidative agent that occurs naturally. With its extra free radical oxygen molecule, ozone is able to destroy germs, viruses, and microbes that may cause surface or air contamination. Furthermore, ozone leaves no chemical residue typical of alternative detergent or synthetic cleaners, and if handled properly—by converting ozone back to oxygen molecules—it can be one of the most effective sterilizing tools.

AMS Biotechnology
For info: +44-(0)-1235-828200
www.amsbio.com/ozilla.aspx

HPLC Columns

Cortecs family of columns now includes a new line of 2.7 µm silica-based, solid-core particle columns that set a new standard for high-performance liquid chromatography (HPLC) column performance. Designed for analytical scientists who need to maximize performance on their existing LC systems, Cortecs 2.7 µm columns run at lower pressures while delivering high efficiencies. This gives the scientist the flexibility to use longer column lengths to improve resolution or higher flow rates to speed instrument analysis times and increase throughput. Available in C18+, C18, and HILIC chemistries, the columns come in 48 unique column configurations and are fully scalable to Cortecs 1.6 µm columns, thus allowing separation scientists who currently run HPLC separations the ability to future-proof their laboratories and seamlessly transfer or migrate their separation to UPLC. Cortecs C18+ columns deliver excellent peak shapes for basic compounds and impart unique selectivity while being a superior low bleed, formic acid-friendly option for LC/mass spectrometry applications.

Waters
For info: 800-252-4752
www.waters.com/cortecs

Scientific Imaging Cameras

Three new scientific imaging cameras are now available, the EFiS, AtoR, and iRiS. Dedicated to low-light imaging applications such as fluorescence imaging, astronomy, X-ray tomography, and single molecule detection, the EFiS, AToR, and iRiS are the ideal candidates when photons are scarce or when fast temporal acquisition is required. A choice of several different software options is offered with these cameras, depending on the customer budget and application. The EFiS is a scientific frame transfer EMCCD camera with a 1004x1002 sensor size enabling optimum data resolution. The frame transfer technology adds the benefit of not requiring a mechanical shutter for ultrafast data acquisition. The AToR is a scientific interline EMCCD camera with a sensor size of 658x496 pixels. The interline transfer technology allows very short integration times without image smearing. The iRiS is a 4.2 megapixel scientific CMOS camera, with a 2048x2048 sensor size that enables a large field of view and ultimate image resolution.

Horiba Scientific
For info: 732-494-8660
www.horiba.com/scientific

Disposable Protein A Chromatography Columns

ProVance pre-packed Protein A columns are a high-performance disposable chromatography solution to help meet the growing demand for downstream purification. Single-use technology offers unparalleled flexibility while reducing risk of contamination at multi-product facilities typical of contract manufacturing organizations. Until now, there has not been a cost-effective Protein A chromatography option for single-use manufacturing facilities. ProVance columns combine Grace proprietary incompressible silica with cost-effective Protein A and disposable column hardware. The high-capacity columns can reduce operating costs by 40%–60% and are ideally suited for single-batch or single-campaign use, eliminating the need for significant cleaning validations and long-term storage. ProVance columns are available in a range of sizes for early screening and up to full-scale GMP manufacturing. Columns for use in GMP manufacturing come complete with documentation for regulatory support, shipping studies, leachables, and extractables.

Grace
For info: 410-531-4000
www.grace.com/provance

Electronically submit your new product description or product literature information! Go to www.sciencemag.org/products/newproducts.dtl for more information.

Newly offered instrumentation, apparatus, and laboratory materials of interest to researchers in all disciplines in academic, industrial, and governmental organizations are featured in this space. Emphasis is given to purpose, chief characteristics, and availability of products and materials. Endorsement by *Science* or AAAS of any products or materials mentioned is not implied. Additional information may be obtained from the manufacturer or supplier.

MERCK'S POSTDOCTORAL RESEARCH FELLOW PROGRAM

Join the Merck Networks for immediate news and recruitment alerts:

merck careers

merckcareers1

merckcareers1

merck

Bringing important medicines and vaccines to people around the world through innovative science is what we do. At Merck, we strive to improve human life, achieve scientific excellence, operate with the highest standards of integrity, expand access to our products and employ a diverse workforce that values collaboration.

Developing Talent, Harnessing Innovation, Building for the Future

Our Postdoctoral Research Fellow Program builds on our legacy of scientific excellence and innovation.

If you join us, you'll be a part of a team of motivated scientists working to discover and develop medicines and vaccines that help meet the world's unmet medical needs. You will work alongside outstanding researchers and collaborators as part of Merck's industry-leading research and development organization. Our postdocs:

- Work in unique laboratory environments with top capabilities, equipment, expertise and knowledge
- Obtain experience in drug discovery and development
- Generate innovative science resulting in high-quality external publications
- Participate in seminars, lectures and meetings, and have the opportunity to interact with the local scientific community
- Are positioned for choice careers in pharma, biotechnology, or academia

As a postdoc, you will receive a competitive salary and access to the full benefits programs offered by Merck.

At Merck, our passion is improving health. This is what keeps us at the forefront of scientific discovery and innovation. We invite you to apply.

Postdoctoral Research Fellow Program

To learn more about the MRL Postdoctoral Research Fellow Program, or to apply for a position, visit www.merck.com/research/fellow/home.html.

MERCK
Be well

NEW ENGLAND BioLabs® Inc.

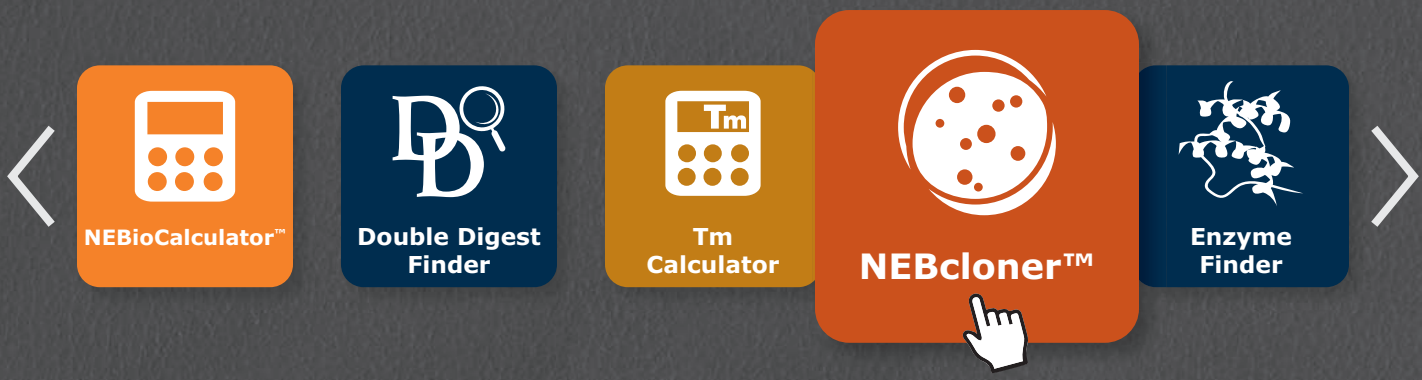

Expand your toolbox

with NEB's interactive tool, NEBcloner™.

Find the right product and protocol for your next cloning experiment with NEBcloner. Answer a few simple questions, and our latest NEBtool will find a solution for you. Or, select the protocol you need, and get started. With NEB®'s online tools, easier experimental design is right at your fingertips.

- For help with scientific conversions and calculations, try **NEBioCalculator™**.
- Identify the restriction enzyme cut sites within your DNA sequence with **NEBcutter®**.
- Calculate the optimal annealing temperature for your PCR with NEB's **Tm calculator**.

Featured NEB Tool

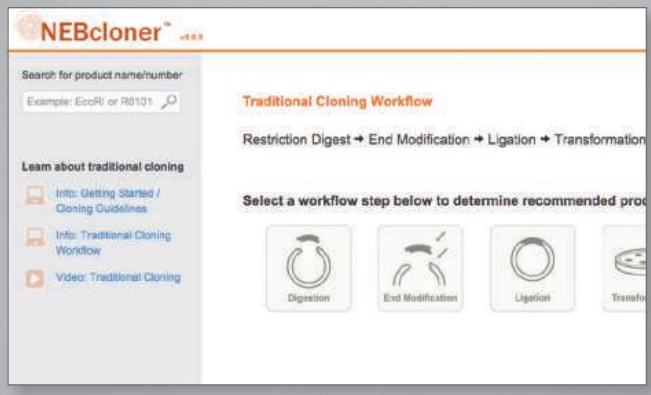

Explore NEB's entire suite of interactive online tools at

www.neb.com/nebtools

NEW ENGLAND BIOLABS®, NEB® and NEBCUTTER® are registered trademarks of New England Biolabs, Inc.
NEBCLONER™ and NEBIOCALCULATOR™ are trademarks of New England Biolabs, Inc.

Science Careers online @sciencecareers.org

Science Careers Advertising

For full advertising details, go to ScienceCareers.org and click For Employers, or call one of our representatives.

Tracy Holmes
Worldwide Associate Director
Science Careers
Phone: +44 (0) 1223 326525

THE AMERICAS
E-mail: advertise@sciencecareers.org
Fax: 202 289 6742

Tina Burks
Phone: 202 326 6577

Nancy Toema
Phone: 202 326 6578

Marci Gallun
Sales Administrator
Phone: 202 326 6582

Online Job Posting Questions
Phone: 202 312 6375

EUROPE / INDIA / AUSTRALIA / NEW ZEALAND / REST OF WORLD
E-mail: ads@science-int.co.uk
Fax: +44 (0) 1223 326532

Axel Gesatzki
Phone: +44 (0) 1223 326529

Sarah Lelarge
Phone: +44 (0) 1223 326527

Kelly Grace
Phone: +44 (0) 1223 326528

JAPAN
Katsuyoshi Fukamizu (Tokyo)
E-mail: kfukamizu@aaas.org
Phone: +81 3 3219 5777

Hiroyuki Mashiki (Kyoto)
E-mail: hmashiki@aaas.org
Phone: +81 75 823 1109

CHINA / KOREA / SINGAPORE / TAIWAN / THAILAND

Ruolei Wu
Phone: +86 186 0082 9345
E-mail: rwu@aaas.org

All ads submitted for publication must comply with applicable U.S. and non-U.S. laws. *Science* reserves the right to refuse any advertisement at its sole discretion for any reason, including without limitation for offensive language or inappropriate content, and all advertising is subject to publisher approval. *Science* encourages our readers to alert us to any ads that they feel may be discriminatory or offensive.

Science Careers
From the journal *Science* AAAS

ScienceCareers.org

Careers in Neuroscience

Special Career Feature

October 31, 2014

Ads accepted until October 27, if space is still available.

There's only one Science

This feature examines the areas and regions where the career possibilities are expanding and offers advice for scientists building their career in neuroscience.

Why you should advertise in these issues of *Science*:

Reach: Your job ad is seen by 570,400 readers around the globe

Bonus distributions to: Society for Neuroscience
15–19 November
Washington, DC

To book your ad: advertise@sciencecareers.org

THE AMERICAS
202-326-6582

JAPAN
+81 3 3219 5777

EUROPE/ROW
+44 (0) 1223 326500

CHINA / KOREA / SINGAPORE / TAIWAN
+86 186 0082 9345

Science Careers | AAAS
FROM THE JOURNAL SCIENCE

Produced by the *Science*/AAAS Custom Publishing Office. | ScienceCareers.org

Employees Thrive on Innovative Design

Science 2014 TOP EMPLOYER

First-in-class drugs and drought-resistant seeds may not seem to have much in common but the transformative technologies being developed to produce these game-changing products do. At the heart of those discoveries are the companies, identified by the 2014 *Science* Careers Top Employer Survey, that foster a spirit of innovation. These 20 biotechnology and pharmaceutical companies have their eyes on transformative prizes and invest in the intellectual capital needed to get there. From encouraging risky research to bolstering academic collaborations, keeping employees engaged and excited about their research is priority number one.

By Virginia Gewin

If there is one budding sentiment in the life sciences these days, it's this: The divide between biotech and pharma is crumbling. Not only are biotech companies loosening pharma's stronghold on small molecules, but pharma is, increasingly, forging biotech research alliances. In fact, pharma companies are setting up shop in biotech-bastions such as Boston, Massachusetts.

A more collaborative era of data-driven discovery—one in which scientists can deftly navigate the regulatory hurdles and development costs necessary to create novel products—is emerging. Adoption of agricultural biotech is at an all-time high. According to a 2013 report by Transparency Market Research, the genetically modified (GM) seed sector is growing at a 9.9% compound annual growth rate, a clear sign of unmet needs in agriculture. And, according to the Pharmaceutical Research and Manufacturers of America, first-in-class therapeutics make up an astounding 70% of the global drug development pipeline.

From new cures to new crops, this year's top employers know that design and diligence go hand in hand. Regeneron Pharmaceutical, Inc.—the top company for the 3rd year in a row—is a biotech bucking to be the next Apple. At the company's 25th anniversary celebration this year, Founding Scientist and Chief Scientific Officer **George Yancopoulos** sought inspirational words to share with his staff. He researched Apple, often cited as the world's most innovative company, at its 25th year mark. He found that, while Apple was considered a solid company, they had yet to invent the iPad or the iPhone. He shared the story at the Regeneron party. "That's our challenge," Yancopoulos told the crowd, "I want us, in 10 years, to be known for the technology we have yet to invent."

The next decade looks equally bright at Novo Nordisk (#2; up from 11 in 2013), the global leader in diabetes drugs. The Danish drug-maker expects a decade's worth of 10% annual growth in revenue. With a 6,000-strong R&D-focused recruitment push by 2023 and a new $180 million headquarters, according to Chief Scientific Officer **Mads Krogsgaard Thomsen**, they are clearly positioning themselves for a new era in the company's history.

There were two fresh names on the 2014 list: the largest U.S. pharma, Johnson & Johnson (J&J), which raked in $28 billion in worldwide pharmaceutical sales last year, reappeared at #19 after a four-year absence, and a newcomer to the list Actelion (#14), a Basel-based biotech currently working on 25 small molecules. "We're the biotech without the large molecules," says **Roland Haefeli**, head of investor relations and public affairs at Actelion.

Perhaps not surprisingly, many of the top 20 companies boast unbelievably low turnover rates, typically lower than 8%. The agricultural-focused biotechs are even lower with roughly 3% of employees at both the #6 top employer, Monsanto Company (up from #14 in 2013), and #9, Syngenta (up from #13 in 2013), voluntarily leaving each year. That's a sharp contrast to a July report from the human resources services company Randstad Pharma that states over 50% of biotech and pharma employees expect to search for a job in the next year.

A common thread runs through the top 20 list: Give employees the intellectual freedom and support necessary to pursue high-risk/high-reward goals—and they'll deliver. Add to this a noble mission, such as increasing food security or decreasing disease suffering, and employers can create a positive feedback loop that maximizes employees' drive and dedication as well as company profits.

Methodology

Each year, *Science* Careers conducts a web-based survey of individuals familiar with biotechnology and continued>

ABSTRACT DESIG: © ISTOCKPHOTO.COM/MATTJEACOCK; PHOTO: © ISTOCKPHOTO.COM/FOTOSTORM

Upcoming Features

Neuroscience Careers—Oct. 31 ■ *Nanotechnology Careers—Nov. 14* ■ *Regional Focus: Europe—Nov. 28*

Top Twenty Employers

2014 Rank	2013 Rank	Employer (Global Headquarters)	Innovative leader in the industry	Treats employees with respect	Has loyal employees	Is socially responsible	Work culture values aligned	Makes changes needed
1	1	**Regeneron Pharmaceuticals, Inc.** *(Tarrytown, NY)*	•		•	•		
2	11	**Novo Nordisk** *(Bagsvaerd, Denmark)*		•	•	•		
3	2	**Genentech** *(South San Francisco, CA)*	•	•			•	
4	3	**Vertex Pharmaceuticals Incorporated** *(Boston, MA)*	•			•	•	
5	5	**Eli Lilly and Company** *(Indianapolis, IN)*		•	•	•		
6	14	**Monsanto Company** *(Creve Coeur, MO)*	•		•			•
7	4	**AbbVie** *(North Chicago, IL)*		•	•	•		
8	16	**Roche**—excluding Genentech *(Basel, Switzerland)*	•		•	•		
9	13	**Syngenta** *(Basel, Switzerland)*		•		•	•	
10	10	**Biogen Idec** *(Weston, MA)*	•	•				•
11	8	**Novartis** *(Basel, Switzerland)*	•			•		•
12	18	**Abbott** *(Abbott Park, IL)*		•	•	•		
13	9	**Boehringer Ingelheim** *(Ingelheim, Germany)*		•	•	•		
14	–	**Actelion** *(Allschwil, Switzerland)*	•		•			•
15	17	**Celgene Corporation** *(Summit, NJ)*		•	•		•	
16	20	**Bayer** *(Leverkusen, Germany)*		•	•	•		
17	12	**DuPont** *(Wilmington, DE)*		•	•	•		
18	19	**Amgen** *(Thousand Oaks, CA)*	•	•		•		
19	–	**Johnson & Johnson** *(New Brunswick, NJ)*		•		•	•	
20	–	**Merck KGaA/Merck Serono/EMD Serono** *(Darmstadt, Germany)*			•	•	•	

The 20 companies with the best reputations as employers and the top three driving characteristics for each company, according to respondents in the 2014 survey undertaken for the *Science*/AAAS Custom Publishing Office. The companies without a 2013 rank did not receive enough mentions to qualify or did not receive a high enough ranking during the 2013 survey.

pharmaceutical employers to determine the best employers in the field. The survey was conducted from March 20 to May 4, 2014. Roughly 65,000 individuals—more than twice the number contacted last year—were invited to take the survey. In all, 5,394 returned surveys served as the basis for the analysis. Roughly 25% of respondents were contacted by direct email; the remaining 75% of surveys were returned following promotion by 573 contacts in human resources at biotech and pharma companies (*Science* Careers database). The top 20 companies were determined using a statistical process that calculates a unique ranking score for each company rated. Only companies rated by 35 or more respondents were eligible for the top 20 best employers list.

The majority of respondents (74%) were current employees of the company who took the opportunity to rate their employer's performance. These are not entry-level staff either; roughly 65% have been in the workforce at least 10 years. Basic researchers made up 22% of the survey respondents, while 27% work in applied research, 36% work in development, and 12% are administrators or executives. This year, of the 19% of respondents who said they were likely to seek a different position in the next year, 39% indicated the primary reason for the change was career advancement, down from 41% in 2012.

Once again, respondents ranked "is an innovative leader in the industry" as the most important driver in choosing the best companies. The remaining drivers: "is socially responsible," "has top leadership that successfully makes changes needed to keep the organization moving in the right direction," "has loyal employees," "treats its employees with respect," and "has work culture values that are aligned with employees' personal values"—suggest today's employees are an idealistic lot.

Novo Nordisk, Monsanto, Roche (excluding Genentech and up 8 places to #8), and Syngenta all made impressive leaps to reclaim spots on the top 10 list.

Genentech (#3), Vertex Pharmaceuticals Incorporated (#4), Eli Lilly and Company (#5), AbbVie (#7), and Biogen Idec (#10) round out the top 10 employers (see chart above).

Innovation, defined

Innovation is, arguably, the most overused word in industry. In fact, it means different things to different people; each company has its own culture of finding a "new" product, process, or pipeline. What works at one company will contrast wildly with what works at another. Yet, despite an almost indefinable quality, our survey reveals that, like good art, employees know innovation when they see it and believe it is the single most important characteristic of a "best employer."

In the last 10 years, Novo Nordisk has developed more of a risk-taking culture to match their grand goal of defeating the growing epidemic of diabetes. "Originally continued>

It takes **great science** to bring medicines to market.

The drive to improve people's lives. It's what turns great ideas into life-changing accomplishments. And it's what defines each and every member of Regeneron's talented and devoted team, universally committed to developing better medicines for serious illnesses. Here, we'll challenge you to expand your knowledge, enhance your expertise and achieve excellence—every day. And we'll support you with world-class resources, outstanding rewards and countless opportunities for professional development and advancement. So you can grow our company's capabilities, while achieving your most ambitious career goals.

Join us at the forefront of new discoveries.
careers.regeneron.com

Regeneron has locations in:
Basking Ridge, NJ
Tarrytown & Rensselaer, NY
Dublin & Limerick, Ireland

REGENERON
science to medicine®

we were not so much into risk taking," says Krogsgaard Thomsen. Now, they are using stem cell research to create insulin-producing cells. "I get questions from research directors at other companies asking if we're serious, and I always answer 'yes,'" he adds. "If we can surpass a barrier to improve the power and convenience of our medicines, we've got to do it." To inspire that spirit of innovation, the new Novo Nordisk headquarters was designed to resemble the hexomer structure of insulin. "Even in our architecture, we're trying to mimic things that exist in the human body," he says.

At Regeneron, critical breakthroughs are tackled by bringing the intellectual firepower under one roof. They call it the "think tank." It's just an ordinary meeting room, except the 10–30 invitees expect marathon meetings, sometimes reassembling over the course of several days to kick around new ideas. "We have great stamina here," says **Neil Stahl**, Regeneron's senior vice president for research and development. Their Veloc-Immune mouse model was an idea which evolved during a "think tank" meeting. The model has been used to produce fully human monoclonal antibodies and was key to creating the 15 antibodies the company currently has in the clinic—among them a cholesterol reducer and a pain reliever. Even though Regeneron now has external scientists bringing innovative ideas to their doorstep, it doesn't change their approach. "A lot of these ideas are clever, but not useful or applicable to the bottlenecks in the drug discovery world," says Yancopoulos. "We understand where innovations are needed to speed drug development and pursue those ideas."

In keeping with the Apple analogy, the most inventive design is often the game-changing idea. For example, they are excited about their new "bi-specific" technology—essentially one antibody, two actions. One arm of the antibody activates T cells and another arm binds to a tumor target. "It's an elegant design—an antibody hybrid, made cleanly, with no artificial pieces unlike other bi-specifics that have more of a 'Rube Goldberg' design," says Stahl. It is Regeneron's first drug candidate that will harness the immune system to attack cancer cells, he says. "That's the kind of stuff that our employees see coming up, and keeps them excited about in the future."

When Janssen Pharmaceuticals, the R&D arm of pharma giant J&J, decided they were going to focus on novel therapeutics of big impact, rather than follow the competition's focus on branded generics or biosimilars, they completely redesigned how they could tackle that goal by opening five so-called innovation centers. The aim is to bring expertise together, rather than reinvent the wheel. Once academic and small company researchers make discoveries, pharma executives can contribute their scientific expertise to help turn those discovery into products. "We want to find the best partners and the best science to develop innovative products," says **Jeffrey Nye**, head of neuroscience innovation and partnership strategy at Janssen R&D and the J&J Innovation Centers. "And it's working." For example, their Boston-based innovation center launched with news of a $12.9 million deal to back Rodin Therapeutics, a Cambridge, Massachusetts-based biotech using epigenetics to develop novel therapeutics for neurological disorders, notably Alzheimer's disease.

It may sound like giving academics money to do a research job, but **Peter Lebowitz**, global head of oncology R&D at Janssen, says that couldn't be further from the truth. "We build a close tie to what these researchers are doing and provide our own expertise," he says. In fact, his neuroscience colleagues are dreaming up unprecedented drug delivery strategies. "We think, in the near future, it will be possible to treat schizophrenia with four injections per year instead of [patients] having to take pills three times a day," says **Husseini Manji**, global head of neuroscience R&D at Janssen. But that's an approach that only one of the largest pharma companies in the world can take.

In contrast, small, young biopharmaceutical companies, like Actelion, carve out their niche through discovery. Actelion is only 15 years old—and their first internally-discovered compound, macitentan, was approved to treat pulmonary arterial hypertension—making 2013 a big year for them. "Science is all about overcoming obstacles and staying excited to do it," says **Oliver Nayler**, Actelion's head of cardiovascular and fibrosis biology. At Actelion, employees are increasingly motivated by visualization technologies, such as automated live-cell imaging and high content screening, that offer new means to view and quantify cellular, even subcellular, processes. "It opens up a whole new world, by letting us see what impact our compounds have on cells, which stimulates our creativity to explore new experimental approaches," says Nayler.

Developing cutting-edge products in the agricultural seed sector, where a constant need to protect crops from drought and disease requires multi-prong strategies, takes on a number of different flavors. For example, both Monsanto and Syngenta have released drought-tolerant seeds. Genomics-based discovery is key for identifying genes of potential interest to plant breeders and biotech seed developers. Monsanto's newest drought-tolerant product, Drought Guard, relies on a gene that creates a chaperone protein to coat a plant's RNA during stressful conditions and maintain the plant's normal cell functions, while Syngenta's hybrid contains novel drought-tolerant gene combinations. Both companies are also exploring RNA interference (RNAi) technology—the use of RNA molecules to inhibit gene expression—to prevent plant diseases. And while Monsanto is digging into which soil continued>

Demographics

Gender:
53% Male, 43% Female, 4% No response

Experience:
66% have 10 or more years work experience

Highest Degree Earned:
40% Doctorate, 28% Master's, 26% Bachelor's, 6% Other

Company Type:
36% Pharma, 33% Biotech, 22% Biopharma, 4% University, 5% Other; More than 9 out of 10 work in private industry

Nature of Work:
36% Development, 27% Applied Research, 22% Basic Research, 12% Administration/Executive, 11% QA/QC/Regulatory Affairs, 8% Production, 13% Other (respondents were able to choose more than one response)

Geography:
70% from North America, 23% from Europe, 6% from Asia/Pacific Rim, 1% from rest of world

PEOPLE ICON: © ISTOCKPHOTO.COM/MEGANEURA

TOP EMPLOYERS Science Careers online @sciencecareers.org

Driving Characteristics of Top Employers

2014	2013
1. Innovative leader in the industry	1. Innovative leader in the industry
2. Treats employees with respect	2. Treats employees with respect
3. Loyal employees	3. Socially responsible
4. Socially responsible	4. Loyal employees
5. Work culture values aligned	5. Has a clear vision
6. Makes changes needed	6. Does important quality research

Driving characteristics are listed in descending order of impact on overall employer rankings.

Shaded backgrounds indicate the characteristics in common for the two years.

microbes might help grow seeds better, Syngenta is hot on uncovering what metabolites can reveal about maximizing plant growth.

Something to believe in

This year's survey responses revealed that employees want to work for a company that holds itself to a high ethic—and walks the walk to prove it. Syngenta employees have long enjoyed a community garden on campus where green thumbs could raise potatoes and carrots from company seeds to donate to a local food bank. In addition, last fall, Syngenta put forward a more global strategy called The Good Growth Plan which makes six commitments to improve resource use efficiency, including finding ways to produce more food with less waste, degradation, and poverty.

For **Hope Hart**, Syngenta's product safety team leader, the company's commitment to social responsibility reinforces her volunteer work at local schools or community groups where she discusses the safety of GM crops or how they help increase small-farm–holders' profits. "I'll go wherever we are invited to share how we know that GM crops are safe because it's an issue that is close to my heart," says Hart.

Monsanto, too, is facing the controversy surrounding genetic engineering head on. A couple of years ago, the company assessed the challenges of, and criticisms against, genetic modification research and realized that they needed to have a more proactive voice on the issue. "We have really started to create a path for employees to engage more in social media or participate in science-based interactions with the public on the questions about the role of science and innovation in agriculture," says **Robb Fraley**, Monsanto's chief technology officer. Their solution, an ambassador program, generated a huge amount of interest. Over 1,000 employees signed up to receive training to be an ambassador and reach out directly to consumers to address question and concerns about science. "You can tell there was a pent-up, innate desire to get more involved. It's been a great employee motivator," adds Fraley. "People really are making a difference in farmer's lives and they want that to continue," he adds.

Fraley says the company's core mission is a critical part of its attraction to potential employees. Internal Monsanto surveys reveal that employee engagement scores are 80%–90%. "That is extraordinary," says Fraley. "We're competing for talent all around the world to expand breeding efforts and having an engaged, diverse workforce is key," he adds.

It's not just the agricultural biotech companies that want to do right by the environment. Actelion has incorporated green building standards in all new construction projects, including the use of solar panels and electric car charging stations, and continues to increase waste recycling efforts. "The young scientists we hire care about these things," says **Tina Kitt**, communications specialist at Actelion. That sentiment is reflected in the survey results as well. Employees are happiest when their work values align with their employer.

But it goes beyond corporate social responsibility. "We are passionate about doing research that helps the patient," says Krogsgaard Thomsen. In fact, Novo Nordisk routinely invites patients to the research facilities to share their experiences. "When we heard that patient outcomes are held back by fear of hypoglycemia (low blood sugar), we created drugs that result in a reduced risk of hypoglycemia," he says.

Novo Nordisk adheres to what they describe as a triple bottom line: doing business that focuses on public health, society, and the shareholders. "Novo Nordisk is consistently one of the top two health care companies in the Dow Jones Sustainability Index, which tracks the sustainability performance of the largest 2,500 companies listed on the Dow Jones Global Total Stock Market Index. When employees can identify with a company's vision, and it goes beyond making a profit, they feel they can really align with shared goals," says Krogsgaard Thomsen.

Not surprisingly, several of these top employers, including Actelion, Syngenta, and Regeneron, also make science education a focus of their social responsibility efforts. Actelion supports the Mobile Bus, a rambling lab equipped with basic science experiments. Yancopoulos says Regeneron sponsors the Westchester Science and Engineering Fair owing largely to two persistent high school science teachers who made him realize that most scientists had, at some point, a science teacher who helped make a difference. "We have to do this for the next generation," he says.

Employee appreciation

The survey data reveals that employee appreciation creates a positive feedback with company loyalty. The company rated highest on "treats employees with respect," Novo Nordisk, also had the highest "loyal employee" rating. "Our international colleagues often comment on how much they appreciate the trust we show in our employees, that it's a sign of respect," says **Ann-Charlotte Hasselager**, corporate vice president of R&D Human Resources at Novo Nordisk. That trust goes both ways. "Every now and then while turmoil surrounds continued>

Scientist's choice – University vs. Industry

There are a few key reasons why outstanding scientists should consider joining big pharma like Roche. Dr. Andrew Thomas, Head of Medicinal Chemistry, Neuroscience at Roche in Basel, explains why he joined one of the leading pharma companies a few years ago.

Dr. Andrew Thomas is Section Head Medicinal Chemistry at Roche in Basel.

What is your current role?
I am a member of our Chemistry Leadership Team, Extended Small Molecule Research Leadership Team, global Non Clinical Drug Safety Committee and I'm directly involved in the discovery and development of new medicines for the therapeutic areas of neuroscience ophthalmology and rare diseases. The goal of my team is design and discover molecules that will one day become medicines. One of the main responsibilities of my current role is to ensure that our department retain a reputation as being an employer of choice for the best scientists in our domain by attracting world class talent to join us.

Why did you decide to join Roche?
There are a few key reasons why I joined Roche. First and foremost – I had an immediate strong and authentic affinity to the outstanding scientists I met during my interviews – which continues to this day. Before I interviewed with Roche I was thinking to become a University Professor – but I was convinced by joining Roche I would be able to get the best of both worlds by generating new knowledge, teaching and mentoring students and more important being to directly impact healthcare through the implementation of medicinal chemistry knowledge. These have all been realised – which is why I have decided to stay with Roche.

What can Roche offer to young scientists?
We are able to offer a unique experience – where we provide the future leading scientists a stimulating and truly enriching environment interacting within very experienced teams where our young scientists gain an authentic insight into the leading capabilities of our organisation. Because we attract leading talents they are regarded right from the beginning as competent researchers and our skill is to support them advancing their own hypotheses and trying out new approaches to their research. The development of novel medicines and diagnostics gives them the opportunity to use their skills in complex areas of science, where there is still so much to discover. Industry has the advantage over academia that we focus very efficiently on the direct application of our research results rather than only generating them for others to use which is often the case in academia. We are able to drive this through our focus on creating new knowledge and value through inventions followed by timely publications. In addition the core of our industry is composed of a team of multi-disciplinary and recognized world experts across all key areas. Having access to experts internally is an asset unique to industry as well as our efficient infrastructure that ensures our company runs smoothly so we can focus on our research.

What would you advise job seekers who want to join Roche?
Make personal contact to our recruiters and departmental representatives who are out in the field at career fairs and/or giving scientific seminars around the world. If you are someone who has the passion to be a world class contributor to the discovery and development of new medicines demonstrate your potential early in your career during your formal education which will catalyse you being recognized by Roche employers.

To apply online for positions visit
careers.roche.ch
Roche is an Equal Opportunity Employer.
The next step is yours.

TOP EMPLOYERS Science Careers online @sciencecareers.org

Comparison of Top Ten's Top Characteristics

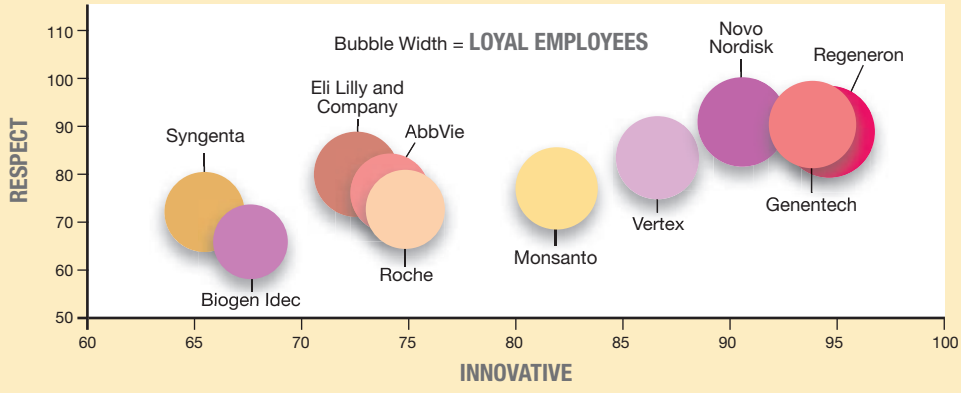

Comparison of the top 10 companies on the basis of the top three drivers (scored out of 100):

- **Innovative leader in the industry** (*x*-axis),
- **Treats employees with respect** (*y*-axis),
- **Has loyal employees** (bubble width).

our company, employees support the company and management. There's not a them [versus] us thing," says Krogsgaard Thomsen. Flexible work policies, especially those that bolster work-life balance, are a way the company demonstrates its respect for employees.

Rewarding top work is perhaps the best employee motivator. Monsanto's strong focus on employee recognition includes quarterly recognition events, as well as an annual "Above and Beyond" awards ceremony, with the highest awards going to scientists who have discovered products. They also have sustainable yield pledge awards for actions, such as improving water availability or increasing crop productivity, that conserve more or improve lives.

Monsanto has also taken a broad view of employee well-being. To better understand employee needs and feedback, Monsanto has opened several lines of communication between employees and management. In addition to a biannual internal survey, they also conduct "pulse" surveys on specific employee populations each quarter.

The goal is to provide an inclusive environment in which employees can thrive. **Melissa Harper**, Monsanto's head of diversity, can rattle off a dozen resource groups designed to support employees—the focus can range from adoption assistance to a lesbian, gay, bisexual, and transgendered network. "We take the time not only to listen but to act on what we're hearing from our employees," says Harper. Similarly, Janssen Pharmaceuticals offers adoption assistance and health care advocacy and support.

During the World Cup, there's one surefire way to acknowledge and appreciate that diversity: televise the soccer matches. In fact, World Cup viewing was a common theme among the top employers. "Our company recognizes that its employees are passionate about sports, and playing the World Cup shows they appreciate our passions as much as they trust us to get our work done," says Hart. Actelion employees are so soccer-crazed, they hold their own tournament each year. "We all get a bit worried because the teams play so hard," says Haefeli. "We keep our medical services nearby—just in case."

The teams that play hard together, work hard together. "When people come together and play on teams, it feels like a family," says **Gaby Scherer**, Actelion director of human resources. Appreciative of that family feel, Actelion recently built an on-site day care because Basel, in particular, has a tight childcare market. They also accommodate employees who choose to work less than full-time, often after having children. In fact, 17% of their workforce is part-time.

Still, most of the top employers cast aside any form of a caste system. "There's not the stereotypical hierarchy at Syngenta," says Hart. "Of course we have levels of management, but everyone's ideas matter." Syngenta's collaborative nature initially unnerved **Michiel van Lookeren Campagne**, Syngenta's head of biotechnology "My first meeting at the company, we sat in a round circle of chairs," he says, "and I wondered 'where did I land?'" But, he found, it's just the company's culture. "When we are meeting, we are all present—no one is typing on a computer."

For scientists, a collaborative culture can matter most. Regeneron was formed, in part, because Yancopoulos, who was discouraged from collaborating during his days in academia, thought that was the wrong way to do science. "Science is interactive and that was one of our core values from day one," says Stahl. Yancopoulos says successful collaborations are all about finding synergies. "Most companies exchange dollars for brains, but we don't work that way," says Yancopoulos. "We have a lot of biologics and antibodies that we want to test in collaborators' systems, but we exchange things of respected value like our technologies, reagents, and know-how." As a result, they are building a company, like Merck KGaA and Genentech (a member of the Roche group) before them, on a foundation of science and technology. "We're not going to just come up with one drug, we're going to build a company that's able to go from basic science into the clinic over and over again."

But, as Janssen's Manji points out, the only way to set up outstanding collaborations is to have a lot of strength on the inside. "When I came here over five years ago, one thing I noted is that we're trying to do things that are so complex, and there is a lot of good science going on outside our walls—we should find ways to work together," he says. "It is not just 'us or them' anymore."

Virginia Gewin is a freelance science writer based in Portland, Oregon.

DOI: 10.1126/science.opms.r1400147

biogen idec

Caring Deeply.
Changing Lives.

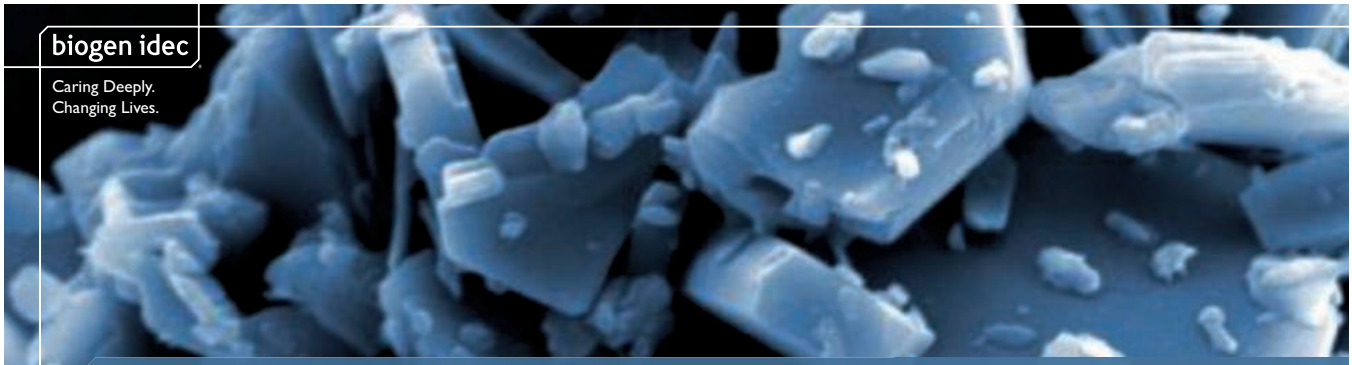

LIFE-CHANGING WORK
More breakthroughs, fewer barriers

It's why you pursued a career in life sciences: an opportunity to change lives – maybe even your own.

Biogen Idec is seeking fearless, creative, entrepreneurial scientists across a variety of disciplines to help create the next generation of innovative drugs for patients and unmet medical needs.

You'll use the latest translational and computational techniques to solve clinical problems and discover new biology. You'll do great science alongside remarkable people. It's life-changing work – and it's waiting for you at Biogen Idec.

biogenidec.com/careers

Biogen Idec has immediate openings in the following areas:

- Molecular Biology
- Immunology
- Fibrosis
- Neurobiology
- Pathology
- Cell Biology
- Antibody Engineering
- Computational Biology
- Postdoctoral Program

Biogen Idec is an Equal Opportunity/Affirmative Action Employer M/F/D/V.

Introducing the new ***Science*** **Careers Jobs app** from Science

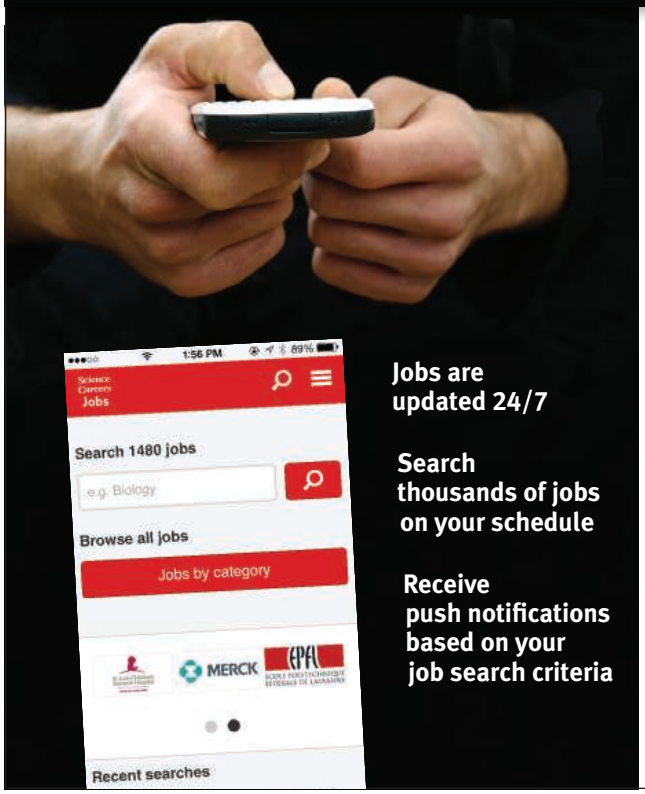

Jobs are updated 24/7

Search thousands of jobs on your schedule

Receive push notifications based on your job search criteria

Get a job on the go.

Search thousands of scientific jobs in academia, industry, and government from around the globe. Keep your finger on the pulse of your field by setting up an alert for the type of job you are looking for and receive push notifications when jobs are posted that meet your criteria. The seamless application process includes linking you directly to job postings from your customized push notifications.

Science Careers
From the journal *Science* AAAS

ScienceCareers.org

Scan this code to download app or visit **apps.sciencemag.org** for information.

NANYANG TECHNOLOGICAL UNIVERSITY

Faculty Positions at School of Chemical and Biomedical Engineering [SCBE]

The School of Chemical and Biomedical Engineering **(http://www.scbe.ntu.edu.sg)**, Nanyang Technological University of Singapore invites applicants to apply for tenure-track faculty positions at the Associate/Assistant Professor level. Applicants should hold a Ph.D. in Chemical Engineering, Bioengineering, Biomedical Engineering, Food Science Technology and Engineering or a related field by the beginning of the appointment period. Candidates with post-doctoral training would be preferred.

The School is particularly interested in:

1) Chemical Engineering candidates with interests in Biochemical Engineering, Synthetic Biology, Food Engineering, Chemical Engineering Process, and Fluids and Colloids.
2) Bioengineering candidates with research interests in Biomaterials, Bioimaging, Biosensors, Biodevices, Bionanotechnologies, Tissue Engineering (musculoskeletal, neuron regeneration, etc), Rehabilitation Neuro-Biomechanics and Translational Biomedical Engineering.

The candidate should have a demonstrated excellence in original research, with good publication records and the ability to teach core Chemical/Food Engineering and Bioengineering courses. Entrepreneurial qualities are also sought after.

Responses received by 30th November 2014 would be given priority.

Emoluments and General Terms and Conditions of Service
The commencing salary will depend on the candidate's qualifications, experience and the level of appointment offered. Information on emoluments and general terms and conditions of service is available at: **http://www.ntu.edu.sg/ohr/CareerOpportunities/TermsandConditions/Pages/FacultyPositions.aspx**.

Application Procedure
Qualified candidates are invited to submit an application. Guidelines for Submitting an Application for Faculty Appointment are available at: **http://www.ntu.edu.sg/ohr/CareerOpportunities/SubmitanApplication/Pages/FacultyPositions.aspx**.
The post applied for should be clearly stated. Electronic submission of application is encouraged and can be forwarded to:

Chairman, Search Committee, School of Chemical and Biomedical Engineering
NANYANG TECHNOLOGICAL UNIVERSITY
E-mail: scbe_recruit@ntu.edu.sg

www.scbe.ntu.edu.sg

Massachusetts Institute of Technology

Come work with us!

Tenure Track Faculty

The Department of Brain & Cognitive Sciences (BCS) (http://bcs.mit.edu) and **The Picower Institute for Learning & Memory at MIT** (http://picower.mit.edu/) are looking to hire up to three (3) tenure-track faculty at the assistant professor level who work in one or more of the following three (3) areas:

i) *Computational* approaches to intelligence, cognition or neuroscience; an experimental component to the candidate's research would be viewed as a positive but is not necessary. An affiliation with Electrical Engineering and Computer Science, the Computer Science and Artificial Intelligence Laboratory (CSAIL), or other allied departments is possible.

ii) *Molecular & cellular:* The Picower Institute is searching for a candidate studying development, function or plasticity of neuronal circuits at the cellular, circuit, and/or systems levels using a multi-faceted approach combining different methodologies and levels of analysis. Candidates with strong cellular/molecular training who are studying development of brain circuits or using stem cell technologies are particularly encouraged to apply.

iii) *Human cognition and/or cognitive neuroscience* using behavioral methods, especially in the areas of language and/or cognitive development OR using fMRI/neuroscience methods.

Successful applicants are expected to develop and lead independent, internationally competitive research programs and to share in our commitment to excellence in undergraduate and graduate education by teaching courses and mentoring graduate and undergraduate research. PhD must be completed by start day of employment and some postdoctoral training is preferred.

Please submit application materials – cover letter, CV, statement of research and teaching interests and representative reprints – online at https://academicjobsonline.org/ajo/jobs/4202. Please state research area in cover letter. To help direct the application, applicants should indicate which of the three areas listed above is their main research area by answering the mandatory questions included in the application. In addition, please arrange to have three letters of recommendation submitted online. Review of applications will begin on November 1, 2014.

MIT is an affirmative action employer, and we encourage applications from women and underrepresented minorities.

http://web.mit.edu

UNIVERSITY OF Miami

Tenure-Track Assistant/Associate Professor

The **Department of Physics** at the **University of Miami** invites applications from highly qualified persons for a faculty position in **Experimental Condensed Matter Physics** focusing on **Energy/Materials**. This appointment will be made at the Assistant or Associate Professor rank to begin Fall 2015. Targeted research agendas include, but are not limited to, energy harvesting, storage, conversion, and optoelectronics. The successful candidate is expected to interact with physics and chemistry faculty. Candidates must have a Ph.D. in physics or related field, a demonstrated record of research achievements, and a strong commitment to teaching and mentoring students at the undergraduate and graduate levels. The physics department is located within the University's attractive Coral Gables campus in the greater Miami area, and has a wide-ranging research expertise and established Ph.D. program.

Application materials, including curriculum vitae with list of publications and statement of research plans, should be sent electronically (as a single PDF) to **energysearch@physics.miami.edu** or to **Energy Search Committee Chair, Department of Physics, University of Miami, Knight Physics Building, Coral Gables, FL 33124**. Applicants should arrange for three letters of recommendation to be sent to the same address. Review of applications will begin on **December 1, 2014** and continue until the position is filled.

The University of Miami is an Equal Opportunity Employer - Females/Minorities/Protected Veterans/Individuals with Disabilities are encouraged to apply. Applicants and employees are protected from discrimination based on certain categories protected by Federal law.

UNIVERSITY OF Miami

Tenure Track Assistant/Associate Professor

The **Department of Physics** at the **University of Miami** invites applications from highly qualified persons for a faculty position in **Experimental Biological Physics** at the Assistant or Associate Professor rank, starting fall 2015. The successful candidate will be expected to complement research activities within the Department involving dynamic processes at the organismal level and complexity science, and to exploit opportunities to collaborate with faculty in the University's Department of Biology and the Miller School of Medicine. Candidates must have a Ph.D. in physics or a related field, a demonstrated record of research achievements, and a strong commitment to teaching and mentoring students at the undergraduate and graduate levels. The Physics Department is located within the University's attractive Coral Gables campus in the greater Miami area, and has a wide-ranging research expertise and established Ph.D. program.

Application materials, including curriculum vitae with list of publications and statement of research plans, should be sent electronically (as a single PDF) to **biosearch@physics.miami.edu** or to **Biological Physics Search Committee Chair, Department of Physics, University of Miami, Knight Physics Building, Coral Gables, Fl. 33124**. Applicants should arrange for three letters of recommendation to be sent to the same address. Review of applications will begin on **December 1, 2014** and continue until the position is filled.

The University of Miami is an Equal Opportunity Employer — Females/Minorities/Protected Veterans/Individuals with Disabilities are encouraged to apply. Applicants and employees are protected from discrimination based on certain categories protected by Federal law.

NUI Galway

NATIONAL UNIVERSITY OF IRELAND GALWAY AND SCIENCE FOUNDATION IRELAND SEEK

GLOBAL RESEARCH LEADERS

IN THE FOLLOWING AREAS:

- Medical Devices
- Innovative Energy Technologies
- Satellite Remote Sensing
- Informatics

If you can make a significant contribution to research in the identified areas then NUI Galway would like to hear from you. To find out more go to nuigalway.ie/aboutus/jobs

SFI Science Foundation Ireland

UNIVERSITY of WASHINGTON

Faculty Position
Eukaryotic Cell Biology
Department of Biology

As part of a long-term strategy to enhance strengths in Cell Biology, the Department of Biology is searching to hire a full-time (9-month) Assistant Professor (Job class 0116) for a tenure-track faculty position in eukaryotic cell biology. We seek candidates who integrate perspectives from multiple disciplines, use quantitative approaches, and appreciate the breadth of research encompassed within the Department. We are especially interested in candidates using experimentally tractable plant, animal or protist systems to investigate fields including but not limited to cell homeostasis, signaling, polarity, proliferation, motility, membrane trafficking, interactions between cells and their environments, developmental cell biology, and evolutionary cell biology.

We are looking for individuals with a record of outstanding achievement or strong indications of outstanding future potential. Priority will be given to applications received by **3 November 2014** at: **http://www.biology.washington.edu/faculty/search/**. Applicants must have earned a doctorate by the date of appointment. All University of Washington faculty engage in teaching, research, and service.

The University of Washington is an Affirmative Action, Equal Opportunity Employer. All qualified applicants will receive consideration for employment without regard to, among other things, race, religion, color, national origin, sex, age, status as protected veterans, or status as qualified individuals with disabilities. The University is building a culturally diverse faculty and staff and strongly encourages applications from women, minorities, individuals with disabilities and covered veterans. The University is the 2006 recipient of the Alfred P. Sloan award for Faculty Career Flexibility, and is committed to supporting the work-life balance of its faculty. Our NSF-supported ADVANCE program http://advance.washington.edu/ is dedicated to increasing the participation of women in STEM disciplines.

Yale UNIVERSITY

Tenure-Track Faculty Positions
(Assistant/Associate/Full Professor)
Department of Genetics,
Yale University School of Medicine

The Department of Genetics at Yale University School of Medicine invites applications for junior or senior tenure-track faculty positions. The search is open to investigators from all areas of biological and biomedical research. We are particularly interested in applicants focused on Functional Genomics, Genome Informatics, Computational Biology or Systems Biology. Applications from investigators working on the interface of these areas and Developmental Biology and Genetics will also be strongly considered. The rank of the appointment will be commensurate with experience.

The Department of Genetics comprises an exceptional group of 22 primary basic science faculty with research interests including fundamental aspects of genetics, genomics and epigenetics, with investigation of model systems including flies, worms, fish and mouse, as well as humans.

Review of applications will begin immediately and will continue until the position is filled. Curriculum vitae, a concise statement of research plans (up to 3 pages), and three letters of recommendation should be sent electronically to: **genetics.admin@yale.edu** to the attention of **Richard Lifton, Chair, Department of Genetics**.

Yale University is an Affirmative Action/Equal Opportunity Employer and welcomes applications from women, persons with disabilities, protected veterans, and members of minority groups.

California State Polytechnic University, Pomona
Biological Sciences Department

TENURE-TRACK FACULTY POSITION
VIROLOGIST

The Biological Sciences Department at California State Polytechnic University, Pomona (Cal Poly Pomona) invites applications for a tenure-track, ASSISTANT PROFESSOR, position in Virology, beginning September 2015. Candidates using various approaches to study viruses are encouraged to apply. A Ph.D. in microbiology or a related field is required. Post-doctoral experience and previous teaching experience are preferred. The successful candidate will have the potential for excellence in undergraduate teaching, and for developing an externally-funded research program that will involve undergraduate and Master's students. Teaching responsibilities will include virology, general microbiology, cell biology, and specialty courses in the candidate's area of expertise, and may involve participation in introductory biology and other courses in microbiology. Cal Poly Pomona is a comprehensive Master's university with a diverse student body. The successful candidate will have demonstrated an ability to be responsive to the educational equity goals of the university and its increasing ethnic diversity and international character. Applicants should forward: (1) a cover letter (maximum 2 pages) that briefly describes the candidate's training, experience, and teaching and research interests; (2) *curriculum vitae*; (3) statement of teaching philosophy (maximum 2 pages); (4) proposed plan of research (maximum 3 pages); (5) maximum of three representative publication reprints; and (6) the names and contact information of three (minimum) to five (preferred) references to: **Chair, Virologist Search Committee, Biological Sciences Department, California State Polytechnic University, 3801 West Temple Avenue, Pomona, CA 91768**. Electronic submission of application materials as a single PDF file is preferred (**microbiol_search@csupomona.edu**). Review of applications begins on **January 12, 2015**. Official transcripts and three letters of reference will be required of all finalists. For further information, visit the Department web site at: **http://www.csupomona.edu/~biology**.

California State Polytechnic University, Pomona is an Equal Opportunity, Affirmative Action Employer.

Memorial Sloan-Kettering Cancer Center

The Sarcoma Medical Oncology Service in the Department of Medicine of Memorial Sloan Kettering Cancer Center is seeking an outstanding **scientist/physician-scientist** with expertise in drug development/discovery and translational research. The successful candidate will be have a research program directed at translational sarcoma research and lead the Jennifer Linn Laboratory of New Drug Development in Sarcoma and Rare Cancers that will interface with the Hospital's sarcoma disease management team. Applicants should have a significant record of research accomplishment, and a proven ability to collaborate with translational physicians on clinically relevant projects. Candidates may have scientific background in any relevant translational field including stem cell biology, epigenetics, metabolomics, cell signaling, etc. Research applicable to sarcoma is desirable but not necessary, but work in the Linn Laboratory will be directed to Sarcoma and rare unidentified cancers.

Interested applicants should forward a cover letter, curriculum vitae, statement of research interests, and list of references to **David Spriggs, M.D, Head of the Solid Tumor Oncology Division, Memorial Sloan Kettering Cancer Center, 300 E 66th Street, 13th Floor, New York, NY 10065**, faxes will be accepted at **646-888-4270** and emails should be sent to **rodrigc4@mskcc.org**.

Memorial Sloan Kettering Cancer Center is an Equal Opportunity Employer with a strong commitment to enhancing the diversity of its faculty and staff. Women and applicants from diverse racial, ethnic and cultural backgrounds are encouraged to apply.

BOSTON UNIVERSITY

Tenure-Track Faculty Position in Human Systems Neuroscience

Tenure-track faculty search, Assistant Professor in Systems Neuroscience, Data Science, Dept. Health Sciences, Boston Univ. Start date: Fall 2015. Candidates who study normal or abnormal brain function using brain imaging (fMRI, MEG/EEG), and/or genetic approaches are especially encouraged to apply. The department includes undergraduate program in human physiology and graduate programs in physiology and neurobiology (MS and PhD). Faculty members have research programs in neurobiology, muscle biology and cytoskeletal signaling. Opportunities for collaborations also exist in other research programs on the Charles River and Medical School campuses, and through interdisciplinary university-wide programs in bioinformatics, computational science, and neuroscience. Applicants should have an earned doctorate in neuroscience, physiology, cell biology, or related field, including post-doctoral training and a strong scholarly record with research funding, or potential for funding from extramural sources, and commitment to departmental undergraduate and graduate programs.

Application deadline is **December 1, 2014**. Applicants should submit a letter of application, curriculum vitae, statement of research plans and names of three individuals who can provide letters of reference to: **Danka Charland, Assistant to the Search Committee, Department of Health Sciences, SAR, Boston University, 635 Commonwealth Avenue, Boston, MA 02215**; E-mail: **charland@bu.edu**.

For more information about BU Sargent College and our programs, visit our website at **bu.edu/sargent**.

We are an Equal Opportunity Employer and all qualified applicants will receive consideration for employment without regard to race, color, religion, sex, national origin, disability status, protected veteran status, or any other characteristic protected by law. We are a VEVRAA Federal Contractor.

UCDAVIS

Associate/Full Professor of Freshwater Fish Ecology

Peter B. Moyle and California Trout Endowed Chair in Coldwater Fishes

Department of Wildlife, Fish, and Conservation Biology

We are recruiting a 9-month (academic year) tenured Freshwater Fish Ecologist at the associate or full professor rank. The appointee will hold the Peter B. Moyle and California Trout Endowed Chair in Coldwater Fishes. The Chair holder needs to be an enthusiastic, experienced and visionary scientist, able to work effectively with diverse interest groups and provide the science leadership to ensure the long-term viability of California's coldwater aquatic ecosystems and their fish fauna. Candidates must have the ability to develop a vigorous, extramurally-funded research and outreach program that addresses questions relevant to the biology and conservation of coldwater fishes in California, and to teach courses in biology and conservation of fishes and other topics. Qualifications include Ph.D. in relevant discipline, and evidence of accomplishment in research, outreach, teaching, and service.

Application materials must be submitted via the following website: **https://recruit.ucdavis.edu/apply**. Inquiries: **Professor Dirk H. Van Vuren, Committee Chair, (530) 752-4181, email: dhvanvuren@ucdavis**.edu. The position will remain open until filled but to ensure consideration, applications should be received by **November 21, 2014**.

UC Davis is an affirmative action/equal employment opportunity employer and is dedicated to recruiting a diverse faculty community. We welcome all qualified applicants to apply, including women, minorities, veterans, and individuals with disabilities.

Direct link to position application:
https://recruit.ucdavis.edu/apply/JPF00404

Brown University Tenured Position in Neuroscience

Brown University's interdisciplinary Institute for Brain Science and the Department of Neuroscience invite applications for a tenured faculty position at the level of Associate Professor or Professor. The successful applicant will use advanced molecular or genetic approaches to address fundamental mechanisms underlying brain development, function, or disorders. Any experimental system will be considered, but a successful candidate will address questions critical to understanding human brain function. We seek an established scientist with an M.D. and/or Ph.D. degree who has an international reputation, a well supported, highly successful independent research program, and an established record of scholarly contribution. A collaborative approach is essential. The incumbent is expected to participate in the educational mission of Brown University. We strongly encourage applications from women and minorities. Further information about the Department, the Graduate Program, and the Brown Institute of Brain Science is available at **http://neuroscience.brown.edu** and **http://www.brainscience.brown.edu**.

The search committee will give full consideration to applications received by **December 1, 2014**. Applicants should submit their curriculum vitae, teaching statement and a two-page description of their research plans and scientific vision to: **apply.interfolio.com/27040**.

Brown University is an Affirmative Action/Equal Opportunity Employer.

Faculty Positions in Biochemistry and Molecular Genetics

Northwestern University Feinberg School of Medicine has committed substantial resources toward expanding interdisciplinary research in Biochemistry and Molecular Genetics. A new Department of Biochemistry and Molecular Genetics has been established and will be led by Dr. Ali Shilatifard, an internationally recognized leader in chromatin biology, gene expression, epigenetics, and cancer biology. We are now seeking candidates to fill several new full-time faculty positions at the Assistant, Associate, and Full Professor ranks. Northwestern University offers superb start-up packages with collegial and collaborative scientific environment that is rich with core facilities, robust cross-disciplinary graduate training programs, and diverse expertise.

Candidates should have a Ph.D., M.D./Ph.D. or M.D. degree, significant research experience, and evidence of sustainable extramural funding. Salary is commensurate with experience. Northwestern University is an Equal Opportunity, Affirmative Action Employer of all protected classes, including veterans and individuals with disabilities. Women and minorities are encouraged to apply. Hiring is contingent upon eligibility to work in the United States. Start date will be within the 2014-2015 academic year. Applications will be accepted until the positions are filled. Please submit by email (as a single PDF) a cover letter, curriculum vitae, summary of research experience, and future plans along with names and contact information for three references to:

Biochemistry and Molecular Genetics
Feinberg School of Medicine
Northwestern University
Chicago, IL 60611
BMG-search@Northwestern.edu

NORTHWESTERN UNIVERSITY FEINBERG SCHOOL OF MEDICINE

ASSISTANT PROFESSOR Sustainable Vegetable Production and Nutrition Systems

The Department of Horticulture (**http://www.hrt.msu.edu**) in the College of Agriculture and Natural Resources at Michigan State University (MSU) invites applications for an Assistant Professor, twelve-month tenure-track position (50% research, 50% extension) to conduct research and extension/outreach programs that promote production of vegetables while maintaining or enhancing environmental quality in Michigan and beyond. The incumbent will develop a nationally and internationally recognized program in vegetable crop nutrition and soil fertility management that builds collaboratively on MSU's strengths in vegetable production and sustainable cropping systems. Research should utilize both basic science and applied approaches while addressing the issues and opportunities facing the Michigan and Midwest vegetable industry. Other potential areas of research focus include development of integrative systems to optimize plant nutrition and soil health; efficient nutrient and water delivery systems tailored to precision agriculture, drip irrigation, microclimate modification or extended season cropping systems; rhizosphere dynamics; or interactions between cropping systems and food quality/human nutrition.

The successful candidate will establish innovative research and outreach programs, secure competitive/extramural funding, publish in high quality refereed journals, advise and mentor students, provide leadership in state-wide vegetable extension programming (including development of educational materials and other outreach tools), establish strong ties with industry leaders and grower groups; and contribute to the on-going programs of MSU's Vegetable Extension Team. The salary is competitive and commensurate with the candidate's experience. A health, dental and retirement benefits program is included.

Qualifications:

Required:
- Ph.D. in horticulture, plant science, plant physiology, soil science or a related field
- Demonstrated capacity to conduct independent research
- Ability to work collaboratively with research and Extension teams
- Excellent oral and written communication skills

Desired:
- Postdoctoral experience in plant nutrition, physiology and vegetable production
- Teaching, Extension, and team management experience
- Three or more years of vegetable production and research experience Plant Sciences at MSU

MSU is a global leader in basic and applied plant sciences, with over 150 faculty members engaged in research on nearly all aspects of crop production and plant science. MSU offers state-of-the-art field, greenhouse, growth chamber, and laboratory facilities to support diverse research and outreach interests.

Application Procedure:
Qualified applicants should submit a letter of application, a summary of research accomplishments and future research objectives, and a description of Extension/outreach interests and philosophy, a current CV, and contact information for at least three references online at **https://jobs.msu.edu**. Select Faculty/Academic Staff and apply to posting **0099** before February 28, 2015. Review of applications will begin March 1, 2015 and will continue until the position is filled.

Questions can be directed to **Dr. Eric Hanson**, Search Committee Chair (**hansone@msu.edu**). Questions on submitting applications through **https://jobs.msu.edu** can be directed to **hrt@msu.edu**.

MICHIGAN STATE UNIVERSITY

MSU is committed to achieving excellence through cultural diversity. The University actively encourages applications and/or nominations of women, persons of color, veterans and persons with disabilities.

MSU is an Affirmative Action, Equal Opportunity Employer.

Yale

Faculty Position at Yale University
Department of Molecular, Cellular and Developmental Biology

The Department of Molecular, Cellular and Developmental Biology at Yale University invites applications for a faculty appointment as an assistant professor from individuals investigating important questions in biology at the cellular or molecular level. The Department encourages applications from candidates using any experimental system, from microbes to multicellular organisms. The broad research interests of the faculty include molecular biology and chemical biology, cellular and developmental biology, computational biology, microbiology, genetics, neurobiology, plant sciences, and biotechnology. We expect the successful candidate will establish an active research group, be an interactive member of the faculty, participate in interdisciplinary research and training, and engage in regular graduate and undergraduate teaching. Teaching skills are essential.

Review of applications will begin **October 1, 2014** and will continue until the position is filled. Submit cover letter, a curriculum vitae and a description of research interests on line to **https://academicjobsonline.org/ajo/Yale**. Request at least three individuals submit letters of recommendation on your behalf to **https://academicjobsonline.org/ajo/Yale**. For questions, please e-mail **mcdb.search@yale.edu**.

Yale University is an Affirmative Action/Equal Opportunity Employer. Yale values diversity among its students, staff, and faculty and strongly welcomes applications from women, persons with disabilities, protected veterans, and underrepresented minorities.

IOWA STATE UNIVERSITY

Assistant Professor in Department of Genetics, Development and Cell Biology

As part of a major interdisciplinary hiring initiative (las.iastate.edu/faculty-careers) in the College of Liberal Arts and Sciences (http://www.las.iastate.edu) at Iowa State University (ISU), a new joint initiative by the Department of Genetics, Development and Cell Biology (http://www.gdcb.iastate.edu) and the Department of Physics and Astronomy (http://www.physastro.iastate.edu) aims to chart a Quantitative Roadmap of the Living Cell. Multiple new hires in the field of Physical Biology are planned for the next 2-3 years and should expect to benefit from and contribute to the interaction and collaboration among these and other departments.

The Department of Genetics, Development and Cell Biology seeks creative individuals for a tenure-track faculty position at the Assistant Professor level with an appointment expected to begin in Fall 2015. This position will establish extramurally funded programs of research that interrogate fundamental cellular or developmental processes, using imaging strategies at the interface of physics and biology in animals, plants or microbes. The selected candidate will teach undergraduate biology or genetics courses and graduate courses in their area(s) of expertise. This position will have a primary appointment in the Department of Genetics, Development and Cell Biology, with the option of having a secondary appointment in the Department of Physics and Astronomy.

Qualified applicants must have a Ph.D. or equivalent in a scientific field and demonstrated potential for superior achievement in research. Please visit **www.iastatejobs.com/postings/search** and search for posting number **400036** to view the entire vacancy and apply electronically. For full consideration, applications must be received by **November 14, 2014**.

Iowa State University is an EO/AA Employer. All qualified applicants will receive consideration for employment without regard to race, color, religion, sex, national origin, disability, or protected Vets status.

CLINICAL ASSISTANT PROFESSOR
Department of Biology
Arts and Science

New York University invites applications for a Clinical Assistant Professor appointment in the Department of Biology to start January 1, 2015 pending budgetary and administrative approval. Responsibilities include developing and teaching courses related to anatomy and physiology at the undergraduate and graduate levels. Teaching duties will include six course equivalents per year annually. Applicants should be able to teach fundamental courses in anatomy, physiology and endocrinology, as well as more specialized courses that emphasize the molecular pathways that control physiological responses. Candidates are expected to have proven teaching ability and recent research experience in a relevant biomedical field. The Department of Biology (http://biology.as.nyu.edu) offers an outstanding and collegial environment.

Candidates should submit applications, including a CV and three letters of references, through the NYU Department of Biology website (**http://biology.as.nyu.edu**), via the "Faculty Recruitment" link. You may use the following address in the cover letter: **Chair of the Anatomy and Physiology Search Committee, Department of Biology, New York University, 1009 Silver Center, 100 Washington Square East, New York, NY 10003**. Closing date: **October 31, 2014.**

NEW YORK UNIVERSITY

EOE/Minorities/Females/Vet/Disabled

2014/2015 SCU Bioengineering Faculty Search Announcement
Tenure-track Faculty Positions Available
Department of Bioengineering
School of Engineering
Santa Clara University

The newly established Department of Bioengineering in the School of Engineering at Santa Clara University is enjoying a rapid expansion in its education and research endeavors (http://www.scu.edu/engineering/bioengineering/). The department has an undergraduate and graduate student body of over 200 students. We are now searching for two new tenure-track faculty members at the rank of assistant professor to join the department beginning academic year of 2015-16.

Candidates in all areas of bioengineering are welcome to apply, although we are particularly interested in receiving applications from qualified candidates with research and teaching interest and expertise in the broad areas of Bio-instrumentation/Bio-device engineering, Biomechanics, and Cellular and Molecular Engineering.

All applicants must have a strong commitment and ability to teach at the undergraduate and graduate levels as well as excellent communication skills. The successful hires are expected to develop independent, externally supported research programs, and to maintain a strong publication record. Successful hires will also advise students, mentor projects, and provide service to the Department, the School and the University. An earned doctorate in bioengineering or a closely related field is required.

All applicants are required to apply through the Santa Clara University website at **www.scu.edu/jobs**. Review of applications will start immediately and will continue until the positions are filled. The proposed starting date is September 1, 2015.

Santa Clara University is an Equal Opportunity/Affirmative Action Employer, committed to excellence through diversity and inclusion, and, in this sprit, particularly welcomes applications from women, persons of color, and members of historically underrepresented groups. All qualified applicants will receive consideration for employment without regard to race, religion, color, national origin, sex, sexual orientation, gender identity or expression, age, status as a protected veteran, status as a qualified individual with a disability, or other protected category in accordance with applicable law.

UCONN HEALTH

Senior Faculty Position Modeling and Analysis of Cellular Systems

The Berlin Center for Cell Analysis and Modeling (**http://www.ccam.uchc.edu/**) (CCAM) at the University of Connecticut Health Center (UCHC) is a multi-disciplinary research center with 15 faculty members focused on development of new photonic, microscopic and computational approaches for the study of cellular systems. CCAM is the home of the Virtual Cell Project (**http://vcell.org**). We occupy a new award winning research building close to the main campus. UCHC is poised to undergo unprecedented growth through the State "Bioscience Connecticut" initiative and through the establishment of the Jackson Laboratory for Genomic Medicine on our campus. We have an opening at the Associate or Full professor level for an established funded investigator whose research program elucidates processes that control cell function. A research program that integrates computational modeling with experiments at multiple scales would be especially appropriate. The successful candidate will be expected to assume a leadership role in the continued growth of CCAM. Opportunities will also be available to participate in the CCAM graduate program. Applications will be accepted until the position is filled. Applicants should submit a letter of application, curriculum vitae, research plan and statement of teaching interests, and names (with address and e-mail address) of at least three references via the University of Connecticut Health Center Employment Services website, **https://jobs.uchc.edu**, search number 2012-1038. Questions regarding this search should be addressed to Leslie Loew at **les@volt.uchc.edu**

Affirmative Action/Equal Opportunity Employer (M/F/M/PwD/PV)

The Noble Foundation launches FORAGE365

The Samuel Roberts Noble Foundation has launched the **FORAGE365** research initiative to develop sustainable, low-input forage systems that will enable ranchers to graze cattle year-round and use less or no hay. This will revolutionize agriculture in the Southern Great Plains, providing significant benefits to ranchers and the environment.

As part of **FORAGE365**, Noble Foundation scientists have developed nine integrated research projects that focus on four pillar forages (alfalfa, bermudagrass, tall fescue, and winter wheat) and relevant model plant species. These projects aim to increase plant nutrient (nitrogen and phosphorus) and water use efficiencies, improve drought tolerance, understand and alter plant root development, harness beneficial plant-microbe interactions, develop informatics tools and databases for genome-assisted plant breeding, and develop superior grazing systems using our target forage species.

To accomplish **FORAGE365** objectives, the Noble Foundation will expand its research staff, adding six postdoctoral fellows, a toolbox developer/curator, a senior research associate, two bioinformatics analysts and five research associates/assistant positions. Each position will have a multi-disciplinary training and research opportunity at one of the country's most renowned centers for agriculture and plant science. We seek candidates with research experience in the areas of plant genetics, genomics, breeding, cell and molecular biology, biochemistry, physiology, microbiology, bioinformatics, or agronomy.

To learn more about **FORAGE365** and the associated job opportunities, please visit www.noble.org or call Human Resources at 580.224.6230. The Noble Foundation is an equal opportunity employer.

THE SAMUEL ROBERTS NOBLE FOUNDATION

Assistant Professors of Biology

Adelphi University invites applications for two tenure-track positions in biology to begin fall 2015. One position is for a molecular biologist, with teaching responsibilities to include biochemistry, molecular biology, and introductory biology. The other position is for an organismal biologist with expertise in anatomy and physiology, with teaching responsibilities to include human anatomy and physiology, animal behavior, and histology. Ph.D required; postdoctoral experience strongly preferred. The successful applicants will have excellent potential as a teacher, a significant record of research accomplishment, and have or be able to develop a fundable independent research program involving undergraduates and master's students.

For more information about the department, visit http://academics.adelphi.edu/artsci/bio/. We encourage applications from members of underrepresented groups. Adelphi is a private university with the spirit of a liberal arts college, committed to combining teaching and scholarship, and located in suburban Long Island within easy reach of New York City. More detailed descriptions of the positions and applications are available through **www.adelphi.edu/positions/faculty/**

Deadline for applications: **November 15, 2014**.

TEXAS STATE UNIVERSITY
The rising STAR of Texas

Texas State University is a member of the Texas State University System.

Assistant Professor
Aquatic Toxicology/Aquatic Hazard Assessment

The Department of Biology at Texas State University (www.bio.txstate.edu) invites applications for a tenure-track Assistant Professor in Aquatic Toxicology/Aquatic Hazard Assessment. The successful candidate will be expected to teach both graduate and undergraduate courses in the Department of Biology and develop an externally funded research program involving graduate students that complements the existing strengths of our 34-member faculty. Required qualifications are a Ph.D. in the life sciences, environmental toxicology or a related field, postdoctoral experience, and a record of published research accomplishments in aquatic toxicology and/or aquatic hazard assessment. Preferred qualifications are a record of externally funded research, a record of interdisciplinary collaboration, and a research area that complements research interests within the Department. Salary and start-up package are negotiable.

Review of applications will begin **December 15, 2014**. A letter of application including a statement of research plans and teaching philosophy, CV, copies of five representative publications, and the names and contact information of five people willing to serve as references should be sent, as a single PDF, to **Toxicology@txstate.edu**. Questions about this position should be addressed to **Dr. Joe Tomasso**, **jt33@txstate.edu**. To ensure full consideration all materials must be received by December 15, 2014.

Texas State University is an Affirmative Action/Equal Opportunity Employer.

Science | Careers

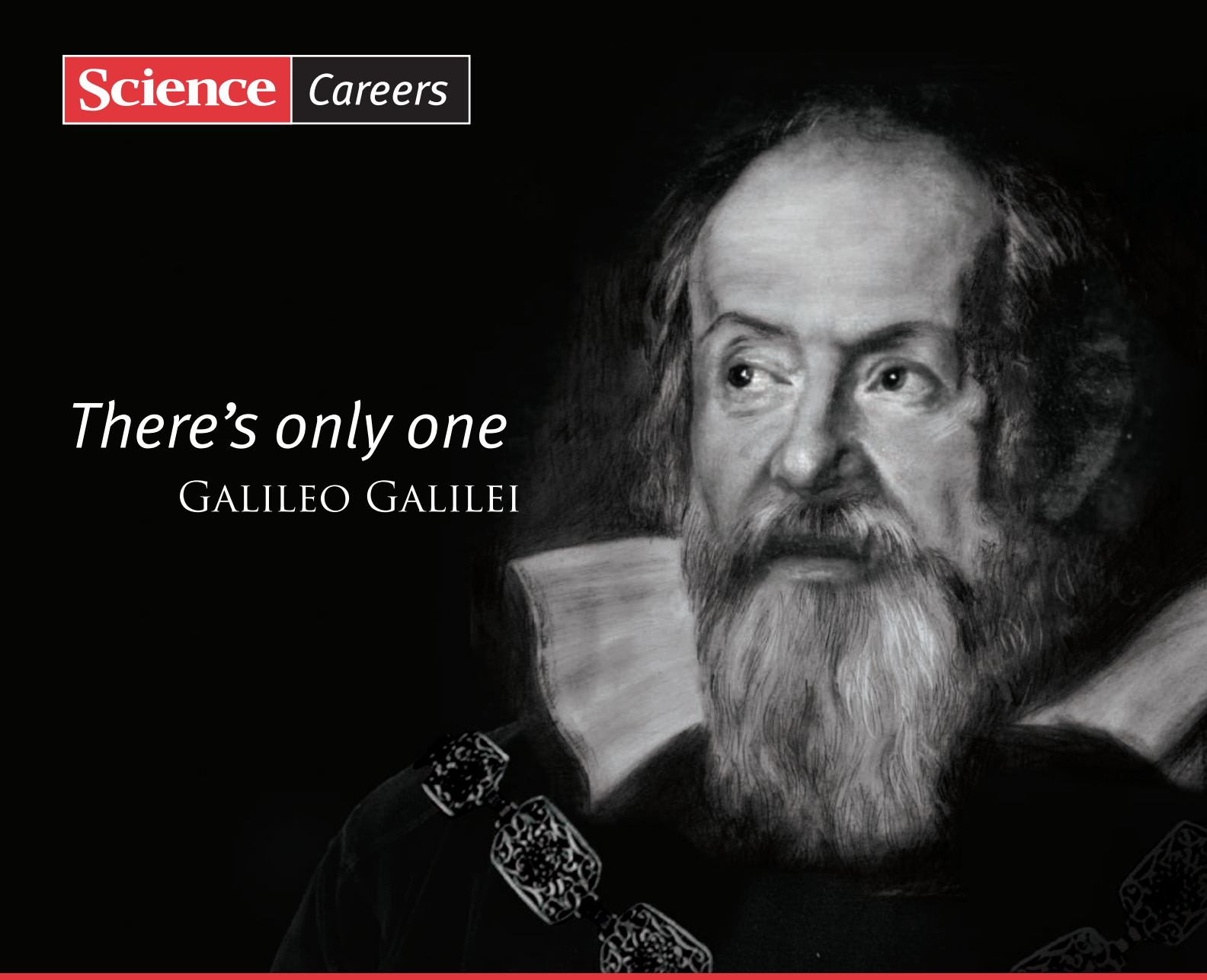

There's only one
GALILEO GALILEI

Born in 1564, Galileo Galilei once contemplated a career in the priesthood. It's perhaps fortunate for science that upon the urging of his father, he instead decided to enroll at the University of Pisa. His career in science began with medicine and from there he subsequently went on to become a philosopher, physicist, mathematician, and astronomer, for which he is perhaps best known. His astronomical observations and subsequent improvements to telescopes built his reputation as a leading scientist of his time, but also led him to probe subject matter counter to prevailing dogma. His expressed views on the Earth's movement around the sun caused him to be declared suspect of heresy, which for some time led to a ban on the reprinting of his works.

Galileo's career changed science for all of us and he was without doubt a leading light in the scientific revolution, which is perhaps why Albert Einstein called him the father of modern science.

Want to challenge the status quo and make the Earth move? At *Science* we are here to help you in your own scientific career with expert career advice, forums, job postings, and more — all for free. For your career in science, there's only one *Science*. Visit **ScienceCareers.org** today.

For your career in science, there's only one Science

AAAS

ScienceCareers.org

Career advice | Job postings | Job Alerts | Career Forum | Crafting resumes/CVs | Preparing for interviews

Dartmouth seeks to hire several new science faculty who are dedicated to leading-edge research and both graduate and undergraduate teaching. This year Dartmouth has active searches in **Applied or Computational Mathematics, Computer Science, Computational Molecular & Cell Biology, Ecology, Geobiology, Materials Chemistry, Psychological and Brain Sciences**, and a chaired position in **Computational Science**. For information on these and all other faculty searches underway, visit **dartgo.org/facjobs**. Dartmouth scientists are also actively seeking ambitious postdoctoral scholars and motivated graduate students to join our research programs.

To create an atmosphere supportive of research, Dartmouth offers new faculty members grants for research-related expenses, a quarter of sabbatical leave for each three academic years in residence, and flexible scheduling of teaching responsibilities. Dartmouth College, a member of the Ivy League, is located in Hanover, New Hampshire. Dartmouth's beautiful, historic campus is located in a scenic area with ample recreational and cultural activities. With an even distribution of male and female students and over one third of the undergraduate student population members of minority groups, Dartmouth is deeply committed to diversity among its student body and its faculty.

Dartmouth is an Equal Opportunity/ Affirmative Action Employer with a strong commitment to diversity. In that spirit, we are particularly interested in receiving applications from a broad spectrum of people, including women, persons of color, persons with disabilities, veterans or any other legally protected group.

NEW YORK UNIVERSITY

FACULTY POSITION

Center for Genomics & Systems Biology
Department of Biology

Arts and Science

CENTER FOR GENOMICS AND SYSTEMS BIOLOGY NEW YORK UNIVERSITY

New York University's Center for Genomics & Systems Biology (**http://cgsb.as.nyu.edu**) in the Department of Biology invites applicants to apply for one open rank faculty position to begin September 1, 2015, or as negotiated pending budgetary and administrative approval. We are interested in applicants who examine how the components of complex biological systems interact. Examples include but are not limited to 1) live imaging approaches that reveal how gene interactions influence cellular, tissue or organismal phenotype, 2) microbial community analysis that takes advantage of high-throughput sequencing, 3) evolutionary questions that use genome-wide information, and 4) computational or mathematical approaches that address biological theory or network inference.

Candidates will be expected to establish an active, externally funded research program and contribute a moderate teaching component in their area of expertise. The Department of Biology (**http://biology.as.nyu.edu**) offers an outstanding, collegial and interdisciplinary research environment that supports ambitious research programs. The department has strong ties to the Courant Institute of Mathematical Sciences and ample resources in robotics, high-throughput sequencing, and high-performance computing.

Application packages should include a cover letter, research statement, teaching statement, curriculum vitae, and three letters of reference. Please apply online via the New York University Department of Biology website (**http://biology.as.nyu.edu**), using the "*Employment*" link. The cover letter should be addressed to: **Chair of the CGSB Search Committee, Department of Biology, New York University, 1009 Silver Center, 100 Washington Square East, New York, NY 10003.** Selection will begin **November 24, 2014**; applications received prior to this date will be guaranteed full evaluation.

EOE/Minorities/Females/Vet/Disabled

AAAS is here –
helping scientists achieve career sucess.

Every month, over 400,000 students and scientists visit ScienceCareers.org in search of the information, advice, and opportunities they need to take the next step in their careers.

A complete career resource, free to the public, *Science* Careers offers hundreds of career development articles, webinars and downloadable booklets filled with practical advice, a community forum providing answers to career questions, and thousands of job listings in academia, government, and industry. As a AAAS member, your dues help AAAS make this service available to the scientific community. If you're not a member, join us. Together we can make a difference.

To learn more, visit
aaas.org/plusyou/sciencecareers

AAAS + U = Δ

NEW YORK UNIVERSITY

CLINICAL ASSISTANT PROFESSOR

Department of Biology and the Center for Genomics and Systems Biology

Arts and Science

CENTER FOR GENOMICS AND SYSTEMS BIOLOGY NEW YORK UNIVERSITY

New York University invites applications for a Clinical Assistant Professor appointment in the Department of Biology to start September 1, 2015 pending budgetary and administrative approval. Responsibilities include developing and teaching courses related to Statistics, Bio-informatics, Genomics, and Systems Biology to support our growing emphasis on training computational biologists. Teaching duties will include six course equivalents per year; candidates should be able to teach fundamental courses in Statistics, Genomics, Systems Biology, and Large Dataset Analysis at the undergraduate and graduate levels. Candidates should have a PhD in Bioinformatics, Computational Biology, or Biology with a concentration in computer studies, and be fluent in programming languages such as R and Perl or Python. Teaching experience is preferred. The Department of Biology (**http://biology.as.nyu.edu**) and NYU's Center for Genomics and Systems Biology (**http://cgsb.as.nyu.edu/page/home**) offer outstanding and collegial environments.

Candidates should submit applications, including a CV and three letters of references, through the NYU Department of Biology website (**http://biology.as.nyu.edu**), via the "Faculty Recruitment" link. You may use the following address in the cover letter: **Chair of the Bio-informatics and Statistics Search Committee, Department of Biology, New York University, 1009 Silver Center, 100 Washington Square East, New York, NY 10003.** *Closing date:* ***November 30, 2014****.*

EOE/Minorities/Females/Vet/Disabled

POSITIONS OPEN

FACULTY POSITION
Johns Hopkins University
School of Medicine
Institute for Cell Engineering

The Institute for Cell Engineering invites applications from outstanding individuals with creative, rigorous, and integrative research approaches to enhance its cell engineering investigational strengths in immunology, stem cell biology, neurosciences, and vascular biology. For additional information about the institute, visit **website: http://www.hopkinsmedicine.org/institute_cell_engineering/**. Candidates should have an M.D. and/or a Ph.D. degree with appropriate postdoctoral experience and an outstanding publication record. Primary department affiliation will be determined by the applicant's qualifications and by relevance of the applicant's research program to departmental initiatives. The successful candidate will have experience in any aspect of stem cell biology or related field. Special attention will be give to investigators in the areas of vascular biology or organogenesis.

To apply, submit curriculum vitae, three letters of reference, copies of relevant publications and a concise description of research interests and research plans (up to three pages) to **e-mail: icesearch@jhmi.edu** to the attention of **Ted M. Dawson**, Director, Institute for Cell Engineering. Applications will be assessed on an ongoing basis and the deadline for submission is December 15, 2014. The appointment is expected to be made in 2015.

The John Hopkins University School of Medicine is an Affirmative Action/Equal Opportunity Employer that embraces diversity.

TENURE-TRACK IMMUNOLOGIST
Assistant Professor Position in Immunology

The Department of Pathology, Microbiology, and Immunology at the University of South Carolina's School of Medicine invites applications for a tenure-track Assistant Professor position in Immunology. The successful candidate is expected to develop a strong extramurally funded research program, and must participate in the teaching mission of the department. Outstanding applicants working in an area complementing our existing faculty research interest (**website: http://pmi.med.sc.edu/**) will be considered. The departmental strengths include the NIH-funded Center for Complementary and Alternative Medicine, and the COBRE on Dietary Supplements and Inflammation. Candidates must have a Ph.D. or equivalent, and at least three years of postdoctoral research experience. Preference will be given to a candidate who has shown evidence of independence with currently active grant funding. Competitive salary and startup funds are available. Please submit curriculum vitae, teaching philosophy, and statement of research plans to: **Dr. Mitzi Nagarkatti, Chair, Department of Pathology, Microbiology, and Immunology, University of South Carolina School of Medicine, Columbia, SC 29208** or **e-mail: pmi.immunology@uscmed.sc.edu.** Kindly arrange to submit three letters of recommendation upon request. The search will start immediately and will continue until the position is filled. *USC Columbia is an Equal Opportunity/Affirmative Action Employer, encourages applications from women and minorities, and is responsive to the needs of dual career couples.*

Stop searching for a job; start your career.

Science Careers
From the journal *Science* AAAS

ScienceCareers.org

POSITIONS OPEN

FACULTY POSITIONS IN IMMUNOLOGY
Boston University School of Medicine

The Department of Microbiology (**website: http://www.bumc.bu.edu/microbiology**) seeks investigators with exceptional records of research achievement and scientific innovation for faculty positions. The successful applicants will join a vibrant and growing community of researchers in an environment that includes the new Center for Immunobiology (**website: http://www.bumc.bu.edu/immunobiology/**), strong translational medicine programs and the state-of-the-art National Emerging Infectious Diseases Laboratories (**website: http://www.bu.edu/neidl**). Applications in all areas of immunology will be considered, but investigators with expertise in the immunology of infectious diseases or adaptive immunity are especially encouraged to apply. Candidates appropriate for any faculty level position will be considered.

To be considered, please submit curriculum vitae, a summary of research accomplishments, a description of future research plans, and the names of at least three references to **Ms. Kathleen Marinelli** (**e-mail: kfurness@bu.edu**). Applications will be considered as they are received, with the positions to be filled after January 1, 2015.

Boston University School of Medicine is an Equal Opportunity/Affirmative Action Employer.

Your career is our cause.

Get help from the experts.

ScienceCareers.org

- Job Postings
- Job Alerts
- Resume/CV Database
- Career Advice
- Career Forum

Science Careers
From the journal *Science* AAAS

☑ More scientists agree—we are the most useful website.

ScienceCareers.org

Nontraditional Careers: Opportunities Away From the Bench

Webinar

Want to learn more about exciting and rewarding careers outside of academic/industrial research? View a roundtable discussion that looks at the various career options open to scientists and strategies you can use to pursue a nonresearch career.

Now Available On Demand
www.sciencecareers.org/webinar

Produced by the *Science*/AAAS Business Office.

Science Careers
From the journal *Science* AAAS

For your career in science, there's only one Science

A career plan customized *for* you, *by* you.

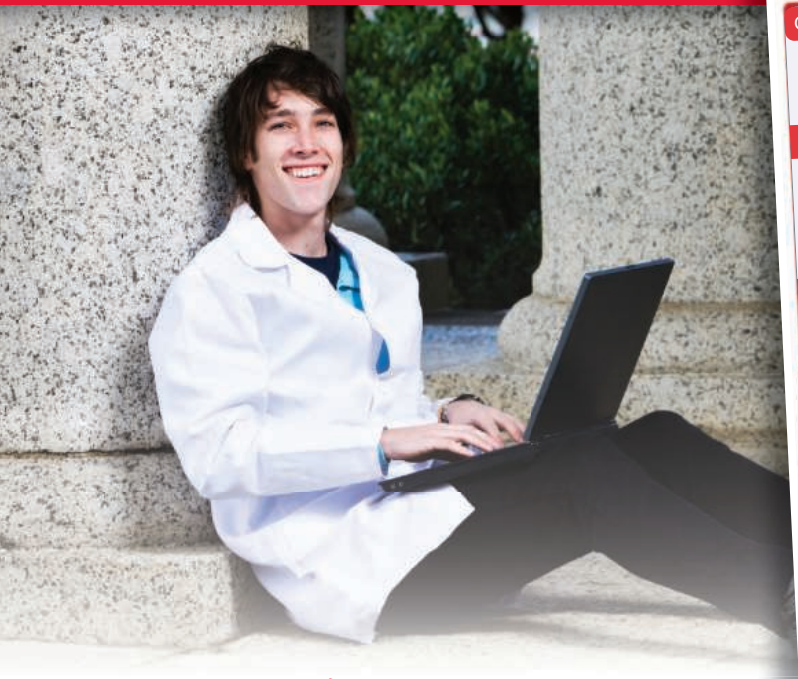

myIDP.sciencecareers.org

Recommended by leading professional societies and endorsed by the National Institutes of Health, an individual development plan will help you prepare for a successful and satisfying scientific career.

my IDP Science Careers

In collaboration with FASEB, UCSF, and the Medical College of Wisconsin and with support from the Burroughs Wellcome Fund, AAAS and *Science* Careers present the first and only online app that helps scientists prepare their very own individual development plan.

Visit the website and start planning today!
myIDP.sciencecareers.org

In partnership with:

advancing the life sciences 1912-2012 FASEB Federation of American Societies for Experimental Biology

UCSF University of California San Francisco

Medical College of Wisconsin

Burroughs Wellcome Fund

By **Sharon Ann Holgate**

Life inspires applications

At first, the abstract beauty of molecules was what drew David Smith to research. During his school days near Manchester, in the United Kingdom, Smith developed a love for physics. But that was before two chemistry teachers and Linus Pauling's book, *The Nature of the Chemical Bond*, inspired him to read chemistry. For his Ph.D. at the University of Oxford, Smith synthesized molecules that could recognize both positively and negatively charged ions in water and studied how they interact. Applications to chemical sensors were easy enough to envision, but he was focused on the fundamental science. He did a postdoc at ETH Zurich and then, in 1999, won a lectureship at the University of York in the United Kingdom.

In York, inspired by the "beauty and symmetry" of the dendritic organic molecules he had worked on for his postdoc, Smith and his lab members worked to create similar molecules. They soon discovered two molecules that readily self-assembled into gel materials. By 2005, Smith's lab—which by then employed eight people—was building an international reputation for its work on the molecular interactions behind this self-assembling behavior. "We were making small, easily synthesized, programmable molecules"—molecules designed and synthesized with parts that control their behavior—"which assembled on the nanoscale into highly functional materials," Smith says.

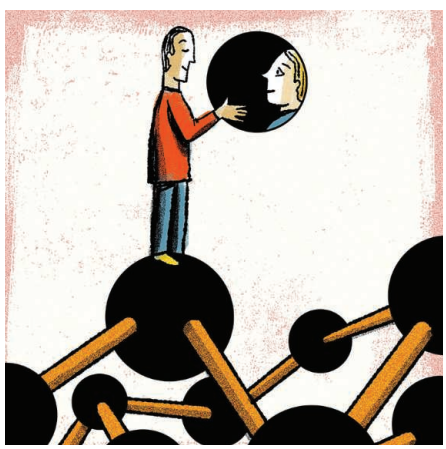

"I didn't know why my work was useful until I was faced with this problem."

Smith had just begun thinking about how this work might be applied when, in 2005, he met Sam. Sam, who would become Smith's husband, has cystic fibrosis (CF). One potential treatment for CF is gene therapy, and a major challenge in gene therapy is packaging replacement genes so they can be delivered to the target cells. The reversible, noncovalent self-assembly processes Smith's team was studying could be harnessed, he realized, to produce molecular systems that could bind and release DNA. By 2009, half his lab was working on gene therapy. "I didn't know why my work was useful until I was faced with this problem," Smith says.

For a fundamental chemist like Smith, the project represented "a different approach to science," he says. Not only was the work multidisciplinary—spanning chemistry, nanotechnology, biology, and medicine—it also required starting out with specific applications in mind and designing the experiments accordingly.

By 2011, Sam's respiratory function had deteriorated to the point where he needed a lung transplant. Smith took an interest in the drugs used during the surgery. As is common in major operations, heparin, a blood-thinning agent, was injected to prevent clotting; the drug must be removed after surgery to allow the patient's wounds to heal. But some patients are allergic to protamine sulfate, the compound now used to remove heparin from the bloodstream.

Smith realized he could create self-assembled nanoscale systems that, when injected, would hunt down and bind circulating heparin and then be excreted. "We had systems that bound DNA, and they can all, in principle, be used to bind heparin as well …, so we could start pretty much instantly," he says.

Smith encourages young researchers to move into applied research—but only after "you've found fundamental techniques that you're good at," he says. "Be prepared to think and hear about plenty of applications where you cannot really help, in order to find the ones you can approach in an innovative way. Treat the application a bit like an academic problem: Consider which small part of it you may be able to do something about, then work from there."

Sam is unlikely to benefit from Smith's work because he is unlikely to need to. His donor lungs don't have the CF gene mutation, and if things continue to go well, he won't need another major surgery. "The inspiration came from Sam," Smith says, "but I think the benefit is likely to be for others in the future." Knowing that your work could potentially save lives, he says, "helps keep research interesting." ■

Sharon Ann Holgate is a freelance science writer in the United Kingdom. For more on life and careers, visit www.sciencecareers.org. Got an interesting career story? Send it to SciCareerEditor@aaas.org.

ILLUSTRATION: ROBERT NEUBECKER

Downloaded from www.sciencemag.org on October 17, 2014

Published by AAAS